Anatomy, systematics, and evolution of Oviraptorosauria (Dinosauria, Theropoda)

by

Gregory Fitzgerald Funston

A thesis submitted in partial fulfillment of the requirements for the degree of

Doctor of Philosophy

In

Systematics and Evolution

Department of Biological Sciences

University of Alberta

ABSTRACT

Here I describe new oviraptorosaur specimens and add to our knowledge of the anatomy, growth, behaviour, ecology, and evolution of oviraptorosaurs. Oviraptorosaurs were a diverse group of theropods known from a long history of discovery and a relatively abundant fossil record. Most analyses divide the toothless members of the clade into three families: Avimimidae, Caenagnathidae, and Oviraptoridae. New avimimid specimens, including bonebed assemblages, show the unusual cranial anatomy of avimimids, compared to other oviraptorosaurs, and add to their diversity. The composition of these bonebeds as revealed by osteohistology indicates that avimimids formed flocks with mixed age representation. Additional caenagnathid material from the Dinosaur Park and Nemegt Formations of Alberta and Mongolia, respectively, improves skeletal representation for these poorly known animals. Osteohistology reveals the growth dynamics of Dinosaur Park Formation caenagnathids and shows that they can be divided into three taxa of varying body sizes and morphologies. A new, well-represented taxon—*Apatoraptor pennatus*—from the Horseshoe Canyon Formation is described and provides information on the skeletal proportions and taxonomy of caenagnathids. Histological analysis of the fused dentaries shows the patterns of mandibular development and confirms the absence of teeth at any point in development. Mongolian oviraptorids are reviewed, including historic specimens and newly discovered material that improves our knowledge of their anatomy. A new, exceptionally preserved oviraptorid is represented by nearly every element and multiple individuals forming an ontogenetic growth series. This unusual, gregarious taxon has a domed cranial crest and only two functional manual digits. Using the new specimens, the gregarious behaviour, ecology, and evolution of oviraptorosaurs is reviewed. New oviraptorosaur assemblages improve our understanding of their gregarious behaviour, which was more ubiquitous than previously recognized and probably persisted throughout ontogeny. Community ecology data show that oviraptorosaurs were a small but stable part of Late Cretaceous ecosystems of the Western Gobi Desert of Mongolia. Incorporation of the new specimens into a phylogenetic analysis provides unprecedented clarity of oviraptorosaur relationships, allowing biogeography, body mass evolution, digit reduction and gregarious behaviour to be analysed in detail. Range expansion played a major role in oviraptorosaur evolution, leading to major taxonomic and morphological radiations in North America and the Western Gobi Desert.

PREFACE

Chapters 2–5 of the thesis contain a mix of previously published and unpublished material (see end of Preface for published and submitted material). Published material has been edited for consistency and improved flow of the thesis as a whole, and in some cases data has been reinterpreted or corrected.

Chapter 2 contains parts of two published articles, listed below, which describe a bonebed of avimimids from the Nemegt Formation and name that species *Avimimus nemegtensis* Funston et al. 2018. The portions included here consist only of my contributions to that collaborative manuscript, which nonetheless benefitted from editorial input by P. Currie, D. Eberth, M. Ryan, C. Tsogtbaatar, and N. Longrich. The descriptions of material from a bonebed at Iren Dabasu have been submitted for publication to Scientific Reports, and are currently accepted with revisions.

Chapter 3 contains portions of one submitted and eight published manuscripts (see below) which describe new caenagnathid specimens. The anatomical descriptions and figures from these manuscripts have been modified for consistency and are interspersed with unpublished descriptions of new material. The discussion section of the chapter takes into account all of the described material and therefore overlaps in content with these manuscripts, but has not been previously published in its entirety. Numerous coauthors contributed to these manuscripts, but the work presented here is my own. P. Currie contributed to each manuscript in the form of editing and providing data. He is lead author on the manuscript describing new material of *Elmisaurus elegans* Osmólska 1981, but I contributed the anatomical descriptions presented here to that manuscript. M. Burns contributed histological sections and analysis to the

manuscript describing new material of *Leptorhynchos elegans* Longrich et al. 2013. I have

reanalyzed the histological sections here. G. Bradley contributed the body mass estimation

equations to the manuscript describing new material of *Caenagnathus collinsi* Sternberg 1940.

Before her passing, H. Osmólska provided data on *Elmisaurus rarus* that contributed to the

manuscript led by P. Currie. W.S. Persons IV contributed his expertise on caudal vertebrae and

measurement data to the manuscript describing new material of *Caenagnathus collinsi*. M.

Rhodes is lead author on a recently submitted project describing new caenagnathid pelvic

material and reconstructing the pelvic musculature. I have contributed the descriptions of ilia and

pubes presented here to that manuscript, but have omitted the musculature reconstructions

created by M. Rhodes. The histological descriptions presented in section 2.2.7 are part of a

recently published manuscript, of which I was lead author, in collaboration with R. Wilkinson,

D.J. Simon, A. LeBlanc, M. Wosik, and P. Currie. The first three collaborators assisted with

analysis of the histology. M. Wosik assisted in polishing and imaging the slides. P. Currie edited

the manuscript. The descriptions of new *Chirostenotes pergracilis* Gilmore 1924 material from

the Dinosaur Park Formation are the basis of a manuscript recently submitted to the Journal of

Vertebrate Paleontology.

Chapter 4 includes material previously published in a review of oviraptorosaurs from the

Nemegt Formation, specifically the descriptions of oviraptorids. This study consists of two

papers: a published dataset and a review of oviraptorosaur taxonomy and an ecological analysis.

These articles were coauthored by S. Mendonca, who helped conceive of the statistical tests, and

P. Currie and R. Barsbold, who contributed data to the study. This chapter also includes parts of

a manuscript submitted to Nature Ecology & Evolution which went to review but was ultimately

declined. Regardless, the revisions suggested by the reviewers have been incorporated.

Chapter 5 builds on previously published material, specifically the phylogeny presented in the article naming *Apatoraptor pennatus* Funston and Currie 2016 and the analyses included in the declined article at Nature Ecology & Evolution. This is supplemented by a biogeographic analysis included in the review of Nemegt oviraptorosaurs. In each case, the phylogeny has been updated and expanded and so the results presented here differ from those previous analyses.

The published, in review, or previously submitted articles incorporated into this thesis are listed here in chronological order:

Chapter 2:

Funston, G. F., Currie, P. J., Eberth, D. A., Ryan, M. J., Tsogtbaatar, Ch., Badamgarav, D., Longrich, N. R. 2016. The first oviraptorosaur (Dinosauria: Theropoda) bonebed: evidence of gregarious behaviour in a maniraptoran theropod. Scientific Reports 6: 35782. DOI: https://doi.org/10.1038/srep35782

Funston, G. F., Mendonca, S. E., Currie, P. J., Barsbold, R. 2018. Oviraptorosaur anatomy, diversity, and ecology in the Nemegt Basin. Palaeogeography, Palaeoclimatology, Palaeoecology 494: 101–120. DOI: https://doi.org/10.1016/j.palaeo.2017.10.023

Funston, G. F., Currie, P. J., Ryan, M. J., and Dong, Z.-M. "Stunted growth and mixed-age flocks in avimimids (Theropoda, Oviraptorosauria". Scientific Reports manuscript number SREP-19-15878 [In Review].

Chapter 3:

Funston, G.F., and Currie, P.J. 2014. A previously undescribed caenagnathid mandible from the late Campanian of Alberta, and insights into the diet of *Chirostenotes pergracilis*

(Dinosauria: Oviraptorosauria). Canadian Journal of Earth Sciences 51: 156–165. DOI: https://doi.org/10.1139/cjes-2013-0186

Funston, G.F., Persons, W.S., Bradley, G.J., and Currie, P.J. 2015. New material of the large-bodied caenagnathid *Caenagnathus collinsi* from the Dinosaur Park Formation of Alberta, Canada. Cretaceous Research 54: 179–187. DOI: https://doi.org/10.1016/j.cretres.2014.12.002

Currie, P.J., Funston, G.F., and Osmólska, H. 2016. New specimens of *Elmisaurus rarus* from Mongolia Acta Paleontologica Polonica 61(1): 143–157. DOI: http://dx.doi.org/10.4202/app.00130.2014

Funston, G.F., Currie, P.J., and Burns, M.E. 2016. New elmisaur specimens from Alberta, Canada, and their relationship to the Mongolian *Elmisaurus rarus*. Acta Paleontologica Polonica 61(1): 159-173. DOI: http://dx.doi.org/10.4202/app.00129.2014

Funston, G.F. and Currie, P.J. 2016. A new caenagnathid (Dinosauria: Oviraptorosauria) from the Horseshoe Canyon Formation of Alberta, Canada, and a reevaluation of the relationships of Caenagnathidae. Journal of Vertebrate Paleontology e1160910: 1-18 DOI: https://doi.org/10.1080/02724634.2016.1160910

Funston, G. F., Mendonca, S. E., Currie, P. J., Barsbold, R. 2018. Oviraptorosaur anatomy, diversity, and ecology in the Nemegt Basin. Palaeogeography, Palaeoclimatology, Palaeoecology 494: 101–120. DOI: https://doi.org/10.1016/j.palaeo.2017.10.023

Funston, G. F., and Currie, P. J. 2018. A small caenagnathid tibia from the Horseshoe Canyon Formation (Maastrichtian): implications for growth and lifestyle in oviraptorosaurs. Cretaceous Research 92: 220–230. DOI: https://doi.org/10.1016/j.cretres.2018.08.020

Funston, G. F., Wilkinson, R. D., LeBlanc, A. H., Wosik, M., and Currie, P. J. 2019. Histology of caenagnathid (Theropoda, Oviraptorosauria) dentaries and implications for development, ontogenetic edentulism, and taxonomy. The Anatomical Record, doi: 10.1002/ar.24205

Funston, G. F. and Currie, P. J. "New material of *Chirostenotes pergracilis* (Theropoda, Oviraptorosauria) from the Campanian Dinosaur Park Formation of Alberta, Canada." Journal of Vertebrate Paleontology manuscript number JVP-2019-0105 [Submitted Aug. 19, 2019].

Chapter 4:

Funston, G. F., Mendonca, S. E., Currie, P. J., Barsbold, R. 2018. Oviraptorosaur anatomy, diversity, and ecology in the Nemegt Basin. Palaeogeography, Palaeoclimatology, Palaeoecology 494: 101–120. DOI: https://doi.org/10.1016/j.palaeo.2017.10.023

Funston, G. F., Mendonca, S. E., Currie, P. J., Barsbold, R. 2018. A dinosaur community composition dataset for the Late Cretaceous Nemegt Basin of Mongolia. Data in Brief 16: 660–666. DOI: https://doi.org/10.1016/j.dib.2017.11.086

Funston, G. F., Tsogtbaatar, C., Khishigjav, T., Yoshitsugu, K., and Currie, P. J. "A huddling group of new oviraptorids and a possible origin of avian sociality". Nature Ecology & Evolution manuscript number NATECOLEVOL-19036495. [Rejected April 25, 2019]

Chapter 5:

Funston, G.F. and Currie, P.J. 2016. A new caenagnathid (Dinosauria: Oviraptorosauria) from

    the Horseshoe Canyon Formation of Alberta, Canada, and a reevaluation of the

    relationships of Caenagnathidae. Journal of Vertebrate Paleontology e1160910: 1-18

    DOI: https://doi.org/10.1080/02724634.2016.1160910

Funston, G. F., Mendonca, S. E., Currie, P. J., Barsbold, R. 2018. Oviraptorosaur anatomy,

    diversity, and ecology in the Nemegt Basin. Palaeogeography, Palaeoclimatology,

    Palaeoecology 494: 101–120. DOI: https://doi.org/10.1016/j.palaeo.2017.10.023

Funston, G. F., Tsogtbaatar, C., Khishigjav, T., Yoshitsugu, K., and Currie, P. J. "A huddling

    group of new oviraptorids and a possible origin of avian sociality". Nature Ecology &

    Evolution manuscript number NATECOLEVOL-19036495. [Rejected April 25, 2019]

For my parents, with love.

ACKNOWLEDGMENTS

Table of Contents

LIST OF TABLES

LIST OF FIGURES

LIST OF INSTITUTIONAL ABBREVIATIONS

CMN, Canadian Museum of Nature, Ottawa, ON, Canada; **IVPP**, Institute of Vertebrate Paleontology and Paleoanthropology, Beijing, China; **MOR**, Museum of the Rockies, Bozeman, Montana, USA; **MPC**, Institute of Paleontology and Geology, Mongolian Academy of Sciences, Ulaanbaatar, Mongolia; **PIN**, Paleontological Institute, Russian Academy of Sciences, Moscow, Russia; **ROM**, Royal Ontario Museum, Toronto, ON, Canada; **RSM**, Royal Saskatchewan Museum, Regina, SK, Canada; **TMP**, Royal Tyrrell Museum of Palaeontology, Drumheller, AB, Canada; **UALVP**, University of Alberta Laboratory for Vertebrate Paleontology, Edmonton, AB, Canada; **ZPAL**, Institute of Paleobiology, Polish Academy of Sciences, Warsaw, Poland.

CHAPTER 1 – INTRODUCTION

1.1 HISTORY OF DISCOVERY

Oviraptorosaurs were an unranked, suprafamilial group of maniraptoran theropod dinosaurs from the Cretaceous of Asia and North America. They were a diverse group, represented by approximately 40 known species (Fig. 1.1; Table 1.1), with an exceptionally abundant fossil record. The first oviraptorosaur remains discovered were the hands of *Chirostenotes pergracilis* Gilmore 1924 from what is now the Dinosaur Park Formation of Alberta, Canada (Gilmore, 1924). Gilmore placed *Chirostenotes* with the coelurosaurs *Ornithomimus* Marsh 1890 and *Dromaeosaurus* Matthew and Brown 1922, but considered it more primitive than *Struthiomimus* Osborn 1917. The same year, Osborn (1924) described *Oviraptor philoceratops* Osborn 1924 based on a more complete skeleton comprising a badly crushed skull and forelimbs. Osborn (1924) noted similarities in the manus of *Chirostenotes pergracilis* and *Oviraptor philoceratops*, which he thought was an ornithomimid on the basis of the toothless jaw. More oviraptorosaur material was discovered in the 1930s and 40s (Sternberg, 1932; Parks, 1933; Sternberg, 1940), but it was not clear that these pertained to the same type of animal as *Chirostenotes* or *Oviraptor*. A long hiatus in the study of oviraptorosaurs followed from 1940 until the 1970s (Fig. 1.1).

Two crucial discoveries were published in 1976, reviving interest in oviraptorosaurs. The first was a study by Osmólska (1976), on new oviraptorid material from Khermiin Tsav in the Gobi Desert of Mongolia. Her material revealed the unusual palatal structure of oviraptorids and drew a link between caenagnathids and oviraptorids based on the mandibles. She united this

material within Caenagnathidae. Barsbold (1976a) described related material (which would come to be *Conchoraptor gracilis* Barsbold 1986 in 1986), and erected Oviraptoridae for this and *Oviraptor philoceratops*. Later, he united the newly named Caenagnathidae and Oviraptoridae in Oviraptorosauria (Barsbold, 1976b).

Throughout the late 1970s and 1980s, Barsbold continued to describe an abundance of new oviraptorids collected from the western Gobi Desert of Mongolia in a series of landmark papers in Russian (Barsbold, 1977, 1981, 1983, 1986, 1988). Osmólska and Currie described new caenagnathids and elmisaurids (Osmólska, 1981; Currie and Russell, 1988; Currie, 1989), under the assumption that these groups were separate but closely related. Meanwhile, Kurzanov described the unusual, diminutive *Avimimus* Kurzanov 1981 (Kurzanov, 1981, 1982, 1983, 1985, 1987), whose unusual mosaic of characters led to wild speculation about its phylogenetic position within Dinosauria (Thulborn, 1984; Norman, 1990; Chatterjee, 1991; Vickers-Rich et al., 2002).

As for many groups of dinosaurs, the 1990s saw a drastic increase in the volume of research. More complete caenagnathid material helped to clarify some aspects of their systematics and anatomy (Currie et al., 1993; Sues, 1997; Makovicky and Sues, 1998), but also raised more questions than answers. New expeditions in China and Mongolia produced a wealth of important oviraptorosaur specimens (Norell et al., 1995; Dong and Currie, 1996; Barsbold, 1997; Maryanska and Osmólska, 1997; Qiang et al., 1998; Clark et al., 1999; Barsbold et al., 2000a; Zhou et al., 2000), including the famous skeletons brooding their nests (Norell et al. 1995; Dong and Currie, 1996) and the first feathered dinosaurs (Qiang et al., 1998).

The early 2000s continued the rampant pace of discovery, and expanded the breadth of Oviraptorosauria. New oviraptorids (Clark et al., 2001, 2002; Lü, 2003; Lü et al., 2004) were

accompanied by an expanded roster of basal oviraptorosaurs, including the newly discovered *Incisivosaurus* Xu et al. 2002—now the most basal oviraptorosaur—and the more derived caudipterygids and avimimids (Zhou et al., 2000; Maryanska et al., 2002; Xu et al., 2002). It is to Maryanska et al. (2002) that we owe our current concept of the membership of Oviraptorosauria, including primitive forms like *Caudipteryx* Qiang et al. 1998 and *Incisivosaurus*, alongside *Avimimus* and the more derived caenagnathoids (Caenagnathidae + Oviraptoridae). This new wave of oviraptorosaur research culminated in the 2004 edition of The Dinosauria (Osmólska et al. 2004)—a comprehensive review of the current systematics of dinosaurs. This volume summarized the complex history of oviraptorosaurs (Osmólska et al., 2004) and conducted the first phylogenetic analysis of the entire group—a data matrix still built upon today (Lamanna et al. 2014; Funston and Currie 2016; Lü et al. 2017).

Since the publication of The Dinosauria II (Osmólska et al. 2004), twenty-seven new oviraptorosaur species have been named—nearly two every year—from all of the constituent groups. Basal oviraptorosaurs include the feathered *Similicaudipteryx* He et al. 2008, which provides information on the ontogeny of feather development (He et al., 2008; Xu et al., 2010). Caenagnathids include the giant *Gigantoraptor* Xu et al. 2007 (Xu et al., 2007), *Hagryphus* Zanno and Sampson 2005 (Zanno and Sampson, 2005), and the most completely known caenagnathid to date: *Anzu* Lamanna et al. 2014 (Lamanna et al., 2014). An explosion of new oviraptorids from the south of China are the result of the work of the late Lü Junchang, whose immeasurable impact on our knowledge of oviraptorosaurs will be sorely missed. Lü's incredible body of work is highlighted by the baby *Yulong* Lü et al. 2013 (Lü et al., 2013), the mired skeleton of *Tongtianlong* Lü et al 2016 (Lü et al., 2016), and the magnificently crested *Corythoraptor* Lü et al. 2017 (Lü et al., 2017), among dozens of other taxa.

Thus, nearly a century after the first report of an oviraptorosaur, our understanding of the diversity, anatomy, and biology of oviraptorosaurs is drastically improved. Most phylogenies recognize four main groups of oviraptorosaurs (Fig. 1.2). Most basal are the toothed caudipterids, which are either recovered as a monophyletic clade or as a series of successive outgroups to the rest of Oviraptorosauria. Toothless oviraptorosaurs comprise *Avimimus* and its sister taxon, Caenagnathoidea, which itself is divided into Caenagnathidae and Oviraptoridae. The relationships within Caenagnathidae and Oviraptoridae are less well-resolved, and various works have inconsistently recovered smaller clades within. Of particular note are "Elmisaurinae", a proposed group of small-bodied caenagnathids with either fused ankles (Currie, 1989), upturned dentaries (Longrich et al., 2013), or both; and "Ingeniinae", a clade of oviraptorids variably grouped as those lacking cranial crests (Balanoff and Norell, 2012) or those with hypertrophied manual digits (Longrich et al., 2010; Fanti et al., 2012).

Certain aspects of oviraptorosaur biology are also well known. For example, the preservation of feather impressions (Fig. 1.3) in both *Caudipteryx* (Qiang et al., 1998) and more derived theropods (Hu et al. 2018) suggests that most, if not all oviraptorosaurs were feathered. This was supported by the discovery of a fused pygostyle in the derived oviraptorosaur *Nomingia* Barsbold et al. 2000a (Barsbold et al., 2000b) and ulnar papillae on the arm of *Apatoraptor* Funston and Currie 2016 (Funston and Currie, 2016), which likely anchored feathers (Fig. 1.3). The diet of oviraptorosaurs is somewhat poorly known, but multiple lines of evidence suggest either strict herbivory (Smith, 1992) or a more generalized omnivorous diet (Zanno and Makovicky, 2011). Regardless, other diets have been proposed, including clams (Barsbold 1986) and eggs (Currie et al. 1993). Skeletons atop their nests (Fig. 1.4) provide insight into the reproductive behaviour. They show that oviraptorids retained the paired oviducts of more basal

archosaurs (Dong and Currie, 1996; Sato, 2005) and brooded their speckled blue eggs (Wiemann et al., 2018) with body heat, rather than substrate (Tanaka et al., 2015, 2018).

Regardless, many gaps in our knowledge remain. A major issue in the study of oviraptorosaurs is that, despite an exceptional fossil record, most studies are concerned solely with the description of new forms or specimens. Each of these studies may include a phylogeny and add new taxa, but this is rarely accompanied by any major revisions to the character matrix or taxonomy of oviraptorosaurs, nor any evolutionary insights. As a result, no study has yet examined any evolutionary aspect of Oviraptorosauria as a whole. Similar issues arise for other aspects of their biology. For example, oviraptorosaurs have been histologically sampled and included as data points in studies of reproductive physiology or growth, but never as the focal points of these works. Accordingly, little is known about the growth patterns of oviraptorosaurs, nor their evolution within the group, despite a more drastic range of body sizes than nearly every other group of theropods in which this is known.

1.2 OBJECTIVES

It is these issues that my thesis work has attempted to address. Building upon an undergraduate thesis, my first oviraptorosaur project described a complete caenagnathid mandible and inferred its omnivorous diet on the basis of biomechanical analysis (Funston and Currie, 2014). Acknowledging numerous issues in the current taxonomy of caenagnathids, my coauthors and I described a wide range of isolated bones in an attempt to create testable operational taxonomic units (Funston et al., 2015; Currie et al., 2016; Funston et al., 2016a). Updated revisions to these groupings based on new specimens and histological insights are provided here. In 2016, my supervisor and I described the relatively complete skeleton of a new

caenagnathid, *Apatoraptor pennatus*, from the Horseshoe Canyon Formation of Alberta (Funston and Currie, 2016). The resulting phylogeny provided the clearest picture of caenagnathid relationships to that point, arguing against a monophyletic "Elmisaurinae". Realizing that some isolated caenagnathid bones may be more valuable for histology than morphology, my coauthors and I assessed the osteohistology of caenagnathid tibiae (Funston and Currie, 2018) and dentaries (Funston et al., In Press). These studies provided information on the early ontogeny of caenagnathids, and the usefulness of caenagnathid dentaries for assessment of skeletal maturity. Additional histological samples are presented in this thesis, and will lead to the publication of a more comprehensive review in the future.

In Mongolia, I worked with a team of collaborators to describe the anatomy and taphonomy of a bonebed of *Avimimus* from Nemegt in the western Gobi Desert (Funston et al., 2016b). A description of a second avimimid bonebed from Iren Dabasu, in China, is currently under review at Scientific Reports. Motivated by descriptions of early oviraptorid holotypes, typically in Russian and lacking in detail, my coauthors and I reviewed the oviraptorosaurs of the Nemegt Basin (Funston et al., 2018a). We provided updated descriptions and figures of the types of *Conchoraptor gracilis*, *"Ingenia" yanshini* (now *Heyuannia yanshini* Barsbold (1981)), and *Rinchenia mongoliensis* Barsbold 1997. Further examination of the *Avimimus* bonebed material indicated that it contained individuals of a new species, *Avimimus nemegtensis* Funston et al. 2018a (Funston et al., 2018a). In addition, using a dataset compiled from nearly 500 skeletons (Funston et al., 2018b), we conducted the first community ecology analysis of the Nemegt Basin, with a special focus on the diversity of oviraptorosaurs and the dynamics of their resource partitioning.

The objective of this thesis is not merely to review my previous work, but also to build upon it. Thus, where new specimens have changed my previously published views, I have revised them to be more correct. In many cases, I have attempted to address gaps in previous work where new specimens allow, or where extra analyses could provide more data. Accordingly, the thesis is a new study, building on past work to provide a synthetic update to our knowledge of Oviraptorosauria.

The thesis contains four parts, focusing on Avimimidae (Chapter 2), Caenagnathidae (Chapter 3), Oviraptoridae (Chapter 4) and the behaviour, ecology, and evolution of Oviraptorosauria as a whole (Chapter 5). Each of the first three parts provides descriptions of new material or redescriptions of important historical specimens.

Chapter 2 tests two main hypotheses. First, I test whether all known avimimid material pertains to the same taxon, as has been assumed in previous biostratigraphic studies. Second, I test whether fusion of the tibiotarsus is a reliable indicator of skeletal maturity, and, subsequently, whether avimimids grew in similar styles to other oviraptorosaurs. To evaluate these questions, I describe new specimens and perform osteohistological analyses.

Chapter 3 tests three hypotheses. First and foremost, I test whether the three recognized genera in the Dinosaur Park Formation are valid, and, if so, which specimens are referable to which taxa. This is part of a larger goal to assess the diversity and relationships of Caenagnathidae in Asia and North America. Second, using osteohistology, I test the assertion of Wang et al. (2018) that caenagnathids lost their teeth via ontogenetic edentulism, and that the complex grooves and ridges of the dentaries are the vestiges of tooth-bearing structures. Finally, I evaluate the growth styles and rates of caenagnathids, and whether they are consistent with other oviraptorosaurs and theropods.

Chapter 4 tests whether our current taxonomic framework of oviraptorids is sufficient, and whether the high species richness of Mongolian oviraptorids is overestimated. In tandem with this, I assess allometric and ontogenetic changes in the skeletons of oviraptorids. Finally, like the other chapters, I evaluate growth styles in oviraptorids, comparing and contrasting them with other oviraptorosaurs.

Chapter 5 focuses on the biology and evolution of oviraptorosaurs. It uses the updated anatomical and taxonomic information from the first three chapters to create a revised phylogeny of Oviraptorosauria. Chapter 5 is divided into three subsections. The first examines evidence of gregarious behaviour throughout the group, speculating on its evolutionary origins and possible functions. In this section, I use taphonomy to evaluate the preservation of mass death assemblages and the information they provide about behaviour in oviraptorosaurs. The second subsection focuses on the ecology of oviraptorosaurs within their communities, using the Nemegt Basin as a case study. Here, I test whether the oviraptorosaur families in the Nemegt Basin occupied the same paleoenvironments, and, if so, how they avoided ecological competition. The last subsection uses the updated phylogeny as a framework for testing the evolutionary patterns of biogeography, body mass, and manual digit reduction. More specifically, I test whether range expansion played a role in the diversification of oviraptorosaurs; if oviraptorosaurs had directional trends in body mass evolution; and if the reduction of the third digit was gradual or punctuated.

1.3 LITERATURE CITED

Balanoff, A. M., and M. A. Norell. 2012. Osteology of *Khaan mckennai* (Oviraptorosauria: Theropoda). Bulletin of the American Museum of Natural History 372:1–77.

Barsbold, R. 1976a. A new Late Cretaceous Family of Small Theropods (Oviraptoridae n. fam.) in Mongolia. Doklady Akademii Nauk SSSR 226:685–688.

Barsbold, R. 1976b. On the evolution and systematics of the late Mesozoic carnivorous dinosaurs [in Russian]. Paleontologiâ i biostratigrafiâ Mongolii. Trudy, Sovmestnaâ Sovetsko−Mongol'skaâ paleontologičeskaâ èkspediciâ 3:68–75.

Barsbold, R. 1977. Kineticism and peculiarities in the maxillary structure of oviraptorids (Theropoda, Saurischia). Transactions of the Joint Soviet Mongolian Paleontological Expedition 4:37–47.

Barsbold, R. 1981. Toothless Dinosaurs of Mongolia. Transactions of the Joint Soviet Mongolian Paleontological Expedition 15:28–39.

Barsbold, R. 1983. Carnivorous dinosaurs from the Cretaceous of Mongolia. Transactions of the Joint Soviet Mongolian Paleontological Expedition 19:5–117.

Barsbold, R. 1986. The predatory dinosaurs - Oviraptors; pp. 210–223 in Herpetologische Untersuchungen in der Mongolischen Volksrepublik. Academia Nauk SSSR.

Barsbold, R. 1988. The bony crest and helmet on the skull of predatory dinosaurs—oviraptors. Transactions of the Joint Soviet Mongolian Paleontological Expedition 34:77–80.

Barsbold, R. 1997. Oviraptorosauria; pp. 505–508 in P. J. Currie and K. Padian (eds.), Encyclopedia of Dinosaurs. Academic Press, Oxford, UK.

Barsbold, R., H. Osmólska, M. Watabe, P. J. Currie, and K. Tsogtbaatar. 2000a. A new

oviraptorosaur [Dinosauria, Theropoda] from Mongolia: the first dinosaur with a

pygostyle. Acta Palaeontologica Polonica 45:97–106.

Barsbold, R., P. J. Currie, N. P. Myhrvold, H. Osmólska, K. Tsogtbaatar, and M. Watabe. 2000b.

A pygostyle from a non-avian theropod. Nature 403:155–156.

Chatterjee, S. 1991. Cranial anatomy and relationships of a new Triassic bird from Texas.

Philosophical Transactions of the Royal Society of London. Series B: Biological Sciences

332:277–346.

Clark, J. M., M. Norell, and L. M. Chiappe. 1999. An oviraptorid skeleton from the late

Cretaceous of Ukhaa Tolgod, Mongolia, preserved in an avianlike brooding position over

an oviraptorid nest. American Museum Novitates 3265:1–36.

Clark, J. M., M. A. Norell, and R. Barsbold. 2001. Two new oviraptorids (Theropoda:

Oviraptorosauria), Upper Cretaceous Djadokhta Formation, Ukhaa Tolgod, Mongolia.

Journal of Vertebrate Paleontology 21:209–213.

Clark, J. M., M. A. Norell, and T. Rowe. 2002. Cranial anatomy of *Citipati osmolskae*

(Theropoda, Oviraptorosauria), and a reinterpretation of the holotype of *Oviraptor*

philoceratops. American Museum Novitates 1–24.

Currie, P., G. Funston, and H. Osmolska. 2016. New specimens of the crested theropod dinosaur

Elmisaurus rarus from Mongolia. Acta Palaeontologica Polonica 61:143–157.

Currie, P. J. 1989. The first records of *Elmisaurus* (Saurischia, Theropoda) from North America.

Canadian Journal of Earth Sciences 26:1319–1324.

Currie, P. J., and D. A. Russell. 1988. Osteology and relationships of *Chirostenotes pergracilis* (Saurischia, Theropoda) from the Judith River (Oldman) Formation of Alberta, Canada. Canadian Journal of Earth Sciences 25:972–986.

Currie, P. J., S. J. Godfrey, and L. Nessov. 1993. New caenagnathid (Dinosauria: Theropoda) specimens from the Upper Cretaceous of North America and Asia. Canadian Journal of Earth Sciences 30:2255–2272.

Dong, Z.-M., and P. J. Currie. 1996. On the discovery of an oviraptorid skeleton on a nest of eggs at Bayan Mandahu, Inner Mongolia, People's Republic of China. Canadian Journal of Earth Sciences 33:631–636.

Fanti, F., P. J. Currie, and D. Badamgarav. 2012. New Specimens of *Nemegtomaia* from the Baruungoyot and Nemegt Formations (Late Cretaceous) of Mongolia. PLoS ONE 7:e31330.

Funston, G. F., and P. J. Currie. 2014. A previously undescribed caenagnathid mandible from the late Campanian of Alberta, and insights into the diet of *Chirostenotes pergracilis* (Dinosauria: Oviraptorosauria). Canadian Journal of Earth Sciences 51:156–165.

Funston, G. F., and P. J. Currie. 2016. A new caenagnathid (Dinosauria: Oviraptorosauria) from the Horseshoe Canyon Formation of Alberta, Canada, and a reevaluation of the relationships of Caenagnathidae. Journal of Vertebrate Paleontology 36:e1160910.

Funston, G. F., and P. J. Currie. 2018. A small caenagnathid tibia from the Horseshoe Canyon Formation (Maastrichtian): Implications for growth and lifestyle in oviraptorosaurs. Cretaceous Research 92:220–230.

Funston, G. F., P. J. Currie, and M. Burns. 2016a. New elmisaurine specimens from North

America and their relationship to the Mongolian *Elmisaurus rarus*. Acta Palaeontologica

Polonica 61:159–173.

Funston, G. F., W. S. Persons, G. J. Bradley, and P. J. Currie. 2015. New material of the large-

bodied caenagnathid *Caenagnathus collinsi* from the Dinosaur Park Formation of

Alberta, Canada. Cretaceous Research 54:179–187.

Funston, G. F., S. E. Mendonca, P. J. Currie, and R. Barsbold. 2018a. Oviraptorosaur anatomy,

diversity and ecology in the Nemegt Basin. Palaeogeography, Palaeoclimatology,

Palaeoecology.

Funston, G. F., S. E. Mendonca, P. J. Currie, and R. Barsbold. 2018b. A dinosaur community

composition dataset for the Late Cretaceous Nemegt Basin of Mongolia. Data in Brief

16:660–666.

Funston, G. F., R. D. Wilkinson, D. J. Simon, A. R. H. LeBlanc, M. Wosik, and P. J. Currie. In

Press. Histology of caenagnathid (Theropoda, Oviraptorosauria) dentaries and

implications for development, ontogenetic edentulism, and taxonomy. The Anatomical

Record.

Funston, G. F., P. J. Currie, D. A. Eberth, M. J. Ryan, T. Chinzorig, D. Badamgarav, and N. R.

Longrich. 2016b. The first oviraptorosaur (Dinosauria: Theropoda) bonebed: evidence of

gregarious behaviour in a maniraptoran theropod. Scientific Reports 6:35782.

Gilmore, C. W. 1924. A new coelurid dinosaur from the Belly River Cretaceous of Alberta.

Canada Geological Survey Bulletin 38:1–12.

He, T., X.-L. Wang, and Z.-H. ZHOU. 2008. A new genus and species of caudipterid dinosaur from the Lower Cretaceous Jiufotang Formation of Western Liaoning, China. Vertebrata PalAsiatica 46:178–189.

Hu, D., J. A. Clarke, C. M. Eliason, R. Qiu, Q. Li, M. D. Shawkey, C. Zhao, L. D'Alba, J. Jiang, and X. Xu. 2018. A bony-crested Jurassic dinosaur with evidence of iridescent plumage highlights complexity in early paravian evolution. Nature Communications 9.

Kurzanov, S. M. 1981. An unusual theropod from the Upper Cretaceous of Mongolia. Transactions of the Joint Soviet Mongolian Paleontological Expedition 15:39–49.

Kurzanov, S. M. 1982. Structural characteristics of the forelimbs of *Avimimus*. Paleontological Journal 3:108–112 [In Russian].

Kurzanov, S. M. 1983. New data on the pelvic structure of *Avimimus*. Paleontological Journal 4:115–116 [In Russian].

Kurzanov, S. M. 1985. The skull structure of the dinosaur *Avimimus*. Paleontological Journal 4:81–89 [In Russian].

Kurzanov, S. M. 1987. Avimimidae and the problem of the origin of birds. Transactions of the Joint Soviet Mongolian Paleontological Expedition 31:1–92.

Lamanna, M. C., H.-D. Sues, E. R. Schachner, and T. R. Lyson. 2014. A New Large-Bodied Oviraptorosaurian Theropod Dinosaur from the Latest Cretaceous of Western North America. PLoS ONE 9:e92022.

Longrich, N. R., P. J. Currie, and D. Zhi-Ming. 2010. A new oviraptorid (Dinosauria: Theropoda) from the Upper Cretaceous of Bayan Mandahu, Inner Mongolia. Palaeontology 53:945–960.

Longrich, N. R., K. Barnes, S. Clark, and L. Millar. 2013. Caenagnathidae from the Upper
    Campanian Aguja Formation of West Texas, and a Revision of the Caenagnathinae.
    Bulletin of the Peabody Museum of Natural History 54:23–49.

Lü, J. 2003. A new oviraptorosaurid (Theropoda: Oviraptorosauria) from the Late Cretaceous of
    southern China. Journal of Vertebrate Paleontology 22:871–875.

Lü, J., Y. Tomida, Y. Azuma, Z.-M. Dong, and Y.-N. Lee. 2004. New oviraptorid dinosaur
    (Dinosauria: Oviraptorosauria) from the Nemegt Formation of Southwestern Mongolia.
    Bulletin of the National Science Museum of Tokyo Series C 30:95–130.

Lü, J., R. Chen, S. L. Brusatte, Y. Zhu, and C. Shen. 2016. A Late Cretaceous diversification of
    Asian oviraptorid dinosaurs: evidence from a new species preserved in an unusual
    posture. Scientific Reports 6:35780.

Lü, J., P. J. Currie, L. Xu, X. Zhang, H. Pu, and S. Jia. 2013. Chicken-sized oviraptorid dinosaurs
    from central China and their ontogenetic implications. Naturwissenschaften 100:165–
    175.

Lü, J., G. Li, M. Kundrát, Y.-N. Lee, Z. Sun, Y. Kobayashi, C. Shen, F. Teng, and H. Liu. 2017.
    High diversity of the Ganzhou Oviraptorid Fauna increased by a new "cassowary-like"
    crested species. Scientific Reports 7.

Makovicky, P. J., and H.-D. Sues. 1998. Anatomy and phylogenetic relationships of the theropod
    dinosaur *Microvenator celer* from the Lower Cretaceous of Montana. American Museum
    Novitates 3240:1–27.

Maryanska, T., and H. Osmólska. 1997. The quadrate of oviraptorid dinosaurs. Acta
    Palaeontologica Polonica 42:361–371.

Maryanska, T., H. Osmólska, and M. Wolsan. 2002. Avialan status for Oviraptorosauria. Acta Palaeontologica Polonica 47.

Norell, M. A., J. M. Clark, L. M. Chiappe, and D. Dashzeveg. 1995. A nesting dinosaur. Nature 378:774–776.

Norman, D. B. 1990. Problematic Theropoda: "Coelurosaurs"; pp. 280–305 in D. B. Weishampel, P. Dodson, and H. Osmólska (eds.), The Dinosauria, 1st ed. University of California Press, Berkeley.

Osborn, H. F. 1924. Three new theropoda, *Protoceratops* zone, central Mongolia. American Museum Novitates 144:1–12.

Osmólska, H. 1976. New light on the skull anatomy and systematic position of *Oviraptor*. Nature 262:683–684.

Osmólska, H. 1981. Coossified tarsometatarsi in theropod dinosaurs and their bearing on the problem of bird origins. Palaeontologia Polonica 42:79–95.

Osmólska, H., P. J. Currie, and R. Barsbold. 2004. Oviraptorosauria; pp. 165–183 in D. B. Weishampel, P. Dodson, and H. Osmólska (eds.), The Dinosauria, 2nd ed. University of California Press, Berkeley, California.

Parks, W. A. 1933. New species of dinosaurs and turtles from the Upper Cretaceous Formations of Alberta. University of Toronto Studies Geological Series 34:1–24.

Qiang, J., P. J. Currie, M. A. Norell, and J. Shu-An. 1998. Two feathered dinosaurs from northeastern China. Nature 393:753–761.

Sato, T. 2005. A Pair of Shelled Eggs Inside A Female Dinosaur. Science 308:375–375.

Smith, D. 1992. The type specimen of *Oviraptor philoceratops*, a theropod dinosaur from the

Upper Cretaceous of Mongolia. Neues Jahrbuch Fur Geologie Und Palaontologie

Abhandlungen 186:365–388.

Sternberg, C. M. 1932. Two new theropod dinosaurs from the Belly River Formation of Alberta.

The Canadian Field-Naturalist 46:99–105.

Sternberg, R. M. 1940. A toothless bird from the Cretaceous of Alberta. Journal of Paleontology

14:81–85.

Sues, H.-D. 1997. On *Chirostenotes*, a Late Cretaceous oviraptorosaur (Dinosauria: Theropoda)

from western North America. Journal of Vertebrate Paleontology 17:698–716.

Tanaka, K., D. K. Zelenitsky, and F. Therrien. 2015. Eggshell Porosity Provides Insight on

Evolution of Nesting in Dinosaurs. PLOS ONE 10:e0142829.

Tanaka, K., D. K. Zelenitsky, J. Lü, C. L. DeBuhr, L. Yi, S. Jia, F. Ding, M. Xia, D. Liu, C.

Shen, and R. Chen. 2018. Incubation behaviours of oviraptorosaur dinosaurs in relation to

body size. Biology Letters 14:20180135.

Thulborn, R. A. 1984. The avian relationships of *Archaeopteryx*, and the origin of birds.

Zoological Journal of the Linnean Society 82:119–158.

Vickers-Rich, P., L. M. Chiappe, and S. M. Kurzanov. 2002. The enigmatic birdlike dinosaur

Avimimus portentosus, comments and a pictorial atlas; pp. 65–86 in L. M. Chiappe and L.

M. Witmer (eds.), Mesozoic Birds, Above the Heads of Dinosaurs. University of

California Press, Berkeley, California.

Wiemann, J., T.-R. Yang, and M. A. Norell. 2018. Dinosaur egg colour had a single evolutionary

origin. Nature 563:555–558.

Xu, X., X. Zheng, and H. You. 2010. Exceptional dinosaur fossils show ontogenetic development of early feathers. Nature 464:1338–1341.

Xu, X., Y.-N. Cheng, X.-L. Wang, and C.-H. Chang. 2002. An unusual oviraptorosaurian dinosaur from China. Nature 419:291–293.

Xu, X., Q. Tan, J. Wang, X. Zhao, and L. Tan. 2007. A gigantic bird-like dinosaur from the Late Cretaceous of China. Nature.

Zanno, L. E., and S. D. Sampson. 2005. A new oviraptorosaur (Theropoda, Maniraptora) from the Late Cretaceous (Campanian) of Utah. Journal of Vertebrate Paleontology 25:897–904.

Zanno, L. E., and P. J. Makovicky. 2011. Herbivorous ecomorphology and specialization patterns in theropod dinosaur evolution. Proceedings of the National Academy of Sciences 108:232–237.

Zhou, Z.-H., X.-L. Wang, F. Zhang, and X. Xu. 2000. Important features of *Caudipteryx* - evidence from two nearly complete new specimens. Vertebrata PalAsiatica 10:241–254.

1.4 FIGURES & TABLES

Fig. 1.1. History of discovery of Oviraptorosauria.

Described oviraptorosaur diversity through time. Caudipterid species shown in purple,

avimimids in yellow, caenagnathids in blue, oviraptorids in red, and the total of all groups in

black.
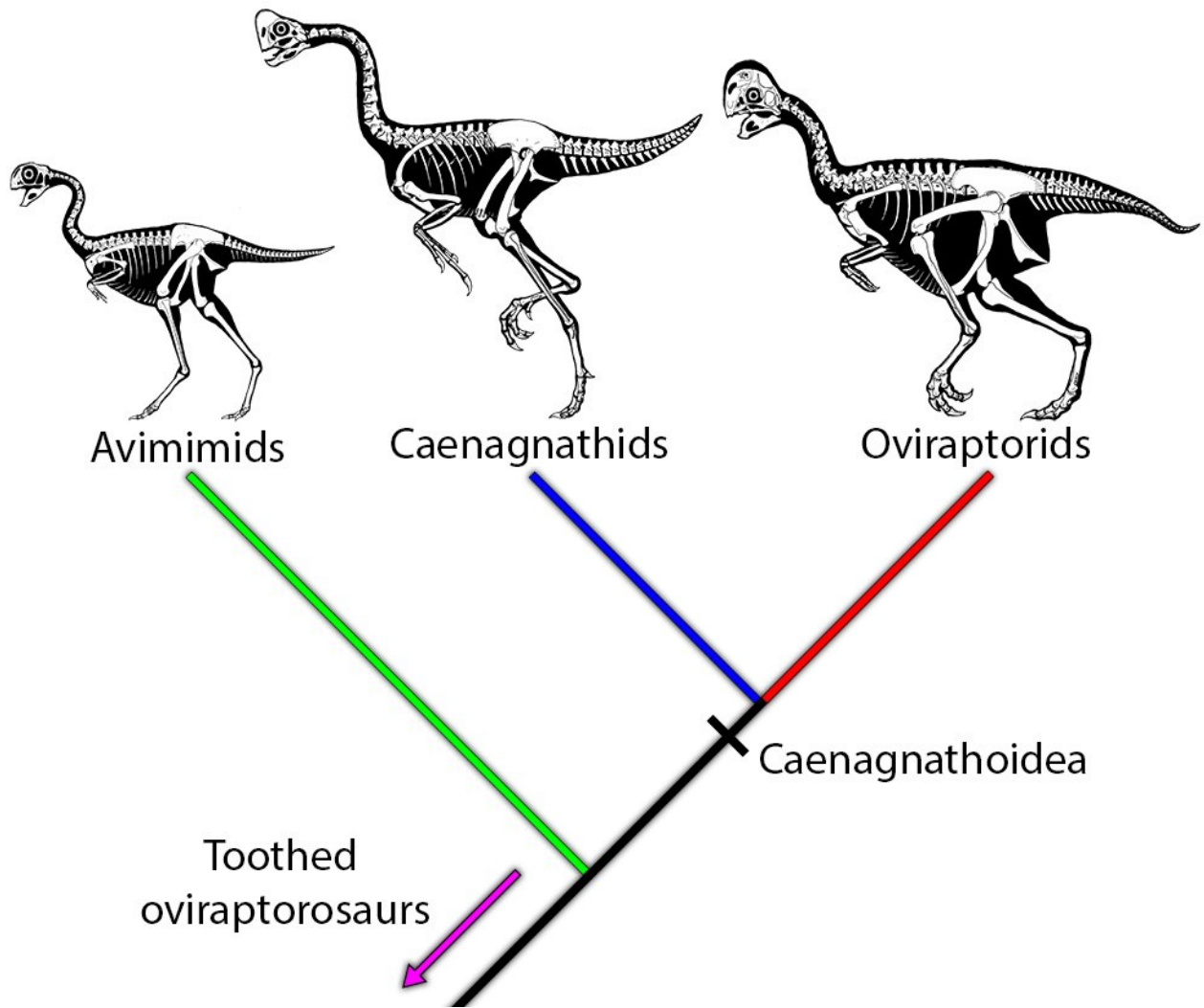
Fig. 1.2. Simplified phylogeny of Oviraptorosauria.

Simplified phylogeny showing the relationships of the three major oviraptorosaur groups as recovered in Chapter 5. Reconstructions show skeletal anatomy and relative body sizes (from left to right: *Avimimus nemegtensis*, *Chirostenotes pergracilis*, and the Guriliin Tsav oviraptorid).
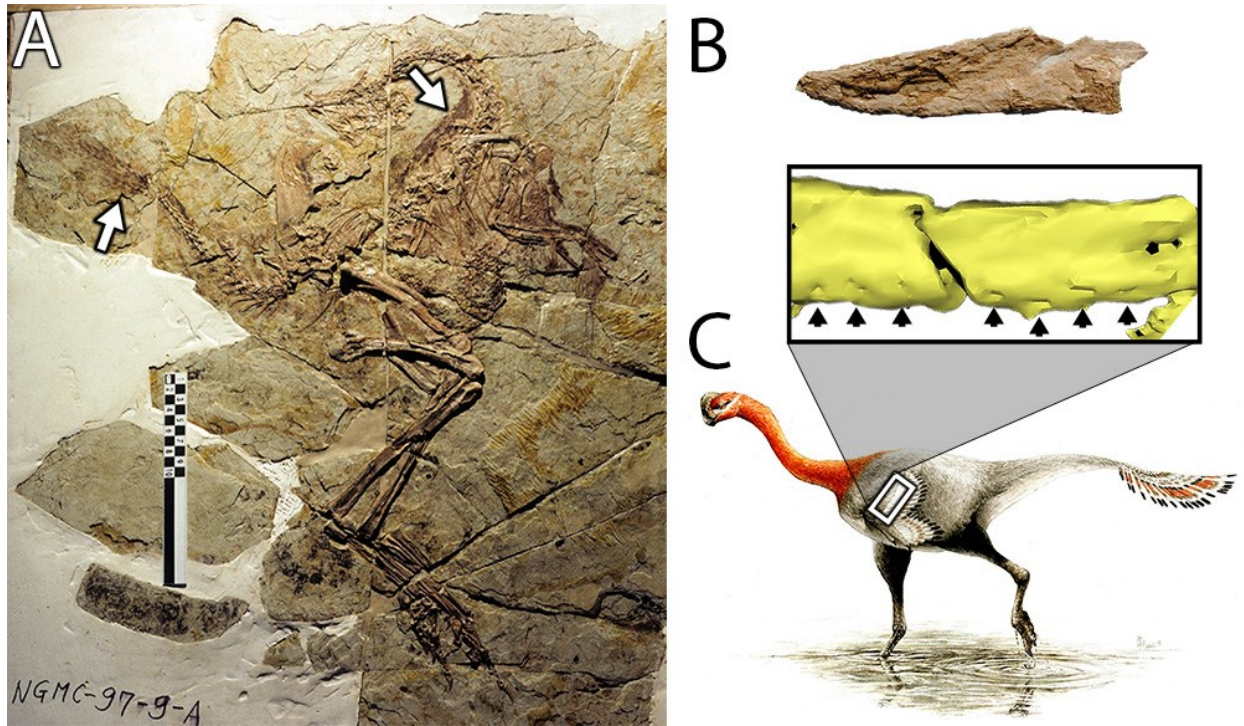
Fig. 1.3. Evidence of feathers in oviraptorosaurs.

Photograph (A) *Caudipteryx* (NGMC-97-9-A), showing feather impressions (arrows). Fused

pygostyle (B) of *Nomingia* in lateral view. Computed tomography rendering (top) and life

reconstruction (bottom) of *Apatoraptor* (C), showing ulnar papillae and hypothesized

integumentary covering.
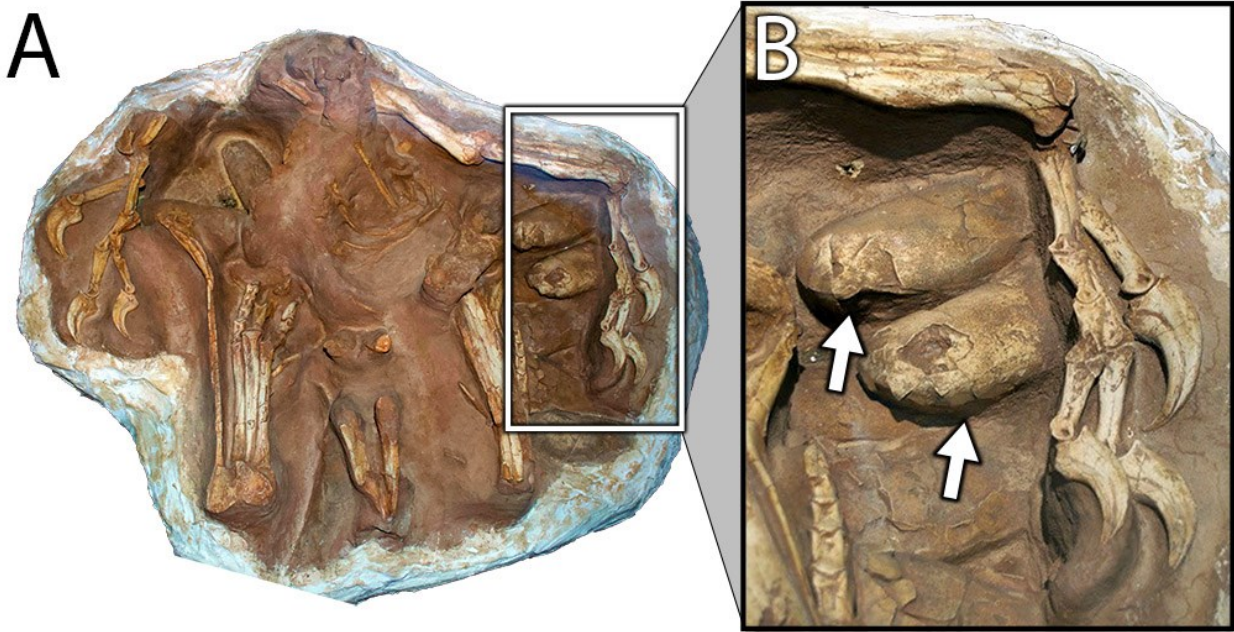
Fig. 1.4. Brooding behaviour in oviraptorids.

MPC-D 100/979 (*Citipati osmolskae*) preserved in brooding position atop a nest of eggs (arrows).

Table 1.1 Previous state of taxonomy of oviraptorosaur taxa examined.

Clade	Family	Genus	Species	Authority	Holotype	Referred specimens	Skeletal representation
Unnamed clade	Avimimidae	*Avimimus*	*portentosus*	Kurzanov, 1981	PIN 3907/1	None	Partial skull and skeleton
Caenagnathoidea	Caenagnathidae	*Chirostenotes*	*pergracilis*	Gilmore, 1924	CMN 2367	CMN 8538, TMP 1979.020.0001, ?TMP 1990.056.0006	?Mandible, hands, pelvis and hindlimb, foot
		Caenagnathus	*collinsi*	Sternberg, 1940	CMN 8776	None	Mandible
		Elmisaurus	*rarus*	Osmólska, 1981	ZPAL MgD-I/98	None	Hands and feet
		Leptorhynchos	*elegans*	Longrich et al. 2013	ROM 781	?TMP 1992.036.0390, TMP 1982.039.0004	Mandible, tarsometatarsus
	Oviraptoridae	*Conchoraptor*	*gracilis*	Barsbold 1986	MPC-D 100/20	MPC-D 100/3006, ZPAL MgD-I/95	Skull
		Rinchenia	*mongoliensis*	Barsbold 1997	MPC-D 100/32-A	None	Nearly complete skeleton
		"Ingenia"	*yanshini*	Barsbold 1981	MPC-D 100/30	MPC-D 100/31–4	postcranial skeleton
	Indeterminate	*Nomingia*	*gobiensis*	Barsbold et al. 2000	MPC-D 100/119	None	Partial postcranial skeleton

? Indicates questionable or uncertain referral.

CHAPTER 2 – AVIMIMIDAE

2.1 INTRODUCTION

Avimimidae was a monogeneric family of oviraptorosaurs from China and Mongolia (Fig. 2.0) that has remained enigmatic since its discovery. *Avimimus portentosus* Kurzanov 1981 was first described by Kurzanov (1981) and its bird-like morphology immediately confused palaeontologists. Although regarded as a non-avian theropod by Kurzanov (1981), other workers interpreted its mosaic of features as similar to those of a flightless avian (Chatterjee, 1991), a sauropod (Norman, 1990), and even an ornithopod (Norman, 1990). These apparently contradictory hypotheses led several authors (Thulborn, 1984; Vickers-Rich et al., 2002) to suggest that the holotype may have been a chimaera, a possibility Kurzanov considered himself (Thulborn, 1984). However, the subsequent discovery of an articulated skeleton (Watabe et al. 2000) indicated that the material did indeed belong to a single taxon. The oviraptorosaurian affinities of *Avimimus* were first recognized by Maryanska et al. (2002), although their analysis also placed oviraptorosaurs within Avialae, a conclusion no longer supported by broad-scale theropod phylogenies (Senter, 2007; Turner et al., 2012). Recent analyses (Lamanna et al., 2014; Funston and Currie, 2016; Lü et al., 2016) have recovered *Avimimus* as an intermediate oviraptorosaur, sister to Caenagnathoidea (=Caenagnathidae + Oviraptoridae).

A series of detailed descriptions of *Avimimus portentosus* in Russian by Kurzanov (1981b, 1982, 1983, 1985, 1987), and their translations, comprise most of the literature on avimimids. Despite the discovery of numerous additional avimimid specimens in the intervening

years, few of these have been described until recently. An expedition led by the Hayashibara Museum of Japan collected a nearly complete skeleton including cranial material (MPC-D 100/129) from Shar Tsav in the eastern Gobi Desert of Mongolia, but, until now, it has not been described beyond conference abstracts (Watabe et al., 2000). In 2006, the same organization discovered a second skeleton in the Nemegt Formation at Bugiin Tsav, in western Mongolia, the cranium of which was recently described (Tsuihiji et al., 2017). Ryan et al. (2001) presented on new material of *Avimimus* from a bonebed in the Iren Dabasu Formation of China, but this material has not been described until now. They also tentatively identified the first avimimid material from North America (Ryan et al., 2001), but re-examination indicates that this material more likely belongs to another small theropod. A bonebed of disarticulated avimimids from the Nemegt Formation of Mongolia was discovered in 2006 (Currie et al., 2008), but was not described until ten years later (Funston et al., 2016b). Subsequent examination of that material determined that it represents a new species, *Avimimus nemegtensis* Funston et al. 2018, based on a suite of cranial and postcranial differences from the holotype of *Avimimus portentosus* (Funston et al., 2018a).

The rarity of avimimid material and its poor history of description has led to several problems in the understanding of these animals. For example, until recently (Funston et al., 2018a), all avimimids were considered one species, which had been used for biostratigraphic correlations of sites in the eastern and western Gobi (Watabe et al., 2006, 2010a). Furthermore, the functional significance and ontogenetic onset of the unusual fused compound bones of the avimimid skeleton have not yet been addressed, although they are assumed to be reliable indicators of skeletal maturity. Here, I test these assumptions by describing the new avimimid material from Erenhot, Nemegt, and Shar Tsav within an oviraptorosaur framework. Histological

sampling of material from Iren Dabasu reveals unexpectedly young ages in some individuals, and suggests that the ontogeny of fused compound elements in oviraptorosaurs is more complex than previously thought. The results help to clarify the enigma of avimimids, their unusual anatomy, and their phylogenetic relationships to other theropods.

2.2 MATERIALS AND METHODS

I examined Late Cretaceous avimimid material in the collections of the MPC and IVPP (on loan to UALVP) firsthand. Photographs were taken using a Nikon D5000, Nikon D7200, or Nikon Coolpix AW120 camera, and measurements were taken with digital calipers to an accuracy of 0.5 mm, or with a fabric measuring tape to an accuracy of 1 mm. Excavation of the *Avimimus* bonebed in 2016 at the Nemegt Locality was undertaken in conjunction with the MPC, under proper permits and supervision. Overburden was removed using shovels and pickaxes, and the relatively hard matrix was excavated manually using hammers, chisels, and pin vises. The bones were mapped using a gridsquare and a baseline established during initial excavation in 2006.

Histological thin-sections of specimens from Iren Dabasu were made by vacuum-embedding the specimens in Buehler Epothin Resin or Castolite AC polyester resin, and cutting the billet using a Hillquist Thin Section Machine or an Isomet 1000 Precision Sectioning Saw. Billets were adhered to plexiglass slides using Buehler Epothin Resin or 3M Cyanoacrylate glue. Thin sections were ground and polished from the mounted slides using a variety of grits on a lapidary wheel or by hand on a glass plate.

2.3.1 *Avimimus portentosus* Kurzanov 1981

Dinosauria Owen, 1842

Saurischia Seeley, 1888

Theropoda Marsh, 1881

Coelurosauria Huene, 1914

Maniraptora Gauthier, 1986

Oviraptorosauria Barsbold, 1976

Avimimidae Kurzanov, 1981

Avimimus Kurzanov, 1981

Avimimus portentosus Kurzanov, 1981

Holotype: PIN 3907/1, partial skeleton.

Referred material: PIN 3906/1, partial skeleton, PIN 3907-2, partial pubis and ischium; PIN 3907-3, partial skeleton including neurocranium and vertebrae; PIN 3907-4, partial axial skeleton; PIN 3907-5, pelvis.

Newly referred material: MPC-D 100/129 (Figs. 2.1–2.4), partial skeleton consisting of cervical, dorsal, sacral and proximal caudal vertebrae, partial forelimbs, partial pelvis, and complete hindlimbs.

Horizon and localities: Djadokhta Formation (Campanian); Shar Tsav, Udan Sayr, and Yagan Khovil; Gobi Desert, Mongolia.

Etymology: *Avi-* , bird, *-mimus*, mimic; *portentosus*, unusual (Latin).

Diagnosis: Small oviraptorosaurian theropod diagnosed by the following features (autapomorphies indicated by asterisk, plesiomorphies indicated by dagger): premaxilla invaded by antorbital fenestra*; fused neurocranium*; low mandible with poorly developed symphyseal shelf†; dorsal vertebrae without lateral pleurocoels*; fused carpometacarpus*; fused tibiotarsus incorporating distal end of fibula*; fused tarsometatarsus lacking first digit and with proximally absent third metatarsal*.

Description

MPC-D 100/129:

This specimen was briefly mentioned by Watabe et al. (2000), who indicated that the skeleton also preserved parts of the cranium, pectoral girdle, and a complete caudal series. Unfortunately, these elements were not mounted with the rest of the skeleton and could not be observed.

Axial skeleton—Ten cervical vertebrae are preserved, but the axis and atlas are not among them. The cervical vertebrae have lateral pleurocoels (Fig. 2.1A–C), which distinguishes them from all but the first of the unusual dorsal vertebrae. All of the cervical vertebrae are amphicoelous, and, where preserved, have infradiapophyseal fossae and infrapostzygapophyseal fossae divided by a lamina. Anterior to the fifth postaxial cervical vertebra (C7; Fig. 2.1A), the vertebrae have anterodorsally to posteroventrally inclined anterior articular faces. Beginning with the fifth postaxial cervical vertebra, both the anterior and posterior articular faces are

vertical relative to the long axis of the vertebra. The neural arches of the anterior vertebrae are mostly broken, but on the fourth postaxial vertebra (C6), the postzygapophyses are low, pointed, and connected to form a U-shaped lamina. The fifth postaxial vertebra is elongate and has a strongly inclined anterior articular face. It is the transition point of the neck. Posterior to it, all of the cervical vertebrae have ventrally-facing postzygapophyses (instead of ventrolateral), low rectangular neural spines, and centra that become successively taller.

The first dorsal vertebra is a cervicodorsal, showing a mosaic of features otherwise exclusive to either cervical or dorsal vertebrae. Unlike the other dorsal vertebrae, it has a large lateral pleurocoel, but it also has a small hypapophysis, which is absent in the cervical vertebrae. The parapophysis is dorsally situated on the centrum, near the neurocentral suture, whereas it is more ventral on the cervical vertebrae. A small transverse process extends from the neural arch, unlike the cervical vertebrae. The second dorsal vertebra (Fig. 2.1D) has a large, rounded anteroventrally projecting hypapophysis, but lacks a lateral pleurocoel. The same is true of the third dorsal vertebra, although its hypapophysis is broken so its full extend cannot be discerned. In other oviraptorosaurs, the second hypapophysis is the largest of the three. The remaining dorsal vertebrae (Fig. 2.1E) each lacks a hypapophysis but has a ventral keel that develops more prominently in successive vertebrae. Posteriorly, each becomes lower dorsoventrally and more rounded transversely. Where preserved, the neural arches have shallow infradiapophyseal fossae that become progressively deeper in more posterior vertebrae, and consistently deep infrapostzygapophyseal fossae. The neural spines become taller and more rectangular posteriorly along the dorsal vertebral series.

There are eight completely fused sacral vertebrae (Fig. 2.1G). The first sacral vertebra has a shallow ventral keel, but a ventral groove extends between two keels along sacral vertebrae

three to seven. The first sacral vertebra has a small pleurocoel, but the others do not. The neural arches are very different than those of most oviraptorosaurs in that they lack tall neural spines and the complex laminae that usually extend lateral to the neural spines. Only the first sacral vertebra has an infradiapophyseal fossa (Fig. 2.1G), which are usually large in oviraptorosaur sacra. The intravertebral canals, which manifest as circular fenestrae, decrease in size sequentially, and are little more than foramina between sacral vertabrae five and six. They are completely absent between sacral vertebrae seven and eight, and these are unusually smooth for sacral vertebrae, lacking any fossae.

Only three caudal vertebrae are mounted with the specimen, despite Watabe et al. (2000) describing a complete caudal series. The first caudal vertebra (Fig. 2.1F) has a tall neural spine and an amphicoelous centrum lacking a pleurocoel or ventral keel. Unlike the other caudal vertebrae, it has an infraprezygapophyseal fossa, although it is shallow. The second caudal vertebra has a posteriorly directed neural spine and a smaller posterior articular surface that is positioned further ventrally than the anterior one. The third caudal vertebra is similar to the second, but has more posteriorly positioned transverse processes and a more ventrally located posterior articular surface. The neural spine of the third caudal vertebra is missing.

Forelimb—Watabe et al. (2000) described a scapulocoracoid for the specimen, but it is not mounted with the rest of the skeleton. The humerus (Fig. 2.2A) is about as long as the forearm, which is typical of oviraptorosaurs (Osmólska et al., 2004b). The medial head is strongly inturned and deltopectoral crest is poorly developed compared to the large, winglike crests of caenagnathids and oviraptorids (Balanoff and Norell, 2012b; Lamanna et al., 2014; Funston and Currie, 2016). A groove separates the head of the humerus from the deltopectoral crest, creating a morphology superficially similar to the humeri of crocodylomorphs and

choristoderes. The shaft of the humerus is relatively straight, rather than curved laterally. The distal condyles are well defined, but the ectepicondylar tuber is small (Fig. 2.2A), unlike the prominent process of oviraptorids (Funston et al., 2018a).

The radius (Fig. 2.2B) is gracile and morphologically simple. The proximal end is rounded and slightly compressed dorsoventrally. The shaft is generally cylindrical and lacks any distinctive ridges or grooves. The distal end has an anterodorsally to posteroventrally inclined distal surface, but lacks a prominent styloid process. The ulna (Fig. 2.2C) has a poorly developed proximal condyle and is transversely compressed. The olecranon process is poorly developed, like other oviraptorosaurs (Funston et al., 2018a), but the coronoid process is moderately developed and rounded. The shaft of the ulna bows ventrally and has two ridges: a thin ventral crest that probably supported the remiges (Kurzanov, 1987; Funston and Currie, 2016), and a shallow lateral ridge.

The carpometacarpus (Fig. 2.2D) is highly unusual compared to other oviraptorosaurs (Osmólska et al., 2004b). The carpal bones and metacarpals are proximally fused into a single unit, which comprises at least the semilunate carpal and the metacarpals. It is unclear whether the radiale is also incorporated into this unit, because it typically lies proximal to the semilunate carpal (Zanno and Sampson, 2005; Balanoff and Norell, 2012b), which clearly forms the main trochlea of the carpometacarpus (Fig. 2.2D). The intermedium and ulnare, if present, may contribute to the fused unit, but if so, they are indistinct. A small protuberance at the proximal end of metacarpal III may represent one of these carpal bones, but which one is not clear. The fused carpal bones form a semicircular trochlea that is thickened along the flexor-extensor plane. On the lateral side of the trochlea, there is a small notch, which may have accommodated the radiale if it is not fused to the other carpals. The trochlea appears to be formed mostly of the

semilunate carpal, and its main articular groove is oriented dorsolaterally to ventromedially. The proximal ends of all three metacarpals are preserved and incorporated into the fused mass, but only the separate shafts of metacarpals II and III are preserved (Fig. 2.2D). Metacarpal II tapers distally and metacarpal III is straplike with a flexor ridge. The broken base of metacarpal I indicates that this metacarpal was broader transversely than the other two, but compressed in the flexor-extensor plane. Its medial edge would have been much thicker than the lateral edge, which, together with the palmar ridge of metacarpal III, would have made the palmar (flexor) surface of the hand concave.

Hindlimb—The partial right pelvis (Fig. 2.3A) is comprised of the ilium, pubis, and ischium, which have fused around the acetabulum. The ilium is missing much of the supracetabular and preacetabular portions, whereas the pubis is complete but in two pieces, and the ischium is represented solely by the proximal end. The preacetabular blade of the ilium is ventrally hooked and would have been shorter than the postacetabular blade when complete. There is a large, rugose antitrochanter on the lateral surface of the ilium, and a large, well-developed brevis shelf on the medial side. The brevis shelf bifurcates posterodorsally, forming a small posterior process and a large, anteromedially extending crest (Fig. 2.3A: sbr). The former is homologous to the brevis shelf of other oviraptorosaurs (Osmólska et al., 2004b; Funston et al., 2018a), whereas the latter probably contacted the neural spine or sacral rib of a sacral vertebra, and is not found in other oviraptorosaurs. The anteromedial projection of this crest forms a deep fossa in the medial surface of the ilium, which is bordered anteriorly by a T-shaped crest that extends ventrally from the dorsal edge of the ilium. Just anterior to its ventral end, there is a prominent mound which represents the attachment of a sacral rib (Fig. 2.3A). The dorsal edge of the postacetabular blade curves ventrally to form a tapered, blunt point with the

straight ventral edge of the ilium. The pubic peduncle is rectangular in lateral view and has a small anterior crest where it meets the pubis. This crest may have accommodated *M. ambiens* (Hutchinson, 2001). The ischiadic peduncle is square in lateral view, rather than triangular as in caenagnathids and oviraptorids, and is transversely wide because of the large antitrochanter.

The pubis has a small anterior process that is continuous with the crest on the ilium for *M. ambiens*. When articulated, the parts of the pubis show that it projected slightly anteriorly, although it is relatively straight, rather than anteriorly concave as in oviraptorids. The pubic apron (Fig. 2.3A: apr) is restricted to the distal third of the shaft and was transversely narrow. The ridge marking the base of the apron is straight and situated in the anteroposterior middle of the shaft of the pubis, like in oviraptorids, rather than having a sinuous outline and being confluent with the anterior surface of the shaft, which is the case in caenagnathids. The pubic boot is relatively small and its distal margin is inclined anteroventrally to posterodorsally. The anterior process is slightly longer than the posterior process, which is upturned and slightly hooked (Fig. 2.3) as in caenagnathids. However, the disparity between anterior and posterior processes is not as great as in oviraptorids. The left and right pubes are fused at the pubic boot, and a small portion of the shaft of the left pubis is preserved dorsal to this. At the distal end of the pubic apron, the pubic fenestra separates the pubes dorsal to the boot. A small cleft can be seen between the pubes on the dorsal surface of the boot. Only the proximal end of the ischium is preserved, and it provides little morphological information other than having a small contribution to the acetabulum.

The femur (Fig. 2.3B, C) has a round, medially-directed head that is separated from the wide greater trochanter by a sulcus. The anterior trochanter is fingerlike and is separated from the greater trochanter by a wide cleft, unlike the tightly appressed trochanters of oviraptorids and

derived caenagnathids. A modest fourth trochanter is present on the posteromedial edge of the

shaft, about a quarter of the length of the femur from the head. This ridge is not as well

developed as that of the type specimen (PIN 3907/1) and is apically flattened, rather than

rounded. The shaft of the femur is cylindrical and is slightly bowed anteriorly (Fig. 2.3C). There

is an anteromedial ridge extending proximally from the medial condyle (Fig. 2.3B). The lateral

condyle is larger than the medial condyle and extends further ventrally. A moderately developed

popliteal fossa separates the condyles posteriorly. A large ectocondylar tuber projects laterally

from the lateral condyle, as in most oviraptorosaurs (Osmólska et al., 2004b).

The tibia (Fig. 2.3D, E) has a large, laterally deflected, proximally restricted cnemial

crest with a ventrally located apex. The fibular condyle is relatively large and projects laterally

from the femoral condyle of the tibia, from which it is separated posteriorly by a small groove.

The fibular crest is located relatively proximally compared to most oviraptorosaurs, and does not

extend more than one third of the length of the tibia from the proximal end. Its length is about

12–13% of the entire length of the tibia. The shaft of the tibia has the semicircular cross-section

typical of oviraptorids (Funston and Currie, 2018), formed by a flat anterior surface devoid of

ridges, and a rounded posterior surface. Only the proximal end of the fibula is preserved (Fig.

2.3D). The head has a medial concavity and projects anteriorly towards the cnemial crest. The

astragalocalcaneum (Fig. 2.3D, E) is completely fused to the tibia and its ascending process

extends proximally about a third of the length of the tibia. At the base of the ascending process,

there is a pit, similar to that of *Anzu wyliei* Lamanna et al. 2014 (Lamanna et al., 2014). A small

rugosity on the lateral surface of the calcaneum represents the distal end of the fibula, which, like

in *Avimimus nemegtensis* (Funston et al., 2018a), is completely fused to the astragalocalcaneum.

The tarsometatarsus (Fig. 2.4A) is a fused unit composed of the distal tarsals and metatarsals II–V. The distal tarsals are coossified with each other and the proximal end of the metatarsals. Unlike in *Avimimus nemegtensis*, they form an anteriorly tapering wedge that creates a posterodorsally to anteroventrally inclined articular surface. Distal tarsal IV has a small proximodorsal process. In contrast to *Avimimus nemegtensis*, metatarsal V is well developed and forms a prominent longitudinal ridge fused to the posterolateral side of the metatarsus (Fig. 2.4A). It is broken on both sides, but its distal end is preserved on the right side adhering to the proximal end of metatarsal IV (Fig. 2.4), showing that it extended much further distally—about one third of the length of the metatarsus—than in *Avimimus nemegtensis*. The proximal coossification of the distal tarsals and metatarsals is somewhat reminiscent of *Elmisaurus rarus* Osmólska 1981 in that it produces a posterior protuberance, which is not the case in *Avimimus nemegtensis*. The shafts of the metatarsals are gracile. Metatarsal III is proximally pinched to form an arctometatarsalian pes (Fig. 2.4A). Metatarsal II is both shorter and narrower in anterior view than metatarsal IV. The posteromedial ridge on the second metatarsal and the posterolateral one on the fourth create a concave plantar surface of the metatarsus. The pedal phalanges (Fig. 2.4B–D) are absolutely and relatively short compared to those of other oviraptorosaurs, especially caenagnathids. Phalanx III-1 (Fig. 2.4C) is the longest by far, and exceeds even the unguals in length. In contrast, phalanges II-1 (Fig. 2.4B) and IV-1 (Fig. 2.4D) are relatively shorter than usual for an oviraptorosaur. Phalanges II-2 and IV-2–IV-4 are highly reduced, so that the proximal and distal articulations of each one are nearly overlapping, and there is no intervening shaft. The unguals are short, blunt, and straight, more reminiscent of the unguals of ornithomimids than oviraptorosaurs.

2.3.2 *Avimimus nemegtensis* Funston et al. 2018

Avimimus Kurzanov, 1981

Avimimus nemegtensis Funston et al. 2018

Holotype:

MPC-D 102/81; partial skull; Nemegt Formation, Nemegt, Mongolia.

Referred Material:

MPC-D 102/15 – MPC-D 102/100 (see Supplement 1 of Funston et al. 2016b). Variety of

elements including crania (Figs. 2.5–2.9) and postcrania (Figs. 2.10–2.14); Nemegt Formation,

Nemegt, Mongolia.

Etymology: *Avi-* , bird, *-mimus*, mimic; *nemegtensis*, from Nemegt.

Diagnosis:

Differs from *Avimimus portentosus* in the following features (autapomorphies indicated

by asterisk, plesiomorphies indicated by dagger): exoccipital with single jugular opening rather

than two*; relatively small foramen magnum; wider pterygoids; laterally bowed quadratojugal*;

dentaries with greater development of symphyseal shelf and shallow lingual ridges*; unfused

ilium and ischium†; ischiadic peduncle of ilium lacking antitrochanter†; ilium with dorsally

expanded and ventrally hooked preacetabular blade†; sigmoidal brevis shelf*; postacetabular

blade lacking suprabrevis ridges†; shallow brevis fossa of postacetabular blade of ilium†.

Description

Craniomandibular Skeleton—The bonebed produced cranial elements that were formerly unknown for *Avimimus* and provide important anatomical information. A jumble of associated bones (MPC-D 102/34) includes the premaxillae and nasals (Fig. 2.5), and an additional two semiarticulated premaxillae (MPC-D 102/108) were recovered (Fig 2.5J, K). The unfused premaxillae are hollow; each has a long dorsal process with a lateral facet for the nasal and a flat medial surface for the adjoining premaxilla. The tomial margin has five denticulations (Fig. 2.5J). Uniquely amongst oviraptorosaurs, the laterally flaring posterior process (Fig. 2.5F, G) that separates the maxilla from the external naris has a deep depression, probably confluent with the antorbital fossa. Although Kurzanov (1981b) reconstructed *Avimimus* with a conjoined naris and antorbital fenestra, the presence of the posterior process, which is missing in the holotype, indicates that it would have separated the naris and antorbital fenestra, as in all other theropods (Fig. 2.6G). The fused nasals (MPC-D 102/46; Fig. 2.5) form an unusual anchor-shaped bone. Posteriorly the nasals have ventrolaterally extending, hatchet-shaped lateral descending processes. Anteriorly there is a longitudinal groove on the dorsal surface, which opens into a slot for the premaxillae (Fig. 2.5). The posterior margin of the fused nasals is concave in dorsal view (Fig. 2.6C), and the nasals would have been largely separated posteriorly by the frontals. There is a longitudinal ridge on the ventral side of the midline process of the nasals. The united nasals have a smooth exterior surface and lack the pneumatic pitting that is present in oviraptorids (Clark et al., 2002b; Osmólska et al., 2004b; Balanoff and Norell, 2012b). Articulating the premaxillae and nasals shows that the snout was short, with a vertical anterior margin and anteriorly facing nares (Fig. 2.6).

A partial skull (MPC-D 102/81; Fig. 2.7) preserves the posterior part of the cranium, which has coossified into a single unit—here called the neurocranial unit—as in birds. The

coossified unit of *Avimimus* incorporates more bones than that of any bird, including the frontals, parietals, postorbitals, pterygoids, quadrates, squamosals, and bones of the braincase. Sutures between bones are obliterated, except for faint lines between the opisthotic-exoccipital unit and the basioccipital. The body of the apneumatic quadrate (Fig. 2.7) fuses along its whole medial margin to the prootic and pterygoid, so that the only communication of the post-temporal fenestra with the region anterior to the quadrate is the foramen for the middle cerebral vein (Fig. 2.7C, D). Dorsally, the pterygoid wing of the quadrate and the fused squamosal are separated from the exoccipital by an anteriorly-facing recess with a large ventral foramen and a smaller dorsal fossa, both for the middle cerebral vein. An aperture in the dorsal part of the exoccipital connects this dorsal fossa to the top of the skull. The quadrate condyles are saddle-shaped as in most oviraptorosaurs, suggesting that propalinal movement of the mandible was possible (Funston and Currie, 2014b). The right quadratojugal is an anteriorly directed prong that is indistinguishably fused to the lateral margin of the quadrate. There is no evidence of a quadratic foramen or fenestra between the quadrate and quadratojugal, a feature that is usually present in oviraptorosaurs (Clark et al., 2002b; Balanoff and Norell, 2012b). The occipital process of the squamosal (Fig. 2.7) is conjoined and fused to the paroccipital process of the exoccipital, which is unusual for oviraptorosaurs. The posterior part of the pterygoid (Fig. 2.7) is relatively large and is horizontal, contrasting with the typical dorsomedial-ventrolateral orientation of the oviraptorid pterygoid. The pterygoid contacts the basisphenoid along most of its length, rather than just at the basipterygoid process. The pterygoid contact with the quadrate is anteroposteriorly extensive and lies far dorsal to the mandibular condyles of the quadrate. In oviraptorids, the pterygoid typically contacts the quadrate just medial to the mandibular condyle (Clark et al., 2002b). Breakage to the ramus of the pterygoid shows that the pterygoid is hollow,

which is unique for oviraptorosaurs (Fig. 2.7). The occipital condyle (Fig. 2.7) is kidney-shaped and smaller than the foramen magnum, which is nearly circular as in oviraptorids (Osmólska et al., 2004b). The basal tubera are large and separated by a shallow median depression, with a possibly pneumatic foramen at its center. There are no basisphenoid recesses. The basipterygoid processes face laterally and are continuous with the greatly expanded posterior wing of the pterygoid, unlike in oviraptorids (Clark et al., 2002b). The supraoccipital has a longitudinal sagittal crest, but lacks a transverse nuchal crest. The opisthotic-exoccipitals form small laterally directed paroccipital processes that do not extend ventrally to the level of the basal tubera (Fig. 2.7). There is only one jugular opening on the posterior surface of each opisthotic-exoccipital— apparently unique for a dinosaur—that presumably served as the exit for cranial nerves IX-XII (Fig. 2.7). This condition is also reflected in MPC-D 100/125 (Tsuihiji et al., 2017), indicating that it is not individual variation. The functional significance of this union is difficult to discern, but it contrasts with the morphology of *Avimimus portentosus*, where there are two foramina per side for these nerves (Fig. 2.8). On the medial wall of the exoccipital portion of the braincase (Fig. 2.7J, K), there are five foramina. The largest of these, dorsal to the others, is a dorsoventrally oriented slit for cranial nerves IX-XI and communicates with the jugular opening on the posterior side of the exoccipital. Of the four smaller, ventral foramina, the anterior one was probably for a blood vessel, and the other three were for branches of cranial nerve XII. The last three foramina merge posteriorly to exit through the large jugular opening on the posterior face of the exoccipital. The medial surface of the braincase is pierced by a large floccular recess, ventral to which is a shallow depression pierced by cranial nerves VII and VIII (Fig. 2.7B, J, K). Anterolaterally, the prootic is pierced by a small anteriorly-facing foramen for the anterior branches of cranial nerve VII. The neurocranium of *Avimimus nemegtensis* is different than that

of *Avimimus portentosus* (PIN 3907-3) in having wider paroccipital processes and a deeper

basioccipital, so that the basal tubera are relatively lower (Fig. 2.8). The foramen magnum is

relatively smaller in *Avimimus nemegtensis* than in *Avimimus portentosus* (Tsuihiji et al., 2017).

The foramina for the middle cerebral vein of *Avimimus nemegtensis* are larger and placed farther

posteriorly to separate the squamosal and quadrate. In *Avimimus portentosus*, they are relatively

more anterior on the lateral side of the braincase. The quadrate condyles are more widely

separated in *Avimimus nemegtensis*, because the pterygoids are broader posteriorly than in

Avimimus portentosus. In addition, the quadratojugal projects laterally from the quadrate condyle

in *Avimimus nemegtensis*, as opposed to anteriorly like in *Avimimus portentosus*, which results in

a relatively wider posterior end of the skull.

The edentulous apneumatic dentaries (MPC-D 102/16) of *Avimimus* are partly coossified,

although a suture is visible ventrally (Fig. 2.9). The lingual surface of the dentary has a complex

series of ridges and grooves, although the relief is not as great as in caenagnathids (Funston and

Currie, 2014b). There is a distinct lingual groove on the occlusal surface of the dentary, which is

bounded medially by a weakly pronounced lingual ridge. There is an incipient symphysial shelf,

similar in development to most oviraptorids (Clark et al., 2002b).The occlusal margin projects

above the rest of the lingual surface, but is not concave in lateral view (Fig. 2.9). The Meckelian

grooves are separated at the midline by a distinctive ventrally tapering buttress of bone (Fig. 2.9),

which demarcates two shallow lateral fossae in posterior view. The lateral surface of the

mandible is marked by several minute foramina, which suggests that there was a keratinous beak

as in birds (Funston and Currie, 2014b). The posterodorsal ramus of the dentary is not bifurcated

transversely, which indicates that its contact with the surangular or coronoid was simple, as in

oviraptorids (Clark et al., 2002b).

Axial skeleton—Bonebed material includes cervical, dorsal, and caudal vertebrae, but sacra have not been discovered. Cervical and dorsal vertebrae are identical to those of *Avimimus portentosus*. The cervical vertebrae (Fig. 2.10) are unremarkable for an oviraptorosaur, but the dorsal vertebrae are unusual in lacking lateral pleurocoels or other signs of pneumatic invasion. A series of eight articulated distal caudal centra (Fig. 2.11) was recovered from the bonebed (Funston et al., 2016b). The centra are small and barrel-shaped, with weakly pronounced ventral ridges. The unfused caudal vertebrae show that this individual did not have a pygostyle, although in other oviraptorosaurs the pygostyle fuses through ontogeny.

Pectoral girdle—A scapulocoracoid (MPC-NEE.2016-257) awaits preparation, but the lateral side was exposed in the field (Fig. 2.10). The scapula and coracoid are fused without a suture, and surround a posteroventrally-facing glenoid. The anterior end of the scapula has a small, laterally everted acromion process and the posterior end is widened. The coracoid is pierced by a large coracoid foramen, and bears a ridge-like coracoid (biceps) tubercle. The posteroventral process is not as strongly recurved as in other oviraptorosaurs, and the anteromedial portion is enlarged, resulting in a triangular coracoid.

Forelimb—Forelimb material is underrepresented in the bonebed, but a radius and a manual phalanx were recovered. The radius is relatively straight and its shaft bears two ridges. One of these is for the interosseous membrane, and the other may be for muscle attachment. The proximal end has a tab-like medial process, and the distal end is weakly expanded. The manual phalanx (Fig. 2.10) is unusual. The proximal articular cotyle faces proximodorsally and is bisected by a ridge. The distal end is mostly broken, but part of the distal condyle is present, indicating that the phalanx was not much longer than preserved.

Pelvis—None of the pelvic bones of *Avimimus nemegtensis* are fused to each other, despite being the same size as PIN 3907-1 (the holotype of *Avimimus portentosus*), and nearly double the size of PIN 3907-5, a pelvis of *Avimimus portentosus* that is completely fused. Although degree of fusion changes through ontogeny, the shape of the ilium is remarkably conservative in oviraptorosaurs, even in young individuals (Norell et al., 2001; Weishampel et al., 2008; Lü et al., 2013; Wang et al., 2016). It is therefore reasonable to interpret the gross morphological differences (Fig. 2.8) in the pelves of *Avimimus portentosus* and *Avimimus nemegtensis* as taxonomic, rather than ontogenetic. The ilium (Figs. 2.8, 2.10) of *Avimimus nemegtensis* is relatively unmodified compared to caenagnathids and oviraptorids, which contrasts with the unusual ilium of *Avimimus portentosus*. In *Avimimus portentosus* (PIN 3907-5; Fig. 2.8), the preacetabular blade is upturned and rounded, and the postacetabular blade is nearly twice the length of the preacetabular process and has a strong antitrochanter (*sensu* Romer, 1923). In contrast, *Avimimus nemegtensis* has a ventrally hooked, dorsally expanded preacetabular blade that is only slightly shorter than the postacetabular blade, and lacks an antitrochanter (Fig. 2.8). The ischiadic peduncle of *Avimimus nemegtensis* is triangular in lateral view, as is typical for oviraptorosaurs, but in *Avimimus portentosus*, it is rectangular. The medial surface of the ilium (Figs. 2.8, 2.10) has an extensive, sigmoidal brevis shelf that overhangs a shallow brevis fossa and lacks the large suprabrevis ridges that characterize *Avimimus portentosus*. In *Avimimus portentosus*, the straight brevis shelf does not extend the full length of the postacetabular process, and meets a prominent dorsoventral suprabrevis ridge. Despite the recognition of a ventrally-hooked preacetabular process in *Avimimus portentosus* (Fig. 2.3), the morphology of the medial surface of the ilium differs greatly between *Avimimus nemegtensis* and *Avimimus portentosus*. In particular, the presence of suprabrevis ridges in *Avimimus portentosus*

starkly contrasts with their absence in *Avimimus nemegtensis*, where the medial surface of the

ilium is more similar to other oviraptorosaurs. The pubis is represented in the bonebed only by

an isolated pubic symphysis (MPC-D 102/50). The symphysis is completely fused, although

there is a shallow groove on the ventral surface where the pubes meet. Dorsally, there is a deep

cleft between the shafts of the pubes at their symphysis, as in *Avimimus portentosus*. The pubic

boot is larger anteriorly than posteriorly, as in all oviraptorosaurs. It appears that the pubic apron

extended far distally, and is separated from the pubic boot by only a small fenestra just proximal

to the pubic symphysis. The ischium of *Avimimus nemegtensis* is known only from a fragment of

the wide shaft, which includes a large, rounded obturator process.

  Hindlimb—The femora of *Avimimus nemegtensis* (Fig. 2.10) are essentially identical to

those of *Avimimus portentosus*. The femoral head is well developed, and projects medially

perpendicular to the shaft of the femur. The anterior trochanter is robust and fingerlike, and

extends proximally to the level of the large greater trochanter. There is a wide gap separating the

anterior trochanter from the greater trochanter, much like in *Caenagnathasia martinsoni* Currie

et al. 1993 (Sues and Averianov, 2015). On the posteromedial side of the shaft there is a

prominent fourth trochanter, which is absent in other oviraptorosaurs (Qiang et al., 1998;

Balanoff and Norell, 2012b; Lamanna et al., 2014). Posteriorly, the distal condyles are well

developed, separated by a deep popliteal fossa, and there is a large ectocondylar tuber.

  The adult tibiotarsus consists of the fused tibia, astragalocalcaneum, and the fibula (Fig.

2.12). The tibia is gracile and long relative to its distal transverse width (Fig. 2.12). The cnemial

crest is thick transversely and laterally deflected, but does not extend far distally down the shaft

of the tibia. The fibular condyle is well developed and separated from the cnemial crest by a deep

incisura tibialis. The fibular crest is deflected anteriorly and extends distally about a quarter of

the length of the shaft (Fig. 2.10). The distal end of the tibia is only slightly expanded

mediolaterally, but, as in *Elmisaurus rarus*, there is a relatively well-developed postfibular

flange. The distal end of the fibula fuses to the calcaneum in adult individuals (Fig. 2.13), but the

proximal end does not fuse to the tibia even in the largest specimens. The astragalus and

calcaneum are fused without a suture in all specimens. The calcaneum has a lateral depression,

but does not have an excavated facet for the fibula, with which it fuses. The astragalus has a tall

and wide ascending process that extends a quarter of the way up the tibia. At the base of the

ascending process, there is a shallow median depression, as in caenagnathids (Lamanna et al.,

2014).

In large specimens, the distal tarsals (Fig. 2.14) are fused to each other and coossified

with the proximal ends of metatarsals II, III, IV and V. On the proximal end of the

tarsometatarsus, the third distal tarsal swells to form a bulbous process that would have

articulated with the depression between the condyles of the astragalocalcaneum (Fig. 2.10). The

fourth distal tarsal has a proximodorsal process that is attenuated into a point, rather than a hook-

like process as in *Elmisaurus rarus* and *Leptorhynchos elegans* Longrich et al. 2013 (Currie et

al., 2016; Funston et al., 2016a). This proximodorsal process is fused to the proximal end of

metatarsal V. The tarsometatarsus has a flat flexor surface, like in oviraptorids, rather than a

deeply incised flexor surface as in caenagnathids. The pedal phalanges are short and robust, but

otherwise unremarkable. Phalanges from digit IV of *Avimimus nemegtensis* are not as reduced as

those of *Avimimus portentosus* (Kurzanov, 1987). The pedal unguals are straight or slightly

curved ventrally, and have less transverse constriction distal to the articular surface than in other

oviraptorosaurs.

2.3.3 Indeterminate avimimid material

Avimimidae Kurzanov, 1981

Gen. et sp. indet.

Referred specimens: IVPP V16313–14, V16316–19, V16321–45, disarticulated bonebed float comprising frontal, vertebrae, forelimb, and hindlimb elements.

Horizon and locality: Iren Dabasu Fm. (?Campanian), Erenhot (Iren Dabasu), Nei Mongol, China

Description

Cranial skeleton:

     Frontal—A partial, highly unusual frontal (IVPP V16342; Fig. 2.15) was collected from the bonebed, but whether it pertains to an avimimid or another oviraptorosaur is uncertain. It can be distinguished from other theropods by the large, incising nasal contact, which is similar to the morphology of *Elmisaurus rarus* (Currie et al., 2016). The preserved portion of the frontal is roughly triangular in dorsal view, tapering anteriorly, but in lateral view it is strongly arched dorsally and the dorsal edge is strongly convex (Fig. 2.15). The dorsal surface of the frontal twists anteriorly, so that it faces laterally at its anterior end. On this lateral surface, there is a small depression, which probably accommodated the lacrimal, pierced by a foramen. The medial edge of the bone twists in unison with the lateral surface, and this forms a broad, angled facet for

the nasal (Fig. 2.15E). Ventral to this, the endocranial cavity is marked by numerous foramina and striations. The orbital rim flares laterally at its posterior end and becomes thinner and more crest-like. Like the dorsal edge of the frontal, it curves dorsally, so the frontal is uniform in thickness in lateral view. Posterior to its transversely widest point, the orbital rim becomes flat. Although the transversely widest point of theropod frontals is typically the postorbital process, it is unlikely that the widest point of the preserved portion of IVPP V16342 is the postorbital process. Instead, it is likely that the frontal was larger than preserved, and the fragment recovered is just the portion of the frontal anterior to the postorbital process. Near the posterior end of the preserved fragment, there is a large foramen on the dorsal surface (Fig. 2.15B). This foramen may communicate with another large foramen on the broken posterior surface, which probably would have been the anterior edge of the cerebral fossa (Fig. 2.15F). The orbital surface of the frontal is concave and has a fibrous texture pierced by numerous small foramina. A raised mound of rugose bone extends medially from the laterally flared part of the orbital rim (Fig. 2.15C).

Axial skeleton:

An assortment of vertebrae from all regions of the spinal column were recovered, including three cervical, four cervicodorsal, and six dorsal vertebrae; three partial sacra; and nine caudal vertebrae. Some other vertebrae were also collected, but they differ from those of avimimids and likely represent another taxon.

Cervical vertebrae—The smallest cervical vertebra (IVPP V16318) is likely from a juvenile, because the neurocentral sutures are open. It has vertical articulating surfaces, which suggests it is from the posterior half of the neck, based on comparison to MPC-D 100/129 (*Avimimus portentosus*). There is a small pleurocoel on each side and numerous smaller foramina

pierce the centrum. IVPP V16329.a (Fig. 2.16) is the most complete and probably represents the last or second last cervical. The articular faces are vertical and shallowly concave. There are two prominent ventral ridges on the centrum, although they do not extend far posteriorly. Lateral to these ridges is a prominent parapophysis and posterior to this is a deep fossa in place of a pleurocoel (Fig. 2.16C). The neurocentral suture is completely obliterated and the neural arch lacks pneumatic excavation except for two small post-diapophyseal fossae. The neural spine is short and square and there is a small anterolateral knob on each side. The hypantral facets are well developed and there is a deep slot dorsal to the hyposphene (Fig. 2.16D). The epipophyses are very small compared to those of other oviraptorosaurs.

Cervicodorsal vertebrae—Two of the cervicodorsal vertebrae (IVPP V16332.a and IVPP V16329.b) appear to be equivalent to the first cervicodorsal of *Avimimus portentosus* (MPC-D 100/129), whereas another (IVPP V16332.b) seems more similar to the last cervical, but lacks a pleurocoel and has a prominent hypapophysis. Accordingly, it is better categorized as a first cervicodorsal, rather than a cervical. Therefore, this avimimid appears to have three cervicodorsal vertebrae, and the first cervicodorsal of *Avimimus portentosus* is equivalent to the second cervicodorsal of this animal. The first cervicodorsal (IVPP V16332.b; Fig. 2.17A, B) has a rounded, bulbous, anteriorly projecting hypapophysis. Dorsolateral to the hypapophysis, there are rounded parapophyses with small foramina posterior to them. The articular face is moderately concave. The neurocentral suture is fused but still open. There are incipient infradiapophyseal fossae on the neural arch. One of the second cervicodorsal vertebrae (IVPP V16329.b) has a broken hypapophysis, whereas in the other (IVPP V16332.a; Fig. 2.17C, D) it is tab-like and prominent, with a rounded ventral edge. It projects slightly anteroventrally, but asymmetrically so, being directed more to the left side of the animal than the right (Fig. 2.17C),

47

which does not appear to be the result of post-burial deformation. The parapophyses are concave and sit on prominent laterally projecting mounds of bone. They vary in shape, being either circular or kidney-shaped. The anterior articular surface is slightly concave and the posterior articular surface is flat. There are no foramina in the centrum and the neurocentral sutures are closed in both specimens. Both specimens have infradiapophyseal and infrapostzygapophyseal fossae, but they are relatively deeper in IVPP V16332.a. In IVPP V16329.b, an extra fossa is situated on the ventrolateral surface of the postzygapophysis, and it is discontinuous with the infrapostzygapophyseal fossa. In both specimens, the neural spine is small, there is a deep slot posterior to it above the hyposphene, and there is an anteriorly facing pit between the hypantra. A third cervicodorsal (IVPP V16323.a) can be identified based on the presence of a small hypapophysis and large parapophyses on the centrum. It lacks most of the neural arch, but the neurocentral suture is closed.

Dorsal vertebrae—Six dorsal vertebrae (Fig. 2.17E–H) were collected and, although it is likely that they represent different regions of the back, none can be confidently identified to a specific position. All of the dorsal vertebrae lack lateral pleurocoels, and all but one have closed neurocentral sutures. Three of the vertebrae have parapophyses preserved, and in each case they are elongate and tear-drop shaped, extending across the neurocentral suture. These three vertebrae also have ventral keels, which indicates that they are from the anterior part of the dorsal column. One vertebra (IVPP V16318.b) has a complete neural arch but lacks parapophyses (Fig. 2.17G, H), indicating it is from the posterior part of the series. The neural arches of the remaining vertebrae are broken, but no parapophyses are present on the centra of these vertebrae, so they are likely from the middle or posterior part of the series. The dorsal vertebrae have infradiapophyseal and infrapostzygapophyseal fossae, the latter of which are

deeper (Fig. 2.17E). The neural spine is low, anteroposteriorly long, and square in lateral view. There is a deep slot anterior to the neural spine for the hypantrum-hyposphene contact, and a deep slot above the hyposphene.

Sacral vertebrae—Three partial sacra were recovered. One of these consists of a single, unfused sacral vertebra (IVPP V16328; Fig. 2.18A–D), whereas the others consist of two fused vertebrae. The latter specimens are both from the posterior end of the sacrum, based on the height and width of the centra and the positions of the sacral ribs. Of these, IVPP V16330 (Fig. 2.18E, F) is both larger and more complete, but also more poorly preserved. The centra lack ventral ridges or grooves, and none have lateral pleurocoels. The neurocentral sutures of the smaller specimen appear unfused and as a result, the neural arch is not preserved (Fig. 2.18B). The neural arch of the larger specimen is preserved but badly damaged, and the neurocentral suture is not visible. The isolated sacral vertebra (IVPP V16328) is from somewhere in the middle of the sacrum, based on the laterally deflected facets for the sacral ribs (Fig. 2.18A–D). The neural arch is missing and there is a clean neurocentral suture, indicating that the neural arch had not yet fused. Similarly, the articular surfaces of the centrum are complete, which indicates that this vertebra had not yet fused to the others in the sacrum. Combined with porous, striated bone texture, this suggests that this individual was young at the time of death. Numerous small foramina pierce the lateral sides of the centrum, but these probably reflect the young age of the individual rather than pneumatization of the vertebra.

Caudal vertebrae—The caudal vertebrae range in size and likely position, although none can be identified to an exact position. The more proximal vertebrae (Fig. 2.18H) have a distinct disparity in the locations of the articular faces: the posterior face is positioned further ventrally when both faces are oriented vertically. On some of the vertebrae, this disparity is

associated with a flat or grooved ventral surface of the centrum, whereas those with less disparity tend to be ventrally rounded. Invariably, the caudal vertebrae lack lateral pleurocoels and any pneumatic fossae on the neural arches. Where preserved, the transverse processes sweep posteriorly (Fig. 2.18K), which tends to be the case in oviraptorosaurs, except for the distal caudal vertebrae, where they are oriented transversely or anteriorly. The prezygapophyses are long and face medially. The postzygapophyses are short and the slot between them is reduced compared to the deep supra-hyposphenal slots of the dorsal vertebrae (Fig. 2.18I, L). The neural spine is relatively tall and located above the posterior half of the vertebra.

Appendicular skeleton:

Forelimb—A partial scapulocoracoid (IVPP V16327; Fig. 2.19A, B) consists of the distal scapula and a portion of the coracoid including the glenoid and biceps tubercle. The scapulocoracoid is completely fused and the suture is obliterated. The acromion process is small and projects laterally, but does not have a prominent facet for the furcula. The glenoid faces posteroventrally but is slightly exposed laterally, as is the case in many oviraptorosaurs. The coracoid has a large, knob-like biceps tubercle and is strongly curved posteroventrally. The coracoid foramen is broken (Fig. 2.19A), but based on the remaining edge, it was large and positioned directly dorsal to the biceps tubercle.

The humerus is represented solely by the proximal head (IVPP V16340), which is rounded and projects medially. The deltopectoral crest was apparently small, as in other avimimids, and appears to have been a small tubercle rather than a square, wing-like crest as in caenagnathids and oviraptorids.

50

A small distal end of a bone (IVPP V16343) is probably the distal end of the first metacarpal (Fig. 2.19C–H). The shaft is strongly compressed in the flexor-extensor plane, which matches the broken outline of metacarpal I of MPC-D 100/129. The presumable medial edge of the shaft is attenuated into a sharp crest, which creates a lens shaped cross-section in proximal view. The distal end of the metacarpal is highly unusual and asymmetrical compared to other oviraptorosaurs (Fig. 2.19C). The medial condyle has a modest ligament pit and is somewhat rounded, but not ginglymoid. The lateral condyle is about half of the size of the medial condyle and there is no articular groove separating them. The lateral condyle is slightly rounded and apparently had a small ligament pit with a posterior flange, although the latter structure is broken.

A small manual ungual (IVPP V16313.a; Fig. 2.19I–M) is clearly oviraptorosaur based on the relatively large flexor tubercle and a proximodorsal process. Its small size means that it may be referable to Avimimidae, but it is possible that it is from a small caenagnathid or oviraptorid. Unfortunately, much of the proximodorsal process is broken, and the proximal articular surface is worn away. The ungual is curved and the flexor tubercle is large but not rugose. There is a small posterior groove separating it from the proximal articular surface, which is also the case in some caenagnathids (Bell et al., 2015; Funston et al., 2015). The lateral vascular canal is broad and less well defined than the medial one, and neither bifurcates proximally. The distal end is missing.

Hindlimb—Two femoral heads (IVPP V16334) were collected, but they differ considerably. One can be identified as avimimid on the basis of a deep cleft between the anterior and greater trochanters (IVPP V16334.a; Fig. 2.20A–F). In the other specimen (IVPP V16334.b), these structures are fused, which suggests that it may be oviraptorid or, more likely,

dromaeosaur. The head of the avimimid femur projects medially and is somewhat spherical, with a distinct lip separating the articular bone from the underlying cortical bone. On the posterior side, there is a notch in the articular bone that extends into a groove on the head for the capitate ligament (Fig. 2.20E). The head is separated from the greater trochanter by a shallow sulcus but the entire proximal surface of the femur is formed of spongy epiphyseal bone. This region of articular bone wraps posteroventrally onto the posterior surface of the shaft until a point level with the ventral edge of the head. The greater trochanter is proximally curved and projects as far dorsally as the head. On the anteromedial side of the greater trochanter, there is a deep, pocket-like fossa (Fig. 2.20B). Posteriorly, the dorsal edge of the greater trochanter terminates in a rugose mound. On the lateral side of the shaft, level with the anteromedial fossa, there is a prominent tubercle, distal to which the shaft is flat, resulting in a posterior ridge. Only the base of the fingerlike anterior trochanter is preserved. It is separated from the greater trochanter by a wide cleft, like in *Caenagnathasia martinsoni* (Sues and Averianov, 2015) and *Microvenator celer* Ostrom 1970 (Makovicky and Sues, 1998). Distal to the medial head, there are two longitudinal ridges on the shaft of the femur that form a shallow groove (Fig. 2.20F). The distal end of a femur (IVPP V16338; Fig. 2.20G–L) is clearly avimimid, but is slightly unusual compared to *Avimimus nemegtensis* and *Avimimus portentosus*. The bone of the shaft is very thin-walled and rectangular in cross-section (Fig. 2.20K). The condyles do not flare as widely transversely as other avimimids, but they are similarly robust. The medial condyle is fairly typical for an oviraptorosaur, but has a rugose mound of bone on its anteromedial surface. The lateral condyle has an exceptionally large ectepicondylar tuber, like all avimimids, and is united with the crista tibiofibularis (Fig. 2.20J), which contrasts with those of other oviraptorosaurs. In

contrast to other avimimids, the condyles are separated distally by a deep groove, which is continuous with the deep popliteal fossa.

Five partial tibiae (Fig. 2.21) were recovered, three from the proximal end (IVPP V16322.a–c) and two from the distal end (IVPP V16320; IVPP V16337). Two of the proximal ends are from the left, and a larger one is from the right side. Unlike other avimimids, the femoral condyle projects posteriorly, which produces a triangular posterior process in medial view (Fig. 2.21C: ppr). The fibular condyle is large and bulbous (Fig. 2.21D), more reminiscent of the condition in *Avimimus portentosus* than the smaller fibular condyle of *Avimimus nemegtensis*. However, the groove separating the fibular condyle posteriorly from the rest of the condyle is much deeper, forming a distinct notch (Fig. 2.21E). The fibular condyle has two main bulbs, the posterior of which is larger (Fig. 2.21E). This condyle is larger, more bulbous, and taller dorsally in the larger specimen, which may be related to differences allometric growth. The same is true of the femoral condyle, except instead of becoming more bulbous, it expands medially. The incisura tibialis is semicircular and is relatively smaller in the larger specimen. The cnemial crest is anteroposteriorly small and proximally restricted (Fig. 2.21C), but robust and transversely thick (Fig. 2.21B). It has a rounded outline in lateral view, but in the smaller specimens cnemial crests are slightly squared off ventrally. The cnemial crest is everted laterally and thickens transversely towards its proximal end, where it is bulbous in anterior view. The larger of the two distal ends of the tibiae (IVPP V16337; Fig. 2.21F–H) is more complete and has fully fused with the astragalocalcaneum. In the smaller specimen (IVPP V16320; Fig. 2.21I–L), the astragalocalcaneum had begun to fuse distally, but the ascending process is free. Each of the tibiae has a flattened anterior surface which lacks a fibular ridge or groove. The postfibular flange is relatively well developed. In the larger, fused specimen, the fibula is visible fused to the

lateral surface of the tibiotarsus (Fig. 2.21H), as in other avimimids. The calcaneum is laterally concave and it is fused to the astragalus in both specimens, although a suture is visible in the smaller one. The astragalus covers the entire transverse surface of the tibia and has an anterior pit above the distal condyles. There is a small process of the astragalus that overlies the calcaneum in anterior view, as in most other oviraptorosaurs.

Numerous partial metatarsals were recovered (Fig. 2.22), all except one of which (IVPP V16335.a) appear to have been fused proximally. Two size classes are apparent in the metatarsal material. The largest specimens (IVPP V16314 and IVPP V16341) are from the right and left, respectively, and may belong to a single individual. An isolated proximal end of a left metatarsal II (IVPP V16321) is the same size. Two left second metatarsals (IVPP V16315 and IVPP V16326) are smaller, especially in the anteroposterior length of the proximal surface of the tarsometatarsus. The fused proximal metatarsus consists of metatarsals II, IV, and V, and distal tarsals III and IV (Fig. 2.22A–F). Metatarsal III apparently did not contribute to this fused unit, or, if it did, its contribution is minimal. Metatarsal II is larger than metatarsal IV, which appears to increase allometrically. A large bulbous boss on the posterior side of metatarsal II appears to be distal tarsal III, which wraps posteroventrally and is restricted anteriorly (Fig. 2.22C). This creates a concavity on the proximal articular surface of metatarsal II. Distal tarsal IV is small, but has a prominent proximodorsal process, which may be partly formed by metatarsal V. The shaft of metatarsal V extends ventrally from the proximodorsal process along the lateral edge of the tarsometatarsus (Fig. 2.22D). Metatarsal IV has a posterior protuberance similar to that formed by distal tarsal III, and together these form a distinct boss, albeit not as large as that of *Elmisaurus rarus*. The shafts of the metatarsals are not well preserved, but they appear to have been relatively straight until their distal ends. Posteromedial and posterolateral ridges on

metatarsal II and IV, respectively, create a posteriorly concave tarsometatarsus, but less so than in *Elmisaurus rarus* because these metatarsals contact each other posterior to metatarsal III. The small, isolated metatarsal IV (IVPP V16335.a; Fig. 2.22J–N) is fused to distal tarsal IV, but a clean, slightly concave articular surface for metatarsal II (Fig. 2.22M) indicates that it had not yet begun to coossify with the other metatarsals. Distal to the articular surface, there is a small depression and a rugose patch of bone, which together would hae formed a slit for *a. tarsalis plantaris*. On the posterior side of the metatarsal, there is a lateral ridge that contacted metatarsal V, which had not yet fused. Medial to this, there is a posterior protuberance (Fig. 2.22L) as in other oviraptorosaurs with fused tarsometatarsi.

Four distal ends of metatarsals are preserved, representing each metatarsal. A single distal end of metatarsal IV (IVPP V16336) was preserved, and it can be articulated with a left metatarsal III and II (IVPP V16335.b–c; Fig. 2.22G–I). The distal condyle of metatarsal II is larger than metatarsal IV. It has a deep lateral ligament pit and a small posterior spur that overhangs this pit slightly. The medial ligament pit is small and bordered posteriorly by a ridge. Metatarsal III has a ginglymoid articular condyle with a larger medial side than lateral side (Fig. 2.22I). The medial ligament pit is deeper, but both are well developed. The shaft is triangular in cross-section and its posterior ridge is rugose distally. Metatarsal IV has a large, rugose facet for metatarsal III and a modest posterolateral ridge. Distal to this ridge, a groove twists from the posterior side to the lateral side as it extends distally. The medial ligament pit is better developed and the condyles are small and transversely narrow.

Thirteen pedal unguals are attributable to an avimimid, but, curiously, no pedal phalanges were recovered. Two morphotypes are represented by the unguals: one is relatively symmetrical and gracile (n = 3; Fig. 2.23E–H), whereas the other is slanted and asymmetrical (n = 10; Fig.

2.23A–D). It is likely that the first morphotype corresponds to ungual III-4, whereas the asymmetrical unguals are from digits II or IV. However, whether each ungual represents ungual II-3 or IV-5 cannot be determined and the unguals are virtually identical. Ungual III-4 is gracile and relatively straight, rather than being curved. The proximal articular surface is teardrop shaped and asymmetrical in some specimens. The vascular grooves are low on the unguals and relatively even in height and depth. There is no flexor tubercle, but in its place there is sometimes a slot or foramen that varies in size and depth (Fig. 2.23F). Ten unguals are the II/IV morphotype. Of these, six slant leftwards in proximal view, and three are angled right. In each case, the direction of inclination corresponds to the side with the more dorsally situated vascular groove, which makes it difficult to tell if these are antimeres or from different digits. Each has a teardrop shaped articulation with a distinct ridge and a prominent posterodorsal process (Fig. 2.23A, D). The unguals are relatively straight in lateral view and have a series of pits, which probably anchored ligaments, in place of a flexor tubercle (Fig. 2.23B). The vascular grooves are prominent and the presumable external groove is lower when the tall axis of the claw is oriented vertically. When the ungual is oriented with its ventral surface horizontal, as in life, the vascular grooves become level with each other.

2.3.4 Histology of Iren Dabasu avimimids

Serial thin sections (Figs. 2.24–2.26) were made from two distal tibiotarsi collected from the bonebed (IVPP V16320, IVPP V16337). These specimens vary in the degree of fusion of the tibia and astragalocalcaneum, and therefore provide information about the mechanism and timing of fusion. As described previously, the astragalocalcaneum of the smaller specimen (IVPP

V16320) is fused distally to the tibia, but the ascending process is not fused. In contrast, these bones are completely and indistinguishably fused in the larger specimen (IVPP V16337), and this fused unit also includes the distal end of the fibula.

IVPP V16320 (Fig. 2.24)—The sections include the tibia and ascending process of the astragalus, but the fibula is not preserved. The tibia of this specimen is composed entirely of primary fibrolamellar bone, but the texture and vascularization vary considerably throughout the cortex. The medullary cavity is large and spanned by several trabeculae of primary bone. The endosteal surface is unfinished in most areas and scalloped Howship's lacunae indicate it was being actively resorbed in these areas. However, some parts of the endosteal margin, especially towards the lateral and posteromedial portions of the bone, have thin endosteal lamellae indicating secondary deposition (Fig. 2.24F). The vascularity of the cortex is highly disorganized, consisting of web-like, predominantly reticular vascular canals. Two notable exceptions are the anterior and posterior surfaces of the tibia, where vascular canals are more organized. On the anterior surface of the tibia (Fig. 2.24E), vascularization is reduced and canals are oriented longitudinally. In the posterior half of the tibia, vascular canals gradually change orientation towards the periosteal surface and become sub-plexiform in orientation. Osteons are moderately well developed and osteocyte lacunar density (~53,000/mm^3) is relatively consistent throughout the cortex. The ascending process of the astragalus is represented by a thin ribbon of bone that is separated from the tibia by a gap of approximately 100 μm. Like the tibia, it is composed entirely of primary fibrolamellar bone, but it differs considerably in vascular orientation. Towards the anterior and posterior edges of the astragalus, vasculature is reticular in orientation, but there is a narrow band in the middle of the bone where vasculature is oriented mostly radially (Fig. 2.24D). Three large vascular canals pierce the lateral part of the ascending

process. The largest evidently separated the tibia and astragalus, and it is lined by endosteal lamellae. Although it is clear that some of the separation between the astragalus and tibia is caused by expansion of post-depositional mineral infill, realigning the broken faces on either side indicates that there would still have been a gap between these bones in life. The bone at the interface of these two elements is unusual in that it has reduced vascularity and a somewhat granular texture under normal light (Fig. 2.24C). There is a clear delineation in colour and opacity between the bone of the tibia and a darker layer that separates it from the astragalus. In some areas, this dark layer appears acellular (Fig. 2.24C), although this may be an artifact of poor light transmission. This unusual tissue spans the gap between the tibia and astragalus in three main regions: at the lateral edge of the astragalus; medial to the largest lateral foramen; and about a quarter of the length of the astragalus from the medial edge, where the tissue is most prevalent. While it is possible that this material is simply mineral infilling, this seems unlikely for several reasons. First, it differs in mineralogical properties from other mineral infilling in the specimen. Second, it is continuous with the osteonal bone of the tibia and astragalus, rather than having a distinct border like the mineral infilling. Third, although it is acellular, it does not appear to be avascular, and several simple vascular canals can be found within the acellular matrix. Finally, in some areas it appears to be interspersed with osteonal bone, and in one area, this osteonal bone is separated from both the tibia and the astragalus by the acellular matrix (Fig. 2.24C).

IVPP V16337—Because more of IVPP V16337 was preserved, sections were made from both the distal end (Fig. 2.25), to elucidate the process of tibiotarsal fusion, and from the proximal end (Fig. 2.26). The latter is closer to the midshaft of the bone and therefore more useful for skeletochronology. The distal thin sections (Fig. 2.25) show the tibia, astragalus, and

fibula, all of which are fused into a single unit. Although the cortex is still predominantly composed of primary fibrolamellar bone, there is significantly more secondary remodelling than IVPP V16320. Unlike IVPP V16320, the entire medullary cavity is surrounded by endosteal lamellae, and anteriorly, these lamellae are thick and formed by multiple generations of deposition (Fig. 2.25F). The primary bone of the anterior part of the tibia has reticular vascularity, but the posterior surface of the tibia has plexiform–laminar vascularity and is primarily parallel-fibered bone (Fig. 2.25E). There is a stark, onlapping transition between these regions (Fig. 2.25E), which may represent the former posterior surface of the tibia. If this is the case, then there must have been significant cortical drift during growth and a significant change in growth style and rate. Osteocyte lacunae are relatively dense ($\sim$45,000/mm^3) throughout the cortex, but they are patchily distributed, because they are denser in the primary bone than the secondary osteons. The contact between the astragalus and tibia has extensive secondarily remodelling (Fig. 2.25C, D), and some of these areas are composed entirely of Haversian bone. In other areas, however, the intervening space between the secondary osteons is formed by either primary osteonal bone, or, more towards the astragalus, by parallel-fibered bone. Indeed, much of the bone of the astragalus is nearly avascular parallel-fibered bone (Fig. 2.25D). There is a notable transition in texture from the reticular fibrolamellar bone of the tibia to the less vascularized parallel-fibered bone of the astragalus. However, these two zones are abutting, rather than separated by a transitional tissue as in the smaller specimen. Like in IVPP V16320, a large vascular canal separates the tibia and astragalus towards the lateral edges of each bone. It is likely that this is the same structure as the former specimen, and it probably conducted nerves and vasculature towards the distal end of the tibiotarsus. No lines of arrested growth (LAGs) are visible in the cortex, although they could possibly have been obscured by secondary remodelling.

However, there is a distinct lineation separating two zones of plexiform vasculature on the posterior surface of the tibia (Fig. 2.25A, B), and it is possible that this represents a growth mark of some kind. Similarly, the onlapping contact between the zone of plexiform bone and reticular bone indicates a change in growth style, which suggests the passage of some time. Furthermore, vasculature is reduced at the periosteal surface of the bone, which is mostly parallel-fibered bone, indicating that growth had slowed significantly (Fig. 2.25E).

The more proximal section (Fig. 2.26) preserves mostly the tibia, and only small fragments of the fibula and ascending process of the astragalus are visible. Like the more distal section, there is significantly more remodelling of the cortex than the smaller specimen (IVPP V16320), and most of the tibia is composed of Haversian bone (Fig. 2.26A, B). Curiously, the secondary osteons are concentrated in a band that is separated from the endosteal surface by a region of primary bone with reticular vascularity (Fig. 2.26D); typically secondary remodelling proceeds from the endosteal surface outwards. The endosteal lamellae are well-formed and, anteriorly, are formed of multiple generations of deposition. As in the more distal section, the posterior surface of the tibia is composed entirely of primary parallel-fibered bone with reticular to plexiform vascularity (Fig. 2.26C, D). However, in contrast to further distally, this bone type encircles the entire periosteal surface, with the exception of the fibula and astragalus. Along the lateral and presumably medial surface (the latter is broken), this region of bone is much narrower and most of the cortex is formed by secondarily remodelled fibrolamellar bone. One LAG is visible in the region of parallel-fibered bone corresponding in position to the lineation in the more distal section (Fig. 2.26C). A second LAG may be preserved near the periosteal surface, but the surface is too damaged to trace it around the entirety of the bone. Regardless, the bone at

the periosteal surface is parallel-fibered and less vascularized, indicating a low rate of growth and possibly incipient development of an external fundamental system (Horner et al. 2011).

2.4 DISCUSSION

2.4.1 Morphology

The anatomy of *Avimimus* (Fig. 2.27) is unusual for oviraptorosaurs, and indeed for theropods in general. Kurzanov (1981, 1987) speculated on the skull structure of *Avimimus portentosus*, but more recent information about oviraptorosaurs (Vickers-Rich et al. 2002; Tsuihiji et al. 2017) suggests that his reconstructions are erroneous, particularly regarding the conjoined naris and antorbital fenestra. The new specimens described here improve our knowledge of the morphology of avimimids, especially in terms of their skull, forelimb, and caudal anatomy.

The skull of *Avimimus* (Fig. 2.6) is dorsoventrally tall and anteroposteriorly compressed, like those of many oviraptorosaurs. The orbit is exceptionally large compared to other oviraptorosaurs, and the preorbital part of the skull is significantly reduced. Regardless, it is clear that avimimids share the basic structure of the skull with other oviraptorosaurs, despite numerous specializations. No evidence exists for a cranial crest in avimimids, although the unusual frontal from the Iren Dabasu Formation (Fig. 2.15) may eventually prove to have participated in a crest. The premaxilla is dorsoventrally tall and has a denticulate tomial margin. The nasals were fused but lacked pneumatic pitting, contrasting with more derived oviraptorosaurs (Fig. 2.5). They arched dorsally and enclosed a large, elongate external naris. The jugal is thin and rodlike, and, at least in *Avimimus nemegtensis*, contacted the postorbital as in all oviraptorosaurs (Tsuihiji et

al., 2017). The bones of the neurocranium, including the postorbital, frontal, parietal, squamosal, quadrate, quadratojugal, and braincase, were indistinguishably fused into a single unit (Fig. 2.7). Like most oviraptorosaurs (Balanoff et al., 2014, 2018), the brain was relatively large and had a well developed flocculus. The palate is poorly known, but the pterygoids were transversely broad. The mandibular condyles of the quadrate allowed propalinal movement of the jaw, which is also the case in all other oviraptorosaurs (Balanoff et al., 2009; Funston and Currie, 2014b). The mandible is low but is typically oviraptorosaur in that it is composed of two fused units: the dentaries and the articular-surangular-coronoid complex. The dentaries are completely fused without a suture, and have an incipient symphysial shelf. There are shallow lingual ridges on the occlusal surface and a ventrally tapering buttress on the posterior surface. The lateral surface has numerous small foramina and a lateral depression that corresponds to the mandibular fossa (Funston and Currie, 2014b) but is not as pronounced.

Unlike most oviraptorosaurs, the caudal vertebrae (Figs. 2.1, 2.18) lack lateral pleurocoels, but they are barrel-shaped, rather than elongate as in other theropods. The articular faces of the proximal caudal vertebrae are offset so that the tail would have sloped ventrally at its base. The distal caudal vertebrae are small and barrel-shaped, but are not fused into a pygostyle (Fig. 2.11), which contrasts with those of oviraptorids and presumably caenagnathids. The length of the tail is unknown, but previous suggestions that avimimids lacked or had a highly reduced tail (Kurzanov, 1987) are unsupported.

The scapulocoracoid is completely fused and relatively large (Figs. 2.10, 2.19). The scapula is straplike and expands at its distal end, a feature which is variable in other oviraptorosaurs (Osmólska et al., 2004b; Funston et al., 2018a). The glenoid faces posteroventrally and the acromion is small and laterally everted. The coracoid is large and has a

well developed biceps tubercle directly ventral to the coracoid foramen. The posteroventral

process is strongly curved and the anterior portion of the coracoid is expanded and winglike. The

humerus has a reduced deltopectoral crest that forms an arc rather than a square flange. The

distal condyles are poorly developed and there is no ectepicondylar tuber. The ulna is bowed

ventrally and has an attenuated ventral edge that likely anchored a pennibrachium. The radius is

straight and featureless. The fused carpometacarpus comprises the metacarpals, semilunate

carpal, and probably the intermedium and ulnare, but apparently not the radiale. Metacarpal I

(Fig. 2.19) is compressed along the flexor-extensor plane, and has an unusual distal condyle that

likely indicates restricted mobility. The only known manual phalanx (Fig. 2.10) is unusual in that

the proximal articulation faces dorsally, but a manual ungual from the Iren Dabasu Formation

bonebed (Fig. 2.19) is relatively typical for an oviraptorosaur.

2.4.2 Taxonomy

Tsuihiji et al. (2017) described the cranium and mandible of a relatively complete

skeleton (MPC-D 100/125) from Bugiin Tsav (Watabe et al., 2010b), under the assumption it

was conspecific with *Avimimus portentosus*. Their description, however, highlighted several

differences between their material and the holotype of *Avimimus portentosus*, including the

relatively smaller foramen magnum and the hollow premaxilla (Fig. 2.8). Instead, the cranial

anatomy of MPC-D 100/125 (Tsuihiji et al. 2017) is identical to material recovered from the

avimimid bonebed at Nemegt (Funston et al., 2016b), rather than the holotype of *Avimimus*

portentosus. This material was split into a new species of *Avimimus* by Funston et al. (2018a).

This species, *Avimimus nemegtensis,* is known primarily from a bonebed, which allowed for

characterization of intraspecific variation. Reexamination of the bonebed material revealed

several anatomical differences from *Avimimus portentosus* throughout the skeleton, most notably in the neurocranium and pelvis. The ilium of *Avimimus nemegtensis* is plesiomorphic, and lacks the unusual specializations that distinguish *Avimimus portentosus* from most other oviraptorosaurs (Fig. 2.8). This is consistent between both specimens from the bonebed and both known ilia of *Avimimus portentosus* (MPC-D 100/129 and PIN 3907-5). Beyond the skeleton described by Watabe et al. (2010) and Tsuihiji et al. (2017), some other undescribed material of *Avimimus* is known from the Nemegt Formation. It is likely that most of this material is referable to *Avimimus nemegtensis*, but this will need to be confirmed on a case-by-case basis.

Unambiguous *Avimimus portentosus* material is only known from localities farther east (Shar Tsav and Udyn Sayr; Watabe et al. 2010), and the delineation of at least two species of *Avimimus* has implications for the biostratigraphy of these eastern Gobi localities. Watabe et al. (2006) suggested that, because of the abundance of *Avimimus portentosus* remains at Yagan Khovil, the type site was probably mistaken with the nearby Udan Sayr. Furthermore, they hypothesized that, based on the shared presence of avimimids at Shar Tsav, Yagan Khovil, and sites in the Nemegt Formation further west, that the former two localities were Nemegtian in age. The taxonomic separation of avimimids from the Nemegt Formation and the sites further east invalidates their use for biostratigraphy, especially because avimimids are also known from probable Djadokhta-equivalent beds in the Iren Dabasu Formation of China (Currie and Eberth, 1993; Ryan et al., 2001). Like *Avimimus nemegtensis*, this material is known primarily from a single bonebed, with a minimum of five individuals based on metatarsals. This site was originally discovered by a Russian expedition in 1959, which used bulldozers to excavate the site. It was revisited in 1987 and 1988 by the Sino-Canadian expedition and numerous fragmentary bones were recovered from the spoil piles left by the Russian bulldozers.

Unfortunately, the material collected by the Russians still awaits preparation and it may never be available for study.

The material from the Iren Dabasu Formation shows several differences from either *Avimimus portentosus* or *Avimimus nemegtensis*. The dorsally arched frontal (Fig. 2.15) with a deep slot for the nasal is unusual, and compares poorly to those of the former taxa. In *Avimimus* spp., the frontals are transversely wide and bulbous dorsally, with small facets for the nasal. Although it is possible that the frontal from the Iren Dabasu Formation bonebed is from another oviraptorosaur, the most parsimonious option is that it is an unusual avimimid. This is supported by other differences in the skeleton. For example, the cervicodorsal vertebrae differ in both number (three with hypapophyses) and morphology from those of *Avimimus* (Figs. 2.1, 2.17). The distal condyles of the femur (Fig. 2.20) are separated much more deeply than is typical in avimimids, and metatarsals II and IV (Fig. 2.22) are much more disparate in size. Unfortunately, the material from the Iren Dabasu bonebed is too incomplete to confidently erect a new taxon, but future preparation of the Russian material (or collection of new material) may result in its taxonomic distinction from other avimimids.

2.4.3 Growth

The tibiotarsi from Iren Dabasu provide information about the growth of avimimids and the process of tibiotarsal fusion. Despite the onset of fusion of the tibia and astragalocalcaneum in IVPP V16320, numerous lines of evidence suggest it was a young, rapidly growing animal. The absence of growth marks suggests that the animal was less than one year old at the time of death, especially considering that secondary remodelling, which could have obscured growth marks, is limited (Fig. 2.24). However, the endosteal margin was clearly subjected to resorption,

as shown by the scalloped Howship's lacunae and the deposition of endosteal lamellae in some areas (Fig. 2.24F). Therefore, it is conceivable that a growth mark has been removed by expansion of the medullary cavity and thus, this individual is best considered as a juvenile less than two years old. The predominance of reticular vasculature indicates that this individual was growing quickly, similar to other young oviraptorosaurs (Funston and Currie, 2018). The unusual acellular bone separating the tibia and astragalus (Fig. 2.24C) probably resulted from polarized deposition of extracellular matrix during direct osteogenesis. It is likely that, after initial endochondral ossification, osteoprogenitor cells from the periosteum of both the tibia and astragalus migrated toward each other, beginning an intramembranous ossification event. Although unusual later in life, a similar process is responsible for much of the pre-hatching circumferential growth of the limbs in avians (Padian and Lamm, 2013). The movement of these cells away from the deposition of osteoid meant that they did not become trapped in the mineralized matrix. However, once these cell populations reached each other, they could no longer evade mineralization, which resulted in two thin bands of acellular bone separated by primary osteonal bone (Fig. 2.24C). This provided a mechanism for rapidly fusing the two bones by ossifying the intervening tissue rather than secondarily remodelling the interface between the elements.

IVPP V16337 (Figs. 2.25, 2.26) reveals aspects of growth after fusion of the tibiotarsus is complete. The absence of parallel-fibered bone in IVPP V16320 (Fig. 2.24) suggests that the unusual, onlapping posterior region of parallel-fibered bone in IVP V16337 was deposited after fusion of the tibiotarsus was complete. The area where it contacts the primary fibrolamellar bone with reticular vascularity (Fig. 2.26D) was probably the posterior edge of the tibia when fusion was completed. Accordingly, considerable cortical drift must have occurred, as this contact has

been eroded in places by the medullary cavity. The cortical drift is probably caused by restriction

of anterior growth by the fused astragalus, which is formed of slow growing parallel-fibered

bone (Fig. 2.25D). Because the tibia could not grow anteriorly, the medullary cavity expanded

only posteriorly, to avoid resorbing the ascending process of the astragalus. Instead of growing

outwards, the interface of the tibia and astragalus remodelled (Fig. 2.25C, D), and new bone was

deposited solely on the posterior surface of the tibia (Figs. 2.25E, 2.26C, D), as recorded by the

zone of parallel-fibered bone. Fusion also explains the reduced thickness of this zone of new

growth on the medial and lateral sides of the tibiotarsus (Fig. 2.26D). Fusion of the tibiotarsus

and tarsometatarsus would have restricted the maximum transverse dimensions of these elements

by fixing the proportions of the ankle joint. Accordingly, less bone was deposited on the

transverse edges of the tibia, and the posterior surface became the primary area for cortical

expansion to compensate for increasing body mass. The growth record of the individual is

therefore recorded in the combination of the primary fibrolamellar region and the subsequently

deposited parallel-fibered region. Because at least one LAG is preserved in the latter zone (Fig.

2.26C), this individual was at least one year older than IVPP V16320, perhaps as old as four

years.

Together, these specimens elucidate the growth patterns of avimimids. Growth was

initially rapid and juveniles approached maximum body size within one or two years. At this

point, fusion of the tibiotarsus occurred, presumably in conjunction with fusion elsewhere in the

skeleton. It is possible that sexual maturity was attained as well, because growth after this point

was much slower. Cortical growth in the tibiotarsus shifted from expanding uniformly in all

directions to solely increasing the anteroposterior thickness of the bone by deposition of parallel-

fibered bone on the posterior surface of the tibia (Fig. 2.26B). Accordingly, body mass was

likely still increasing, accommodated for by anteroposterior expansion of the tibiotarsus, but it is unlikely that the linear dimensions of the hindlimb or animal increased appreciably. This appears to be evident in the material collected from the *Avimimus nemegtensis* bonebed at Nemegt, where fused tibiotarsi vary in length by less than 10% (Funston et al., 2016b). Although achieved by different means, this process would have effectively resulted in determinate growth like in birds, mammals, and presumably many dinosaurs. Why avimimids limited growth in this way is unclear, but one clue may be found in the absence of extensive pneumatism of the vertebrae. Unlike other oviraptorosaurs, avimimids lack lateral pleurocoels in the post-cervical vertebrae (Figs. 2.1, 2.16–2.18), which suggests that they lacked the associated thoracic, sacral, and caudal air sacs. This may have limited the maximum body size at which intense aerobic activity was still possible. As highly cursorial animals, it is possible that behavioural constraints meant avimimids could not achieve large body sizes. Fusion of the hindlimb bones would have also had a beneficial effect on their cursorial ability (Snively et al., 2004), and limiting body size could have reduced the effects of negative allometry of the hindlimb that are prevalent in other theropods.

2.5 CONCLUSIONS

The specimens described here provide new insights into the anatomy, diversity, and growth of avimimid oviraptorosaurs. New elements of the skull, tail, and forelimb fill the gaps in our knowledge of these regions and solidify the oviraptorosaurian affinities of avimimids. More abundant material has led to the recognition of separate taxa from the eastern and western Gobi,

which raises doubts about their use for biostratigraphy. A new avimimid bonebed from China

supports widespread gregarious behaviour in these animals and shows some morphological

differences from other known avimimids. Histological analysis of tibiotarsi from the site reveals

the pattern of ankle fusion in avimimids and suggests that this phenomenon was linked to

determinate growth.

2.6 LITERATURE CITED

Balanoff, A. M., and M. A. Norell. 2012. Osteology of *Khaan mckennai* (Oviraptorosauria:

Theropoda). Bulletin of the American Museum of Natural History 372:1–77.

Balanoff, A. M., G. S. Bever, and M. A. Norell. 2014. Reconsidering the Avian Nature of the

Oviraptorosaur Brain (Dinosauria: Theropoda). PLoS ONE 9:e113559.

Balanoff, A. M., M. A. Norell, A. V. C. Hogan, and G. S. Bever. 2018. The Endocranial Cavity

of Oviraptorosaur Dinosaurs and the Increasingly Complex, Deep History of the Avian

Brain. Brain, Behavior and Evolution 91:125–135.

Balanoff, A. M., X. Xu, Y. Kobayashi, Y. Matsufune, and M. A. Norell. 2009. Cranial Osteology

of the Theropod Dinosaur *Incisivosaurus gauthieri* (Theropoda: Oviraptorosauria).

American Museum Novitates 3651:1–35.

Bell, P. R., P. J. Currie, and D. A. Russell. 2015. Large caenagnathids (Dinosauria,

Oviraptorosauria) from the uppermost Cretaceous of western Canada. Cretaceous

Research 52:101–107.

Chatterjee, S. 1991. Cranial anatomy and relationships of a new Triassic bird from Texas. Philosophical Transactions of the Royal Society of London. Series B: Biological Sciences 332:277–346.

Clark, J. M., M. a. Norell, and T. Rowe. 2002. Cranial Anatomy of *Citipati osmolskae* (Theropoda, Oviraptorosauria), and a Reinterpretation of the Holotype of *Oviraptor philoceratops*. American Museum Novitates 3364:1–24.

Currie, P., G. Funston, and H. Osmolska. 2016. New specimens of the crested theropod dinosaur *Elmisaurus rarus* from Mongolia. Acta Palaeontologica Polonica 61:143–157.

Currie, P. J., and D. A. Eberth. 1993. Palaeontology, sedimentology and palaeoecology of the Iren Dabasu Formation (Upper Cretaceous), Inner Mongolia, People's Republic of China. Cretaceous Research 14:127–144.

Currie, P. J., N. R. Longrich, M. J. Ryan, D. A. Eberth, and D. Badamgarav. 2008. A bonebed of *Avimimus* sp. (Dinosauria: Theropoda) from the Late Cretaceous Nemegt Formation, Gobi Desert: insights into social behaviour and development in a maniraptoran theropod. Journal of Vertebrate Paleontology 28:67A.

Funston, G. F., and P. J. Currie. 2014. A previously undescribed caenagnathid mandible from the late Campanian of Alberta, and insights into the diet of Chirostenotes pergracilis (Dinosauria: Oviraptorosauria). Canadian Journal of Earth Sciences 51:156–165.

Funston, G. F., and P. J. Currie. 2016. A new caenagnathid (Dinosauria: Oviraptorosauria) from the Horseshoe Canyon Formation of Alberta, Canada, and a reevaluation of the relationships of Caenagnathidae. Journal of Vertebrate Paleontology 36:e1160910.

Funston, G. F., and P. J. Currie. 2018. A small caenagnathid tibia from the Horseshoe Canyon

    Formation (Maastrichtian): Implications for growth and lifestyle in oviraptorosaurs.

    Cretaceous Research 92:220–230.

Funston, G. F., P. J. Currie, and M. Burns. 2016a. New elmisaurine specimens from North

    America and their relationship to the Mongolian *Elmisaurus rarus*. Acta Palaeontologica

    Polonica 61:159–173.

Funston, G. F., W. S. Persons, G. J. Bradley, and P. J. Currie. 2015. New material of the large-

    bodied caenagnathid *Caenagnathus collinsi* from the Dinosaur Park Formation of

    Alberta, Canada. Cretaceous Research 54:179–187.

Funston, G. F., S. E. Mendonca, P. J. Currie, and R. Barsbold. 2018. Oviraptorosaur anatomy,

    diversity and ecology in the Nemegt Basin. Palaeogeography, Palaeoclimatology,

    Palaeoecology 494: 101–120.

Funston, G. F., P. J. Currie, D. A. Eberth, M. J. Ryan, T. Chinzorig, D. Badamgarav, and N. R.

    Longrich. 2016b. The first oviraptorosaur (Dinosauria: Theropoda) bonebed: evidence of

    gregarious behaviour in a maniraptoran theropod. Scientific Reports 6:35782.

Hutchinson, J. 2001. The evolution of pelvic osteology and soft tissues on the line to extant birds

    (Neornithes). Zoological Journal of the Linnean Society 131:123–168.

Kurzanov, S. M. 1981. An unusual theropod from the Upper Cretaceous of Mongolia. Joint

    Soviet Mongolian Paleontological Expedition 15:39–49.

Kurzanov, S. M. 1982. Structural characteristics of the forelimbs of *Avimimus*. Paleontological

    Journal 3:108–112 [In Russian].

Kurzanov, S. M. 1983. New data on the pelvic structure of *Avimimus*. Paleontological Journal

    4:115–116 [In Russian].

Kurzanov, S. M. 1985. The skull structure of the dinosaur *Avimimus*. Paleontological Journal 4:81–89 [In Russian].

Kurzanov, S. M. 1987. Avimimidae and the problem of the origin of birds. Transactions of the Joint Soviet Mongolian Paleontological Expedition 31:1–92. [In Russian]

Lamanna, M. C., H.-D. Sues, E. R. Schachner, and T. R. Lyson. 2014. A New Large-Bodied Oviraptorosaurian Theropod Dinosaur from the Latest Cretaceous of Western North America. PLoS ONE 9:e92022.

Lü, J., R. Chen, S. L. Brusatte, Y. Zhu, and C. Shen. 2016. A Late Cretaceous diversification of Asian oviraptorid dinosaurs: evidence from a new species preserved in an unusual posture. Scientific Reports 6:35780.

Lü, J., P. J. Currie, L. Xu, X. Zhang, H. Pu, and S. Jia. 2013. Chicken-sized oviraptorid dinosaurs from central China and their ontogenetic implications. Naturwissenschaften 100:165–175.

Makovicky, P. J., and H.-D. Sues. 1998. Anatomy and phylogenetic relationships of the theropod dinosaur *Microvenator celer* from the Lower Cretaceous of Montana. American Museum Novitates 3240:1–27.

Maryanska, T., H. Osmólska, and M. Wolsan. 2002. Avialan status for Oviraptorosauria. Acta Palaeontologica Polonica 47.

Norell, M. A., J. M. Clark, and L. M. Chiappe. 2001. An Embryonic Oviraptorid (Dinosauria: Theropoda) from the Upper Cretaceous of Mongolia. American Museum Novitates 3315:1–20.

Norman, D. B. 1990. Problematic Theropoda: "Coelurosaurs"; pp. 280–305 in D. B. Weishampel, P. Dodson, and H. Osmólska (eds.), The Dinosauria, 1st ed. University of California Press, Berkeley.

Osmólska, H., P. J. Currie, and R. Barsbold. 2004. Oviraptorosauria; pp. 165–183 in D. B. Weishampel, P. D. Dodson, and H. Osmolska (eds.), The Dinosauria, 2nd Edition. University of California Press.

Padian, K., and E.-T. Lamm. 2013. Bone Histology of Fossil Tetrapods: Advancing Methods, Analysis, and Interpretation. University of California Press, Berkeley, 285 pp.

Qiang, J., P. J. Currie, M. A. Norell, and J. Shu-An. 1998. Two feathered dinosaurs from northeastern China. Nature 393:753–761.

Romer, A. S. 1923. The ilium in dinosaurs and birds. Bulletin of the AMNH; v. 48, article 5. .

Ryan, M. J., P. J. Currie, and A. P. Russell. 2001. New material of *Avimimus portentosus* from the Iren Dabasu Formation (Upper Cretaceous) of the Erenhot region of Inner Mongolia. Journal of Vertebrate Paleontology 21:95A.

Senter, P. 2007. A new look at the phylogeny of coelurosauria (Dlnosauria: Theropoda). Journal of Systematic Palaeontology 5:429–463.

Snively, E., A. P. Russell, and G. L. Powell. 2004. Evolutionary morphology of the coelurosaurian arctometatarsus: descriptive, morphometric and phylogenetic approaches. Zoological Journal of the Linnean Society 142:525–553.

Sues, H.-D., and A. Averianov. 2015. New material of *Caenagnathasia martinsoni* (Dinosauria: Theropoda: Oviraptorosauria) from the Bissekty Formation (Upper Cretaceous: Turonian) of Uzbekistan. Cretaceous Research 54:50–59.

Thulborn, R. A. 1984. The avian relationships of *Archaeopteryx*, and the origin of birds. Zoological Journal of the Linnean Society 82:119–158.

Tsuihiji, T., L. M. Witmer, M. Watabe, R. Barsbold, K. Tsogtbaatar, S. Suzuki, and P. Khatanbaatar. 2017. New information on the cranial morphology of *Avimimus* (Theropoda: Oviraptorosauria). Journal of Vertebrate Paleontology e1347177.

Turner, A. H., P. J. Makovicky, and M. A. Norell. 2012. A Review of Dromaeosaurid Systematics and Paravian Phylogeny. Bulletin of the American Museum of Natural History 371:1–206.

Vickers-Rich, P., L. M. Chiappe, and S. M. Kurzanov. 2002. The enigmatic birdlike dinosaur *Avimimus portentosus*, comments and a pictorial atlas; pp. 65–86 in L. M. Chiappe and L. M. Witmer (eds.), Mesozoic Birds, Above the Heads of Dinosaurs. University of California Press, Berkeley, California.

Wang, S., S. Zhang, C. Sullivan, and X. Xu. 2016. Elongatoolithid eggs containing oviraptorid (Theropoda, Oviraptorosauria) embryos from the Upper Cretaceous of Southern China. BMC Evolutionary Biology 16.

Watabe, M., S. Suzuki, and K. Tsogtbaatar. 2006. Geological and geographical distribution of bird-like theropod, *Avimimus* in Mongolia. Journal of Vertebrate Paleontology 26:136–137A.

Watabe, M., K. Tsogtbaatar, S. Suzuki, and M. Saneyoshi. 2010a. Geology of dinosaur-fossil-bearing localities (Jurassic and Cretaceous: Mesozoic) in the Gobi Desert: Results of the HMNS-MPC Joint Paleontological Expedition. Hayashibara Museum of Natural Sciences Research Bulletin 3.

Watabe, M., D. B. Weishampel, R. Barsbold, K. Tsogtbaatar, and S. Suzuki. 2000. New nearly complete skeleton of the bird-like theropod, *Avimimus*, from the Upper Cretaceous of the Gobi Desert, Mongolia. Journal of Vertebrate Paleontology 20:77A.

Watabe, M., S. Suzuki, K. Tsogtbaatar, T. Tsubamoto, and M. Saneyoshi. 2010b. Report of the HMNS-MPC Joint Paleontological Expedition in 2006. Hayashibara Museum of Natural Sciences Research Bulletin 3:11–18.

Weishampel, D. B., D. E. Fastovsky, M. Watabe, D. Varricchio, F. Jackson, K. Tsogtbaatar, and R. Barsbold. 2008. New oviraptorid embryos from Bugin-Tsav, Nemegt Formation (Upper Cretaceous), Mongolia, with insights into their habitat and growth. Journal of Vertebrate Paleontology 28:1110–1119.

Zanno, L. E., and S. D. Sampson. 2005. A new oviraptorosaur (Theropoda, Maniraptora) from the Late Cretaceous (Campanian) of Utah. Journal of Vertebrate Paleontology 25:897–904.

2.7 FIGURES

Fig. 2.0. Map of eastern Asia illustrating localities where avimimids have been found.
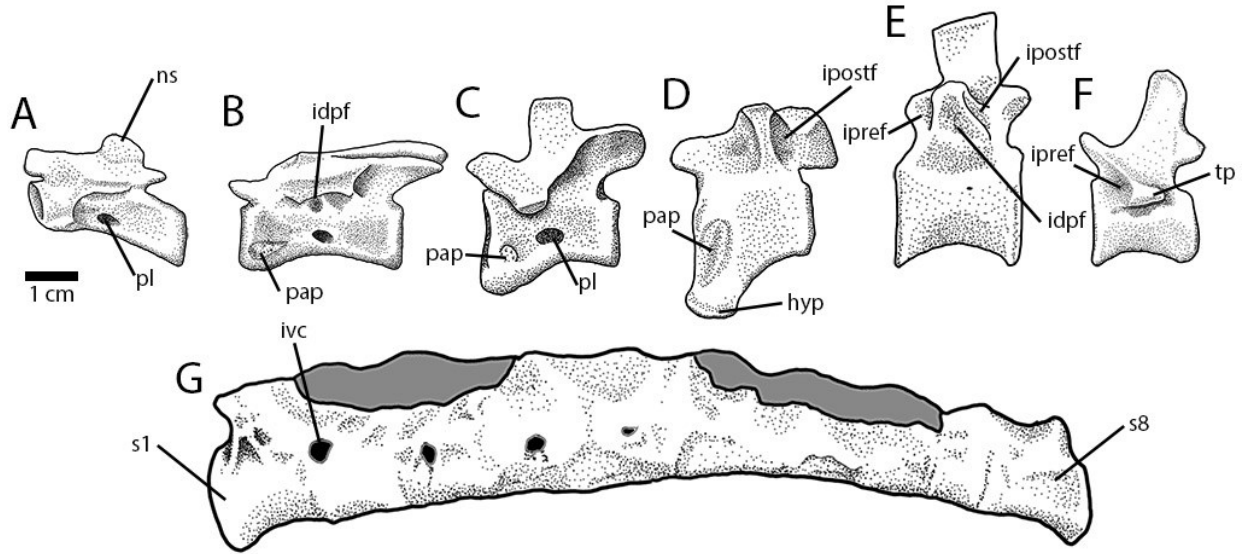
Fig. 2.1. Vertebrae of *Avimimus portentosus* (MPC-D 100/129).

Reconstructed anterior cervical (A), mid-cervical (B), and posterior cervical (C) in lateral view.

Reconstructed first cervicodorsal (D) in lateral view. Posterior dorsal (E) in lateral view.

Anterior caudal (F) in lateral view. Sacrum (G) in lateral view, shaded areas are missing. Scale

applies to all images. **Abbreviations: hyp,** hypapophysis; **idpf,** infradiapophyseal fossa; **ipostf**,

infrapostzygapophyseal fossa; **ipref**, infraprezygapophyseal fossa; **ivc**, intravertebral canal; **ns**,

neural spine; **pap**, parapophysis; **pl**, pleurocoel; **s1**, sacral 1, **s8**, sacral 8; **tp**, transverse process.
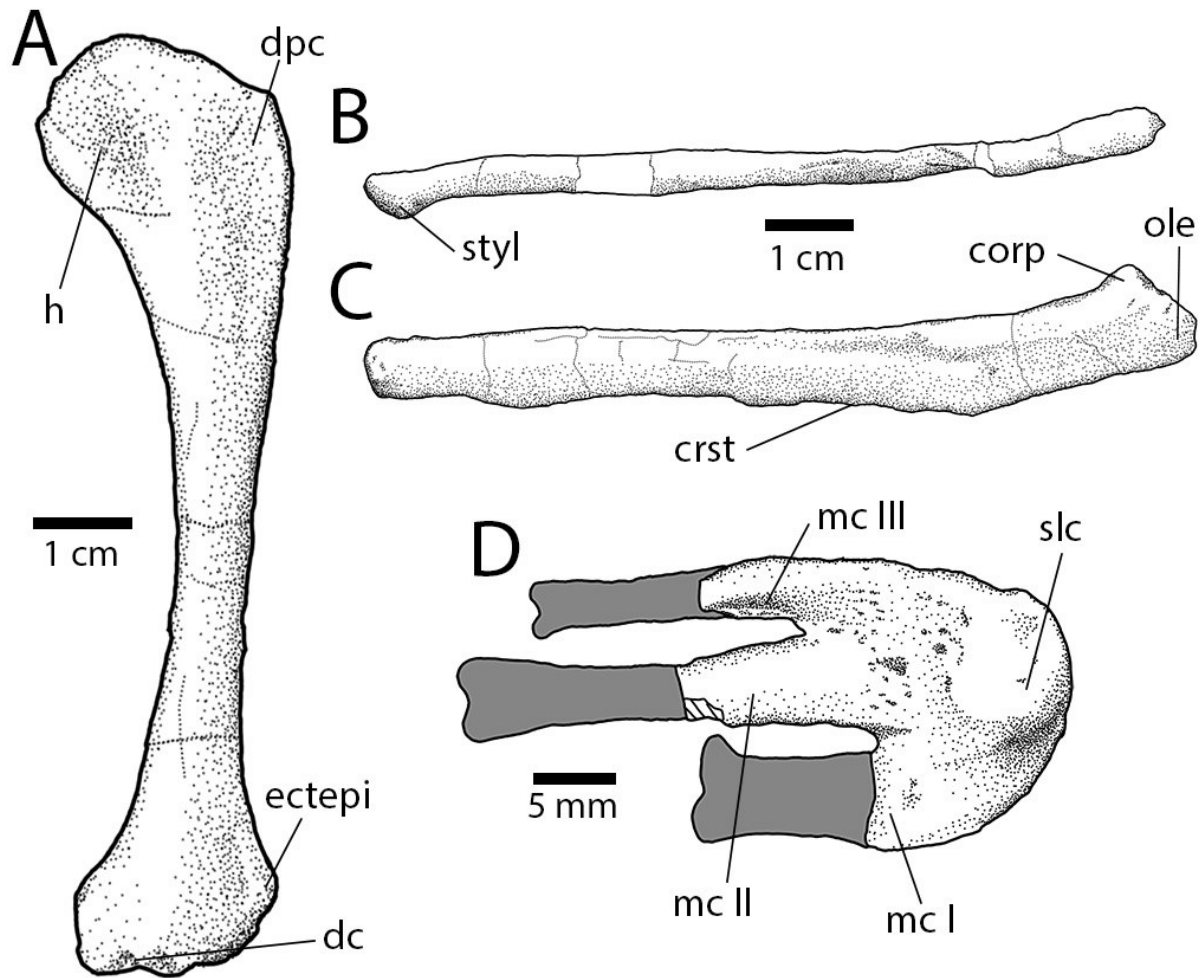
Fig. 2.2. Forelimb material of *Avimimus portentosus* (MPC-D 100/129).

Left humerus (A) in anterior view. Left radius (B) and ulna (C) in lateral view. Right carpometacarpus (D) in extensor (lateral) view, shaded areas are missing. **Abbreviations: crst**, crest; **corp**, coronoid process; **dc**, distal condyles; **dpc**, deltopectoral crest; **ectepi,** ectepicondylar tuber; **h**, head; **mc I**, metacarpal I; **mc II**, metacarpal II; **mc III**, metacarpal III; **ole**, olecranon process; **slc**, semilunate carpal; **styl**, styloid process.
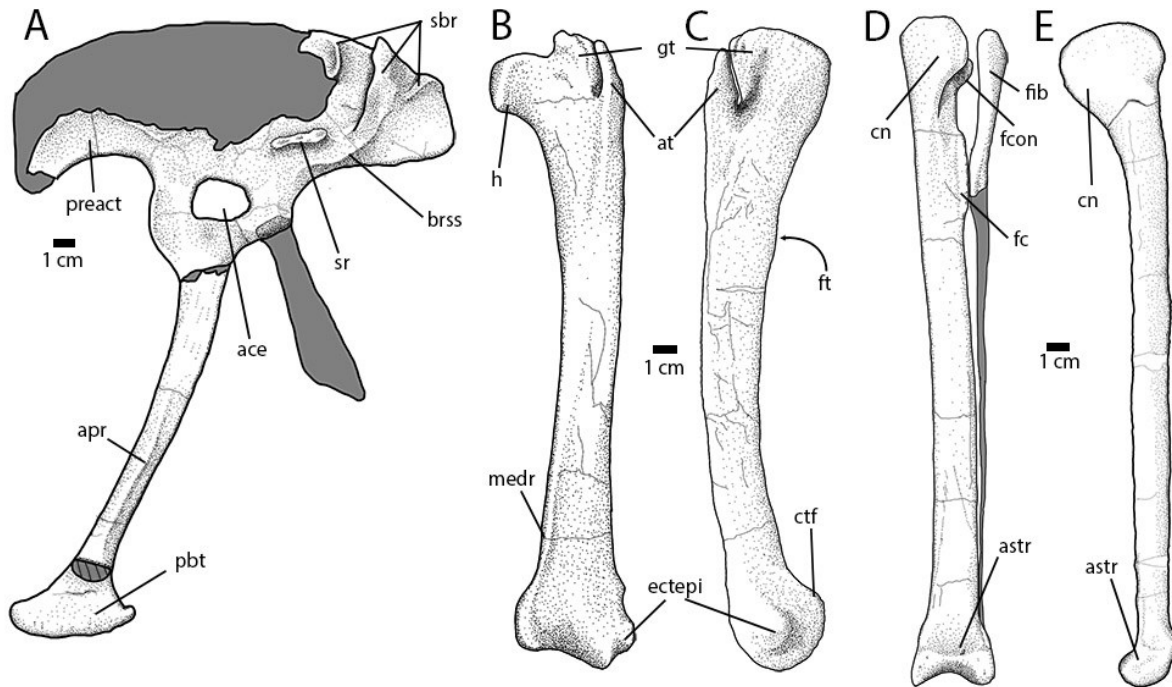
Fig. 2.3. Pelvis and proximal hindlimb elements of *Avimimus portentosus* (MPC-D 100/129).
Reconstructed right pelvis (A) in medial view. Left femur in anterior (B) and lateral (C) views.
Left tibia in anterior (D) view. Right tibia in medial (E) view. Shaded portions are missing.
Abbreviations: ace, acetabulum; **apr,** pubic apron; **astr,** astragalus; **at**, anterior trochanter; **brss**,
brevis shelf; **ctf**, crista tibiofibularis; **cn**, cnemial crest; **ectepi**, ectepicondylar tuber; **fc**, fibular
crest; **fcon**, fibular condyle; **ft**, fourth trochanter; **gt**, greater trochanter; **h**, head; **medr**, medial
ridge; **pbt**, pubic boot; **preact**, preacetabular process; **sbr**, suprabrevis ridges; **sr**, sacral rib.
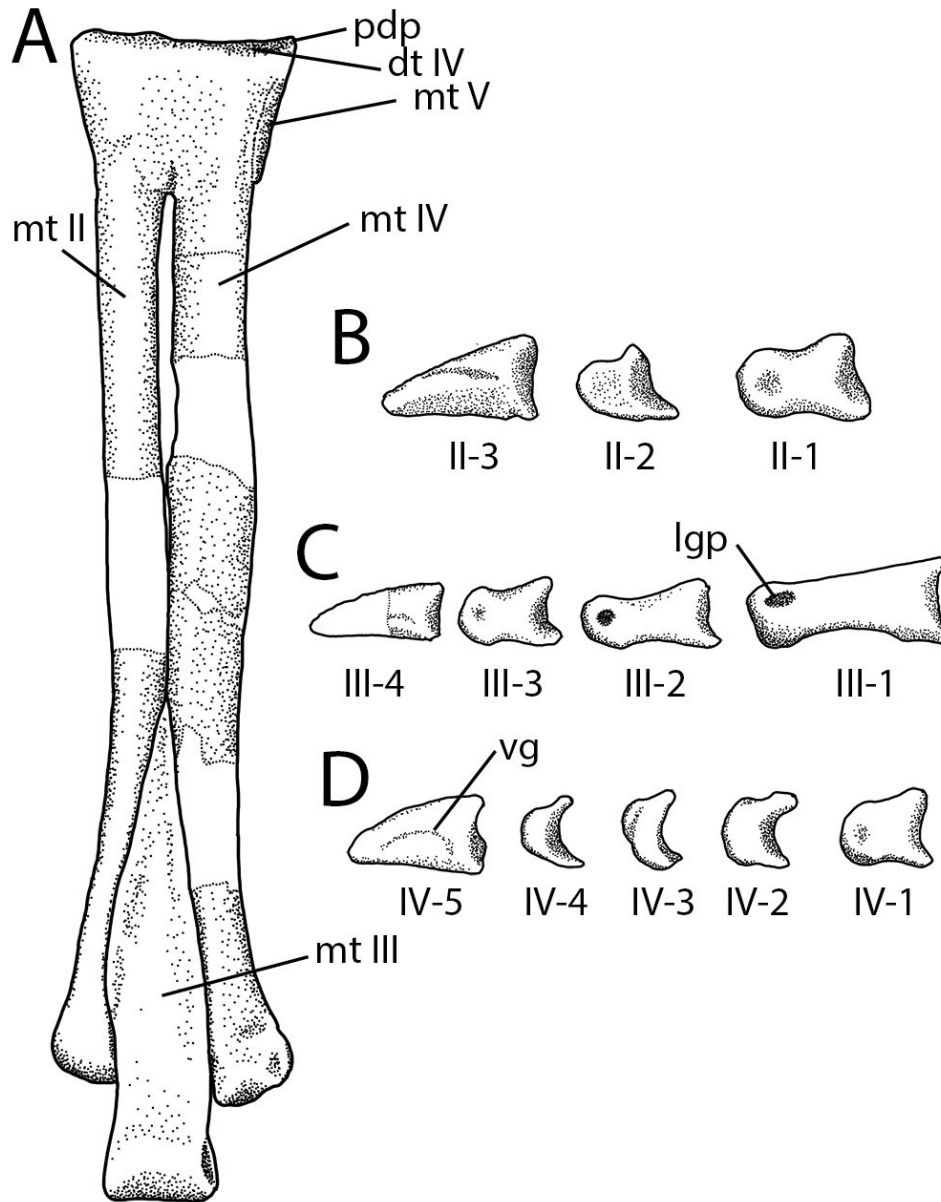
Fig. 2.4. Pedal material of *Avimimus portentosus* (MPC-D 100/129).

Left tarsometatarsus in anterior (A) view. Pedal digit II in lateral (B) view. Pedal digit III in lateral (C) view. Pedal digit IV in medial (D) view. Unshaded areas are reconstructed. Numbers below phalanges correspond to phalanx number. **Abbreviations: dt IV**, distal tarsal IV; **lgp**, ligament pit; **mt II**, metatarsal II; **mt III**, metatarsal III; **mt IV**, metatarsal IV; **mt V**, metatarsal V; **pdp**, proximodorsal process; **vg**, vascular groove.
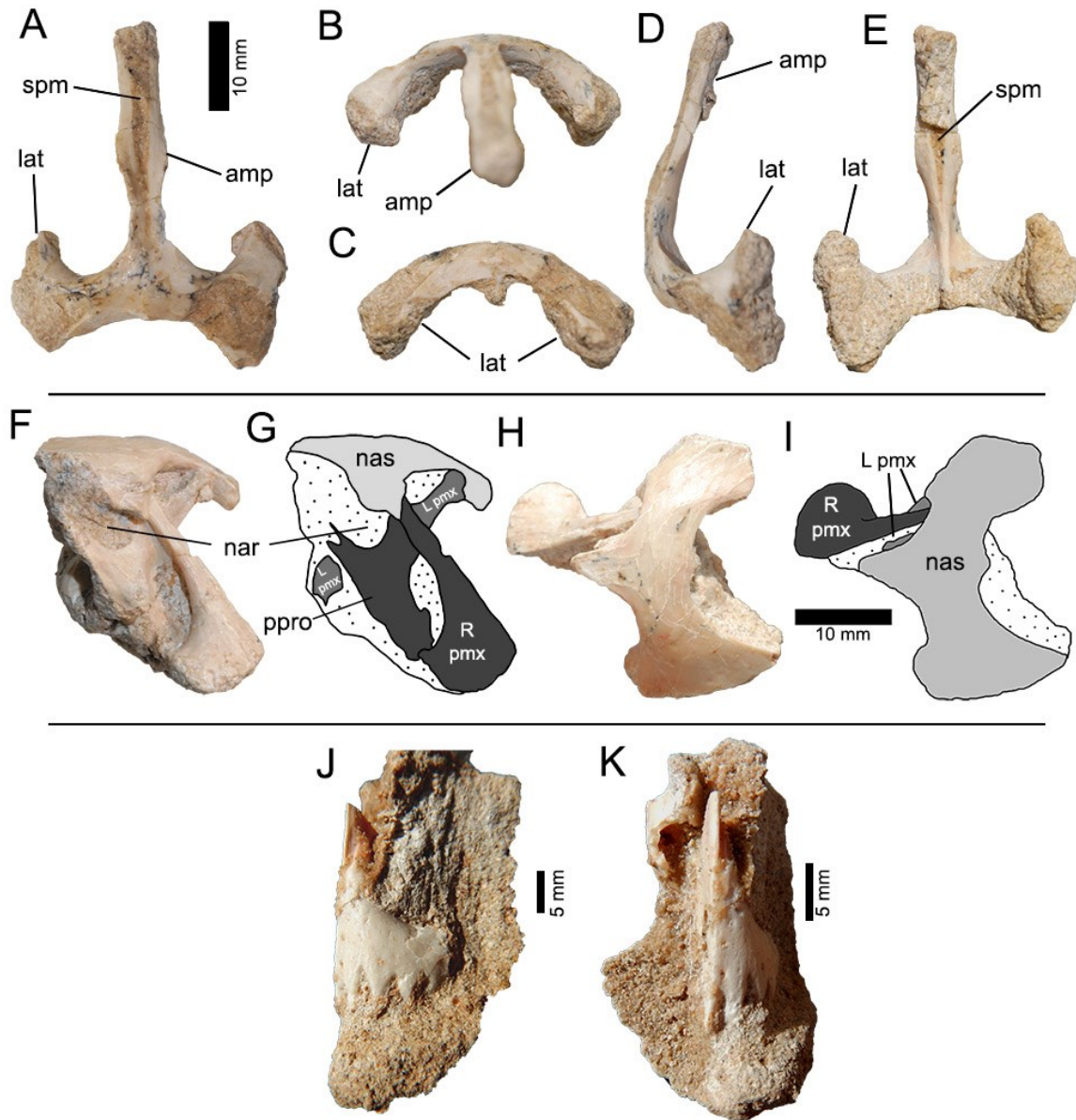
Fig. 2.5. Cranial elements of *Avimimus nemegtensis* (MPC-D 102/46).

Fused nasals in dorsal (A), anterior (B), posterior (C), right lateral (D), and ventral (E) views.
MPC-D 102/34, block containing right premaxilla, maxilla and fused nasals in lateral (F, G) and
dorsal (H, I) views. **Abbrevations**: **amp**, anterior midline process; **lat**, lateral descending
process; **mx**, maxilla; **nas**, nasal; **pmx**, premaxilla; **spm**, slot in nasal for premaxilla.
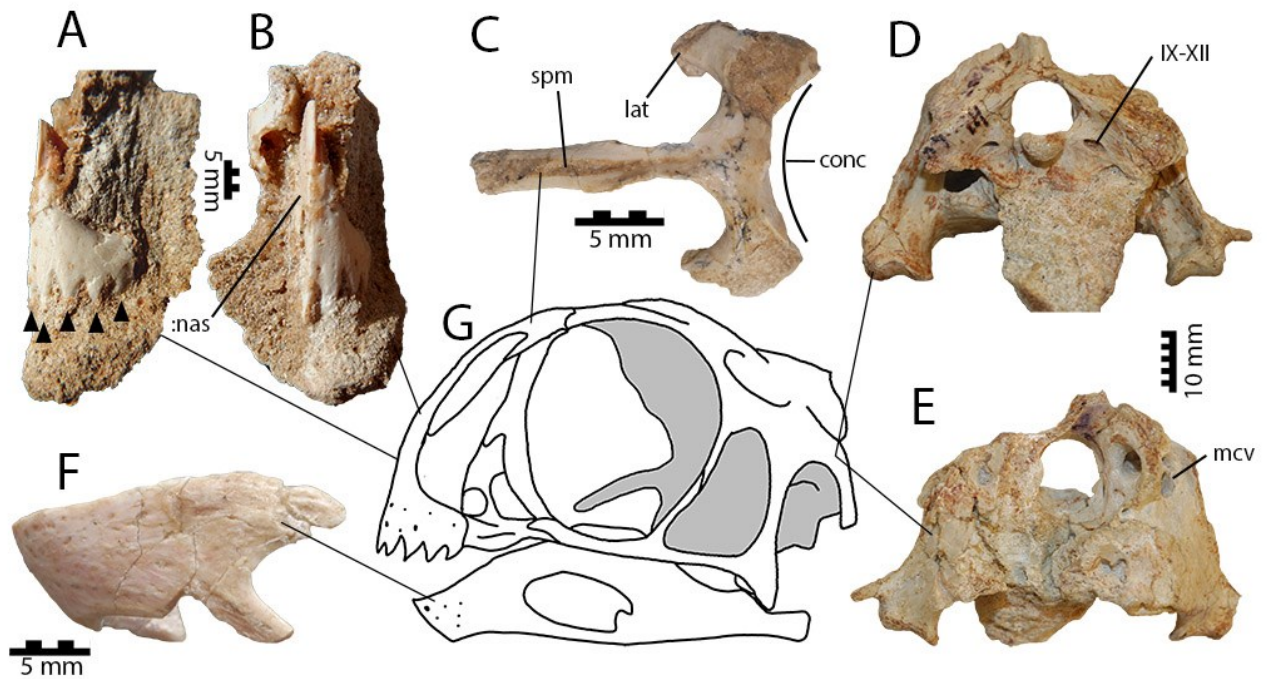
Fig. 2.6. Cranial material of *Avimimus nemegtensis*.

Premaxilla in lateral (A) and anterior (B) views; nasal in dorsal view (C); coossified

neurocranium in posterior (D) and anterior (E) views; dentary in lateral view (F); and

hypothetical reconstruction of the skull in left lateral view (G). Images modified from Funston et

al. (2016b). **Abbreviations**: **conc**, concavity; **IX-XII**, jugular foramen for cranial nerves IX to

XII; **lat**, lateral descending process; **mcv**, foramina for the middle cerebral vein; **spm**, slot in

nasal for premaxilla.
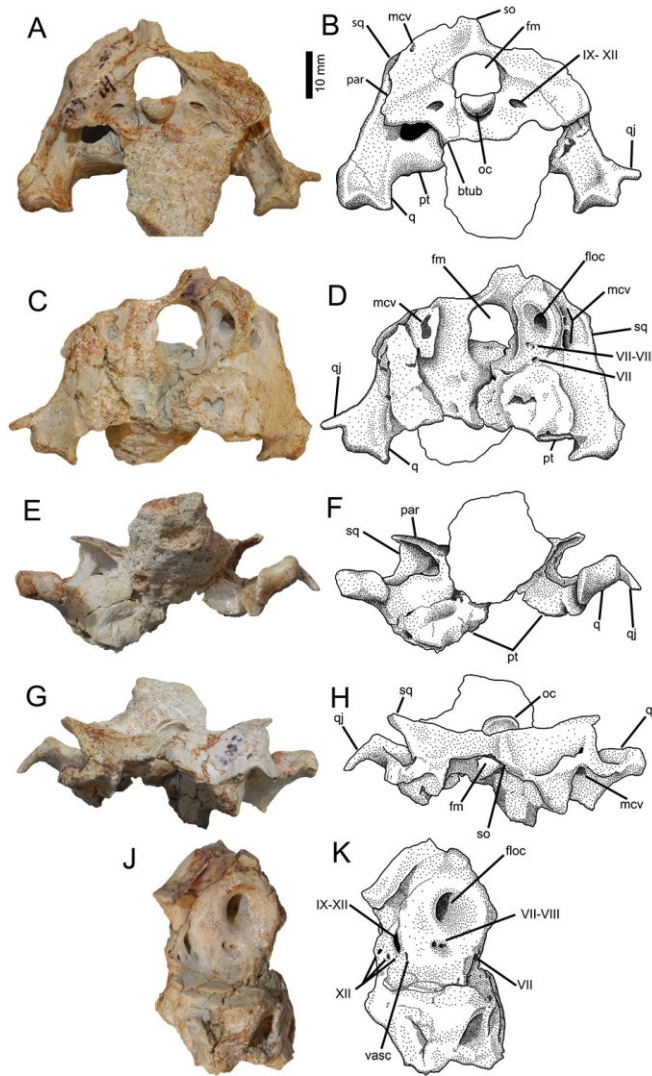
Fig. 2.7. Fused neurocranium of *Avimimus nemegtensis* (MPC-D 102/81).

Partial braincase in posterior (A, B), anterior (C, D), ventral (E, F) and dorsal (G, H) views.

Detail of medial wall of exoccipital (J, K), not to scale. **Abbreviations: floc**, floccular fossa; **fm**,

foramen magnum; **mcv**, foramina for middle cerebral vein; **oc**, occipital condyle; **pt**, pterygoid;

q, quadrate; **qj**, quadratojugal; **so**, supraoccipital; **sq**, squamosal; **vasc**, vascular foramen; **VII**,

foramen for facial nerve; **VII-VIII**, foramina for branches of the facial nerve and

vestibulocochlear nerve; **IX-XII**, foramen for glossopharyngeal, vagus, accessory, and

hypoglossal nerves; **XII**, foramina for hypoglossal nerve.
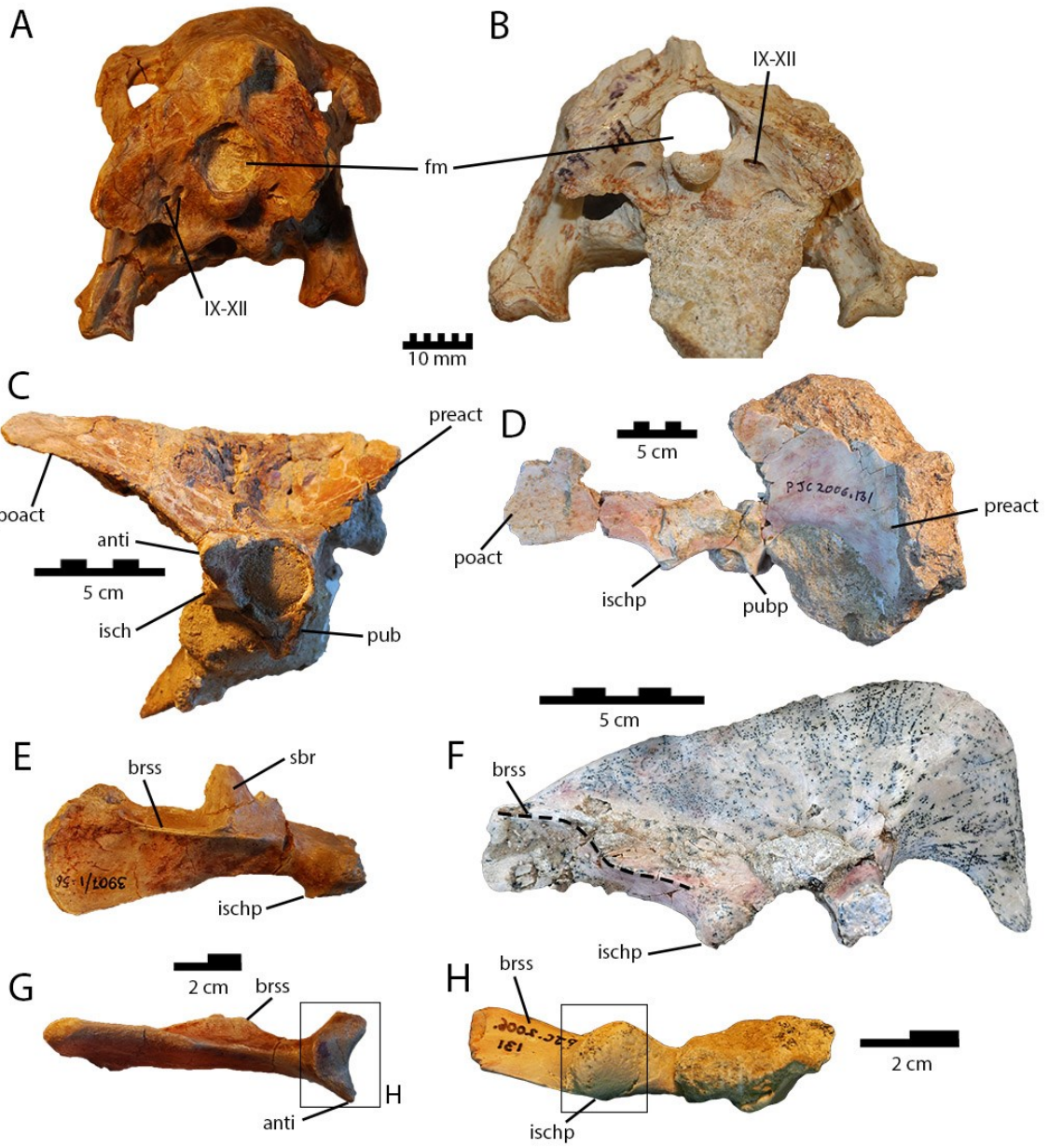
(Previous page)
Fig. 2.8. Comparison of *Avimimus portentosus* and *Avimimus nemegtensis*.

Neurocrania of *Avimimus portentosus* (A) and *Avimimus nemegtensis* (B) in posterior view.

Pelvis of *Avimimus portentosus* (C) in lateral view. Ilium of *Avimimus nemegtensis* (D) in lateral

view. Postacetabular process of *Avimimus portentosus* in medial view (E). Ilium of *Avimimus*

nemegtensis in medial view (F), dashed line indicates brevis shelf. Postacetabular process of

Avimimus portentosus in ventral view (G), box corresponds to highlighted region in (H).

Acetabulum and postacetabular process of *Avimimus nemegtensis* in ventral view, reversed (H).

Abbreviations: anti, antitrochanter; **brss**, brevis shelf; **isch**, ischium; **ischp***, ischiadic peduncle;

IX-XII, jugular foramen for cranial nerves IX to XII; **poact**, postacetabular process; **pub**, pubis;

pubp, pubic peduncle; **preact**, preacetabular process; **sbr**, suprabrevis ridge.
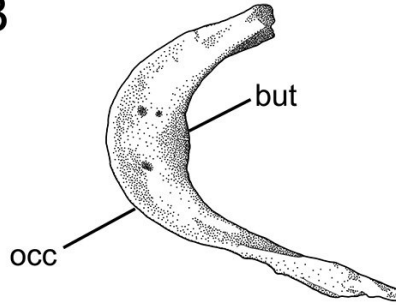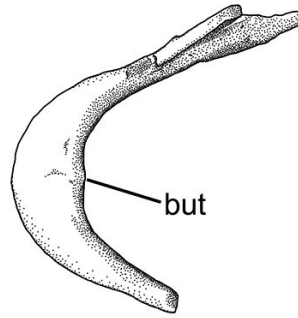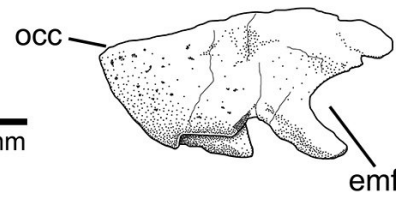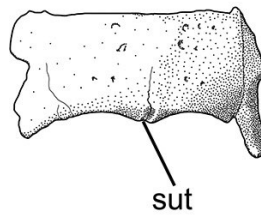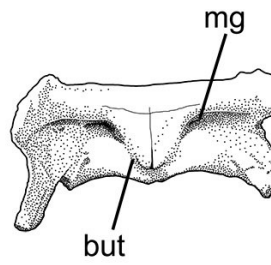
(Previous page)
Fig. 2.9. Dentaries of *Avimimus nemegtensis* (MPC-D 102/16).

Partial dentaries in dorsal (A, B), ventral (C, D), anterior (E, F), left lateral (G, H), and posterior

(I, J) views. **Abbreviations: but**, symphyseal buttress; **emf**, external mandibular foramen; **mg**,

Meckelian groove; **occ**, occlusal margin, **sut**, symphyseal suture.
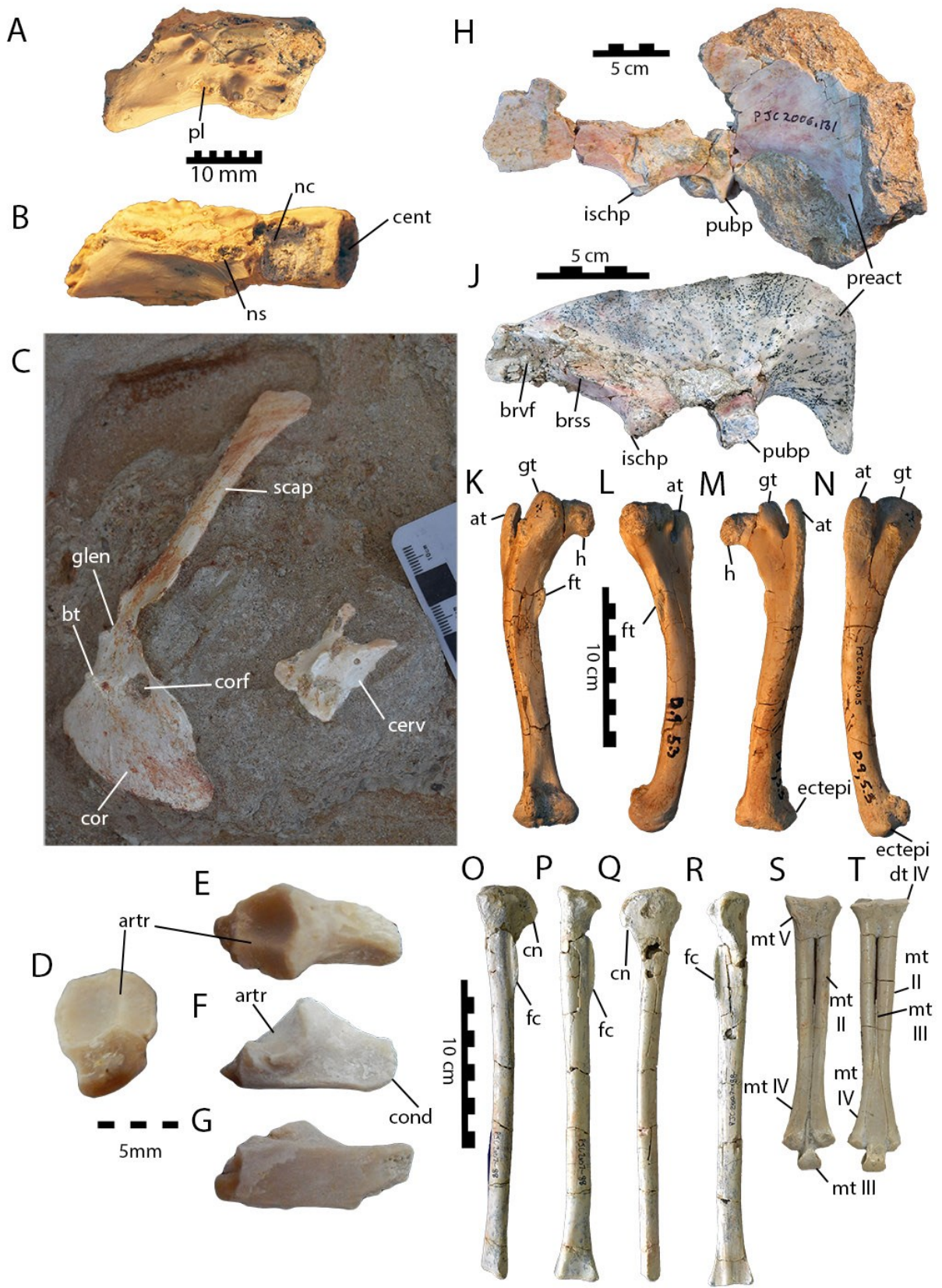
Fig. 2.10. Postcranial material of *Avimimus nemegtensis*.

Cervical vertebra in left lateral (A) and dorsal view (B). Field photo (C) of exposed scapulocoracoid (left) and cervical vertebra (right). Photo has been modified by darkening the matrix to make the bones more easily discernable. Manual phalanx in proximal (D), dorsal (E), lateral (F) and ventral (G) views. Right ilium in lateral view (H) and left ilium in medial view (J). Left femur in posterior (K), medial (L), anterior (M), and lateral (N) views. Right tibia in lateral (O), posterior (P), medial (Q), and anterior (R) views. Left tarsometatarsus in posterior (S) and anterior (T) views. **Abbreviations**: **artr**, articular ridge; **at,** anterior trochanter; **bt**, biceps tubercle; **brvf**, brevis fossa; **brss**, brevis shelf; **cent**, centrum; **cerv**, cervical vertebra; **cond**, condyle; **cor**, coracoid; **corf**, coracoid foramen; **cn**, cnemial crest; **dt IV**, distal tarsal IV; **ectepi**, ectocondylar tuber; **fc**, fibular crest; **ft**, fourth trochanter; **glen**, glenoid; **gt**, greater trochanter; **h**, femoral head; **ischp**, ischiadic peduncle; **mt II**, metatarsal II; **mt III**, metatarsal III; **mt IV**, metatarsal IV; **mt V**, metatarsal V; **nc**, neural canal; **ns**, neural spine; **pl**, pleurocoel; **preact**, preacetabular process; **pubp**, pubic peduncle; **scap**, scapula.
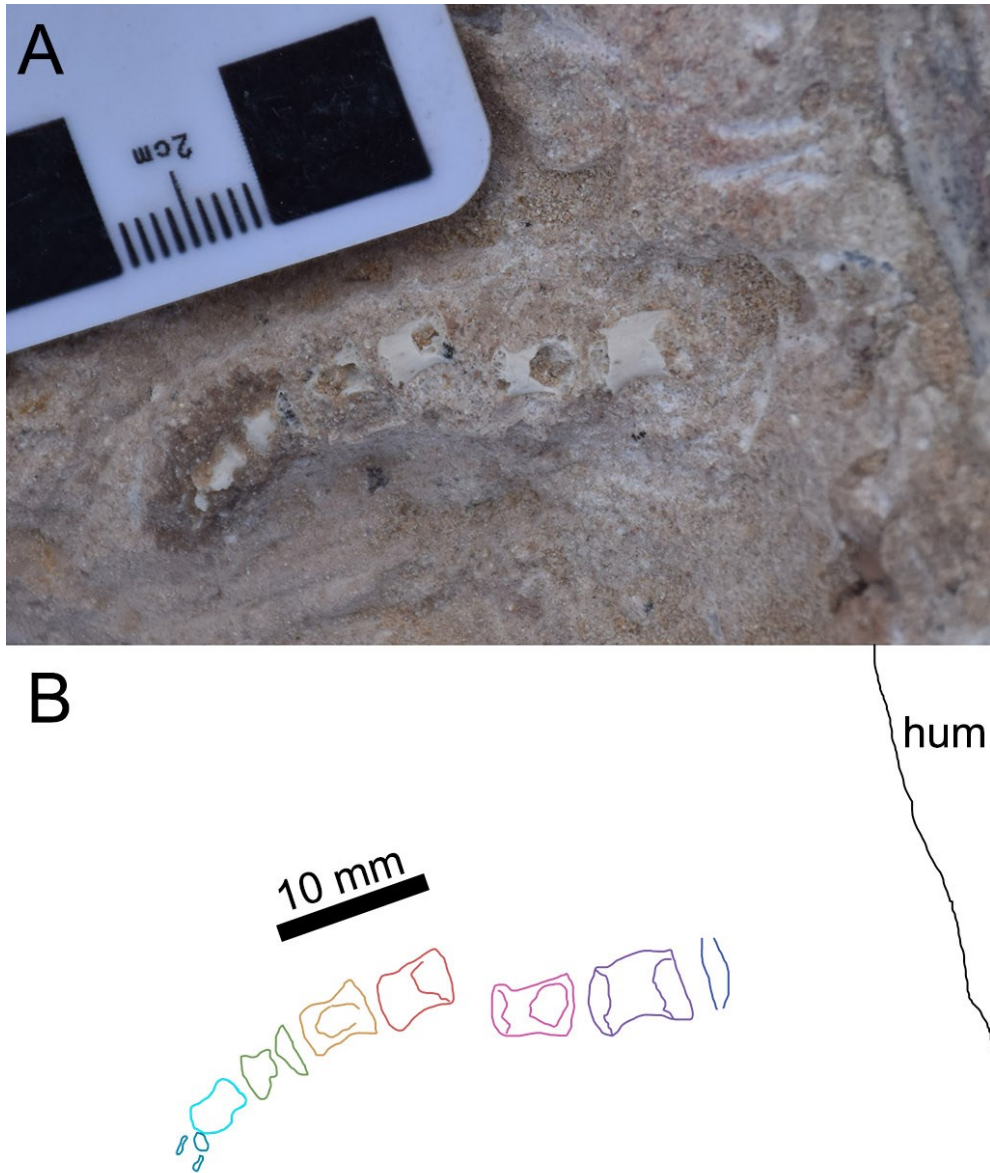
Fig. 2.11. Distal caudal vertebrae of *Avimimus nemegtensis*.

Photograph (A) and illustration (B) of distal caudal vertebrae as preserved at the avimimid bonebed at Nemegt. Each caudal vertebra is illustrated in a different colour. **Abbreviations: hum**, humerus.
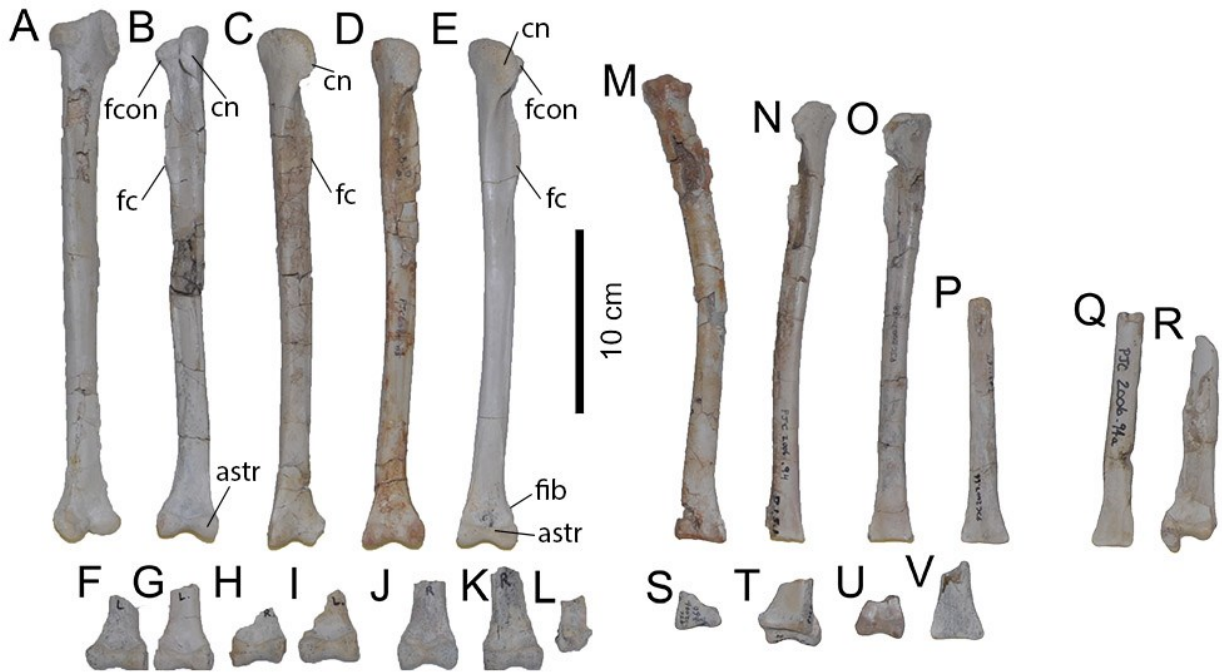
Fig. 2.12. Tibiotarsi of *Avimimus nemegtensis* arranged by total length.

Tibiotarsi arranged to demonstrate size dichotomy between tibiotarsi fused with

astragalocalcanei (A–L) and tibiotarsi unfused to astragalocalcanei (M–V). MPC-D 102/92 (A);

MPC-D 102/94 (B); MPC-D 102/42 (C); MPC-D 102/84 (D); MPC-D 102/90 (E); MPC-D

102/83 (M); MPC-D 102/74 (N); MPC-D 102/105 (O); MPC-D 102.86 (P); MPC-D 102/74a

(Q); and MPC-D 102/26 (R) in anterior view. **Abbreviations: astr**, astragalus; **cn**, cnemial crest;

fc, fibular crest; **fcon**, fibular condyle; **fib**, fibula.

Fig. 2.13. Fusion of fibula to the tibiotarsus in *Avimimus nemegtensis*.

Field photography of left tibia (right) in lateral view, showing adhered portion of distal fibula

(arrow), and left fibula (left) in medial view.
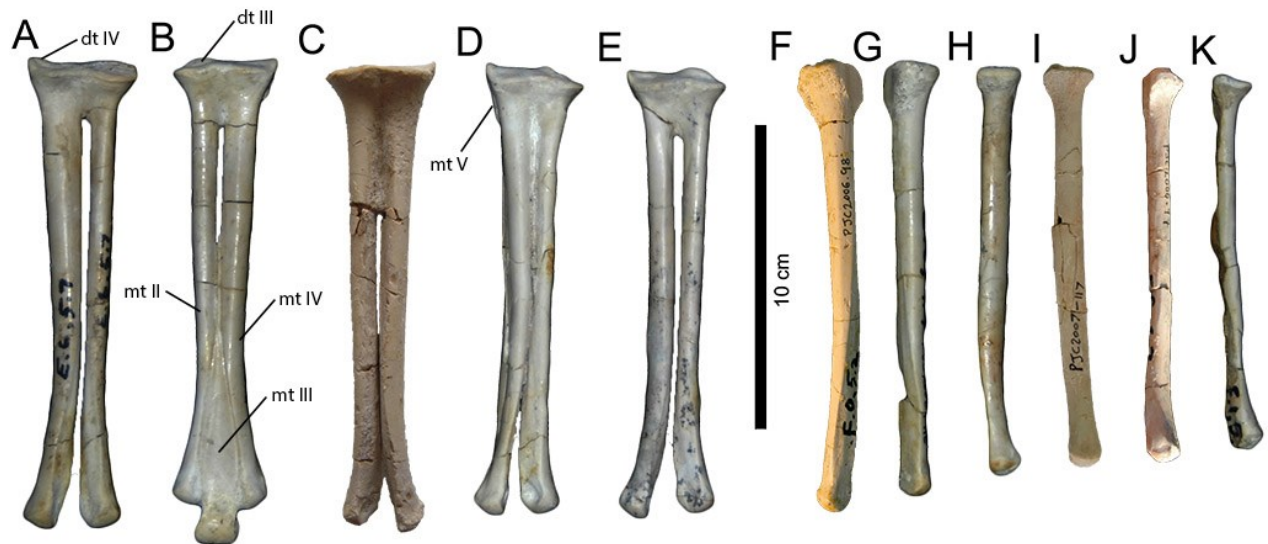
Fig. 2.14. Tarsometatarsi recovered from the *Avimimus nemegtensis* bonebed arranged by size.

Tarsometatarsi arranged to demonstrate size dichotomy between fused elements (A-E) and isolated elements (F-K). Note small degree of variation in length of fused tarsometatarsi. MPC-D 102/37 (A); MPC-D 102/89 (B); MPC-D 102/93 (C); MPC-D 102/76 (D); MPC-D 102/96 (E); MPC-D 102/78 (F); MPC-D 102/40 (G); MPC-D 102/48 (H); MPC-D 102/106 (I); MPC-D 102/77 (J); MPC-D 102/39 (K). **Abbreviations: dt III**, distal tarsal III; **dt IV**, distal tarsal IV; **mt II**, metatarsal II; **mt III**, metatarsal III; **mt IV**, metatarsal IV; **mt V**, metatarsal V.
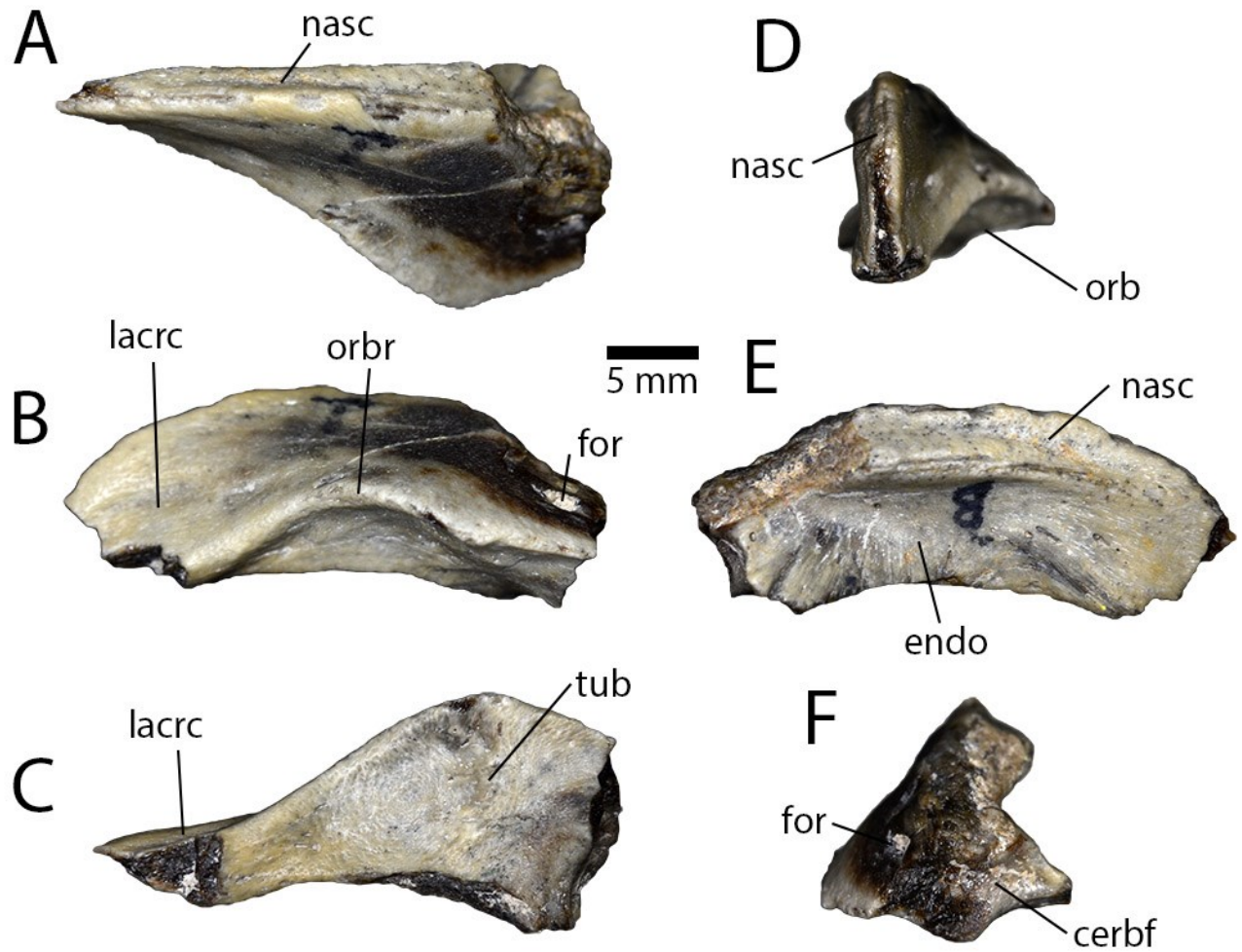
Fig. 2.15. Cranial material from the Iren Dabasu avimimid bonebed.

Partial left frontal (IVPP V16342) in dorsal (A), lateral (B), ventral (C), anterior (D), medial (E), and posterior (F) views. **Abbreviations: cerbf**, cerebral fossa; **endo**, endocranial cavity; **for**, foramen; **lacrc**, lacrimal contact; **nasc**, nasal contact; **orb**, orbit; **orbr**, orbital rim; **tub**, tubercle.
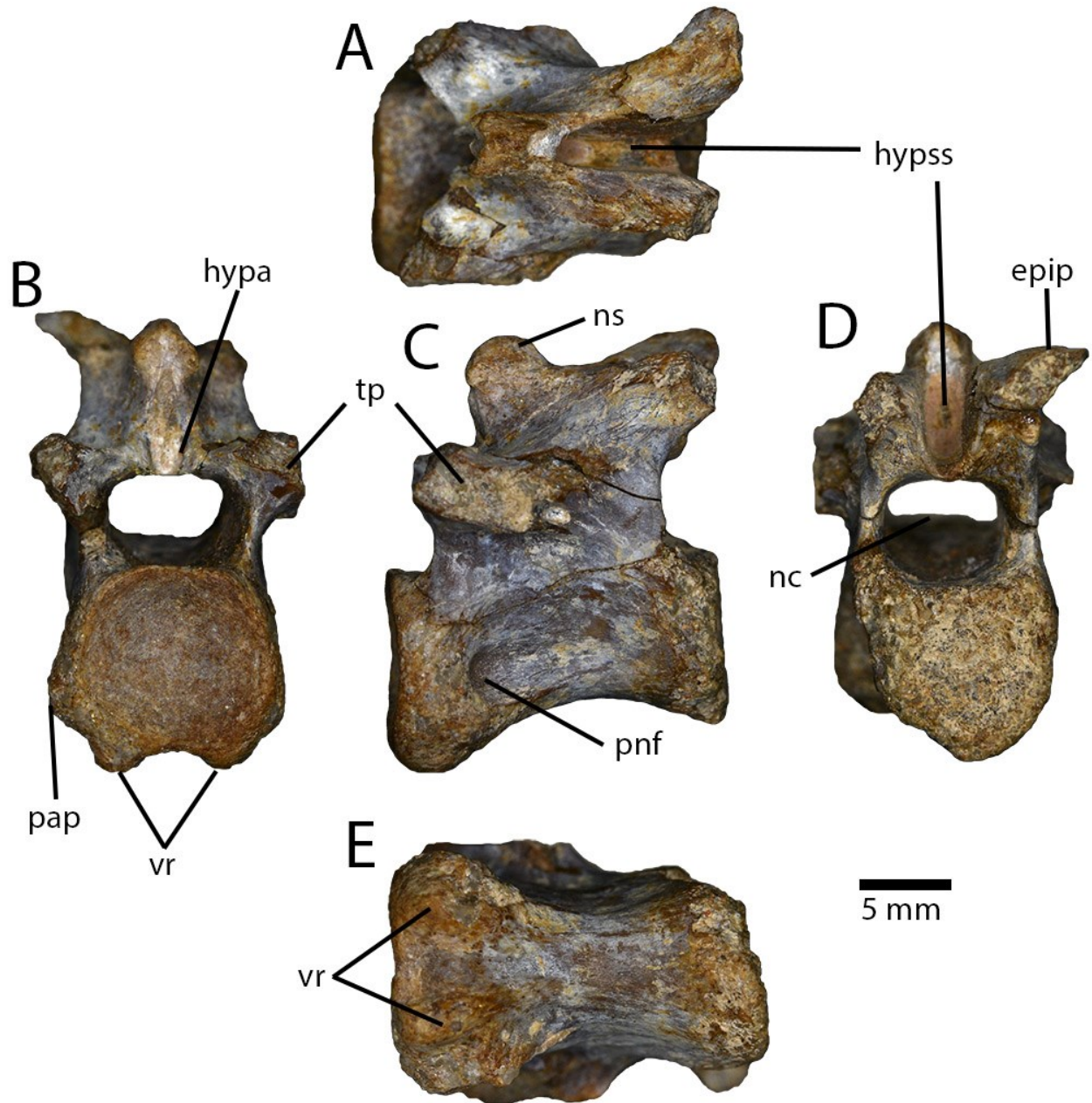
Fig. 2.16. Cervical vertebra from the Iren Dabasu avimimid bonebed.

Posterior cervical vertebra (IVPP V16329.a) in dorsal (A), anterior (B), lateral (C), posterior (D),

and ventral (E) views. **Abbreviations: epip**, epipophysis; **hypa**, hypantrum; **hypss**, hyposphenal

slot; **nc**, neural canal; **ns**, neural spine; **pap**, parapophysis; **pnf**, pneumatic fossa; **vr**, ventral

ridges.
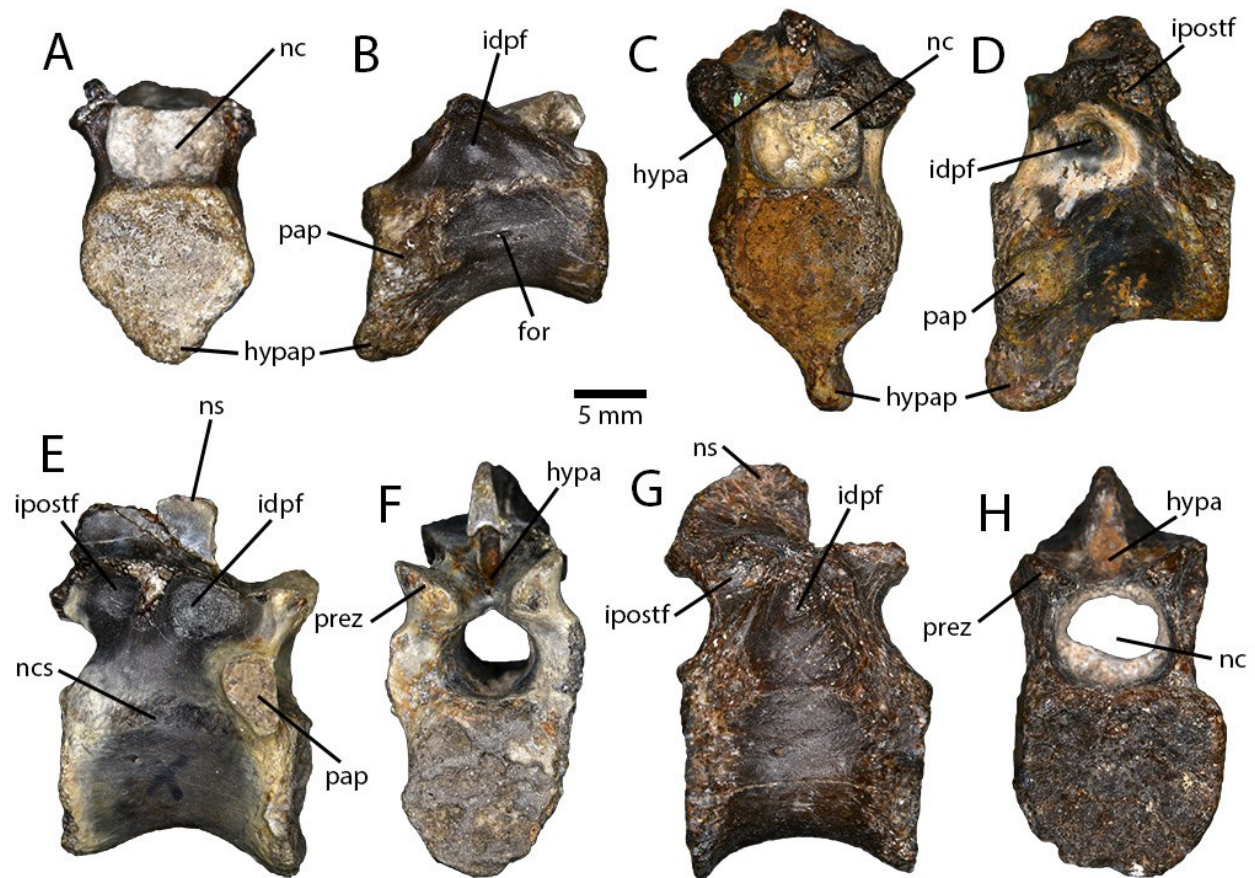
Fig. 2.17. Dorsal vertebrae from the Iren Dabasu avimimid bonebed.

First cervicodorsal vertebra (IVPP V16332.b) in anterior (A) and lateral (B) views. Second cervicodorsal (IVPP V16332.a) in anterior (C) and lateral (D) views. Anterior dorsal (IVPP V16318.a) in lateral (E) and anterior (F) views. Posterior dorsal (IVPP V16318.b) in lateral (G) and anterior (H) views. **Abbreviations: for**, foramen; **hypa**, hypantrum; **hypap**, hypapophysis; **idpf**, infradiapophyseal fossa; **ipostf**, infrapostzygapophyseal fossa; **nc**, neural canal; **ncs**, neurocentral suture; **ns**, neural spine; **pap**, parapophysis; **prez**, prezygapophysis.
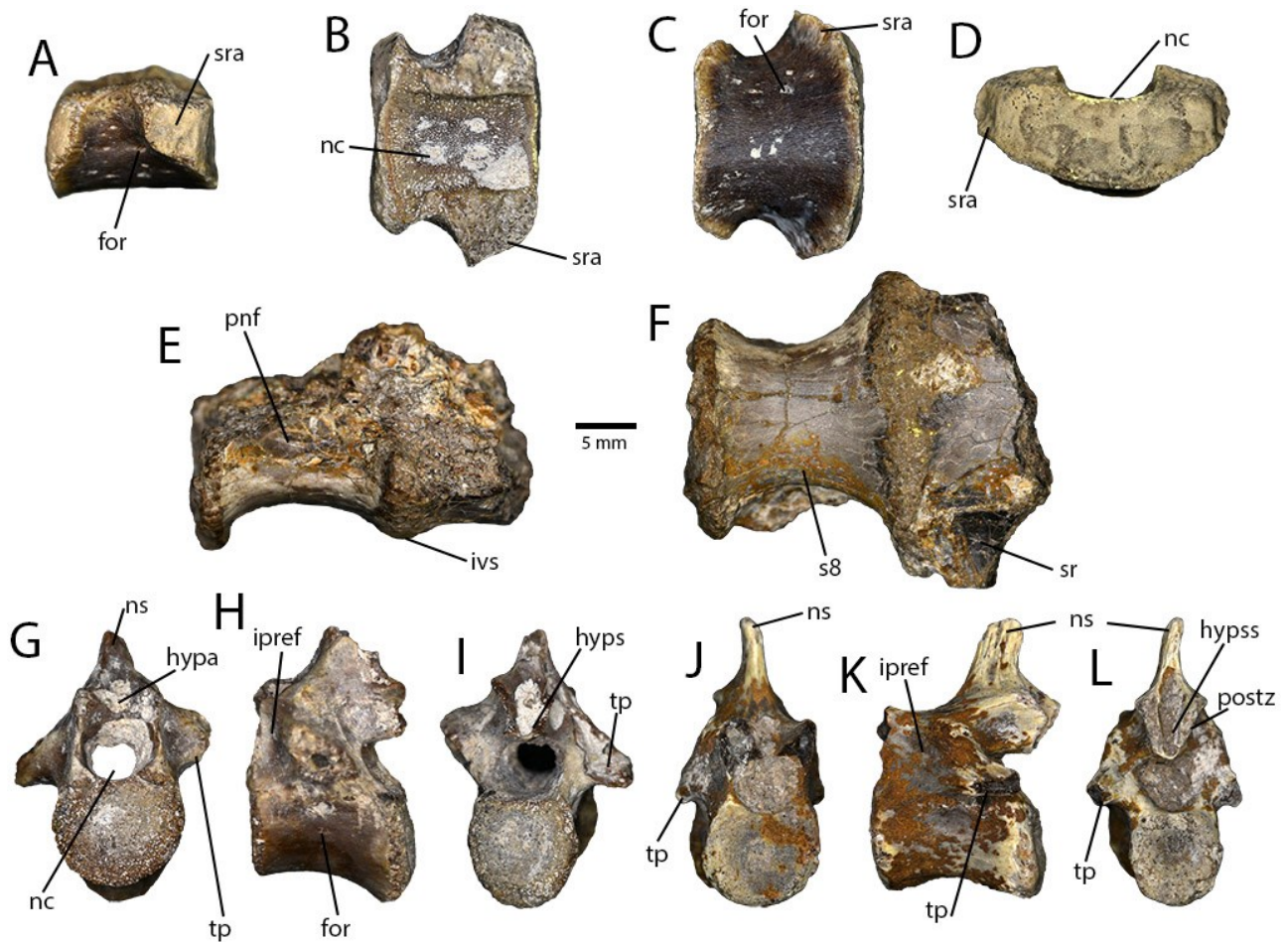
Fig. 2.18. Sacral and caudal vertebrae from the Iren Dabasu avimimid bonebed.

Isolated juvenile mid-sacral vertebra (IVPP V16328) in lateral (A), dorsal (B), ventral (C), and anterior (D) views. Partial sacrum (IVPP V16330) in lateral (E) and ventral (F) views. Proximal caudal vertebra (IVPP V16317.a) in anterior (G), lateral (H), and posterior (I) views. Mid-caudal vertebra (IVPP V16317.b) in anterior (J), lateral (K), and posterior (L) views. **Abbreviations: for**, foramen; **hypa**, hypantrum; **hyps**, hyposphene; **hypss**, hyposphenal slot; **ipref**, infraprezygapophyseal fossa; **ivs**, intravertebral suture; **nc**, neural canal; **ns**, neural spine; **pnf**, pneumatic fossa; **postz**, postzygapophysis; **s8**, sacral vertebra eight; **sr**, sacral rib; **sra**, sacral rib attachment; **tp**, transverse process.
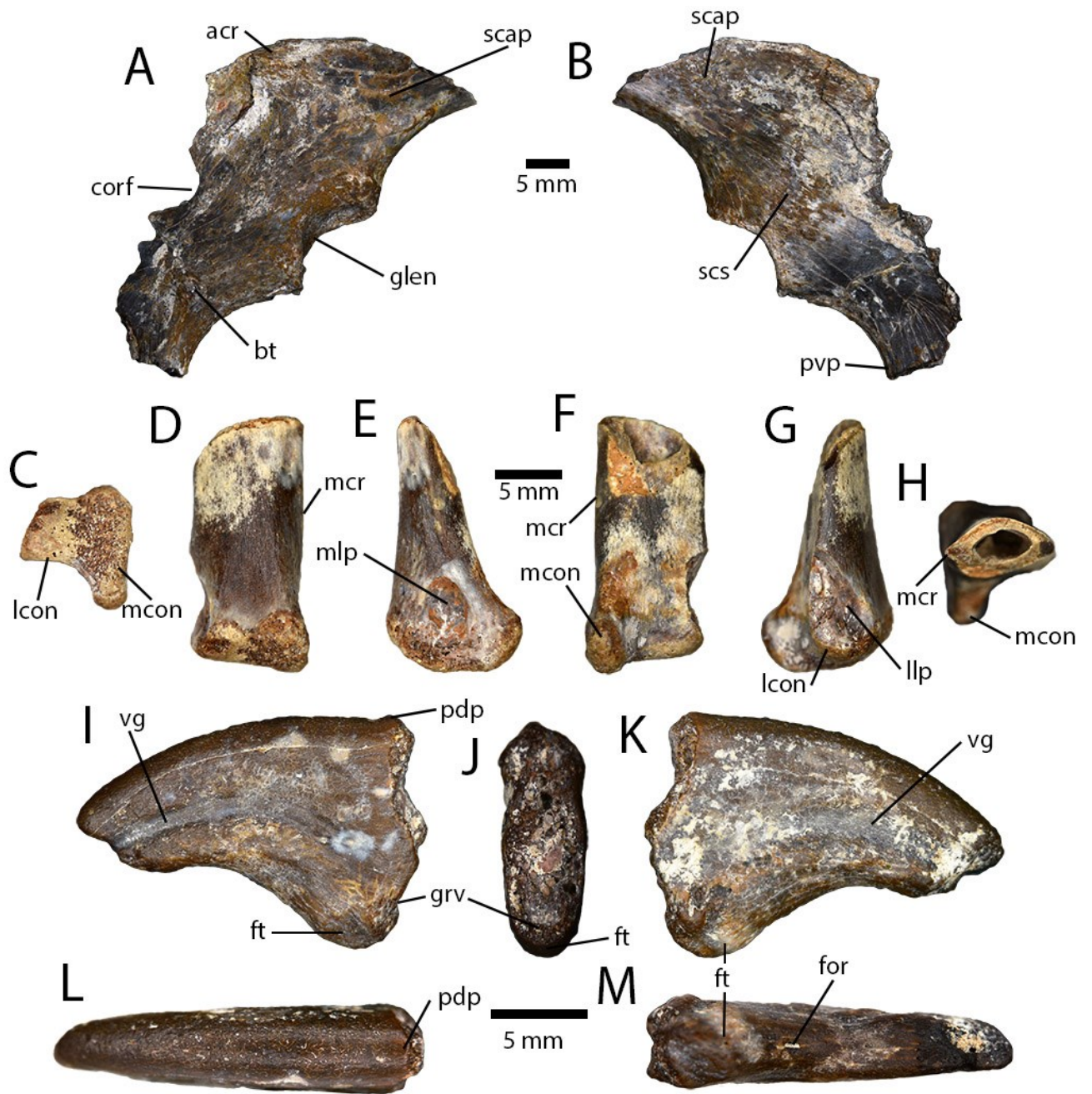
(Previous page)
Fig. 2.19. Forelimb material from the Iren Dabasu avimimid bonebed.

Partial scapulocoracoid (IVPP V16327) in lateral (A) and medial (B) views. Distal end of right metacarpal I (IVPP V16343) in distal (C), extensor (D), medial (E), flexor (F), lateral (G) and proximal (H) views. Right manual ungual ?I (IVPP V16313.a) in medial (I), proximal (J), lateral (K), dorsal (L), and ventral (M) views. **Abbreviations: acr**, acromion process; **bt**, biceps tubercle; **corf**, coracoid foramen; **for**, foramen; **ft**, flexor tubercle; **glen**, glenoid; **grv**, groove; **lcon**, lateral condyle; **llp**, lateral ligament pit; **mcon**, medial condyle; **mcr**, medial crest; **mlp**, medial ligament pit; **pdp**, proximodorsal process; **pvp**, posteroventral process; **scap**, scapula; **vg**, vascular groove.
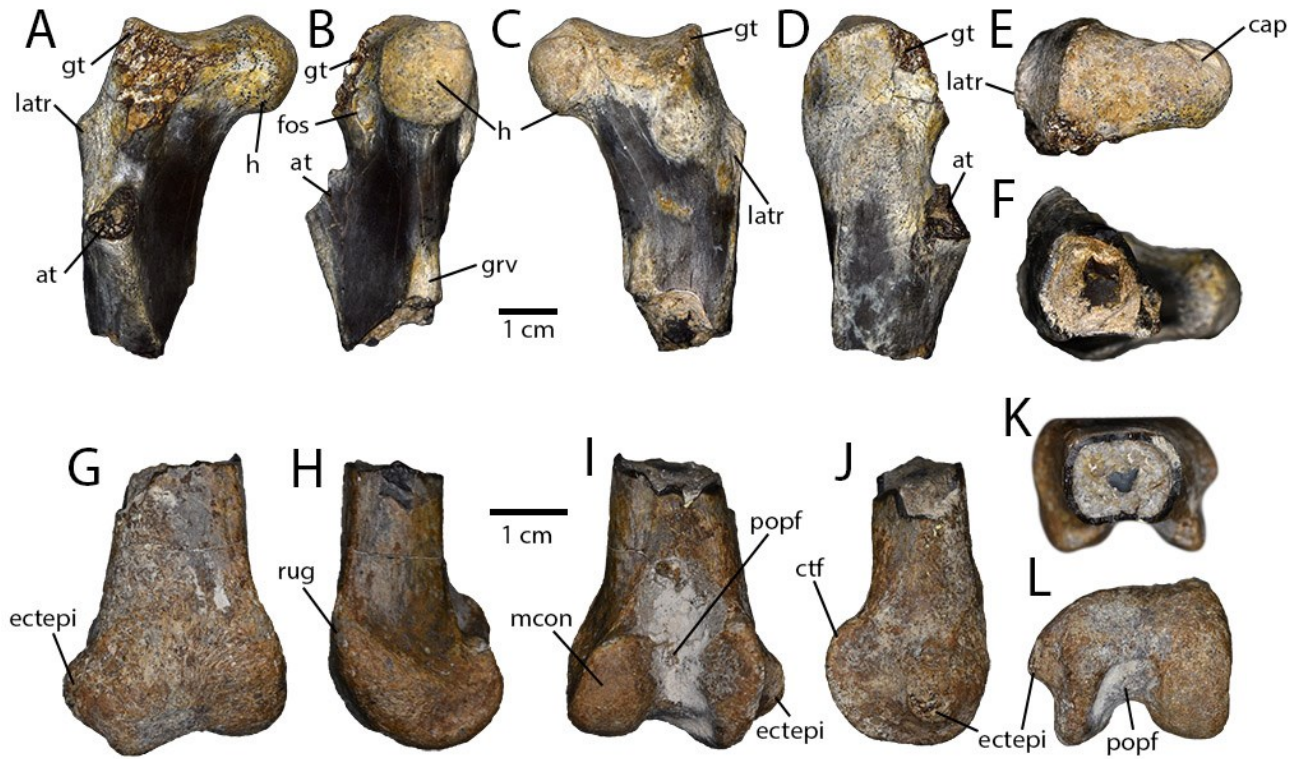
Fig. 2.20. Femora collected from the Iren Dabasu avimimid bonebed.

Proximal right femur (IVPP V16334.a) in anterior (A), medial (B), posterior (C), lateral (D), proximal (E) and distal (F) views. Distal right femur (IVPP V16338) in anterior (G), medial (H), posterior (I), lateral (J), proximal (K), and distal (L) views. **Abbreviations: at**, anterior trochanter; **cap**, capitate ligament scar; **ctf**, crista tibiofibularis; **ectepi**, ectepicondylar tuber; **fos**, fossa; **grv**, groove; **gt**, greater trochanter; **h**, head; **latr**, lateral ridge; **mcon**, medial condyle; **popf**, popliteal fossa; **rug**, rugosity.
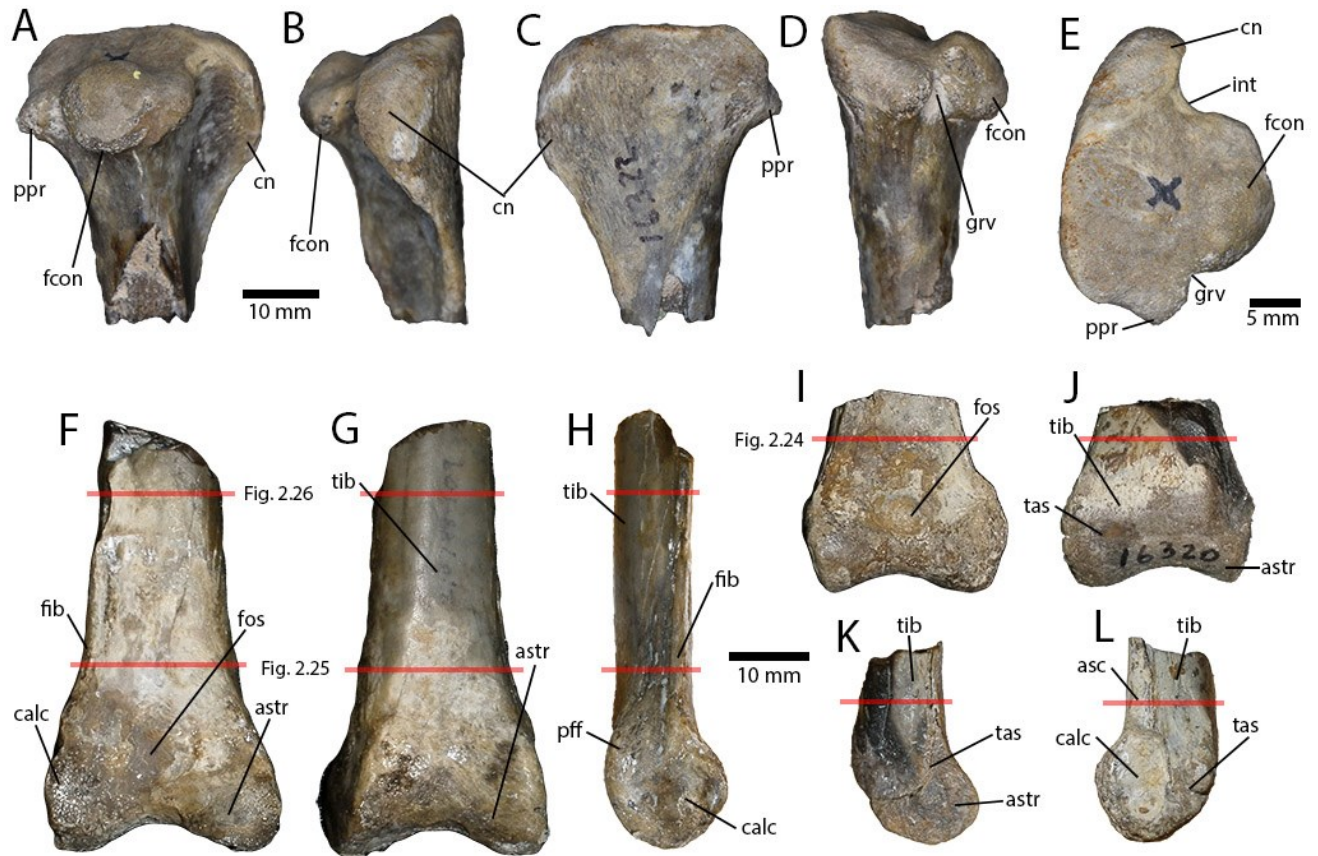
Fig. 2.21. Tibiotarsi recovered from the Iren Dabasu avimimid bonebed.

Proximal right tibiotarsus (IVPP V16322.a) in lateral (A), anterior (B), medial (C), posterior (D), and proximal (E) views. Adult distal right tibiotarsus (IVPP V16337) in anterior (F), posterior (G), and lateral (H) views. Juvenile distal left tibiotarsus (IVPP V16320) in anterior (I), posterior (J), medial (K), and lateral (L) views. Red lines in F–L indicate locations of thin sections and corresponding figure numbers. **Abbreviations: asc,** ascending process of astragalus; **astr**, astragalus; **calc**, calcaneum; **cn**, cnemial crest; **fcon**, fibular condyle **fib**, fibula; **fos**, fossa; **grv**, groove; **int**, incisura tibialis; **pff**, postfibular flange; **ppr**, posterior process; **tas**, tibia-astragalus suture; **tib**, tibia.
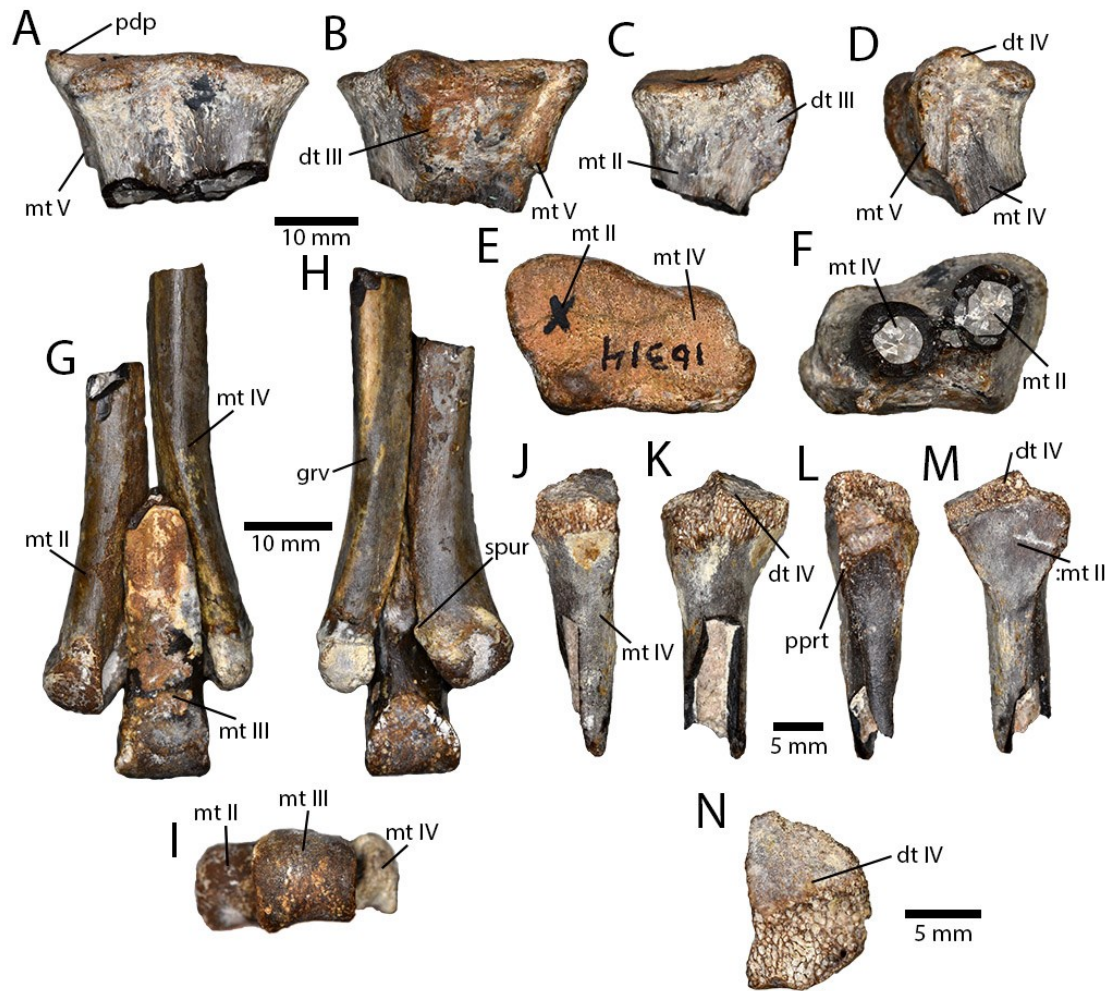
Fig. 2.22. Tarsometatarsi recovered from the Iren Dabasu avimimid bonebed.

Proximal right tarsometatarsus (IVPP V16314) in anterior (A), posterior (B), medial (C), lateral (D), proximal (E), and distal (F) views. Rearticulated distal metatarsus (IVPP V16336 and IVPP V16335.b–c) in anterior (G), posterior (H), and distal (I) views. Unfused proximal end of right metatarsal IV (IVPP V16335.a) in anterior (J), lateral (K), posterior (L), medial (M), and proximal (N) views. **Abbreviations: dt III**, distal tarsal III; **dt IV,** distal tarsal IV; **grv**, groove; **mt II**, metatarsal II; **mt III**, metatarsal III; **mt IV**, metatarsal IV; **mt V**, metatarsal V. **pdp**, proximodorsal process; **pprt**, posterior protuberance; **spur**, posterolateral spur; **:mt II**, contact for metatarsal II.
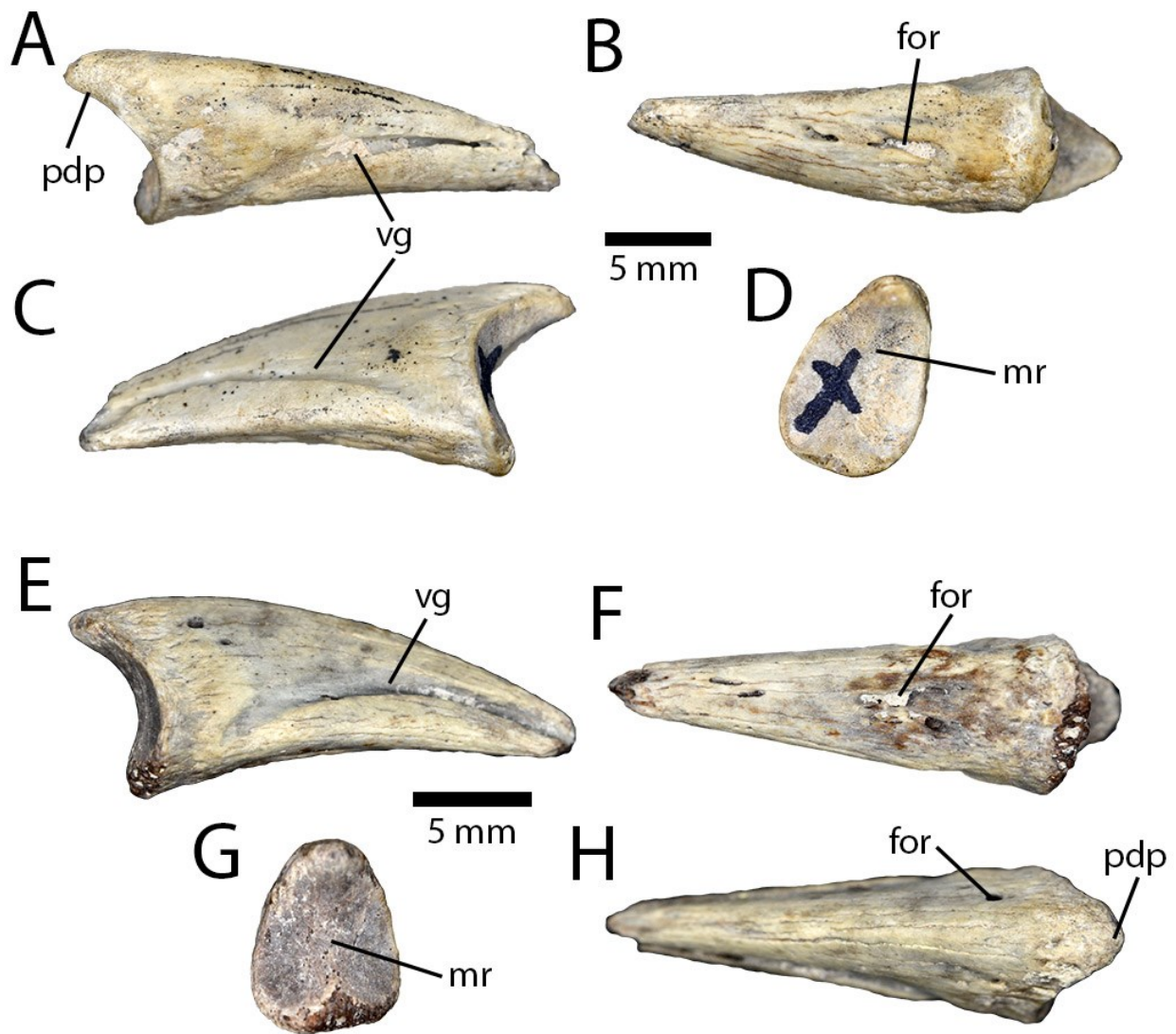
Fig. 2.23. Pedal unguals from the Iren Dabasu avimimid bonebed.

Digit II or IV ungual (IVPP V16316.a) in right lateral (A), ventral (B), left lateral (C), and proximal (D) views. Ungual III-4 (IVPP V16316.b) in right lateral (E), ventral (F), proximal (G) and dorsal (H) views. **Abbreviations: for**, foramen; **mr**, median ridge; **pdp**, proximodorsal process; **vg**, vascular groove.
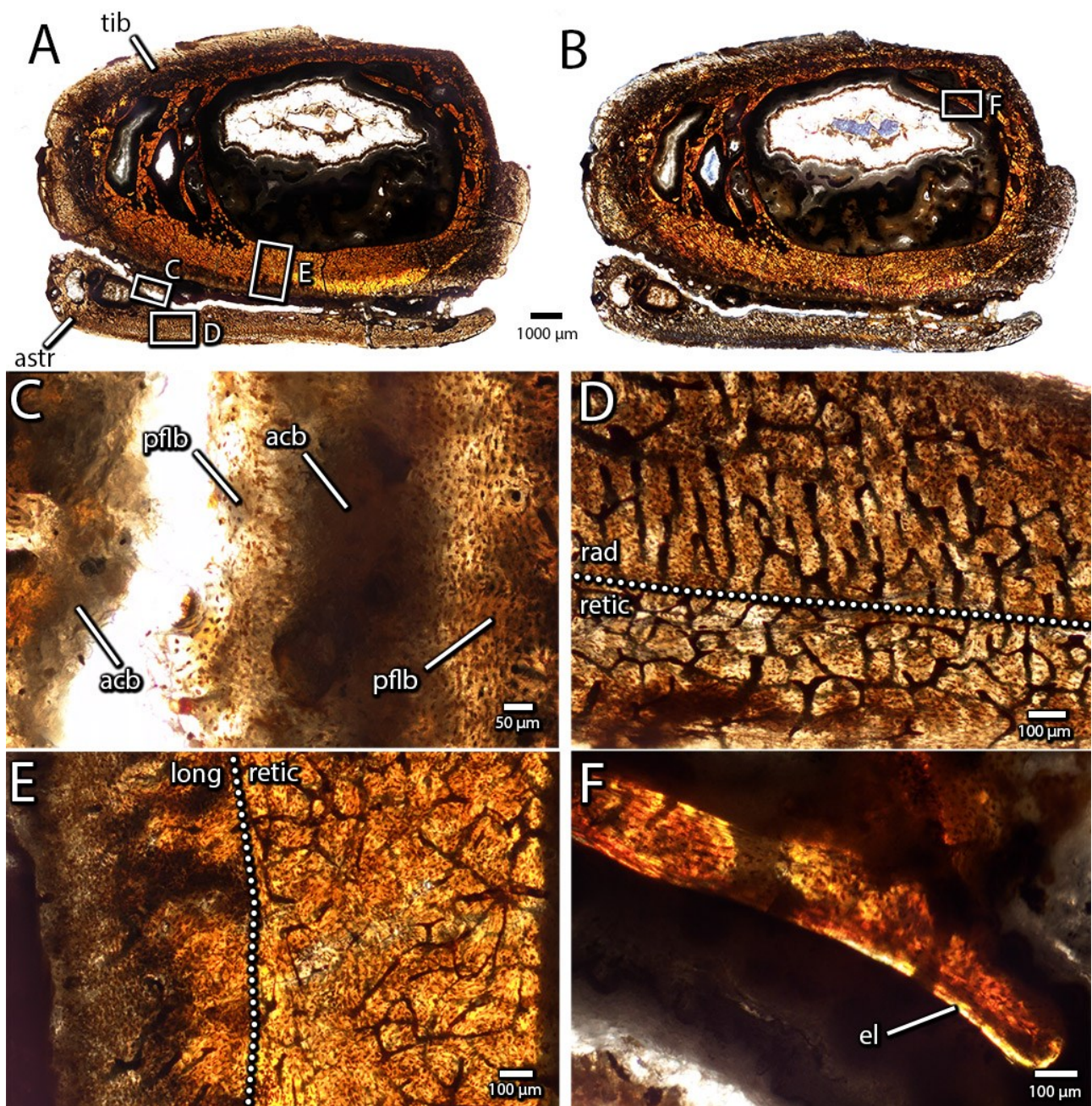
(Previous page)
Fig. 2.24. Histology of the distal end of an unfused avimimid tibiotarsus (IVPP V16320).

Overview of slide under normal light (A) and cross-polarized light (B), showing tibia, unfused astragalus, and locations of close-up images. Detail (C) of tibia-astragalus interface under normal light, showing granular, acellular bone interspersed with primary fibrolamellar bone. Detail (D) of zone of radially-oriented vasculature in the astragalus under normal light. Detail (E) of anterior surface of tibia under normal light, showing transition from reticular vasculature (right) to longitudinal vasculature (left). Detail (F) of endosteal surface of tibia under cross-polarized light, showing incipient development of endosteal lamellae. **Abbreviations: acb**, aceullular bone; **astr**, astragalus; **el**, endosteal lamellae; **long**, longitudinal vasculature; **pflb**, primary fibrolamellar bone; **rad**, radial vasculature; **retic**, reticular vasculature; **tib**, tibia.
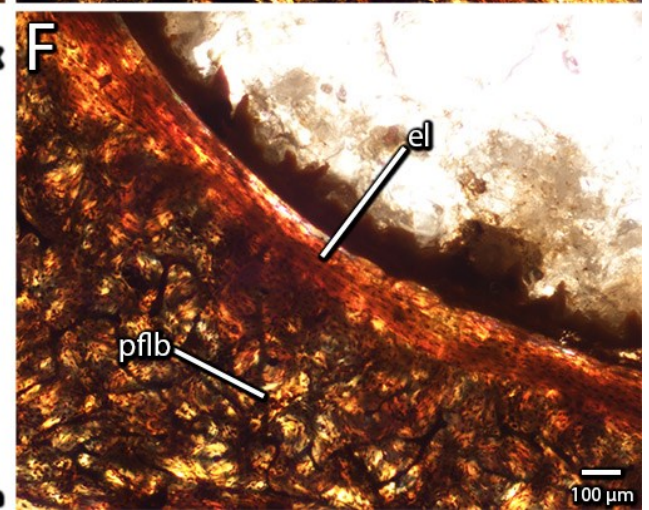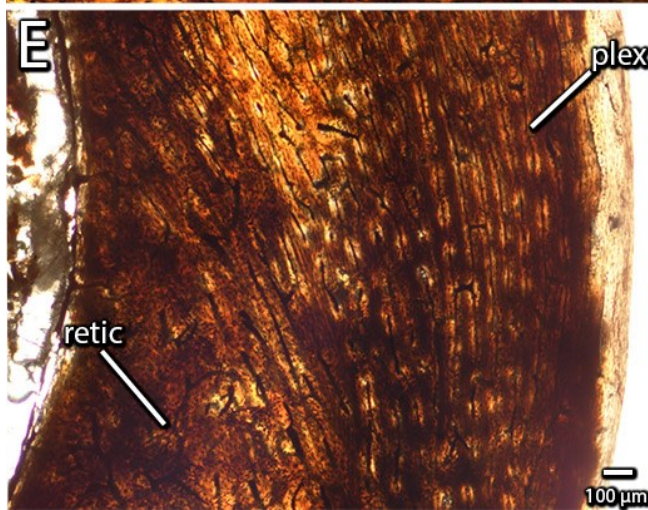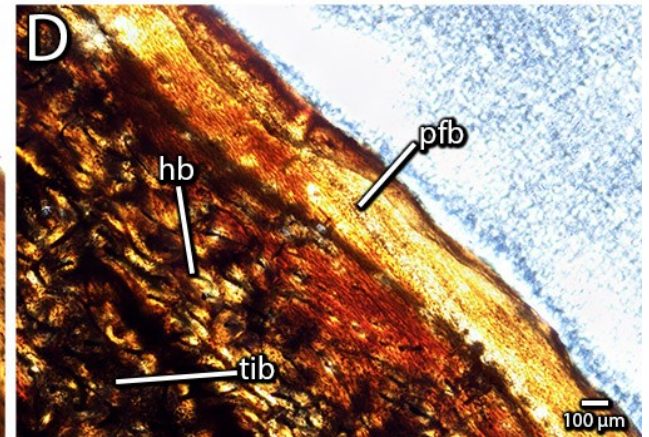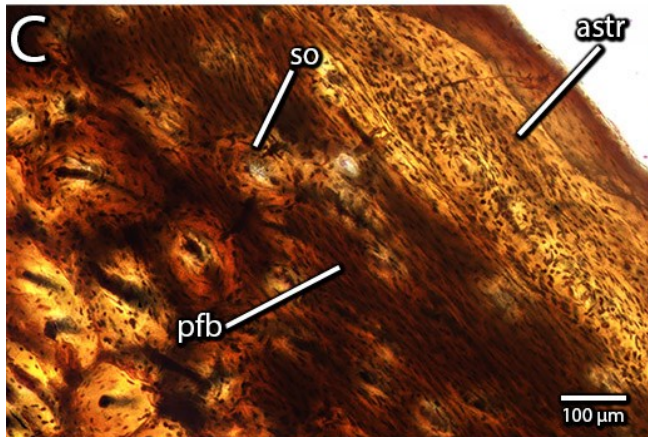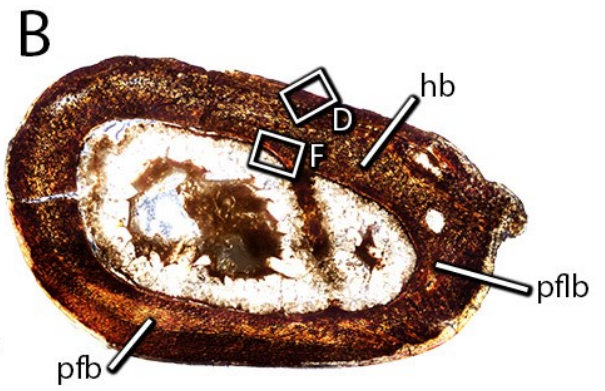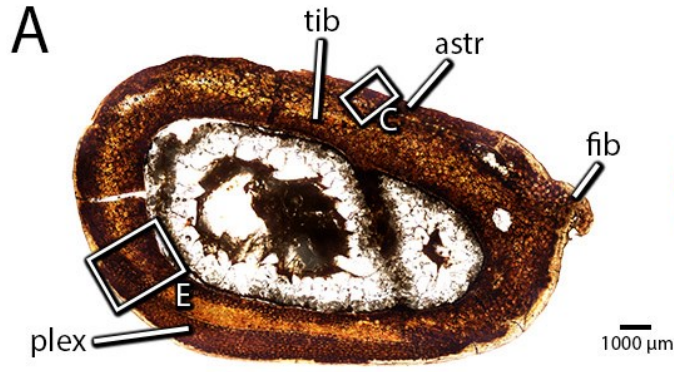
(Previous page)

Fig. 2.25. Histology of the distal end of a fused avimimid tibiotarsus (IVPP V16337).

Overview of slide under normal light (A) and cross-polarized light (B), showing fusion of tibia, astragalus, and fibula, and locations of close-up images. Detail (C) of tibia-astragalus interface under normal light, showing variation in vasculature. Detail (D) of tibia-astragalus interface under cross-polarized light, showing transition from fibrolamellar bone (left) to parallel-fibered bone (right) and presence of secondary remodeling at the contact. Detail (E) of contact between reticular bone and plexiform bone on the posterior surface of the tibia under normal light. Detail (E) of endosteal lamellae and primary fibrolamellar bone near the periosteal surface of the anterior part of the tibia under cross-polarized light. **Abbreviations: astr,** astragalus; **el**, endosteal lamellae; **fib**, fibula; **hb**, Haversian bone; **pfb**, parallel-fibered bone; **pflb**, primary fibrolamellar bone; **plex**, plexiform vascularity; **retic,** reticular vascularity; **so**, secondary osteon; **tib**, tibia.
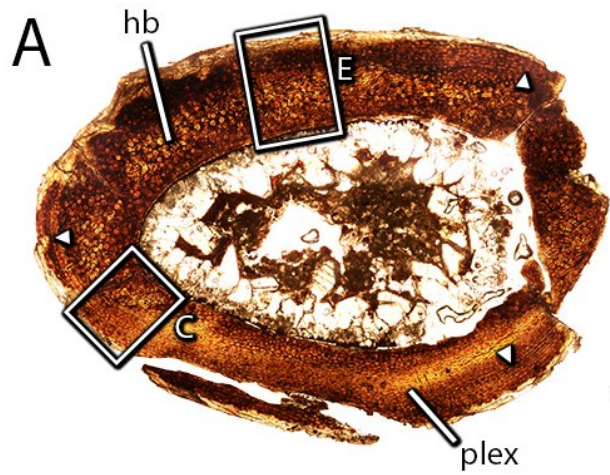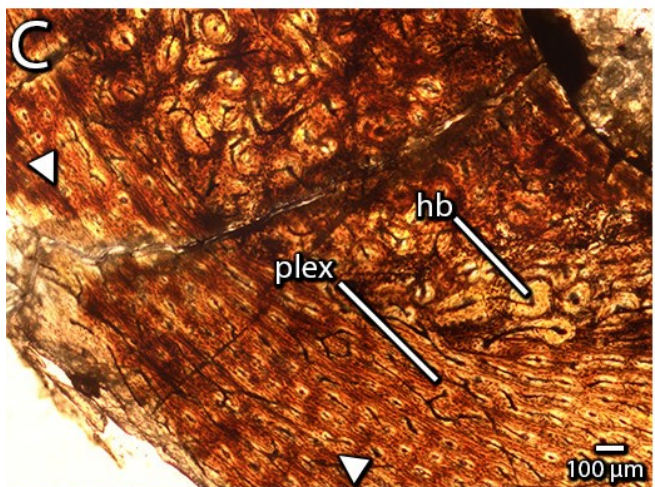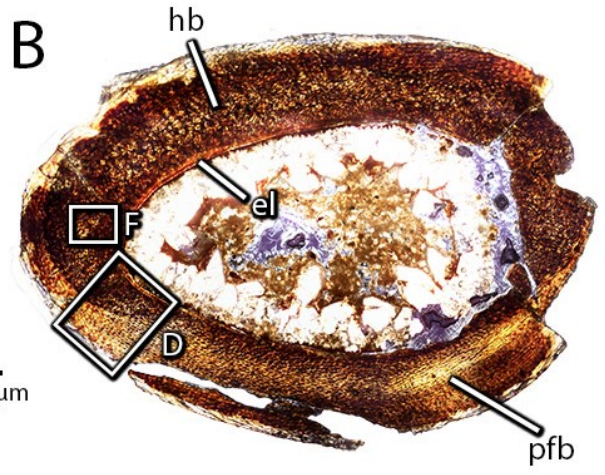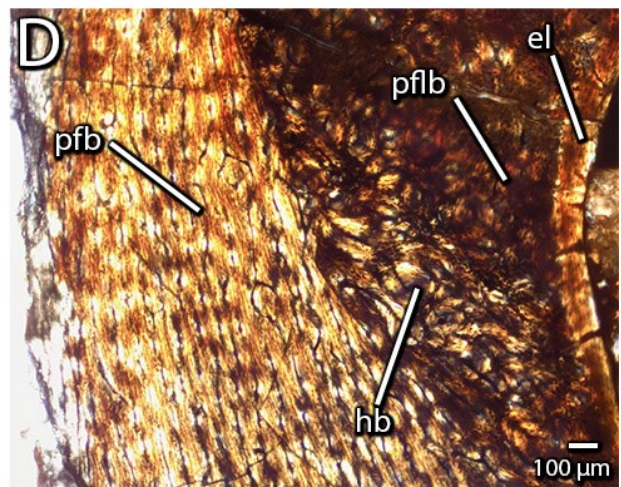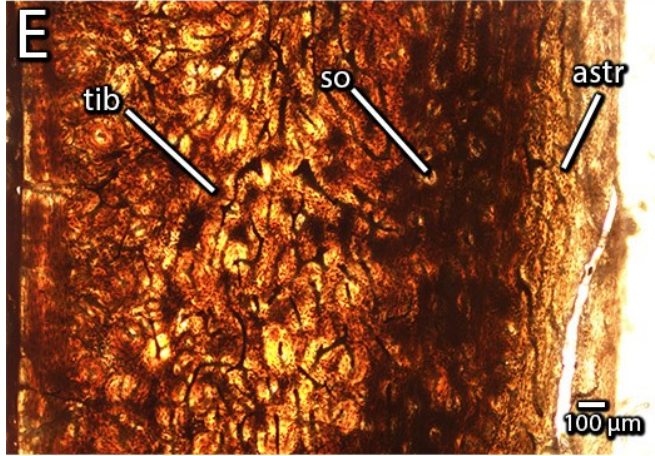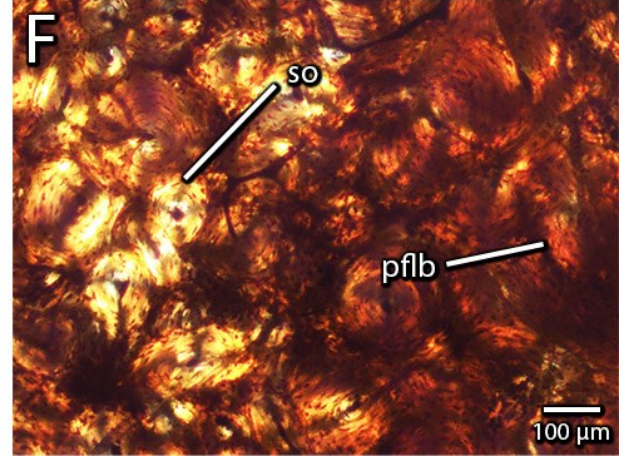
(Previous page)

Fig. 2.26. Histology of the midshaft of a fused avimimid tibiotarsus (IVPP V16337).

Overview of slide under normal light (A) and cross-polarized light (B) showing posterior zone of parallel-fibered bone and dense secondary remodeling of most of the cortex, as well as locations of close-up images. Detail (C) of contact between zone of plexiform, parallel-fibered bone, and secondarily remodeled primary fibrolamellar bone, on the posterolateral side of the tibia. Note line of arrested growth (arrows). Detail (D) of transition from endosteal lamellae (far right) to primary fibrolamellar bone (right) to secondarily remodeled Haversian bone (center right) to parallel-fibered bone with plexiform vasculature, under cross-polarized light. Detail (E) of tibia-astragalus interface, showing small portion of astragalus (right) and heavily remodeled tibia (left) under normal light. Detail (F) of secondary osteons and primary fibrolamellar bone in the inner cortex of the lateral part of the tibia under cross-polarized light. **Abbreviations: astr**, astragalus; **el**, endosteal lamellae; **hb**, Haversian bone; **pfb**, parallel-fibered bone; **pflb**, primary fibrolamellar bone; **plex**, plexiform vascularity; **so**, secondary osteon; **tib**, tibia.
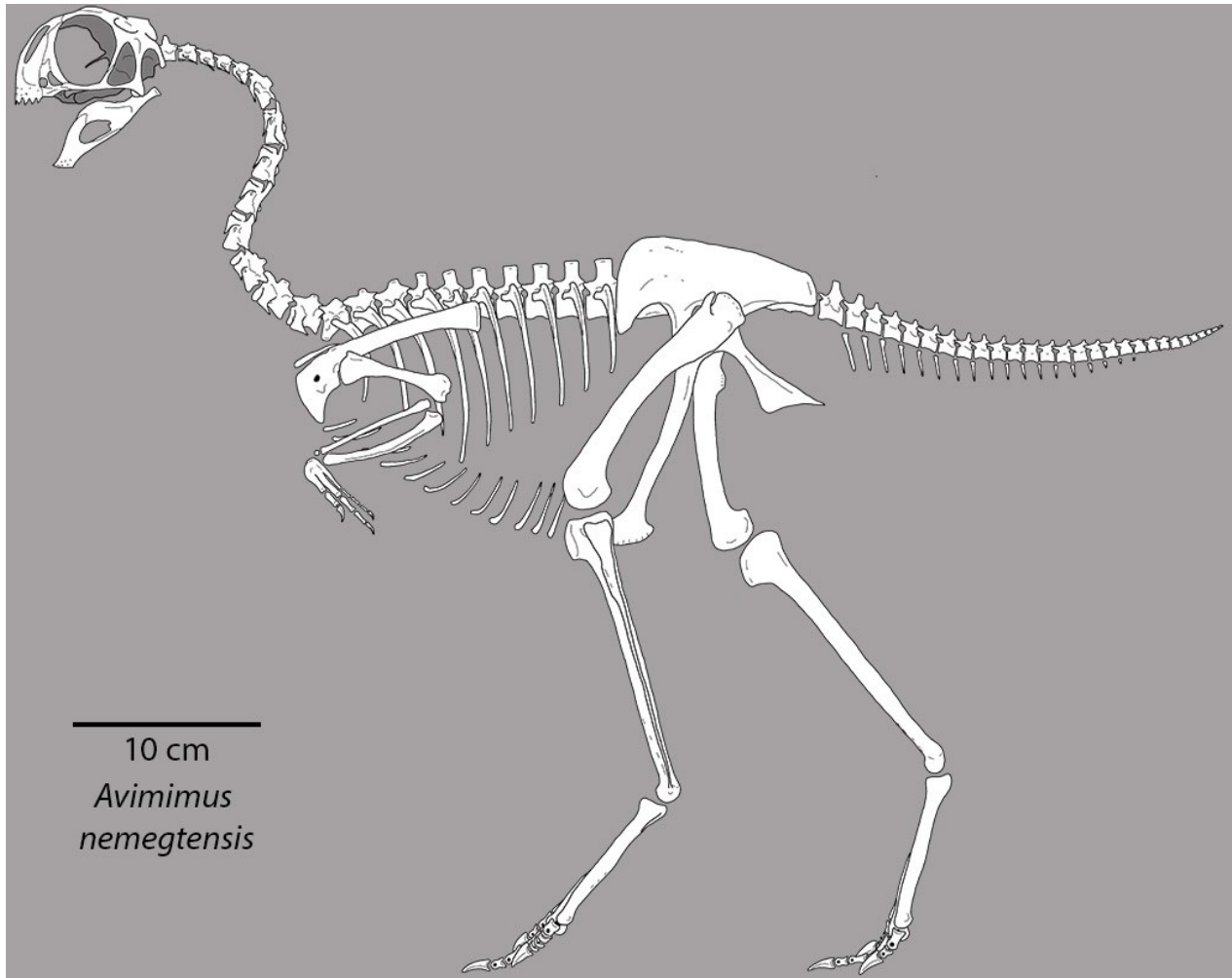
Fig. 2.27. Skeletal reconstruction of *Avimimus nemegtensis*.

Missing portions of skeleton and proportions reconstructed based on *Avimimus portentosus*

(MPC-D 100/129) or material from the Iren Dabasu avimimid bonebed.

CHAPTER 3 – CAENAGNATHIDAE

3.1 INTRODUCTION

Caenagnathidae is a clade of maniraptoran theropods from the Cretaceous of Asia and North America (Fig. 3.0). In contrast to oviraptorids, which are known from multiple complete skeletons, caenagnathids are typically represented by fragmentary material, despite an equally long history of discovery (Gilmore, 1924; Osborn, 1924). Gilmore (1924) described a set of elongate hands from the Upper Cretaceous (Campanian) Dinosaur Park Formation (DPF) and named them *Chirostenotes pergracilis* Gilmore 1924. Subsequent work by C.M. Sternberg (1932, 1934), Parks (1933), and R.M. Sternberg (1940) described feet and a mandible, but only much later would this material be united within Oviraptorosauria as Caenagnathidae (Osmólska, 1976, 1981; Currie, 1989). A partial skeleton of *Chirostenotes pergracilis* (Currie and Russell, 1988) revealed more of the anatomy, and a plethora of mandibular material (Currie et al., 1993) highlighted the diversity within the group. Another partial skeleton (ROM 43250), collected by G.E. Lindblad in 1923 from the Upper Cretaceous (Campanian-Maastrichtian) Horseshoe Canyon Formation (HCF) and described by Sues (1997), cemented the monophyly of Caenagnathidae but stimulated debate about which specimens were conspecific.

Since that time, a number of new discoveries have ameliorated our understanding of the anatomy of caenagnathids. Xu et al. (2007) described the appropriately named *Gigantoraptor erlianensis* Xu et al. 2007 on the basis of a giant skeleton with clear oviraptorosaur affinities. Subsequent cladistic analyses (Lamanna et al., 2014; Funston and Currie, 2016) placed

Gigantoraptor as a basal caenagnathid, mostly on the basis of the mandible. Ma (2017) described

the mandible of *Gigantoraptor* in more detail, and assessed the functional morphology of its

intermediate shape. Although significantly smaller than *Gigantoraptor*, *Anzu wyliei* Lamanna et

al. 2014 is the largest caenagnathid known from North America (Lamanna et al. 2014). It is

represented by three reasonably complete skeletons from the Upper Cretaceous (Maastrichtian)

Hell Creek Formation, which show that it had a prominent cranial crest and a short tail with

modified pygostyle-like distal vertebrae. Sues and Averianov (2015) described additional

material of the miniscule *Caenagnathasia martinsoni* Currie et al. 1993, including vertebrae and

a femur. Yao et al. (2015) described another partial mandible of *Caenagnathasia*, but from the

Iren Dabasu Formation of China, expanding the stratigraphic and geographic range of

Caenagnathasia. Tsuihiji et al. (2015) described a pair of giant mandibles from the Bayn Shiree

Formation of Mongolia, noting similarities to *Gigantoraptor erlianensis*. The same authors then

described much smaller, fused dentaries probably referable to *Elmisaurus rarus* Osmólska 1981

from the Nemegt Formation exposed at Bugiin Tsav (Tsuihiji et al., 2016). Recently, Pu et al.

(2017) published the long-awaited description of 'Baby Louie', interpreting it as a new, giant

caenagnathid closely related to *Gigantoraptor erlianensis*. Yu et al. (2018) subsequently named

an intermediately-sized caenagnathid, *Anomalipes zhaoi* Yu et al. 2018, from the Late

Cretaceous of China, filling the former gap in body sizes of Chinese caenagnathids between

Caenagnathasia and *Gigantoraptor*. In a series of controversial papers, Wang et al. (2017, 2018)

argued that, based on tooth-loss patterns in a Jurassic ceratosaur, caenagnathids experienced

ontogenetic edentulism. On this basis, they argued that the complex structures on the occlusal

surfaces of the dentaries were the vestiges of tooth-bearing structures.

Despite these advances, the anatomy, taxonomy, growth, and phylogenetics of caenagnathids are still unresolved, in part because of fragmentary and non-overlapping specimens. This is especially true of caenagnathids from North America, where multiple taxa coexist in the same formations. Currie (1989) separated material with fused tarsometatarsi and referred it to *Elmisaurus elegans* Parks (1933) based on similarities to the Mongolian *Elmisaurus rarus*. Sues (1997) argued that material from *Elmisaurus elegans* was congeneric with *Chirostenotes pergracilis*, and referred ROM 43250 to the latter. Sullivan et al. (2011) suggested that ROM 43250 (Sues 1997) was sufficiently distinct to merit its own genus, *Epichirostenotes* Sullivan et al. 2011, and named *Ojoraptorsaurus* Sullivan et al. 2011 for pubic material from New Mexico. Longrich et al. (2013) grouped mandibles by size, and proposed a new genus, *Leptorhynchos* Longrich et al. 2013, for material from Texas and Alberta. Within this genus, they erected *Leptorhynchos elegans* Parks (1933) for the fused metatarsi referred by Currie (1989) to *Elmisaurus* and small, upturned mandibles from the DPF (Longrich et al., 2013). Lamanna et al. (2014) countered this, arguing that without overlapping material to unite mandibles and metatarsi in *Leptorhynchos elegans*, it was more conservative to use a taxonomic approach using only species with unambiguous mandibular material.

In recent years, numerous additional caenagnathid specimens have been recovered throughout North America and Asia (Fig. 3.0). Here I use this new material to assess the diversity and growth of caenagnathids. Specifically, I test whether the new specimens from the DPF support the delineation of the three proposed genera (*Caenagnathus collinsi* Sternberg 1940, *Chirostenotes pergracilis*, and *Leptorhynchos elegans*), and, if so, which specimens are referable to which taxon. I also describe new specimens from the Nemegt and Horseshoe Canyon Formations, to document the diversity in those formations. Using osteohistology, I evaluate the

hypothesis of Wang et al. (2018) that caenagnathids lost their teeth through their lifetimes, by testing whether the dentaries have vestiges of tooth-bearing tissues. Finally, I evaluate caenagnathid growth styles using the skeletochronology of individuals of varying size, comparing and contrasting patterns in caenagnathids with other oviraptorosaurs and theropods. Together, these analyses help to resolve some of the ambiguities surrounding caenagnathid anatomy, growth, and phylogeny.

3.2 MATERIALS AND METHODS

Late Cretaceous caenagnathid material in the collections of the CGMP, CMN, MPC, ROM, TMP, and UALVP was examined firsthand. Casts of the type (CM 78000) and paratype (CM 78001) of *Anzu wyliei* were examined for comparison. The material was measured using digital calipers to an accuracy of 0.5 mm or a fabric measuring tape to an accuracy of 1 mm (Appendix 1). Photographs were taken using a Nikon D5000, a Nikon D7200, or a Nikon Coolpix AW120 using conventional photographic techniques. Three-dimensional models of some material were generated using photogrammetric reconstruction in Agisoft Photoscan Standard v. 1.4.3. Some material was scanned using computed tomography using either a Skyscan 1174 or a Siemens Sensation 64 Medical CT scanner. Reconstructed slices were segmented using Mimics 14.0, Dragonfly 3.1, or 3DSlicer 4.8.

Histological thin-sections were made by vacuum-embedding the specimens in Buehler Epothin Resin or Castolite AC polyester resin, and cutting the billet using a Hillquist Thin Section Machine or an Isomet 1000 Precision Sectioning Saw. Billets were adhered to plexiglass slides using Buehler Epothin Resin or 3M Cyanoacrylate glue. Thin sections were ground and

polished from the mounted slides using a variety of grits on a lapidary wheel or by hand on a

glass plate. Slides were imaged under plane polarized and cross-polarized light using NIS

Elements on a Nikon Eclipse E600POL trinocular polarizing microscope with an attached Nikon

DXM 1200F digital camera. Panoramic images of the entire slide were generated by stitching

smaller images together, or by photographing them with transmitted light using a Nikon D7200.

For enhanced clarity and depth of field, some pictures were generated using Z-stacked images.

<p style="text-align:center">3.3 RESULTS</p>

3.3.1 *Caenagnathus collinsi* Sternberg 1940

<p style="text-align:center">Dinosauria Owen, 1842</p>

<p style="text-align:center">Saurischia Seeley, 1888</p>

<p style="text-align:center">Theropoda Marsh, 1881</p>

<p style="text-align:center">Coelurosauria Huene, 1914</p>

<p style="text-align:center">Maniraptora Gauthier, 1986</p>

<p style="text-align:center">Oviraptorosauria Barsbold, 1976</p>

<p style="text-align:center">Caenagnathidae R. M. Sternberg, 1940</p>

<p style="text-align:center">*Caenagnathus collinsi* R.M. Sternberg, 1940</p>

<p style="text-align:center">Figs. 3.1–3.10</p>

Holotype: CMN 8776, mandible

Newly referred material: TMP 1979.014.0001, manual ungual I-2; TMP 1982.019.0222, manual ungual I-2; TMP 1986.036.0323, right femur; TMP 1993.036.0197, right metatarsal II; TMP 1993.036.0198, right metatarsal II; TMP 1993.036.0475, manual ungual II-3; TMP 1993.036.0631, partial left astragalocalcaneum; TMP 1993.075.0049, nearly complete right astragalocalcaneum; TMP 2009.003.0029, manual ungual I-2; UALVP 55725, partial caudal vertebra; UALVP 56638, nearly complete pubes; UALVP 59791, partial ilium.

Horizon and locality: Upper Cretaceous (Campanian) Dinosaur Park Formation. All specimens recovered from Dinosaur Provincial Park, Alberta, Canada.

Etymology: *Caen-* , new, *agnathus*, toothless jaw; *collinsi*, in honour of D. H. Collins.

Revised diagnosis: Large caenagnathid oviraptorosaur diagnosed by the following combination of features and autapomorphies (asterisks): elongate dentary symphysis* (shared with *Anzu wyliei*); low articular ridge of mandible; posterior protuberance on proximal end of metatarsal II*; groove between proximal articular surface and flexor tubercle present in manual ungual II-3 but not I-2*; rounded ventral edge of preacetabular blade; low ilium above the acetabulum; inclined ventral edge of pubic peduncle.

Osteological Description

Mandible:

CMN 8776 (Fig. 3.1) is a nearly complete mandible described by Sternberg (1940) and Currie et al. (1993). It is the largest caenagnathid mandible recovered from the DPF (Table 3.1). The right angular has been reconstructed below the external mandibular fenestra, which has resulted in medial displacement of the right ramus of the mandible (Fig. 3.1A). The dentary can be distinguished from those of other caenagnathids, besides *Anzu wyliei*, by its low occlusal margin and anterior elongation. Like other caenagnathids, the symphysis is fused without a suture. However, the symphysis is much longer anteroposteriorly than most caenagnathids and is not upturned anteriorly into a sharp occlusal margin (Fig. 3.1B). The features of the occlusal surface of the dentary (Fig. 3.1E) are less relieved than those of TMP 2001.012.0012 (*Chirostenotes pergracilis*) and TMP 1992.036.0390 (*Leptorhynchos elegans*). For example, the lingual groove and ridge are shallower and the tubercle of the lingual ridge is level with the low

occlusal margin of the dentary. The symphyseal sulcus is shallow and tapers anteriorly instead of posteriorly, unlike the condition in TMP 2001.012.0012 and TMP 1992.036.0390. At its anterior end, there is a prominent midline tubercle (Fig. 3.1E), which is absent in other caenagnathids, including *Anzu wyliei*. Anterolateral to this tubercle, there is a circular fossa that corresponds to the anterior occlusal groove of other caenagnathids. However, there is no midline anterior occlusal groove, which is usually present. The symphyseal sulcus is bordered laterally by a shallow lingual ridge with a poorly developed tubercle. Lateral to this ridge, the occlusal surface is slightly depressed into a lingual groove, bordered laterally by six lateral occlusal grooves separated by five lateral occlusal ridges (Fig. 3.1E). The lateral occlusal ridges and grooves are more pronounced anteriorly and become less prominent successively. The lateral surface of the dentary is marked by several distinct foramina, but lacks a deep mandibular fossa, which is present in TMP 2001.012.0012 and TMP 1992.036.0390. Instead, there is a shallow depression underneath a poorly-developed lateral shelf (Fig. 3.1B, D). This shelf is similar in position to the lateral flange of *Anzu wyliei*, but is less well developed. Two large foramina, probably pneumatopores, pierce this depression, similar to the pneumatopores in the mandibular fossae of other caenagnathid dentaries. The ventral surface of the dentary is much flatter than those of 'deep-beaked' caenagnathids, but is similarly pierced by numerous foramina. The Meckelian grooves extend along the ventromedial surfaces of the dentaries and converge anteriorly at the posterior end of the symphysis. A vascular canal extends anteromedially from each Meckelian groove, and these canals converge just anterior to the poorly-defined attachment for *M. genioglossus*. The posterodorsal ramus of the dentary is dorsoventrally broad and tapers to a pointed posterior end. The posteroventral ramus is anteroposteriorly longer and dorsoventrally

narrower than the posterodorsal ramus. It inserts onto the lateral surface of the angular and is slight bowed both laterally and ventrally.

Postdentary bones— Caenagnathid mandibles are characterized by a fusion of the articular, surangular, and coronoid, termed the articular-surangular-coronoid (ASC) complex (Currie et al., 1993). Both of the ASC complexes are preserved in CMN 8776, but the left side is slightly better preserved. The anterior part of the surangular has an interdigitating contact with the dentary. The anteroposterior length of this contact is greater than in *Chirostenotes* (TMP 2001.012.0012) or *Leptorhynchos* (TMP 1992.036.0390), extending posteriorly to the level of the coronoid process. Ventral to this contact, the surangular flares laterally as it forms the dorsal edge of the external mandibular fenestra, but not to the same degree as in *Chirostenotes* (TMP 2001.012.0012). The coronoid process is rugose and medially inturned, but does not project far above the highest point of the dentary (Fig. 3.1D), contrasting with the condition in *Chirostenotes* (TMP 2001.012.0012). The dorsoventrally broad ramus of the surangular descends towards the articular, which is in the form of a low ridge. There is no surangular foramen, but there is a shallow fossa on the medial surface of the surangular posterior to the external mandibular fenestra. The medial glenoid of the articular is larger transversely and anteroposteriorly than the lateral one. The retroarticular process is hatchet-shaped and directed posteroventrally and slightly laterally. The angular is mostly missing on the right side, and its reconstruction has distorted the right ramus of the mandible, pulling it medially. On the left side, it is completely preserved and well articulated with the dentary (Fig. 3.1D). Anteriorly, it is sheetlike and inserts on the medial surface of the dentary. It tapers dorsoventrally towards its midshaft, becoming more rodlike where it underlies the external mandibular fenestra. Here, it has a prominent lateral ridge underlain by a groove, which accommodate the posteroventral ramus of

the dentary. Posterior to the external mandibular fenestra, the angular becomes platelike and lies against the lateral surface of the surangular. It extends to the posterior end of the mandible and forms the lateral portion of the retroarticular process. The splenial is a thin splint of bone that extends along the medial surface of the angular. Posteriorly, it underlies the prearticular, which is also rodlike in this region. The prearticular expands dorsoventrally towards its posterior end, where it is platelike as it underlies the medial glenoid of the articular region. It contributes to the medial and ventral parts of the retroarticular process.

Axial skeleton:

      Caudal Vertebra—UALVP 55725 consists of the right side of the centrum and the lower portion of the neural arch (Fig. 3.2). The centrum is large (39.7 mm long), amphicoelous, and spool-shaped, with a large (12.5 mm) lateral pleurocoel (Fig. 3.2C). The anterior articular surface (31.5 mm dorsoventrally) would have been pentagonal in shape, with a midline ventral keel (Fig. 3.2D). The posterior articular surface (31.4 mm dorsoventrally) is more rounded than the anterior articular surface and lacks a midline ventral keel (Fig. 3.2B). The pleurocoel pierces the lateral wall of the vertebra and is inclined dorsolaterally to ventromedially. The neural arch is fused indistinguishably to the centrum. There is a shallow depression at the base of the postzygapophysis that may be pneumatic in origin. The pre- and postzygapophyses are divided by a V-shaped transverse groove, which is likely the ventral margin of a large infradiapophyseal fossa (Fig. 3.2C). There is no caudal rib (transverse process), but the caudal rib would have been positioned dorsal to the infradiapophyseal fossa and above the portion of the neural arch that is preserved. The interior of the centrum is composed of camellate bone (Britt, 1993), which is exposed where the centrum is weathered. On the medial side of the neural arch, the lateral wall

of the neural canal is preserved (Fig. 3.2E). The neural canal has a flat bottom and would have been wider ventrally than dorsally.

Appendicular skeleton:

Manual Unguals—In addition to the material described by Bell et al. (2015), two large manual unguals I-2 (Fig. 3.3 TMP 1979.014.0001, TMP 1982.019.0222) from the DPF of Dinosaur Provincial Park, Alberta, are referable to *Caenagnathus collinsi*. Both specimens are strongly curved and have well-developed, distally positioned flexor tubercles. The proximodorsal lip is well developed in both specimens, and the lateral and medial vascular grooves do not bifurcate proximally, as they do in manual ungual II-3 (TMP 1979.014.0499, TMP 1993.036.0475). TMP 1982.019.0222 is larger (91 mm around outside curve) than TMP 1979.014.0001 (~90 mm around outside curve), although both are comparable to TMP 2009.003.0029 (85 mm around outside curve). Neither of the unguals I-2 has a transverse groove separating the flexor tubercle from the proximal articular surface, which appears to distinguish them from *Chirostenotes pergracilis* (CMN 2367) and the larger unguals from the Frenchman Formation (CMN 346).

Ilium—A relatively large ilium (UALVP 59791; Fig. 3.4) was collected in the summer of 2018 near Iddesleigh in the eastern part of Dinosaur Provincial Park. The ilium preserves a complete preacetabular process and the acetabulum, but the postacetabular process is entirely missing. The preacetabular blade is ventrally expanded below the level of the pubic peduncle and its ventral edge is rounded (Fig. 3.4A), as in *Nomingia gobiensis* Barsbold et al. 2000b. The dorsal edge of the preacetabular blade is complete and curves gently at its anterior end, but is more straight posteriorly. This contrasts with the morphology of TMP 1979.020.0001

(*Chirostenotes pergracilis*; see section 3.3.2), where this edge is curved posteriorly. Furthermore,

UALVP 59791 is dorsoventrally shorter above the acetabulum than is TMP 1979.020.0001,

despite the much greater size of the acetabulum and therefore the individual. In ventral view

(Fig. 3.4C), the preacetabular blade is deflected slightly laterally, resulting in a large cuppedicus

fossa. On the medial side of the ilium (Fig. 3.4B), this cuppedicus fossa is bordered dorsally by a

prominent ridge with a large facet, probably for the first sacral rib. This ridge tapers in transverse

thickness anteriorly, but continues to the anterior edge of the ilium as a shallow lip separating the

insertion for *M. puboischiofemoralis internus 2* from the dorsal portion of the preacetabular

blade. The pubic peduncle is large compared to other oviraptorosaurs and its ventral edge is

anterodorsally inclined, as in TMP 1979.020.0001. However, it extends much further ventrally

than TMP 1979.020.0001 relative to the cuppedicus shelf. Also, its anterior end protrudes from

the base of the peduncle, giving it a bootlike profile in lateral view (Fig. 3.4A), which is not the

case in TMP 1979.020.0001 or TMP 1981.023.0034–5 (*Leptorhynchos elegans*; see section

3.3.4). In ventral view (Fig. 3.4C), it has a triangular outline, expanding posteriorly towards the

acetabulum. There is no foramen on its lateral surface, contrasting with the condition in TMP

1981.023.0034–5. Like all oviraptorosaurs, the acetabulum constricts in transverse thickness

towards its midpoint, expanding transversely towards either peduncle. The acetabular surface is

slightly concave posterior to the pubic peduncle, but there are no deep grooves on its dorsal

surface. The ischiadic peduncle is triangular in lateral view (Fig. 3.4A), but expands transversely

towards its ventral end, contrasting with the ventrally tapering peduncles of other

oviraptorosaurs. This gives the ischiadic peduncle a square aspect in anteroposterior view. The

ischiadic peduncle is slightly everted laterally, as is the case in TMP 1979.020.0001, resulting in

slight lateral exposure of the acetabular articular surface. The medial surface of the ilium shows

evidence of a shallow anterior depression and a ridge that would have separated this from the intermediate depression, but the posterior depression is broken. Ventral to these depressions, the ilium is transversely thickened, forming a promontory for the attachments of the sacral ribs, of which four are preserved. However, this promontory is not as well developed as TMP 1981.023.0034–5 (*Leptorhynchos elegans*; see section 3.3.4), despite the much greater size of UALVP 59791. The first sacral rib attachment is likely represented by the facet on the cuppedicus ridge (Fig. 3.4B). Posterior to this, there is a small fossa that separates it from the second sacral rib attachment, which is just dorsal to the pubic peduncle. The third sacral rib attachment is directly dorsal to the midpoint of the acetabulum, and the fourth is directly dorsal to the ischiadic peduncle. Together, these attachment sites form a gentle arc descending from anterior to posterior, congruent with the descent of the sacral ribs on successive sacral vertebrae.

Pubis— UALVP 56638 (Fig. 3.5) is a large, nearly complete pair of pubes, missing only the anterior portion of the pubic boot. No locality data accompanies the specimen because it was mislabelled, but the excellent preservation and associated matrix are consistent with the DPF. The pubes are relatively straight in anterior view (Fig. 3.5B), and lack the sinuate profile of TMP 1994.012.0603. Thus, they are relatively narrower proximally than other caenagnathid pubes. The proximal end has a transversely wide, semicircular-trapezoidal iliac contact surface, and a roughly triangular ischiadic contact. The ischiadic contact is less offset from the shaft (Fig. 3.5A) than in other caenagnathids. Separating these two contact surfaces is a relatively small, poorly excavated portion of the acetabulum. Medial to the ischiadic contact is a deep fossa (Fig. 3.5B), bordered posteriorly by a thin crest of bone. Just ventral to the ischiadic contact, on the lateral side, there is a low, rounded ridge. Proximally, the shaft of the pubis is transversely flattened, but distally it is more round in cross-section. The shafts are relatively straight in lateral view,

especially distally, but the proximal end is slightly curved anteriorly. As in TMP 1980.016.2095 (Caenagnathidae indet.; see Section 3.3.6), a proximodistal ridge continuous with the proximal end of the pubic apron extends toward the ischiadic contact until merging with the shaft approximately halfway. The pubic apron begins just proximal to half the length of the pubes from the proximal end (Fig. 3.5B). Its proximal edge is dorsally concave in anterior view (Fig. 3.5B), but this outline is curved rather than pointed as in TMP 1994.012.0603 (Caenagnathidae indet.; see Section 3.3.6). The apron is narrow and continuous with the anterior surfaces of the shafts, creating a posterior concavity. There is a small, slit-like pubic fenestra (Fig. 3.5B, C), which contrasts with the larger oval fenestra of TMP 1994.012.0603. The posterior portion of the pubic boot forms a quarter-circle in lateral view (Fig. 3.5D). The lateral surface of the boot is slightly scalloped, especially towards the ventral edge. The proximal end is attenuated to a point, and its dorsal surface would have been parallel to the vertebral column. From this point, the boot expands transversely towards the anterior end, resulting in a triangular profile in ventral view. On the ventral surface of the boot, there is a shallow groove that marks the union of the pubes, even though they are completely fused.

Femur—A large right femur (Fig. 3.6), TMP 1986.036.0323, was recovered from the DPF of Dinosaur Provincial Park, Alberta. The shaft is 114 mm in circumference, and nearly straight, with little anterior convexity. The proximal articular head is well developed and meets the long axis of the femur at nearly a right angle. The greater trochanter is large and separated from the femoral head by a shallow concavity. The fingerlike anterior trochanter is level with and pressed against the greater trochanter, but separated by a small furrow (Fig. 3.6D, E). Distal to the anterior trochanter is an accessory trochanteric crest (Fig. 3.6B) similar to that of *Anzu wyliei* (Lamanna et al., 2014), *Chirostenotes pergracilis* (Currie and Russell, 1988), and

Microvenator celer Ostrom 1970 (Makovicky and Sues, 1998). The lateral distal condyle extends further distally than the medial condyle, and the two are separated by a deep popliteal fossa. The lateral distal condyle has an ectocondylar tuber and a deep notch separating it from the crista tibiofibularis (Fig. 3.6F).

Astragalocalcaneum—Two large astragalocalcanei (TMP 1993.075.0049, TMP 1993.036.0631) have been recovered from the DPF of Dinosaur Provincial Park. TMP 1993.075.0049 (Fig. 3.7) is from the right side, and is more complete than TMP 1993.036.0631, which is from the left. In both, the astragalus and calcaneum are fused, though there is a posterior suture that opens into a furrow (Fig. 3.7E). There is a well-developed fibular facet on both the astragalus and calcaneum. The calcaneum has a poorly developed medial tuber, and the astragalus is only slightly invaginated posteriorly for the calcaneum. The base of the ascending process has a median fossa instead of a transverse groove, as in other oviraptorosaurs, but unlike *Anzu wyliei* (Lamanna et al., 2014), which has a rugose tuberosity. The astragalocalcanei can be distinguished from those of ornithomimids and deinonychosaurs by the simple contact of the astragalus and calcaneum, the deeply excavated fibular facet on the dorsal surface of the calcaneum, and the median fossa of the ascending process of the astragalus in place of a transverse groove.

Metatarsal II—Two large second metatarsals (TMP 1993.036.0197, TMP 1993.036.0198) are referable to *Caenagnathus collinsi* (Fig. 3.8). They are both from the right side, and TMP 1993.036.0197 is larger than TMP 1993.036.0198. The proximal end has a well-developed, anteriorly projecting facet for metatarsal IV (Fig. 3.8C, D, I, J), and a posterior concavity for metatarsal III. On TMP 1993.036.0198, there is a posterior process (Fig. 3.8B, C) on the proximal end that makes the articular surface C-shaped in proximal view (Fig. 3.8E), and

distinguishes these metatarsals from *Chirostenotes pergracilis*. This process appears to have been broken in TMP 1993.036.0197. The shaft of the second metatarsal is straight with no medial deflection of the distal condyle and a poorly developed but faceted posteromedial ridge. The facet for the third metatarsal is wide distally, but narrows proximally and terminates about halfway up the shaft (Fig. 3.8C, I). In *Chirostenotes pergracilis*, this facet continues proximally for at least three-quarters of the length of the shaft. There is no rugosity proximal to the distal condyle for the insertion of *M. tibialis cranialis* in either TMP 1993.036.0197 or TMP 1993.036.0198*,* which distinguishes them from *Leptorhynchos elegans*. The second metatarsals can be distinguished from the smaller *Chirostenotes pergracilis* by the anterior projection of the facet for metatarsal IV on the proximal end, the posterior process on the proximal end, and the relatively short facet for metatarsal III on the medial side of the shaft. They can be distinguished from *Leptorhynchos elegans* by the lack of coossification with the distal tarsals, the poorly developed posteromedial ridge, and the lack of the rugose insertion of *M. tibialis cranialis*.

Osteohistology

       UALVP 56638—A fragment of the proximal shaft of UALVP 56638 was thin sectioned to examine growth (Figs. 3.9, 3.10). Unlike the limb bones of caenagnathids, the pubes lack a hollow medullary cavity, and therefore preserve a more complete growth record of the individual. The histological texture of the cortex of UALVP 56638 differs greatly between the anterior and posterior sides of the bone (Fig. 3.9B). Whereas anteriorly the cortex is composed of primary bone, posterior to its midpoint, the cortex is densely remodeled by numerous generations of secondary osteons (Fig. 3.10D). Separating these regions are numerous erosive cavities forming the spongy medullary region. Trabeculae between these cavities are composed of low

vascularity parallel-fibered bone (Fig. 3.10A), indicating several pulses of erosion and deposition. Any evidence of embryonic bone has been destroyed by expansion of these cavities. The anterior portion of the cortex preserves an exceptional growth record, and at least 12 lines of arrested growth (LAGs) can be detected alongside several other growth marks (Fig 3.9C, D). LAGs decrease in spacing gradually towards the periosteal surface, but there is a distinct transition in LAG spacing after the fifth LAG (Fig. 3.9A). All LAGs are roughly parabolic in shape, and therefore become more closely spaced on the medial and lateral sides of the cortex. On the lateral side, this results in a thick band of avascular parallel-fibered bone at the periosteal surface, which contains at least nine LAGs (Fig. 3.9A). On the medial side of the cortex there are only four LAGs preserved, and the rest have been obliterated by resorption at the periosteal surface as a result of cortical drift. The wide spacing between the LAGs on the anterior side of the cortex resulted from deposition of fibrolamellar bone in the intervening spaces (Fig. 3.9C, D), rather than parallel-fibered bone. This bone is vascularized, which provides more information about growth between the deposition of LAGs (Fig. 3.10 E, F). Throughout the first eight LAGs, vasculature in these intervening areas is oriented longitudinally and primary osteons are well-developed. There is one unusual concentration of large secondary osteons near the midpoint of the cortex (Fig. 3.10B), possibly related to remodeling from biomechanical stress. The first four LAGs are more widely spaced, but the distance between LAGs four and five is about half of the previous three. Subsequent LAGs are evenly but tightly spaced, averaging about 350 μm between LAGs and therefore per year. However, the final five growth marks are more widely spaced than the previous six, which would apparently indicate an increase in growth rate after a prolonged decrease. However, this is possibly the result of cortical drift, as these growth marks coalesce on the medial and lateral sides, and therefore bone was only being deposited on

the anterior surface of the pubis. This results in a smaller area of deposition and an overall decrease in the volume of bone being deposited (and therefore growth rate), despite appearing to indicate the opposite. Between the outer LAGs, the primary bone shows a different pattern of growth than the inner LAGs. The bone in the more endosteal part of the intervening space, which would have been deposited early during the year, has radial orientation of the vascular canals (Fig. 3.10F), indicating a relatively high growth rate. However, this grades into longitudinal vascularity later during the year, and finally an annulus of avascular parallel-fibered bone (Fig. 3.10C) is deposited preceding the next LAG. Like in hadrosaurs (Horner et al., 2000; Woodward et al., 2015; Woodward, 2019), this likely indicates that this individual experienced seasonal differences in growth. Between some of the LAGs, there are linear features that could be mistaken for cyclical growth marks at low magnification, but closer examination suggests that they do not reflect a cessation of growth. Instead, they are formed by alignment of osteocyte lacunae and changes in their density (Fig. 3.10E, F). It is likely that these osteocytes are aligned at what was the periosteal surface when they were deposited, and therefore they possibly indicate inconsistent growth rates within a single year. It is possible that these marks reflect stress or other life events that temporarily decreased growth rate, or, conversely, favourable conditions that resulted in an increase in growth rate.

Remarks

The mandibles of *Caenagnathus collinsi* were first described by Sternberg (1940), who suggested they were those of a large bird. No unambiguous material of *Caenagnathus collinsi* has been discovered since, but large size and morphological differences in several isolated elements from the DPF suggests they may pertain to *Caenagnathus collinsi*. These large isolated

bones produce estimates of femoral length ranging from 360–400 mm based on the proportions of other caenagnathids. These estimates are significantly larger than known specimens of *Chirostenotes pergracilis*, which can be assumed to be osteologically mature on the basis of osteohistology, as discussed subsequently (see Section 3.3.2). Furthermore, systematic differences in the morphology of the unguals, pubes, and metatarsals suggests that these elements are not referable to *Chirostenotes pergracilis* or *Leptorhynchos elegans*. Although it could be argued that these differences are the result of allometry, this seems unlikely because they are not incipiently developed in smaller specimens. For example, the presence of grooves between the flexor tubercle and proximal articular surface of the manual unguals appears to be opposite the pattern in *Chirostenotes pergracilis*, although no comparable material exists for *Leptorhynchos elegans*. Similarly, a posterior process on metatarsal II is completely absent in *Chirostenotes pergracilis* and *Leptorhynchos elegans*. The ilium (UALVP 59791; Fig. 3.4) is much larger than those known for *Chirostenotes pergracilis* (TMP 1979.020.0001; TMP 2002.012.0103; see Section 3.3.2), and is morphologically different. Whereas the ilium of *Chirostenotes pergracilis* is tall above the acetabulum and has a convex dorsal edge, UALVP 59791 is absolutely shorter above the acetabulum (despite greater size of the element) and its dorsal edge is straight. Similarly, the morphology of the pubic peduncle differs from that of TMP 1979.020.0001 in that it has an anterior process. The large pubes (UALVP 56638; Fig. 3.5) represent an individual comparable in size to the types of *Anzu wyliei*, much larger than *Chirostenotes pergracilis* or *Leptorhynchos elegans*. They are also morphologically similar to those of *Anzu wyliei*, although the pubic boots of each taxon are badly broken. If these pubes are referable to *Caenagnathus collinsi*, they suggest that it was similar in maximum body size to *Anzu wyliei*, much larger than sympatric caenagnathids. Although it is possible that these

elements are simply aberrantly large individuals of *Chirostenotes pergracilis* or *Leptorhynchos elegans*, it is more reasonable to interpret them as representatives of *Caenagnathus collinsi*, which is expected to be larger on the basis of the holotype mandible (CMN 8776). This is further supported by their systematic morphological differences from elements that can be unambiguously referred to *Chirostenotes pergracilis* or *Leptorhynchos elegans*. Together, these specimens elucidate the anatomy of *Caenagnathus collinsi* (Fig. 3.11) and greatly improve our understanding of its biology.

Osteohistology of UALVP 56638 shows that this individual was at least 14 years old and approaching maximum body size. It can therefore be considered a mature individual. As expected in any theropod, growth was initially rapid, but continued at a slower pace later in life (Fig. 3.12). It is likely that sexual maturity corresponded with the stark decrease in LAG spacing (Castanet et al., 2004; Erickson et al., 2007; Lee and Werning, 2008; Köhler et al., 2012), after the fifth or sixth year of life. Despite the large size of this individual, comparable in size to the holotype of *Anzu wyliei*, it was still increasing the anteroposterior thickness diameter of the pubis late in life. This may be related to muscular function of the pubis, or possibly prolonged cortical drift. However, the transverse diameter of the pubis was not increasing, and therefore it is unlikely that the animal was increasing body mass significantly. Accordingly, the bone on the lateral surface can be characterized as an external fundamental system (Woodward et al., 2011a). The maximum body size of *Caenagnathus collinsi* was therefore similar to *Anzu wyliei*, assuming that the type specimen of the latter is close to maximum body size.

3.3.2 *Chirostenotes pergracilis* Gilmore 1924

Chirostenotes Gilmore, 1924

Chirostenotes pergracilis Gilmore, 1924 sensu Longrich et al., 2013

Figs. 3.13–3.43

Holotype: CMN 2367, left and right hands.

Referred material: CMN 2690, partial articular and surangular; CMN 8538 (*"Macrophalangia canadensis"* Sternberg 1932), right partial tibia, astragalus, and foot; TMP 1979.20.1, partial skeleton; TMP 1990.56.6, dentary.

Newly Referred Material: TMP 1984.043.0070, partial dentaries; TMP 1992.036.1237, partial dentaries; TMP 2001.12.12, nearly complete mandible; UALVP 59400, partial skeleton including mandible, cervical vertebrae, caudal vertebrae, distal end of tibia, astragalus, and distal tarsal III.

Horizon and Locality: Upper Campanian of the Dinosaur Park Formation. All specimens found within Dinosaur Provincial Park, Alberta, Canada.

Etymology: *Chiro-* , hand, *stenos*, narrow; *per-*, throughout; *gracilis*, slender.

Revised Diagnosis (modified from Currie and Russell 1988): Medium-bodied caenagnathid oviraptorosaur diagnosed by the combination of the following features and autapomorphies (asterisks): mandible with upturned occlusal edge; tall articular ridge of mandible steeply offset from ramus of articular-surangular-coronoid complex; six sacral vertebrae with pleurocoels; digit III of manus longer than digit I, but with slender phalanges, having a diameter of less than half that of pahalanges in other digits*; well-developed posterodorsal lip on manual unguals; groove between proximal articular surface and flexor tubercle present in manual ungual I-2 but not II-

3*; dolichoiliac, prepubic pelvis; inclined ventral edge of pubic peduncle; tall ilium above the acetabulum; distal tarsals not fused to proximal metatarsus at maturity; proximal metatarsals not coossified at maturity; short tail with anteroposteriorly broad chevrons.

Description

Skeletons

CMN 2367:

The type of *Chirostenotes pergracilis* was described by Gilmore (1924), but has received little attention since, except for comparison with TMP 1979.020.0001 (Currie and Russell 1988). The specimen (Fig. 3.13) entails two partial articulated hands, the right slightly more complete than the left. In 2018, the type site was revisited, and a small portion of the right ungual II-3 was found. Unfortunately, it provides no additional anatomical data.

Phalanges I-1, II-1, II-2 and III-1 from the left hand are preserved, alongside the unguals I-2 and II-3 (Fig. 3.13). Phalanx I-1 is mostly complete, although it is missing its proximal end. The shaft is straight and cylindrical, although its ventral surface is flattened distally. The condyle is nearly symmetrical, and the lateral and medial portions are equal in size. However, the medial ligament fossa is deeper and more circular than the lateral one. Ungual I-2 is complete except for a small part of the distal tip. It is strongly recurved and has a large flexor tubercle. The proximodorsal lip is well-developed. The flexor tubercle has a flat ventral surface and is separated from the proximal articular surface by a pronounced sulcus, which differentiates it from *Caenagnathus collinsi*. The medial and lateral vascular grooves are well developed but neither bifurcates proximally. Phalanx II-1 is crushed and only the distal half is preserved. The shape of the shaft is deformed by crushing, but it is generally cylindrical with slight elongation

along its dorsoventral axis. The distal condyle is asymmetrical, with a ventrally directed medial portion and a dorsally deflected lateral portion. Accordingly, the sulcus between the two condyles is inclined ventromedial to dorsolateral. Phalanx II-2 is complete and, despite some crushing and fragmentation, is relatively undeformed. The proximal end is saddle-shaped, and the median ridge and saddles correspond in inclination to the offset distal condyles of phalanx II-1. The shaft of phalanx II-2 is slightly twisted, which results in the lateral surface of the distal condyle being more exposed in dorsal view. The distal condyles are relatively equal in size, but the lateral condyle is further dorsal and slightly inclined, as previously described. Ungual II-3 is relatively straight, like that of *Apatoraptor pennatus* Funston and Currie 2016 (Funston and Currie 2016) and other caenagnathids in general. The flexor tubercle is distally positioned and is greatly reduced compared to ungual I-2 and even other unguals II-3 of other caenagnathids, like *Anzu wyliei*, *Apatoraptor pennatus*, and those described by Bell et al. (2015). In contrast, the proximodorsal lip is pronounced, and extends further dorsally than the flexor tubercle extends ventrally. Separating the crescentic proximal articulation from the flexor tubercle is a wide but shallow sulcus, contrasting with the deeper grooves of *Anzu wyliei*, *Apatoraptor pennatus*, and those described by Bell et al. (2015). Each side has a vascular canal extending from the blunt distal tip of the ungual. Neither bifurcates proximally, and the lateral groove is both deeper and positioned further dorsally than the medial one. Phalanx III-3 is the only phalanx from the third digit preserved on the left side. It is small and the proximal end is missing. The shaft is roughly cylindrical, although it is slightly compressed mediolaterally, and it is flattened dorsally just proximal to the condyles. The distal condyles do not protrude dorsally beyond the shaft, which contrasts with the other phalanges preserved from the left hand. Like phalanx II-1, the distal condyles are inclined dorsaterally to ventromedially. Although ungual III-4 is shown in

Gilmore's (1924) original plates, it is not currently present in the CMN collection. It is possible that it was damaged during collection, or that it has been lost since.

The right hand includes parts of metacarpals I and II, phalanges I-1, II-1, II-2, III-3 and unguals I-2 and III-4. Metacarpal I is represented by the distal third of the bone. The shaft is ovate in cross-section, with the long axis inclined dorsolateral to ventromedial relative to the condyles. The condyles are unequal, and the medial is larger and protrudes further distally. Phalanx I-1 is nearly complete, missing only the dorsal part of the distal condyles. The proximal articulation is asymmetrical and the lateral facet is larger than the medial one. Similarly, the medial facet is excavated more deeply than the lateral facet, which complements the more distally projecting medial condyle of metacarpal I. The shaft of phalanx I-1 is gently arched dorsally, but not to the same degree as *Apatoraptor pennatus* (Funston and Currie 2016). The distal condyles are damaged, but there is no reason to suspect that they differ from those of the left phalanx I-1. The right ungual I-2 is slightly larger than the left, but is consistent in morphology. The flexor tubercle is well developed and there is a groove separating it from the proximal articular surface. The proximodorsal lip has been removed by erosion. Metacarpal II is represented by a portion of the shaft and the distal condyles. The shaft is slightly elliptical in cross-section, and there is a facet on its dorsolateral surface that probably accommodated metacarpal III. The lateral distal condyle is mostly missing, but together the condyles appear to have formed a saddle-shaped articulation. The distal outline of the medial condyle is cresentic, and both condyles appear to have protruded dorsally and ventrally past the margins of the shaft. The medial ligament fossa is shallow and roughly oval in shape. Phalanx II-1 is complete except for the lateral side of the proximal end. The medial facet of the proximal end faces posteromedially, rather than directly posteriorly, which accommodates the large crescentic

medial condyle of metacarpal II. The shaft is mediolaterally compressed and has a small groove

on its ventrolateral surface similar to that on phalanx II-2 of *Anzu wyliei* (Lamanna et al. 2014),

but it is not as well developed. Like in the left hand, the distal end of phalanx II-1 is

asymmetrical, with a larger, more dorsally-directed lateral condyle. Only the proximal part of

phalanx II-2 is preserved, and it is badly crushed. The proximal articular surface is identical to

that on the left hand, and is roughly symmetrical with a median ridge. The shaft is mediolaterally

compressed and lacks the groove on the ventrolateral surface that is present in *Anzu wyliei*

(Lamanna et al. 2014). Gilmore's (1924) original plates show at least one phalanx from the third

digit articulating with the ungual, and based on their position below the second digit, it is

possible that the entire third digit was preserved. Regardless, only the ungual remains in the

CMN collection. Ungual III-4 is small and intermediate in curvature between I-2 and II-3, but

more gracile than either. The flexor tubercle is large, square, and positioned far from the

proximal articular surface, which is broken. A moderately deep groove would have separated

these features. The proximodorsal lip is broken, but Gilmore's (1924) plates show it was small

regardless.

TMP 1979.020.0001:

This partial skeleton was described by Currie and Russell (1988), but new insights into

caenagnathid anatomy mean a redescription is warranted. The specimen consists of a sacrum,

right coracoid, partial hand, partial pelvis, and a relatively complete but crushed right hindlimb.

Sacrum—Like those of other caenagnathids, the sacrum of TMP 1979.020.0001 (Fig.

3.14) incorporates six vertebrae. The neural arches are indistinguishably fused, but sutures can

still be discerned between the centra of the first five vertebrae. The centrum of the sixth vertebra

does not appear to be fused to the fifth sacral (Fig. 3.14D). With the exception of the first centrum, which is barrel-shaped, the centra are progressively flattened dorsoventrally. The first five centra have deep lateral pleurocoels, but these decrease in size successively. The ventral surfaces of sacral vertebrae 2–5 have a midline sulcus, which is best developed on sacral 3. Fusion of the neural spines forms a tall fan that decreases in height posteriorly (Fig. 3.14A). There is a gap between the neural spines of sacral vertebrae 3 and 4; this same condition is present in another sacrum, TMP 1984.163.102 (see section 3.3.6), which suggests it is not the result of breakage. Each neural arch is invaded by a series of pneumatic fossae, and these depressions are separated by tall ridges on the lateral sides of the neural spines. The sacral ribs are positioned lower on the neural arches successively, with the exception of sacral rib 4, which is directed more dorsally. Most of the sacral ribs are represented only by their bases, which are fused to the sacrum, but the left sacral rib 5 is fully preserved. It is hatchet shaped in ventral view and expands posteriorly into a pointed process (Fig. 3.14C, D).

Coracoid—The coracoid (Fig. 3.15A, B) is relatively complete, missing only its dorsal edge. It was unfused to the scapula, based on clean bone surface on the posterior edge. The glenoid is transversely thickened compared to the rest of the bone, and it forms the posterior part of a raised platform that connects with the biceps tubercle. Dorsal to this, a small coracoid foramen pierces the bone, and it opens dorsally because of the raised platform. The dorsal portion of the coracoid is platelike but it thickens transversely towards the caudoventral process. This process (Fig. 3.15A) is relatively short for an oviraptorosaur, but strongly curved posteriorly into a hook-like process. The medial surface of the coracoid is concave, following the convex profile of the lateral surface. There is a small fossa medial to the biceps tubercle, as is the case in MPC-D 100/33, an oviraptorid from the Nemegt Formation of Mongolia.

Manus—The left manus of TMP 1979.020.0001 (Fig. 3.15C) consists of the distal end of metacarpal I, phalanges I-1, II-1, II-2, III-3, and unguals I-2 and II-3. Currie and Russel (1988) figured phalanx III-1 of the specimen, but that element is no longer accessioned with the rest of the material. It has perhaps been lost or damaged in the intervening period. Metacarpal I has a crescentic distal end, virtually identical to that of CMN 2367. Like in that specimen, the lateral part of the condyle is slightly larger than the medial part. As is typical of caenagnathids, phalanx I-1 is comparable in length and width to II-1 (Fig. 3.15C), rather than being much longer and more robust, as is the case in heyuannines. The shaft is relatively straight, rather than being curved dorsally as in *Apatoraptor*. Ungual I-1 is smaller than II-3. It has a prominent proximodorsal lip, but the flexor tubercle is missing. Phalanx II-1 is about equal in length to II-2, but has larger, more gingylmoid distal condyles. Phalanx II-2 is the longest of the hand. Unlike *Anzu*, it lacks a ventral groove for flexor tendons (Fig. 3.15C). Ungual II-3 is elongate and straighter than typical in oviraptorosaurs, but not as straight as in *Apatoraptor*. It has a large proximodorsal lip and a modest flexor tubercle separated from the proximal articulation by a shallow transverse groove. Phalanx III-3 is gracile and would have had a relatively ginglymoid distal condyle. Its length relative to other phalanges of the third digit cannot be determined, although Currie and Russell (1988) figured it longer than phalanx III-1, which is typical of oviraptorosaurs.

Ilium—The left ilium (Fig. 3.16A–C) is nearly complete, but is missing a small portion of the preacetabular process. The ilium is tall and strongly dolichoiliac, with a small, pointed postacetabular blade and a large, anteriorly downturning preacetabular blade. In these features it differs from *Nomingia gobiensis*, where the postacetabular blade is broad and rounded, and the preacetabular blade is not as downturned. The cuppedicus fossa is relatively well developed (Fig.

3.16B), but is only minimally exposed laterally. The pubic peduncle is larger than the ischiadic

peduncle and its straight ventral edge is inclined anterodorsal-posteroventral relative to the long

axis of the ilium. It is extends further ventrally than the ischatic peduncle. The acetabulum is

circular and the dorsal articular surface is transversely constricted towards its midpoint. The

ischiadic peduncle is triangular and flares slightly laterally, although there is not a well-

developed antitrochanter. The postacetabular blade has a straight ventral edge and a curved

dorsal edge that converge into a pointed posterior process (Fig. 3.16A). The medial surface of the

iliac blade has three concavities separated by ridges (Fig. 3.16C). The anteriormost concavity is

small and shallow, occupying the area just dorsal to the pubic peduncle. The middle concavity is

the smallest but deepest and has a parabolic outline, opening dorsally. The posterior concavity is

large and occupies the entire area dorsal to the brevis shelf on the postacetabular blade. Whereas

posteriorly its ventral border is confluent with the brevis shelf, there is a flat platform separating

these features anteriorly. The brevis fossa is small compared to that of most oviraptorosaurs and

occupies only the posterior half of the postacetabular blade.

Ischium—The right ischium (Fig. 3.16D, E) is relatively well preserved. The proximal

head has widely separated contacts for the ilium and pubis, suggesting that it contributed

significantly to the acetabulum, unlike in oviraptorids. The pubic contact is badly crushed, so the

exact angle at which it contact the pubis cannot be determined, but it extends ventrally to a lesser

degree than in *Anzu wyliei* (Lamanna et al., 2014)*, Epichirostenotes curriei* (Sues, 1997; Sullivan

et al., 2011), and *Nomingia gobiensis* (Barsbold et al., 2000a), and is not distinctively hooked

like it is in those taxa. The acetabular portion is relatively straight, rather than rounded as in most

oviraptorosaurs. The shaft of the ischium is narrow in dorsoventral breadth, and curves strongly

posterodorsally. A constricted neck separates the head from a large, tablike obturator process

(Fig. 3.16D). Unlike in oviraptorids, this process is less than half the length of the ischium from the head, and is not accompanied by a wide sheet of bone. The obturator process protrudes more from the rest of the ischium than in *Anzu wyliei* or *Epichirostenotes curriei*, partly because the distal end of the ischium is narrower dorsoventrally. The ventral edge of the ischium distal to the obturator process is relatively straight, and the bone thickens transversely at its distal end, rather than forming a wing-like sheet of bone as in oviraptorids.

Femur—The right femur (Fig. 3.17) is badly crushed, but some features can still be discerned. The proximal head is rounded and would have been separated from the greater and anterior trochanters by a shallow groove, if any (Fig. 3.17A). The anterior trochanter is tightly appressed to the anterior edge of the greater trochanter, and a small cleft can be observed between them (Fig. 3.17F). This contrasts with the femora of *Caenagnathasia martinsoni* and *Avimimus* spp. Kurzanov 1981, which have an anteriorly projecting, fingerlike anterior trochanter that is separated from the greater trochanter by a wide space. Distal to the anterior trochanter of TMP 1979.020.0001, there is an accessory trochanteric ridge similar to that of *Anzu wyliei*, although this feature may be exaggerated by anteroposterior crushing of the femur. The shaft of the femur is badly crushed, but appears to have bowed anteroposteriorly in life. There is no trace of a fourth trochanter on the posterior surface of the shaft. Instead, a slight ridge occupies the posterolateral surface of the middle third of the shaft. Distally, the distal condyles are well developed and are separated posteriorly by a deep, proximally-tapering popliteal fossa (Fig. 3.17E). A small ectocondylar tuber occupies the lateral surface of the lateral condyle, it is separated from the crista tibiofibularis by a groove paralleling the popliteal fossa. The medial condyle is well developed and rounded in distal view. The lateral condyle extends further ventrally and is separated from the crista tibiofibularis by a wide but shallow gap.

Tibia—The right tibia (Fig. 3.18) is complete, but like the femur, is crushed anteroposteriorly. Neither the astragalus nor fibula were recovered, which indicates that these bones had not yet fused, unlike the tibiotarsus of *Avimimus* spp. The cnemial crest is restricted to the distal end of the tibia (Fig. 3.18A, C), but the extent of its anterior projection has been obscured by crushing. Its apex is at its ventral end, in contrast to the dorsal apices of ornithomimid cnemial crests, and it is thickened. The fibular condyle projects laterally (Fig. 3.18A, B), but it has been badly crushed and the shape of the incisura tibialis cannot be determined. It appears that a small groove may have separated it from a posterior condyle, but, again, this is mostly obscured by crushing. The fibular crest has been shifted medially by crushing, and faces anteriorly instead of laterally (Fig. 3.18A). It begins just distal to the cnemial crest, and extends about 7 cm distally, where it grades into the shaft of the tibia. Although it may be deformed by crushing, it appears more robust than that of *Elmisaurus rarus*, which projects laterally as a thin sheet of bone. Near the distal end of the fibular crest of TMP 1979.020.0001, on its posterior side, there is a nutrient foramen associated with a dorsal groove, as is characteristic for many oviraptorosaurs. The shaft of the tibia is badly crushed, but rounded medial and lateral shoulders indicate that it would have shared the semicircular cross-section of all caenagnathids (Funston and Currie, 2018). The distal end of the tibia flares only slightly mediolaterally, and is anteriorly flattened for the astragalus. Like in *Anzu wyliei*, this facet is bisected into medial and lateral parts by a shallow longitudinal ridge (Fig. 3.18A). On the posterior part of the lateral malleolus, there is a distinctly ridged postfibular flange, however, it is less pronounced than those of *Elmisaurus rarus* and *Leptorhynchos elegans*.

Pes—The right metatarsus (Fig 3.19) is represented by all of the metatarsals. Although Currie and Russell (1988) did not comment on the distal tarsals, they are present on the proximal

ends of the metatarsals. Distal tarsal III is represented by badly crushed fragments adhered to the proximal ends of metatarsals II and III (Fig. 3.19C, D). It tapers in thickness anteriorly, which is best observed on the fragment attached to metatarsal II. Distal tarsal IV covers the proximal end of metatarsal IV (Fig. 3.19H, I) and a suture can be discerned between these bones. It is thinner than distal tarsal III, but also tapers anteriorly. On its anterolateral edge, there is a tall proximodorsal process, as described in *Elmisaurus rarus* and *Leptorhynchos elegans*. The full length of this process cannot be determined because its proximal end is broken. The position of the proximodorsal process is unusual, but it is possible that this can be accounted for by the direction in which the metatarsal was crushed. Mediolateral crushing has flattened the metatarsal so that the anterior and lateral surfaces are on the same side, opposite the medial and posterior sides.

Metatarsal I (Fig. 3.19A, B) is small composed of a tapering shaft and a bulbous condyle. These two features are separated by a slightly constricted neck. The shaft tapers proximally and, in combination with the constricted neck, gives the proximal part of the metatarsal a spearhead shape. The distal condyle is larger medially and strongly ginglymoid. There is a small triangular process extending laterally from its lateral surface, just posterior to the shallow lateral ligament pit.

Metatarsal II (Fig. 3.19C, D) is badly crushed transversely, which has deformed its shape and proportions. Regardless, it would have been the shortest of the three weight-bearing metatarsals. The proximal end has a large, distally tapering posterior facet for metatarsal III and a smaller anterior facet for metatarsal IV; these have been crushed to lie in the same plane. The lateral surface of the shaft is marked by a proximally-tapering facet for metatarsal III. The posteromedial ridge is modestly developed, its protrusion from the metatarsal may be enhanced

by crushing. The distal condyle would have been bulbous, although it has been compressed into a single plane. The medial ligament pit is shallow, whereas the lateral one is deeper.

Metatarsal III (Fig. 3.19E–G) is complete and has suffered less crushing than the other metatarsals. It is the longest of the metatarsals, but is also the most gracile. However, its proximal end is crushed anteroposteriorly, which artificially increases its transverse width. The proximal head of the metatarsal is poorly preserved, but clearly expanded from the proximal end of the shaft. It is not clear whether a posterior protuberance was present on the posterior surface of the proximal head of metatarsal III, as is the case in *Elmisaurus rarus*. The shaft of metatarsal III is strongly compressed anteroposteriorly, and it is overall much wider transversely than it is deep anteroposteriorly. On the posterior surface of the shaft there are two longitudinal ridges (Fig. 3.19G) that correspond to the cruciate ridges described for *Elmisaurus elegans* and *Leptorhynchos elegans* (Currie et al., 2016; Funston et al., 2016a), however, these ridges are not continuous with the condylar ridges as they are in those two taxa. Instead, these ridges end about one fifth of the way from the distal end. In addition to the discontinuous cruciate ridges, the posterior surface of the distal end of metatarsal III has an accessory ridge that is continuous with the medial edge of the metatarsal. The distal condyle is ginglymoid and its articular surface extends more than 180°. Both collateral ligament pits are shallow.

Metatarsal IV (Fig. 3.19H, I) appears more robust than the other metatarsals, and is slightly longer than metatarsal II. It has been crushed mediolaterally, which artificially increases its anteroposterior breadth and has deformed it. For example, the proximodistal process of the distal tarsal appears to be on the medial side of the metatarsal, rather than the lateral side, although this is probably because it has been flattened. Like in other caenagnathids, the proximal end of metatarsal IV has a notch just posterior to the proximodorsal process of distal tarsal IV,

which accommodated metatarsal V. The shaft of metatarsal IV is badly crushed, but does not appear to have a pronounced posterolateral ridge, unlike the condition in *Elmisaurus rarus* and *Leptorhynchos elegans*. The distal condyle has a shallow lateral ligament pit, and the articular surface is slightly bulbous but not nearly as ginglymoid as metatarsal III.

Metatarsal V (Fig. 3.19J, K) is a small, crescentic splint of bone. What is presumably the distal end is tapered, and oriented nearly perpendicular to the proximal end, although its orientation relative to the rest of the metatarsus cannot be determined.

Two pedal phalanges (Fig. 3.19L–O) are preserved. One is likely phalanx I-1 (Fig. 3.19L, M), based on its small size and flattened medial surface. It is virtually identical to phalanx I-1 of CMN 8538 ("*Macrophalangia*"). The other can be identified as phalanx III-1 (Fig. 3.19N, O) on the basis of its cup-shaped proximal articulation and general symmetry. It is relatively elongate and its distal condyle is strongly ginglymoid compared to other theropods.

UALVP 59400:

This specimen (Figs. 3.20–3.27) consists of a partial articulated skeleton including the mandible, four cervical vertebrae, eleven caudal vertebrae and associated chevrons, a partial pubis and ischium, fragments of a femur and tibia, both astragali, and a right distal tarsal IV. The bones are transversely crushed but otherwise relatively well preserved. Some evidence of integumentary preservation is evident along the dorsal surface of the articulated cervical vertebrae, as well as in between the neural spines of the caudal vertebrae.

Mandible—The mandible (Fig. 3.20) is relatively complete, consisting of a badly crushed dentary and portions of both articular-surangular-coronoid (ASC) complexes. The angulars are preserved as a collection of fragments which likely represent a significant

proportion of the bones, but cannot be reconstructed. The left dentary is more complete and can be rearticulated with the corresponding ASC complex (Fig. 3.20A–D), which is less complete than the right side (Fig. 3.20E–J). The mandible is overall remarkably similar to TMP 2001.012.0012 in morphology, but it is slightly smaller in size. The dentary is transversely crushed but still preserves much of the morphology. The anterior occlusal grooves ridges are shallow and lack nodules, in contrast to TMP 1992.036.0390. There are four lateral occlusal ridges (Fig. 3.20C, D), which become successively smaller posteriorly. They border a deep lingual groove, which itself lies lateral to the well-developed lingual ridge. The tubercle of the lingual ridge is distorted by crushing, but it does not appear to have been as prominent as that of TMP 1992.036.1237, nor does it have the small nodules present in the latter. The symphyseal sulcus is mostly missing. The lateral surface of the dentary is pierced by numerous foramina (Fig. 3.20A, B), which, like in TMP 2001.012.0012, are arranged into three rows (Funston and Currie 2014). A mandibular fossa is present and apparently deep, but it is deformed by transverse and dorsoventral crushing. The ventral surface of the dentary is only preserved at its posterior end, near the attachment of *M. genioglossus*. This scar is roughly heart-shaped and foramina demarcate its posterior border. The Meckelian grooves converge towards the midline, and open posteroventrally on the posterior surface of the dentary. The rami of the dentaries bifurcate around a large external mandibular fenestra. The dorsal ramus is strap-like and forms an interfingering joint with the ASC complex. The ventral ramus tapers posteriorly and lies lateral to the angular, which has a deep groove for this contact. The ASC complex has a rugose, medially deflected coronoid process, which, like in TMP 2001.012.0012, has a distinct ventral suture (Fig. 3.20E, F). This suggests that the coronoid is present and forms part of this fused unit. A small foramen pierces the medial surface of the surangular near its contact with the angular,

but this does not form a fenestra in the way that it does in oviraptorids. The articular has a tall

median ridge which presumably was flanked by tongue-like medial and lateral cotyles as in TMP

2001.012.0012, although these are missing. The slope of the anterior part of the articular ridge,

where it meets the surangular, is less steep than in TMP 2001.012.0012, but it is more

pronounced than in *Anzu wyliei* and *Caenagnathus collinsi*. It is most similar to that of

Apatoraptor pennatus.

       Cervical vertebrae—Four cervical vertebrae are preserved, three of which remain in

articulation (Fig. 3.21). Two mid-cervical vertebrae, probably representing postaxial cervical

vertebrae 7–8 based on comparison to *Apatoraptor pennatus*, are better preserved. The

morphologies of their centra are difficult to discern, but the neural arches are well preserved. The

neurocentral suture is obliterated in all of the vertebrae. The centrum of the anterior vertebra

appears to have a longitudinal ridge underlying the infrapostzygapophyseal fossa on the neural

arch (Fig. 3.21). Ventral to this, there is a large lateral pleurocoel that opens posteriorly. The

diapophysis is connected to the postzygapophysis by a broad lamina that forms the dorsal edge

of the infrapostzygapophyseal fossa. The neural spine is dorsoventrally short and rounded in

lateral view (Fig. 3.21). The postzygapophysis faces ventrally and the epipophysis is small or

absent. The posterior cervical vertebra preserves the entire neural arch, but it is more damaged

than the anterior one. The prezygapophysis is upturned, which may be taphonomically modified

but also appears to be the case in postaxial cervical vertebra eight of *Apatoraptor pennatus*. The

neural spine is low and rounded. The postzygapophyses face ventrally and also seem to lack

epipophyses. Like the anterior vertebra, the neural arch has a broad lamina that connects the

postzygapophysis to the diapophysis. The diapophysis is apparently fused to the cervical rib,

although this region is damaged and this cannot be determined without doubt. Dorsal to the two

better preserved cervical vertebrae is a patch of matrix with apparently filamentous stains (Fig. 3.21). There is a distinct border between these stains and the matrix further away from the specimen, and the filaments appear to have a preferred orientation extending posterodorsally from the vertebrae. Accordingly, they likely represent preservation of integument. Their filamentous nature suggests that they may be feathers rather than collagen bundles, but no unambiguous branching can be identified.

Caudal vertebrae—A series of eleven articulated caudal vertebrae (Figs 3.22, 3.23) were preserved with the skeleton. Orange staining of the matrix between their neural spines suggests that some of the integument was preserved, but this has been prepared away to reveal the morphology of the vertebrae. The caudal vertebrae likely represent the penultimate part of the tail, with the exception of the pygostyle. This is evident from the position of the neural spine posterior to the articular face of the corresponding vertebra and the anteriorly directed transverse processes on the posteriormost caudal vertebrae (Fig. 3.23). The anterior caudal vertebrae (Fig. 3.22) have barrel-shaped centra with large lateral pleurocoels, which decrease in size posteriorly along the tail. In the posterior caudal vertebrae, these pleurocoels are slit-like, underlying the infradiapophyseal fossa, and they are absent in the last three vertebrae preserved. The neural spines are low and triangular in lateral view. The transverse processes are elliptical in cross section, tongue-like in dorsal view, and extend posterolaterally in the anterior caudal vertebrae (Fig. 3.22). Posteriorly, they become more platelike, taper at their distal ends, and become successively more directed anteriorly. In the anterior caudal vertebrae, there is a well developed infradiapophyseal fossa and a smaller infraprezygapophyseal fossa, but the presence of an infrapostzygapophyseal fossa cannot be determined because this area is overlain by the fingerlike prezygapophyses. The last two vertebrae are slightly disarticulated and lie nearly perpendicular

to the rest of the series (Figs. 3.22, 3.23). The centra of these vertebrae are transversely wider than they are dorsoventrally tall, and they have a groove ventrally along the midline (Fig. 3.23). The transverse processes extend from the widest point of the centrum and curve anteriorly from their bases. In these respects, they are similar to the penultimate caudal vertebrae of *Nomingia gobiensis*, and they likely represent the corresponding elements. If this is the case, only five additional vertebrae would be missing from the anterior part of the caudal vertebral series.

Chevrons—The chevrons (Fig. 3.24) are exceptionally large compared to other oviraptorosaurs, especially considering the distal positions of the corresponding caudal vertebrae. Anteriorly, the chevrons are elongate and taper towards their rounded distal ends. Posteriorly, they become shorter and more platelike (Fig. 3.22), but do not decrease in anteroposterior length and their proximal ends. The result is that the posterior chevrons are nearly in contact, and the posteriormost chevrons are longer anteroposteriorly than their corresponding vertebrae. A similar morphology is present in *Nomingia gobiensis*, but not to the same extreme as in UALVP 59400.

Pelvis—Small portions of a pubis and ischium (Fig. 3.25) are represented by fragments collected as float. A single fragment of the pubis is from the proximal end where it would have contacted the ilium. The ischium is better represented, and most of a shaft can be reconstructed, although it is likely some fragments are from opposite sides. The reconstructed morphology of the ischium (Fig. 3.25) is similar overall to that of TMP 1979.020.0001 in that it is posteriorly concave and has a tab-like obturator process.

Hindlimb—The hindlimb is known from fragments of the femur, tibia, both astragalocalcanei (Fig. 3.26), and a distal tarsal IV (Fig. 3.27). It is likely that some of the float fragments pertain to other hindlimb bones including metatarsals, but these cannot be identified with certainty. The femur and tibia are represented by indistinct fragments that do not provide

any morphological information, and so were histologically sampled. The distal end of the right tibia is preserved in articulation with the badly crushed astragalocalcaneum (Fig. 3.26). All that can be said of these is that they were not fused, the postfibular flange of the tibia was small, and the astragalocalcaneum extended onto the posterior surface of the tibia as in CMN 8538. The left astragalocalcaneum is less crushed and shows that there was a transverse groove above the distal condyles (Fig. 3.26), rather than a median tubercle as in *Anzu wyliei*. The right distal tarsal IV (Fig. 3.27) is well preserved and relatively complete. It is roughly triangular in proximal view and tapers in proximodistal thickness towards its anterior edge. The proximodorsal process is broken off, but posterior to it there is a notch for metatarsal V (Fig. 3.27F), which contrasts with the morphology of *Leptorhynchos elegans*, where metatarsal V contacts and fuses with the proximodorsal process. The medial edge of the distal tarsal is mostly broken, but some intact surface indicates that this tarsal was not fused to distal tarsal III. Similarly, the intact ventral (distal) articular surface (Fig. 3.27D) indicates that distal tarsal IV had not fused to the proximal metatarsus, despite histological maturity of this individual (see Section 3.3.7). This strongly suggests that this individual did not have a proximally fused metatarsus, which contrasts with all known specimens of *Leptorhynchos elegans*, but is similar to the known specimens referred to *Chirostenotes pergracilis*.

Isolated Mandibles

TMP 2001.012.0012:

A remarkably preserved mandible (TMP 2001.12.12) was recovered in 2001 from Bonebed BB048 (50 degrees 49.045 minutes, 111 degrees 34.918 minutes) in the DPF of Dinosaur Provincial Park near Steveville, AB. The horizon lies in the base of a cross-bedded

sandstone unit above an overbank mudstone. The deposit likely represents a crevasse splay, as suggested for other fossiliferous sandstones within the DPF (Eberth, 1990).

The symphyseal region of TMP 2001.12.12 (Fig. 3.28A) is completely preserved, and both mandibular rami are at least partially preserved. The left ramus is best preserved, but has some damage to the ventral margin. The angular is nearly complete on the left side, but was broken and has been left in the position in which it was found. No angular is present on the right side (Fig. 3.28C). The prearticular is preserved only as a small wafer of bone medial to the angular, and possibly a sheet of bone forming the medial surface of the retroarticular process. In the description of *Caenagnathus collinsi* by Sternberg (1940), he illustrated a hypothetical cross-section showing the relationship of the prearticular to the angular, based on his observations of CMN 8776, which has a prearticular. His illustration shows that the prearticular is plate-like, and lies medial to the angular, along its entire length. Based on his illustrations of CMN 8776, it is likely that the prearticular is not fully preserved in TMP 2001.12.12, but would have been comparable to CMN 8776 in life. Even so, the prearticular of TMP 2001.12.12 is not complete enough to provide any useful information (Fig. 3.29: ?pa).

The articular region is complete on the left side, although some compression appears to have distorted the contact of the angular with the ASC complex (Fig. 3.28). The left retroarticular process is intact. On the right side, the dorsal part of the ASC complex is preserved, but not the ventral surface of the articular region. This includes the median ridge and the medial portion of the glenoid, but little of the lateral portion of the glenoid. It appears that the splenial is completely absent, unless a small suture posterior to the *M. genioglossus* attachment is evidence of fusion (Fig. 3.29B).

On the whole, the mandible is long, narrow and low (Figs. 3.29D), unlike those of most oviraptorosaurs, but retains the large external mandibular fenestra typical of oviraptorosaurs. The mandible is 188 mm long, and the rami are bowed laterally, reaching a maximum transverse width of 73.8 mm and converging again towards the articular region.

Dentary—The dentary of TMP 2001.12.12 is composed of an anterior, beak-like portion, a robust symphyseal shelf, and posteriorly diverging rami. The occlusal margin is upturned anteriorly, forming a sharp edge (Fig. 3.28). The anterolabial surface of the dentary is subvertical. In lateral aspect, the beak appears concave, because the midline of the occlusal edge is more dorsally extended than the lateral edges (Figs. 3.28B).

The mandibular symphysis is fused, with no evidence of sutural separation (Figs. 3.28A,D). Anterior and medial to the Meckelian groove (Fig. 3.29B), there is a slight furrow on its ventral surface. The beak of the dentary increases in thickness ventrally until its junction with the symphyseal shelf. The ventral surface of the margin produces a distinct 'chin', with the apex anterior to the Meckelian grooves. This 'chin' is marked by a heart-shaped attachment for *M. genioglossus* (Fig. 3.29B: "gen"). In the most anterolateral portions of the attachment of the *M. genioglossus* there is a foramen. This area of muscle origin is unlike those in other specimens of *Caenagnathus*, which are hourglass-shaped (Currie et al., 1993).

The labial surface of the dentary is marked by three anteroposterior rows of foramina (Figs. 3.28B, C). Of these, the upper is the longest and has the most openings, with at least ten foramina. It is 5 mm from the occlusal margin, and parallel to it. This row of foramina extends from the midline to the mandibular fossa and each foramen opens dorsally and labially. The most anterior foramen of the top row is the largest, and Currie et al. (1993) noted that it probably represent an exit for a branch of the inferior alveolar nerve and associated blood vessels. The

intermediate row is comprised of at least two small foramina, unseen in other specimens that possess only two rows of openings. It appears that the foramina on TMP 2001.12.12 are asymmetrical, because three small foramina are present on the right side (Fig. 3.28C), and two on the left (Fig. 3.28B). However, breakage on the right side obscures the positions of the other foramina, so it is impossible to determine the degree of asymmetry in this specimen. If the middle row of foramina is present on both sides, this is unique among caenagnathids, but it appears that foramen position is individually variable. The bottom row comprises eight foramina, each smaller in size than those of the upper row, but equal in size to those in the intermediate row (Figs. 3.28B). These foramina follow the ventral margin of the dentary, and extend from the midline to a point 10 mm anterior to the mandibular fossa.

Work by Currie et al. (1993) indicated pneumatization of the dentary in CMN 8776, and this is confirmed in TMP 2001.12.12. Breakage on the right side reveals a smooth-walled chamber, anterior to the broken mandibular fossa (Fig. 3.28C). The extent of the chamber is obscured by matrix, but it appears to extend almost to the midline. Computed tomography (CT) images confirm the presence of the pneumatization (Fig. 3.30). The left dentary preserves a depression on the lateral surface of the mandible, here called the mandibular fossa. There is a pneumatopore within the anterior margin of the mandibular fossa (Fig. 3.29C). In CMN 8776 and TMP 1990.56.6, the pneumatopore lies outside the mandibular fossa. It is not clear whether this is taxonomically significant, or is the result of individual variation.

The Meckelian grooves are mediolaterally narrow but dorsoventrally deep, and extend towards the midline of the mandible on the posterior and ventral surfaces of the dentaries (Fig. 3.29B). They do not reach into the symphysis, but end in deep pits 5 mm from the midline. Within these pits are foramina that connect the grooves to the interior of the symphyseal region.

If there is a continuous cavity across the midline because of pneumatization, it is reasonable that these foramina open into this cavity.

The lingual surface of the dentary is complex (Figs. 3.28A, 3.29A). The symphyseal shelf has a deep midline sulcus, here called the symphyseal depression (Fig. 3.29A: "Sd"), which may have accommodated a large tongue. The symphyseal depression tapers posteriorly to the posterior margin of the dentary on the midline. The lateral edges of the symphyseal depression are marked by longitudinal vascular grooves, with foramina extending into the bone at their anterior ends (Fig. 3.29A: "vg"). The symphyseal depression and well-developed attachment of *M. genioglossus* may be evidence of a powerful tongue in *Chirostenotes*, because *M. genioglossus* is the main tongue protruder in most amniotes (Smith, 1988). This tongue may have been used for food gathering or manipulation within the mouth.

The anterolingual surface of the occlusal margin is shallowly fluted, as in CMN 8776, TMP 1990.56.6, and TMP 1991.144.1. The fluting in TMP 2001.12.12 is comprised of one midline depression, and one depression on each side (Fig. 3.29A: A1, A2, respectively). The ridges separating the depressions join posteroventrally, but do not have the ventral rugosity described by Currie et al. (1993). There is, however, a small (1 mm) tubercle below the convergence of the ridges, but it is quite distinct from the large tubercle of CMN 8776, which is formed by the lingual ridges.

Lateral to the symphyseal depression, lingual ridges extend subparallel to the symphyseal depression but diverge posteriorly (Figs. 3.28A, 3.29A). At the anterior end of each of the lingual ridges, there is a tubercle. Lateral to each lingual ridge, a longitudinal groove is widest and deepest anteriorly. The longitudinal grooves are bordered laterally by the grooved occlusal margin of the dentary, which has three lateral occlusal grooves per side (Figs. 3.28A). The lateral

occlusal grooves are strongest anteriorly, and each extends ventrally into a pit. Each lateral occlusal ridge is rugose. The lateral occlusal ridges are less pronounced posteriorly, where the longitudinal grooves become shallow. Posterior to the third lateral occlusal ridge, the occlusal margin is straight and sharp.

Posteriorly, the ramus of each dentary is split into a dorsal and ventral portion (Fig. 3.28). The dorsal portion contacts the ASC complex, and the ventral portion meets the angular and possibly prearticular (Figs. 3.28A, 3.29). The junction of the two portions is rounded, and forms the anterior border of the mandibular fenestra. The dorsal portion is mediolaterally bifurcated where it contacts the ASC complex (Figs. 3.28A, 3.29). The medial flange of this bifurcation is longer than in other specimens, and is more than half the length of the lateral flange. This creates a double-locking contact and would allow only limited if any intramandibular movement. Where the lateral flange of the dorsal portion inserts on the ASC complex, it forms a dorsal ridge. This flange also tapers posteriorly, creating a Z-shaped suture in lateral view (Figs. 3.28B, 3.29).

The ventral portion of the dentary inserts onto the lateral surface of the angular, and contributes to the ventral margin of the external mandibular fenestra (Fig. 3.29). It tapers posteriorly, although its posterior extent is unknown due to breakage.

ASC Complex—The ASC complex is well fused (Figs. 3.28A) and does not show any evidence of sutures, unless a scar at the base of the articular condyle is the remnant of the original articular-surangular contact (Fig. 3.29A). There may also be a coronoid suture, which will be discussed subsequently.

The surangular forms the dorsal margin of the external mandibular fenestra (Fig. 3.28), and contacts the angular, articular and possibly prearticular posterior to the fenestra. Anteriorly, the surangular interdigitates with the dentary. The ventral flange of the anterior part of the

surangular excludes the dentary from the dorsal margin of the external mandibular fenestra and forms the lateral surface of the mandibular ramus (Fig. 3.28). The medial portion of the surangular lies between the two prongs of the dentary, and appears to extend just medial to the mandibular fossa. Where it overlies the external mandibular fenestra, the surangular is laterally deflected, producing a distinct lip of bone below a shallow groove on the lateral surface (Fig. 3.28B).

The coronoid is completely fused to the surangular. There is, however, a possible remnant of a suture, preserved as a small ridge just anteromedial to the coronoid rugosity, and a small channel extending on the ventral surface of the ASC above the external mandibular fenestra (Fig. 3.29B). The coronoid process is medially inflected, but not to the same degree as that of CMN 8776. The coronoid is roughened and is dorsally excavated, with rugosities on the medial and lateral edges.

Posteriorly, the dorsal edge of the surangular becomes rounded, and widens mediolaterally where it fuses with the articular. There may be evidence of a suture here, just posterior to the dorsal deflection of the surangular (Fig. 3.29A), but this may also have been caused by abrasional damage to the specimen.

The articular process is marked by a longitudinal ridge, convex in lateral aspect, with a steeper curve anteriorly and a flatter descent behind the apex (Fig. 3.28). The medial portion of the glenoid on the articular process is larger than the lateral portion, and is convex in both anteroposterior and mediolateral views (Fig. 3.28). This creates a platform, which thins towards its edges. The inferior surface of the medial portion of the glenoid is roughened, and the superior surface is porous. The medial portion of the glenoid is widest immediately behind its anterior margin, and then narrows posteriorly until it ends near the back of the articular ridge (Fig.

3.29A). The lateral glenoid is much narrower than the medial one, and reaches its maximum width midlength. Posteriorly, it joins the articular ridge to form a tuber overlying the retroarticular process. As with the medial glenoid, it is convex in lateral aspect, but mediolaterally it forms a continuous slope with the articular ridge, tapering to a thin lateral edge (Fig. 3.28).

The retroarticular process is composed of the angular ventrally, of the articular laterally, and of the prearticular, if it is present, medially. No obvious suture is present, but a longitudinal groove extending the length of the retroarticular process may separate the angular and prearticular (Fig. 3.29B). The retroarticular process is hatchet-shaped, with a semi-circular posterior edge.

Prearticular—The prearticular may or may not be preserved in TMP 2001.12.12 but was certainly present in life. The best evidence for the prearticular is a sheet of bone that forms the medial retroarticular process, but this may be the angular (Fig. 3.29B). A small wafer of bone was found medial to the angular at its anterior end (Fig. 3.29A). If this is the prearticular, then it would have extended as a thin plate medial to the angular (Sternberg, 1940).

Angular—The angular is robust posteriorly, but thins anteriorly. At its anterior end, it lies medial to both the dentary and surangular (Fig. 3.29A). It forms most of the ventral margin of the external mandibular fenestra (Figs. 3.28B, 3.29). Its anterior end has three grooves—one medial, one dorsal, and one lateral. The medial groove is for the prearticular, and extends until the posterior margin of the external mandibular fenestra, where it merges with a faceted ridge. The lateral groove is for the insertion of the dentary (Fig. 3.28), and turns ventrally as it extends and narrows posteriorly. It becomes shallow posteriorly and merges into a deep depression

ventral to the articular process. The dorsal groove is shallow at its anterior end but deepens posteriorly. It extends only to the posterior margin of the external mandibular fenestra.

Posteriorly, the angular forms a depression underlying the articular process and lateral portion of the glenoid (Fig. 3.29), as described by Currie et al. (1993). Breakage obscures the contact of the angular with the ASC complex, but the angular seems to turn from a medial position anteriorly to a lateral position posteriorly. This means that the angular and likely the prearticular form the ventral margin of the jaw, with a groove between them (Fig. 3.29B).

TMP 1985.043.0070:

This specimen (Fig. 3.31A–C) is a small (Table 3.1), fragmentary mandibular symphysis with parts of both dentaries, recovered from the DPF of Alberta, Canada. The left tubercle of the lingual ridge is preserved, but the right tubercle has been broken off, revealing the camellate bone inside (Fig. 3.31A). The symphyseal sulcus is pierced by two asymmetrical foramina; the left one is anterior to the right one. The symphyseal sulcus is bordered laterally by two shallow vascular grooves, which extend longitudinally (Fig 3.31A; vg). On the left, the vascular groove extends into the foramen in the symphyseal sulcus. On the right, however, the foramen is situated more medially, so it does not communicate with the vascular groove. The symphysis is completely fused, and there is no evidence of a mandibular suture on either the occlusal or ventral surfaces of the dentaries. Furthermore, the cross-sectional view provided by breakage of the anterior and posterior margins of the symphyseal depression shows that there is no internal suture. The ventral surface of the symphysis is convex, and has a fibrous exterior appearance (Fig. 3.31C). The attachment of *M. genioglossus* is composed of multiple webs of bone, rather than the smooth depression of most caenagnathids.

TMP 1992.036.1237:

This is a large (Table 3.1) and relatively well-preserved symphysis (Fig. 3.31D–F), including the anterior portion of the beak. The right dentary is slightly more complete than the left dentary, but both are broken just posterior to the mandibular symphysis. The rim of the occlusal margin is broken, revealing the hollow interior. The left lingual ridge is broken, but the right lingual ridge is well developed and has a tubercle anteriorly (Fig. 3.31D). This tubercle is rugose and has several small nodules of bone at its apex. The lingual groove is deep and pierced by several foramina. The first lateral occlusal ridge is level with the tubercle of the lingual ridge in dorsal view. The symphyseal sulcus is bordered by two pronounced vascular grooves that end anteriorly in foramina (Fig. 3.31D). Posteriorly the vascular grooves converge before descending towards the Meckelian grooves. At the anterior end of the symphyseal sulcus, there is an accessory longitudinal groove medial to the larger vascular groove. This groove extends posteriorly from a small foramen and ends just anterior to the level of the tubercles of the lingual ridge. The upturned occlusal margin of the beak has a midline anterior occlusal groove and a lateral anterior occlusal groove (Fig. 3.31D). Separating these two grooves is a shallow ridge that lacks any rugosity, unlike TMP 1992.036.0390, where these ridges have small nodules. The labial surface of the dentary is excavated by branching vascular grooves, in addition to the foramina typical of caenagnathid beaks (Fig. 3.31 E, F). These vascular grooves are especially prominent laterally, where they contribute to the rugose texture of the labial surface of the dentary. The attachment of *M. genioglossus* is well developed but damage to the bone in this area obscures its shape. The presence of a mandibular fossa cannot be determined because of

breakage, but there is a pneumatic pocket in the broken right dentary that is consistent with a mandibular fossa.

Isolated Postcrania

TMP 2002.012.0103:

This partial right ilium (Fig. 3.32) includes the pubic peduncle and the parts of the ilium posterior to it. There is a lip at the anterior edge of the acetabulum on the lateral surface. The acetabulum has some transverse constriction and a slight longitudinal groove (Fig. 3.32C). The pubic peduncle is broken anteriorly so its lateral extent cannot be determined with certainty. Ventrally, it is wide and has a square posterior edge (Fig. 3.32C). The ischiadic peduncle is completely preserved and projects laterally past the lip on the pubic peduncle (Fig. 3.32C). Its posterior end is slightly hooked and dorsal to the peduncle is a small anteroposterior strip of rugose bone. Anterior to the ischiadic peduncle, there is a slight lateral swelling that coincides with the texture change on the dorsal surface of the acetabulum (Fig. 3.32C). On the lateral surface (Fig. 3.32A), the postacetabular process has less rugose bone that is restricted to the ventral region. At the anterior end of the rugose patch, there is a slightly swollen mound with some associated foramina (Fig. 3.32A). The dorsal edge of the ilium is broken. The brevis fossa is overhung by what would have been a relatively large brevis shelf (Fig. 3.32B), but it is broken. Just posterior to the ischiadic peduncle is a small mound of rugose bone in the brevis fossa. The middle sacral attachment is preserved, at what would have been the base of the anterior ridge dorsal to the acetabulum (Fig. 3.32B). The medial side of the ilium is badly broken, so the limits of the pneumatic concavities cannot be determined. There are clearly three concavities, and the middle one appears to reach further ventrally, with a small ventral platform and foramina as in

TMP 1998.093.0013 (see section 3.3.6). The ridges are marked only by their broken bases, and the posterior one is the best preserved. It appears to extend dorsally over the posterior concavity slightly, but not to the same degree as TMP 1981.023.0035 (see section 3.3.4). It cannot be determined if the posterior concavity is continuous with the brevis shelf because this area is broken to reveal an internal pneumatic chamber.

TMP 1993.036.0181:

TMP 1993.036.0181 (Fig. 3.33) is a pathological partial tarsometatarsus, including metatarsals II and IV and the distal tarsals III and IV. Although initially described as a representative of *Leptorhynchos elegans* (Funston et al., 2016a), several features suggest it more likely represents *Chirostenotes pergracilis*. For example, it is the largest fused tarsometatarus recovered from Alberta (Appendix 1), comparable in size with the holotype of "*Macrophalangia*", CMN 8538 (Sternberg, 1932), but is not proximally coossified. This is most evident in the absence of metatarsal III, which shows it had not coossified, despite being fused with metatarsals II and IV in all other individuals of *Leptorhynchos elegans*. Similarly, the distal tarsals are not coossified with the metatarsals, and a clear suture is visible between them.

Metatarsal II is 221 mm in length, and if the proportions are similar between TMP 1982.016.0006 and TMP 1993.036.0181, the total length of the tarsometatarsus would exceed 250 mm. The shaft of metatarsal II is mediolaterally expanded by a large tuberosity of twisted bone (Fig. 3.33B, C). Two holes pierce the distal shaft near the tuberosity, one on the medial side oblique to the shaft, and one on the lateral side parallel with the long axis of the shaft. Metatarsal IV is 221 mm long and appears unaffected by the pathology. Distal tarsal III covers metatarsals II and IV (Fig. 3.33A) and there is a distinct suture between distal tarsal III and metatarsal II.

Distal tarsal IV has the posterodorsal process typical of *Elmisaurus rarus* and *Leptorhynchos elegans*, although metatarsal V is missing, indicating that they were not fused. The proximal tarsometatarsus is 50 mm wide transversely, narrower than *"Macrophalangia"* despite the greater lengths of the metatarsi.

The proximal end of metatarsal II is not coossified with metatarsal IV, nor with metatarsal III, as indicated by the clean bone surface on the facet for metatarsal III. The shaft of metatarsal II is pathologically deformed, but the posteromedial ridge is still discernable. The distal condyle is rounded and faces ventrolaterally. The shaft of metatarsal IV has a prominent anterior ridge, separated from the facet for metatarsal III by a groove. The distal condyle faces laterally, and there is a poorly developed scar for the insertion of the *M. tibialis cranialis*, which contrasts with the better developed scars of most specimens of *Leptorhynchos elegans*. The proximal end of metatarsal IV (TMP 1993.036.0181) is separated from metatarsal II posteriorly by the wedge-shaped proximal end of metatarsal III, which is missing. These bones apparently had not coossified or fused, as the edge between metatarsals II and IV is natural, despite the great size (>250 mm) of the tarsometatarsus.

Mandibular Osteohistology

TMP 1985.043.0070:

The partial dentaries of this specimen are composed predominantly of highly vascularized primary fibrolamellar bone with small regions of secondarily remodeling. Vasculature and collagen fiber orientation vary considerably throughout the specimen. Several large openings are evident throughout the bone (Fig. 3.34A). Some of these openings show

evidence of expansion into the surrounding tissue matrix: bone texture truncates abruptly against cavity walls and internal lamellar bone deposition is present (Fig. 3.35B). However, it is unclear if these cavities possess active resorption fronts as Howship's lacunae are not evident. None of the ground sections show evidence of a suture at the midline, nor is there any evidence of metaplastic bone (Horner et al. 2016). These tissues might be expected if the symphysis were fused through ontogenetic mineralization of a soft-tissue structure (Horner et al., 2016). Similarly, the mandibles lack chondroid bone, which can function in suture closure and rapid embryonic growth (Bailleul et al., 2016b). In each section, primary osteons extend transversely across the midline of the mandible and the bone microtexture is continuous across the two sides of the mandible. Osteocyte lacunae are uniformly dense (~44,000/mm^3) throughout the mandible and most are oriented parallel to osteons within lamellar bone. This value is high compared to other theropods (Cullen et al., 2014), although theropod mandibles have never been histologically sampled. However, it is in line with similarly elevated measurements from postcrania of other caenagnathids (Benner et al., 2016; Funston and Currie, 2018). Because osteons vary in orientation throughout the dentaries, osteocyte lacunae are captured in various planes, and thus differ in apparent size and shape (Fig. 3.35D).

Section A—Anterior to the symphyseal sulcus, the dentaries consist mainly of primary, fibrolamellar bone (Fig. 3.35A). As in other sections, Section A shows highly vascularized fibrolamellar bone with a combination of reticular, plexiform, and longitudinal vascular canals. The fibrolamellar bone matrix results in variable birefringence under cross-polarized light, but some distinct zonal banding is evident between regions with differing matrix organization (Fig. 3.35C). Vasculature is dense and canals are more consistently longitudinal in some of these bands and more plexiform-laminar in others. Osteocyte lacunae in these bands are perpendicular

in orientation to the other osteocyte lacunae in this region, indicating a change in the direction of growth. The more endosteal layers, which are predominantly oriented perpendicular to the periosteal surface, were probably deposited first. These bands alternate dorsoventrally through the sections. Large cavities excavate the internal regions of the dentaries, truncating the primary bone. These cavities are lined with thin layers of lamellar bone (Fig. 3.35B), indicating they were gradually expanding into the surrounding bone, followed by periodic deposition of thin layers of secondary bone within the cavity. The thickness of the secondary bone lining these resorption cavities varies, which suggests drift of the internal cavities, similar to cortical drift in long bones (Enlow, 1962). The largest of these cavities, hereafter called the major labial cavity (Fig. 3.34 A), extends posteriorly through all of the serial sections, and is mirrored on both sides of the midline. Smaller cavities are present along the midline of the mandible and are asymmetrical in shape and number, but located in consistent positions, suggesting they are formed by similar processes. Some of these are associated with Volkmann's canals and may represent branching blood vessels.

Section B—Secondary remodeling is evident at the anterior end of the symphyseal sulcus, there is more secondary remodeling (Fig. 3.36B). Haversian bone is concentrated generally along occlusal areas, rather than dispersed throughout the mandible. At the occlusal surface of the symphyseal sulcus, just ventral to the midline tubercle, there is a patch of relatively dense secondary osteons and primary bone with dense Sharpey's fibers is visible between these (Fig. 3.36B). Secondary osteons are also concentrated along the lingual surface of the lingual ridge, and are present, but not as concentrated, on the labial portion. The ventral part of the mandible is mostly composed of primary bone, similar in texture to the fibrolamellar bone anterior to the symphyseal sulcus. Sharpey's fibers are visible around the entire periosteal

surface of the bone (Fig. 3.36C), except where it is broken or secondarily remodeled. The major labial cavity is larger in this more posterior serial section and extends further labially to underlie the lingual ridge. Foramina communicate between this cavity and both the ventral and occlusal surfaces of the mandible (Fig. 3.36D). Secondary lamellae surround more of the major labial cavity here than at its anterior end, although there are unlined portions of the perimeter. An additional major cavity is present just dorsolingual to the major labial cavity, and another lies within the lingual ridge. Each of these cavities is only partly lined by secondary lamellae.

Section C—Just anterior to the tubercle of the lingual ridge, the internal part of the mandible is perforated by many more cavities than in the more anterior sections (Fig. 3.37A). Several labial cavities branch from the major labial cavity and the dorsolingual cavity. Two additional midline cavities are also present in this section (Fig. 3.37D). These spaces are relatively symmetrical, but do not appear to extend far anteroposteriorly, as they are absent in other ground sections. The more ventral of these two cavities is entirely lined by secondary lamellae, whereas the dorsal one lacks secondary lamellae altogether (Fig. 3.37D). The cavity within the lingual ridge is divided into five smaller canals of varying size (Fig. 3.37C).

Vascular orientation is more consistent throughout the mandible in this region than in the anterior sections, and at the labial edges of the beak, vascular canals are predominantly laminar (Fig. 3.37B). Along the ventral and labial surfaces of the dentary, osteons are predominantly oriented transversely, and in the lingual ridges primary and secondary osteons extend anteroposteriorly. More internally, the osteons in the primary bone that form the trabeculae are randomly oriented. Secondary remodeling is concentrated on both sides of the lingual ridge (Fig. 3.37C) and is also present on the occlusal surface of the symphyseal sulcus at the midline. There

is a small region of secondary remodeling near the ventral surface of the jaw on either side of the midline, just labial to the *M. genioglossus* attachment.

      Section D—In the transverse plane at the tubercles of the lingual ridges, vascularization is reduced near the midline occlusal surface (Fig. 3.38C, D). Under cross-polarized light, the extinction pattern of this bone sweeps transversely. Just lingual to the dorsolingual cavities, which are each bisected by a thin web of bone, there are triangular regions of bone that differ in orientation from the rest of the symphyseal bone. An area of cancellous bone is present near the midline, dorsal to the *M. genioglossus* attachment. Bone in this region is resorbed, although Howship's lacunae are absent, and most of the trabeculae consist of primary bone, with no secondary lamellar bone lining. At the ventral surface of the mandible, flanking the midline, osteocyte lacunae are elongate, flattened, and have a predominantly transverse orientation (Fig. 3.38B). The ventrolabial parts of the dentaries have more organized bone with uniform collagen fiber orientation. Vascular canals in these areas are enlarged, and some have secondary lamellae, so that they resemble large secondary osteons. Two small regions of secondary remodeling exist near the periosteal surface of the ventrolabial parts of the dentaries. The lingual ridge has fewer secondary osteons than the anterior ground sections, but this may be the result of increased excavation by the lingual ridge cavity, which has split into ten canals lined with endosteal lamellae (Fig. 3.38A). The periosteal margin of the occlusal surface has a distinct but small band of Sharpey's fibers, as does the lingual ridge. Sharpey's fibers are also present at the *M. genioglossus* attachment, but are more subtle (Fig. 3.38B).

TMP 1992.036.1237:

This specimen (Fig. 3.39) is composed predominantly of fibrolamellar bone with plexiform–laminar vasculature, and shows a higher degree of overall tissue organization and more secondary remodeling than TMP 1985.043.0070. Additionally, a relatively greater proportion of the mandible is occupied by hollow internal cavities compared to TMP 1985.043.0070 (Fig. 3.39A). This is the result of both expansion of cavities present in the latter specimen, as well as an increase in the number of cavities in several regions of the dentaries. Like in the smaller specimen, there is no evidence of a suture or change in bone texture at the midline. Osteocyte lacunae are relatively dense (~50,000/mm^3), and do not vary appreciably in density throughout the sections. The primary osteons towards the ventral and lingual parts of the dentaries are very well developed (i.e., consist of a large amount of lamellar bone surrounding each vascular space). This type of lamellar primary bone is also present along the lingual ridges and lateral occlusal ridges. The labial surfaces of the mandibles are composed of fibrolamellar bone with laminar vasculature (Fig. 3.39E), as are the areas separating the lingual ridges and the symphyseal sulcus. The primary bone of the labial portions of the beak is highly organized and forms annuli similar to those in the limb bones of sauropods and ornithischians (Fig. 3.39E). Dark lines between layers of circumferential vasculature are probably the result of hypermineralization during slow growth (Woodward et al., 2014). At least seven lines are present, but it is possible that more have been obscured by expansion of internal cavities and secondary remodeling. Similar lines are present in the primary bone of the ventral surface of the mandibles, and in the lingual ridges (Fig. 3.39B), where they appear in conjunction with cement lines. The consistency in number and appearance of these lines—and their association with cement lines in the lingual ridge—strongly suggests that they are lines of arrested growth (LAGs). In contrast to TMP 1985.043.0070, the internal structures of TMP 1992.036.1237 are

more consistent between the anterior sections and the posterior sections, and no major differences can be distinguished between the three ground sections. Accordingly, only Section A is described here, as it is representative of the other sections.

Section A—In the anterior part of the dentary, level with the first lateral occlusal ridge, the major labial cavity extends dorsally towards the occlusal edge of the beak (Fig. 3.39). Here, it is divided by several trabeculae, which are asymmetrical and become reduced posteriorly. Between the major labial cavities the dentary is hollowed by numerous cavities of varying size (Fig. 3.39A). These smaller cavities are separated by trabeculae formed almost exclusively of endosteal lamellar bone, although some remodeled secondary bone is present in the more ventral trabeculae. Although cavities likely homologous to those in TMP 1985.043.0070 are present in TMP 1992.036.1237, they are less distinct. Rather, it appears as though the cavities have united into one large field that extends across the dentaries, but which is disrupted by incomplete trabeculae (Fig. 3.39A). The bone of the symphyseal sulcus dorsal to the united internal cavity is secondarily remodeled and secondary osteons are oriented transversely. Like in the primary bone of TMP 1985.043.0070, the extinction under cross-polarized light sweeps transversely. The lateral occlusal ridge is heavily remodeled, but primary bone is still visible on the labial and lingual sides (Fig. 3.39C). On the labial side, there is no discernible transition between the external portion of the mandible and the lateral occlusal ridge. Unremodeled portions of the lateral occlusal ridge show the same highly organized bone and laminar vasculature as in the labial portion of the dentary. Similarly, primary bone on the lingual side of the lateral occlusal ridge is continuous with the bone of the lingual ridge and the floor of the lingual groove. These regions, in turn, are consistent in texture, vasculature, and orientation with the bone of the symphyseal sulcus. Sharpey's fibers are present along the entire perimeter of the lateral occlusal

ridge, and are oriented in different directions. Along the labial surface of the mandible, they are directed approximately 45° ventrolabially (Fig. 3.39C). Sharpey's fibers on the lingual surface of the lateral occlusal ridge are parallel to those on the labial surface, and therefore face dorsolingually. In contrast, Sharpey's fibers on the labial surface of the lingual ridge are oriented dorsolabially, perpendicular to those on the lateral occlusal ridge.

Postcranial Osteohistology

UALVP 59400:

Thin sections were made from fragments of the femur and tibia. The fragment of the femur was identifiable as the proximal portion by a rugose lateral surface and a cleft that presumably separated the greater and lesser trochanters. The fragment of the tibia probably represents the posterior surface of the bone.

Femur—The femur (Fig. 3.40) is composed mostly of primary fibrolamellar bone with plexiform vascularity, but there is an unusual pathological region of the bone discussed later. At least six growth marks are preserved in the cortex of the femur, but these are less obvious than those in the tibia, described subsequently. Of these, only one, just periosteal to the pathological bone, is associated with a cement line. The remaining growth marks consist of annuli of parallel-fibered bone indicative of relatively slow growth. These growth marks generally decrease in spacing towards the periosteal surface, but not in a regular fashion. Vascularity decreases towards the periosteal surface, and in some areas the external bone is nearly avascular (Fig. 3.40F). This region likely represents an incipient external fundamental system (EFS), but in any case, it indicates a much slower rate of growth just before the animal perished. Secondary

remodelling is concentrated towards the endosteal surface, particularly in a region on the right side of the slide, where there are also some larger erosive cavities. A small portion of the endosteal lamellae are preserved just endosteal to this region. Sharpey's fibers are visible on the periosteal surface around the bone (Fig. 3.40F), but there are also some larger bundles extending periosteally from the region of secondary remodelling, suggesting that this area anchored musculature.

About halfway through the cortex, there is a wedge of unusual woven bone with heavy secondary remodelling (Fig. 3.40C). Several aspects of this region suggest it represents a pathology. First, it differs considerably in orientation and bone texture from other regions of the cortex. Second, it has a clean, sharp border with the more endosteal part of the cortex (Fig. 3.40D, E), which suggests it was deposited on top of the 'normal' cortical bone. Finally, it transitions periosteally back to the 'normal' condition, suggesting that its deposition was temporally restricted, rather than a permanent change in bone formation style. Some features of this bone provide information on the type of pathology that formed it. The clean boundary between it and the underlying 'normal' cortical bone eliminates infectious periostitis and osteomyelitis as possible candidates. In these pathologies, infection of the periosteum results in necrosis of the surrounding bone, which would have produced a resorptive boundary marked by Howship's lacunae and cross-cut osteons. This is not the case (Fig. 3.40D, E), and it is clear that the pathological bone was deposited on top of the 'normal' cortical bone without resorptive action. This is further supported by the texture and morphology of the bone itself. Periosteal reactive bone deposited during periostitis or avian osteopetrosis is typically formed of radial spicules of fibrolamellar bone. This is not the case in UALVP 59400, where the pathological bone is clearly woven bone with reticular vascularity. Similarly, the fact that the pathological

bone is uneven in thickness around the cortex suggests that this was a localized injury. Indeed, the uneven thickness of the pathological bone provides a clue to the nature of the pathology. To account for the wedge-like morphology of the pathological bone, the post-pathological bone also tapers, in order to provide a smooth exterior surface. This is accompanied by uneven resorption of the endosteal surface of the bone, so that the periosteal and endosteal surfaces are parallel and the cortex is even in thickness throughout. This is evidence of significant cortical drift after the pathology, which is not the case in periostitis or other infectious pathologies. This cortical drift suggests that this part of the bone was displaced from its original location and that post-pathological growth corrected for this issue. In these features, the pathology is similar to a fracture callus described in *Psittacosaurus* Osborn 1923 (Hedrick et al., 2016) . Like in UALVP 59400, that callus is composed mostly of woven bone, and distal to the injury, the pathological bone is overlain by 'normal' cortical bone. These calluses differ slightly because vascularity of the pathological bone in UALVP 59400 is reticular, rather than radial, but this may reflect a less grievous injury.

Tibia—The tibia (Fig. 3.41) is not pathological, which makes it more useful for skeletochronology. Like the femur, it is composed primarily of fibrolamellar bone, but the vascularity varies between plexiform and reticular (Fig. 3.41C). At least ten growth marks are preserved in the cortex, but two pairs of these are doublet LAGS, marking just a single annual cycle. Another annulus of parallel-fibered bone is preserved between the first and second LAGs, but it does extend around the whole cortex. Therefore, it is best interpreted as a non-cyclical sign of slower growth, possibly coinciding with the injury to the femur. Like in the femur, the growth marks decrease in spacing towards the periosteal surface (Fig. 3.41C), but this is more regular than in the femur. The last seven LAGs (marking six years of growth) are tightly spaced near the

periosteal surface. Most of these are separated by just a single generation of longitudinal vascular canals. Their spacing and the change in vascularity suggests that this individual was approaching maximum body size, and had slowed growth considerably. Secondary remodelling is restricted to a region endosteal to the first LAG (Fig. 3.41D), and primary bone is still visible between the secondary osteons. Two or three successive generations of endosteal lamellae are preserved on the endosteal surface (Fig. 3.41D, E), forming a thick layer of parallel-fibered bone. Between two of these, there is an unusual patch of primary fibrolamellar bone with osteon development and some secondary remodelling (Fig. 3.41D, E). It is cross-cut by the most internal generation of endosteal lamellae, suggesting that it was deposited in between generations of endosteal lamellae deposition. Its position therefore indicates that it was deposited on what was formerly the endosteal surface of the bone, internal to the endosteal lamellae. Based on its position, origin, and clear signs of resorption, this bone is likely homologous to avian medullary bone, deposited during the egg-laying phase. Although it could be argued that it is pathological bone, this is unlikely because the tibia shows no signs of pathology, and the fracture callus in the femur is unlikely to cause spontaneous deposition of endosteal bone in the tibia. Furthermore, the bone itself is dissimilar to endosteal bone induced by avian osteopetrosis, which is highly vascularized and consists of radial spokes of bone. The tissue satisfies all conditions of medullary bone proposed by O'Connor et al. (2018) for which it can be scored. It occurs in the medullary cavity and is of endosteal origin, and its collagen fibers have a woven arrangement, although there is also some deposition of lamellar bone, probably from infill of the vascular spaces. It is vascularized, which contrasts with the endosteal lamellae, which are avascular and therefore not subject to secondary remodelling. It co-occurs with a periosteal surface free from pathologies (Fig. 3.41A), and it is clearly demarcated from the cortex of the bone by thick endosteal

lamellae. Although its timing can not be deduced with certainty, the closely-spaced LAGs at the periosteal surface of the tibia indicate that this individual had a decreased growth rate, which probably corresponds to achievement of sexual maturity. Some of the criteria of O'Connor et al. (2018) cannot be satisfied, particularly concerning its distribution throughout the medullary cavity and in other bones. However, this is because this region of bone in UALVP 59400 were medullary bone, it would only be a remnant of a previous generation of medullary bone that evaded resorption and was enclosed by subsequent deposition of endosteal lamellae.

Remarks

Anatomy:

Chirostenotes pergracilis was first described by Gilmore (Gilmore, 1924) on the basis of a pair of articulated hands. A second, more complete skeleton was described by Currie and Russell (1988), illustrating other aspects of the anatomy and solidifying the caenagnathid identity of *Chirostenotes*. Despite being among the best known caenagnathids, the lack of definitive mandibular material has made it difficult to refer isolated specimens to *Chirostenotes pergracilis*. This makes the discovery of UALVP 59400 particularly important, because it preserves a relatively complete mandible in association with an unfused distal tarsal IV. The lack of fusion between distal tarsal IV and the metatarsus of UALVP 59400, despite histological maturity (see Section 3.3.7) shows that this specimen is distinct from *Leptorhynchos elegans*, whereas the mandible shows that it is distinct from *Caenagnathus collinsi*. However, elements that overlap between this skeleton and TMP 1979.020.0001, like the ischium and distal tarsals, are identical. Accordingly, it is best referred to *Chirostenotes pergracilis*, filling numerous gaps

in the anatomy of this taxon. It includes cervical vertebrae, which have not yet been recovered

from the DPF, as well as a series of articulated caudal vertebrae. Critically, referral of a

relatively complete mandible to *Chirostenotes pergracilis* allows for referral of isolated

mandibular material, including TMP 2001.012.0012, an exceptionally complete mandible.

Other isolated specimens overlap with TMP 1979.020.0001 but reveal more of the

morphology of those elements. Reexamination of a pathological tarsometatarsus (TMP

1993.036.0181) previously referred to *Leptorhynchos elegans* suggests that it more likely

represents *Chirostenotes pergracilis*. Although less complete than the metatarsals of TMP

1979.020.0001, the excellent preservation of this specimen provides additional information on

the pedal structure of *Chirostenotes pergracilis*. Importantly, this specimen elucidates the

morphology of the proximodorsal process of distal tarsal IV, which is similar to that of

Leptorhynchos elegans.

The discovery of the new skeletons and referral of isolated specimens results in a clearer

picture of the skeletal proportions and anatomy of *Chirostenotes pergracilis* (Fig. 3.42). Notably,

Chirostenotes pergracilis has exceptionally long legs compared to other oviraptorosaurs, paired

with elongate hands adapted for grasping. In tandem with a mandible well adapted for omnivory,

these lines of evidence suggest that *Chirostenotes pergracilis* relied heavily on prey capture as a

major portion of its diet.

Osteohistology:

The osteohistological sections provide a wealth of information regarding ontogeny and

growth in *Chirostenotes* and other caenagnathids.

Mandibles—Thin sections of isolated dentaries (TMP 1985.043.0070 and TMP 1992.036.1237) provide information about the ontogeny and development of caenagnathid dentaries. The predominance of primary bone and the random orientation of the collagen fibers indicating rapid growth (Figs. 3.35–3.39) suggest that TMP 1985.043.0070 was young, possibly less than one year old, when it died. While the absence of cyclical growth marks makes it difficult to assess the exact age at death, their presence in TMP 1992.036.1237 suggests that they might be expected in an individual over one year old. However, some evidence (Funston and Currie, 2018) suggests that caenagnathids may not have deposited a conventional LAG during the first year as they were growing rapidly, possibly leading to underestimation of age in these animals. Furthermore, the presence of some secondary remodeling argues against this individual being a hatchling. Therefore, this individual is best interpreted as simply a young juvenile of indeterminate age, perhaps less than one year old.

TMP 1992.036.1237 has seven LAGs recorded in the labial surface of the dentary (Fig. 3.39). Current evidence suggests that LAGs generally reflect annual hormonal changes and slowing of growth in response to seasonal indicators, regardless of metabolism (Köhler et al. 2012, Padian and Lamm 2013). However, LAG count is known to vary between bones of the same individual, complicating age estimation from single elements (Horner et al., 2000; Cullen et al., 2014). Additionally, little work has been conducted to correlate LAG number between craniomandibular bones and postcranial bones, so it is unclear if the mandibular LAGs found here reflect annual cycles. While correlation between LAG counts of mandible and long-bone material has not yet been established within caenagnathids, the presence of seven cyclical growth marks in TMP 1992.036.1237, combined with the moderate degree of secondary remodeling, suggests that this specimen was relatively more mature at time of death than TMP

1985.043.0070. Presuming each cyclical growth mark present in the mandible represents an annual indicator of growth, TMP 1985.043.0070 may have approximately reached seven years at its time of death. However, because it is likely that some of the LAGs have been obliterated by secondary remodeling and expansion of internal cavities, or deposited at different rates than the postcrania, this individual may have been considerably older than seven years. Regardless of its age in years, the highly organized and less vascularized bone around the periphery of the specimen indicates that it had slowed its growth. However, it lacks an EFS, and can best be interpreted as approaching but not yet at maximum body size (Woodward et al., 2011b).

This evidence shows that, in contrast to the suggestion of Longrich et al. (2013), the fusion of the mandibular symphysis in caenagnathids occurs early in ontogeny. There are no differences in degree of suture closure between the ontogenetic stages examined here. Therefore, fusion of the mandibular symphysis does not indicate maturity in caenagnathids. This is consistent with previous assessments of suture closure and maturity, as synostosis or closure of sutures does not always mark maturity (Bailleul et al., 2016a).

Although fragmentary, the specimens examined here show remarkably little variation in terms of the gross morphological structures of the dentaries. Despite a wide range of ontogenetic stages, the specimens are consistent in the relative development of the lingual ridges, symphyseal sulcus, and vascular grooves in the symphyseal sulcus. In each specimen, the lingual ridges are prominent and have a well-developed anterior tubercle (Fig. 3.31). In TMP 1985.043.0070, this tubercle is smooth, whereas in TMP 1992.036.1237, it is capped by several small nodules of bone (Fig. 3.43E). These nodules may appear through ontogeny, but some evidence suggests that they are better interpreted as individual variation. For example, similar nodules are visible on the anterior occlusal ridges of TMP 1992.036.0390 (*Leptorhynchos elegans;* Fig 3.43F), but not on

its lingual ridges. Furthermore, UALVP 55639 lacks these nodules, despite being more histologically mature than TMP 1992.036.1237. Similarly, TMP 2001.012.0012 lacks any nodules, despite being almost equal in size to TMP 1992.036.1237. Furthermore, some dentaries have nodules on both the anterior occlusal ridges and lingual ridges (TMP 1992.040.0044), some on only the anterior occlusal ridges (TMP 1990.036.0390), others on only the lingual ridges (TMP 1992.036.1237), and some dentaries lack these nodules altogether (TMP 1990.056.0006; TMP 2001.012.0012). Therefore, the presence or absence of these rugose patches is probably best explained by individual variation.

The fibrous external bone texture of TMP 1985.043.0070 (Fig. 3.43A, C) may be a potential external indicator of immaturity. Fibrous external bone texture has been used in ceratopsians as a sign of relative immaturity (Tumarkin-Deratzian, 2009), but it is not clear to what extent this applies to caenagnathid theropods. It is possible that this feature indicates a young ontogenetic stage, but it may also be pathological, taphonomic, indicative of rapid growth regardless of age, or individually variable. Similar bone texture is apparent in TMP 1990.040.0044 and to a lesser extent in TMP 1992.036.0390, the holotype of *Leptorhynchos elegans*. However, the ontogenetic stages of these specimens are unknown. In TMP 1985.043.0070, there may be some histological features related to the fibrous bone texture. For example, this individual lacks the organized, cyclical bone that forms the labial surface of the mandible in TMP 1992.036.1237 (Figs. 3.35C,D; 3.39E). Also, under cross-polarized light, there are bands of bone that alternate in orientation on the ventral portion of the mandible of TMP 1985.043.0070 (Fig. 3.35C), which may represent the strands of fibrous bone. However, it is unclear how these alternating bands relate to growth and ontogeny in TMP 1985.043.0070, and they may simply represent a more rapid rate of osteogenesis than in TMP 1992.036.1237.

Although a promising candidate for an external indicator of immaturity, additional specimens and histological samples are necessary to confirm this suspicion.

The development of the *M. genioglossus* attachment may change throughout the ontogeny of caenagnathid dentaries (Fig. 3.43). Musculature, as indicated by osteological muscle correlates, generally increases in size through ontogeny, although it is rarely used for age assessment. The poor definition of the *M. genioglossus* attachment in TMP 1985.043.0070 contrasts starkly with the well-defined marks on TMP 1992.036.1237 and UALVP 55639 (Fig. 3.43). Examination of other known caenagnathid dentaries suggests that this muscle attachment is subject to considerable variation in shape, but is consistently defined among most specimens. In addition to TMP 1985.043.0070, two other specimens have poorly developed *M. genioglossus* attachments: TMP 1979.008.0622 and TMP 1990.040.0044. In both of these specimens, the bone surrounding the M. genioglossus attachment is fibrous in texture (Fig. 3.43C), and the attachment consists of two small, poorly defined depressions. In contrast, the M. genioglossus attachments of other caenagnathid dentaries are hourglass or dumbbell-shaped, glossy in texture, and with a defined lip demarcating their extents (Fig. 3.43D). Additional histological samples are required to evaluate whether the specimens with poorly defined *M. genioglossus* attachments are of a similar ontogenetic stage to TMP 1985.043.0070.

Postcrania—Sections of UALVP 59400 show that this individual was a previously gravid female and approaching maximum body size. Reticular and plexiform vascularity in the inner cortex of the femur and tibia of UALVP 59400 (Fig. 3.41) suggest that this individual had relatively rapid rates of growth early in life. This is similar to the outer cortex of UALVP 57349, a small caenagnathid tibia from the HCF (see Section 3.3.6). Retrocalculation of missing growth

marks based on spacing of the three internal LAGs suggests that up to three additional growth marks may be missing, which would result in a total age of at least 12 years at death.

The possible presence of partly resorbed medullary bone between endosteal lamellae is important. In addition to providing an indicator of sex, it also suggests that medullary bone has a chance of being detected outside of the gravid period. In this case, only a small wedge of bone is preserved, and it is unclear why it was not fully resorbed. No study has yet qualified the degree of medullary bone resorption, and it is not clear whether it can persist after the egg-laying cycle in modern avians. It is possible that it was not fully resorbed in UALVP 59400 because, being large compared to a bird, relatively more calcium was available from other sources in the skeleton. On the other hand, it is possible that it remained because UALVP 59400 apparently still experienced some growth after achieving sexual maturity. In this case, normal growth processes, including expansion of the medullary cavity, continued during the egg-laying cycle, and osteocytes responsible for resorbing the medullary bone were displaced by osteoblasts depositing endosteal lamellae. As a result, the underlying medullary bone could not be fully resorbed and it was entrapped within the endosteal lamellae.

Although the timing of medullary bone deposition cannot be determined with certainty, it is likely that it coincides with or followed the stark decrease in LAG spacing, because sexual maturity is usually reflected by a decrease in growth rate. If this is the case, UALVP 59400 was at least six years old when reproductive maturity was reached, and may have had as many as five reproductive seasons before death. This estimate is roughly similar to estimates of the growth rate of the similarly sized *Troodon formosus* Leidy 1856 (three to five years to adult size). However, the reticular–plexiform vascular patterns in UALVP 59400 suggest a more rapid growth rate than in *Troodon formosus,* where vasculature is plexiform–laminar. This difference

in growth rate likely accounts for the larger body size in *Chirostenotes pergracilis*, despite

similar duration of maximum growth periods.

3.3.3 *Elmisaurus rarus* Osmólska 1981

Elmisaurus Osmólska 1981

Elmisaurus rarus Osmólska 1981

Figs. 3.44–3.55

Holotype: ZPAL MgD-I/98, partial skeleton including vertebrae, manus, partial pelvis, and nearly complete hindlimb.

Newly referred specimens: MPC-D 102/006, right tarsometatarsus; MPC-D 102/007; partial skeleton including frontal, vertebrae, ribs, partial manus, and partial hindlimb; MPC-D 102/008, left metatarsal IV; MPC-D 102/009, proximal end of right tarsometatarsus; MPC-D 102/010, vertebra and tibia.

Horizon and locality: All specimens are from the Nemegt Formation exposed in the Central or Northern Sayrs at the Nemegt locality, Omnogövi Province, Mongolia.

Etymology: *Elmyi-* , pes (Mongolian), *-saurus*, lizard; *rarus*, rare.

Revised Diagnosis (modified from Osmólska 1981): Small caenagnathid oviraptorosaur diagnosed by the following features and autapomorphies (asterisks): frontal divided anteriorly by slot for lacrimal and nasal*; metacarpal I more than half the length of metacarpal II; tibia with large postfibular flange; distal tarsals III and IV coossified to each other and the proximal metatarsus at maturity; prominent posterior protuberance on proximal end of tarsometatarsus*; metatarsal III with prominent cruciate ridges on posterior surface.

Description

Axial skeleton:

Frontal—An isolated cranial bone (50.5 mm long) of *Elmisaurus rarus* was found with MPC-D 102/007. It can be identified as a frontal (Fig. 3.44) because the lower surface includes the roofs of the orbit and the brain cavity, and there are clear sutures for laterosphenoid, parietal and postorbital. The bone is less than 2 mm thick and does not appear to be pneumatized. The interfrontal suture is dorsoventrally thin posteriorly (4 mm), dorsoventrally deep (15.2 mm) anteriorly, and lightly striated longitudinally. The nasal contact is a large, deep slot between the interfrontal suture and the orbital margin; the nasal extended posteriorly to a position between the supratemporal openings. There are no obvious sutures for either the prefrontal or the lacrimal, which suggests that the large nasal contact was also at least partially filled by the lacrimal. Unfortunately, the anterolateral tip of the frontal is incomplete. The slot is open ventrally almost to the back of the orbit, posterior to which it becomes a depression in the dorsal surface of the frontal. The frontals formed a flat dorsal surface between the upper temporal fenestra. There is a strong suture (7.5 mm long anteroposteriorly) that overlapped the front of the parietal. In dorsal view, the anteriormost margin of the parietal is on the midline. However, a thin process extended anterolaterally along the margin of the frontal to contact the laterosphenoid and postorbital as in most theropods; the suture is only visible in lateral and ventral views. The postorbital process of the frontal is almost perpendicular to the medial orbital margin. This is the widest part of the bone. As in other theropods, the dorsal surface of this process slopes posteroventrally into the supratemporal fenestra. There is a distinct suture posterolaterally for the postorbital bone. The ventral margin the postorbital process has a transverse groove for the postorbital process of the laterosphenoid. Overall, the postorbital process is similar to that of any dromaeosaurid. The domed, ventral surface over the brain has the impressions of blood vessels, suggesting the animal was highly encephalized (Osmólska, 2004a).

Vertebrae—Three vertebrae were recovered with MPC-D 102/007 (Fig. 3.45). An anterior to mid cervical neural arch is relatively small (21.4 mm long) and tapered, and resembles the third to fifth cervical vertebrae of dromaeosaurids and oviraptorosaurs. The second preserved vertebra is a posterior cervical or anterior dorsal that in cross-section tapers ventrally into a midline keel. The 26.4 mm long centrum is pierced laterally by a single pleurocoel (sometimes termed a lateral excavation), close to the posterior margin. There is no sign of the suture between the neural arch and centrum, and the coosification suggests that the specimen was mature at the time of death. Only the base of the neural arch is preserved, but on the right side it forms the margin of a large infradiapophysial fossa**.** The third vertebra of MPC-D 102/007 is an anterior dorsal that lacks the neural spine and transverse processes (Fig. 3.45). The 27.7 mm long centrum has a large (5 mm) pleurocoel on each side. The anterior edge of the centrum extends ventrally far below the ventral margin of the central part of the vertebra, and as a consequence the centrum is 22.5 mm high anteriorly. The ventral surface of this extension (hypapophysis) is unfinished. The hypapophysis suggests that this is a cervicodorsal vertebra, of which there are two or three in oviraptorids and alvarezsaurids. The parapophysis is positioned on the lateral surface at the anteroventral margin of the neural arch, which is consistent with the identification of this vertebra as an anterior dorsal. The neurocentral suture is fused but still discernable for most of its length. An intricate system of laminae and ridges outline the infraprezygapophysial, infradiapophysial, and infrapostzygapophysial pneumatic fossae (Britt, 1993). In addition to the highly angled zygapophyses, there are paired hyposphene and hypantrum articulations.

Two fragmentary mid-sacral vertebrae (ZPAL MgD-I/98) show that the ventral surfaces of these vertebrae are almost flat, and that there were no longitudinal furrows along the ventral surfaces of the mid-sacral centra. Such a furrow has been reported (Currie and Russell, 1988;

Norell and Makovicky, 1997) in some other maniraptorans, although it is usually present in only the more posterior vertebrae. On each of the two sacral vertebrae a deep, elongate pleurocoel is ventrolaterally present as in caenagnathids (Currie and Russell 1988), oviraptorids (Balanoff and Norell, 2012a), tyrannosaurids (Brochu, 2003), dromaeosaurs, megaraptorines, ornithomimids, therizinosaurs, and birds.

Ribs—Three of the rib heads, all from the left side, are reasonably well preserved (Fig 3.46). The proximal shafts of both the two larger anterior dorsal and the smaller posterior dorsal ribs were hollow and were clearly pneumatic. A pneumatopore pierces the base of the lateral surface of the web joining the tuberculum and capitulum in the largest specimen (Fig. 3.46A). The ribs are generally similar to those of oviraptorosaurs, although the ridges along the anterolateral and posterolateral margins of the proximal part of the shaft are more pronounced.

Appendicular skeleton:

Scapula—There is a fragment of scapula preserved in specimen ZPAL MgD-I/98 (Fig. 3.47). It represents a proximal portion of the bone that has an almost complete glenoid surface and most of the basal portion of the acromial process. The latter is thick across the base and inclines laterally, which suggests that its missing distal part might provide an attachment surface for the clavicular epicleideum. The supraglenoid ridge is not pronounced. Just above the margin of the glenoid and close to the coracoscapular suture, there is a small irregular depression on the lateral surface of the scapula with two to three tiny foramina. On the ventromedial side of the scapular fragment, there is a small nutrient foramen positioned close to the glenoidal surface. The portion of the ventral margin adjoining to the glenoid is rough and thick where it forms an elongate tuberosity. As only the proximal portion of the bone is preserved, the relationship of the

scapula to the rib cage, and orientation of the glenoid, whether ventral or lateral, cannot be shown beyond doubt. In theropods with ventrally (or ventroposteriorly) facing glenoids, the scapular portion of the glenoid faces anteroventrally as in *Gallimimus bullatus* Osmólska et al. 1972, and the oviraptorids *Citipati* n. sp. Clark et al. 2001 (MPC-D 100/42), *Conchoraptor gracilis* Barsbold 1986 (ZPAL MgD-I/099), and *Heyuannia yanshini* Barsbold (1981) (MPC-D 100/30). In this specimen of *Elmisaurus rarus*, the glenoid faces somewhat lateroventrally as in dromaeosaurids, *Apatoraptor pennatus* (Funston and Currie 2016) and some therizinosaurs, which clearly have more lateral orientations to their glenoids (Kirkland and Wolfe, 2001). The angle to the lateral surface of the blade is approximately 110-120° in *Elmisaurus rarus*, whereas it is around 90° in most other theropods.

Manus—In addition to the incomplete manus described by Osmólska (1981), four elements of the hand were recovered with MPC-D 102/007 (Fig. 3.48). Phalanx II-2 lacks the proximal end, so the total length is unknown. The shaft is 7.3 mm deep and 5.4 mm wide. The distal width is 8.5 mm, which is less than the 10 mm width of ZPAL MgD-I/98 (Osmólska 1981). Like all theropod penultimate phalanges, the collateral ligament pits (foveae ligamentosae) are deep on both sides, and are positioned high on the medial and lateral surfaces of the distal expansion. One ungual was recovered and lacks only the disal tip. It is about 10% smaller than the ungual described for ZPAL MgD-I/98. The absence of a proximodorsal lip is due to breakage (Fig. 3.48F). The smaller size of MPC-D 102/007 plus the more open curvature, the more distally positioned flexor tubercle and the fact that it articulates well with II-2 indicate that this ungual is phalanx II-3. The ungual described for ZPAL MgD-I/98 (Osmólska 1981) is almost certainly I-2. Phalanges III-1 and III-3 are very slender elements as in other elmisaurids

(Osmólska, 1981), and have shaft diameters that are less than two-thirds the width of phalanx II-2. The smaller of the two phalanges has a shallow concave proximal articulation that indicates it is phalanx III-1. The longer phalanx has the high collateral ligament pits that identify it as phalanx III-3. The lateral pit is deeper than the medial one in *Elmisaurus* (Osmólska 1981) and other theropods, indicating that this element is from the left hand. Both third digit phalanges have measurements (Appendix 1) comparable with, but slightly smaller than, ZPAL MgD-I/98 (Osmólska 1981).

Pelvis—The preserved proximal part of the right pubis of ZPAL MgD-I/98 (Fig. 3.47B) is associated with the adjoining portion of the ischium forming the ventral margin of the acetabulum. The iliac process of the pubis is broken off, and the ischiadic process is reduced to a thickened lip. Judging by the preserved proximal portion of the left pubic shaft, the shaft may have been somewhat concave anteriorly. In addition to the proximal part of the right ischium (ZPAL MgD-I/98), there are incomplete shafts of both ischia. They show that the shaft was relatively long and massive, and was only slightly flattened mediolaterally. The distal ends of the shafts are missing, and only the bases of the thin obturator processes are preserved.

Femur—The head of the left femur (ZPAL MgD-I/98) is cylindrical, somewhat higher than the greater trochanter, and is separated from the latter by a broad, shallow depression (Fig. 3.47). On the posterior surface of the head, there is a wide groove for the capital ligament. The anterior (lesser) trochanter is not complete, but is prolonged into a mediolaterally flattened and anteriorly extended ridge. The preserved thickness of the trochanter is 8 mm. Its shape and orientation seems to suggest that the anterior trochanter was a wing-like rather than a finger-like structure. On the medial side of the shaft, a short distance below the head, there is a shallow, longitudinally oval depression. It corresponds to similarly positioned depressions (or a scars) in

ornithurine birds, oviraptorids and ornithomimids (*Gallimimus bullatus*). On the posterolateral surface of the proximal end of the femur, some distance (25- 30 mm) below the upper margin of the greater trochanter, there is a large but low protuberance resembling in its position the "posterior trochanter" of *Deinonychus antirrhopus* Ostrom 1969 (Ostrom, 1969). Similar protuberances seem be present in several other theropods, including *Bagaraatan ostromi* Osmólska 1996 (Osmólska, 1996) and *Gallimimus bullatus*. The preserved shaft of the left femur of MPC-D 102/007 has a circumference of 70 mm. A formula (0.8685x + 0.7654, where 'x' and 'y' are the log transformed values of shaft circumference and femoral length respectively; n is 106, and the r^2 value is 0.9808) comparing the femur shaft circumference with femur length in 106 coelurosaurs (Currie, 2003), can be used to estimate the length of the femur of MPC-D 102/007 as 233 mm. Using transverse shaft width produces a slightly different result where the estimated value of the femur is 236 mm. Finally, comparison of femoral versus tibial lengths in oviraptorosaurs produces an estimate of 270 mm. The last comparison is tightly constrained (0.9377x + 0.229, where 'x' and 'y' are the log transformed values of femoral and tibial length respectively; n is 43, and the r^2 value is 0.99385). The three measurements were averaged for an estimated femur length of 246 mm. The head of the femur was badly eroded when found but shows a few characters of interest. Like the head of ZPAL MgD-I/98, the lesser trochanter appears to have been a tall, winglike structure as in most theropods; it does not seem to have been the closely appressed, fingerlike lesser trochanter that is seen in oviraptorids. The shaft circumference suggests that this elmisaurid weighed about 18–31 kg (Table 3.2), using the method of Campione et al. (2014).

Tibia—Tibiae (Fig. 3.49), previously undescribed for *Elmisaurus*, were recovered in two specimens (MPC-D 102/007, MPC-D 102/010). The average length (323 mm) of the right and

left tibiae of MPC-D 102/007 suggests that this animal stood approximately 75-80 cm high at the hips. The tibia is somewhat more gracile and elongate than those of similar sized oviraptorids. For example, MPC-D 102/007 (*Elmisaurus*) has a femur slightly longer (an estimated length of 246 mm) than that (an estimated length of 242 mm) of MPC-D 102/11 (Unnamed Guriliin Tsav oviraptorid), but the tibia of MPC-D 102/007 is 25% longer, even though the shaft circumference is 10% less. The unfinished anterior surface of the prominent cnemial crest slopes anteroventrally from the articulation for the medial condyle of the femur (Fig. 3.49). The cnemial crest is separated from the outer (fibular) condyle by a deep incisura tibialis (Fig. 3.49D, E). The outer condyle would have contacted more than half the anteroposterior length of the proximal end of the fibula. Its lateral articular surface for the fibula is oriented posterolaterally. This surface is separated from a low ridge extending from the fibular condyle by a shallow concavity. The groove separating the outer and inner condyles is shallow, whereas it tends to be more pronounced in oviraptorids. The rugose edge for the interosseum tibiofibular ligament attachment (Fig. 3.49G) is more than 4 cm long, and is oriented anterolaterally. This is 35% of the way down the shaft of the tibia from the proximal end, whereas it is 41% in the unnamed Guriliin Tsav oviraptorid (MPC-D 102/11). Just posterior to the distal end of the fibular crest is a small foramen at a distal end of a shallow canal. The canal enters the bone where it forms the lateral corner between the flat anterior and convex posterolateral surfaces of the bone. This is the same in *Heyuannia yanshini* (MPC-D 100/032), *Khaan* Clark et al. 2001 (Balanoff and Norell, 2012a) and other oviraptorosaurs. The shaft of the tibia has a flat anterior face, which produces a semicircular cross section. Distally, the anterior surface of the tibia is flat for its contact with the ascending process of the astragalus. This surface extends medially and laterally into sharply defined ridges, the latter of which is the postfibular flange (Fig. 3.49F). A groove on the anterior

surface of the postfibular flange marks the distal position of the fibula. This groove extends dorsally for almost half the length of the tibia. Its presence shows that the fibula extended to the tarsus and was closely appressed distally to the lateral edge of the anterior surface of the tibia. A more medial impression shows that the ascending process was at least 65 mm high (20% of tibia length). Overall, the anatomy of the tibia is virtually the same as an oviraptorid tibia. Whereas the tibia of MPC-D 102/007 is only 25% longer than that of an oviraptorid of equivalent size, the tarsometatarsus is relatively longer in *Elmisaurus*; the tarsometatarsus is 70% of femur length in MPC-D 102/007, whereas the average in 22 oviraptorid specimens is only 55%, with a maximum of 60% in the chicken-sized *Yulong mini* Lü et al. 2013 (Lü et al., 2013).

Tarsals—The third and fourth distal tarsals form part of the fused tarsometatarsus in MPC-D 102/006 (Fig. 3.50A). A third distal tarsal that is not fused to the metatarsus is preserved in association with the second metatarsal of MPC-D 102/007 (Fig. 3.50B). It caps the posterior third of the proximal articulation of the second metatarsal in both this specimen and that of MPC-D 102/006. The third distal tarsal extends medially to reach the medial margin of the tarsometatsus, whereas this never happens in oviraptorids. The third distal tarsal also completely covers the proximal articular surface of the third metatarsal. In oviraptorids (for example MPC-D 102/12), the third distal tarsal contacts the posterolateral margin of the proximal articulation of the second metatarsal, but does not overlap it to any great extent. As the lateral surface is broken (Fig. 3.50D), it is not possible to know if it was fused to the fourth distal tarsal before death and burial. In MPC-D 102/006, it is fused to both the fourth distal tarsal and posterodistally to both the second and third metatarsals. In outline, it is similar to the same elements in dromaeosaurids, ornithomimids, oviraptorids, and tyrannosaurids. It is 23.5 mm wide, 14.4 mm anteroposteriorly, and covers the posterior half of the proximal surfaces of the second and third metatarsals. The

distal surface of the third tarsal extends posteroventrally around the back of the proximal end of the metatarsals (Fig. 3.50F). Fusion between the distal tarsals and the metatarsus proceeded from posterior to anterior (there is no fusion in MPC-D 102/007, posterior fusion in MPC-D 102/006, and complete fusion in ZPAL MgD-I/172). The fourth distal tarsal of MPC-D 102/006 is indistinguishably fused to the third distal tarsal (Fig. 3.50A), and to metatarsals III, IV and V. As pointed out by Osmólska (1981), a process projects dorsally from the posterolateral corner of the bone. Unlike any other theropods, it arches distally to meet the upper end of the fifth metatarsal (Fig. 3.50G).

Tarsometatarsus—The tarsometatarsus in MPC-D 102/006 (Fig. 3.51A, Appendix 1), is 15% longer than ZPAL MgD-I/172 but is not as completely fused. Nevertheless in this specimen, the third and fourth distal tarsals are fused to each other, and are fused posteriorly to the second to fifth metatarsals. Their anterior margins are still distinct and had not coossified with the second to fourth metatarsals. The second to fourth metatarsals are also coossified posteriorly, but remain distinct in anterior view, which is similar to ZPAL MgD-I/172 (Osmólska 1981). The fifth metatarsal is closely appressed to the fourth but is not fused to it (Fig. 3.50G). The isolated fourth metatarsal (MPC-D 102/008, Fig. 3.51C) is 164 mm long (12% longer than ZPAL MgD-I/172) but was not found with either the distal tarsals or the other metatarsals. However, the posterior part of the proximal surface was damaged when the specimen was found, suggesting that it had been fused posteriorly to the rest of the tarsometatarsus but had broken away before burial and fossilization. The metatarsals of the associated specimen MPC-D 102/007 are about 15% larger than the equivalent parts of ZPAL MgD-I/172, and show no signs of fusion to each other. However, the third distal tarsal had remained associated with the head of the second metatarsal, suggesting that coossification had begun between these elements. There is therefore

some variability in the onset of tarsometatarsal coossification in *Elmisaurus rarus*. The

metatarsus of MPC-D 102/007 (Fig. 3.51B) is 53% the length of the tibia, which is more

elongate than in most oviraptorosaurs (43 to 48%), but is less than most arctometatarsalian

theropods. A section across the mid-length of the metatarsus is deeply concave on the plantar

side (Fig. 3.52). This is because metatarsals II and IV are deep between the extensor and flexor

surfaces, especially at tarsometatarsus midheight. As a result, the outer and inner surfaces of

these metatarsals are flat, with sharply defined, posteroventral edges. These edges are

surmounted by thick and rough ridges along their plantar edges, which are most easily seen in

specimens MPC-D 102/006 and ZPAL MgD-I/172. On the fourth metatarsal, a wide but shallow

groove is present along approximately the distal fifth of the shaft length. The groove starts

somewhat proximal to the lateral ligament pit and extends upward (proximally) and posteriorly

onto the plantar side of Metatarsal IV, and distally bounds the thickened portion of the metatarsal

edge. The inner sides of metatarsals II and IV form steep and deep walls (lateral and medial

respectively) of a plantar trough (Fig. 3.52), the narrow bottom of which is formed by the weakly

concave surface of metatarsal III. The anterior (dorsal) surface of the metatarsus is concave

along about its proximal half, but much less than the plantar surface. Proximally, there is a short

slit between the otherwise tightly connected (or fused) metatarsals III and IV (Osmólska 1981).

This slit occurs in ZPAL specimens Mg-D I/127, 98 (Osmólska 1981: pls 20: 2; 21: 1) and MPC-

D 102/007 (Fig. 3.51B, atp). Its position is comparable to that of the lateral proximal vascular

foramen in modern birds, and *Confuciusornis sanctus* Hou et al. 1995 (Chiappe et al., 1999); it

probably transmitted *a. tarsalis plantaris* to the plantar aspect of the foot. On all adequately

preserved metatarsi, there is a second, narrower slit located between metatarsal II and the

somewhat medially incised metatarsal III (Fig. 3.51B, vs). This slit is placed more distally than

the former, but also cuts through the metatarsus. A similarly located slit is also present in species of *Velociraptor* Osborn 1924. On the anterior (dorsal) surfaces of metatarsals II-IV (Fig. 3.51A), there is a tripartite protuberance proximally (Osmólska 1981). A similarly placed tubercle is present on metatarsal II in an undetermined dromaeosaurid specimen, probably a species of *Velociraptor* (Norell and Makovicky, 1997) and in *Confuciusornis sanctus* (Chiappe et al., 1999). These authors suggest that the tubercle probably marks the insertion of *M. tibialis cranialis*.

Metatarsals II, III and IV are the same in the new specimens as they are in ZPAL MgD-I/127 (Osmólska 1981) and little needs to be added to their description. Because the elements of MPC-D 102/007 are separate, some of the contacts between the metatarsals can be seen well. Relatively small (12 mm high, 7 mm anteroposteriorly) facets on metatarsals II and IV contact each other anterior to the proximal end of the third metatarsal (Fig. 3.51E). The posterior surface of the third metatarsal has two longitudinal ridges (cruciate ridges) that are continuous with the posterior articular ridges. These ridges cross distally, forming a distinctive chiasmata (Fig. 3.53), as in *Leptorhynchos elegans* from Alberta (Funston et al., 2016a).The fifth metatarsal extends proximally beyond the proximal surfaces of the distal tarsals. When found, it formed an ossified arch with the top of the distinctive protuberance (Osmólska 1981) of the fourth distal tarsal. Unfortunately, this fragile arched structure was damaged during collection, although the outline is still visible and it is clear that the fifth metatarsal was fused into the tarsometatarsus as in *Avimimus*. The fifth metatarsal is 70.3 mm long, which is 38% the length of the third. The long tapering fifth metatarsal contacts most of the margin of the ridge along the posterolateral edge of the fourth metatarsal (Fig. 3.51B) rather than arching away from it as it does in other theropods (Currie and Peng, 1993). Although the first metatarsal was not recovered with MPC-D 102/007,

the rest of the digit from the right side was (Fig. 3.54). The medial collateral ligament pit is deeper than the lateral one in pedal phalanx I-1. In both size and shape, it is similar to I-1 of ZPAL MgD-I/98.

Remarks

A suite of manual and pedal characters ties *Elmisaurus* to Caenagnathidae, including the elongate metacarpal I, the proximodorsal "lip" on the unguals, and the flat, proximally pinched metatarsal III. This indicates that "Elmisauridae" is best considered the junior synonym of Caenagnathidae. Within Caenagnathidae, *Elmisaurus rarus* is most similar to *Leptorhynchos elegans*: the paired cruciate ridges on the posterior surface of metatarsal III, the fusion of the distal tarsals to each other, and their coossification with metatarsals II, III, and IV, are unique to both taxa. Sues (1997) suggested that material assigned to *"Elmisaurus" elegans* by Currie (1989) was probably synonymous with *Chirostenotes pergracilis*. The abundance of additional material described here shows that *Elmisaurus rarus* and *Leptorhynchos elegans* ("*Elmisaurus*" of Currie, 1989) can be consistently distinguished from *Chirostenotes pergracilis*. Despite their similar proportions and the distinctive metatarsal III, the fusion of the proximal end of the tarsometatarsus in *Elmisaurus rarus* and *Leptorhynchos elegans* distinguishes them from *Chirostenotes* (CMN 8538, TMP 1979.020.0001, UALVP 59400), which have larger but unfused tarsometatarsi. Although previously suggested that isolated metatarsals can be confidently identified based on the development of the posteromedial ridge of metatarsal II, presence of the cruciate ridges on metatarsal III, and the development of the posterolateral ridge of metatarsal IV (Currie et al. 2016; Funston et al. 2016), reexamination suggests these features are also present in *Chirostenotes pergracilis* and *Anzu wyliei* (S. Williams, T. Holtz, pers. comm.) Instead, fusion of

the distal tarsals to the proximal end of the metatarsus, a posterior protuberance on metatarsals II and IV, and the rugose insertions of *M. tibialis cranialis* on all three metatarsals are better characters for distinguishing these taxa. Overall it appears that the feet of *Elmisaurus rarus* and *Leptorhynchos elegans* were more consolidated units, with fused proximal tarsometatarsi and a closer association between the shafts of metatarsals II, III, and IV.

The new specimens provide a wealth of new anatomical information, allowing the skeleton of *Elmisaurus rarus* to be reconstructed (Fig. 3.55). The frontal of *Elmisaurus rarus* suggests it was an encephalized theropod that had a tall nasal crest, possibly analogous to that of *Anzu wyliei* (Lamanna et al. 2014). The vertebrae are similar to those of other caenagnathids, with large pleurocoels and pneumatized neural arches. The scapulocoracoid is similar to other theropods, but the scapular portion of the glenoid faces lateroventrally, as in some therizinosaurs. The manual unguals are tightly curved, instead of elongate and broadly curved as in other caenagnathids. The tibia is anatomically similar to those of dromaeosaurids and oviraptorosaurs, but is more elongate and gracile. The relatively large protuberance on the posterolateral margin of the proximal surface of the fourth distal tarsal extended to contact the proximal end of the fifth metatarsal, which also protrudes above the articulation between the proximal and distal tarsals. The distal tarsals and the metatarsals were probably fused in all mature specimens of *Elmisaurus* and *Leptorhynchos*. The posteromedial and posterolateral longitudinal ridges of metatarsals II and IV are well developed in elmisaurines. This creates a deeply concave posterior margin of the foot in cross section. The third metatarsal has two distinct longitudinal ridges on the posterior surface – one medial and one lateral – that are separated by a sulcus; in cross section, the shaft of the proximal half of the bone is wider mediolaterally than anteroposteriorly long, and is rectilinear rather than triangular.

The lateral orientation of the glenoid of the scapulocoracoid is similar to TMP 1993.051.0001, the holotype of *Apatoraptor pennatus* from the HCF of Alberta, Canada. In TMP 1993.051.0001, the biceps tubercle of the coracoid and the deltopectoral crest are expanded. The manual structures of *Elmisaurus* and TMP 1993.051.0001 are similar, so perhaps the lateral orientations of the glenoids in these taxa represent an adaptation for a stronger grasp. In any case, the lateral position of the glenoid increases the flexibility of the arm, allowing it to reach farther anteriorly when extended.

3.3.4 *Leptorhynchos elegans* (Parks 1933)

Leptorhynchos Longrich et al. 2013

Leptorhynchos elegans (Parks 1933) Longrich et al. 2013

Figs. 3.56–3.71

Holotype: ROM 781, partial tarsometatarsus, Dinosaur Park Formation, Dinosaur Provincial Park

Referred specimens: ROM 37163, distal metatarsal II; TMP 1979.008.0622, partial fused dentaries; TMP 1982.039.0004, proximal tarsometatarsus; TMP 1991.144.0001, partial fused dentaries; TMP 1992.036.0390, nearly complete fused dentaries.

Newly Referred specimens: TMP 1981.023.0034–35 + TMP 1981.023.0039, partial left and right ilium and associated last sacral vertebra; TMP 1982.016.0006, complete right tarsometatarsus; TMP 1984.163.0036, distal end of metatarsal III; TMP 1986.036.0186, distal end of metatarsal III; TMP 1988.036.0104, distal half of metatarsal II; TMP 1993.036.0630, distal end of metatarsal III; TMP 1994.012.0880, left tibia; TMP 1996.012.0141, left

tarsometatarsus; TMP 2005.049.0190, right metatarsal III; UALVP 55585, distal shaft of metatarsal III; UALVP 55639, partial fused dentaries; UALVP 59606, complete metatarsal IV and distal tarsal IV.

Horizon and locality: All specimens are from the Dinosaur Park Formation of Dinosaur Provincial Park, Alberta, Canada.

Etymology: *Lepto-*, small; *-rhynchos*, beak; *elegans*, elegant.

Revised Diagnosis (modified from Longrich et al. 2013): Small caenagnathid oviraptorosaur diagnosed by the following combination of features and autapomorphies (asterisks): tip of beak strongly upturned, with anterior occlusal margin projecting vertically; anterior margin of symphysis straight, chin squarish in lateral view; ilium with horizontal ventral edge of pubic peduncle*; dorsal margin of ilium thickened into a platform*; distal tarsals III and IV coossified with each other and proximal metatarsus at maturity; metatarsal III with prominent cruciate ridges on posterior surface.

Description

Dentaries:

UALVP 55639—This specimen is a relatively small, fragmentary pair of dentaries (Fig. 3.56). The left dentary is represented solely by the symphyseal region and the tubercle of the lingual ridge. The right dentary is more complete and preserves part of the occlusal margin, most of the lingual ridge including the tubercle, the symphyseal region, and the ventral surface of the symphysis. The occlusal margin is low, but thin sections show that this is the result of taphonomic wear on its apical surface (Fig. 3.56B). The occlusal margin extends only slightly

above the tubercles of the lingual ridges, which are smooth instead of rugose. On the right side, the occlusal margin is scalloped by three lateral occlusal ridges, the anteriormost of which is the best developed (Fig. 3.56A). The posterior part of the right ramus preserves a slight depression on its lateral side, although whether this is the mandibular fossa cannot be determined. The symphyseal sulcus does not taper posteriorly, and is marked by anterior and posterior pairs of foramina. The vascular grooves of the symphyseal sulcus are pronounced, and diverge posteriorly to meet the Meckelian grooves, which open posteroventrally. The ventral surface of the symphysis is root etched, which makes it difficult to distinguish the shape of the M. genioglossus attachment (Fig. 3.56C). There are two foramina that mark the posterolateral extent of the M. genioglossus attachment. The ventral surface of the symphysis appears flat transversely, rather than convex as in most caenagnathids. However, this may be because only the posterior end of the symphysis is preserved, as this region is also flat in TMP 1992.036.0390.

Sacral Vertebra:

 TMP 1981.023.0039—This specimen (Fig. 3.57H–M) is an isolated last sacral vertebra. The centrum is relatively low and wide, resulting in a barrel shape similar to the proximal caudal vertebrae of most oviraptorosaurs. The anterior articular surface is unbroken (Fig. 3.57H), indicating that it had not fused to the preceding sacral vertebra, as in TMP 1979.020.0001. The anterior articular face is convoluted, with a median ridge and adjacent lateral depressions towards the dorsal side. The posterior articular surface is deeply concave and is inclined to face posterodorsally (Fig. 3.57I, J). It is roughly trapezoidal in posterior view, with a transversely wider ventral edge than dorsal edge. On the lateral surface of the centrum there is a small, posteroventrally opening foramen just ventral to the sacral rib. This likely corresponds to the

lateral pleurocoels of more anterior sacral vertebrae, but it is much smaller. Dorsal to this foramen, there is a second, larger opening that pierces the posterior side of the sacral rib (Fig. 3.57I, L). The ventral surface of the centrum has a wide, shallow midline sulcus. The neural canal is consistent in transverse width for its length, and is roughly elliptical in anteroposterior view. The sacral ribs are indistinguishably fused to the centrum, but the area where they lap onto the dorsal part of the centrum can be distinguished. Little can be discerned about the morphology of the sacral ribs because they are broken just lateral to their contact with the centrum.

Ilium:

TMP 1981.023.0034—A partial left ilium (Fig. 3.57C, E, G) preserves the ventral parts of the pre- and postacetabular blades and the acetabulum. Only the base of the preacetabular portion is preserved, but a ridge on its lateral surface shows that the cuppedicus fossa was well developed. On its medial surface (Fig. 3.57E), there is a deep fossa dorsal to a promontory that the sacral ribs contacted. The pubic peduncle is much larger than the ischiadic peduncle and is square in lateral view. Its ventral edge is horizontal, rather than anterodorsally inclined as in TMP 1979.020.0001. There is a ventrally opening foramen near its anterior edge on the lateral surface. The acetabulum is constricted transversely at its midpoint (Fig. 3.57G), expanding towards the pubic and ischiadic peduncles. Its dorsal surface is pockmarked by numerous small foramina and striations. The ischiadic peduncle is small and triangular in lateral view. It is less everted laterally than that of TMP 1979.020.0001, which means less of the articular surface of the posterior acetabulum is visible in lateral view. The postacetabular blade has a patch of rugose bone on its lateral surface (Fig. 3.57C) and breakage indicates that this region would have overhung the brevis fossa in lateral view. Brevis fossa terminates anterior to the ischiadic

peduncle and in this region the brevis shelf merges with the thickened promontory for attachment to the sacral ribs. Dorsal to this, there is a deep concavity. Only fragments of the dorsal edge of the ilium were recovered, and they cannot be reconstructed with the rest of the specimen. However, these fragments show that, like TMP 1981.023.0035, the dorsal edge was transversely thickened.

TMP 1981.023.0035—Most of a right ilium (Fig. 3.57A, B, D, F) is missing the preacetabular process and some of the body between the acetabulum and dorsal margin. Where the bone is broken on the ilium, it reveals trabeculae of camellate bone throughout. The acetabulum is semicircular, moderately lipped towards the anterior portion, and has a thick, rounded lateral edge. It is relatively wide in ventral view (Fig. 3.57F) and constricted somewhat towards the midpoint. The anterior part of the ventral surface has a circular pit and there is a longitudinal groove that shallows posteriorly along its dorsal surface. The pubic peduncle is large, nearly the same anteroposterior length as the acetabulum, and robustly built (Fig. 3.57A, D). On its anterolateral surface, there is a ventrally-opening foramen (Fig. 3.57A). Directly dorsal to this there is what appears to be a tooth mark. The pubic peduncle is nearly rectangular in cross-section, with a tapering anterior end and a squared-off posterior end (Fig. 3.57F). Its ventral edge is parallel to the dorsal margin of the ilium and when these planes are horizontal it extends far past the ischiadic peduncle. The ischiadic peduncle is small and triangular in lateral view. It projects only slightly beyond the lateral surface of the ilium, although its most ventral corner is broken. The lateral surface of the blade is smooth except towards its dorsal edge. Here, a raised platform of rugose bone forms a ridge that is directed posteroventrally (Fig. 3.57A). It becomes less pronounced posteriorly and ends halfway between the ischiadic peduncle and posterior end of the postacetabular blade. The dorsal surface of the ilium is thick and flat (Fig.

3.47B); posteriorly it widens, becomes rounded, and curves medially. The posterior end of the

lateral side of the ilium bears a rectangular patch of rugose bone. The medial surface of the ilium

(Fig. 3.57D) is complexly excavated. There are three broken areas where the sacral ribs would

have attached (Fig. 3.57D). The most anterior one is at the anterior end of the pubic peduncle,

and its long axis is anterodorsal-posteroventral. The middle contact—the smallest—is directly

above the middle of the acetabulum, and is situated at the base of a dorsoventral ridge that

separates two deep concavities on the medial side of the ilium. The posterior attachment is the

longest, and its long axis is nearly horizontal. It is above the ischiadic peduncle, but is longer

anteroposteriorly than the peduncle. Between it and the acetabulum, there is a depressed area

bisected by a rugose ridge. The brevis fossa is relatively shallow, and its lateral surface is

inclined dorsomedially-ventrolaterally (Fig. 3.57D). The ventral edge of the ilium is broken here,

but appears to have been rugose and raised slightly from the natural curve of the brevis fossa.

This raised area is demarcated dorsally by a slight groove. There are two foramina in the brevis

fossa, the anterior approximately double the length of the posterior one. The brevis shelf is

broken, but based on the sacral rib contacts, cannot have extended much further medially. There

are three large depressions (Fig. 3.57D) on the medial side of the iliac blade, probably to

accommodate air sacs. They are pierced by numerous foramina and are composed of woven,

fibrous, pneumatic bone webs. The anterior one is the largest, and is bounded posteriorly by an

anteriorly concave ridge that overhangs it medially. Towards the dorsal end of this ridge, there is

a dorsally-opening foramen. The concavity is separated from the medial side of the pubic

peduncle by a rounded ridge. The middle concavity is the smallest, and is roughly triangular in

shape, with the apex directed ventrally. The posterior concavity is nearly circular in outline, and

is separated from the middle concavity by a posteriorly concave ridge that extends along the

dorsal edge of the concavity. On its ventral edge, the concavity appears to have been confluent with the brevis shelf, but this region is broken.

TMP 1992.036.0674—TMP 1992.036.0674 (Fig. 3.58) is a pathological specimen that includes both the pubic and ischiadic peduncles, part of the preacetabular process, and the postacetabular process. The acetabulum lacks a longitudinal groove, but has moderate transverse constriction in ventral view (Fig. 3.58C). The pubic peduncle is large and square in lateral view, and triangular in ventral view (Fig. 3.58C). It has a slight posterior lip, and, where it is level with the ischiadic peduncle it has a horizontal ventral edge, which is unlike the anteriorly-inclined pubic peduncle of *Chirostenotes pergracilis* (TMP 1979.020.0001). The ischiadic peduncle is triangular, but is broken so that the extent of its projection cannot be discerned (Fig. 3.58A). Dorsal to the ischiadic peduncle on the lateral surface of the ilium is a deep foramen that opens ventrally into a curving groove. Posterodorsal to this foramen, the ilium is swollen and breakage reveals cross-hatched trabeculae (Fig. 3.58A). The surface of this swelling is pebbled, irregular, and offset laterally from the rest of the ilium by a step-like crack, which extends anterodorsally to posteroventrally. The brevis fossa is greatly reduced by the ventral extension of the swollen region. The area where the fossa would have been is horizontal in lateral view and rounded ventrally. The brevis shelf is present posteriorly, but anteriorly engulfed by the ventral swelling of the postacetabular process. The posterior end of the postacetabular blade has a wide medial facet (Fig. 3.58B) that is absent in other caenagnathid ilia. The sacral rib contacts are in the same places as TMP 1981.023.0035, but the arrangement of pneumatic cavities on the medial side of the ilium differs from both TMP 1979.020.0001 and TMP 1981.023.0035. The ridge separating the anterior and middle cavities is wider and composed of three rami, rather than two, and the middle concavity extends further ventrally to separate the anterior ridge from the posterior ridge,

which does not extend as far posteriorly. In these aspects, the pneumatic concavities are more similar to TMP 1998.093.0013. The circular anterior concavity is bounded anteriorly by the attachment site for a sacral rib, which is dorsoventral in orientation, and has a slight depression anterior to it. The cuppedicus fossa is wide and flat with only a slight transverse arch. The lateral side of the ilium is broken above it, but its breakage indicates that a lateral flange of the preacetabular process would have overhung the cuppedicus fossa laterally as in TMP 1979.020.0001.

Tibia:

 TMP 1994.012.0880—A crushed left tibia (Fig. 3.59), TMP 1994.012.0880 is similar to those of *Elmisaurus rarus* (Currie et al., 2016), but there are some differences. The tibia is 280 mm long, shorter than that of MPC-D 102/007 (*Elmisaurus elegans*), but still more gracile than those of oviraptorids. The cnemial crest is laterally deflected, with a deep incisura tibialis separating it from the fibular condyle. The fibular crest has a rugose posterolateral surface, with a shallow groove for the interosseum tibiofibular ligament. There is a foramen at the distal base of this groove, as in *Elmisaurus rarus, Heyuannia yanshini* (Barsbold, 1981), and *Khaan mckennai* (Clark et al., 2001; Balanoff and Norell, 2012a). The anterior surface of the shaft is flat, and the posterior surface is curved, resulting in a semi-circular shaft in cross section. The distal condyles are worn, especially the lateral (fibular) condyle, which nevertheless has a prominent postfibular flange (Fig. 3.59A, D). The contact with the ascending process of the astragalus is slightly concave mediolaterally.

Tarsometatarsus:

ROM 781—ROM 781 (Fig. 3.60D–F), the holotype for *Leptorhynchos elegans*, has been described in detail (Parks, 1933; Currie, 1989), so only salient details will be noted here. The metatarsus is small but well fused, leading Currie (1989) to infer that it was a mature specimen of a small taxon. The metatarsus approaches arctometatarsalian form, with metatarsal III pinched between metatarsals II and IV. Only the most proximal part of metatarsal III is obscured in anterior view by the contact of metatarsi II and IV. The posterior (palmar) surface of metatarsal III has two longitudinal (cruciate) ridges that extend most of the height of the bone and are separated by a longitudinal sulcus. The distal articular end extends onto the posterior surface as a pair of ridges. The medial one becomes less pronounced proximally until it crosses the back of the metatarsal to become continuous with the lateral cruciate ridge. The lateral ridge from the distal articulation crosses to the medial side to meet the ventral end of the medial cruciate ridge. The intersecting 'X' shape (Fig. 3.61) is more distinct in *Leptorhynchos elegans* than in *Elmisaurus rarus*, but this distinctive feature is present to a lesser degree in *Chirostenotes pergracilis* (TMP 1979.020.0001) and *Anzu wyliei* (T. Holtz, S. Williams, pers. comm.). It is also absent in all of the oviraptorids examined in the collections of the Mongolian Paleontological Center. These ridges, and the medial and lateral facets they demarcate, indicate a closer association between metatarsals II and III than between metatarsals III and IV. There is a prominent faceted posteromedial ridge on metatarsal II, which gives the metatarsus a posteriorly concave outline in cross section (Fig. 3.62); the distal part of this ridge likely contacted metatarsal I. This posteromedial ridge is absent in *Caenagnathus collinsi* (Funston et al., 2015) and is poorly developed in *Chirostenotes pergracilis* (Currie and Russell, 1988). Metatarsal IV of ROM 781 has a rugose posterolateral ridge, and a sharp anteromedial ridge. The latter ridge is variably present in other caenagnathid specimens from the DPF. Distal tarsal IV is fused to the

proximal surface of metatarsal IV, and its lateral margin is attenuated into a posterodorsal hook-like process. In all respects the tarsometatarsus of ROM 781 is nearly identical to *Elmisaurus rarus* (MPC-D 102/006, ZPAL MgD-I/127). It differs in that the proximal ends of metatarsals II and IV do not coossify as extensively posteriorly, and that the distal part of metatarsal III of ROM 781 does not have the prominent horizontal sulcus seen in MPC-D 102/006 above the distal articulation.

ROM 37163—ROM 37163, a metatarsal II assigned by Currie (1989) to *Elmisaurus elegans*, is slightly smaller than ROM 781 but nearly identical otherwise. In place of the medial rugosity on metatarsal II of ROM 781, ROM 37163 has a small flange of bone in the same position. This suggests that this is the insertion for the *M. tibialis cranialis*, which may become stronger and more pronounced with age. In addition, the medial condylar fossa is shallower in ROM 37163 than ROM 781, likely a result of muscle development in older specimens. The posteromedial ridge is strong, which is unlike *Caenagnathus collinsi* and *Chirostenotes pergracilis*. The development of this ridge helps to distinguish *Leptorhynchos* and *Elmisaurus* from other caenagnathids.

TMP 1982.016.0006—TMP 1982.016.0006 (Figs. 3.60A–C, 3.63) is an almost complete right tarsometatarsus that lacks the first metatarsal and is somewhat crushed. It shows that the distinct proximal fusion of ROM 781 is not a result of pathology and solidifies the close relationship of *Elmisaurus* from Asia and *Leptorhynchos* in North America. The distal tarsals are fused to each other and to the proximal face of the metatarsus. The third and fourth distal tarsals are fused indistinguishably and cover the proximal surfaces of metatarsals II-IV (Fig. 3.63A). The fourth distal tarsal is arched posterodorsally into a hook-like process (Fig. 3.63B), which contacts and is fused to the fifth metatarsal. In proximal view (Fig. 3.63A), the proximal surface

of the tarsometatarsus is oval in shape, but wider transversely and narrower anteroposteriorly than in *Elmisaurus rarus*. This is due in part to the lack of the posterior protuberance caused by the coossification of the distal tarsals and metatarsals in *Elmisaurus rarus*.

Metatarsal II of TMP 1982.016.0006 is straight along most of its length (152 mm), but the distal condyle is deflected medially. The proximal end is semi-circular in proximal view, and lacks the posterior protuberance of *Caenagnathus collinsi* (Funston et al. 2015). Near the proximal end of the shaft, there is an oval slit separating the second and third metatarsals, but there is no separation between the third and fourth metatarsi proximal to this region. In *Elmisaurus rarus* there are two holes between the metatarsi: proximally, there is a foramen between the third and fourth metatarsi, and distal to this point, there is a slit between the second and third metatarsi. Currie et al. (2016) suggest that the proximal slit between the second and third metatarsi accommodated the *a. tarsalis plantaris*. It is likely that in *Leptorhynchos elegans*, the more distal slit between the second and third metatarsals played the same role. This suggests that the proximal slit between the third and fourth metatarsal conducts another artery or vein. As other specimens of *Elmisaurus rarus, Leptorhynchos elegans*, *Velociraptor mongoliensis* (Norell and Makovicky 1997), and *Confuciusornis sanctus* (Hou et al., 1995; Chiappe et al., 1999), there is a rugosity on both metatarsi II and IV, for the insertion of the *M. tibialis cranialis*, on the lateral side of the shaft just proximal to the distal condyle. The posteromedial ridge of metatarsal II bows laterally, probably to accommodate metatarsal I. There is a prominent ridge on the posterior surface of the distal condyle of metatarsal II that extends from the proximal edge of the articular surface.

As in other oviraptorosaurs, metatarsal III of TMP 1982.016.0006 is the longest (172 mm) bone of the foot (Appendix 1), and the shaft is widest (12.5 mm) about a quarter of its

length from the distal end. Proximally, metatarsal III is fused with the third distal tarsal, although a distinct suture is still present. Metatarsal III tapers dorsally on the anterior surface, and its proximal end is covered anteriorly by the contact between the second and fourth metatarsals. There is a horizontal groove on the anterior surface just proximal to the distal articular surface, although it is not as well developed as in MPC-D 102/006. Metatarsal III has nearly symmetrical distal condyles. On the posterior (palmar) surface of metatarsal III, there are two cruciate ridges that extend most of the height of the bone and are separated by a vertical sulcus that contributes to the deep longitudinal concavity of the tarsometatarsus. On the palmar surface, the third metatarsal is thinnest at mid-height but expands dorsally to separate the proximal heads of metatarsals II and IV posteriorly.

The minimum shaft width of metatarsal IV (TMP 1982.016.0006) is wider (11.4 mm) than that of metatarsal II (8.4 mm) in anterior view. Metatarsal IV is straight along its entire length (160 mm). At its proximal end, it is wide (19.9 mm) and fused indistinguishably with distal tarsals III and IV. A well-developed anterior ridge ends just proximal to the distal condyle. Although the posterior (palmar) surface of metatarsal IV is damaged, it appears that it would have had a posterolateral ridge that would have accentuated the concave posterior surface of the tarsometatarsus. The distal condyle of metatarsal IV is rounded but broken.

The fifth metatarsal (Fig. 3.63B) of TMP 1982.016.0006 (Fig. 3.60A–C) is relatively short (44.3 mm) and splint-like, and has an anteriorly deflected distal end. Metatarsal V is straighter along its length in *Elmisaurus* and *Leptorhynchos* (MPC-D 102/6, TMP 1982.016.0006) than in other caenagnathids (Currie and Russell, 1988) and theropods (Currie and Peng 1993). It is fused to the hooklike posterodorsal process of distal tarsal IV, and closely associated but not fused with metatarsal IV proximally.

TMP 1982.039.0004—A fused proximal tarsometatarsus (TMP 1982.039.0004) was described by Currie (1989). The proximal ends of those metatarsi have coossified and are fused with the distal tarsals. Distal tarsal IV has a hook-like posterodorsal process that would have contacted and fused with metatarsal V. Currie (1989) notes that the shape of the proximal face of the tarsometatarsus has a posteromedial emargination that is not seen in *Elmisaurus rarus*. This emargination is present to a lesser degree in other specimens of *Leptorhynchos elegans* (TMP 1993.036.0181; TMP 1996.012.0141), but it may serve to distinguish *Leptorhynchos* from *Elmisaurus*. This feature is not present in TMP 1982.016.0006, probably because of post-mortem crushing. Posteriorly, between metatarsal III and IV, there is a rounded hole, which probably accommodated the *a. tarsalis plantaris*. The second slit between the second and third metatarsals, which are completely fused, cannot be seen, but it may have been situated more distally.

TMP 1996.012.0141—Another partial tarsometatarsus, TMP 1996.012.0141 (Fig. 3.60G–I) includes the distal tarsals III and IV and metatarsals II, III, IV. The distal tarsals are fused without visible sutures to metatarsals II, III and IV, and the posterodorsal process of distal tarsal IV is present but worn. Most of the shafts of metatarsals II and IV are preserved, as well as the distal condyles of each. Metatarsal II is fused to distal tarsal III and proximally to metatarsals III and IV, and there is a suture between metatarsals II and III. The shaft of metatarsal II has a well-developed and rugose posteromedial ridge, and a distinct facet for metatarsal III extends onto the anterior face of the shaft. The distal condyle is rounded and bulbous, and has a distinct lateral rugosity proximal to the distal condyle for *M. tibialis cranialis* with a medial rugosity opposite it.

The third metatarsal of TMP 1996.012.0141 is preserved only proximally, where it is appressed between metatarsals II and IV, to which it is fused (Fig. 3.60H). It is triangular in cross section, but the anterior wedge does not separate metatarsals II and IV anteriorly, as it does in *Elmisaurus rarus*. Metatarsal IV of TMP 1996.012.0141 is fused indistinguishably with metatarsals II and IV and distal tarsals III and IV at its proximal end. There is a strong anteromedial ridge on the shaft, and a well-developed posterolateral ridge. The shaft is teardrop-shaped in cross section as a result. The distal condyle is gnarled and rugose, with a prominent medial rugosity for *M. tibialis cranialis*.

UALVP 59606—This specimen (Fig. 3.64) is a complete left metatarsal IV and associated distal tarsal IV. The distal tarsal is wedge-shaped, tapering in dorsoventral thickness anteriorly (Fig. 3.64D). The distal tarsal is incompletely fused to the metatarsal and a gap can be seen around the entirety of the distal tarsal. The proximodorsal process is broken, so its size cannot be determined. Posterior to this process, there is a fossa in the distal tarsal that is continuous with a groove on the posterolateral surface of the proximal end of metatarsal IV (Fig. 3.64E). These features would have accommodated metatarsal V, which is fused in some other specimens of *Leptorhynchos elegans*. The medial edge of the distal tarsal is broken where it would have fused to distal tarsal III. This reveals that the internal trabeculae of the metatarsal and distal tarsal are continuous and fusion had begun internally.

Metatarsal IV is elongate and elliptical in cross-section. The proximal end is roughly semicircular in proximal view (Fig. 3.64E). Posteriorly, the proximal head has a mound that overhangs the shaft (Fig. 3.64B, C), similar to the posterior protuberance in *Elmisaurus rarus*. Proximally, the posterolateral edge of the metatarsal is attenuated into a ridge anterior to where metatarsal V would have attached. This ridge is continuous with the more distal posterolateral

ridge that contributes to the posterior concavity of the tarsometatarsus. Medially, the proximal head has two facets for articulation: the larger, more posterior one is for metatarsal III, whereas the other projects medially to contact metatarsal II anterior to metatarsal III. A small gap separates the triangular proximal facet for metatarsal III from the distally expanding contact for metatarsal III on the rest of the shaft. Presumably, this gap accommodated *a. tarsalis plantaris*, as in *Elmisaurus rarus* (Currie et al. 2016). Distally, the facet for metatarsal III invades the anterior surface of the shaft. Lateral to this, the anterior surface of the shaft has a ridge oriented proximomedial-distolateral. There is also a small ridge, oriented the same way, on the posterior surface of the shaft just proximal to the lateral condylar ridge. The distal condyle is bulbous and its main articular part is nearly spherical (Fig. 3.64F). On its lateral side, it flares into a triangular process behind the shallow lateral ligament pit. The medial ligament pit is deeper and teardrop-shaped, with its apex pointing dorsally. Just anterior to this pit, there is a small, rugose tubercle for *M. tibialis cranialis*. Posteriorly, the condylar ridges are separated by a shallow concavity.

Isolated *Leptorhynchos* Metatarsals—Six isolated metatarsal IIIs (Fig. 3.65) and one isolated metatarsal II attributable to *Leptorhynchos elegans* have been recovered from North America. The metatarsal IIIs (TMP 1984.163.0036, TMP 1986.036.0186, TMP 1993.036.0630, TMP 1996.005.0012, TMP 2005.049.0190 and UALVP 55585) all include the distal portions of the shafts. Invariably, the shaft is flat anteroposteriorly, and expands mediolaterally towards the distal end. The posterior surface has two cruciate ridges (medial and lateral), which are continuous with the lateral and medial postcondylar ridges (Fig. 3.61). In each case, the crossing of these ridges forms a chiasmata, which distinguishes them from the more poorly developed ridges of *Chirostenotes pergracilis*. Where the distal condyle is present, it is invariably thicker

anteroposteriorly than wide mediolaterally, a feature that distinguishes *Leptorhynchos elegans* from *Elmisaurus rarus* and *Chirostenotes pergracilis*.

One of these metatarsals, UALVP 55585 (Fig. 3.66), was thin-sectioned to determine its histological age. The specimen represents the distal portion of the shaft, which is anteriorly concave and has well-developed, paired cruciate ridges (Fig. 3.66). The minimum transverse shaft width is 11.4 mm, which is intermediate in size compared to other isolated elmisaurine third metatarsals.

The isolated metatarsal II (TMP 1988.036.0104) has several characters that distinguish it as *Leptorhynchos elegans*. Unfortunately only the distal half is preserved, so it is unclear if the proximal end was fused to the other metatarsals. The facet for metatarsal III invades the anterior face of the shaft and there is a distinct lateral rugosity for *M. tibialis cranialis*, both features absent in *Chirostenotes*. The distal shaft is deflected anteriorly, and there is a large, well-developed posteromedial ridge with a rugose apex. The strong development of the posteromedial ridge and the rugosity for *M. tibialis cranialis* are features that appear to be present only in *Elmisaurus rarus* and *Leptorhynchos elegans*, so they can be used to identify second metatarsals of these taxa.

Osteohistology

Mandibular Histology:

UALVP 55639—This specimen is almost completely secondarily remodeled (Fig. 3.67B, D, F, H), and the only primary bone is a thin band around the periphery of the jaw. Accordingly, the bone texture does not change between the four sections, although the shapes and sizes of the internal cavities do change. Osteocyte lacunar density ($46,666/mm^3$) is intermediate between

TMP 1985.043.0070 and TMP 1992.036.1237. Throughout most of the mandible secondary osteons are oriented anteroposteriorly, but in some regions, like the symphysis, they are oriented mediolaterally. Along the lateral portions of the mandible, especially towards the tip of the occlusal edge, osteons are oriented dorsoventrally, parallel to the lateral surface of the beak.

The internal cavities are more distinct and differ in arrangement from those of TMP 1985.043.0070 and TMP 1992.036.1237 (Fig. 3.67A, C, E, G). The major lateral cavity is relatively smaller than either of the other specimens, and is not united with the cavities closer to the midline (Fig. 3.67A, C, E, G). The dorsomedial cavity is larger and highly asymmetrical, as are the smaller midline cavities. Small trabeculae within cavities are absent, likely as a result of resorption during cavity expansion. The larger trabeculae that remain are composed entirely of secondary osteons of varying orientation or of multiple generations of endosteal lamellae (Fig. 3.68A). Many of these osteons are cross-cut by endosteal lamellae, which indicates that remodeling occurred before expansion of the cavities. Indeed, active zones of expansion are present along the ventral and lateral sides of the major lateral cavity, and osteons along this frontier have been eroded.

The lingual ridges are heavily remodeled, and in some areas as many as five generations of secondary osteons are present (Fig. 3.68C). In contrast to TMP 1992.036.1237, there are fewer, smaller cavities within the lingual ridge, each of which is surrounded by multiple generations of endosteal lamellae. The lateral occlusal ridge has been entirely remodeled, but there is some primary bone along the lateral surface of the beak (Fig. 3.68D). Like the primary bone elsewhere in the specimen, it is completely avascular and has prominent, well-developed Sharpey's fibers (Fig. 3.68A, B). These fiber bundles are particularly thick and extensive along the lateral surface of the mandible, where they are oriented ventrolaterally. Like in TMP

1992.036.1237, Sharpey's fibers along the lateral and medial sides of the lingual ridge are perpendicular to each other, and face dorsolaterally and dorsomedially, respectively.

Postcranial Histology:

UALVP 55585— The cortex of UALVP 55585 (Fig. 3.69) is extensively remodeled, which has obliterated most of the primary bone near the endosteal surface of the bone. However, some primary bone remains along the periosteal surface, especially on the anterolateral side. In this region, the primary bone is parallel-fibered and its vasculature is predominantly laminar in orientation. Medially and posteriorly to this area, the bone transitions to a fibrolamellar matrix with longitudinal vascular canals. Bone in these regions shows abundant Sharpey's fibers, and on the medial and posterior surfaces of the metatarsal, these are accompanied by large collagen bundles (Fig. 3.69E). On the lateral side of the metatarsal, there is a thin layer of primary woven-fibered bone on the periosteal surface (Fig. 3.69C). Vascular canals in this area are simple and longitudinally oriented. This bone indicates accelerated growth in this region, possibly in response to mechanical loads or interaction with the fourth metatarsal. Most of the inner cortex of UALVP 55585 is Haversian bone with well developed secondary osteons (Fig. 3.69F). These osteons appear to be from a single generation, because no cross-cutting can be detected. The secondary osteons are crosscut, however, by the endosteal lamellae (Fig. 3.69D), indicating that secondary remodeling began before expansion of the medullary cavity ceased. The endosteal lamellae are composed of multiple generations of avascular parallel-fibered bone, and they line the entirety of the medullary cavity. They are thickest medially and thinnest anterolaterally, where Howship's lacunae indicate they are being actively resorbed. This is possibly the result of new bone deposition on the periosteal surface of this area, resulting in cortical drift.

No lines of arrested growth can be detected in the primary bone, although this is likely

the result of extensive remodeling. This precludes determination of the exact age at death of this

individual. However, bone at the periosteal surface around most of the cortex, with the exception

of the region of new growth, is poorly vascularized and parallel-fibered, indicative of slow

growth. In these traits, the osteohistology of UALVP 55585 is similar to that of UALVP 55639,

where the cortex is entirely remodeled and the primary bone remaining is poorly vascularized

and parallel-fibered. In both specimens, endosteal lamellae are composed of several generations

of deposition and secondary osteons are well developed, showing multiple internal lamellae.

These lines of evidence suggest that UALVP 55585 was subject to considerable mechanical

stress, which resulted in heavy remodeling. The region of new bone growth on the anterolateral

surface of the metatarsal is unusual, and it is possible that this area represents some kind of

pathology, or that it is simply a reaction to interaction with metatarsal IV.

UALVP 59606—A broken segment of metatarsal IV was sectioned (Fig. 3.70), which

allowed the fragments to be repositioned to their original locations. The cortex is composed

predominantly of primary fibrolamellar bone (Fig. 3.70C, F), although there is a region of

concentrated secondary remodeling on the posterolateral side (Fig. 3.70F), and another smaller

region towards the endosteal surface of the anterior side. The medullary cavity is entirely lined

with endosteal lamellae, which are thicker towards the anterior side (Fig. 3.70E). In this area, the

endosteal lamellae are penetrated by simple vascular canals that communicate with the secondary

osteons just periosteal to the endosteal lamellae. This likely indicates that secondary this

secondary remodeling occurred after deposition of the endosteal lamellae. Throughout the

cortex, vasculature is oriented predominantly longitudinally (Fig. 3.70C), although this varies

and some areas have patches of reticular or even plexiform vasculature. Osteocyte lacunae are

uniformly dense throughout the cortex. At least six LAGs are preserved in the cortex (Fig. 3.70C, D). The innermost LAG is truncated by the endosteal lamellae, indicating that it was resorbed by expansion of the medullary cavity, and that some cortical drift occurred during growth. LAGs become more tightly packed towards the periosteal surface; this is most prominent between LAGs 1–2 and 2–3, where the latter growth interval is less than half the size of the previous one. At the periosteal surface, at least three LAGs are densely packed in a zone of avascular parallel-fibered bone, representing an external fundamental system (Fig. 3.70D).

Remarks

Three caenagnathid elements (Fig. 3.57), including a left and right ilium and an isolated last sacral vertebra, were recovered in 1981 from the same site, although they were not articulated. The ilia are identical to each other in size, morphology, and style of preservation, which suggests that they pertained to the same individual. The isolated last sacral vertebra is the correct size for the associated ilia, and is clearly from a caenagnathid. Accordingly, these specimens are best interpreted as representing the same individual, and together with the other material, provides valuable information about body size and morphology of *Leptorhynchos* (see Section 3.4.1 for details on their referral to this taxon).

Osteohistological sections of the mandibles and metatarsals of *Leptorhynchos elegans* show that this taxon had a small body size at maturity. The mandibles (UALVP 55639) are heavily remodeled and the remaining primary bone is low in vascularity, indicating slow growth. Although there is no EFS present, it is likely that this individual had more or less ceased growth, and was close to maximum body size. Despite their histological maturity, these mandibles are considerably smaller than those of *Caenagnathus collinsi* and *Chirostenotes pergracilis*. This

213

suggests that *Leptorhynchos elegans* had a smaller body size at maturity than the former two taxa. The metatarsals (UALVP 59606 and UALVP 55585) support this assertion. The stark decrease in LAG spacing in the cortex of UALVP 59606 indicates a decreasing growth rate, and the closely packed LAGs at the periosteal surface are consistent with an EFS, suggesting cessation of growth. Accordingly, this individual can be interpreted as a mature adult. However, the clean surfaces for metatarsals II and III show that the tarsometatarsus of this individual had not yet fused. This may indicate that fusion of the tarsometatarsus is more variable than currently recognized, or that it is more strongly tied to size and body mass than to maturity. The metatarsal III (UALVP 55585) has an unusual combination of histological features. The endosteal portion of the cortex is heavily remodeled, but there are no growth marks and the periosteal surface shows indications of slow but continuous growth. Although this was initially interpreted as indicating subadult age (Funston et al., 2016a), it is more likely that this is a juvenile which had nonetheless experienced significant mechanical loads on the foot, resulting in secondary remodeling.

The new material shows that the hindlimb of *Leptorhynchos elegans* is significantly different from those of *Caenagnathus collinsi* and *Chirostenotes pergracilis*. Whereas the ilium of *Chirostenotes pergracilis* is dorsoventrally tall, that of *Leptorhynchos elegans* is shorter above the acetabulum and much thicker transversely (Fig. 3.57). This gives it a more robust appearance overall, despite smaller size. This is also reflected in the muscular attachments, and the attachment site for *M. flexor tibialis externus* is much more rugose and defined than that of *Chirostenotes pergracilis*. Few comparisons can be made with the ilium of *Caenagnathus collinsi*, but the ischiadic peduncle of *Leptorhynchos elegans* is neither laterally exposed nor ventrally expanding. The tibia is relatively similar to that of *Chirostenotes pergracilis* and

Elmisaurus rarus, but is slightly more elongate for its distal width. However, this may be a result of negative allometry, rather than a meaningful difference. The tarsometatarsus is intermediate in morphology between *Chirostenotes pergracilis* and *Elmisaurus rarus*: whereas it is fused proximally (Fig. 3.60), it is not a robust nor as coossified as that of *Elmisaurus rarus*. Advanced histological maturity in UALVP 59606 suggests that fusion of the distal tarsals to the metatarsals indicates skeletal maturity, and that it precedes coossification of the metatarsals to each other. In this case, fused tarsometatarsi (TMP 1982.016.0006; TMP 1982.039.0004; TMP 1996.012.0141) can be considered to represent adult individuals, further supporting previous arguments of small body size in adult *Leptorhynchos elegans*.

3.3.5 *Apatoraptor pennatus* Funston and Currie 2016

Apatoraptor Funston and Currie 2016

Apatoraptor pennatus Funston and Currie 2016

Figs. 3.72–3.85

Holotype: TMP 1993.051.0001, articulated partial skeleton (Fig. 3.72) with right palatine, nearly complete left and fragmentary right mandibles, left and fragmentary right ceratobranchials, axis and complete post-axial cervical series, complete dorsal series, partial left and complete right pectoral girdle, right sternal plate, right forelimb, partial right ilium, partial right femur, partial right tibia, and partial right fibula.

Horizon and locality: Horsethief Member (just above coal 7) of the Horseshoe Canyon Formation (Eberth and Braman, 2012), recovered 3km west of the Royal Tyrrell Museum of Palaeontology (Fig 3.73; UTM 12U 374600, 5705950).

Etymology: *Apate-* , goddess of deception; *-raptor*, thief; *pennatus*, feathered.

Diagnosis: Small caenagnathid theropod diagnosed by the following autapomorphies: ventral flange of angular underlying posteroventral ramus of the dentary; anterior constriction of external mandibular fenestra by posteroventral ramus of the dentary; medial fossa anterior to articular region of mandible; articular region of mandible with low articular ridge offset from dorsal margin of articular-surangular-coronoid complex; metacarpal I less than half as long as metacarpal II; manual I-1 longest phalanx of hand; manual phalanx II-1 longer than II-2.

Also distinguished by the unique combination of the following characters: thin retroarticular process of mandible oriented posterolaterally; cervical vertebrae with infradiapophyseal fossae in addition to infrapre- and infrapostzygapophyseal fossae; fusion of

cervical ribs to vertebrae; fingerlike uncinate processes on dorsal ribs; glenoid of scapulocoracoid directed laterally; enlarged coracoid with relatively straight posteroventral process; manual ungual I-2 lacking transverse groove between proximal articular surface and flexor tubercle; anterior margin of preacetabular portion of ilium rounded; and tibia with expanded cnemial crest.

Description

Cranial Skeleton:

　　Palatine—A right palatine (Fig. 3.74) was revealed by CT scans, situated below the ceratobranchial and medial to the mandible. The palatine fragment is a quadrangular plate of bone about 25 mm long, with a long anterior process that contacted the maxilla and a long posterior pterygoid process. The bone is overall similar in shape to that of *Epichirostenotes curriei* (Sues, 1997), although the vomerine process is longer and the anteromedial process is less offset from the body of the palatine.

　　Dentary—The left mandible (Fig. 3.75) is approximately 165 mm long (Table 3.1), and is preserved with the ventral and lateral sides exposed. The left dentary is relatively long and shallow, and the lateral surface has a deep mandibular fossa perforated by a pneumatopore. The posterodorsal ramus of the dentary contacts the articular-surangular-coronoid complex in an interlocking dentary-surangular suture. In *Apatoraptor pennatus* the dentary-surangular suture (Fig. 3.74C) does not extend posteriorly to the coronoid process, whereas it does in *Anzu wyliei* (CM 78000), *Caenagnathus collinsi* (CMN 8776), and *Chirostenotes pergracilis* (TMP 2001.012.0012). The posteroventral ramus of the dentary contacts the angular and forms the ventral border of the external mandibular fenestra.

Angular—The angular is medial to the posteroventral ramus of the dentary, but it has a ventral flange underlying the posteroventral ramus of the dentary (Fig. 3.75). This ventral flange is unique to *Apatoraptor pennatus*. Together, the angular and dentary bow ventrally beneath the external mandibular fenestra, similar to *Anzu wyliei* (CM 78000) and *Chirostenotes pergracilis* (TMP 2001.012.0012), but unlike *Caenagnathus collinsi* (CMN 8776).

Prearticular—The prearticular (Fig. 3.74C) is a thin plate-like bone medial to the angular and can be seen in CT scans. It becomes transversely thick posteriorly where it meets the articular and forms the medial part of the retroarticular process.

Articular-Surangular-Coronoid (ASC) Complex—The ASC complex is fused without a suture, as in other caenagnathids (Currie et al. 1993). There is a lateral flange on the surangular at the dorsal margin of the external mandibular fenestra, which extends from the coronoid process posteriorly to the end of the external mandibular fenestra. CT scans show that where the ASC complex meets the angular just anterior to the articular region, there is a deep fossa on the medial surface of the mandible (Fig. 3.74C). The articular region was revealed by CT scans (Fig. 3.75C). There is a convex articular ridge, as in all caenagnathids, and well-developed medial and lateral glenoids. The articular ridge is not as well developed as in *Chirostenotes pergracilis* (TMP 2001.012.0012) and is more similar to that of *Caenagnathus collinsi*; however, it is more offset from the dorsal margin of the surangular than it is in the latter genus. The retroarticular process is formed of the articular laterally and the prearticular medially. It is directed posterolaterally and has a narrow hatchet-shaped distal end in dorsal view. The external mandibular fenestra is anteroposteriorly elongate (51 mm), as in other caenagnathids, but it is constricted anteriorly by the posteroventral ramus of the dentary.

Hyoid—The left ceratobranchial of the hyoid apparatus (Fig. 3.75A,B) is thin and rodlike, with slightly expanded anterior and posterior ends. It is 68.4 mm long, roughly 41% the length of the mandible; the maximum shaft diameter (2.0 mm) is 3% of its length. Parts of the hyoid apparatus have been previously reported in three oviraptorosaurs: *Caudipteryx zoui* Qiang et al. 1998 (Qiang et al., 1998), *Citipati osmolskae* Clark et al. 2001 (Clark et al., 2002a), and *Khaan mckennai* (Balanoff and Norell, 2012). In *Caudipteryx zoui* and *Khaan mckennai*, the ceratobranchial is straight, but in *Citipati osmolskae* it bows laterally. The ceratobranchial (Appendix 1) of TMP 1993.051.0001 is straight, but appears to be relatively longer (41%) compared to the mandible than in *Caudipteryx zoui* (~20%), and more gracile compared to its length than in *Khaan mckennai*, where the ceratobranchial is more robust and has a more pronounced anterior expansion. There are no muscle scars on the ceratobranchial of TMP 1993.051.0001, so no inferences about the strength of the lingual apparatus can be made.

Axial Skeleton:

Vertebrae—There would have been 13 cervical vertebrae in life (Figs. 3.72, 3.76), but only 11 are well preserved. These include all of the postaxial cervical vertebrae and the posterior end of the axis, but not the atlas. This count excludes the cervicodorsal vertebrae, of which only two are present, contrasting with the condition in most other oviraptorosaurs. The neck is 680 mm long and the longest centrum in the neck is the tenth cervical, which is 61.5 mm long. The centra of the anterior cervical vertebrae are elongate, but the aspect ratio (length: height) decreases posteriorly. On the lateral side of the centrum, there is a pneumatic depression. The cervical ribs obscure the anterolateral parts of the centra, but CT scans reveal the presence of the pleurocoels described by Sues (1997) and Lamanna et al. (2014). Unlike *Caenagnathasia*

martinsoni (Sues and Averianov 2015), there are no pleurocoels on the lateral surfaces of the centra posterior to the parapophyses. As in *Epichirostenotes curriei* (Sues, 1997), the parapophyses extend anteroventrally, and a lateral ridge extends on the ventral surface of the centrum posteriorly from each parapophysis. The articular surfaces of the anterior cervical vertebrae face anteroventrally. Posterior cervical vertebrae have anterior articular surfaces that are perpendicular to the longitudinal axis of each vertebra. The neurocentral sutures are closed, as in *Epichirostenotes curriei*, suggesting that both specimens represent relatively mature individuals (Brochu, 1996; Sues, 1997). There are three pneumatic fossae delimited by the laminae of the neural arches: infraprezygapophyseal, infrapostzygapophyseal, and infradiapophyseal (Fig. 3.76C). An infradiapophyseal fossa is not present in ROM 43250, but is present in *Elmisaurus rarus* from Mongolia (Currie et al., 2016). The infraprezygapophyseal fossa is deep in TMP 1993.051.0001, unlike ROM 43250. The transverse processes of the anterior cervical vertebrae are small, in contrast to the large wing-like transverse processes of ROM 43250. The neural spines are low and anteroposteriorly elongate, as in most oviraptorosaurs. Starting with the third or fourth postaxial vertebra, the posterior cervical ribs are fused to the centra as in *Anzu wyliei* (Lamanna et al. 2014), *Avimimus portentosus* (Kurzanov, 1981a) and *Khaan mckennai* (Balanoff and Norell, 2012), but unlike ROM 43250 (Sues, 1997).

There are nine dorsal vertebrae, including the cervicodorsal vertebrae (Figs. 3.72, 3.77). The first cervicodorsal vertebra is visible without CT scans; it has a reduced rib and a prominent hypapohysis. Unlike *Anzu wyliei*, the hypapophysis are triangular in lateral view, not rounded. The transverse process and the neural spine of the first cervicodorsal vertebra are triangular in lateral view and the neural spine is dorsoventrally tall. The infraprezygapophyseal fossa is deep. The neural spines of the posterior vertebrae are quadrangular in shape, and become progressively

taller posteriorly. Reexamination of CT scans (Fig. 3.77) show the dorsal vertebrae and the left ribs, although contrast is poor. The anterior two dorsal vertabrae have prominent hypapophyses, but the third dorsal vertebra appears to lack a hypapophysis. The centra of the dorsal vertebrae are barrel-shaped, as in other oviraptorosaurs, and each bears a large lateral pleurocoel. The neurocentral sutures appear to be unfused, but this could be due to breakage or lower density in the suture than the surrounding bone. The neural arches each have infradiapophyseal, infrapostzygapophyseal, and infraprezygapophyseal fossae. The neural spines are relatively tall and square in lateral view. In the anterior vertebrae they project slightly posteriorly, but in the more posterior vertebrae they are more vertical.

Ribs—There are nine dorsal ribs per side (Fig. 3.72) and at least three sets of sternal ribs. There is a foramen piercing the lamina that connects the capitulum and tuberculum in each rib, suggesting that the ribs are pneumatized. On dorsal ribs five, six, and seven there are fingerlike uncinate processes (Fig. 3.72) that are attached but not fused to the posterior surfaces of the rib shafts. CT scans (Fig. 3.77) show the presence of uncinate processes on the left side of the body as well, associated with ribs. These uncinate processes are slightly wider at the base, curve dorsally, and taper to points distally. Uncinate processes have been reported in *Caudipteryx* (Zhou et al., 2000) and *Citipati* (Clark et al., 1999; Norell et al., 2018), where they are wide and plate-like proximally, and taper distally into rounded ends. The uncinate processes of *Apatoraptor pennatus* are unlike those of *Caudipteryx* and *Citipati* and more similar in shape to those of *Velociraptor mongoliensis* (Norell and Makovicky, 1999). Unusually, on both sides, a long, rod-like bone extends posterodorsally from the second dorsal rib and overlies the third dorsal rib (Fig. 3.72). Although it is possible that they are dislodged sternal ribs, it is more likely that it is an elongate, poorly ossified uncinate process.

Appendicular Skeleton:

    Pectoral Girdle—The coracoid (Fig. 3.78) of *Apatoraptor pennatus* is relatively and

absolutely larger (96 mm across the widest breadth) than that of *Chirostenotes pergracilis* (66

mm), despite the similarly sized manus. The manus of TMP 1993.051.0001 and TMP

1979.020.0001 are close in length, based on the length of digit II excluding the metacarpal (203

mm vs. 213 mm, respectively). The posteroventral process of the coracoid is large, and its

posterior margin is strongly concave, but it is straighter than that of *Chirostenotes pergracilis*.

The coracoid tubercle is relatively closer to the glenoid in *Apatoraptor pennatus* than in

Chirostenotes pergracilis, which would shorten the lever arm for adduction of the humerus. The

glenoid faces laterally, as in *Elmisaurus rarus*, rather than posteroventrally as in most theropods.

The two bones of the scapulocoracoid are unfused but tightly sutured. The right scapula (Fig.

3.78) is long (215 mm in a straight line to the glenoid) and strap-like (22 mm midshaft diameter),

without a pronounced distal expansion. The acromion process is directed dorsolaterally but

mostly obscured by matrix.

    The right sternal plate (Fig. 3.79) is smooth and unornamented, and there is no sternal

keel. It cannot be determined whether the left and right sternal plates diverge posteriorly as in

Khaan mckennai (Balanoff and Norell, 2012). The sternal plate is quadrangular and 112 mm

long anteroposteriorly. The anterior margin has a shallow coracoid sulcus that is exposed

because it is disarticulated from the coracoid. The sternocoracoidal process is rounded and

bulbous, and a hole penetrating the sternocoracoidal process may be a vascular foramen. The

lateral trabecula is broken; it appears to be triangular and narrower mediolaterally than the

sternocoracoidal process. The posterolateral region of the right sternal plate lacks the foramen described by Lamanna et al. (2014) in *Anzu wyliei*.

Humerus—The head of the humerus (Fig. 3.80) is rectangular, and has a poorly developed articulation similar to those of *Anzu wyliei* (Lamanna et al. 2014) and *Khaan mckennai* (Balanoff and Norell, 2012). The deltopectoral crest is large, but the shape of its apex cannot be determined because it is broken. In *Anzu wyliei* (Lamanna et al., 2014) and *Gigantoraptor erlianensis* (Xu et al., 2007), the apex of each deltopectoral crest is rounded, whereas in derived oviraptorids the apices are pointed (Balanoff and Norell, 2012). The deltopectoral crest is 56 mm long proximodistally, 27% of the length of the humerus (206 mm), and occupies more than one-third the length of the humeral shaft. This is similar to *Falcarius utahensis* Kirkland et al. 2005 and *Khaan mckennai*, in which the deltopectoral crest is expanded to one-third the length of the humerus. In therizinosaurs, expansion of the deltopectoral crest compared to basal coelurosaurs is tied to greater tensile loads in adduction of the arm (Zanno, 2006). As in other maniraptorans, the humerus twists midshaft, and as in *Anzu wyliei* (Lamanna et al. 2014), the humerus bows laterally. CT scans (Fig. 3.81) revealed the left humerus preserved underneath the body, but it provides little additional information.

Ulna and Radius—Near the proximal end, the shaft of the ulna (Fig. 3.80) is straight, but distally it bows posteriorly for most of its length (167 mm). The olecranon and coronoid processes are weakly developed and form a shallow trochlear notch for the humerus. CT scanning revealed seven small, evenly spaced depressions on the posterolateral surface of the ulna (Fig. 3.80C). The position and size of these depressions is consistent with ulnar papillae (quill marks) in *Velociraptor mongoliensis* (Turner et al., 2007), *Ornithomimus edmontonicus* Sternberg 1933 (Zelenitsky et al., 2012), *Conchavenator corcovatus* Ortega et al. 2010 (Ortega et

al., 2010), and the modern Great Blue Heron, *Ardea herodius* Linnaeus 1758 (UAMZ B6969).

On the exposed (flexor) side of the ulna there are four small, donut-shaped depressions that are

likely ulnar papillae from the anconal series (sensu Edington and Miller 1942). The depressed

donut shape of these marks is nearly identical to those described in the male White Stork

(*Ciconia alba* Linnaeus 1758) by Edington and Miller (1942). Based on the spacing between the

ulnar papillae (5 mm) in *Apatoraptor* and the proportion of the ulna occupied by secondary

feathers in modern birds, there would be room for about 16-18 secondaries in *Apatoraptor*. This

is consistent with its relatively large size, and the presence of a similar number in modern birds

with similarly sized ulnae. Based on ulnar measurements from Wang et al. (2011), these include:

Bubo scandiacus (Linnaeus 1758)*, with a 169 mm ulna and 16 secondaries (Solheim, 2012);

Ardea purpurea (Linnaeus 1766) with a 159 mm ulna and 16 secondaries (GF pers. obs.); *Bubo

bubo* Linnaeus 1758 with a 183 mm ulna and 15-16 secondaries (Solheim, 2011); *Branta

canadensis* (Linnaeus 1758) with a 161 mm ulna and 16 secondaries (GF pers. obs.); and *Larus

marinus* Linnaeus 1758 with a 170 mm ulna and 24 secondaries (Ingolfsson, 1970).

The radius (Fig. 3.80) is straighter than the ulna, but has a slight anterior curve at its

midpoint. The proximal end of the radius is square in outline, and the distal end is expanded,

with a large medial flange for the ulnar notch, a small styloid process, and a concave facet for the

carpals. The radius is narrower in diameter than the ulna but is equal to it in length.

Carpals and Manus—The preservation of the carpal region (Fig. 3.82) is poor, and

neither of the two potential carpals can be positively identified. There may be a semilunate carpal

overlying the proximal ends of the first and second metacarpals. There may also be a radiale, but

this could be the compressed proximal end of metacarpal I. In *Hagryphus giganteus* Zanno and

Sampson 2005 (Zanno and Sampson, 2005), four carpals are preserved—the semilunate, radiale,

and two smaller carpals (likely homologous with the intermedium and ulnare). It is likely that *Apatoraptor pennatus* possessed all four of these carpals in life, but they have not been preserved.

All of the phalanges of the manus (Fig. 3.82), except ungual III-4, are preserved to some degree. Digit II (metacarpal II plus phalanges II-1, II-2 and II-3) is the longest digit, and digit III is longer than digit I, as in other caenagnathids (Fig. 3.82C). The second metacarpal is the longest (105 mm) and most robust of the three, and metacarpal III (75 mm) is longer than metacarpal I (52 mm), but more gracile (Appendix 1). Unlike the condition in other caenagnathids, metacarpal I is less than half the length of metacarpal II. Digits I and II are complete, including unguals, but digit III is missing most of phalanx III-1, and the ungual (III-4). The phalanges are elongate and gracile, as in all caenagnathids, and the unguals are long and sharply curved. Phalanx I-1 is the longest phalanx of the hand (82.4 mm), and bows dorsally midshaft. This is unlike all other caenagnathids, in which phalanx I-1 is shorter than or subequal to phalanx II-1. Phalanx I-2 has a pronounced flexor tubercle and proximodorsal lip, both characteristics of caenagnathids. Phalanx I-2 measures 39 mm in a straight line from the middle of the proximal articular surface to the tip, and 47 mm around the outside curve. This ungual is similar in shape to those of *Elmisaurus rarus* (Osmólska, 1981; Currie et al., 2016), although it is shorter proximodistally, and lacks the transverse groove between the articular surface and the flexor tubercle, which is also present in large unguals from the Frenchman Formation (Bell et al., 2015). Phalanx II-1 is the longest of the second digit (77.7 mm), as opposed to *Chirostenotes pergracilis* (CMN 2367, TMP 1979.020.0001), in which II-2 is noticeably longer than both I-1 and II-1 (Gilmore, 1924; Currie and Russell, 1988). In *Elmisaurus rarus* and *Hagryphus giganteus*, manual phalanges II-1 and II-2 are subequal in length, and in oviraptorids II-1 tends

to be longer than II-2. Phalanx II-2 (72.4 mm) has a straight dorsal margin, unlike *Chirostenotes pergracilis* (CMN 2367, TMP 1979.020.0001), where the distal condyle extends dorsally. The ungual, II-3, is much longer proximodistally (57 mm) than I-2, but is less strongly curved (65.5 mm around the outside curve). There is a well-developed proximodorsal lip, but the flexor tubercle is not as pronounced as in I-2. Most of phalanx III-1 is missing, but its distal end is preserved near the proximal end of III-2. Phalanx III-2 is complete, and much smaller than phalanges of the other digits (32 mm in length). Phalanx III-3 is at least as long as III-2, but the distal end is absent. Ungual III-4 is not present, but in other caenagnathids this ungual is similar in morphology to I-2 but smaller (Gilmore, 1924; Currie and Russell, 1988).

Ilium—Only the preacetabular blade of the ilium (Fig. 3.72) is preserved. The anterior edge of the preacetabular blade is dorsoventrally tall, smooth, and rounded. The anteroventral portion of the preacetabular blade has been broken so that it lies below the lateral surface of the ilium. This suggests that there was at least a shallow cuppedicus fossa, as in *Nomingia gobiensis* (Barsbold et al., 2000a, 2000b). From the location of the break, it is clear that the anteroventral portion of the preacetabular blade extended ventrally past the cuppedicus fossa, and was possibly level with the pubic peduncle. The shape of the anteroventral process of the preacetabular blade cannot be determined, but in *Anzu wyliei* (Lamanna et al., 2014) and probably *Chirostenotes pergracilis* (Currie and Russell, 1988), the anterior margin of the preacetabular blade is straight. This is also true for *Khaan mckennai* (Balanoff and Norell, 2012); however, the unnamed Guriliin Tsav oviraptorid (MPC-D 102/11, MPC-D 102/12) and *Nomingia gobiensis* (Barsbold et al. 2000a, 2000b) have downturned, rounded preacetabular blades.

Femur—The exposed portion of the right femur (Fig. 3.83) is 220 mm long, with an anteroposterior midshaft diameter of 31.8 mm, although this has likely been increased by

crushing. Using other oviraptorosaurs for comparison, femoral length can be estimated based on humerus length and femoral midshaft diameter. In both cases, these produce estimates of 345 mm in TMP 1993.051.0001. *Chirostenotes pergracilis* (TMP 1979.020.0001) has a complete femur 304 mm long, relatively shorter than *Apatoraptor pennatus*, despite similarly sized manus. A v-shaped ridge on the posterolateral surface of the shaft of the femur in TMP 1993.051.0001 represents the insertion of *M. caudofemoralis*. The shaft of the femur gently bows anteriorly and laterally, although this latter feature may be the result of taphonomy. There is no fourth trochanter on the femur, like in most oviraptorosaurs except *Avimimus* and *Caenagnathasia*. Using the anteroposterior dimensions of the crushed right femur, femoral circumference was estimated at 107 mm. However, direct measurement from the CT scans indicate that femoral circumference was more likely about 98 mm.

Tibia and Fibula—The tibia (Fig. 3.83) has an anteriorly enlarged anterior cnemial crest for anchoring the *quadriceps femoralis*, like in *Anzu wyliei* (Lamanna et al., 2014) and *Elmisaurus rarus* (Currie et al., 2016). In both of those taxa, the tibia is elongate, suggesting that most caenagnathids were relatively fast runners. The cnemial crest of *Apatoraptor pennatus* extends at least 35 mm anterior to the fibular condyle, more than that of *Elmisaurus rarus* (25 mm–MPC-D 102/7), despite being similar in size.

The exposed portion of the fibula (Fig. 3.83) is 54 mm long proximodistally, and covers the lateral surface of the tibia. At its proximal end, the fibula is 45.7 mm wide anteroposteriorly, and it tapers distally to 21.2 mm wide. The presence of a medial fossa, present in other caenagnathids (but not oviraptorids), cannot be determined without disarticulating the specimen, but the convex lateral surface of the proximal end is consistent with a medial fossa.

Remarks

Comparison to other caenagnathid taxa:

Epichirostenotes curriei—The close temporal and geographic proximity of *Apatoraptor* and *Epichirostenotes* obligates a comparison of the two taxa. Despite relatively little overlapping material between ROM 43250 and TMP 1993.051.0001, some important observations can be made. Comparison of the preserved cervical vertebrae of ROM 43250 to the complete axial series of TMP 1993.051.0001 allows their positions to be determined. The anteriormost cervical of ROM 43250 is distinguished by greatly enlarged posterolaterally directed lateral processes, and an anteroposteriorly short centrum with inclined articular faces. The neural spine is a short triangular process that does not extend as far dorsally as the prezygapophyses, which are large, fingerlike, and directed anterodorsally. The postzygapophyses are small and their articular facets are nearly vertical. The centrum has a sigmoidal ventral margin, and is pierced by a single pneumatic foramen just ventral to the large transverse process on the left side. The cervical ribs of this vertebra are reduced and fused to the centrum and transverse processes, producing a single wing-like lateral process on either side of the vertebra. Based on its size relative to the other cervical vertebrae and the short, sigmoidal centrum, it is likely that this vertebra represents the anteriormost postaxial cervical vertebra (C3). Two other preserved cervical vertebrae of ROM 43250 are less distinctive, and it is therefore more difficult to determine their exact positions. Based on the height to length ratio of the centra, they appear to represent postaxial cervical vertebrae four and five (i.e. C6 and C7). This is supported by the large, wide transverse processes that descend close to the parapophyses, the low neural spines, and the flat ventral margins. The presence of laminae connecting the transverse processes to the postzygapophyses—absent in the posterior cervical vertebrae of *Apatoraptor pennatus* but

present anterior vertebrae of *Chirostenotes pergracilis* (UALVP 59400)—is also evidence that these vertebrae are from the anterior part of the neck. The largest and best preserved cervical vertebra of ROM 43250 is probably more posterior than the other vertebrae, as noted by Sues (1997). It is likely the sixth postaxial vertebra (C8), but could be from further posterior. Its proximity in size (85mm ventral length) compared to C7 (81mm in ventral length) suggests that the two vertebrae are either consecutive in the cervical series or separated by only a single vertebra.

With the approximate positions of the cervical vertebrae in ROM 43250, better comparisons can be drawn between *Apatoraptor pennatus* and *Epichirostenotes curriei*. The first postaxial vertebra of *Apatoraptor* has unfused cervical ribs, as do most oviraptorosaurs, and lacks the wing-like transverse processes of *Epichirostenotes*. The laminae connecting the neural spine to the transverse processes of C6 and C7 are not as well developed in *Apatoraptor* as in *Epichirostenotes*, especially in their posterior extent. The sixth cervical of *Epichirostenotes* has a lamina that connects the transverse process to the postzygapophysis, which appears to be absent in *Apatoraptor*. In ventral view, the parapophyses of *Apatoraptor,* especially on C6 and C7, extend much further anteriorly and are separated by a deeper depression than in *Epichirostenotes*. The ambiguous C8 of *Epichirostenotes* has a much more dorsally displaced transverse process, indicating that the cervical rib in this position has a larger dorsal process than in *Apatoraptor*. Alternatively, this could be evidence that this cervical is in fact from further posterior. In any case, the lack of infradiapophyseal fossae on this vertebra distinguishes it from *Apatoraptor*, in which all vertebrae posterior to C4 have infradiapophyseal fossae.

Comparisons can also be drawn between the ribs of *Apatoraptor pennatus* and *Epichirostenotes curriei*. In *Apatoraptor*, the tubercula of the ribs decrease in size posteriorly, as

does the degree of proximal expansion of the shaft. The preserved dorsal rib of *Epichirostenotes* has a large tuberculum and a proximally expanded shaft, which indicates, as suggested by Sues (1997), that it comes from the mid-dorsum. In *Apatoraptor*, all but the posterior three ribs have a lamina of bone that connects the tuberculum to the capitulum, and encloses a pneumatic opening. Both the opening and the lamina appear to be absent in *Epichirostenotes*, as are the uncinate processes that mark the ribs of *Apatoraptor pennatus*. However, with only a single complete rib preserved from *Epichirostenotes*, the absence of these structures is uncertain.

Based on the lengths of the seventh cervical vertebrae of ROM 43250 (81 mm) and TMP 1993.051.0001 (53.2 mm), *Epichirostenotes* would have been 52% larger than *Apatoraptor*. Both specimens have closed neurocentral sutures in the cervical vertebrae, which tentatively indicates that they represent relatively mature individuals (Brochu, 1996). The obliteration of sutures in the braincase in ROM 43250 and the fusion of cervical ribs to the centra in TMP 1993.051.0001 support this assertion.

Other caenagnathids—*Apatoraptor pennatus* has several features that distinguish it from all other known caenagnathid species. The angular has a ventral flange that underlies the posteroventral ramus of the dentary, which, itself, constricts the external mandibular fenestra anteriorly. The dentary-surangular suture does not extend posteriorly to the coronoid process, which is unlike all other known mandibles. *Apatoraptor* differs from *Anzu* in several features of the postcranium. *Apatoraptor* lacks the foramen that pierces the posterolateral region of the sternum in *Anzu*, and also lacks the fusion between the scapula and the coracoid. Phalanx II-2 of *Apatoraptor* lacks the distinctive ventral groove of *Anzu*, and the unguals of *Apatoraptor* do not have a transverse groove between the flexor tubercle and the articular surface. In *Apatoraptor pennatus*, manual phalanx II-2 is distinctly shorter in length than I-1 and II-1, which contrasts

with *Chirostenotes pergracilis*, and phalanx I-1 is the longest of the hand, unlike all other caenagnathids. *Apatoraptor pennatus* is similar to *Elmisaurus rarus* in the presence of the infradiapophyseal fossa in the cervical vertebrae, the lateral orientation of the glenoid of the scapulocoracoid, and the expanded cnemial crest of the tibia. Elliptical regression estimate (ELLR-anteroposterior) of femoral circumference from Bradley et al. (2015) based on the anteroposterior diameter of the right femur produces a circumference estimate of 107.1 mm for the femur of *Apatoraptor*. Using this estimate and the technique of Campione et al. (2014), where $\log_{10}BM_{biped} = 2.754$ x $\log_{10}(C_{femur}) - 0.683$, the body mass of *Apatoraptor pennatus* (Table 3.2) would have been 80.8 kg (lower limit: 60.6 kg; upper limit: 101.0 kg). However, the right femur is transversely crushed, which may have artificially increased its anteroposterior diameter. Using the measured circumference from the CT scans of the right femur (98 mm), the body mass of *Apatoraptor pennatus* would have been 63.2 kg (lower limit: 47.4 kg; upper limit: 79.0 kg). These are considerably different results, but it is likely that the lower estimate (63.2 kg) is more accurate, as this is similar to estimates of similar sized oviraptorids for which undistorted femora are known.

Mandibular morphology—The mandible of TMP 1993.051.0001 is incomplete anteriorly, but has several features that allow inference of the shape of the beak. Comparison to *Anzu wyliei*, *Caenagnathus collinsi*, *Chirostenotes pergracilis*, and *Leptorhynchos elegans* (Longrich et al. 2013), all of which have relatively complete mandibles, reveals a suite of characters that suggest a 'deep-beaked' morphology for *Apatoraptor pennatus*. The dentaries of *Apatoraptor* (Fig. 3.75), *Chirostenotes*, and *Leptorhynchos* all have deep mandibular fossae on their lateral sides, in contrast to the shallow mandibular fossae of *Anzu* and *Caenagnathus*. Similarly, the mandibles of *Apatoraptor* and *Chirostenotes* have only one apex on the dorsal

margin of the mandible (Fig. 3.75, cor), whereas *Anzu* and *Caenagnathus* have two: one anterior to the external mandibular fenestra, and one directly above the midpoint of the external mandibular fenestra. The articular ridge of *Apatoraptor* is low compared to *Chirostenotes*, but is well offset from the dorsal margin of the surangular, contrasting with both *Anzu* and *Caenagnathus*, in which the articular ridge is confluent with the surangular. Other features better developed in *Apatoraptor* and *Chirostenotes* than in *Anzu* and *Caenagnathus*—like a well-developed lateral surangular flange, and the strong ventral bow of the angular and dentary below the external mandibular fenestra—support this interpretation.

Paleobiological Implications of *Apatoraptor pennatus*:

     Ulnar papillae— In modern birds, the presence of ulnar papillae is highly variable, and does not appear to be tied to flight style or performance (Hieronymus 2015). Ulnar papillae are produced by an exostosis at the attachment site of the follicular ligament to the ulna, and their relative development is linked to feather musculature (Edington and Miller 1942). In modern birds, feather movement is controlled by networks of integumentary muscles and ligaments, the complexity and size of which reflect feather function (Stettenheim 2000). These muscles and ligaments work in tandem with hydrostatic pressure (Homberger and de Silva 2000). Feather arrector muscles contract to raise the feathers and upon relaxation, subcutaneous fat and the elasticity of the skin move the calamus back into resting position (Homberger and de Silva 2000). The secondaries of modern birds are muscularized by two main muscles, the *flexor sublimis digitorum* and the *flexor carpi ulnarum*, which connect to a network of follicular ligaments (Lowe 1942). The morphology of ulnar papillae in the pennibrachia of feathered

theropods, therefore, is probably linked to the development of these muscles or their homologues.

Though well-preserved ulnae are known from many oviraptorid taxa (e.g. *Citipati*, *Conchoraptor* Barsbold 1986, *Heyuannia* Barsbold (1981), and *Khaan*), none shows any trace of ulnar papillae. The presence of complex branched feathers and a pennibrachium in basal oviraptorosaurs like *Caudipteryx*, however, suggests that pennibrachia were present throughout oviraptorosaurs. The presence of ulnar papillae in *Apatoraptor*, therefore, likely reflects a relative increase in the development of feather arrector musculature in *Apatoraptor*, rather than a lack of pennibrachia in oviraptorids. Multiple oviraptorid skeletons have been found in brooding posture (Dong and Currie 1996; Clark et al. 1999; Hopp and Orson 2004; Fanti et al. 2012), with their arms over their nests. The position of the arms in these specimens is congruent with the use of remiges for insulation or protection of the eggs (Hopp and Orson 2004). The consistent lack of ulnar papillae on oviraptorids, despite excellent preservation, suggests that brooding behaviour was not impeded by relatively poorly developed feather arrector musculature. Ulnar papillae, therefore, are unlikely to reflect an adaptation for brooding behaviour, though it is likely that *Apatoraptor* did engage in brooding behaviour. Pennibrachia are unlikely to contribute significantly to insulation, or to have aided with foraging. Even if either case were true, it is difficult to conceive an associated adaptive pressure that would promote the development of arm feather musculature. Because the large size of *Apatoraptor* precludes it from flight, the increased feather musculature must be explained in another manner.

One possible explanation is that this structure was used for display (Foth et al. 2014; Koschowitz et al. 2014). The late ontogenetic development of pennibrachia (and therefore the associated arrector musculature) in *Ornithomimus* Marsh 1890 led Zelenitsky et al. (2012) to

suggest that pennibrachia were used for sexual display in that taxon. Although the ontogenetic

timing of pennibrachium development in *Apatoraptor* is unknown, the presence of a well-

muscled pennibrachium could be reasonably explained as a secondary sex characteristic. Further

support for increased feather musculature in conjunction with display comes from feather

musculature patterns in modern birds. Lowe (1942) notes that in the male Gould's Manakin

(*Manacus vitellinus* Gould 1843), which uses its wings in an elaborate courtship display, the

flexor sublimis digitorum and the *flexor carpi ulnarum* are greatly hypertrophied. Similarly,

Stettenheim (2000) notes that, especially in males, feather musculature is larger in display

feathers than in non-display feathers.

     Sexual display—Hypotheses about sexual display in oviraptorosaurs have been

presented by several authors, though most studies have focused on the tail and its associated

feathers (Ji et al. 1998; Barsbold et al. 2000; Pittman et al. 2013; Persons et al. 2014).

Oviraptorids, which frequently develop fused pygostyles or cranial crests (see Chapter 4), may

have used those structures for display instead of pennibrachia. Thus, the presence of a

pennibrachium potentially associated with sexual display in *Apatoraptor* (Fig. 3.84) expands on

the known display structures of oviraptorosaurs. There is now evidence for three types of display

in oviraptorosaurs: tail display (Persons et al. 2014); cranial crests (Clark et al. 2002); and

pennibrachia (Fig. 3.84). The widespread presence and frequent convergence of sexual display

features in oviraptorosaurs (see Chapter 5) suggests that sexual display was an important factor

in the evolution of this group. This has important ramifications for cladistic analysis of

oviraptorosaurs, as several features cited as taxonomic differences may, in fact, be homoplastic,

ontogenetic, or sexually dimorphic. For example, as recovered in the analyses of Funston and

Currie (2016), the development of a cranial crest has evolved at least three separate times, and

cranial crests have been lost once. Furthermore, the fusion of the distal caudal vertebrae into a pygostyle—potentially associated with a fan of feathers for display—appears to be independent of phylogeny, with differing morphology even in closely related taxa (e.g. MPC-D 100/42 and *Citipati osmolskae*). Indeed, the most parsimonious explanation for the evolution of pygostyles requires at least five separate convergent events. It is likely that the presence or absence of a pygostyle is controlled by ontogeny and possibly sexual dimorphism, rather than taxonomy. At the moment, however, there is not a sufficient sample size in the literature to examine this possibility. As ontogeny and individual variation in oviraptorosaurs become better known, it may be necessary to reevaluate the use of certain characters in cladistic analyses and their impact on our understanding of oviraptorosaur relationships.

3.3.6 Indeterminate caenagnathid material

Dinosaur Park Formation:

Gen. et sp. indet.

Figs. 3.86–3.89

Newly referred material: TMP 1980.016.2095, partial left pubis; TMP 1981.019.0252, parietals; TMP 1981.023.0035, partial right ilium; TMP 1992.036.0674, partial right ilium; TMP 1994.012.0603, nearly complete pubes; TMP 1996.012.0142, partial dentaries; TMP 1998.093.0013, partial right ilium; TMP 2001.012.0216, partial right quadrate; TMP 2002.012.0103, partial right ilium.

Horizon and locality: Dinosaur Park Formation, Dinosaur Provincial Park, Alberta, Canada.

Description

Parietals:

   TMP 1981.019.0252—A pair of indistinguishably fused parietals (Fig. 3.86) shows a number of unusual features compared to other oviraptorosaurs and theropods. The parietals are dorsally arched but lack any development of a sagittal crest along the midline. They are incomplete posteriorly, as indicated by Currie (1992), but comparison to other oviraptorosaurs suggest that they would not have extended much further. As a result, they are nearly as wide transversely as long anteroposteriorly, which is unusual for most theropods, but more similar to the broad parietals of oviraptorosaurs. The anterior edge is rounded in dorsal view (Fig. 3.86C)

and has a prominent W-shaped shelf. Along the midline, there is an anteriorly-tapering triangular process that would have separated the posterior parts of the frontals on the dorsal surface of the skull. A depressed, posteriorly-slotted shelf in the parietal would have accommodated each frontal, and their positions indicate that the frontals were widely separated at their posterior ends. The degree of separation indicated by these facets is both wider transversely and further anteroposteriorly than is typically the case in oviraptorosaurs. Currie (1992) suggested that the parietals had an anteriorly-projecting lateral process that would have contributed to the postorbital bar and formed part of the supratemporal fenestra. Instead, this process closely resembles the anterior process of the laterosphenoid in oviraptorids, and it is more likely that it represents a portion of the laterosphenoid fused to the parietal. This interpretation is supported by a crack with a finished edge separating the parietal from this structure on the left and a change in bone texture in this region on the right, where the process is broken off (Fig. 3.86A, B). The dorsal surface of each parietal has an unusual, circular, raised platform that is rugose and pitted. These plateaus are symmetrical and show no evidence of pathology. As suggested by Currie (1992), they likely represent attachment sites for mandibular adductor musculature, but which muscles they hosted is uncertain. No other oviraptorosaur has similar features, although no other caenagnathid parietals are known. The ventral surface of the parietals (Fig. 3.86D) has an unusual, prominent transverse sulcus just posterior to their widest point, bordered anteriorly and posteriorly by shallow ridges. The lateral parts of the sulcus are slightly deeper than the medial parts, and it is likely that these represent the fossa for the optic tectum (Osmólska, 2004b; Balanoff et al., 2018). Accordingly, the transverse sulcus likely indicates that the optic tecta were dorsomedially expanded relative to other oviraptorosaurs. At the anterior end of the ventral surface, a slightly thicker region of bone with a posterior lip underlies the midline process of the

237

parietal. Unlike the parietals described by Osmólska (2004), TMP 1981.019.0252 lacks any evidence of vascular impressions, nor is there a longitudinal ridge signifying a cerebral fissure.

Quadrate:

TMP 2001.012.0216—This specimen is a partial quadrate with clear oviraptorosaur affinities (Fig. 3.87). The mandibular articulation is saddle-shaped and deeply incised to accommodate the tall articular ridge of the mandible. The medial glenoid is larger than the lateral glenoid, but the lateral glenoid projects further ventrally. The lateral surface of the quadrate (Fig. 3.87C) has a rounded facet that faces dorsolaterally for articulation with the quadratojugal. The posterior edge of this facet is broken, so the shape of the quadratojugal cannot be determined. Medial to this facet, a finished dorsal edge marks the ventral extent of the quadratojugal foramen. This foramen is much larger than those of oviraptorids and occupies nearly one third of the transverse width of the quadrate (Fig. 3.87A). The ascending portion of the quadrate is missing, but the broken base reveals that it shared a similar cross-section with oviraptorids. The medial edge of surface of the quadrate has a large process that would have contacted the pterygoid. This process is oval-shaped in medial view and is divided into two concave regions (Fig. 3.87D). The dorsal concavity is small, deep and elliptical, with its long axis oriented anteroposteriorly. It is separated from the larger, shallower concavity by a rugose semi-circular ridge. A small channel oriented anteroventral-posterodorsal communicates between these two concavities. The anterior surface of the quadrate is somewhat convex, although there is a depression ventral to the quadratojugal facet and a deep groove separating the condyles from the pterygoid process. The posterior surface of the quadrate is concave, but otherwise unremarkable. At the base of the ascending process, on the posterior side, there is a small depression that

suggests that the posterior surface of the ascending process was deeply concave, as in oviraptorids.

Sacrum:

TMP 1984.163.0102—This is a relatively complete sacrum (Fig. 3.88A–F), missing portions of the neural spines. As in other caenagnathids, six fused vertebrae form the sacrum, which measures 221 mm in length, slightly larger than TMP 1979.020.0001 (199 mm). Like in TMP 1979.020.0001, the centra are low and wide, and each has a deep lateral pleurocoel. They decrease in transverse width towards the posterior end of the sacrum. The centra are completely fused to each other, but a crack is visible between the last sacral vertebra and the preceding one (Fig. 3.88C). This crack appears to be natural, extending around the entirety of the centrum. This indicates that although the neural arch of the last sacral is extensively fused to the rest of the sacrum, that the centrum of this vertebra was not. There is no midline groove along the ventral surface of the sacrum, but this is highly variable in oviraptorosaurs. The neural arches are tall and indistinguishably fused, except for a gap between neural spines three and four (Fig. 3.88A, D). The neural spines decrease in height in each successive vertebra, so that the sacrum is much taller overall at its anterior end than its posterior end. Like in TMP 1979.020.0001, the neural arches are invaded by a complex series of pneumatic fossae divided by delicate laminae of bone. On the first sacral vertebra, these include two infradiapophyseal fossae, but these are displaced in the posterior vertebrae by the fused sacral ribs. The sacral ribs are placed lower on the centrum in each successive vertebra, and on the posterior three vertebrae, there is a large process that extends laterally from the neural arch above the sacral rib (Fig. 3.88D, F: adp). The fifth and sixth sacral ribs are largest and each is expanded into a hatchet-like process at its lateral end.

TMP 1980.016.1503—This is a partial sacrum comprising parts of the anterior four vertebrae (Fig. 3.88 J–M). Parts of the neural arches are adhered to the dorsal surfaces of the centra, but they are badly damaged and do not include the neural spines. The bases of the sacral ribs are present and fused to the centra, but the rest of the ribs have been broken. Each vertebra has a large lateral pleurocoel, which is low on the centrum, nearly flush to its ventral surface (Fig. 3.88J). These pleurocoels decrease in size posteriorly along the series. The first sacral is lower dorsoventrally than TMP 1984.163.0102, but is wider transversely. Its infradiapophyseal fossa is divided into anterior and posterior pits, rather than dorsal and ventral pits as in TMP 1984.163.0102. The first three centra are fused and the sutures between them are obliterated. The third and fourth vertebrae seem to be less well fused than the other vertebrae, and a suture is still visible between them (Fig. 3.88L). No midline groove is apparent on the ventral surfaces of the centra. The neural arches are badly damaged, but it is clear nonetheless that they hosted numerous complex pneumatic fossae, including infradiapophyseal and infrapostzygapophyseal fossae.

TMP 1981.019.0285—This partial sacrum (Fig. 3.88G–I) comprises complete sacral vertebrae five and six, and the posterior portion of sacral four. The centra are completely fused with each other and the sacral ribs, including the last sacral. The last sacral measures 31.5 mm, which is slightly smaller than the last sacral vertebrae of TMP 1984.163.0102 (38 mm), despite more complete fusion to sacral five (Fig. 3.88H). Each centrum has small lateral pleurocoels, and in sacral six, these are nearly flush to the ventral surface of the centrum. The neural arches have deep infraprezygapophyseal fossae that are divided by a lamina, as well as supradiapophyseal fossae that invade the space above the sacral ribs. The neural spines are broken but in sacral five, a broken region probably represents the base of a lateral process for attachment to the ilium, like

in TMP 1984.163.0102. Sacral six has an inclined posterior articular face, which faces posterodorsally. Like in TMP 1981.023.0039, it is deeply concave and roughly trapezoidal in shape (Fig. 3.88I).

Ilium:

TMP 1998.093.0013—TMP 1998.093.0013 (Fig. 3.89A–C) is the posterior half of a right ilium, without the pubic peduncle or preacetabular process. The acetabulum has a rounded, slightly raised dorsal edge. Its dorsal surface lacks a longitudinal groove, but is broken where this groove would have been pronounced. The bone texture changes from the anterior to posterior parts of the dorsal surface: anteriorly, it is glossy, but posteriorly, including on the anterior face of the ischiadic peduncle, it is pebbled and porous, typical of articular faces. A distinct but low-relief ridge between these regions is oriented posterolaterally-anteromedially. The ischiadic peduncle is triangular in outline and also projects only slightly beyond the lateral side of the ilium (Fig. 3.89B), but the ventral corner is broken. The lateral surface of the blade of the ilium is smooth, with a slight concavity above the acetabulum, and textured bone at the dorsal edge. This region does not have a raised ridge as in TMP 1981.023.0035. The dorsal edge of the ilium is transversely rounded (Fig. 3.89A), rather than flat, but also becomes wider and medially directed posteriorly. The postacetabular blade has a square area of rugose bone, which occupies two-thirds of its anteroposterior length. The sacral rib attachments are less visible than in TMP 1981.023.0035, and appear to be in slightly different locations (Fig. 3.89C). The most posterior one is directly above the ischiadic peduncle, but appears to be more similar in length to it, rather than longer. The middle contact surface appears to be closely appressed to the posterior one, rather than at the base of the ridge that separates the anterior two medial concavities. The

anterior ridge separating the concavities branches into two major rami, the posterior one of which is larger than the anterior one (Fig. 3.89C). They are separated by a large foramen anteriorly, and a slight depression. The middle concavity does not extend as far ventrally as in TMP 1981.023.0035; instead, the anterior and posterior ridges unite into a platform with at least four large, dorsally-opening foramina. The posterior ridge does not extend over the posterior concavity as far posteriorly as in TMP 1981.023.0035, and instead becomes shallow and triangular at about half the length of the concavity. The posterior concavity is oval, not circular, and is not confluent with the brevis shelf: a flat platform separates them anteriorly. The brevis shelf is shallow, as is the fossa, and it lacks any grooves (Fig. 3.89B, C). It has four large, posteriorly-opening foramina.

Pubis:

   TMP 1980.016.2095—A left pubis (Fig. 3.89G–I) is missing most of the end proximal to the ischiadic process, as well as all of the pubic boot. The shaft is sinuous in anterior view (Fig. 3.89G), but does not bow as far laterally at the proximal end as does TMP 1994.012.0603. The proximal end is missing the iliac contact and only the base of the ischiadic process is preserved. Medial to the latter, there is a posteriorly-rimmed fossa (Fig. 3.89I: pf) that characterizes caenagnathid pubes (Sullivan et al. 2011). The proximal end of the shaft is more strongly curved anteriorly than TMP 1994.012.0603, but the distal end is straight in lateral view. On the medial side of the shaft, a proximodistal ridge extends from the proximal end of the pubic apron (Fig. 3.89I), becoming confluent with the shaft about halfway between the apron and the ischiadic contact. In medial view, the pubic apron is slightly sinuous: its proximal third is concave anteriorly, and the distal two-thirds are convex anteriorly. Although proximally it is near the

posterior side of the shaft, distally it is continuous with the anterior surface and forms a posterior concavity. In anterior view (Fig. 3.89G), the pubic apron is narrower transversely than TMP 1994.012.0603, although its medial edge shows some breakage. At its ventral end, there is an invagination that indicates a pubic fenestra was present, but its size and shape cannot be discerned.

TMP 1994.012.0603—The paired pubes of TMP 1994.012.0603 (Fig. 3.89D–F) are nearly complete, missing only the anterior part of the fused pubic boot and its ventral surface. The pubes are sinuous in anterior view (Fig. 3.89D), bowing medially about one-third of the distance from the proximal end. In lateral view (Fig. 3.89E), they are nearly straight-shafted, in contrast with the strongly curved pubes of oviraptorids (Osmólska et al. 2004). The proximal ends are composed of a dorsal peduncle for the ilium and a posterior facet for the ischium, separated by a quarter-circle portion of the acetabulum margin. The iliac contact is roughly semicircular in dorsal view, but with a flattened anterolateral edge (Fig. 3.89D–F, ilc). Posteriorly, the acetabular rim tapers transversely towards the ischiadic contact. There is a pronounced circular area that protrudes slightly from the rest of the acetabulum on its ventral surface, just anterior to the contact with the ischium (Fig. 3.89E, ace). The ischiadic contact is triangular, is widest proximally, and tapers to a point distally (Fig. 3.89E–F, iscc). Medial to it, the pubis has a deep concavity (Fig. 3.89D, pf); this depression is bordered posteriorly by a raised lip of the ischiadic contact as in other caenagnathids (Sullivan et al. 2011). As in *Anzu wyliei*, *Elmisaurus rarus*, and *Nomingia gobiensis*, the ischiadic contact protrudes further from the shaft of the pubis than in oviraptorids (Funston et al., 2018a). A faint, proximodistal ridge extends from the proximal end of the pubic apron toward the ischiadic contact, terminating about halfway. The pubic apron is much narrower than the inter-acetabular width and is not extensive

proximodistally (Fig. 3.89D,F, apr). It tapers in transverse width distally and is separated from the pubic boot by an oval pubic fenestra (Fig. 3.89D,F, pfen). The apron is flush with the anterior surfaces of the shafts of the pubes, which results posteriorly in a slightly concave area between the shafts. The pubic boot is inclined anteroventrally-posterodorsally relative to the shaft of the pubis and the suture between the pubes at the pubic boot is entirely obliterated by fusion (Fig. 3.90D, pb). The posterior part (Fig. 3.89E–F, pbt) is dorsally concave in lateral view, but lacks a cleft between the pubes as is found in *Avimimus* and some oviraptorids (Funston et al., 2018a).

Remarks

Numerous isolated bones from the DPF pertain to caenagnathids, but cannot be assigned to a taxon because they are either not distinctive enough, or do not overlap with specimens of known affinities.

The parietals and quadrate are the first unambiguous caenagnathid cranial elements from the DPF. Currie (1987) mentioned the parietals, and they were briefly described in a symposium paper (Currie 1992). As mentioned by Currie (1992), although they are likely oviraptorosaur, they cannot currently be assigned to any caenagnathid taxon because no overlapping material exists. These parietals differ from those of avimimids and oviraptorids in the presence of pitted plateaus that likely anchored temporal musculature, but the functional significance of these features is unknown. The quadrate has the saddle-shaped articulation that is typical of oviraptorosaurs, but is more deeply incised to match the tall articular ridge of the mandibles. Because *Caenagnathus collinsi* has lower articular ridges than *Chirostenotes pergracilis* or *Leptorhynchos elegans*, it is more likely that the quadrate pertains to one of these latter taxa than

to the former. Several features distinguish the quadrate from those of oviraptorids, particularly the large quadratojugal foramen and the large, protruding process for the pterygoid.

Isolated sacra known from the DPF show little variation, although most of their overlap is in the centra. The only complete isolated sacrum incorporates six vertebrae, as is the case in *Anzu wyliei, Chirostenotes pergracilis,* and *Epichirostenotes curriei*, suggesting that sacral number varied minimally in caenagnathids. All caenagnathid sacra known show prominent lateral pleurocoels on the anterior centra and fusion of the neural spines into a broad plate. The last two sacral ribs are much larger than the rest, and expand laterally into wide, hatchet-shaped processes. The last sacral vertebra is frequently less well fused to the rest of the sacrum, and usually has in inclined, concave posterior articular surface. Unfortunately, consistency in the morphology of the known sacra from the DPF means that they cannot be assigned with confidence to a taxon unless associated with other material. Therefore, it is not clear whether all known isolated sacra pertain to *Chirostenotes pergracilis*, to which they are identical, or if the sacra of *Caenagnathus collinsi* and *Leptorhynchos elegans* differed minimally from the former.

Several isolated pelvic elements from the DPF can be identified as caenagnathids by a number of features. Ilia can be distinguished by the absence of a supraacetabular crest and a tall iliac blades. Ornithomimids and tyrannosaurs both have supracetabular crests, whereas dromaeosaurs and troodontids also lack this feature but have low, elongated ilia. Pubes can be identified as caenagnathid by a posteriorly enclosed medial fossa on the proximal end; relatively straight, mesopubic shafts; transversely narrow pubic aprons; and, where preserved, a pubic booth with a longer anterior process than posterior. Although the pelvic elements cannot be referred to particular taxa with confidence, they do show variation which can be used to provisionally assign them (see Sections 3.3.2 and 3.3.4). The ilia also appear to show variation

that is not taxonomic. The medial side of the ilium has either three ridges developed between the anterior depression and middle depression (TMP 1992.036.0674, TMP 1998.093.0013), or only two (TMP 1981.023.0035, TMP 2002.012.0103). The middle depression is variable in its ventral extent, as is the development of a platform separating it from the acetabulum. Furthermore, the posterior depression varies in its relationship to the brevis fossa, in that it appears to be confluent with the brevis shelf in TMP 1981.023.0034 and TMP 1981.023.0035, but not in the other specimens. It is likely that much of this is simply individual variation because the states do not co-vary. Other features, however, like the inclination of the pubic peduncle and the relative height of the ilium, may be more useful for distinguishing taxa. In TMP 1981.023.0035 and TMP 1992.036.0674 (which is pathological), the ventral surface of the pubic peduncle is horizontal, rather than inclined as in *Chirostenotes pergracilis* (TMP 1979.020.0001) and TMP and TMP 2002.012.0103. Similarly, these specimens share a relatively lower ilium over the acetabulum. Although it is possible that these traits vary allometrically or ontogenetically, some evidence shows that the individual represented by TMP 1981.023.0034–5 and TMP 1981.023.0039 is of roughly equivalent ontogenetic stage as TMP 1979.020.0001 (*Chirostenotes pergracilis*). Unfortunately, the incomplete nature of TMP 1998.093.0013 means that it cannot be linked to either *Chirostenotes pergracilis* nor *Leptorhynchos elegans*. However, the transverse thickening of the dorsal edge of the ilium and its medial curvature towards the posterior end are more similar to *Leptorhynchos elegans* (TMP 1981.023.0034–5) than to *Chirostenotes pergracilis* (TMP 1979.020.0001).

Three isolated caenagnathid pubes have been recovered from the DPF, so they taxa to which they pertain are ambiguous. However, it is likely that those described here represent at least two taxa. One major difference is the size range of the pubes, as UALVP 56638 (See

section 3.3.1) is more than twice the size of TMP 1994.012.0603. Although slightly larger, TMP 1980.016.2095 is closer in size to TMP 1994.012.0603 and is more consistent in morphology. Despite being half the length of UALVP 56638, TMP 1994.012.0603 is nearly as broad proximally, partly because the shafts bow laterally at the proximal end. In contrast, the pubic shafts of UALVP 56638 are more or less straight in anterior view. TMP 1980.016.2095 shares the proximally bowed morphology of TMP 1994.012.0603, rather than the straight shafts of UALVP 56638. Similarly, the proportion of the pubes occupied by the pubic apron differs between these morphotypes. In UALVP 56638, the pubic apron occupies about two-thirds of the proximodistal length of the pubes, whereas in the other specimens this ratio is closer to one half. The pubic fenestra also differs in shape between UALVP 56638, where it is slit-like, and TMP 1994.012.0603, where it is more oval and rounded. Its shape cannot be determined in TMP 1980.016.2095. Although far from certain, it is likely that the larger UALVP 56638 is referable to *Caenagnathus collinsi*, because it is comparable in size to the pubes of *Anzu wyliei*, to which *Caenagnathus collinsi* is assumed to be closely related in size and morphology on the basis of the mandible. The smaller pubes are probably representative of either *Chirostenotes pergracilis* or *Leptorhynchos elegans*, but which of these cannot be determined.

Frenchman Formation:

Gen. et sp. indet.

Fig. 3.90

Newly referred material: RSM P2600.1, Partial hindlimb comprising distal tibia, astragalocalcaneum, and metatarsals II and III; RSM P2161.1, Second metatarsal.

Horizon and locality: Frenchman Formation, Grasslands National Park, Saskatchewan, Canada.

Description

A partial skeleton (RSM P2600.1; Fig. 3.90A–H) and an isolated second metatarsal (RSM P2161.1; Fig. 3.90I–N) have been recovered from the Frenchman Formation of Saskatchewan. Lack of fusion of the tarsometatarsus or the distal tarsals suggests they are more closely allied with *Chirostenotes pergracilis* than *Leptorhynchos elegans*, but it is possible that this is the result of ontogeny.

RSM P2600.1—The partial skeleton (RSM P2600.1) is composed mostly of hindlimb elements, including the distal end of a left tibia and some of the metatarsals (Fig. 3.90A–H). The distal end of the tibia is similar in shape to *Leptorhynchos elegans* from Alberta, but is relatively wider where it contacts the astragalus and calcaneum, which are fused. The astragalocalcaneum lacks a horizontal groove distal to the ascending process and extends far onto the posterior surface of the tibia (Fig. 3.90B, D). The distal condyle of the second metatarsal faces ventromedially, and there is a rugosity for *M. tibialis cranialis* proximal to the condyle. The shaft of the third metatarsal is broader transversely than the distal condyle and is anteriorly concave. The posterior surface has two cruciate ridges, as in *Leptorhynchos elegans* and *Elmisaurus rarus*. The facets for the contacts with the second and fourth metatarsals appear asymmetrical and suggest a closer association between the second and third metatarsals than the third and fourth metatarsals. The distal condyle is as mediolaterally wide as it is anteroposteriorly deep, whereas in *Leptorhynchos elegans* from Alberta, it is deeper than wide.

RSM P2161.1—A second metatarsal (RSM P2161.1; Fig. 3.90I–N) from the left foot was recovered from Grasslands National Park in Saskatchewan. The proximal end (Fig. 3.90N)

has a flat posterior surface for the contact with the third distal tarsal, which does not appear to have coossified in this individual. The proximal end lacks the posterior process of *Caenagnathus collinsi*, and is nearly identical in shape to *Leptorhynchos elegans* (TMP 1982.016.0006). The shaft, however, is straight and not deflected medially at its distal end, unlike *Leptorhynchos elegans*. There is a large posteromedial ridge on the shaft, as in *Leptorhynchos elegans* and *Elmisaurus rarus*.

Remarks

The recovery of caenagnathid material from the Maastrichtian Frenchman Formation of Saskatchewan expands the geographic range of caenagnathids, although they are known from both further east and further north. More importantly, it increases the diversity of latest Cretaceous oviraptorosaurs, showing the presence of a small caenagnathid in addition to *Anzu wyliei* during this interval. Unfortunately, the material is not complete enough to allow for referral to a genus or species, although it resembles *Leptorhynchos elegans* and *Elmisaurus rarus* in features of the metatarsals. Regardless, some morphological differences exist, which should be expected, considering the ~10 ma gap between the DPF and the Frenchman Formation. Despite the limited nature of the current material, its excellent preservation and association of the elements is promising for the discovery of more material in the future.

Horseshoe Canyon Formation:

Gen. et sp. indet.

Figs. 3.91–3.93

Newly referred material: UALVP 57349, Partial right tibia.

Horizon and locality: Tolman Member of Horseshoe Canyon Formation, Tolman Bridge, Alberta, Canada (Eberth and Braman, 2012).

Description

       Morphology—UALVP 57349 (Fig. 3.91) is a small tibia comprising the distal end, most of the shaft, and an unconnected proximal end. Based on the profile and width of the proximal end where it would have connected to the remainder of the shaft, the missing portion of the shaft was probably small. UALVP 57349 is elongate and gracile relative to its distal width. Towards the proximal and distal ends, the shaft has been crushed anteroposteriorly, and the fragments are slightly telescoped. Otherwise, the specimen is well preserved and shows no signs of pre-burial damage or weathering.

       The proximal end is missing most of the cnemial crest and fibular condyle, and the femoral articular surface is eroded (Fig. 3.91A, F). The cnemial crest does not extend far distally (~20% of the length of the tibia) as in most caenagnathids (Currie and Russell, 1988; Lamanna et al., 2014; Currie et al., 2016; Funston and Currie, 2016; Funston et al., 2016a). However, it would have been pronounced, based on the preserved portion. The eroded fibular condyle is separated from the inner condyle by a small notch (Fig. 3.91F), as it is in other caenagnathids (Currie et al., 2016; Funston et al., 2016a). As in *Elmisaurus rarus* and *Chirostenotes pergracilis*, this produces a small protrusion on the posterolateral surface of the femoral condyle (Fig. 3.91F). The incisura tibialis is deep and semicircular in profile. The fibular crest is mostly missing, but the distal end is preserved as a small, rugose ridge. The fibular crest ends 156 mm from the distal end, at about 25% of the estimated length of the tibia. Posterior to this crest, there

is a large nutrient foramen that opens proximally (Fig. 3.91D), as in *Elmisaurus rarus*, *Heyuannia yanshini*, *Khaan mckennai*, and *Leptorhynchos elegans* (Balanoff and Norell, 2012; Currie et al., 2016; Funston et al., 2016a).

The uncrushed midshaft of the tibia is flat anteriorly and rounded posteriorly, creating the half-circle cross-section typical of oviraptorosaurs (Currie et al., 2016; Funston et al., 2018, 2016a). The shaft is 41 mm in circumference. Distal to the fibular crest on the anterolateral surface of the shaft, there is a short, shallow longitudinal groove that may have accommodated vasculature. A similar groove is visible—although situated more distally—in *Avimimus nemegtensis* Funston et al. 2018b (Funston et al., 2016b).

The distal end of the tibia flares mediolaterally but is compressed anteroposteriorly. It is transversely wide—16% of the estimated length of the tibia—similar to *Chirostenotes pergracilis* (TMP 1979.020.0001; 13%) and *Elmisaurus rarus* (MPC-D 102/007; 14%). A region of glossy bone on the anterior surface hosted the ascending process of the astragalus (Fig. 3.91G); it extends proximally at least 57 mm (27% of the length of the tibia). It tapers proximally, but is not significantly deflected medially or laterally. As in *Anzu wyliei* (Lamanna et al., 2014) and *Chirostenotes pergracilis* (Currie and Russell, 1988), this concavity is bisected by a shallow, longitudinal ridge. The medial malleolus has a flat anterior surface and a convex posterior surface, which meet in a sharp crest (Fig. 3.91E) as in *Anzu wyliei* (Lamanna et al., 2014), *Chirostenotes pergracilis* (Currie and Russell, 1988), *Elmisaurus rarus* (Currie et al., 2016), and *Leptorhynchos elegans* (Funston et al., 2016a). The lateral malleolus is posteriorly deflected and has a small postfibular flange, in contrast with the larger postfibular flanges of *Elmisaurus rarus* (Currie et al., 2016) and *Leptorhynchos elegans* (Funston et al., 2016a). On the posterior surface of the tibia, there is a shallow concavity separating the lateral and medial

malleoli. A porous articular surface extends from the distal end of the tibia onto a small portion of the posterior side, suggesting that the astragalocalcaneum wrapped around the distal end of the tibia onto its posterior surface.

Osteohistology—The thin sections (Figs. 3.92, 3.93) confirm that the cross-sectional shape is not the result of deformation, although the bone is extensively fractured. The entirety of the cortex, which ranges from $2.5 - 3.5$ mm in thickness, is formed of primary fibrolamellar bone (Fig. 3.92A). There are no obvious lines of arrested growth, and no secondary osteons. The orientation of vasculature changes throughout the cortex from predominantly reticular endosteally (Fig. 3.92E) to primarily plexiform (Fig. 3.92D) towards the periosteal surface. The periosteal margin is vascularized and lacks any circumferential lamellae, indicating that UALVP 57349 was still growing rapidly when it died. The endosteal margin is encircled by a layer of avascular lamellar bone representing endosteal lamellae (Fig. 3.92A; 3.93B). This layer cross-cuts the primary osteons of the cortex with a scalloped resorption line, and in some areas it has become taphonomically detached at this contact. Throughout the cortex, osteocyte lacunae are relatively dense ($46,005/mm^3$) compared to other theropods (Cullen et al., 2014), but are similar to *Anzu* (Benner et al. 2016). This is not surprising, considering that there is a negative trend between body size and osteocyte lacunar density (Bromage et al., 2009), and UALVP 57349 likely belonged to a small animal. While osteocyte lacunar density does not change appreciably from the inner to outer cortex ($48972/mm^3$ and $52968/mm^3$, respectively), there is a distinctive thin band of decreased osteocyte lacunar density ($29452/mm^3$) about 1500 μm from the periosteal surface (Fig. 3.93A). Endosteal to this band, osteocyte lacunae are relatively small and flat, whereas periosteally they are larger and more globose (Fig. 3.93A). This transition

corresponds to a significant colour change of the bone matrix (Fig. 3.92A, B), as well as the onset of predominantly plexiform vasculature.

About 700 μm from the periosteal surface, a layer of parallel-fibered bone appears under cross-polarized light (Fig. 3.92C, 3.93C, D). In plane-polarized light it is difficult to discern, although in some regions, it results in a slightly wider layer of bone between rings of plexiform vascular canals and a bright line at low magnification (Fig. 3.93C). This zone can be traced around the entirety of the cortex, and it is roughly parallel to the periosteal surface. In some regions of the bone, just periosteal to this parallel-fibered bone, there is a reduction in the number of circumferential vascular canals. This results in a discontinuity between two zones of plexiform vasculature, similar to vascular changes described in *Maiasaura* Horner and Makela 1979 (Woodward et al., 2015). The development of parallel-fibered bone indicates a temporary decrease in growth rate, and it is likely that this zone represents the first cyclical growth mark, similar to annuli of *Psittacosaurus* Osborn 1923 (Erickson, 2000). However, growth did not cease during this period, and this individual was still growing at a relatively rapid rate.

Remarks

Although the tibia of *Apatoraptor* is known from nearby deposits of the HCF, only the cnemial crest is visible in the specimen (Funston and Currie, 2016). The cnemial crest of *Apatoraptor* compares favourably in terms of position with that of UALVP 57349, but it was not included in CT scans, and so no more comparisons can be made. UALVP 57349 is geologically younger than either *Apatoraptor* or *Epichirostenotes*, which are both from the Campanian portion of the HCF, but it may become referable to either taxon as more material is discovered. At 210 mm, the individual represented by UALVP 57349 would have stood about 48 cm at the

hip, based on the same measurements in *Elmisaurus rarus* (Currie et al., 2016), for which the entire hindlimb is known. A linear relationship ($R^2 = 0.9856$) between $\log(B_M)$ and $\log(T_L)$ in caenagnathids (Fig. 3.94) suggests that UALVP 57349 would have weighed approximately 7.95 kg (± 2.05 kg). These data also show that caenagnathids had relatively longer tibiae for their body mass than did oviraptorids (Fig. 3.94). The slope of the best-fit lines indicates that in oviraptorosaurs as a group, the length of the tibia is negatively allometric to body mass. Whether this is an ontogenetic trend cannot be determined.

Nemegt Formation:

<div align="center">

Family Caenagnathidae Sternberg 1940

cf. *Elmisaurus rarus*

Figs. 3.95–3.97

</div>

Newly referred material: MPC-D NatGeo.2018.040 (field number), partial skeleton comprising partial postorbital, partial angular, partial cervical vertebra, nearly complete scapulacoracoid, nearly complete left pubis, partial right pubis, partial astragalus, and partial left tarsometatarsus.

Horizon and locality: Nemegt Formation (?Maastrichtian), Bugiin Tsav, Gobi Desert, Mongolia. Collected approximately 20 m south of the type quarry of *Nomingia gobiensis*.

Description

Craniomandibular skeleton:

Two fragmentary bones are tentatively identified as craniomandibular bones, although it is possible that they are small portions of other bones.

Unidentified bone—A small triangular fragment of bone (Fig. 3.95A–E) cannot be identified with certainty, although it appears to have surrounded one of the cranial fenestrae. The bone tapers towards one side, and is broken on the opposite side. One edge of the bone is straight, whereas the other is rounded into a tab-like flange. On what is presumably the lateral surface of this flange, there is a small groove into which another bone may have inserted (Fig. 3.95A: :sq?). The opposite, presumably medial surface of the bone has a longitudinal ridge that separates it into two concave portions (Fig. 3.95C: rdg). The portion closest to the straighter edge is smaller and shallows towards the tapering end of the bone. The other portion is larger and has two shallow grooves the run perpendicular to the medial ridge. The end of the bone opposite the tapering process is broken, but there is a region of finished surface that indicates either the bone was hollow, or that it branched into multiple processes which are broken. Although the bone is complex, it cannot be positively identified because caenagnathid crania are so poorly known and there is little comparative material. The most likely option is that it represents an unusual postorbital, but it is possible that it represents a heavily worn fragment of the frontal, the lacrimal, or a palatal bone.

Dentary and angular—A small fragment of bone (Fig. 3.95F) represents part of the right mandible below the external mandibular fenestra. Most of this fragment is comprised of the angular, which has a deep, posteriorly tapering groove on its lateral surface (Fig. 3.95F: :dent). Within this groove, a small portion of the splint-like posteroventral ramus of the dentary is preserved. Together, these two bones bow ventrally, as is the case in *Chirostenotes pergracilis* (Funston and Currie 2014) and *Apatoraptor pennatus* (Funston and Currie 2016). The medial surface of the angular has a slight depression, resulting in an hourglass-like cross-section of the bone.

Axial skeleton:

   Cervical vertebra—A small portion of a cervical vertebra (Fig. 3.95G, H) was recovered. It includes the base of the neural arch and the left prezygapophysis. The prezygapophysis faces anterodorsally and is rounded in dorsal view (Fig. 3.95G). Its medial edge extends posteriorly as a ridge and curves medially to overhang a pocket above the neural canal. It is difficult to determine which part of the neck the prezygapophysis represents, but based on the depth of the fossa overlying the neural canal and the proportion of the prezygapophysis occupied by articular area, it likely represents an anterior vertebra.

Appendicular skeleton:

   Scapulocoracoid—The left scapula and coracoid (Fig. 3.96A–C) are relatively complete, but the scapula is missing its distal end. The scapula has a transversely thick, medially curving blade. The acromion is damaged but appears to have been narrow and directed anterolaterally. The long anterior portion of the scapula is downturned relative to the shaft, so the glenoid is situated more anteriorly and ventrally than in other oviraptorosaurs. In lateral view (Fig. 3.96A), the posterior edge of the glenoid is anterior to the level of the acromion process. In contrast, in oviraptorids (MPC-D 100/33) the anterior edge of the glenoid is directly ventral to the apex of the acromion process. The scapular portion of the glenoid of MPC-D NatGeo.2018.040 is small and circular, rather than elongate. It is slightly inclined to face laterally, though not as extremely as in *Apatoraptor pennatus*. Just posterior to the glenoid is a small nutrient foramen, and posterior to this, the scapula is rugose along its ventral edge. The scapula has a long contact with the coracoid, which is inclined about 45° anterodorsal–posteroventral, depending on the orientation of the scapula within the body. The result is a large area of bone that projects anteriorly between the glenoid and the acromion process (Fig. 3.96A). The medial surface of this

area (Fig. 3.96B) is concave and is penetrated by several small foramina. Unlike the scapula of oviraptorids, this area lacks a longitudinal groove conducting the vasculature from the coracoid foramen towards the blade of the scapula. However, this may be explained by the dorsal position of the coracoid foramen, which places it above the dorsal edge of the scapula.

The coracoid (Fig. 3.96A, C) is well preserved and is complete except for its dorsal and anteroventral edges. The glenoid is less only slightly inclined relative to the posterior edge of the coracoid, which results in a more posterior orientation of the entire glenoid, rather than ventral. Just anterior to the coracoid portion of the glenoid there is a small depression, and the surface anterior to this is rugose. The biceps tubercle is positioned relatively far dorsally for an oviraptorosaur, entirely dorsal to the glenoid (Fig. 3.96A). It is large and mounded, but does not protrude as much as those of most oviraptorids. The coracoid foramen is directly dorsal to the biceps tubercle (Fig. 3.96C), rather than posterodorsal, and as noted previously, this situates it above the dorsal edge of the scapula. The posteroventral process curves posteriorly, although it is straighter than that of most oviraptorosaurs. Its apex is broken. On the medial side of the coracoid, there are no fossa underlying the biceps tubercle, unlike the condition in MPC-D 100/33.

Pubis—Parts of both pubes are preserved (Fig. 3.96D–F), but the left is far more complete. The head is nearly completely preserved, as is most of the shaft, but the pubic boot is missing. The iliac process of the head is eroded, exposing the medullary cavity, which suggests it was rotten before burial. The acetabular portion is roughly trapezoidal, with the shorter side facing laterally, and is dorsally concave. The ischiadic contact is elliptical and its lateral edge protrudes from the head of the pubis. There is a ventral groove underlying the ischiadic contact, but otherwise it does not protrude posteriorly (Fig. 3.96D), which is also the case in *Anzu wyliei*,

Elmisaurus rarus, and *Nomingia gobiensis* (Funston et al., 2018a). The medial surface of the

pubic head is concave, and the ischiadic contact protrudes medially to form a posterior lip around

this concavity (Fig. 3.96E, F: pf), suggested to be a synapomorphy for caenagnathids (Sullivan et

al., 2011). The lateral surface of the proximal pubic head is rugose, whereas the bone further

distally is more fibrous. The shaft of the pubis is also rugose, but posteriorly it is pitted and pock-

marked, which suggests that this texture is the result of weathering before burial. The shaft of the

pubis is relatively straight throughout its length in lateral view, although it is anteriorly concave

as in all oviraptorosaurs. The entire proximodistal length of the pubic apron is preserved, but its

medial edge is worn, which reduces its transverse width. Regardless, rearticulation with the right

pubis indicates that the pubic apron would have been transversely narrow (Fig. 3.96F), as is the

case in most oviraptorosaurs.

Astragalus—A small portion of the medial condyle and ascending process of the left

astragalus is preserved (Fig. 3.97A, B). Most of the ascending process is broken, but there is a

shallow transverse sulcus at its base, and a depression dorsal to this. The articular surface of the

medial condyle is rounded and has a finished, rather than porous surface. The union of the

ascending process and the articular portion forms an angle of 90° where the tibia would have

inserted.

Tarsometatarsus—The proximal ends of the left metatarsals III and IV are preserved

(Fig. 3.97 C–I), as well as the distal end of the right metatarsal IV (Fig. 3.97 J–N). Other

fragmentary shafts of bone are likely metatarsals as well, but they cannot be positively identified.

The distal tarsals are missing; the clean proximal surfaces of the metatarsals suggests that no

coossification of the distal tarsals or metatarsals had begun. Metatarsal III is small and

trapezoidal in cross-section proximally (Fig. 3.97 H, I). The medial face curves anterolaterally

where it would have contact metatarsal II, but it is broken. The anterior surface is triangular and has a small, ventrally-tapering flat area where it would have been exposed anteriorly. The posterior surface is anteromedially inclined and has a flat face that contributed to the posterior protuberance (Fig. 3.97H). The proximal end of metatarsal IV is somewhat semicircular in proximal view (Fig. 3.97G). On the medial surface there is a small anterior facet for metatarsal II and a recessed posterior facet for metatarsal III. The posterior side has a square, protruding buttress with a ventromedially-inclined ventral edge. Lateral to this is a small facet into which metatarsal V inserted. The right metatarsal IV preserves the distal end and part of the shaft (Fig. 3.97J–N). The medial surface of the shaft has two ridges that outline the facet for metatarsal III (Fig. 3.97M). Unlike in ornithomimids and oviraptorids, this facet does not cover the entire medial face, and there would have been a posterior concavity to the tarsometatarsus. The distal condyle is small and bulbous, facing directly distally, rather than being deflected laterally. Both of the ligament pits are well-developed, and the shallower lateral one is bordered posteriorly by a winglike triangular process (Fig. 3.97N).

Remarks

This specimen can be identified as an oviraptorosaur on the basis of the pubis, which is mesopubic and anteriorly curved. The pubis contrasts with those of oviraptorids, however, in being relatively straight distally instead of anteriorly convex. This distinction is supported by the preserved proximal end of metatarsal III, which is pinched, indicating an arctometatarsalian condition. Although portions of the skeleton overlap with specimens of *Elmisaurus rarus* (ZPAL MgD-I/98) and *Nomingia gobiensis* (MPC-D 100/119), these regions are not distinctive enough to determine to which taxon MPC-D NatGeo.2018.040 belongs. For example, although part of

the scapula is known for *Elmisaurus rarus*, and compares well with MPC-D NatGeo.2018.040, this element is not known for *Nomingia gobiensis*, and so it cannot be used to distinguish between them. Similarly, the proximal end of the pubis is known for each specimen, but they are all identical. The astragalus of MPC-D NatGeo.2018.040 is virtually identical to that of *Nomingia gobiensis*, but, again, this element is not known for *Elmisaurus rarus*, nor is it highly variable within caenagnathids. The proximal ends of the metatarsals are similar to *Elmisaurus rarus* in having a pronounced posterior protuberance, but they differ in that they are not fused to each other or the distal tarsals. It is possible that this is the result of ontogeny or allometry, because MPC-D NatGeo.2018.040 is slightly smaller than ZPAL MgD-I/98. However, the metatarsals and their degree of fusion are unknown in *Nomingia gobiensis*. The similarity of MPC-D NatGeo.2018.040 to both of these taxa provides further—albeit inconclusive—support for the synonymy of *Elmisaurus rarus* and *Nomingia gobiensis*, as well as the caenagnathid identity of the latter. In particular, it supports the notion that caenagnathid material from the Nemegt Formation belongs to a single morphotype, rather than representing multiple taxa.

3.4 DISCUSSION

3.4.1 Taxonomy and diversity of caenagnathids

Dinosaur Park Formation—Most lines of evidence suggest that three taxa coexisted in the DPF. Unfortunately, there is little anatomical overlap between associated skeletons and isolated specimens, which prevents confident referral of specimens. This is especially problematic for *Caenagnathus collinsi* and *Leptorhynchos elegans*. For these taxa, only mandibles and tarsometatarsi, respectively, can be referred unequivocally. However, more complete material of *Chirostenotes pergracilis* means that some specimens can be referred by exclusion from this taxon. For example, the pubes UALVP 56638 are too large to be reasonably referred to *Chirostenotes pergracilis*, for which an individual approaching maximum body size is known (UALVP 59400). Because *Leptorhynchos elegans* is generally considered to be smaller at maturity than *Chirostenotes pergracilis* on the basis of the tarsometatarsi and maturity in UALVP 59606, *Caenagnathus collinsi* is the only plausible option for the identity of UALVP 56638. Similarly, some isolated dentaries (TMP 1992.036.0390, TMP 1992.040.0044, UALVP 55639) are morphologically different from both *Caenagnathus collinsi* and UALVP 59400, which is referable to *Chirostenotes pergracilis*. These specimens are therefore best regarded as representatives of *Leptorhynchos elegans*. Following this logic—and the assumption that *Caenagnathus collinsi* was larger than *Leptorhynchos elegans* at maturity—most isolated bones from the DPF can be provisionally referred to one of the three taxa (Table 3.3; Fig. 3.98).

Osteohistology provides some insight into the taxonomy of DPF caenagnathids. The morphological similarity of TMP 1985.043.0070 and TMP 1992.036.1237 suggests that they pertain to the same taxon. This is supported by their osteohistology, which shows that the considerably smaller TMP 1985.043.0070 (Fig. 3.34) is substantially younger than TMP 1992.036.1237. The entire dentary of TMP 1985.043.0070 would fit within the central zone of trabeculae of TMP 1992.036.1237, which suggests that little—if any—corresponding tissue is preserved in the latter specimen. This indicates that TMP 1985.043.0070 still required considerable growth before approaching the size of TMP 1992.036.1237 at its earliest recorded LAG. It is possible that these specimens pertain to separate taxa, but this is unlikely for several reasons. First, the gross morphology and proportions of the mandibles are virtually identical, and previous surveys of other caenagnathid material from the DPF support the distinction of only three taxa (Longrich et al. 2013; Funston et al. 2015; Funston et al. 2016a). Second, although it could be argued that the size disparity between TMP 1985.043.0070 and TMP 1992.036.1237 is not large enough to account for at least seven years of growth, two main factors argue against this. Chief among these is that the difference in linear dimensions of the dentaries is misleading with regards to the size of the individual they represent. For example, assuming isometry between the dentary and femur, a doubling in the width of the dentary (and therefore femoral diameter) would result in a six-fold increase in body mass (based on femoral circumference). Secondly, although TMP 1992.036.1237 is at least six years older than TMP 1985.043.0070, it is clear from the spacing of the growth marks that it was not growing at a rapid rate during the last six years of its life, and did not increase drastically in size during this period. Evidence from other caenagnathids (Funston and Currie 2018) suggests that they grew rapidly early in life, and it is possible that TMP 1992.036.1237 achieved most of its growth in only a few years. In this

case, TMP 1985.043.0070 would be in the size range expected for a young juvenile of the same taxon, in the rapid growth phase of development.

The advanced age of UALVP 55639 has ramifications for the diversity of DPF caenagnathids. Longrich et al. (2013) suggested that small, sharply upturned dentaries with fused symphyses are distinctive enough to be considered a new taxon, *Leptorhynchos elegans*. This contrasted with the interpretations of Currie et al. (1993), who hesitated to establish new taxa without a better understanding of ontogenetic and intraspecific variation in caenagnathids. While histological evidence shows that fusion of the symphysis—considered a sign of adulthood by Longrich et al. (2013)—is not an indicator of maturity, the extensive secondary remodeling (Fig. 3.68) in UALVP 55639 does indicate that this individual was of advanced age. In contrast, the much larger TMP 1992.036.1237 is less remodeled, and suggests that this individual was approaching but had not yet attained maximum body size. These results suggest that these individuals represent two taxa of different adult body size; the larger (TMP 1992.036.1237) probably corresponds to *Chirostenotes pergracilis*, whereas the smaller (UALVP 55639) is likely *Leptorhynchos elegans*. This supports the distinction of three caenagnathid taxa (including *Caenagnathus collinsi*) in the DPF based on mandibles. In turn, the referral of TMP 1992.036.1237 to *Chirostenotes pergracilis* on the basis of the associated mandible and distal tarsal IV of UALVP 59400 suggests that UALVP 55639 represents *Leptorhynchos elegans*. Although no overlapping material exists, this provides more confidence in the association between small, anteriorly upturned mandibles and proximally fused tarsometatarsi.

Pelvic material from the DPF (Figs. 3.4, 3.5, 3.16, 3.57, 3.89) shows variation that may be useful for taxonomy. Small ilia so far recovered from the DPF appear to represent two morphotypes: a taller, more gracile morphotype with an inclined pubic peduncle, and a lower,

more robust morphotype with a straight pubic peduncle. The former morphotype is exemplified by TMP 1979.020.0001 (Fig. 3.16), which indicates that it is the condition in *Chirostenotes pergracilis*. Another ilium, TMP 2002.012.0103 also shows this morphology and represents an individual of approximately the same size. The other morphotype is exhibited by two associated ilia (TMP 1981.023.0034 and TMP 1981.023.0035; Fig. 3.57), which were also recovered alongside a sacral vertebra. These ilia are identical in size and morphology, indicating that they are from a single individual and that the morphology is not the result of pathology. They differ greatly from the ilia of *Chirostenotes pergracilis* in that the dorsal edge is much lower above the acetabulum and is transversely expanded to form a robust, flattened facet. The dorsal edge curves medially towards its posterior end, which differs markedly from the straight dorsal edge of TMP 1979.020.0001. The ventral edge of the pubic peduncle of this morphotype is straight, unlike the anterodorsally inclined ventral edge of the pubic peduncle of TMP 1979.020.0001. Furthermore, the smaller, more robust ilia have prominent foramina on the lateral surface of the pubic peduncle, which are absent in the more gracile morphotype. The associated sacral vertebra (TMP 1981.023.0039) is the last caudosacral, and a clean anterior articular surface shows that it was not fused to the rest of the sacrum. However, this is also the case in TMP 1979.020.0001, which suggests that they are roughly equivalent in ontogenetic stage. Furthermore, the sacral ribs are fused indistinguishably with the centrum, which suggests that this individual was not a juvenile. Based on their roughly equivalent ontogenetic stages and the stark differences in morphology, it is likely that these specimens represent separate taxa, *Chirostenotes pergracilis* (TMP 1979.020.0001) and probably *Leptorhynchos elegans* (TMP 1981.023.0034–5, TMP 1981.023.0039). A much larger ilium, UALVP 59791, probably pertains to *Caenagnathus collinsi* on the basis of size and morphology (see Section 3.3.1). This specimen shows that at

least some caenagnathids had rounded preacetabular blades, a feature which formerly linked

Nomingia gobiensis to oviraptorids. Its presence in an inequivocal caenagnathid strengthens the

interpretation of *Nomingia gobiensis* as a caenagnathid rather than an oviraptorid.

Horseshoe Canyon Formation—Two caenagnathids are currently known from the

HCF: *Apatoraptor pennatus* (Funston and Currie, 2016) and *Epichirostenotes curriei* (Sullivan et

al., 2011). In addition to the holotype skeletons of each of these taxa, two isolated caenagnathid

elements are known from the HCF. One of these, a metatarsal II (CMN 9570), was described by

Currie and Russell (1988). It is considerably larger than the metatarsals of *Chirostenotes*

pergracilis (TMP 1979.020.0001 and CMN 8538), suggesting it pertained to a large animal.

Elements of *Epichirostenotes pergracilis* are approximately 55% larger than the corresponding

bones of *Apatoraptor pennatus*, which, itself, is similar in size to *Chirostenotes pergracilis*. This

suggests that CMN 9570 is more likely referable to *Epichirostenotes curriei* than to *Apatoraptor*

pennatus, but this is highly speculative. The other isolated element is a small tibia (UALVP

57349; Fig. 3.91) described by Funston and Currie (2018). Tibiae of *Apatoraptor pennatus* and

Epichirostenotes curriei are incompletely known, so no comparisons can be made to refer

UALVP 57349 to either taxon. It is noteworthy, however, that this specimen is from a

significantly younger portion of the HCF than either *Apatoraptor pennatus* or *Epichirostenotes*

curriei. In any case, it is likely that the diversity of HCF caenagnathids is underestimated

because of their rarity. Unlike the DPF, caenagnathid material in the HCF tends to comprise

associated or articulated skeletons, but these are exceedingly rare. Regardless, this provides

promise for future study of HCF caenagnathids.

Nemegt Formation—Like the HCF, two caenagnathid taxa are currently established for

material from the Nemegt Formation. However, little overlap exists between material from these

taxa, *Elmisaurus rarus* and *Nomingia gobiensis*. Furthermore, elements that do overlap between the specimens are virtually identical, although they represent bones that tend to show little variation in caenagnathids in general. More numerous skeletons of *Elmisaurus rarus* are known, but these tend to be less complete than the type specimen of *Nomingia gobiensis*. Beyond the type skeleton of *Elmisaurus rarus* (ZPAL MgD-I/98), which preserves the hand, a partial pelvis and hindlimb, and a relatively complete foot, three other specimens are known. The most complete of these is a partial skeleton (MPC-D 102/007; Figs. 3.44–46; 3.48–54) with a frontal, some vertebrae, a hand, and a partial hindlimb. Vertebrae of this specimen (Fig. 3.45) compare well with the anterior dorsal vertebrae of *Nomingia gobiensis*, and few differences can be discerned. Similarly, the proximal ends of the partial pubes, ischia, and femur preserved with ZPAL MgD-I/98 (Fig. 3.47) are nearly identical to those of *Nomingia gobiensis*. A second partial caenagnathid skeleton (MPC-D NatGeo.2018.040; Figs. 3.95–97) was discovered approximately 20 m east of the *Nomingia gobiensis* type quarry. Comparison of this material to both *Elmisaurus rarus* and *Nomingia gobiensis* reveals no differences with either taxon, and therefore cannot be referred to either taxon. However, this also increases the number of identical overlapping elements between these taxa. Based on this lack of characters distinguishing these taxa, it is possible that they are synonymous, in which case *Elmisaurus rarus* has priority. However, future material may support their distinction and therefore they are best regarded as separate taxa until more complete material is known.

3.4.2 Mandibular Osteohistology

Ontogenetic edentulism—The histology of the lingual and lateral occlusal ridges is incompatible with Wang et al.'s (2017, 2018) hypothesis that they represent vestiges of tooth-bearing structures. In tetrapods with thecodont implantation, including dinosaurs, interdental septa and plates are remnants of multiple generations of alveolar bone and other dental tissues that accumulate passively during tooth migration (LeBlanc et al., 2017b, 2017a). In ground sections, this bone is distinct in texture and orientation, and is accompanied by reversal lines at the margins of alveolar resorption (LeBlanc et al., 2017b). Ground sections of the lingual and lateral occlusal ridges of TMP 1992.036.1237 and UALVP 55639 show that these structures are continuous with and identical in nature to the jawbone (Fig. 3.39C). The lateral occlusal ridges and grooves both lack any evidence of a reversal line, which indicates that they are not formed by resorption during the formation of the tooth and its alveolus. The lingual ridges have LAGs, which cannot be formed in the woven alveolar bone that would be present in an interdental plate, because these tissues are deposited by a different developmental pathway than fibrolamellar bone (LeBlanc et al. 2017a). The bone underlying the lingual groove curves naturally to form this structure; it has not been resorbed as would be expected if it were homologous with alveolar bone or interdental plates. These results indicate that teeth were not present and then lost in these specimens.

Other evidence from caenagnathids also supports the conclusion that caenagnathids did not possess teeth at any point of their development. For example, the caenagnathid *Beibeilong* Pu et al. 2017 lacks teeth as a perinate (Pu et al., 2017), which contrasts starkly with the expectation that teeth are lost during ontogeny. Wang et al. (2018) propose three explanations for this discrepancy with their hypothesis. The first is that *Beibeilong* is unusual amongst oviraptorosaurs

and was always edentulous, rather than losing its teeth through ontogeny. However, our current understanding of caenagnathid phylogeny makes this an unlikely explanation. *Beibeilong* and *Gigantoraptor* are consistently recovered as basal caenagnathids (Pu et al. 2017), along with *Microvenator* Ostrom 1970, which also lacks complex occlusal structures on the dentary (Makovicky and Sues, 1998). Furthermore, *Avimimus* is consistently situated as a sister to Caenagnathoidea, and it lacks occlusal ridges or grooves on the dentaries (Funston et al., 2016b, 2018a; Tsuihiji et al., 2017). It is likely, therefore, that occlusally simple dentaries are the ancestral condition of the more derived caenagnathids, including *Caenagnathasia* and the taxa examined here. While it is possible that derived caenagnathids re-evolved teeth only to lose them through ontogeny, this seems unreasonable, and is refuted by the histological results presented here. Alternatively, Wang et al. (2018) suggest that teeth were present in *Beibeilong*, but that they were lost before eruption of the null generation of teeth. This would require a delay in rhamphotheca development and a change in the rate of ontogenetic edentulism in more derived caenagnathids. Again, this would necessitate that more derived caenagnathids reacquire functional teeth from an essentially edentulous ancestor. This seems unlikely, however, because if teeth do not erupt and are lost before hatching, they provide little to no adaptive benefit. It is therefore difficult to envision a scenario in which they are selected for, in exchange for delaying the development of the rhamphotheca. Finally, Wang et al. (2018) suggest that teeth erupted later and were lost quicker in *Beibeilong*, and so vestigial tooth structures should be present in more mature individuals. This is a less parsimonious explanation that requires two developmental shifts in tooth formation. Furthermore, it is incongruent with current evidence from *Gigantoraptor*, the mandible of which is remarkably similar to that of *Beibeilong* (Ma et al., 2017; Pu et al., 2017). The dentaries of *Gigantoraptor* lack any occlusal ridges or grooves (Ma et

al., 2017), despite presumably being relatively mature compared to *Beibeilong*, and therefore contradict Wang et al.'s (2018) suggestion. It is possible that *Gigantoraptor* and *Beibeilong* differed in the development of the mandible, but their close phylogenetic relationship and the similarity of their mandibles makes this unlikely. In summary, the evidence from *Beibeilong* strongly refutes the hypothesis of ontogenetic edentulism.

These conclusions call into question the reinterpretations of caenagnathid dentary homology put forth by Wang et al. (2017) and Wang et al. (2018). First, the occlusal structures in caenagnathids cannot be homologous to alveoli, because they fail Patterson's (1982) test of similarity by differing in developmental and histological nature. Accordingly, the nature of the so-called 'alveolar canal' described by Wang et al. (2018) requires reexamination. CT evidence from a more complete *Caenagnathasia* (CGMP 402/12457; Fig. 3.99) and *Chirostenotes pergracilis* (Funston and Currie 2014; Fig. 3.99) shows that this canal is the same structure as the major labial cavity described here. This vacuity is connected anteriorly with the mandibular canal, and externally to a large foramen on the labial surface of the dentary just anterior to the external mandibular fenestra (Fig. 3.99). This foramen has been considered a pneumatopore by several authors (Currie et al., 1993; Longrich et al., 2013; Funston and Currie, 2014a), which would make this cavity pneumatic in nature. This is supported by the criteria of O'Connor (2006), which indicate that, in extant birds, fossae and foramina connected to large internal cavities are consistent indicators of pneumaticity. Other evidence suggests that the major labial cavities are pneumatic rather than alveolar in nature. The major labial cavities are complexly divided by trabeculae, which should not form in alveoli, because they are resorbed from a single centre by the dental lamina. Similarly, the histology of the major labial cavity shows that it was expanding and changing shape through ontogeny, rather than contracting as would be expected if

it were formed of alveoli enclosed by bone. Wang et al. (2018) suggest that the major labial cavity (=alveolar canal) was coopted for innervation and vasculature of the rhamphotheca, on the basis of foramina that connect it to the external surface of the bone. Histological results support this function, and show that this cavity is connected to both the occlusal and labial surfaces of the dentary by numerous foramina. The histological evidence therefore suggests that the major labial cavity is a pneumatic chamber, which may have housed an air sac or adipose tissue as well as vasculature and nerves for the rhamphotheca. Similar chambers exist in modern avians (Genbrugge et al., 2012; Van Hemert et al., 2012), where they house adipose tissues or large blood vessels.

       Developmental origin and functions of the occlusal features of the dentary—The histological data presented here indicate that the lingual and lateral occlusal ridges are elaborations of the jawbone (*sensu* Leblanc et al. 2017). Currie et al. (1993) suggested that the lingual groove of caenagnathids was homologous with the alveolar or dental groove of other theropod dinosaurs, which fits reasonably well with the histological evidence. In this case, the lingual ridge, instead of being a novel feature, is simply an enlarged lingual wall of the dental groove, which is typically thin and plate-like in most small theropods (Currie, 1987, 1995; Kobayashi and Barsbold, 2005).

       The homology of the lateral occlusal ridges is difficult to establish, but it is clear that they are composed of jawbone of the dentary. Superficially similar structures are apparent in young *Alligator mississippiensis* Daudin (1802) (LeBlanc et al., 2017b), where jawbone forms the initial separation between alveoli. However, it is unlikely that these features are homologous, because the shape of these interdental separations in *Alligator* are the result of erosion by the replacement crypt of the developing tooth. As histological evidence shows that caenagnathids

lacked teeth during development, and because the occlusal ridges and lingual groove show no sign of erosion or resorption (Fig. 3.39C), they cannot have formed by this mechanism. Instead, they share morphological similarities with the textured rhamphotheca of ducks, turtles, ornithomimids, and hadrosaurs (Barrett, 2005). However, in these examples, the ridges are more numerous and are not manifested in the dentary itself. In birds and turtles, the rhamphotheca generally reflects the shape of the underlying dentary, although it can be more complex and differ slightly in proportions (Genbrugge et al., 2012; Van Hemert et al., 2012; Urano et al., 2018). Therefore, it is likely that the complex occlusal structures of the caenagnathid dentary were also reflected in the overlying rhamphotheca. In this case, these features were likely adaptations to enhance food processing capabilities, as suggested by Funston and Currie (2014). The increased secondary remodeling in these areas (Fig. 3.39B,C; Fig. 3.68C) suggests that these regions were subject to relatively higher stress than the surrounding bone. This is further supported by the increased size and density of Sharpey's fibers near the apex of the occlusal margin of UALVP 55639 (Fig. 3.68A, B). In the beaks of extant finches, larger bundles of Sharpey's fibers are associated with regions of higher stress (Genbrugge et al., 2012). This tentatively supports the interpretation that these features supported structures of the rhamphotheca that were used for food processing.

The bone of the symphysis and the symphyseal shelf differ considerably from those of other theropods. In most non-avian theropods—including tyrannosaurs, ornithomimids, dromaeosaurs and oviraptorids—the dentaries are separate and are connected by soft-tissue, but in caenagnathids these bones are fully fused. The presence of primary bone extending across the midline in TMP 1985.043.0070 suggests that the mandibular processes had merged early in development, at least before one year of age, as indicated by TMP 1985.043.0070. This is the

case in nearly all extant animals with completely fused mandibles, including birds and some mammals (Beecher, 1977; Ten Cate, 1998; Mina, 2001). This would suggest that, if they ever possessed it, caenagnathids lost the midline suture early in ontogeny, possibly before hatching, as in many birds (Jollie, 1957; Maxwell, 2009). However, this is complicated by *Beibeilong*, in which the dentaries are not fused despite relatively high degrees of ossification elsewhere in the skeleton (Pu et al., 2017). Assuming that *Beibeilong* represents the general condition in other caenagnathids, the evidence presented here suggests that the symphysis fused within the first year of life. The hatching status of *Beibeilong* is somewhat ambiguous, however, and it is possible that synostosis of the dentaries occurred late in embryological ontogeny. Studies in extant mammals with fused mandibular symphyses suggest that fusion is an adaptation to facilitate the transfer of bite force to the opposing side, and to resist the resulting dorsoventral shear forces when processing tough foods (Beecher, 1977; Scott et al., 2012). These functions seem reasonable for caenagnathids, especially in light of the enhanced shearing capability of the dentary (Funston and Currie, 2014a).

3.4.3 Growth in caenagnathids

No ontogenetic series of caenagnathids is yet known, but some insights into their general growth patterns can be made from the material sampled here. The most complete growth record is preserved in the pubes of *Caenagnathus collinsi*, UALVP 56638 (Fig. 3.12). The earliest LAG in this specimen represents a stage when this individual was approximately 30% of adult size. Two subsequent growth intervals represent growth of about 20% of adult size, so it is possible that the earliest LAG represents the first year's annual growth mark, rather than the second. In this case, this individual grew to 30% of linear dimensions in the first year, about 50% in the

second year, and 70% in the third year (Fig. 3.12). However, it is also possible that one or more growth marks have been eroded by expansion of the medullary cavity. Regardless, the LAG spacing shows that, like other theropods, caenagnathids had high growth rates during the early stages of life, followed by a transitional point after which growth is significantly slowed. This transition occurs between the fourth and fifth preserved LAGs in UALVP 56638, after reaching about 80% of maximum body size. The final growth interval prior to this transition is significantly shorter than the previous intervals, but still longer than the subsequent intervals. It is likely that sexual maturity was achieved during this interval (Fig. 3.12), because this phenomenon results in slowed growth in extant tetrapods that take longer than one year to reach reproductive maturity (Castanet et al., 2004; Lee and Werning, 2008; Köhler et al., 2012; Botha-Brink et al., 2016). Accordingly, this specimen likely reached sexual maturity prior to the fifth or sixth growth mark, before growth significantly decreased. This transitional interval is also recorded in two other specimens: UALVP 59400 (*Chirostenotes pergracilis*) and UALVP 59606 (*Leptorhynchos elegans*). Conveniently, this asymptote provides a biologically meaningful point at which the growth curves of these individuals can be aligned (Fig. 3.100). The resulting compound curve shows little variation between the taxa, suggesting that growth patterns of DPF caenagnathids did not vary widely (3.100). This curve can therefore also be used to retrocalculate the number of missing growth marks in UALVP 59400 and UALVP 59606, assuming that the growth record of UALVP 56638 is relatively complete. In the case of UALVP 59400, this method estimates fewer missing growth marks (one) than conventional retrocalculation (three). This suggests that this individual was between 10 and 12 years old, and reached reproductive maturity by 4–6 years old, similar to estimates produced for other theropods (Erickson et al. 2007). The LAGs in UALVP 59400 vary in spacing around the cortex, and are more widely

spaced on the medial and lateral sides than the posterior side, which was used for conventional retrocalculation. It is conceivable, therefore, that this leads to the discrepancies in this estimation. In UALVP 59606, both methods estimate two missing growth marks, suggesting that this individual was nine years old and reached reproductive maturity between ages 4 and 6.

Most of the bone deposited during the first few years of life in UALVP 56638 is resorbed by erosive cavities (Fig. 3.10), so little information can be gleaned on growth rates during this period. Fortunately, this interval is preserved in the inner cortex of UALVP 57349, a tibia from the HCF (Figs. 3.92–93). Vascularity in this region varies from longitudinal to reticular, indicating a relatively rapid rate of growth, but slower than the subsequent zone of plexiform vascularization. This specimen preserves a possible first growth mark as an annulus of parallel-fibered bone (Fig. 3.93), rather than a LAG, indicating rapid growth rates and incomplete cessation of growth during the annual nadir. Just prior to this growth mark, there is a transition in vasculature, bone matrix, and osteocyte lacunar density that likely reflects a biological change at this time. Unfortunately without additional specimens, the nature of this change cannot be determined. In any case, the earliest growth of caenagnathids can probably be characterized as slower than the maximum growth rate, and involving some kind of biological change like fledging, cessation of parental care, or dietary change.

These combined lines of evidence suggest that the growth curves of caenagnathids were sigmoidal, beginning with a period of moderate growth, sustaining maximum growth rates for 3–4 years until age 5 or 6, and tapering off after sexual maturity was reached (Fig. 3.100). Unfortunately an absolute value for maximal growth rate can not be determined because there is insufficient data to establish accurate body mass estimates for the individuals sampled. Future work using femora or tibiae may allow absolute growth rates in kg/day to be determined. The

timing of sexual maturity appears to be relatively consistent in the taxa examined, achieved around the fifth year of life. This suggests that differences in adult body sizes of DPF caenagnathids are the result of changes in growth rate, rather than growth period.

3.5 CONCLUSIONS

The material described and sampled here greatly improves our knowledge of caenagnathid anatomy, taxonomy, and development. New specimens confirm the hypothesis that at least three genera were present in the DPF. A partial skeleton referable to *Chirostenotes pergracilis* (UALVP 59400) is a keystone specimen that allows testable referral of isolated specimens to one of three taxa in the DPF. In turn, this provides numerous inferences on differences in morphology, body size, and growth rates in DPF caenagnathids. A large pair of pubes now referable to *Caenagnathus collinsi* provides a model growth curve for a caenagnathid. Together with representatives from *Chirostenotes pergracilis* and *Leptorhynchos elegans*, this shows that body size differences DPF caenagnathids were achieved by variations in growth rate, not growth period. Osteohistology of isolated mandibles from the DPF indicates: 1) the presence of a small-bodied taxon (*Leptorhynchos elegans*); 2) that suture closure does not indicate maturity; and 3) that caenagnathids did not lose their teeth through ontogenetic edentulism. Additional specimens from the HCF reveal the presence of a new taxon, *Apatoraptor pennatus*, and aspects of the early ontogeny of caenagnathids, specifically rapid growth rates and cryptic growth marks. New specimens of *Elmisaurus rarus* show that this caenagnathid possessed a cranial crest, and fill in the blanks in its anatomy. An indeterminate caenagnathid skeleton from close to the type quarry of *Nomingia gobiensis* highlights the similarity and possible synonymy

of this taxon to *Elmisaurus rarus*. Osteohistology shows that caenagnathids were similar to other theropods in growth styles and longevity, apparently reaching sexual maturity in 4–6 years. These advances provide an important foundation for future work on caenagnathids, which have historically been among the most enigmatic theropods from the Late Cretaceous.

3.6 LITERATURE CITED

Bailleul, A. M., J. B. Scannella, J. R. Horner, and D. C. Evans. 2016a. Fusion patterns in the skulls of modern archosaurs reveal that sutures are ambiguous maturity indicators for the Dinosauria. PloS One 11:e0147687.

Bailleul, A. M., C. Nyssen-Behets, B. Lengelé, B. K. Hall, and J. R. Horner. 2016b. Chondroid bone in dinosaur embryos and nestlings (Ornithischia: Hadrosauridae): Insights into the growth of the skull and the evolution of skeletal tissues. Comptes Rendus Palevol 15:49–64.

Balanoff, A. M., and M. A. Norell. 2012. Osteology of *Khaan mckennai* (Oviraptorosauria: Theropoda). Bulletin of the American Museum of Natural History 372:1–77.

Balanoff, A. M., M. A. Norell, A. V. C. Hogan, and G. S. Bever. 2018. The Endocranial Cavity of Oviraptorosaur Dinosaurs and the Increasingly Complex, Deep History of the Avian Brain. Brain, Behavior and Evolution 91:125–135.

Barrett, P. M. 2005. The diet of ostrich dinosaurs (Theropoda: Ornithomimosauria).

Palaeontology 48:347–358.

Barsbold, R. 1981. Toothless Dinosaurs of Mongolia. Transactions of the Joint Soviet Mongolian

Paleontological Expedition 15:28–39.

Barsbold, R., H. Osmólska, M. Watabe, P. J. Currie, and K. Tsogtbaatar. 2000a. A new

oviraptorosaur [Dinosauria, Theropoda] from Mongolia: the first dinosaur with a

pygostyle. Acta Palaeontologica Polonica 45:97–106.

Barsbold, R., P. J. Currie, N. P. Myhrvold, H. Osmólska, K. Tsogtbaatar, and M. Watabe. 2000b.

A pygostyle from a non-avian theropod. Nature 403:155–156.

Beecher, R. M. 1977. Function and fusion at the mandibular symphysis. American Journal of

Physical Anthropology 47:325–335.

Bell, P. R., P. J. Currie, and D. A. Russell. 2015. Large caenagnathids (Dinosauria,

Oviraptorosauria) from the uppermost Cretaceous of western Canada. Cretaceous

Research 52:101–107.

Benner, E., T. M. Cullen, and D. C. Evans. 2016. Morphological and histological analysis of a

new large-bodied caenagnathid specimen (Theropoda: Oviraptorosauria) from the Hell

Creek Formation (Montana). Vertebrate Anatomy Morphology Palaeontology CSVP

2016 Abstracts:9.

Botha-Brink, J., D. Codron, A. K. Huttenlocker, K. D. Angielczyk, and M. Ruta. 2016. Breeding

Young as a Survival Strategy during Earth's Greatest Mass Extinction. Scientific Reports

6.

Britt, B. B. 1993. Pneumatic postcranial bones in dinosaurs and other archosaurs. Ph.D.

Dissertation, University of Calgary, Calgary, 393 pp.

Brochu, C. A. 1996. Closure of neurocentral sutures during crocodilian ontogeny: implications for maturity assessment in fossil archosaurs. Journal of Vertebrate Paleontology 16:49–62.

Brochu, C. A. 2003. Osteology of *Tyrannosaurus rex*: Insights from a nearly complete skeleton and high-resolution computed tomographic analysis of the skull. Journal of Vertebrate Paleontology 22:1–138.

Bromage, T. G., R. S. Lacruz, R. Hogg, H. M. Goldman, S. C. McFarlin, J. Warshaw, W. Dirks, A. Perez-Ochoa, I. Smolyar, D. H. Enlow, and A. Boyde. 2009. Lamellar Bone is an Incremental Tissue Reconciling Enamel Rhythms, Body Size, and Organismal Life History. Calcified Tissue International 84:388–404.

Campione, N. E., D. C. Evans, C. M. Brown, and M. T. Carrano. 2014. Body mass estimation in non-avian bipeds using a theoretical conversion to quadruped stylopodial proportions. Methods in Ecology and Evolution 5:913–923.

Castanet, J., S. Croci, F. Aujard, M. Perret, J. Cubo, and E. de Margerie. 2004. Lines of arrested growth in bone and age estimation in a small primate: Microcebus murinus. Journal of Zoology 263:31–39.

Chiappe, L. M., J. Shu'An, J. Qiang, and M. A. Norell. 1999. Anatomy and Systematics of the Confuciusornithidae (Theropoda: Aves) from the Late Mesozoic of Northeastern China. Bulletin of the American Museum of Natural History 242:1–89.

Clark, J. M., M. Norell, and L. M. Chiappe. 1999. An oviraptorid skeleton from the late Cretaceous of Ukhaa Tolgod, Mongolia, preserved in an avianlike brooding position over an oviraptorid nest. American Museum Novitates 3265:1–36.

Clark, J. M., M. A. Norell, and R. Barsbold. 2001. Two new oviraptorids (Theropoda: Oviraptorosauria), Upper Cretaceous Djadokhta Formation, Ukhaa Tolgod, Mongolia. Journal of Vertebrate Paleontology 21:209–213.

Clark, J. M., M. A. Norell, and T. Rowe. 2002. Cranial anatomy of *Citipati osmolskae* (Theropoda, Oviraptorosauria), and a reinterpretation of the holotype of *Oviraptor philoceratops*. American Museum Novitates 1–24.

Cullen, T. M., D. C. Evans, M. J. Ryan, P. J. Currie, and Y. Kobayashi. 2014. Osteohistological variation in growth marks and osteocyte lacunar density in a theropod dinosaur (Coelurosauria: Ornithomimidae). BMC Evolutionary Biology 14:231.

Currie, P., G. Funston, and H. Osmolska. 2016. New specimens of the crested theropod dinosaur *Elmisaurus rarus* from Mongolia. Acta Palaeontologica Polonica 61:143–157.

Currie, P. J. 1987. Bird-like characteristics of the jaws and teeth of troodontid theropods (Dinosauria, Saurischia). Journal of Vertebrate Paleontology 7:72–81.

Currie, P. J. 1989. The first records of *Elmisaurus* (Saurischia, Theropoda) from North America. Canadian Journal of Earth Sciences 26:1319–1324.

Currie, P. J. 1992. Saurischian dinosaurs of the Late Cretaceous of Asia and North America; pp. in Aspects of Nonmarine Cretaceous Geology: International Symposium on Nonmarine Cretaceous Correlations. China Ocean Press, Beijing.

Currie, P. J. 1995. New information on the anatomy and relationships of *Dromaeosaurus albertensis* (Dinosauria: Theropoda). Journal of Vertebrate Paleontology 15:576–591.

Currie, P. J. 2003. Allometric growth in tyrannosaurids (Dinosauria: Theropoda) from the Upper Cretaceous of North America and Asia. Canadian Journal of Earth Sciences 40:651–665.

Currie, P. J., and D. A. Russell. 1988. Osteology and relationships of *Chirostenotes pergracilis* (Saurischia, Theropoda) from the Judith River (Oldman) Formation of Alberta, Canada. Canadian Journal of Earth Sciences 25:972–986.

Currie, P. J., and J.-H. Peng. 1993. A juvenile specimen of *Saurornithoides mongoliensis* from the Upper Cretaceous of northern China. Canadian Journal of Earth Sciences 30:2224–2230.

Currie, P. J., S. J. Godfrey, and L. Nessov. 1993. New caenagnathid (Dinosauria: Theropoda) specimens from the Upper Cretaceous of North America and Asia. Canadian Journal of Earth Sciences 30:2255–2272.

Eberth, D. A. 1990. Stratigraphy and sedimentology of vertebrate microfossil sites in the uppermost Judith River Formation (Campanian), Dinosaur Provincial Park, Alberta, Canada. Palaeogeography, Palaeoclimatology, Palaeoecology 78:1–36.

Eberth, D. A., and D. R. Braman. 2012. A revised stratigraphy and depositional history for the Horseshoe Canyon Formation (Upper Cretaceous), southern Alberta plains. Canadian Journal of Earth Sciences 49:1053–1086.

Edington, G. H., and A. E. Miller. 1942. XII.—The Avian Ulna: Its Quill - Knobs. Proceedings of the Royal Society of Edinburgh. Section B. Biology 61:138–148.

Enlow, D. H. 1962. A Study of the Post-Natal Growth and Remodeling of Bone. American Journal of Anatomy 110:79–101.

Erickson, G. 2000. Growth curve of *Psittacosaurus mongoliensis* Osborn (Ceratopsia: Psittacosauridae) inferred from long bone histology. Zoological Journal of the Linnean Society 130:551–566.

Erickson, G. M., K. Curry Rogers, D. J. Varricchio, M. A. Norell, and X. Xu. 2007. Growth patterns in brooding dinosaurs reveals the timing of sexual maturity in non-avian dinosaurs and genesis of the avian condition. Biology Letters 3:558–561.

Funston, G. F., and P. J. Currie. 2014. A previously undescribed caenagnathid mandible from the late Campanian of Alberta, and insights into the diet of *Chirostenotes pergracilis* (Dinosauria: Oviraptorosauria). Canadian Journal of Earth Sciences 51:156–165.

Funston, G. F., and P. J. Currie. 2016. A new caenagnathid (Dinosauria: Oviraptorosauria) from the Horseshoe Canyon Formation of Alberta, Canada, and a reevaluation of the relationships of Caenagnathidae. Journal of Vertebrate Paleontology 36:e1160910.

Funston, G. F., and P. J. Currie. 2018. A small caenagnathid tibia from the Horseshoe Canyon Formation (Maastrichtian): Implications for growth and lifestyle in oviraptorosaurs. Cretaceous Research 92:220–230.

Funston, G. F., P. J. Currie, and M. Burns. 2016a. New elmisaurine specimens from North America and their relationship to the Mongolian *Elmisaurus rarus*. Acta Palaeontologica Polonica 61:159–173.

Funston, G. F., W. S. Persons, G. J. Bradley, and P. J. Currie. 2015. New material of the large-bodied caenagnathid *Caenagnathus collinsi* from the Dinosaur Park Formation of Alberta, Canada. Cretaceous Research 54:179–187.

Funston, G. F., S. E. Mendonca, P. J. Currie, and R. Barsbold. 2018. Oviraptorosaur anatomy, diversity and ecology in the Nemegt Basin. Palaeogeography, Palaeoclimatology, Palaeoecology.

Funston, G. F., P. J. Currie, D. A. Eberth, M. J. Ryan, T. Chinzorig, D. Badamgarav, and N. R. Longrich. 2016b. The first oviraptorosaur (Dinosauria: Theropoda) bonebed: evidence of gregarious behaviour in a maniraptoran theropod. Scientific Reports 6:35782.

Genbrugge, A., D. Adriaens, B. De Kegel, L. Brabant, L. Van Hoorebeke, J. Podos, J. Dirckx, P. Aerts, and A. Herrel. 2012. Structural tissue organization in the beak of Java and Darwin's finches. Journal of Anatomy 221:383–393.

Gilmore, C. W. 1924. A new coelurid dinosaur from the Belly River Cretaceous of Alberta. Canada Geological Survey Bulletin 38:1–12.

Hedrick, B. P., C. Gao, A. R. Tumarkin-Deratzian, C. Shen, J. L. Holloway, F. Zhang, K. D. Hankenson, S. Liu, J. Anné, and P. Dodson. 2016. An Injured *Psittacosaurus* (Dinosauria: Ceratopsia) From the Yixian Formation (Liaoning, China): Implications for *Psittacosaurus* Biology: Psittacosaurus Fibular Fracture. The Anatomical Record 299:897–906.

Horner, J. R., A. De Ricqlès, and K. Padian. 2000. Long bone histology of the hadrosaurid dinosaur *Maiasaura peeblesorum* : growth dynamics and physiology based on an ontogenetic series of skeletal elements. Journal of Vertebrate Paleontology 20:115–129.

Horner, J. R., H. N. Woodward, and A. M. Bailleul. 2016. Mineralized tissues in dinosaurs interpreted as having formed through metaplasia: A preliminary evaluation. Comptes Rendus Palevol 15:176–196.

Hou, L., Z. Zhonghe, L. D. Martin, and A. Feduccia. 1995. A beaked bird from the Jurassic of China. Nature 377:616–618.

Ingolfsson, A. 1970. The moult of remiges and retrices in Great Black-backed Gulls *Larus marinus* and Glaucous Gulls *L. hyperboreus* in Iceland. Ibis 112:83–92.

Jollie, M. T. 1957. The head skeleton of the chicken and remarks on the anatomy of this region in other birds. Journal of Morphology 100:389–436.

Kirkland, J. I., and D. G. Wolfe. 2001. First definitive therizinosaurid (Dinosauria; Theropoda) from North America. Journal of Vertebrate Paleontology 21:410–414.

Kobayashi, Y., and R. Barsbold. 2005. Reexamination of a primitive ornithomimosaur, *Garudimimus brevipes* Barsbold, 1981 (Dinosauria: Theropoda), from the Late Cretaceous of Mongolia. Canadian Journal of Earth Sciences 42:1501–1521.

Köhler, M., N. Marín-Moratalla, X. Jordana, and R. Aanes. 2012. Seasonal bone growth and physiology in endotherms shed light on dinosaur physiology. Nature 487:358–361.

Kurzanov, S. M. 1981. An unusual theropod from the Upper Cretaceous of Mongolia. Transactions of the Joint Soviet Mongolian Paleontological Expedition 15:39–49.

Lamanna, M. C., H.-D. Sues, E. R. Schachner, and T. R. Lyson. 2014. A New Large-Bodied Oviraptorosaurian Theropod Dinosaur from the Latest Cretaceous of Western North America. PLoS ONE 9:e92022.

LeBlanc, A. R. H., D. O. Lamoureux, and M. W. Caldwell. 2017a. Mosasaurs and snakes have a periodontal ligament: timing and extent of calcification, not tissue complexity, determines tooth attachment mode in reptiles. Journal of Anatomy 231:869–885.

LeBlanc, A. R. H., K. S. Brink, T. M. Cullen, and R. R. Reisz. 2017b. Evolutionary implications of tooth attachment versus tooth implantation: A case study using dinosaur, crocodilian, and mammal teeth. Journal of Vertebrate Paleontology 37:e1354006.

Lee, A. H., and S. Werning. 2008. Sexual maturity in growing dinosaurs does not fit reptilian growth models. Proceedings of the National Academy of Sciences 105:582–587.

Longrich, N. R., K. Barnes, S. Clark, and L. Millar. 2013. Caenagnathidae from the Upper

    Campanian Aguja Formation of West Texas, and a Revision of the Caenagnathinae.

    Bulletin of the Peabody Museum of Natural History 54:23–49.

Lü, J., P. J. Currie, L. Xu, X. Zhang, H. Pu, and S. Jia. 2013. Chicken-sized oviraptorid dinosaurs

    from central China and their ontogenetic implications. Naturwissenschaften 100:165–

    175.

Ma, W., J. Wang, M. Pittman, Q. Tan, L. Tan, B. Guo, and X. Xu. 2017. Functional anatomy of

    a giant toothless mandible from a bird-like dinosaur: *Gigantoraptor* and the evolution of

    the oviraptorosaurian jaw. Scientific Reports 7.

Makovicky, P. J., and H.-D. Sues. 1998. Anatomy and phylogenetic relationships of the theropod

    dinosaur *Microvenator celer* from the Lower Cretaceous of Montana. American Museum

    Novitates 3240:1–27.

Maxwell, E. E. 2009. Comparative ossification and development of the skull in palaeognathous

    birds (Aves: Palaeognathae). Zoological Journal of the Linnean Society 156:184–200.

Mina, M. 2001. Regulation of Mandibular Growth and Morphogenesis. Critical Reviews in Oral

    Biology & Medicine 12:276–300.

Norell, M. A., and P. J. Makovicky. 1997. Important features of the dromaeosaur skeleton:

    information from a new specimen. American Museum Novitates 3215:1–28.

Norell, M. A., and P. J. Makovicky. 1999. Important features of the dromaeosaurid skeleton II:

    Information from newly collected specimens of *Velociraptor mongoliensis*. American

    Museum Novitates 3282:1–45.

Norell, M. A., A. M. Balanoff, D. E. Barta, and G. M. Erickson. 2018. A Second Specimen of *Citipati Osmolskae* Associated With a Nest of Eggs from Ukhaa Tolgod, Omnogov Aimag, Mongolia. American Museum Novitates 3899:1–44.

O'Connor, J., G. M. Erickson, M. Norell, A. M. Bailleul, H. Hu, and Z. Zhou. 2018. Medullary bone in an Early Cretaceous enantiornithine bird and discussion regarding its identification in fossils. Nature Communications 9.

O'Connor, P. M. 2006. Postcranial pneumaticity: An evaluation of soft-tissue influences on the postcranial skeleton and the reconstruction of pulmonary anatomy in archosaurs. Journal of Morphology 267:1199–1226.

Ortega, F., F. Escaso, and J. L. Sanz. 2010. A bizarre, humped Carcharodontosauria (Theropoda) from the Lower Cretaceous of Spain. Nature 467:203–206.

Osborn, H. F. 1924. Three new theropoda, *Protoceratops* zone, central Mongolia. American Museum Novitates 144:1–12.

Osmólska, H. 1976. New light on the skull anatomy and systematic position of *Oviraptor*. Nature 262:683–684.

Osmólska, H. 1981. Coossified tarsometatarsi in theropod dinosaurs and their bearing on the problem of bird origins. Palaeontologia Polonica 42:79–95.

Osmólska, H. 1996. An unusual theropod dinosaur from the Late Cretaceous Nemegt Formation of Mongolia. Acta Palaeontologica Polonica 41:1–38.

Osmólska, H. 2004a. Evidence on relation of brain to endocranial cavity in oviraptorid dinosaurs. Acta Palaeontologica Polonica 49.

Osmólska, H. 2004b. Evidence on relation of brain to endocranial cavity in oviraptorid dinosaurs. Acta Palaeontologica Polonica 49.

Ostrom, J. H. 1969. Osteology of *Deinonychus Antirrhopus*, an Unusual Theropod from the

    Lower Cretaceous of Montana. Bulletin 30 of the Peabody Museum of Natural History,

    Yale University, New Haven, Connecticut, 172 pp.

Parks, W. A. 1933. New species of dinosaurs and turtles from the Upper Cretaceous Formations

    of Alberta. University of Toronto Studies Geological Series 34:1–24.

Patterson, C. 1982. Morphological Characters and Homology; pp. 21–74 in K. A. Joysey and A.

    E. Friday (eds.), Problems of Phylogenetic Reconstruction. vol. Systematics Association

    Special Volume No. 21. Academic Press, London and New York.

Pu, H., D. K. Zelenitsky, J. Lü, P. J. Currie, K. Carpenter, L. Xu, E. B. Koppelhus, S. Jia, L.

    Xiao, H. Chuang, T. Li, M. Kundrát, and C. Shen. 2017. Perinate and eggs of a giant

    caenagnathid dinosaur from the Late Cretaceous of central China. Nature

    Communications 8:14952.

Qiang, J., P. J. Currie, M. A. Norell, and J. Shu-An. 1998. Two feathered dinosaurs from

    northeastern China. Nature 393:753–761.

Scott, J. E., A. S. Hogue, and M. J. Ravosa. 2012. The adaptive significance of mandibular

    symphyseal fusion in mammals: Diet and mandibular symphyseal fusion. Journal of

    Evolutionary Biology 25:661–673.

Smith, K. K. 1988. Form and function of the tongue in agamid lizards with comments on its

    phylogenetic significance. Journal of Morphology 196:157–171.

Solheim, R. 2011. Moult pattern of primaries and secondaries in Eagle Owls *Bubo bubo*. Ornis

    Norvegica 34:1–9.

Solheim, R. 2012. Wing feather moult and age determination of Snowy Owls *Bubo scandiacus*.

    Ornis Norvegica 35:48–67.

Sternberg, C. M. 1932. Two new theropod dinosaurs from the Belly River Formation of Alberta. The Canadian Field-Naturalist 46:99–105.

Sternberg, C. M. 1934. Notes on certain recently described dinosaurs. The Canadian Field-Naturalist 48:7–8.

Sternberg, R. M. 1940. A toothless bird from the Cretaceous of Alberta. Journal of Paleontology 14:81–85.

Sues, H.-D. 1997. On *Chirostenotes*, a Late Cretaceous oviraptorosaur (Dinosauria: Theropoda) from western North America. Journal of Vertebrate Paleontology 17:698–716.

Sues, H.-D., and A. Averianov. 2015. New material of *Caenagnathasia martinsoni* (Dinosauria: Theropoda: Oviraptorosauria) from the Bissekty Formation (Upper Cretaceous: Turonian) of Uzbekistan. Cretaceous Research 54:50–59.

Sullivan, R. M., S. E. Jasinski, and M. P. A. Van Tomme. 2011. A new caenagnathid *Ojoraptorsaurus boerei*, n. gen., n. sp (Dinosauria, Oviraptorosauria), from the Upper Ojo Alamo Formation (Naashoibito Member), San Juan Basin, New Mexico. New Mexico Museum of Natural History and Science Bulletin 53:418–428.

Ten Cate, A. R. 1998. Oral Histology: Development, Structure, and Function, 5th ed. University of Michigan, Ann Arbor, pp.

Tsuihiji, T., M. Watabe, R. Barsbold, and K. Tsogtbaatar. 2015. A gigantic caenagnathid oviraptorosaurian (Dinosauria: Theropoda) from the Upper Cretaceous of the Gobi Desert, Mongolia. Cretaceous Research 56:60–65.

Tsuihiji, T., M. Watabe, K. Tsogtbaatar, and R. Barsbold. 2016. Dentaries of a caenagnathid (Dinosauria: Theropoda) from the Nemegt Formation of the Gobi Desert in Mongolia. Cretaceous Research 63:148–153.

Tsuihiji, T., L. M. Witmer, M. Watabe, R. Barsbold, K. Tsogtbaatar, S. Suzuki, and P. Khatanbaatar. 2017. New information on the cranial morphology of *Avimimus* (Theropoda: Oviraptorosauria). Journal of Vertebrate Paleontology e1347177.

Tumarkin-Deratzian, A. R. 2009. Evaluation of Long Bone Surface Textures as Ontogenetic Indicators in Centrosaurine Ceratopsids. The Anatomical Record: Advances in Integrative Anatomy and Evolutionary Biology 292:1485–1500.

Turner, A. H., P. J. Makovicky, and M. A. Norell. 2007. Feather Quill Knobs in the Dinosaur Velociraptor. Science 317:1721–1721.

Urano, Y., K. Tanoue, R. Matsumoto, S. Kawabe, T. Ohashi, and S. Fujiwara. 2018. How does the curvature of the upper beak bone reflect the overlying rhinotheca morphology? Journal of Morphology 279:636–647.

Van Hemert, C., C. M. Handel, J. E. Blake, R. M. Swor, and T. M. O'Hara. 2012. Microanatomy of passerine hard-cornified tissues: Beak and claw structure of the black-capped chickadee (Poecile atricapillus). Journal of Morphology 273:226–240.

Wang, S., Q. Zhang, and R. Yang. 2018. Reevaluation of the Dentary Structures of Caenagnathid Oviraptorosaurs (Dinosauria, Theropoda). Scientific Reports 8.

Wang, S., J. Stiegler, P. Wu, C.-M. Chuong, D. Hu, A. Balanoff, Y. Zhou, and X. Xu. 2017. Heterochronic truncation of odontogenesis in theropod dinosaurs provides insight into the macroevolution of avian beaks. Proceedings of the National Academy of Sciences 201708023.

Wang, X., A. J. McGowan, and G. J. Dyke. 2011. Avian Wing Proportions and Flight Styles: First Step towards Predicting the Flight Modes of Mesozoic Birds. PLoS ONE 6:e28672.

Woodward, H. N. 2019. Maiasaura (Dinosauria: Hadrosauridae) Tibia Osteohistology Reveals Non-annual Cortical Vascular Rings in Young of the Year. Frontiers in Earth Science 7.

Woodward, H. N., J. R. Horner, and J. O. Farlow. 2011a. Osteohistological Evidence for Determinate Growth in the American Alligator. Journal of Herpetology 45:339–342.

Woodward, H. N., J. R. Horner, and J. O. Farlow. 2014. Quantification of intraskeletal histovariability in *Alligator mississippiensis* and implications for vertebrate osteohistology. PeerJ 2:e422.

Woodward, H. N., T. H. Rich, A. Chinsamy, and P. Vickers-Rich. 2011b. Growth dynamics of Australia's polar dinosaurs. PLoS One 6:e23339.

Woodward, H. N., E. A. Freedman Fowler, J. O. Farlow, and J. R. Horner. 2015. *Maiasaura*, a model organism for extinct vertebrate population biology: a large sample statistical assessment of growth dynamics and survivorship. Paleobiology 41:503–527.

Xu, X., Q. Tan, J. Wang, X. Zhao, and L. Tan. 2007. A gigantic bird-like dinosaur from the Late Cretaceous of China. Nature.

Yao, X., X.-L. Wang, C. Sullivan, S. WANG, T. Stidham, and X. Xu. 2015. *Caenagnathasia* sp. (Theropoda: Oviraptorosauria) from the Iren Dabasu Formation (Upper Cretaceous: Campanian) of Erenhot, Nei Mongol, China. Vertebrata PalAsiatica 53:291–298.

Yu, Y., K. Wang, S. Chen, C. Sullivan, S. Wang, P. Wang, and X. Xu. 2018. A new caenagnathid dinosaur from the Upper Cretaceous Wangshi Group of Shandong, China, with comments on size variation among oviraptorosaurs. Scientific Reports 8.

Zanno, L. E. 2006. The pectoral girdle and forelimb of the primitive therizinosauroid *Falcarius Utahensis* (Theropoda, Maniraptora): analyzing evolutionary trends within Therizinosauroidea. Journal of Vertebrate Paleontology 26:636–650.

Zanno, L. E., and S. D. Sampson. 2005. A new oviraptorosaur (Theropoda, Maniraptora) from the Late Cretaceous (Campanian) of Utah. Journal of Vertebrate Paleontology 25:897–904.

Zelenitsky, D. K., F. Therrien, G. M. Erickson, C. L. DeBuhr, Y. Kobayashi, D. A. Eberth, and F. Hadfield. 2012. Feathered Non-Avian Dinosaurs from North America Provide Insight into Wing Origins. Science 338:510–514.

Zhou, Z.-H., X.-L. Wang, F. Zhang, and X. Xu. 2000. Important features of *Caudipteryx* - evidence from two nearly complete new specimens. Vertebrata PalAsiatica 10:241–254.

3.7 FIGURES & TABLES
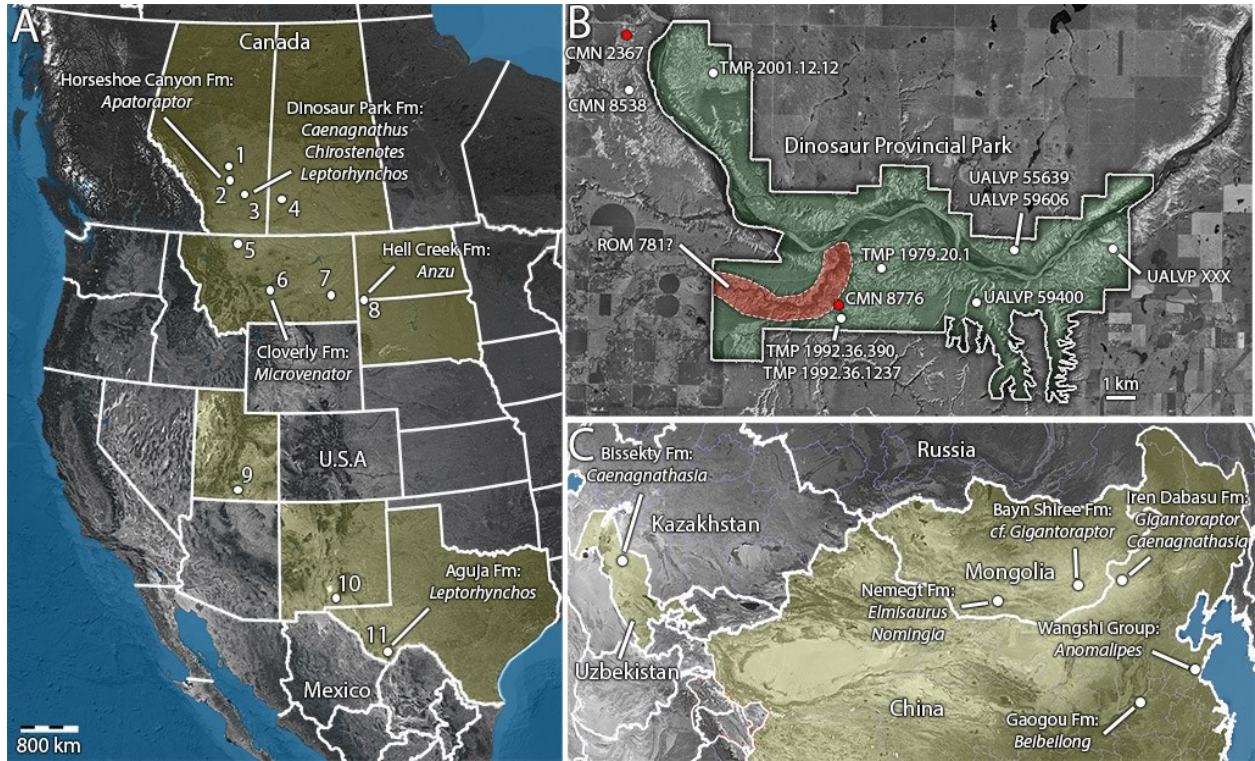
(Previous page)
Fig. 3.0. Maps of caenagnathid occurrences.

Map (A) of North America, showing provinces and states from which caenagnathids have been collected (highlighted), and formations where caenagnathids are known to occur. Names and horizons are provided for caenagnathids for which mandibular material has been found. Map (B) of Dinosaur Provincial Park in Alberta, Canada (highlighted), showing locations of notable caenagnathid specimens. Types are highlighted in red. Red area indicates uncertainty in the provenance of ROM 781. Map (C) of western Asia, showing countries where caenagnathids have been found (highlighted), with names and horizons of named taxa. **Abbreviations: 1**, Scollard Formation (Maastrichtian); **2**, Horseshoe Canyon Formation (Campanian-Maastrichtian), **3**, Dinosaur Park Formation (Campanian); **4**, Frenchman Formation (Maastrichtian), **5**, Hell Creek Formation, Northern Montana (Maastrichtian); **6**, Cloverly Formation (Aptian-Albian); **7**, Hell Creek Formation, Eastern Montana (Maastrichtian); **8**, Hell Creek Formation, North and South Dakota (Maastrichtian); **9**, Kaiparowitz Formation (Campanian); **10,** Ojo Alamo Formation (Maastrichtian); **11**, Aguja Formation (Campanian).
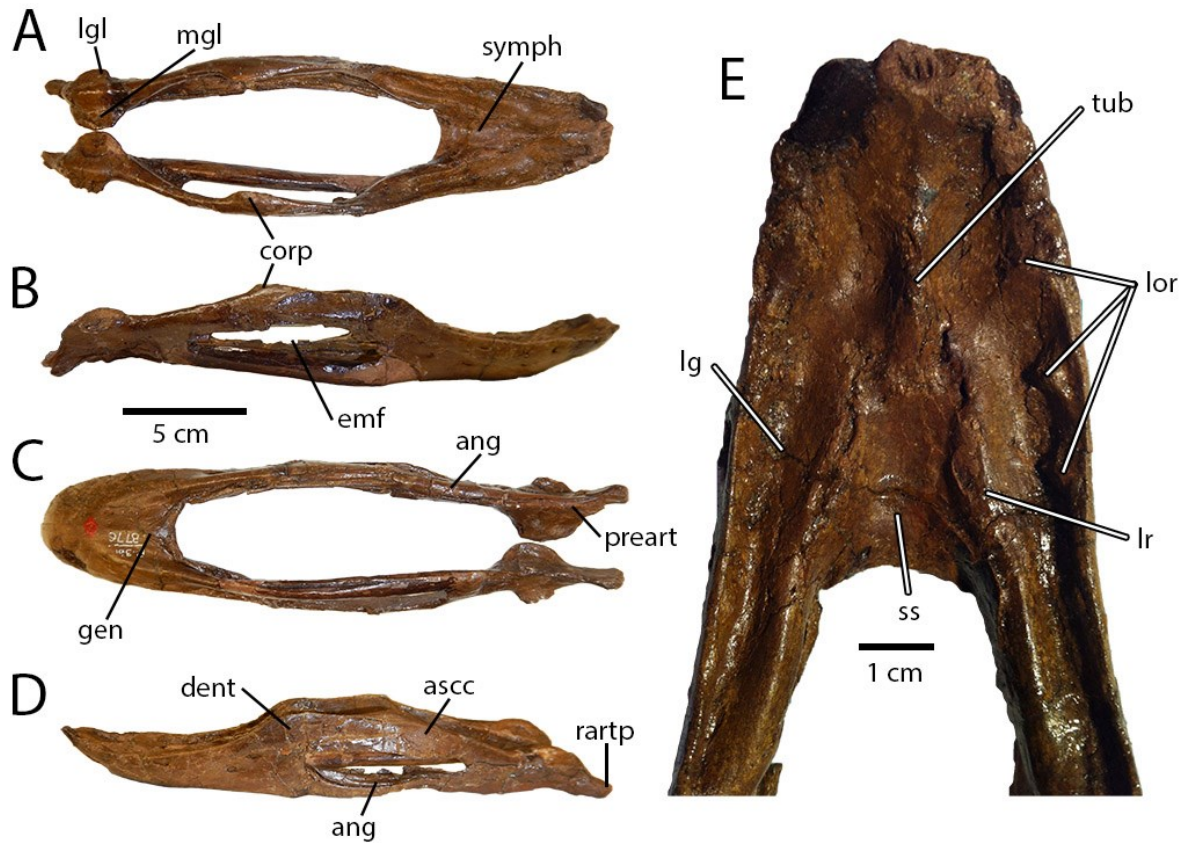
Fig. 3.1. CMN 8776, holotype mandible of *Caenagnathus collinsi.*

Photographs of CMN 8776 in dorsal (A), right lateral (B), ventral (C), and left lateral (D) views.

Detail (E) of occlusal surface of dentaries in dorsal view. **Abbreviations: ang**, angular; **ascc**, articular-surangular-coronoid complex; **corp**, coronoid process; **dent**, dentary; **emf**, external mandibular fenestra; **gen**, attachment of *m. genioglossus*; **lg**, lingual groove; **lgl**, lateral glenoid; **lor**, lateral occlusal ridges; **lr**, lingual ridge; **mgl**, medial glenoid; **preart**, prearticular; **rartp**, retroarticular process; **ss**, symphyseal sulcus; **symph**, symphysis; **tub**, tubercle.

294
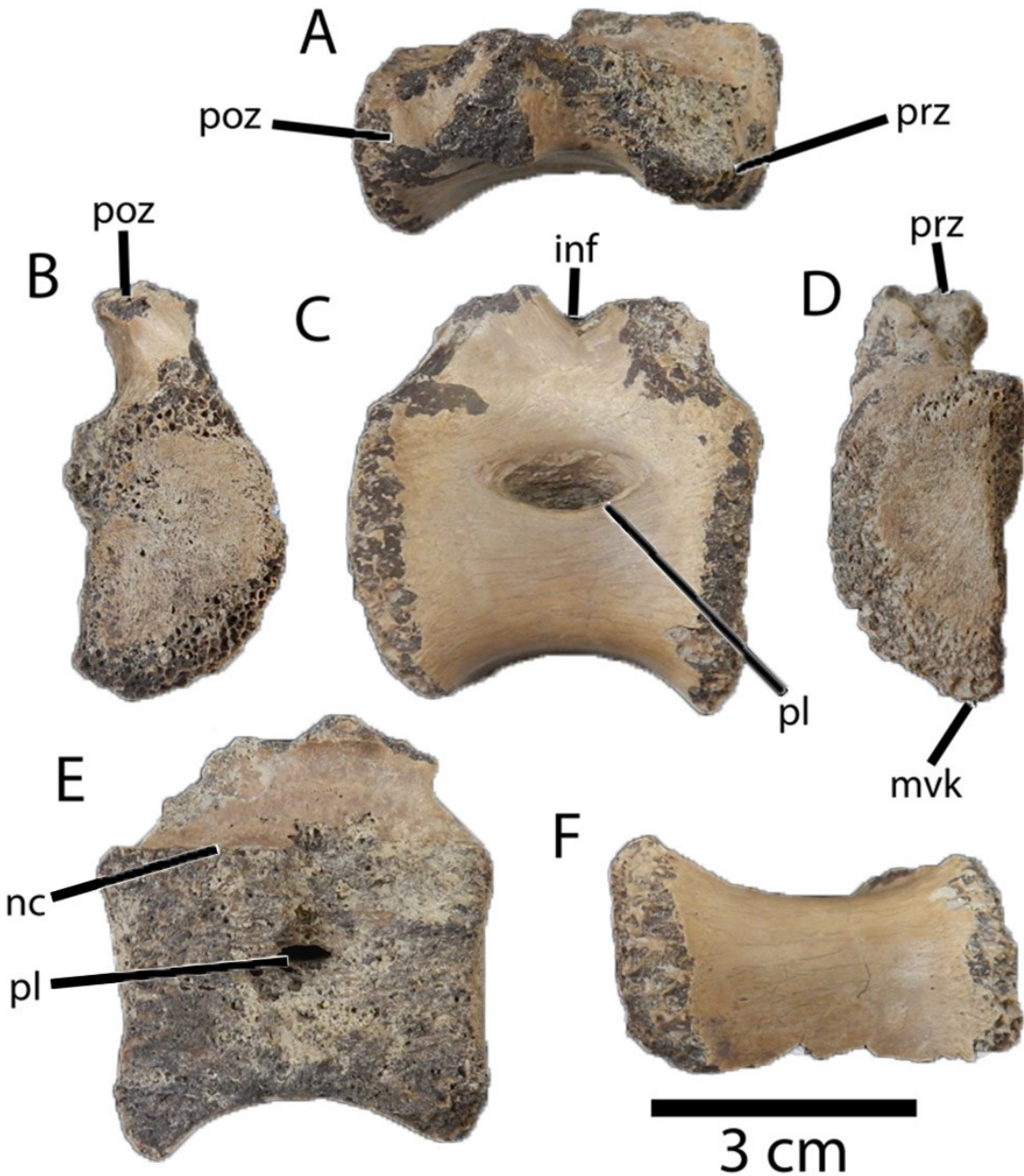
Fig. 3.2. UALVP 55725, partial caudal centrum of *Caenagnathus collinsi.*

UALVP 55725 in dorsal (A), posterior (B), lateral (C), anterior (D), medial (E), and ventral (F)

views. **Abbreviations: inf,** infradiapophyseal fossa; **mvk,** midline ventral keel; **nc,** neural canal;

pl, pleurocoel; **poz,** base of the postzygapophysis; **prz,** base of the prezygapophysis.
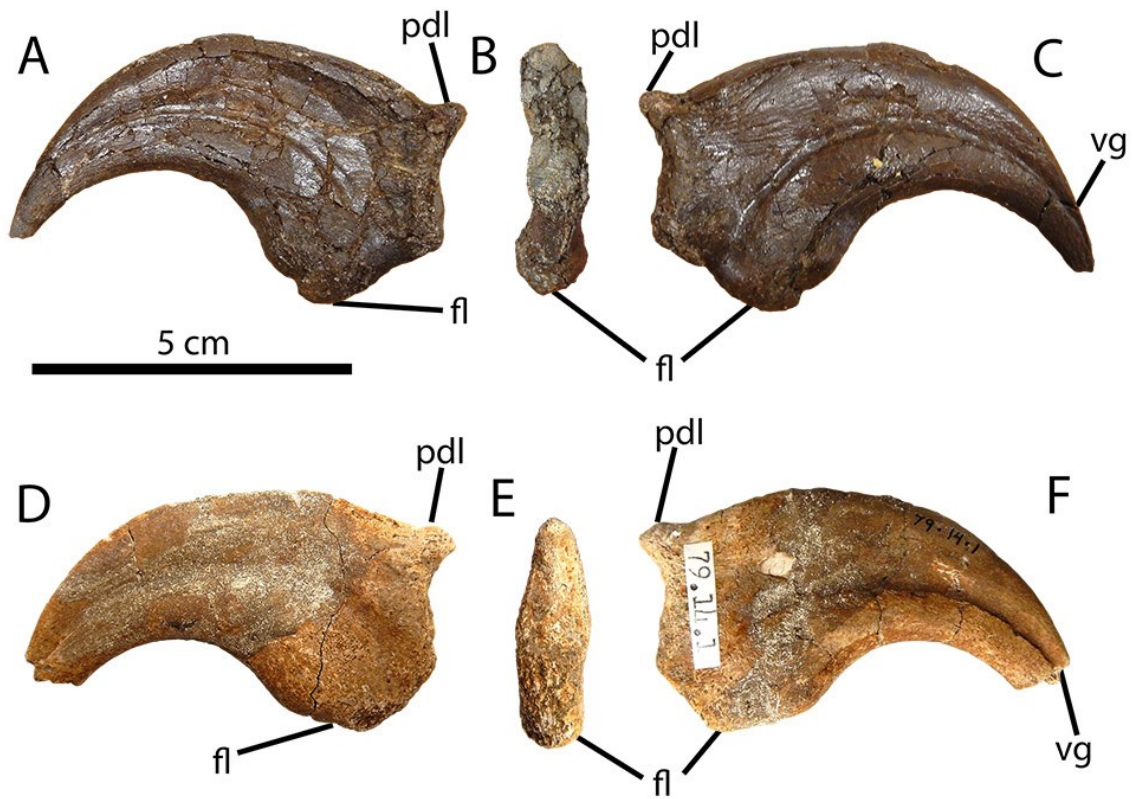
Fig. 3.3. Manual unguals I-2 of *Caenagnathus collinsi*.

TMP 1982.019.0222 in medial or lateral (A), proximal (B) and medial or lateral (C) views. TMP 1979.014.0001 in medial or lateral (D), proximal (E), and medial or lateral (F) view.

Abbreviations: fl, flexor tubercle; **pdl**, proximodorsal lip; **vg**, vascular groove.
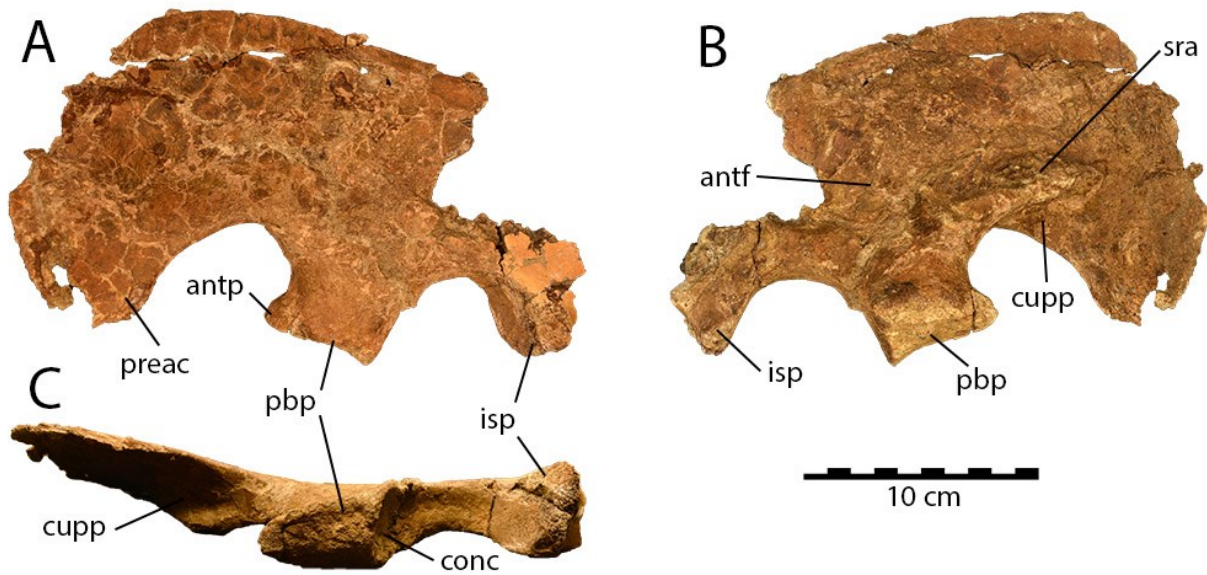
Fig. 3.4. Partial left ilium of *Caenagnathus collinsi*.

UALVP 59791 in lateral (A), medial (B), and ventral (C) views. **Abbreviations: antf**, anterior fossa; **antp**, anterior process of pubic peduncle; **conc**, concavity; **cupp,** cuppedicus fossa; **isp**, ischiadic peduncle; **pbp**, pubic peduncle; **preac**, preacetabular process; **sra**, sacral rib attachment.
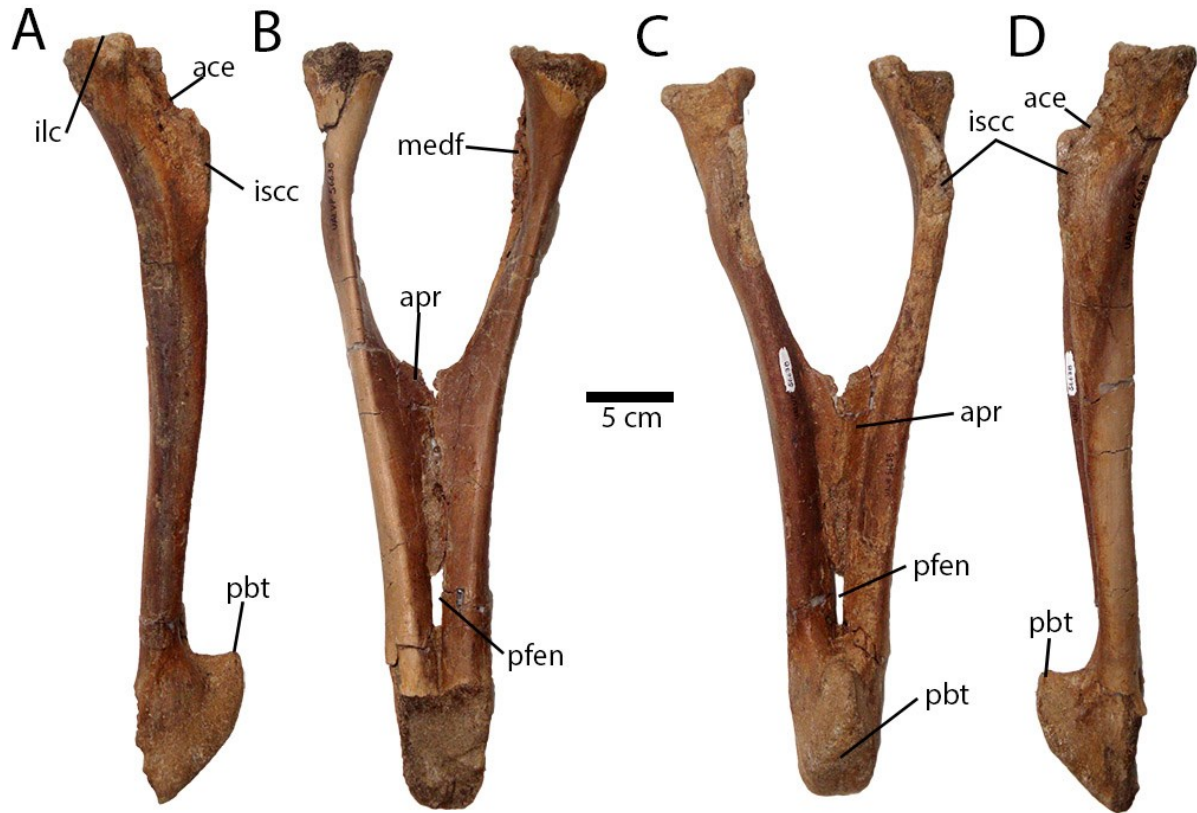
Fig. 3.5. Pubes of *Caenagnathus collinsi.*

UALVP 56648 in left lateral (A), anterior (B), posterior (C), and right lateral (D) views.

Abbreviations: ace, acetabulum; **apr**, pubic apron; **ilc**, iliac contact; **iscc**, ischiadic contact;

medf, medial fossa; **pbt**, posterior process of pubic boot; **pfen**, pubic fenestra.
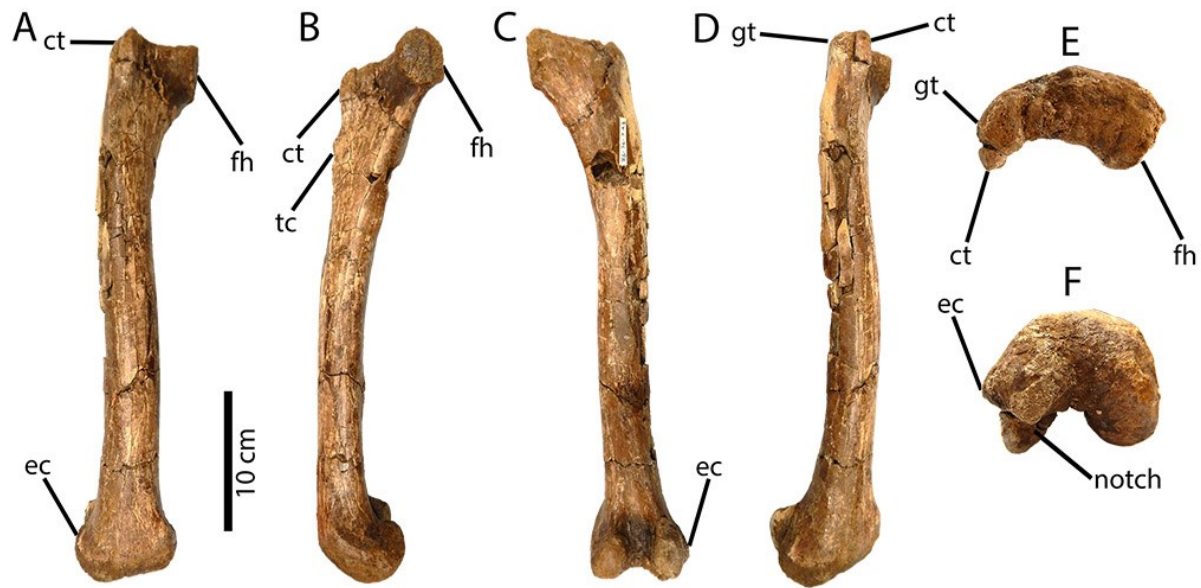
Fig. 3.6. Femur of *Caenagnathus collinsi*.

TMP 1986.036.0323, right femur in anterior (A), medial (B), posterior (C), lateral (D), proximal

(E), and distal (F) views. E and F not to scale. **Abbreviations**: **ct**, anterior trochanter; **ec**,

ectocondylar tuber; **fh**, femoral head; **gt**, greater trochanter; **notch**, notch between anterior and

posterior parts of lateral distal condyle.
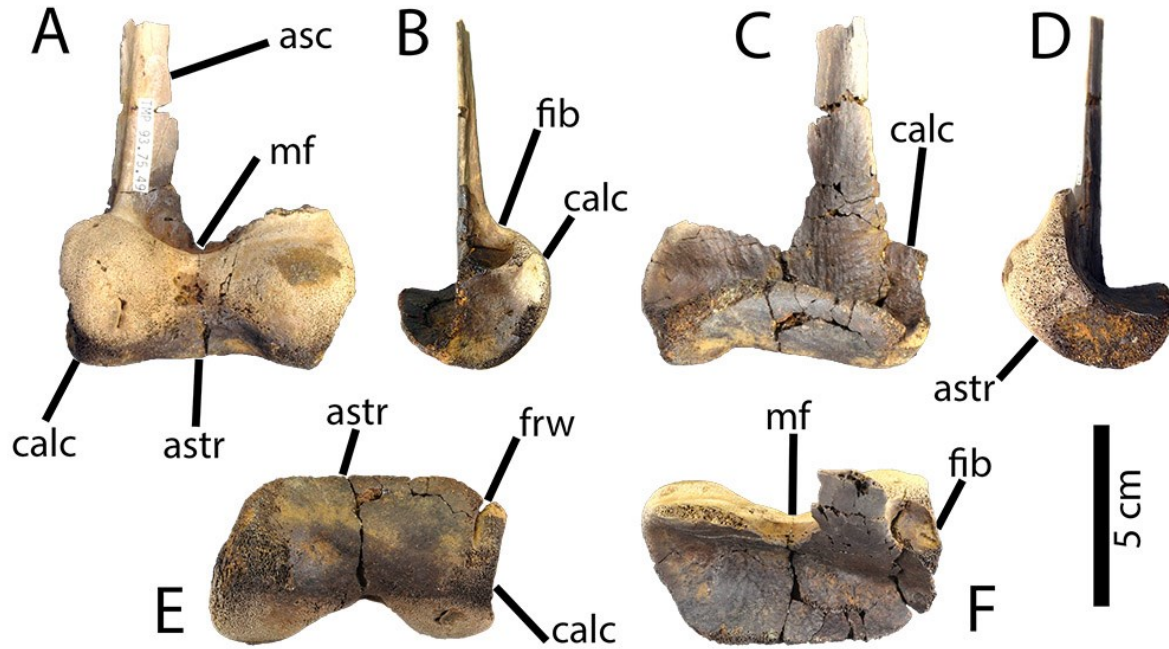
Fig. 3.7. Astragalocalcaneum of *Caenagnathus collinsi*.

TMP 1993.074.0049, right astragalocalcaneum in anterior (A), lateral (B), posterior (C), medial (D), distal (E), and proximal (F) views. **Abbreviations**: **asc**, ascending process of astragalus; **astr**, astragalus; **calc**, calcaneum; **fib**, fibular contact; **frw**, furrow separating astragalus and calcaneum posteriorly; **mf**, median fossa of astragalus.
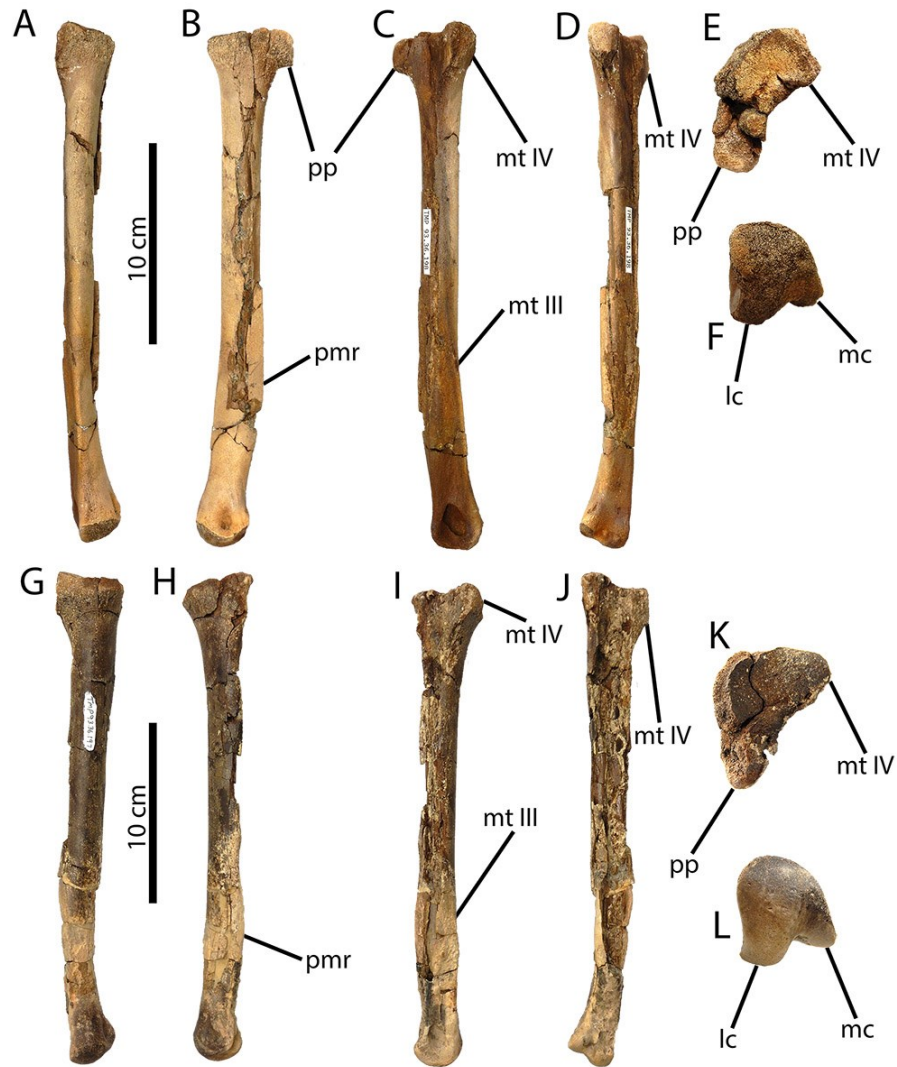
Fig. 3.8. Metatarsi of *Caenagnathus collinsi*.

TMP 1993.036.0198, right second metatarsal in anterior (A), medial (B), lateral (C), posterior (D), proximal (E), and distal (F) views. TMP 1993.036.0197, right second metatarsal in anterior (G), medial (H), lateral (I), posterior (J), proximal (K), and distal (L) views. E, F, K, and L not to scale. **Abbreviations**: **lc**, lateral condyle; **mc**, medial condyle; **mt III**, facet for third metatarsal; **mt IV**, facet for fourth metatarsal; **pmr**, posteromedial ridge; **pp**, posterior process of proximal articular surface.

A

8–12
7
6
5

4

3

2

1

500 μm

B

A

Fig. 3.10D

Fig. 3.10A

C, D

2500 μm

C

Fig. 3.10F

Fig. 3.10E

1000 μm

D

Fig. 3.10C

Fig. 3.10B

302
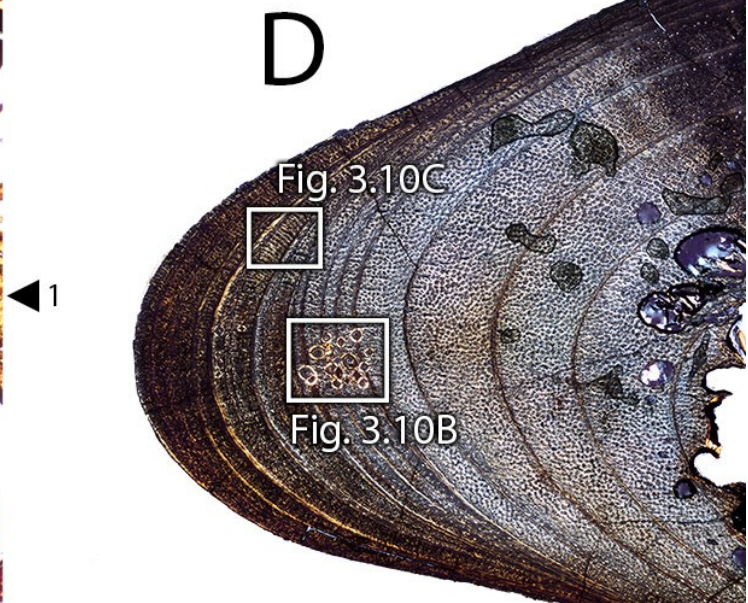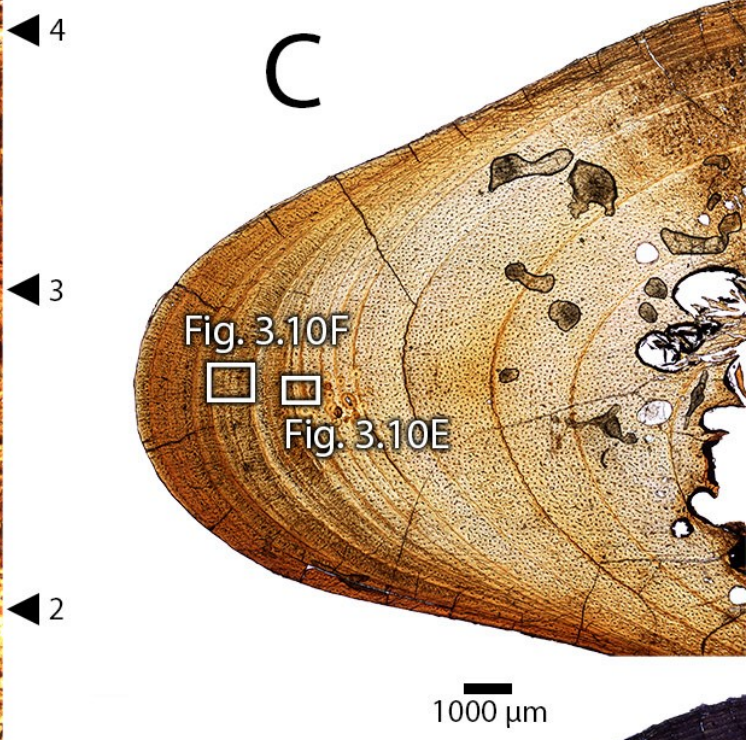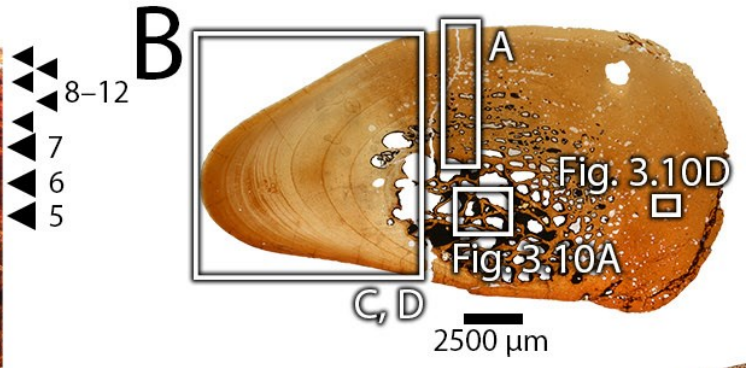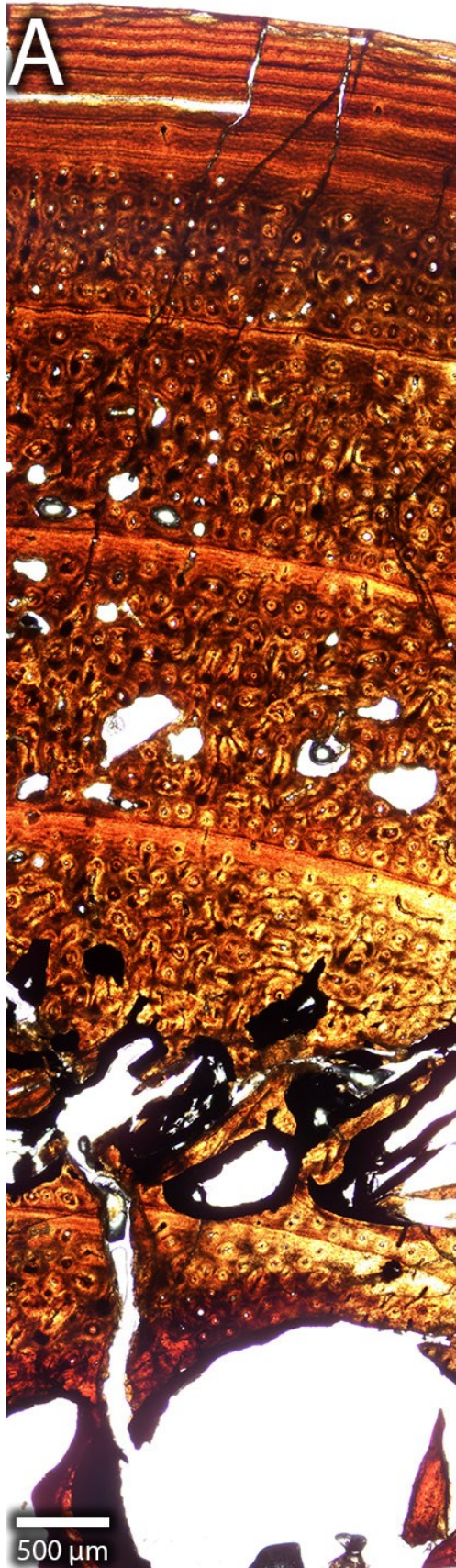
(Previous page)

Fig. 3.9. Osteohistology of UALVP 56638 (*Caenagnathus collinsi*).

Detail (A) of cortex of UALVP 56638 in plane-polarized light, showing cyclical growth marks (arrows). Overview (B) of thin section of UALVP 56638 in plane-polarized light, showing primary bone on the anterior side and densely remodeled Haversian bone on the posterior side, as well as the locations of close-ups in Fig. 3.10. Details (C, D) of anterior portion of UALVP 56638 in plane-polarized (C) and cross-polarized (D) light, showing cyclical growth marks, predominantly primary bone tissue, and locations of close-ups in Fig. 3.10.
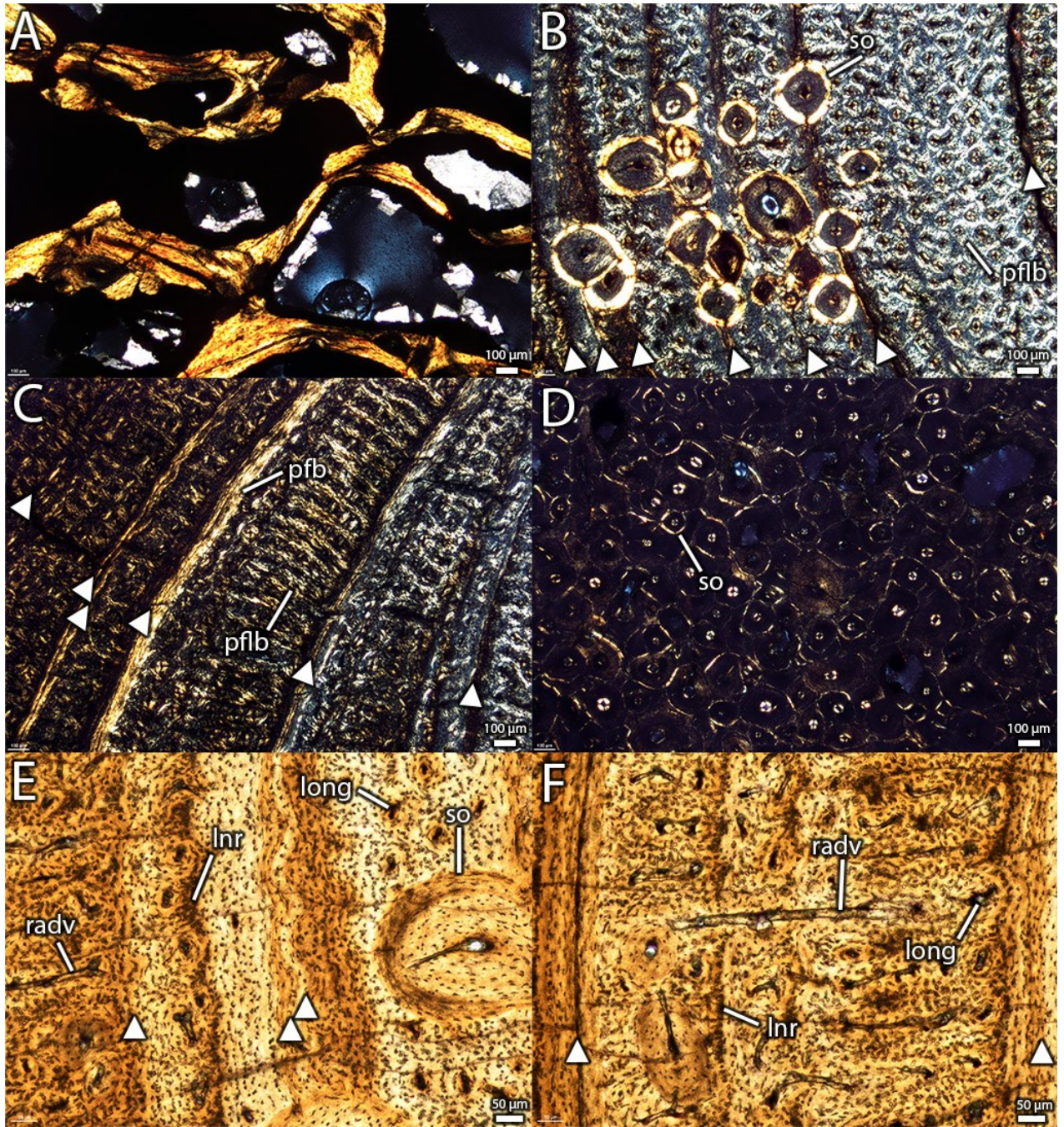
(Previous page)

Fig. 3.10. Osteohistological aspects of UALVP 56638 (*Caenagnathus collinsi*).

Close-up (A) of endosteal lamellae and large erosive cavities in the medullary region of the pubis in cross-polarized light. Detail (B) of localized secondary remodeling with well-developed secondary osteons, cyclical growth marks (arrows), and longitudinally oriented vasculature in the primary bone of the anterior portion of the pubis in cross-polarized light. Detail (C) of parallel-fibered bone and primary fibrolamellar bone in association with cyclical growth marks (arrows) in the exterior cortex of the pubis under cross-polarized light. Detail (D) of dense Haversian bone in the posterior cortex of the pubis under cross-polarized light. Close-up (E) of variation in primary bone texture, alignment of osteocyte lacunae, and cyclical growth marks (arrows) in the anterior portion of the cortex under plane-polarized light. Close-up (F) of variation in vascular orientation and alignment of osteocyte lacunae between cyclical growth marks (arrows) in the cortex of the pubis under plane-polarized light. **Abbreviations: lnr**, linear features created by alignment and density changes of osteocyte lacunae; **long**, longitudinal vasculature; **pfb**, parallel-fibered bone; **pflb**, primary fibrolamellar bone; **radv**, radial vasculature; **so**, secondary osteon.
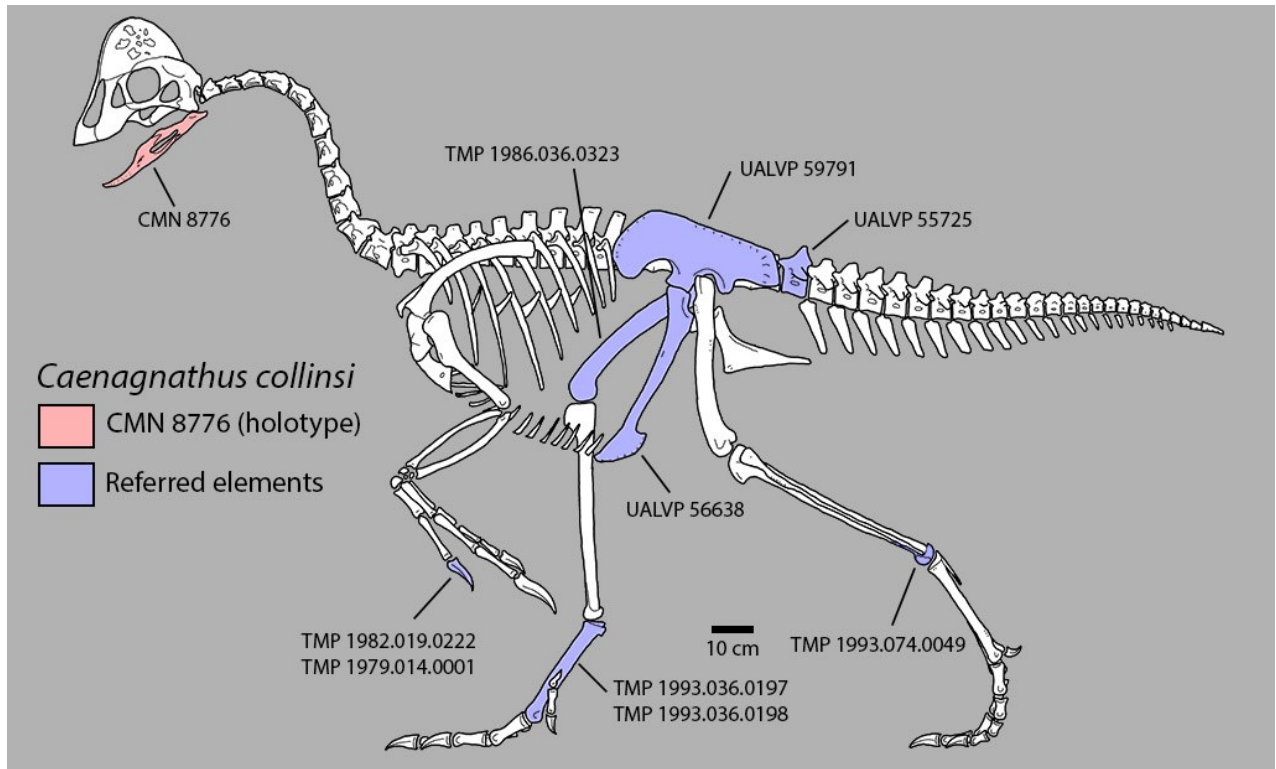
Fig. 3.11. Skeletal reconstruction of *Caenagnathus collinsi*.

Skeletal reconstruction based on *Anzu wyliei*, modified with elements referred to *Caenagnathus collinsi*. Proportions of *Anzu wyliei* taken from Lamanna et al. (2014), as reconstructed by Scott Hartman.
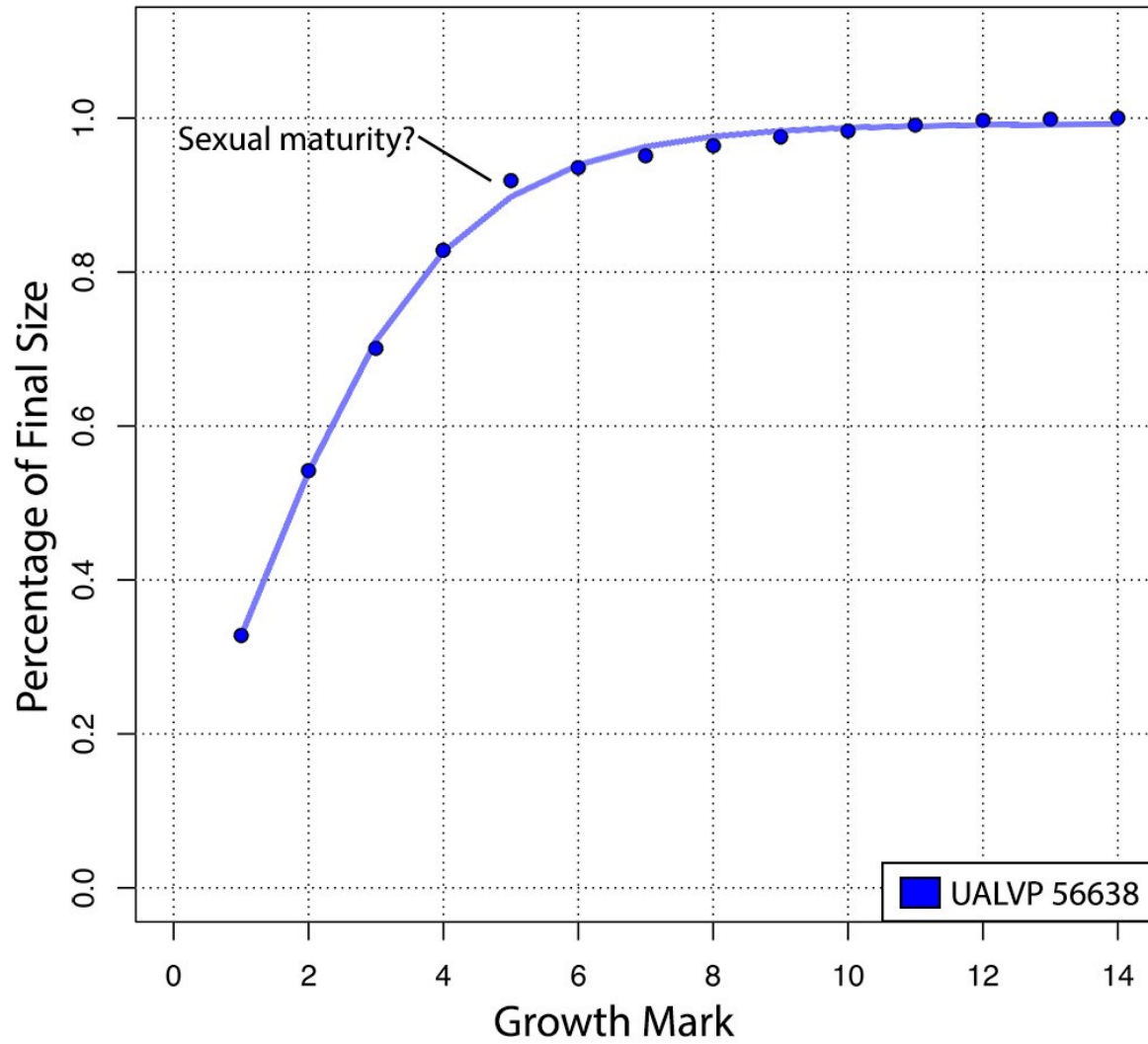
Fig. 3.12. Reconstructed growth curve for UALVP 56638 (*Caenagnathus collinsi*).

Gompertz growth curve model based on line of arrested growth spacing and percentage of final body size for UALVP 56638.
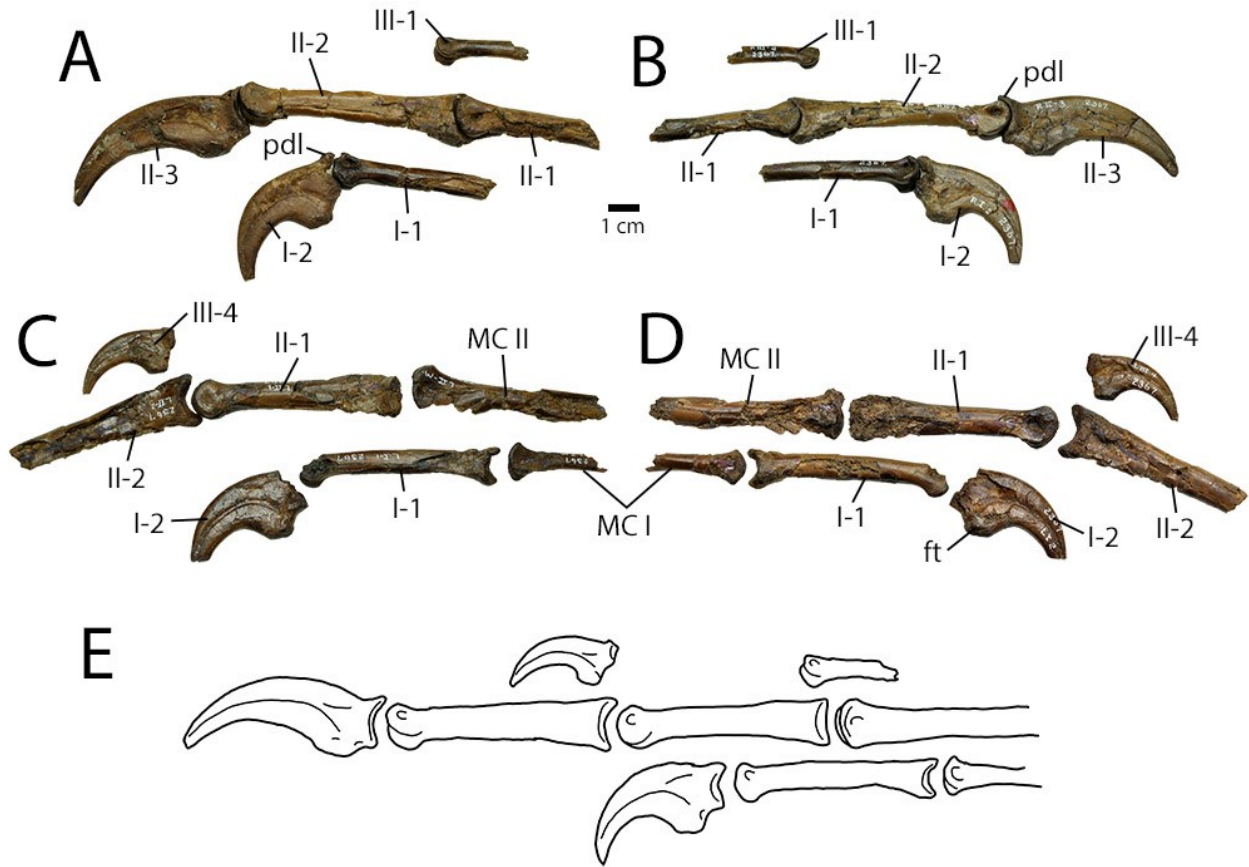
Fig. 3.13. Holotype manus of *Chirostenotes pergracilis*.

Right manus of CMN 2367 in medial (A) and lateral (B) views. Left manus of CMN 2367 in lateral (C) and medial (D) views. Reconstruction (E) of right manus of CMN 2367 in medial view based on composite of both manus. **Abbreviations: ft,** flexor tubercle; **MC I**, metacarpal I; **MC II**, metacarpal II; **pdl**, proximodorsal lip.
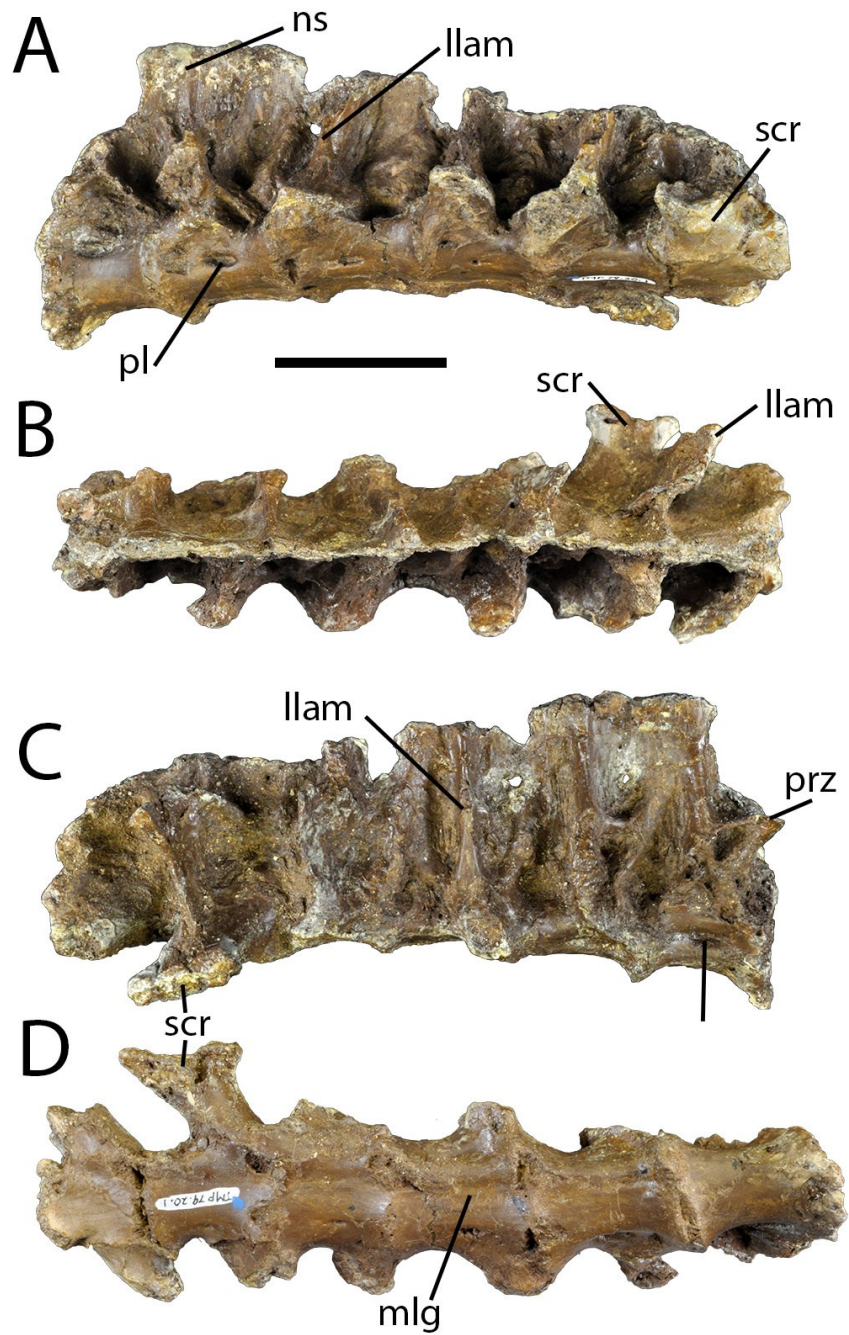
Fig. 3.14. Sacrum of *Chirostenotes pergracilis* (TMP 1979.020.0001).

Sacrum of TMP 1979.020.0001 in left lateral (A), dorsal (B), right lateral (C) and ventral (D)

views. **Abbreviations: llam**, lateral lamina; **mlg**, midline groove; **ns**, neural spine; **pl**,

pleurocoel; **prz**, prezygapophysis; **scr**, sacral rib.
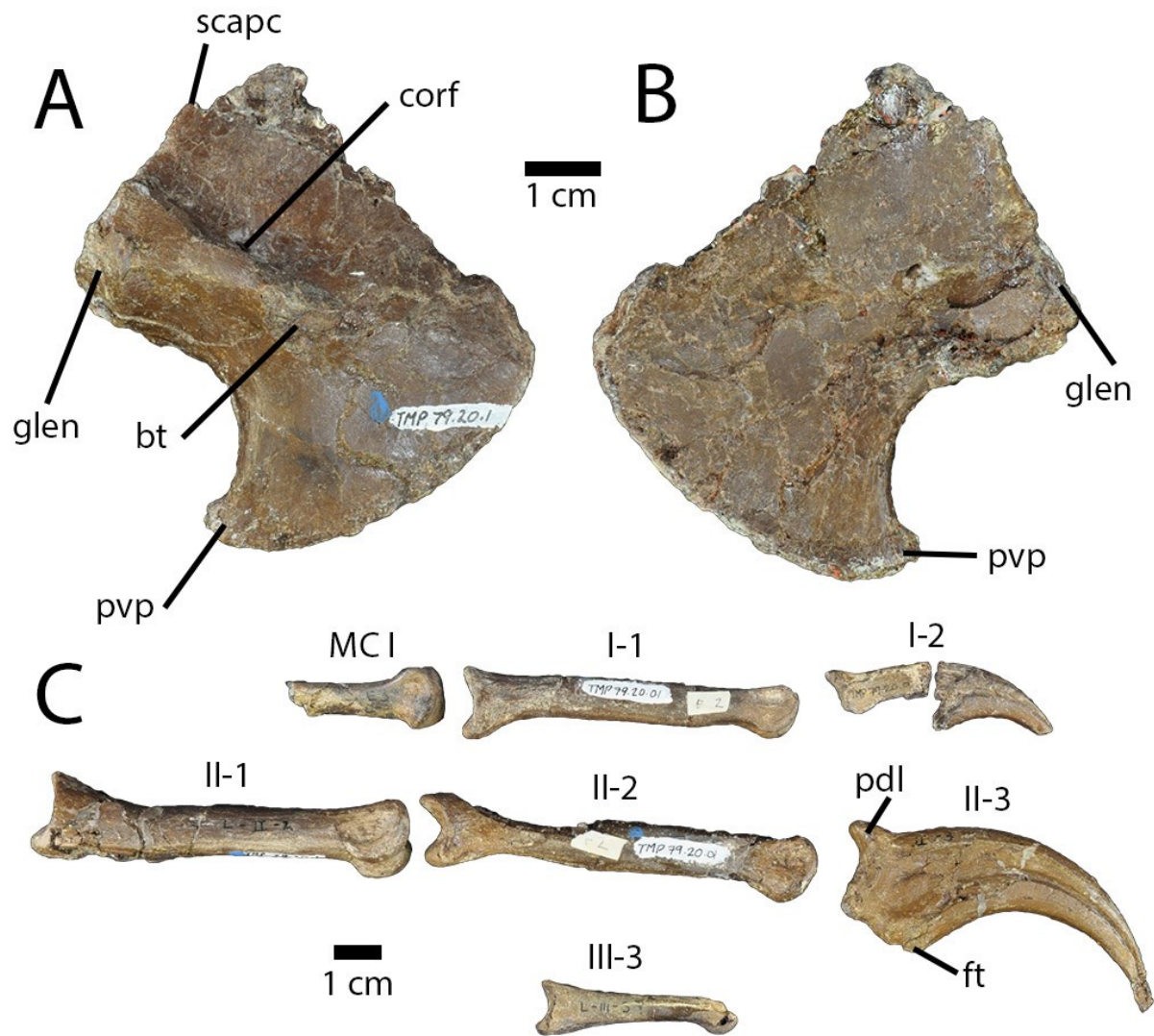
Fig. 3.15. Forelimb elements of *Chirostenotes pergracilis* (TMP 1979.020.0001).

Coracoid of TMP 1979.020.0001 in lateral (A) and medial (B) views. Partial left manus of TMP 1979.020.0001 in medial (C) view. **Abbreviations: bt,** biceps tubercle; **corf**, coracoid foramen; **ft**, flexor tubercle; **glen**, glenoid; **pdl**, proximodorsal lip; **pvp**, posteroventral process; **scapc**, scapular contact.
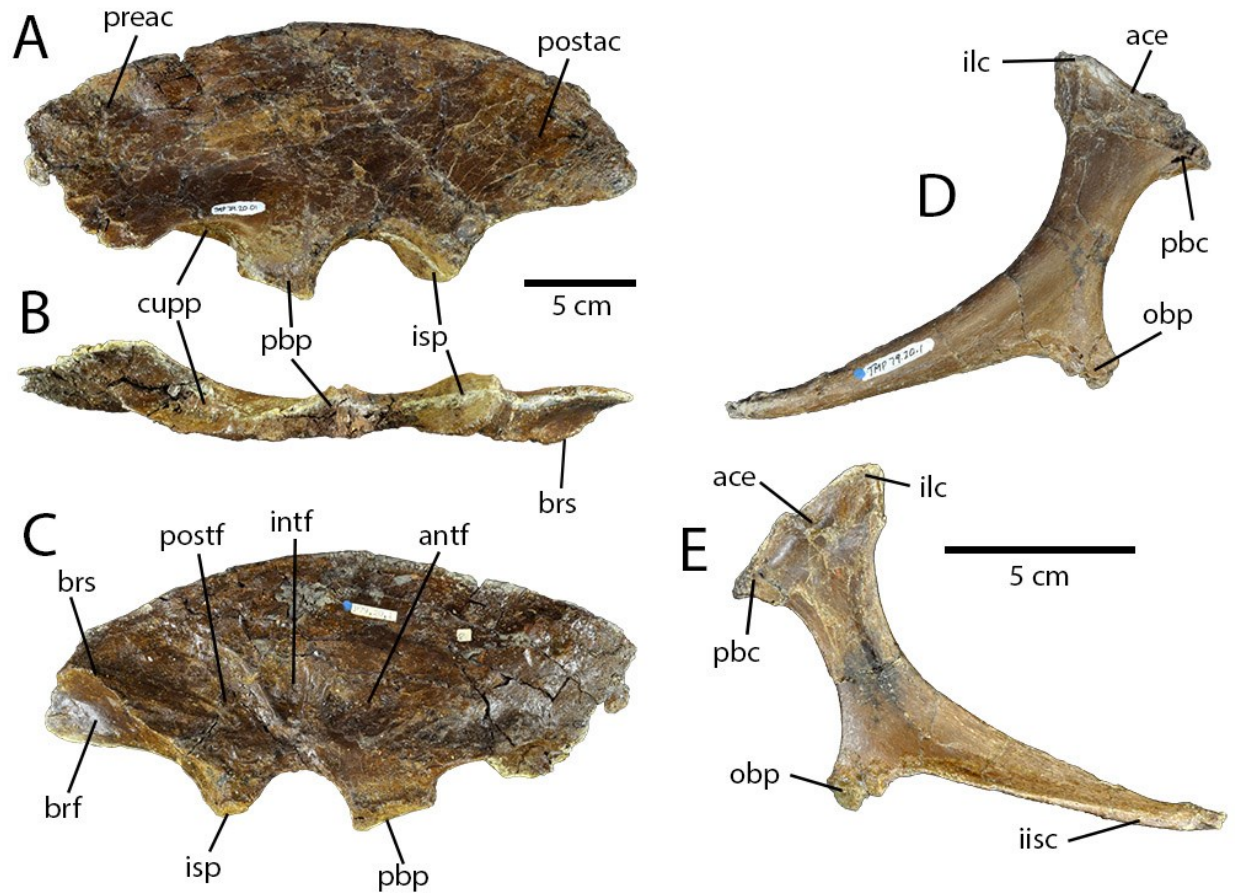
Fig. 3.16. Pelvic elements of *Chirostenotes pergracilis* (TMP 1979.020.0001).

Left ilium of TMP 1979.020.0001 in lateral (A), ventral (B), and medial (C) views. Right ischium of TMP 1979.020.0001 in lateral (D) and medial (E) views. **Abbreviations: ace**, acetabulum; **antf**, anterior fossa; **brf**, brevis fossa; **brs**, brevis shelf; **cupp**, cuppedicus fossa; **iisc**, interischiadic contact; **ilc**, iliac contact; **intf**, intermediate fossa; **isp**, ischiadic peduncle; **obp**, obturator process; **pbc**, pubic contact; **pbp**, pubic peduncle; **postf**, posterior fossa; **postac**, postacetabular process; **preac**, preacetabular process.
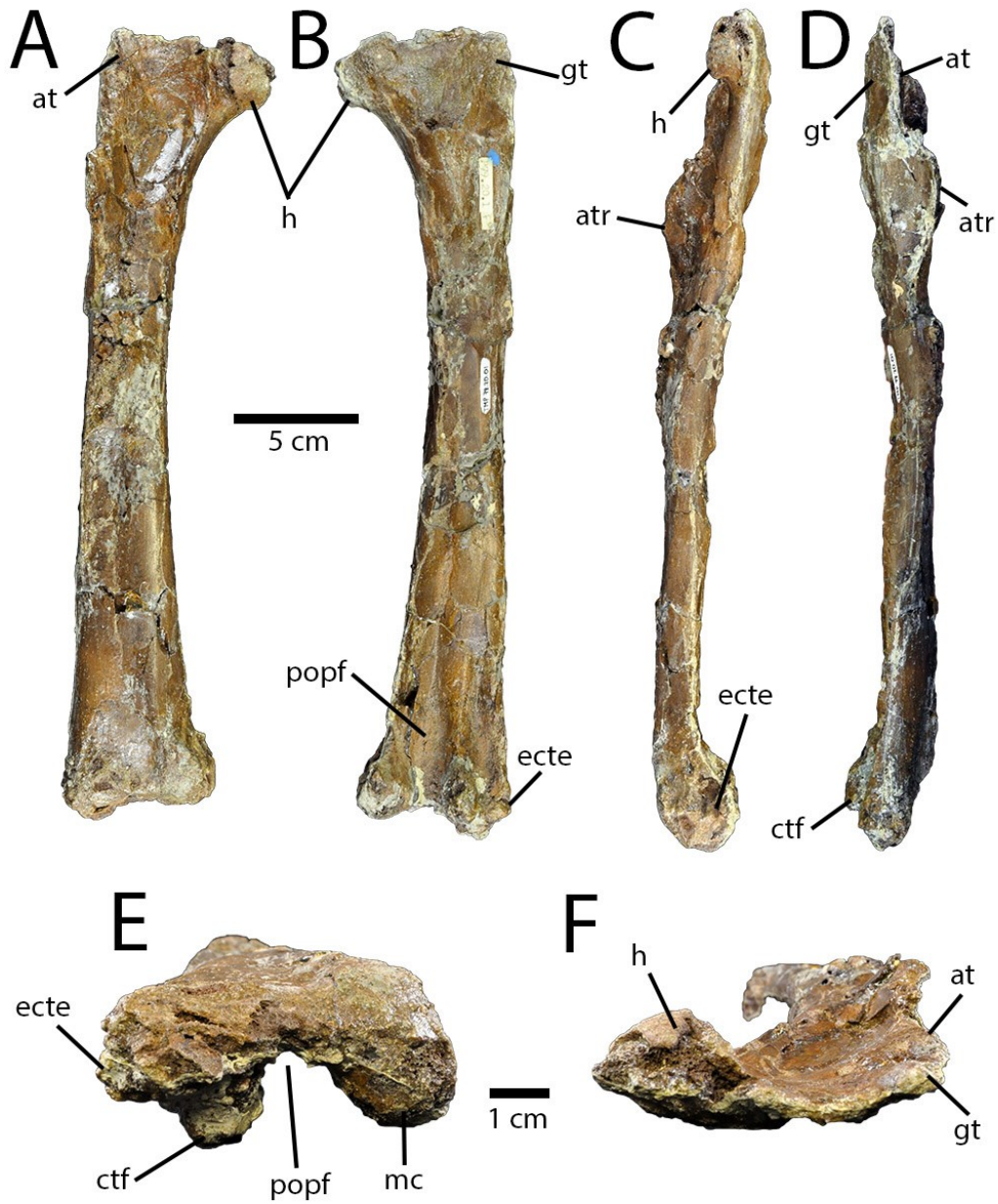
Fig. 3.17. Femur of *Chirostenotes pergracilis* (TMP 1979.020.0001).

Right femur of TMP 1979.020.0001 in anterior (A), posterior (B), medial (C), lateral (D), distal (E), and proximal (F) views. **Abbreviations: at**, anterior trochanter; **atr**, accessory trochanteric ridge; **ctf**, crista tibiofibularis; **ecte**, ectepicondylar tuber; **gt**, greater trochanter; **h**, head; **mc**, medial condyle; **popf**, popliteal fossa.
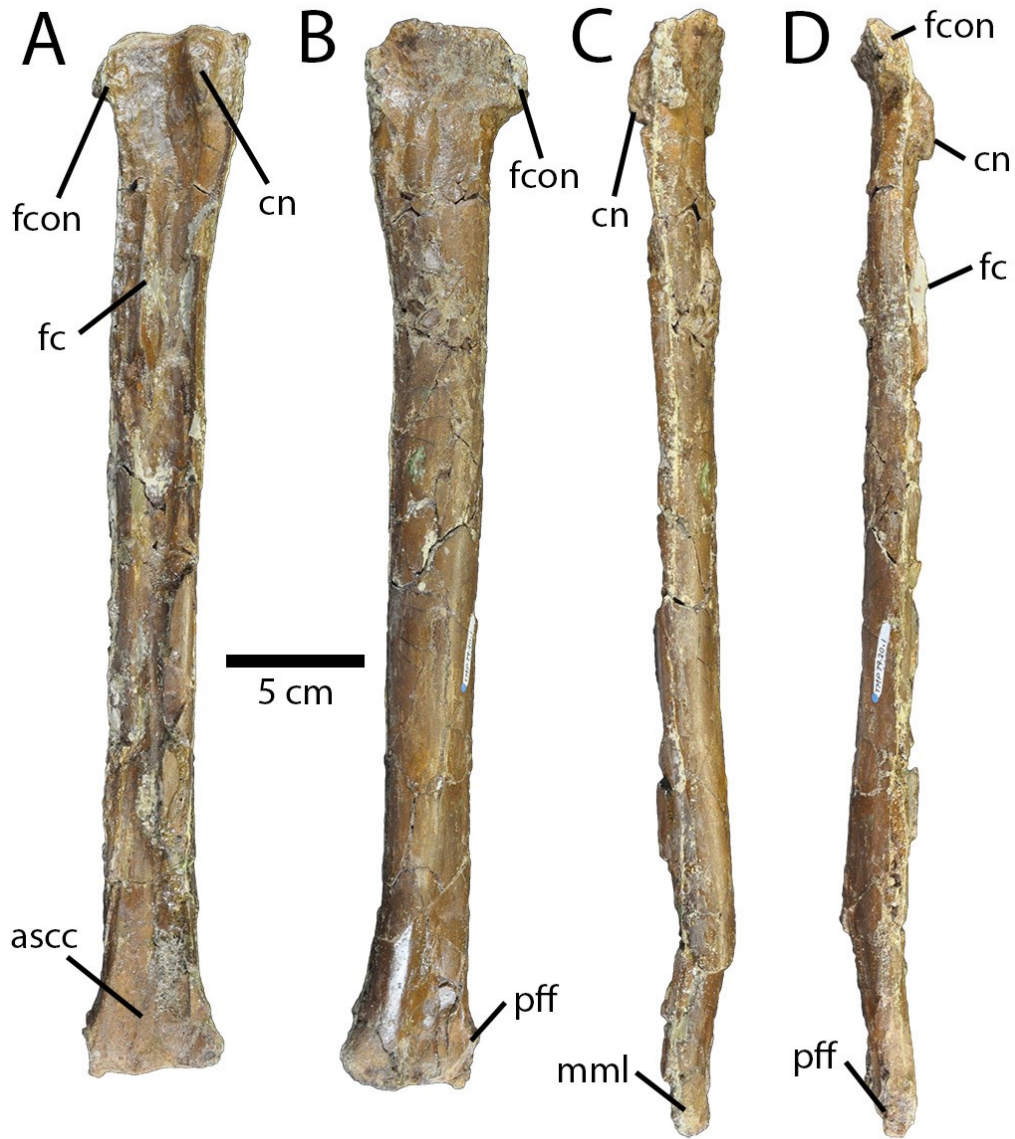
Fig. 3.18. Tibia of *Chirostenotes pergracilis* (TMP 1979.020.0001).

Right tibia of TMP 1979.020.0001 in anterior (A), posterior (B), medial (C) and lateral (D)

views. **Abbreviations: ascc**, contact for the ascending process of the astragalus; **cn**, cnemial

crest; **fc**, fibular crest; **fcon**, fibular condyle; **mml**, medial malleolus; **pff**, postfibular flange.
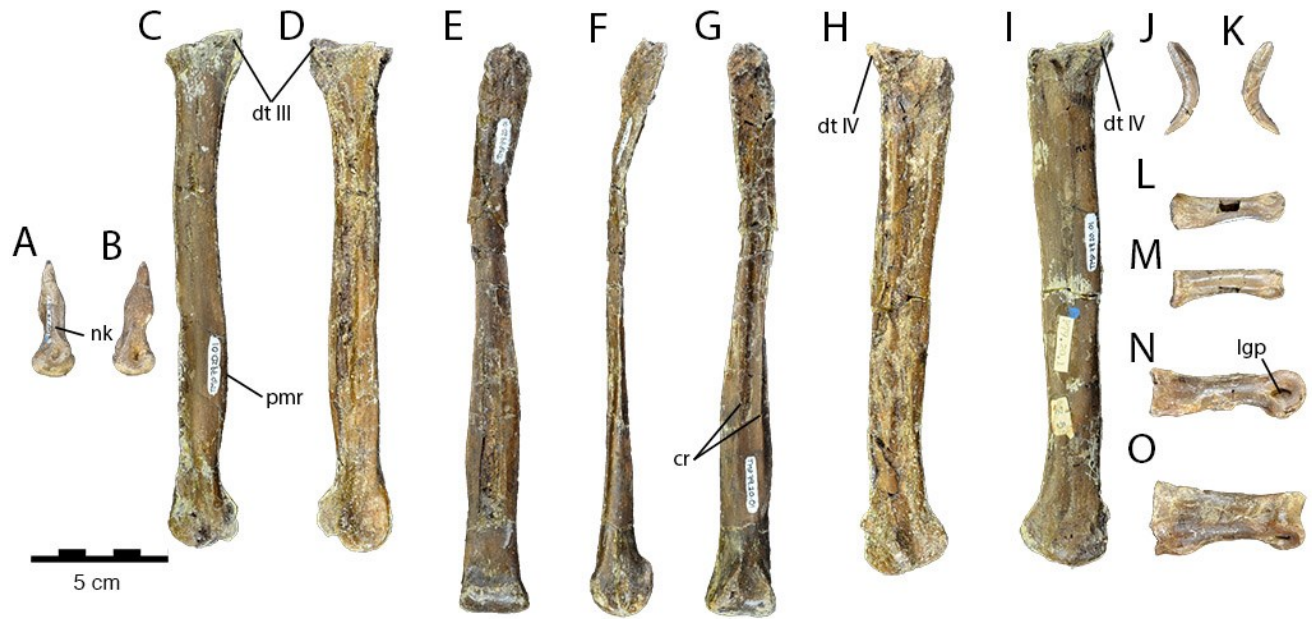
Fig. 3.19. Pedal elements of *Chirostenotes pergracilis* (TMP 1979.020.0001).

Right metatarsal I in medial (A) and lateral (B) views. Right metatarsal II in medial (C) and lateral (D) views. Right metatarsal III in anterior (E), medial (F), and posterior (G) views. Right metatarsal IV in medial (H) and lateral (I) views. ?Left metatarsal V in lateral (J) and medial (K) views. Right phalanx I-1 in lateral (L) and dorsal (M) views. Right phalanx III-1 in lateral (N) and dorsal (O) views. **Abbreviations: cr**, cruciate ridges; **dt III**, distal tarsal III; **dt IV**, distal tarsal IV; **lgp**, ligament pit; **nk**, neck; **pmr**, posteromedial ridge.
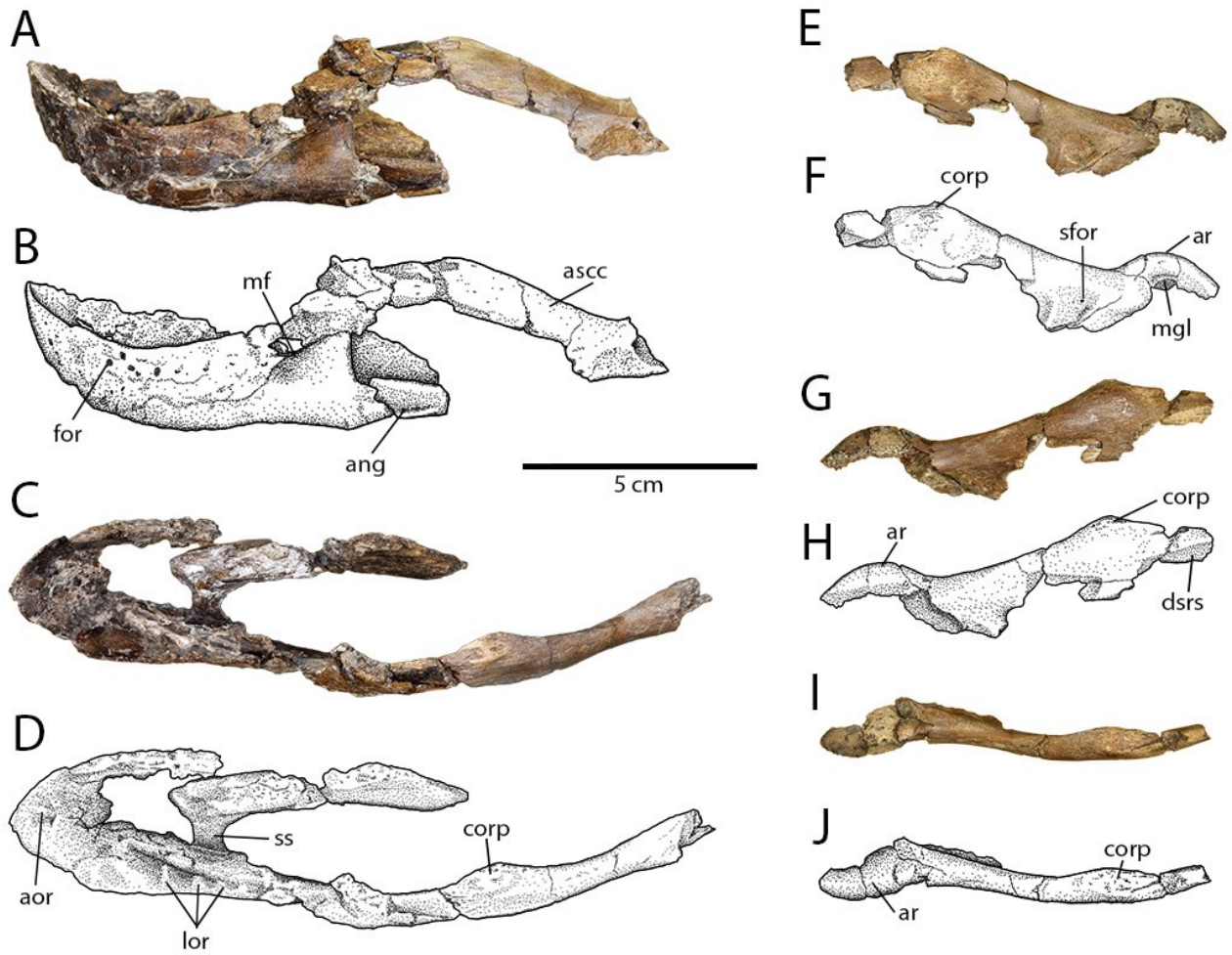
Fig. 3.20. Mandibles of *Chirostenotes pergracilis* (UALVP 59400).

Photographs (A, C) of mandibles of UALVP 59400 in left lateral (A) and dorsal (C) views.

Illustrations (B, D) of the same. Photographs (E, G, I) of right articular-surangular-coronoid

complex in medial (E), lateral (G), and dorsal (I) views. Illustrations (F, H, J) of the same.

Abbreviations: ang, angular; **aor**, anterior occlusal ridge; **ar**, articular ridge; **ascc**, articular-

surangular-coronoid complex; **corp**, coronoid process; **dsrs**, dentary-surangular suture; **for**,

foramen; **lor**, lateral occlusal ridges; **mf**, mandibular fossa; **mgl**, medial glenoid; **sfor**, surangular

foramen; **ss**, symphyseal sulcus.
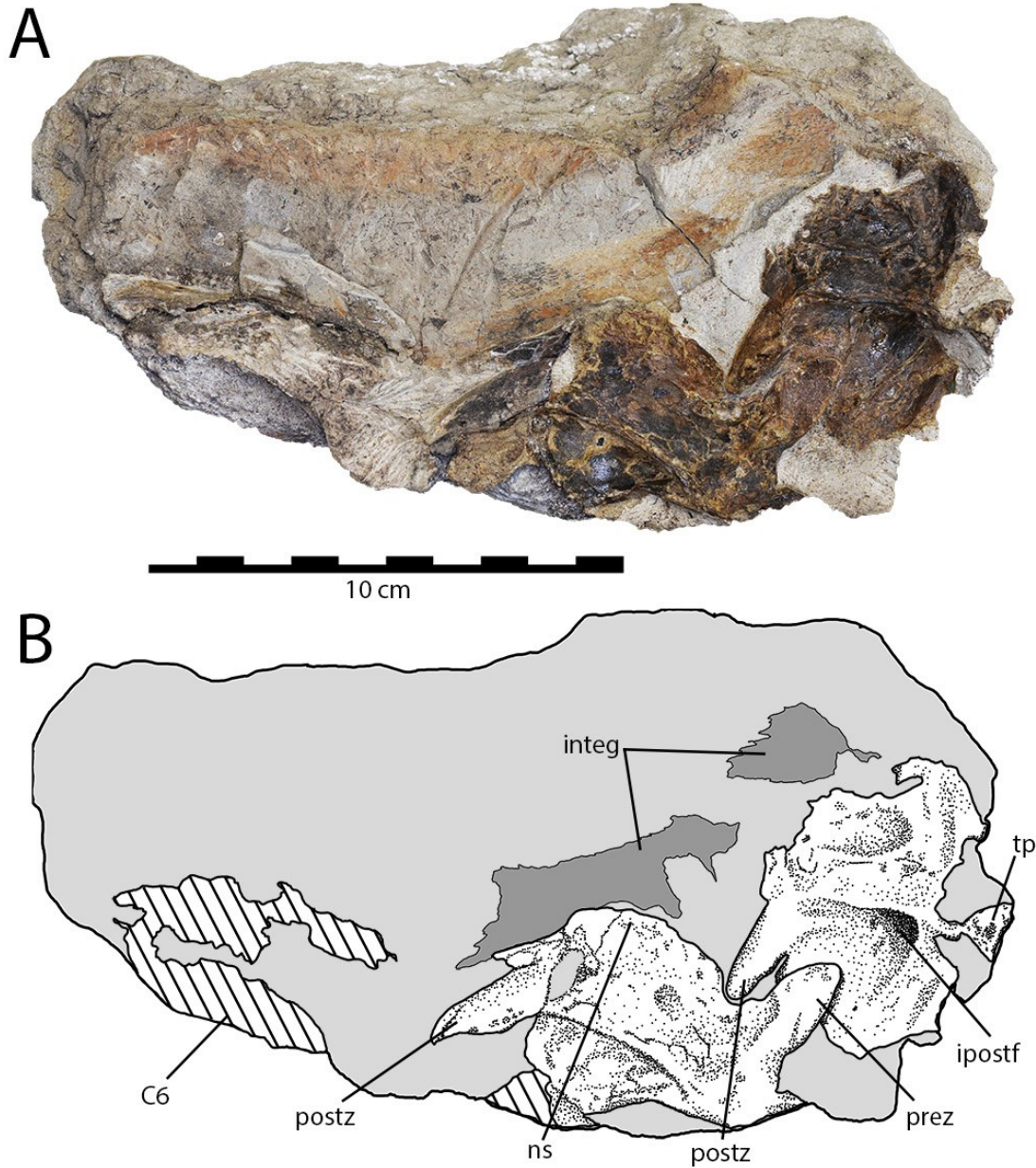
Fig. 3.21. Cervical vertebrae of *Chirostenotes pergracilis* (UALVP 59400).

Photograph (A) and illustration (B) of postaxial cervical vertebrae four, five, and six in right lateral view. Note possible integument preserved dorsal to the neural arches. **Abbreviations: C6**, postaxial cervical vertebra six; **integ**, possible integumentary structures; **ipostf**, infrapostzygapophyseal fossa; **ns**, neural spine; **postz**, postzygapophysis; **prez**, prezygapophysis; **tp**, transverse process.
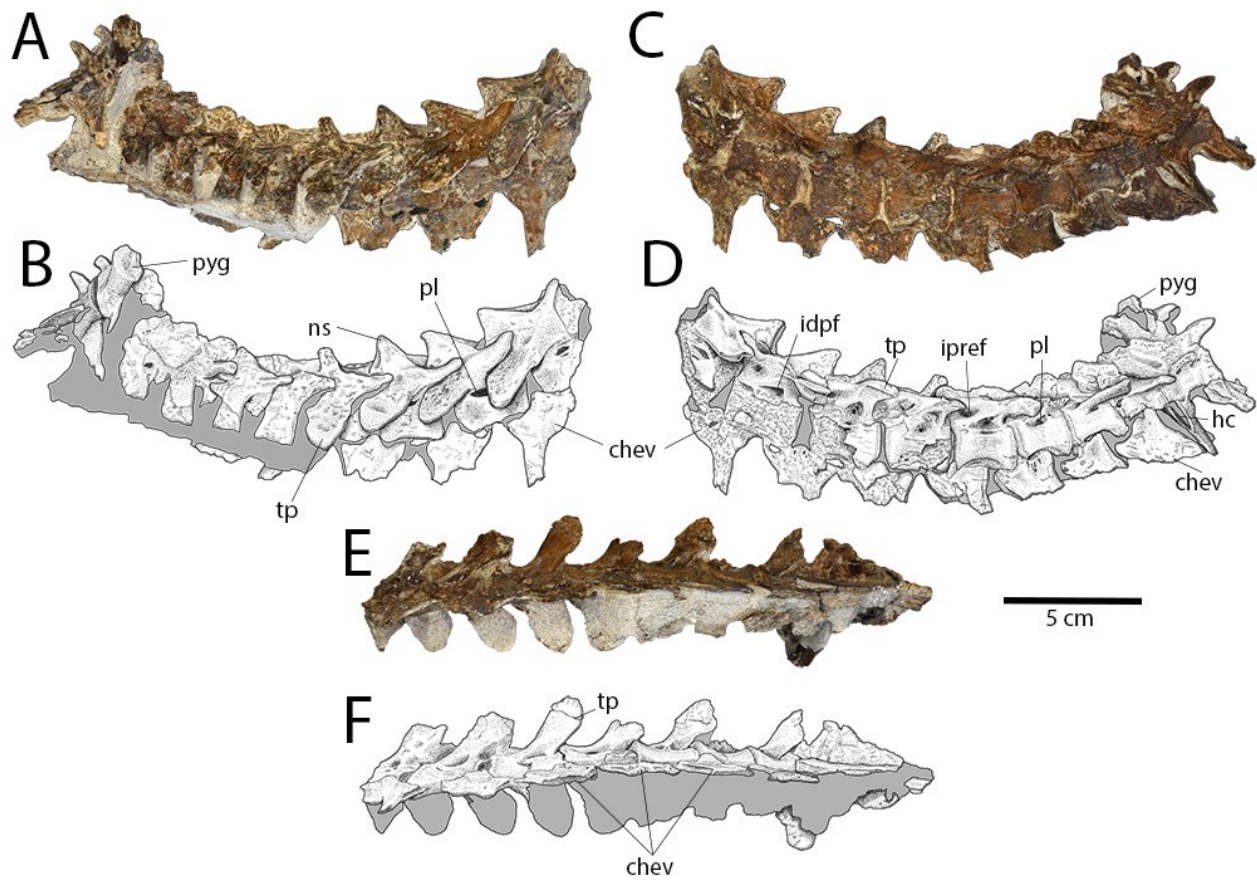
Fig. 3.22. Caudal vertebrae of *Chirostenotes pergracilis* (UALVP 59400).

Photographs (A, C, E) and illustrations (B, D, F) of articulated distal caudal series of UALVP 59400 in right lateral (A, B), left lateral (C, D), and ventral (E, F) views. **Abbreviations: chev**, chevron; **hc**, haemal canal; **idpf**, infradiapophyseal fossa; **ipref**, infraprezygapophyseal fossa; **ns**, neural spine; **pl**, pleurocoel; **pyg**, pre-pygal vertebra; **tp**, transverse process.
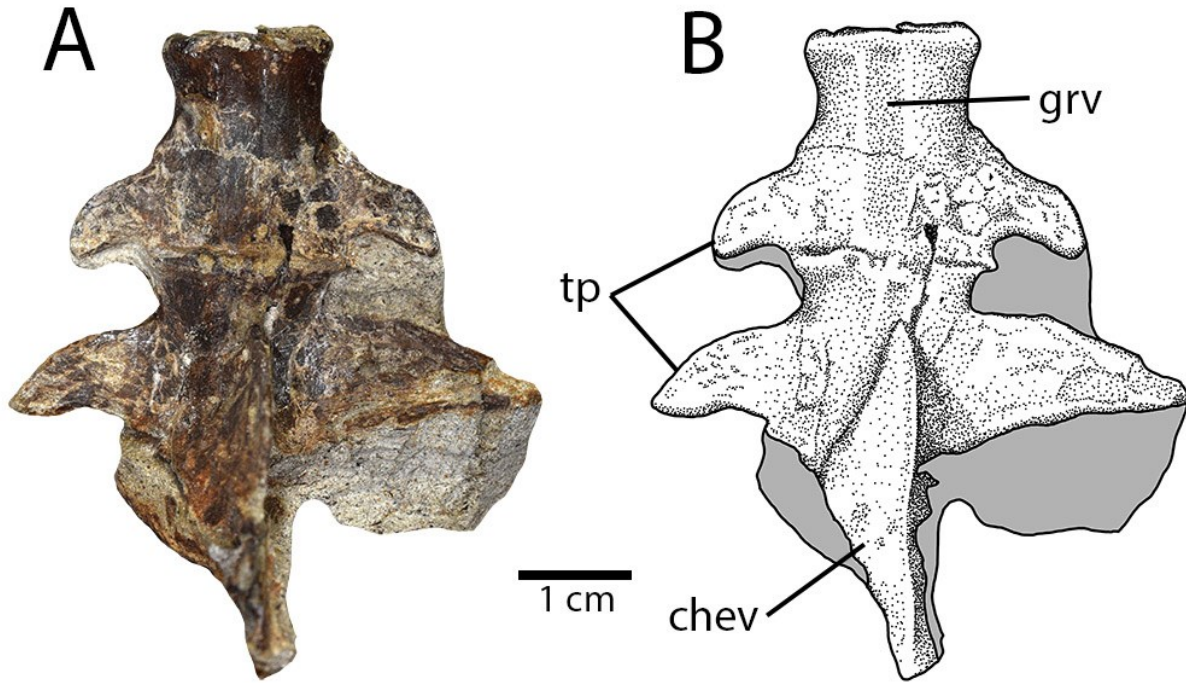
Fig. 3.23. Distal caudal vertebrae of *Chirostenotes pergracilis* (UALVP 59400).

Photograph (A) and illustration (B) of pre-pygal caudal vertebrae of UALVP 59400 in ventral view, showing anteriorly-directed transverse processes, midline ventral groove, and large, platelike chevrons. Anterior is downwards, distal (posterior) is upwards, and lateral is to either side. **Abbreviations: chev,** chevron; **grv**, groove; **tp**, transverse process.
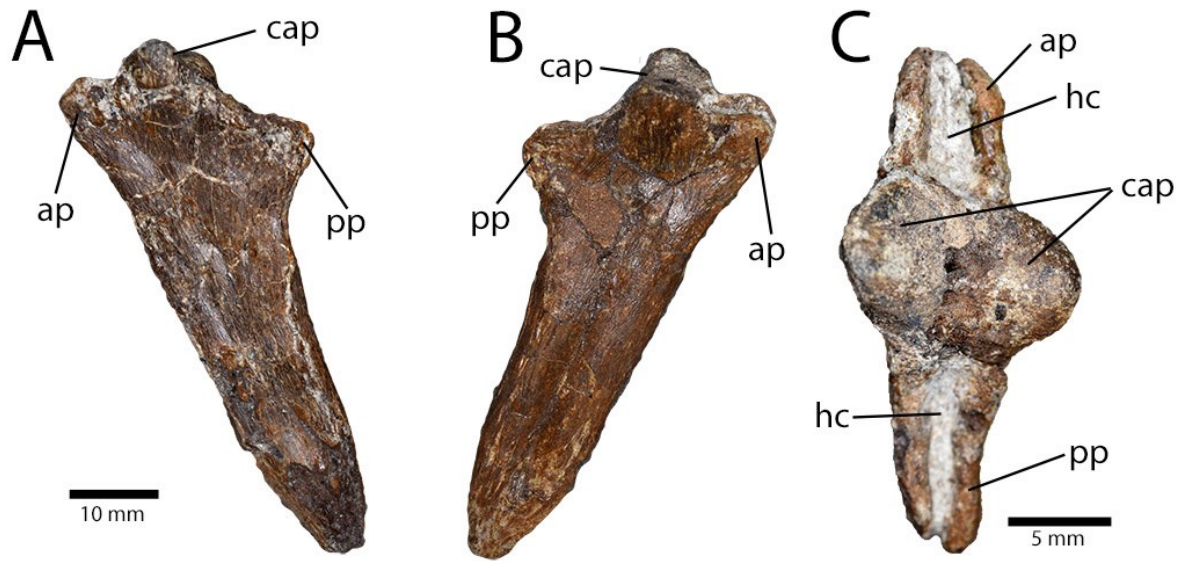
Fig. 3.24. Chevron of *Chirostenotes pergracilis* (UALVP 59400).

Anterior chevron in left lateral (A), right lateral (B) and proximal (C) views. **Abbreviations: ap**, anterior process; **cap**, caudal articular processes; **hc**, haemal canal; **pp**, posterior process.
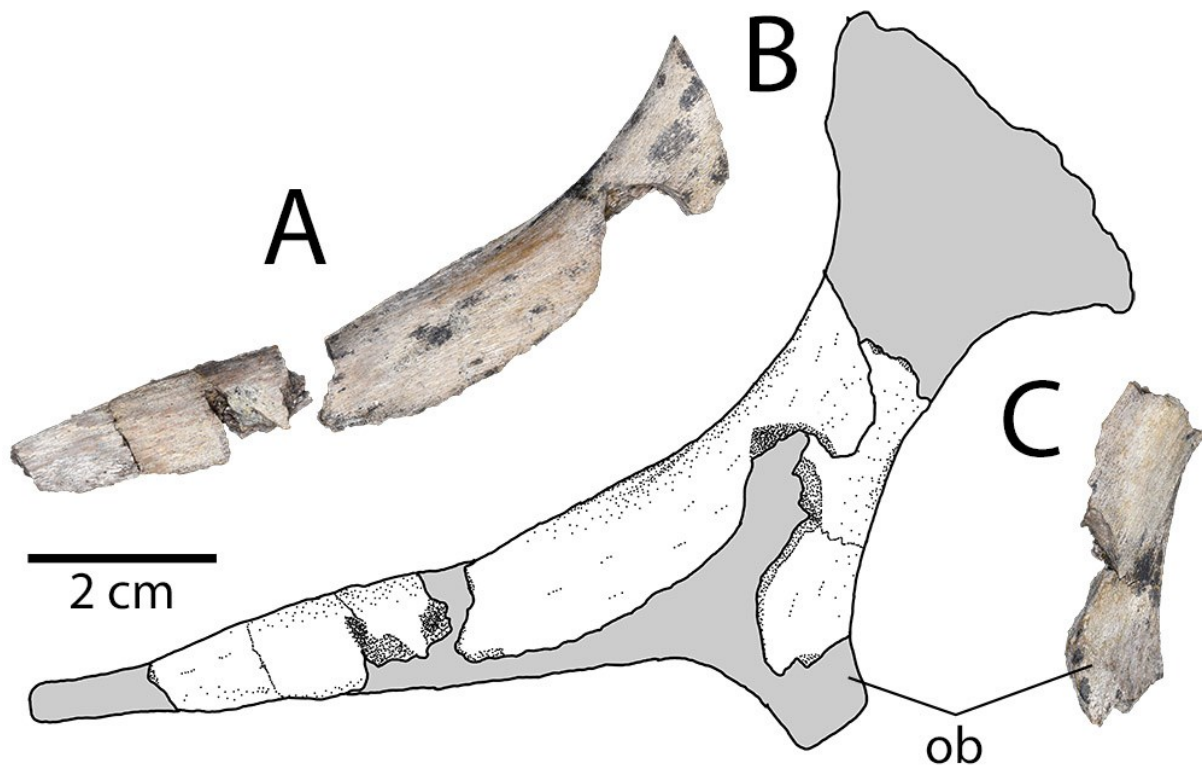
Fig. 3.25. Ischium of *Chirostenotes pergracilis* (UALVP 59400).

Fragments of right ischium in lateral (A) view. Composite reconstruction (B) of ischium of

UALVP 59400 based on fragments of left and right ischia, reconstructed using the complete

ischium of TMP 1979.020.0001. Fragment (C) of right ischium in medial view. **Abbreviation:**

ob, obturator process.
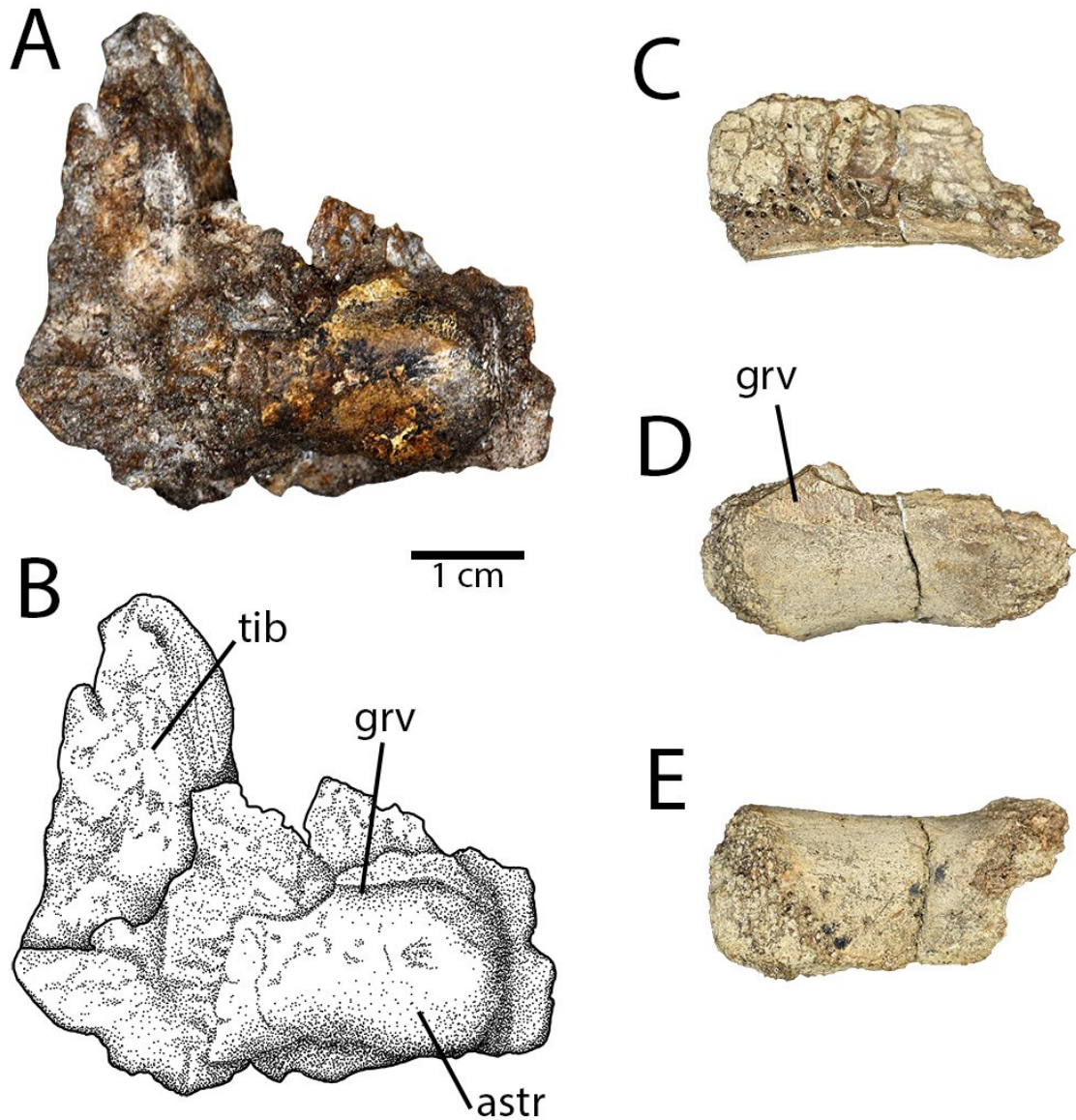
Fig. 3.26. Astragalocalcanei of *Chirostenotes pergracilis* (UALVP 59400).

Photograph (A) and illustration (B) of right distal tibia and astragalocalcaneum of UALVP 59400 in anterior view. Photographs (C–E) of left astragalocalcaneum of UALVP 59400 in dorsal (C), anterior (D), and ventral (E) views. **Abbreviations: astr,** astragalus; **grv**, groove; **tib**, tibia.
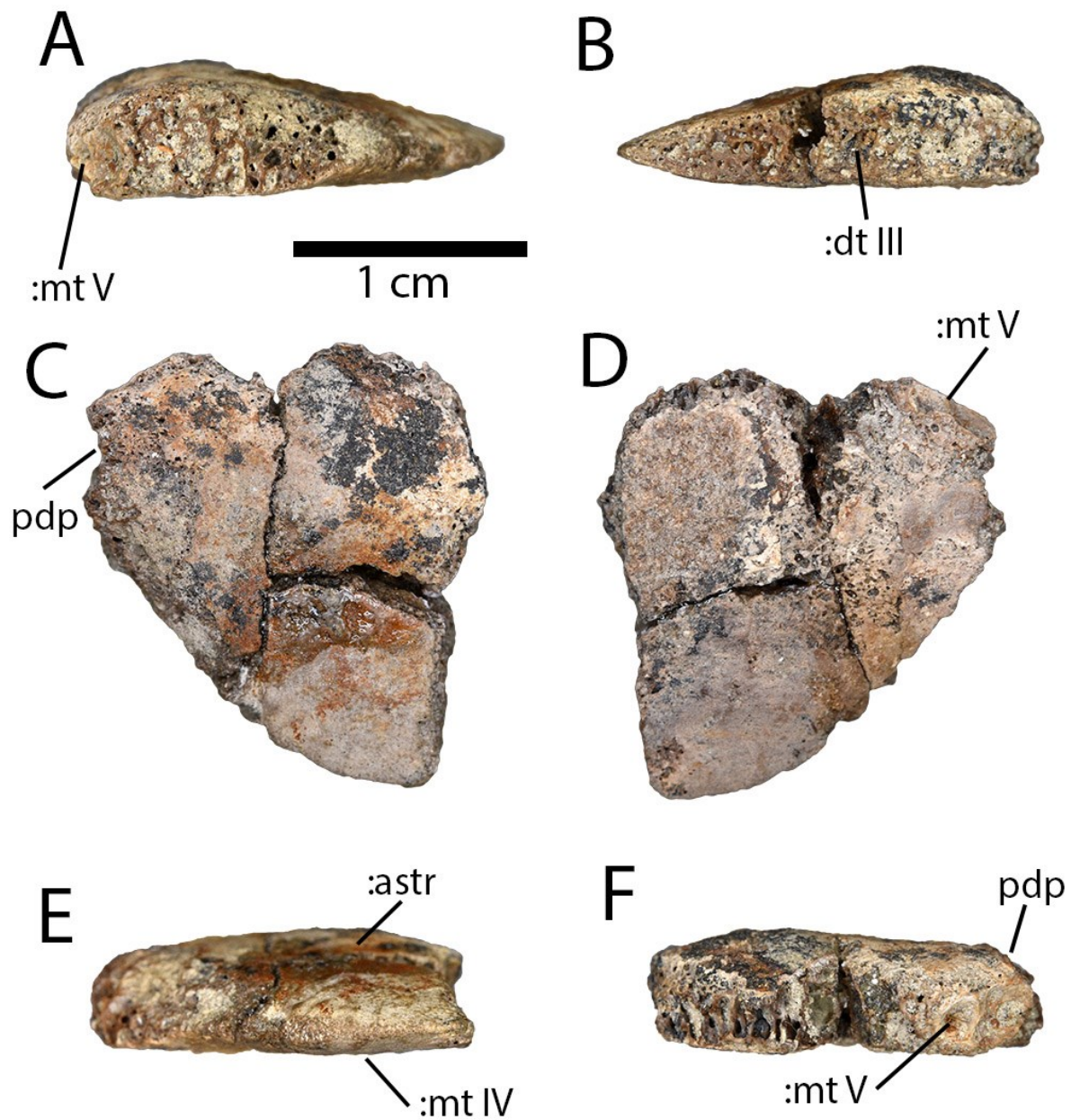
Fig. 3.27. Distal tarsal IV of *Chirostenotes pergracilis* (UALVP 59400).

Right distal tarsal IV in lateral (A), medial (B), proximal (C), distal (D), anterior (E), and

posterior (F) views. Note intact distal surface, indicative of lack of fusion to the proximal end of

metatarsal IV. **Abbreviations: :astr,** contact for astragalus; **:dt III**, contact for distal tarsal III;

:mt IV, contact for metatarsal IV; **:mt V**, contact for metatarsal V; **pdp**, proximodorsal process.
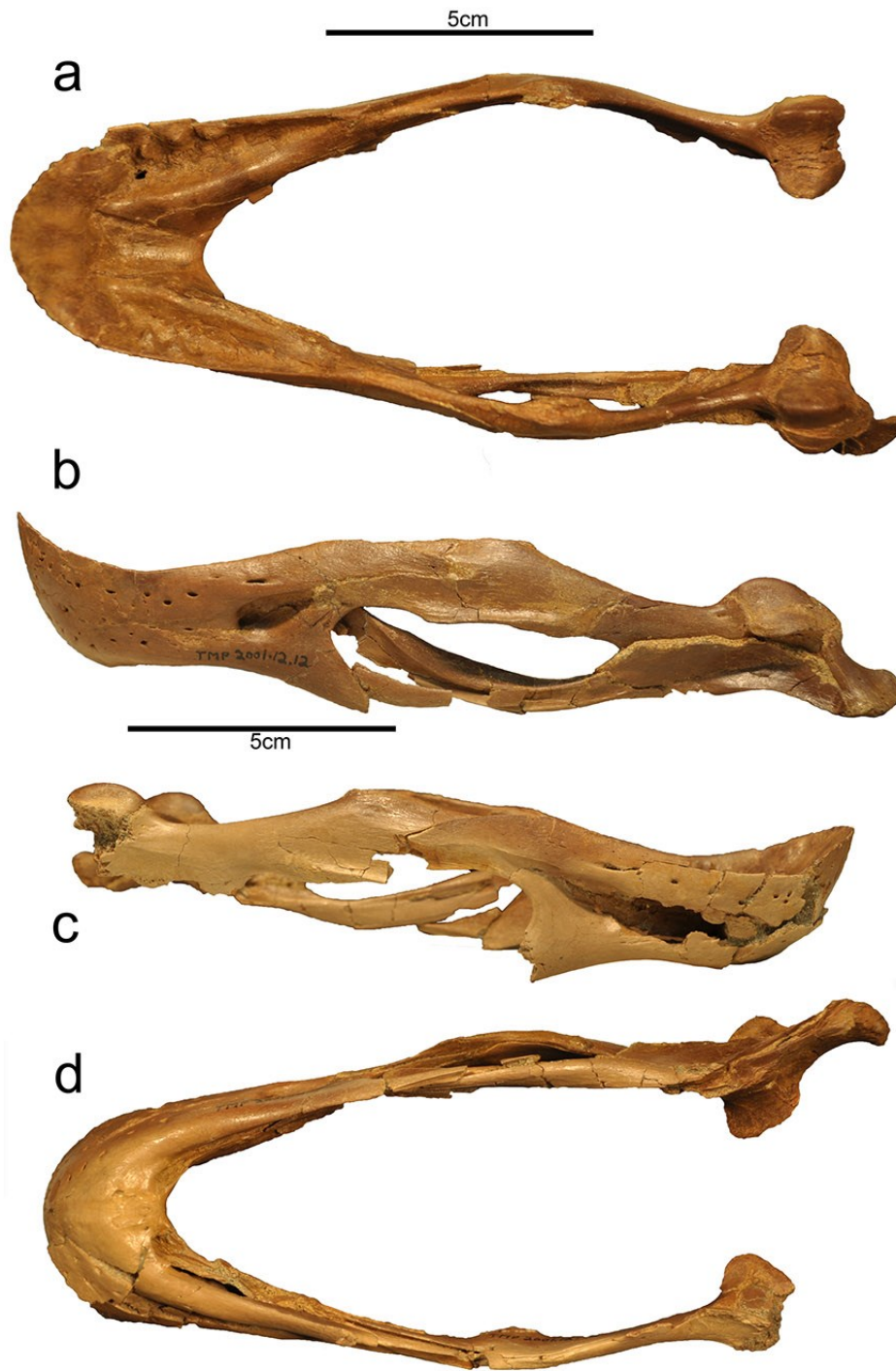
Fig. 3.28. Mandible of *Chirostenotes pergracilis* (TMP 2001.012.0012).

Photographs of mandible of TMP 2001.012.0012 in dorsal (A), left lateral (B), right lateral (C)

and ventral (D) views.
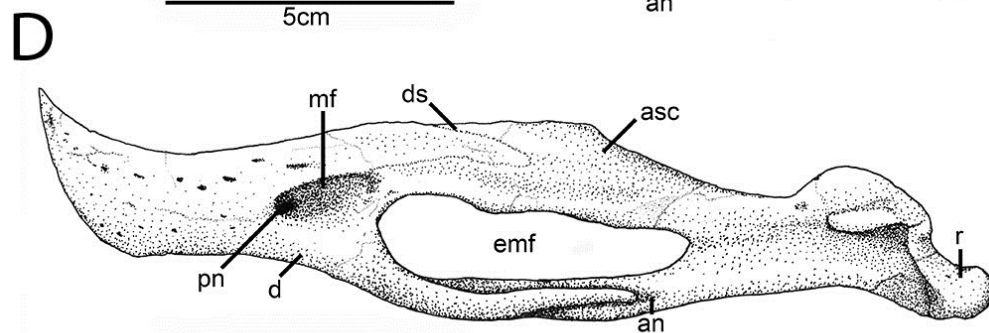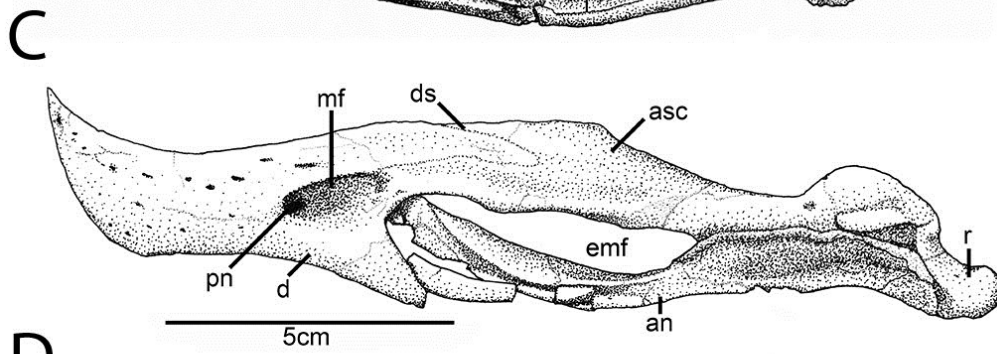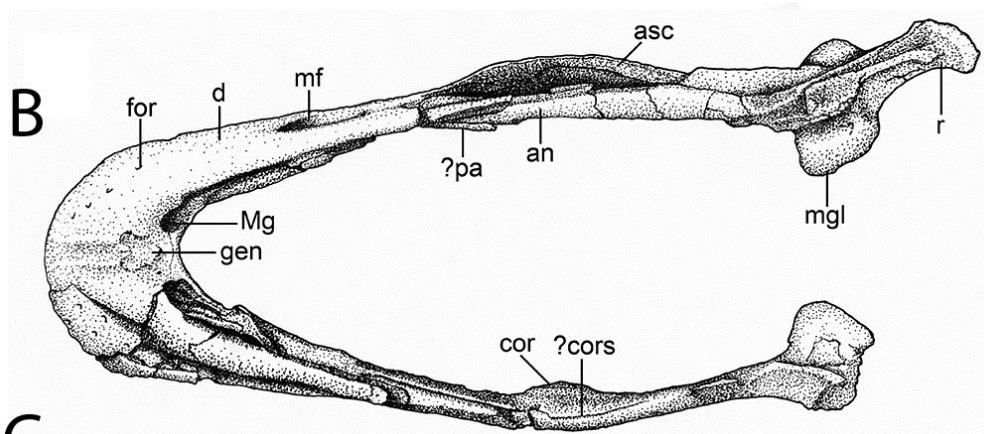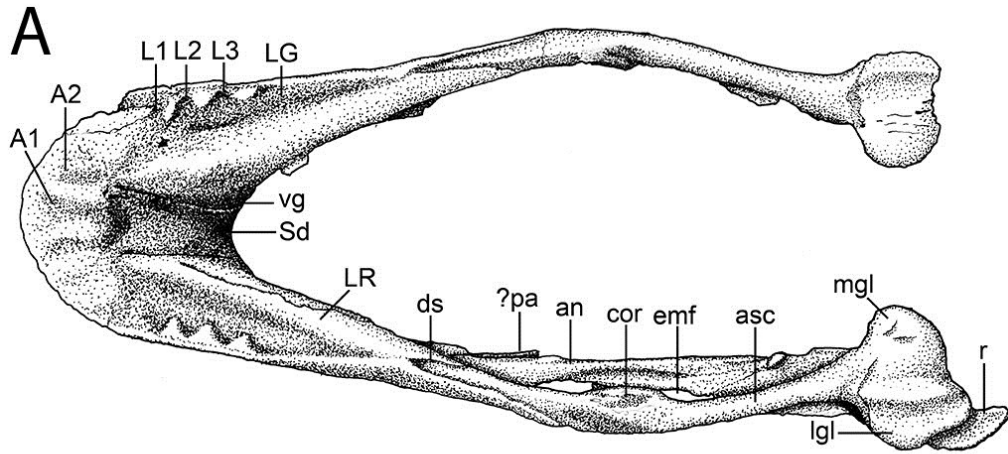
Fig. 3.29. Mandible of *Chirostenotes pergracilis* (TMP 2001.012.0012).

Illustrations of mandible of TMP 2001.012.0012 in dorsal (A), ventral (B), and left lateral (C) views. Reconstruction (D) of mandible in left lateral view. **Abbreviations: A1**, anterior occlusal ridge 1; **A2**, anterior occlusal ridge 2; **an**, angular; **asc**, articular-surangular-coronoid complex; **cor**, coronoid process; **?cors**, possible coronoid suture; **d**, dentary; **ds**, dentary-surangular suture; **emf**, external mandibular fenestra; **gen**, attachment of *m. genioglossus*; **L1–L3**, lateral occlusal grooves 1–3; **LG**, lingual groove; **lgl**, lateral glenoid; **LR**, lingual ridge; **mf,** mandibular fossa; **Mg,** Meckelian groove; **mgl**, medial glenoid; **?pa**, possible prearticular; **pn**, pneumatopore; **r**, retroarticular process; **Sd**, symphyseal depression (=sulcus); **vg**, vascular groove.
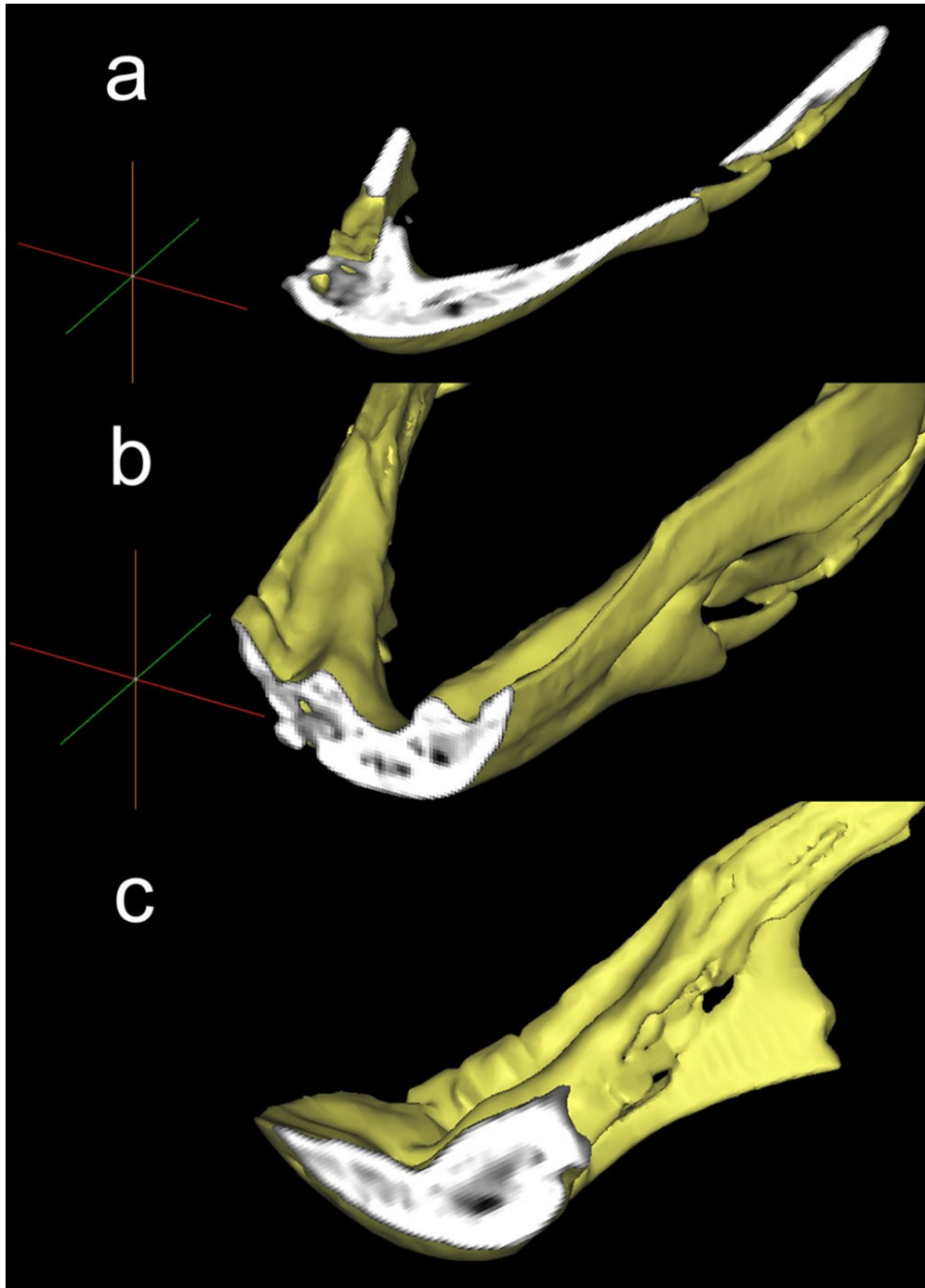
Fig. 3.30. Internal structures of the mandible of *Chirostenotes pergracilis.*

Cross-sectional images generated using computed tomography of the dentaries of TMP

2001.012.0012 sectioned longitudinally (A), transversely (B), and sagitally (C).
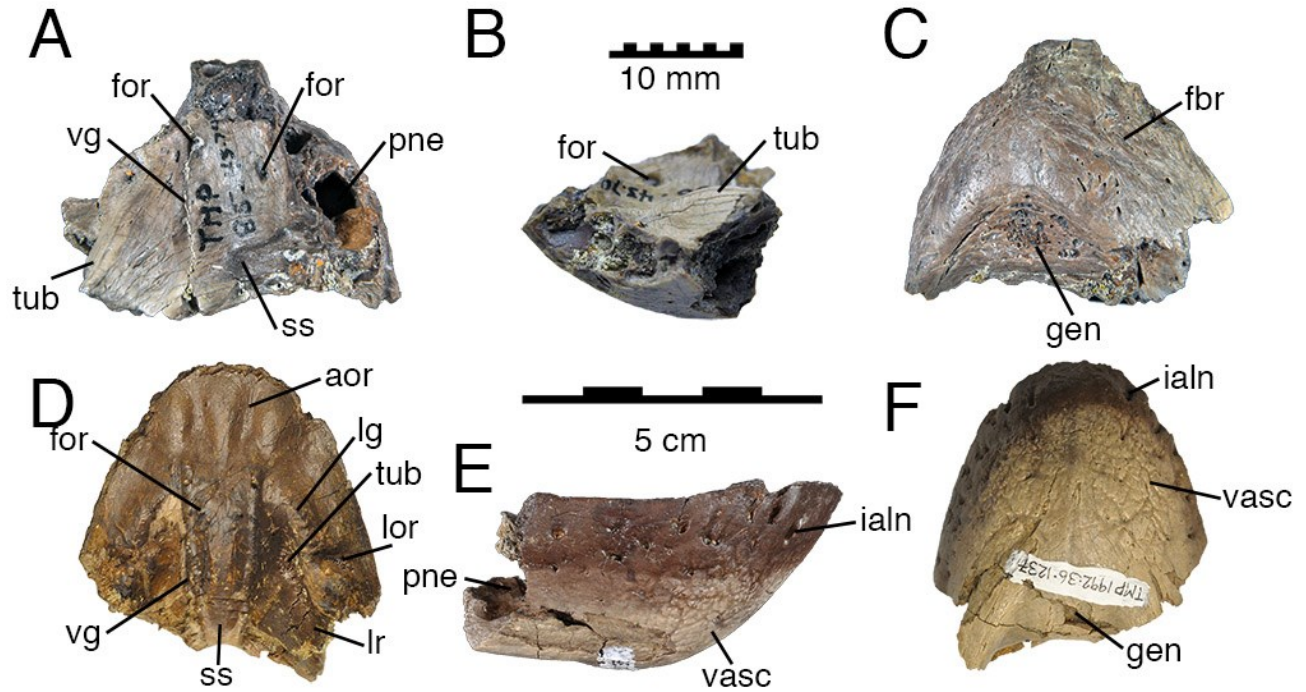
Fig. 3.31 Isolated dentaries of *Chirostenotes pergracilis*.

TMP 1985.043.0070 (A–C) in dorsal (A), left lateral (B), and ventral (C) views. TMP

1992.036.1237 (D–F) in dorsal (D), right lateral (E), and ventral (F) views. **Abbreviations: aor**,

anterior occlusal ridge; **fbr**, fibrous bone texture; **for**, foramen; **gen**, attachment of *m.*

genioglossus; **ialn**, foramen for the inferior alveolar nerve; **lg**, lingual groove; **lor,** lateral

occlusal ridge; **lr**, lingual ridge; **pne**, pneumatopore; **ss**, symphyseal sulcus; **tub**, tubercle; **vasc**,

vascular impressions; **vg**, vascular groove.
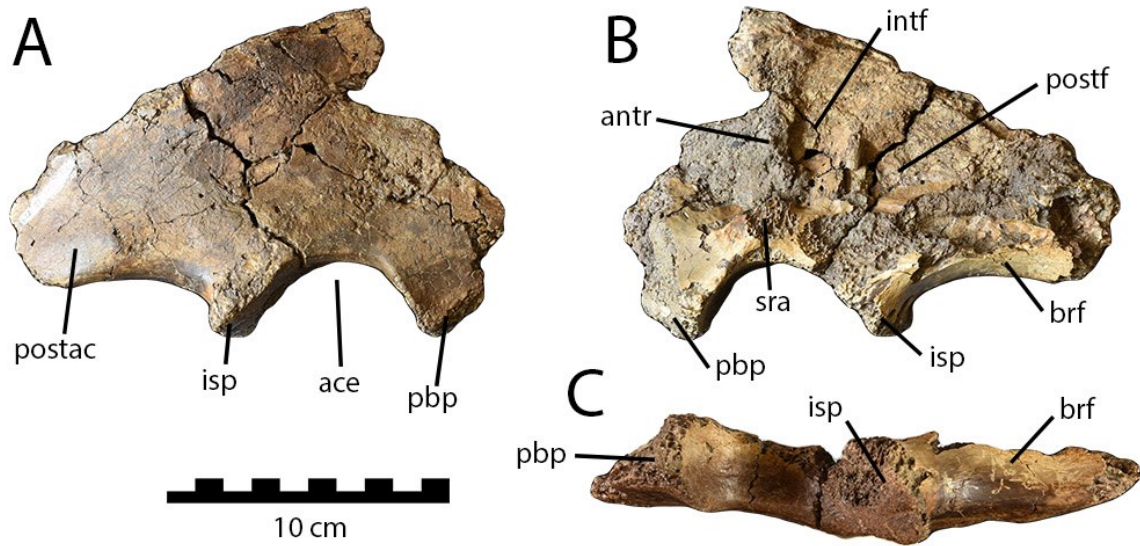
Fig. 3.32. Partial ilium of Chirostenotes pergracilis.

Partial right ilium (TMP 2002.012.0103) in lateral (A), medial (B), and ventral (C) views.

Abbreviations: ace, acetabulum; **antr**, anterior ridge; **brf**, brevis fossa; **intf**, intermediate fossa; **isp**, ischiadic peduncle; **pbp**, pubic peduncle; **postac,** postacetabular blade; **postf**, posterior fossa; **sra**, sacral rib attachment.
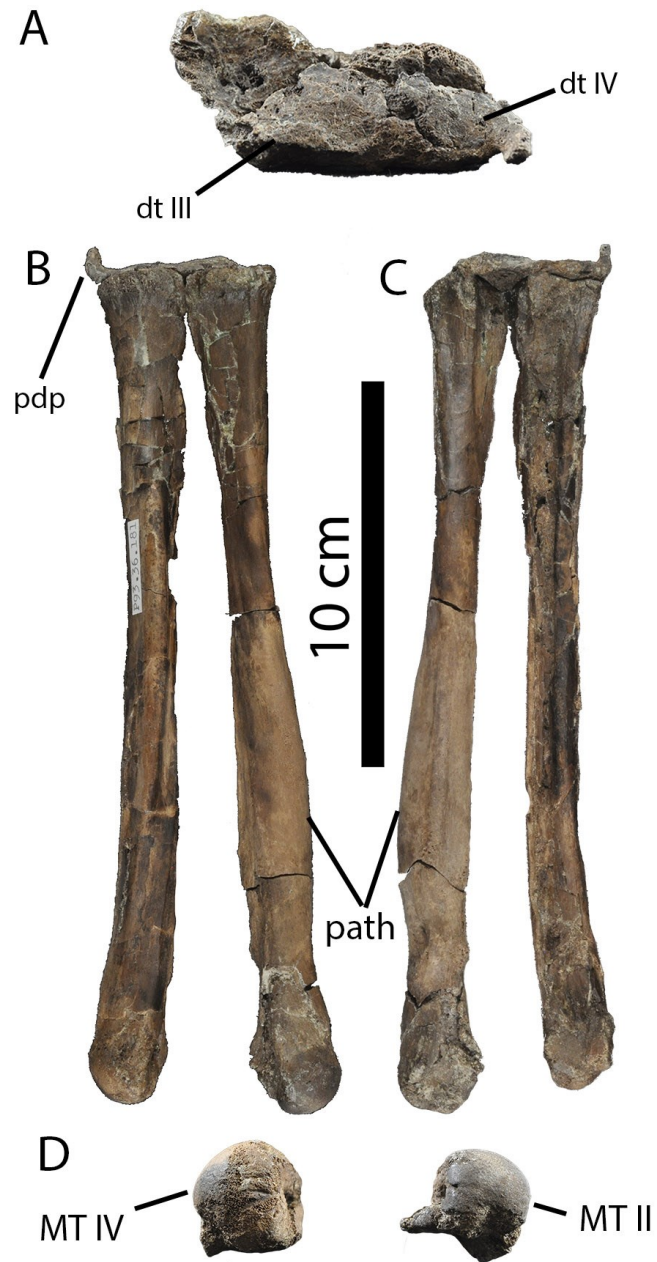
Fig. 3.33. Pathological tarsometatarsus of *Chirostenotes pergracilis*.

Partial right tarsometatarsus (TMP 1993.036.0181) comprising distal tarsals III and IV, and

metatarsals II and IV in proximal (A), anterior (B), posterior (C), and distal (D) views.

Abbreviations: dt III, distal tarsal III; **dt IV**, distal tarsal IV; **MT II**, metatarsal II; **MT IV**,

metatarsal IV; **path**, pathological region; **pdp**, proximodorsal process.
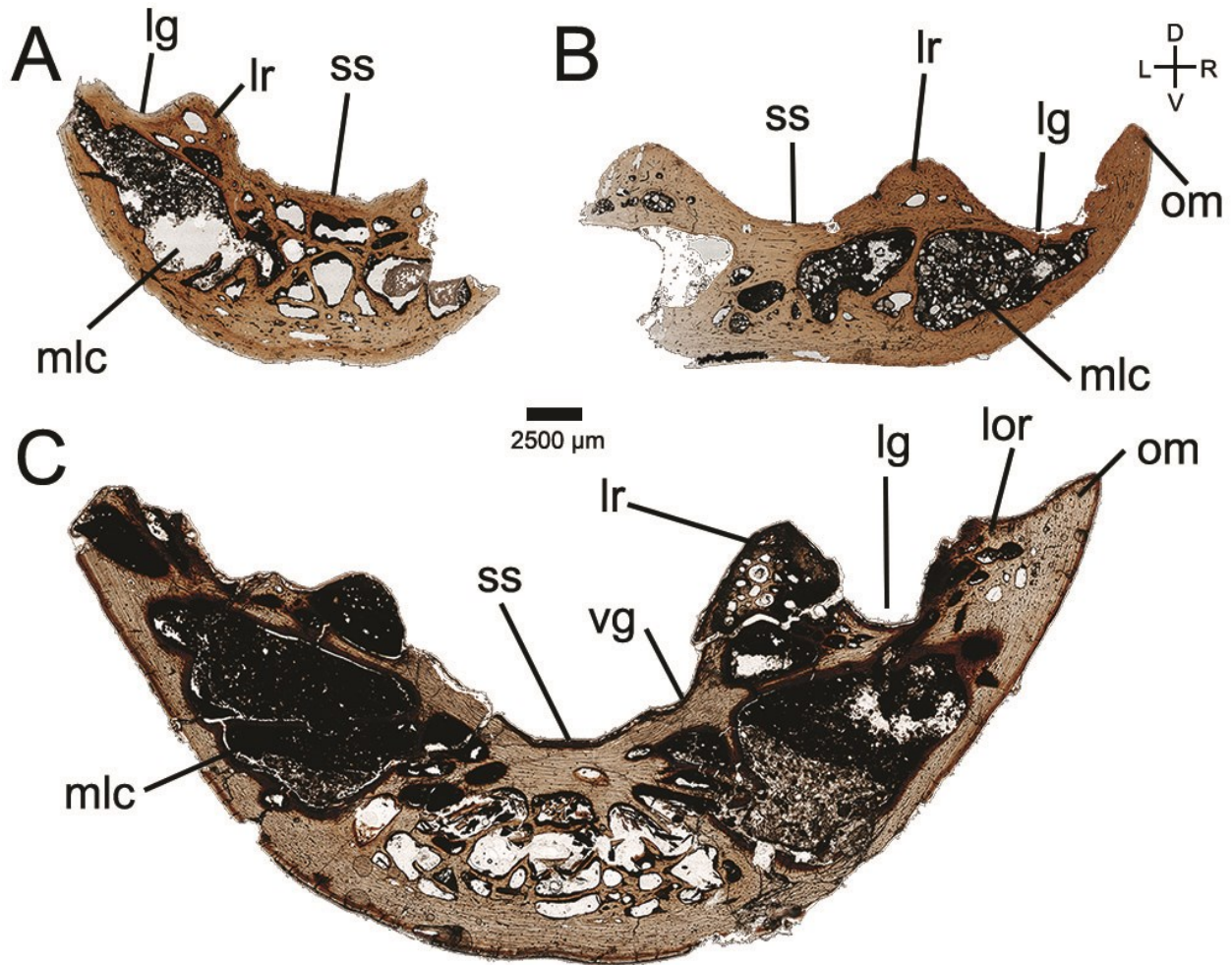
Fig. 3.34. Overview of transverse ground sections of caenagnathid dentaries.

TMP 1985.043.0070 (A), UALVP 55639 (B), and TMP 1992.036.1237 (C) under normal light.

Note variation in size of dentaries as well as arrangement of internal pneumatic cavities.

Orientation of all slides given in top-right corner. **Abbreviations: lg**, lingual groove; **lor,** lateral

occlusal ridge; **lr**, lingual ridge; **mlc**, major lateral cavity; **om**, occlusal margin; **ss,** symphyseal

sulcus; **vg**, vascular groove.
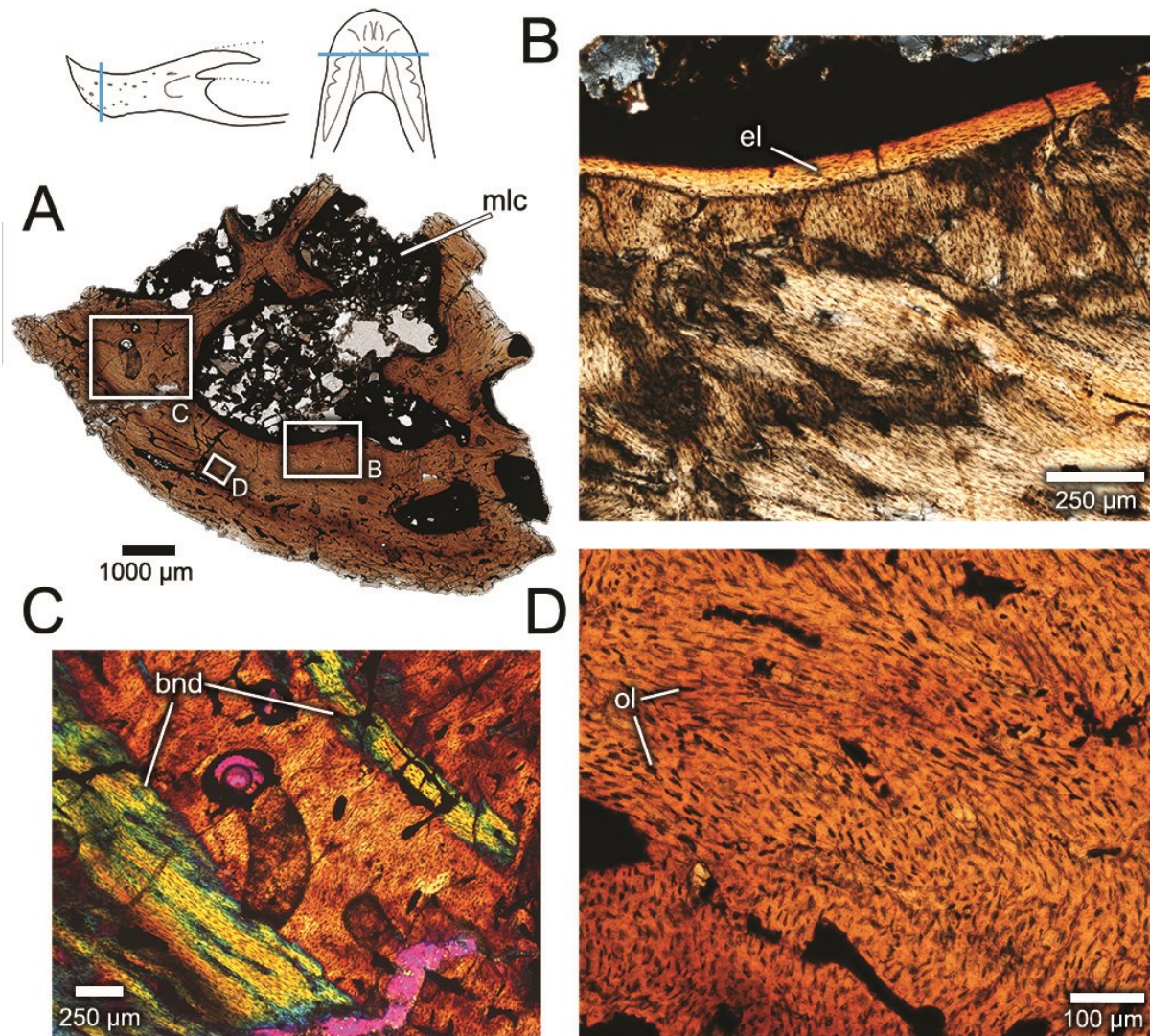
Fig. 3.35. Histological features of Section A of TMP 1985.043.0070.

Overview of entire slide (A) under normal light, showing regions of close-up images (boxes) and position of slide (top). Detail (B) of endosteal lamellae surrounding major labial cavity under cross-polarized light. Detail (C) of bands of opposite orientation composing primary fibrolamellar bone of the ventrolateral surface of the dentary under cross-polarized light with a lambda filter. Detail (D) of primary fibrolamellar bone matrix, showing varying orientation and size of osteocyte lacunae. **Abbreviations: bnd**, banding; **el,** endosteal lamellae; **mlc**, major lateral cavity; **ol**, osteocyte lacunae.
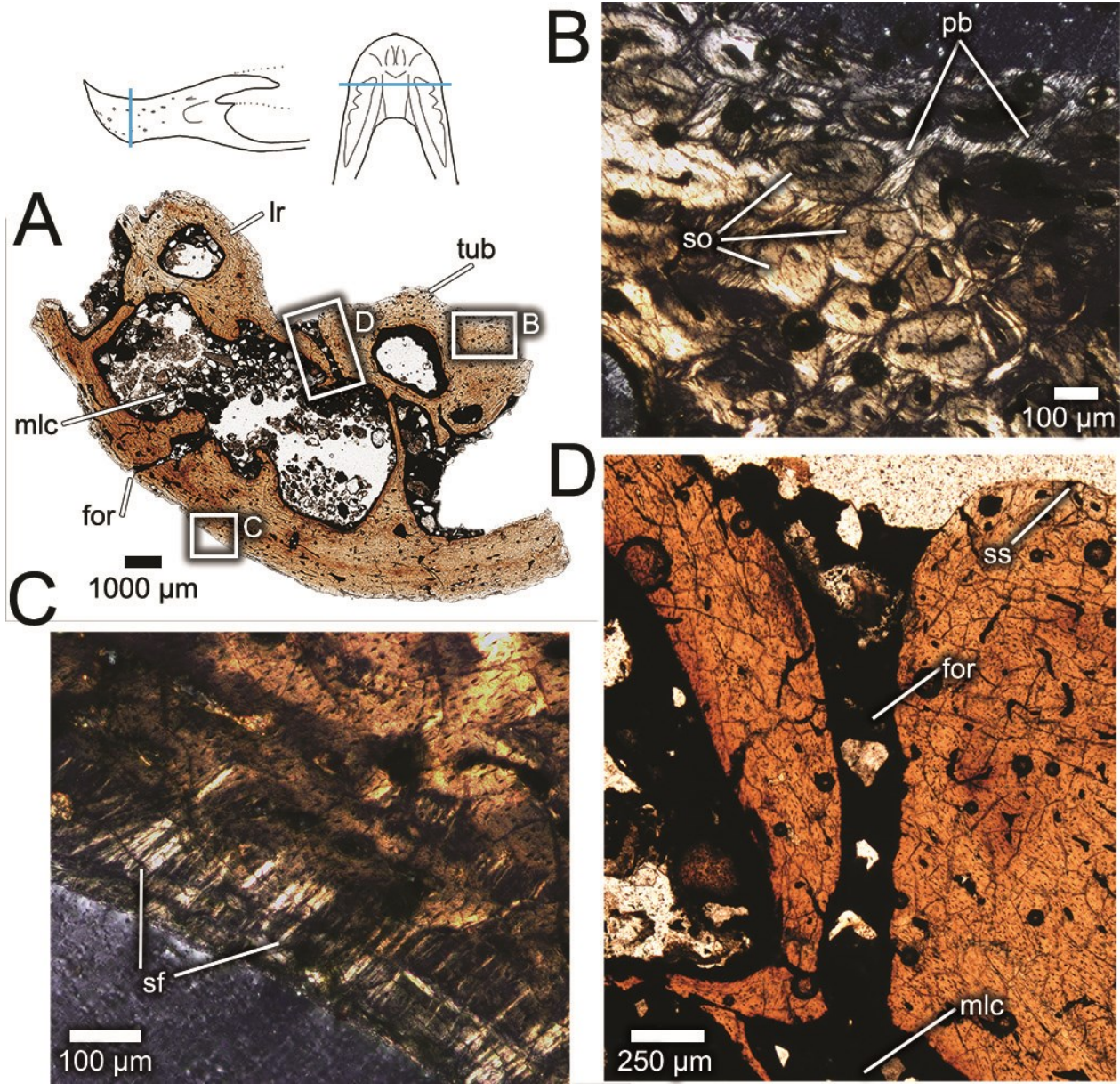
(Previous page)
Fig. 3.36. Histological features of Section B of TMP 1985.043.0070.

Overview of entire slide (A) under normal light, showing regions of close-up images (boxes) and position of slide (top). Detail (B) of secondary osteons cross-cutting primary bone with Sharpey's fibers in the symphyseal sulcus under cross-polarized light. Detail (C) of well-developed Sharpey's fibers in primary bone on the ventrolateral surface of the dentary under cross-polarized light. Detail (D) of foramen connecting major labial cavity and external surface of the dentary at the symphyseal sulcus under normal light. **Abbreviations: for**, foramen; **lr**, lingual ridge; **mlc**, major lateral cavity; **pb**, primary bone; **sf**, Sharpey's fibers; **so**, secondary osteons; **ss**, symphyseal sulcus; **tub**, tubercle.
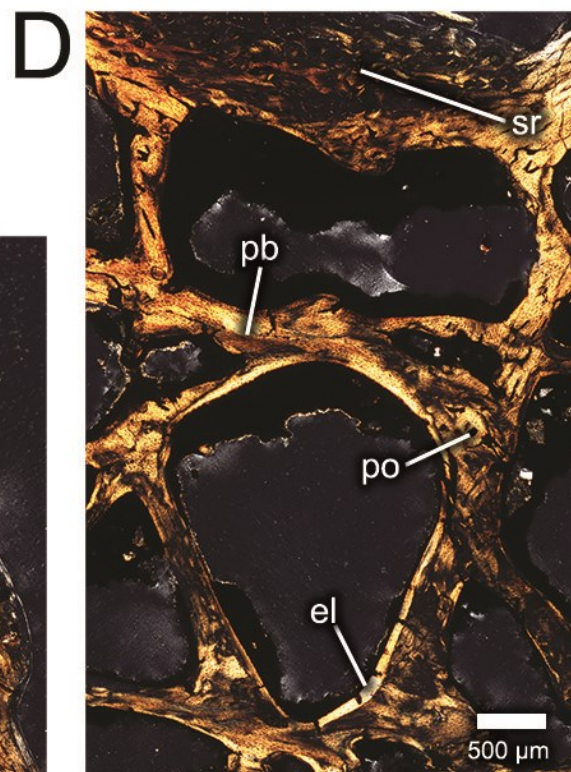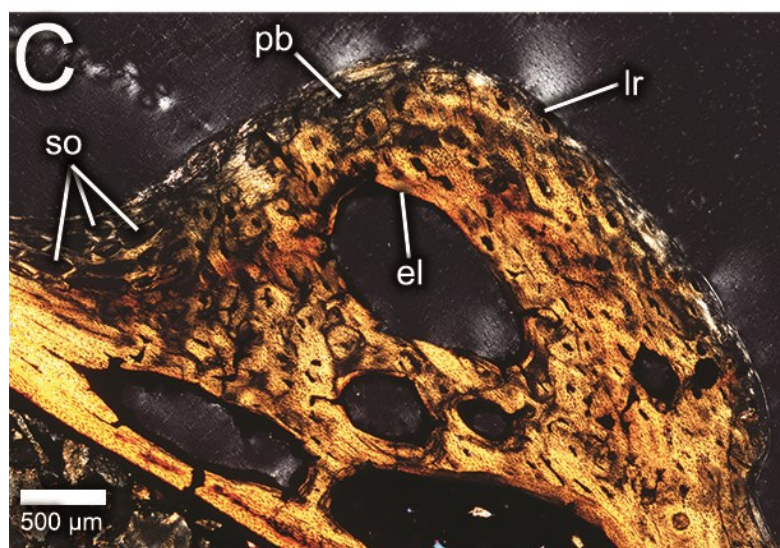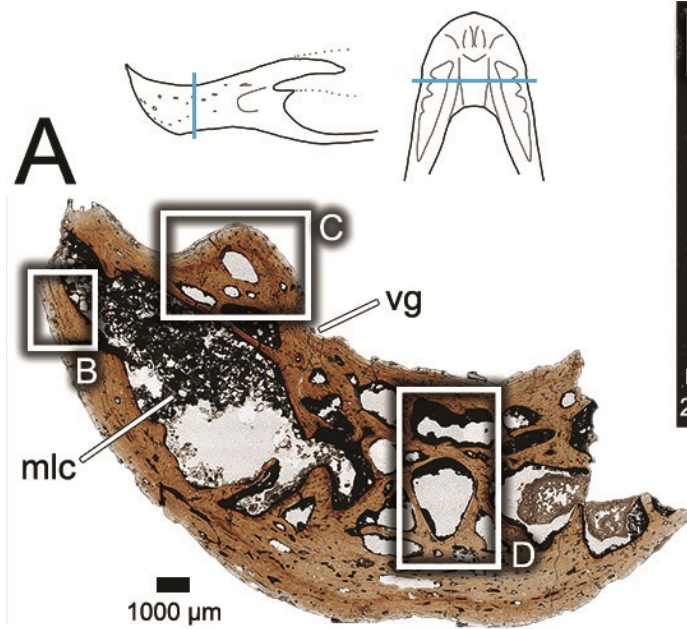
(Previous page)
Fig. 3.37. Histological features of Section C of TMP 1985.043.0070.

Overview of entire slide (A) under normal light, showing regions of close-up images (boxes) and position of slide (top). Detail (B) of labial side of dentary under cross-polarized light, showing orientation of primary osteons parallel to external surface of the bone. Detail (C) of lingual ridge under cross-polarized light, showing internal cavities and secondary remodeling. Detail (D) of midline cavities under cross-polarized light, showing endosteal lamellae and secondary remodeling. **Abbreviations: el**, endosteal lamellae; **lr**, lingual ridge; **mlc**, major lateral cavity; **pb**, primary bone; **po**, primary osteon; **sr**, secondary remodeling; **vg**, vascular groove.
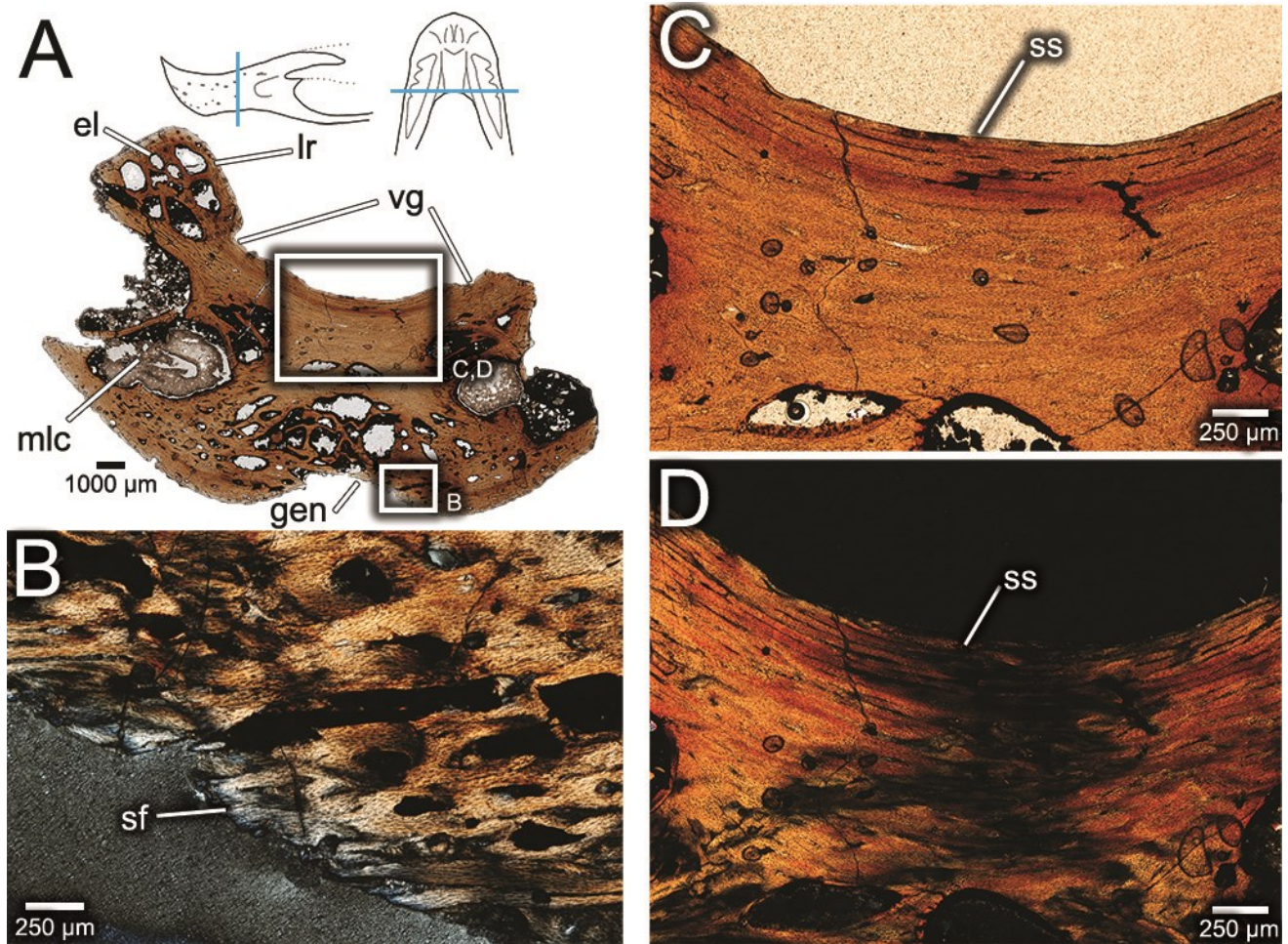
Fig. 3.38. Histological features of Section D of TMP 1985.043.0070.

Overview of entire slide (A) under normal light, showing regions of close-up images (boxes) and position of slide (top). Detail (B) of M. genioglossus attachment under cross-polarized light, showing subtle Sharpey's fibers and unfinished periosteal surface of the bone. Detail (C, D) of nearly avascular symphyseal region of dentary under normal (C) and cross-polarized (D) light, showing sweeping extinction of bone tissue indicating curvature of primary osteons.

Abbreviations: el, endosteal lamellae; **gen**, attachment of *m. genioglossus*; **lr**, lingual ridge; **mlc**, major lateral cavity; **sf**, Sharpey's fibers; **ss**, symphyseal sulcus; **vg**, vascular groove.
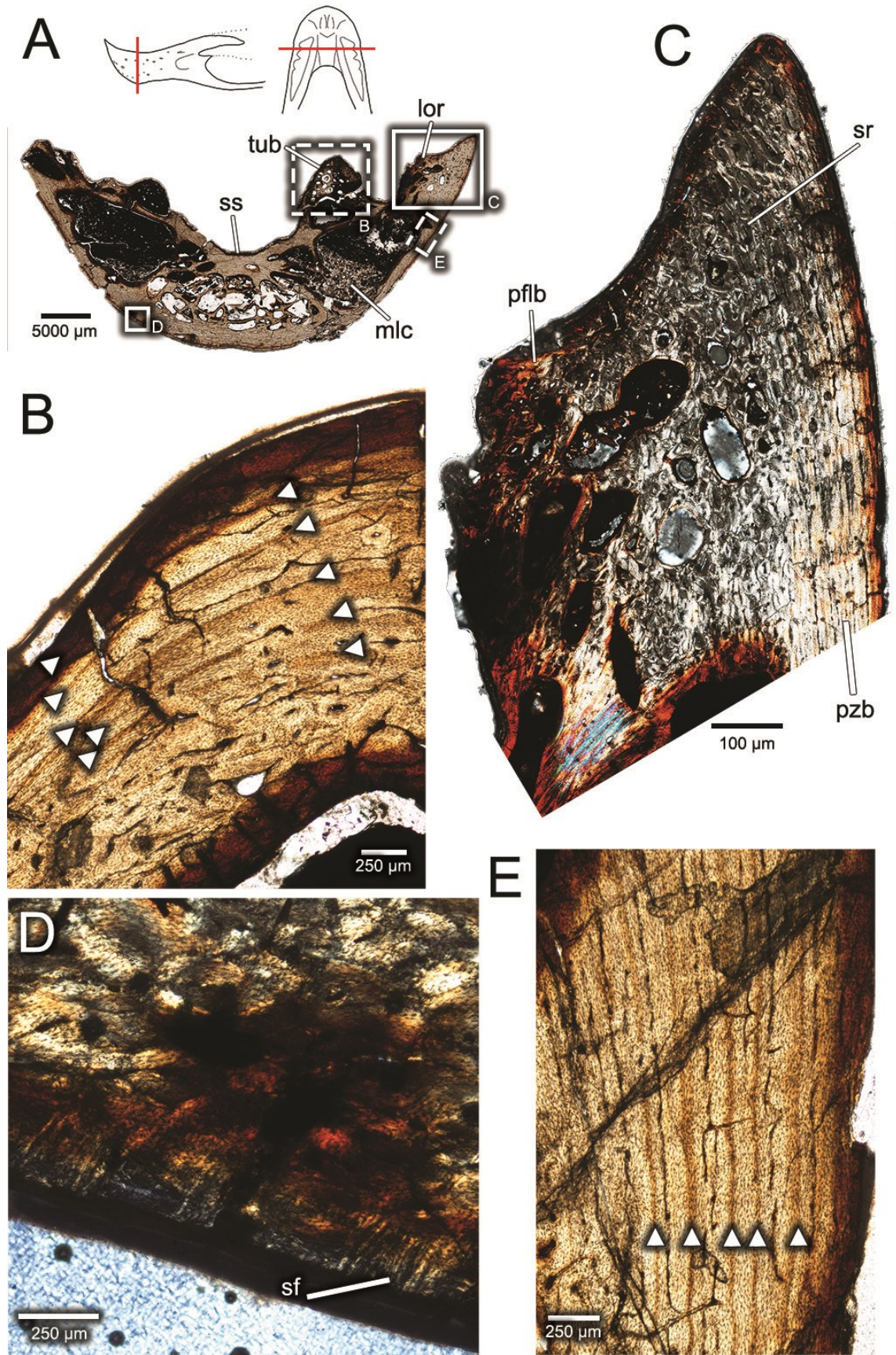
(Previous page)

Fig. 3.39. Histological features of mandible of TMP 1992.036.1237.

Overview of Section A (A) under normal light, showing regions of close-up images (boxes) and position of slide (top). Dashed boxes indicate regions of close-ups taken from Sections B and C, solid boxes indicate regions of close-ups from Section A. Detail (B) of lingual ridge of Section C under normal light, showing lines of arrested growth (arrows). Detail (C) of lateral occlusal ridge of Section A under cross-polarized light, showing primary fibrolamellar bone on lingual and labial sides and a region of secondary remodeling between them. Detail (D) of Sharpey's fibers along the ventrolateral portion of Section A under cross-polarized light. Detail (E) of lines of arrested growth and zonal primary bone (arrows) on the labial surface of Section C.

Abbreviations: lor, lateral occlusal ridge; **mlc**, major lateral cavity; **pflb**, primary fibrolamellar bone; **pzb**, primary zonal bone; **sf**, Sharpey's fibers; **sr**, secondary remodeling; **ss**, symphyseal sulcus; **tub**, tubercle.

A–F. Photomicrographs of bone histology.
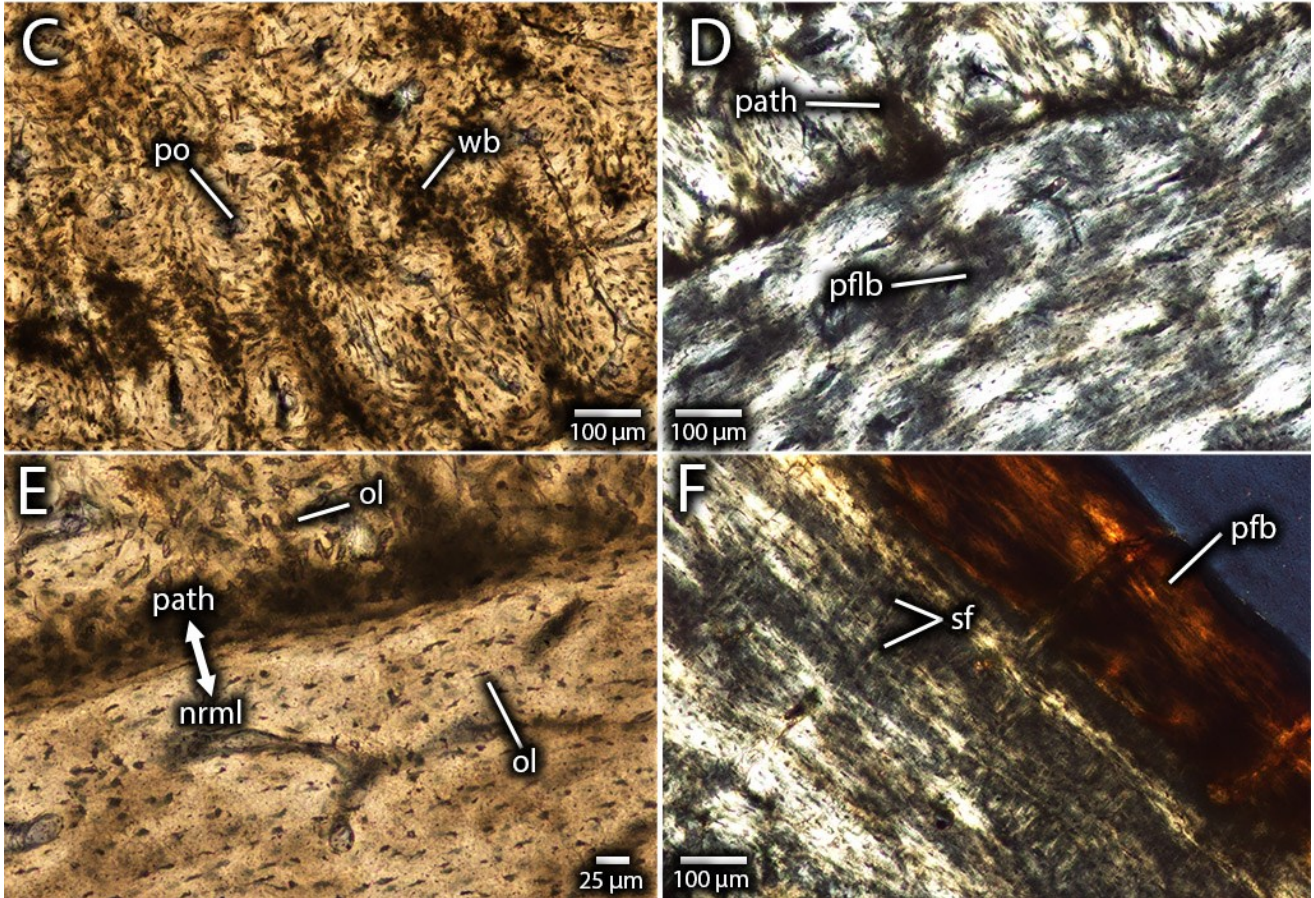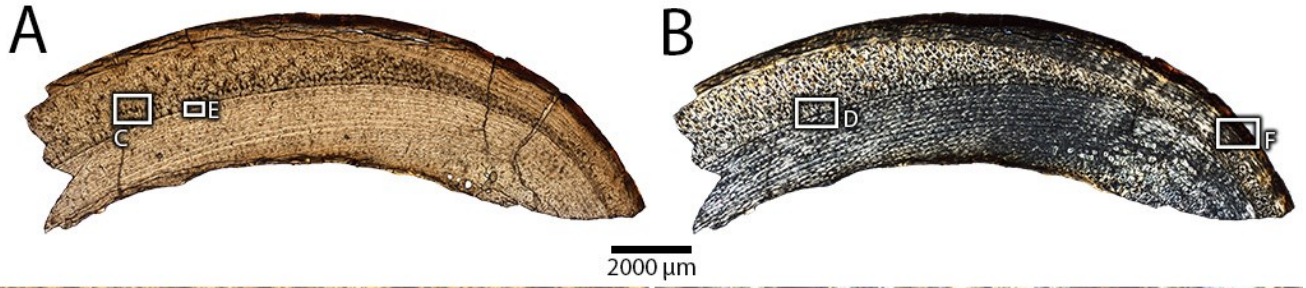
(Previous page)
Fig. 3.40. Femoral osteohistology of *Chirostenotes pergracilis* (UALVP 59400).

Transverse thin section of fragment of femur from UALVP 59400 in plane-polarized (A) and cross-polarized (B) light. Detail (C) of pathological woven bone in the mid-cortex of the femur under plane-polarized light. Detail (D) of interface between normal bone (bottom) and pathological bone (top) in cross-polarized light. Close-up (E) of interface between normal bone (bottom) and pathological bone (top), showing no evidence of resorption at the former periosteal surface, under plane-polarized light. Detail (F) of external cortex, showing well-developed Sharpey's fibers and external zone of parallel-fibered bone indicative of slow growth.

Abbreviations: nrml, normal bone; **ol,** osteocyte lacuna; **path**, pathological bone; **pfb**, parallel-fibered bone; **pflb**, primary fibrolamellar bone; **sf**, Sharpey's fibers; **wb**, woven bone.
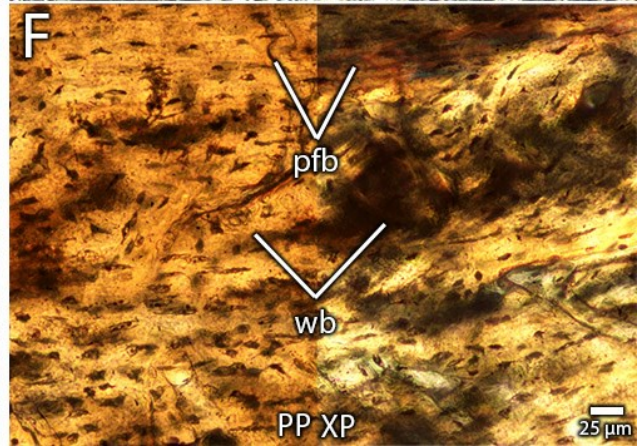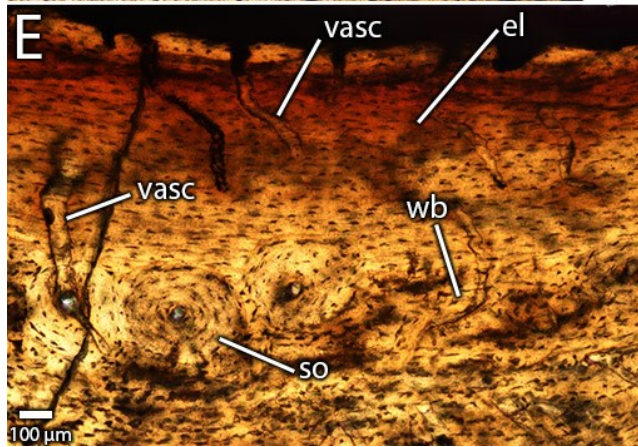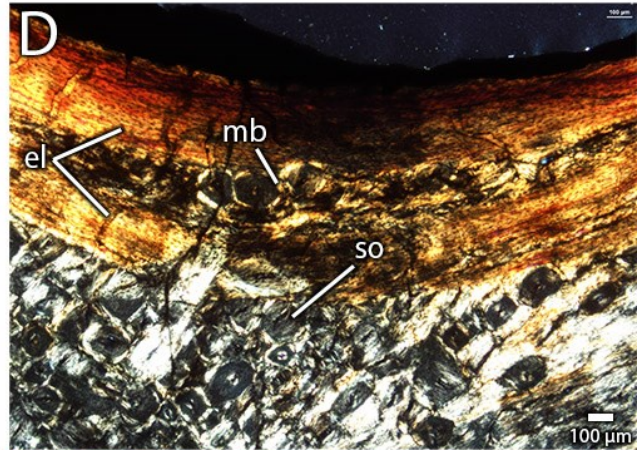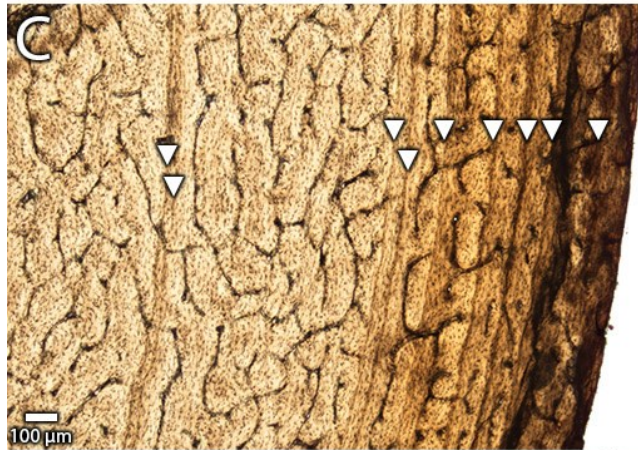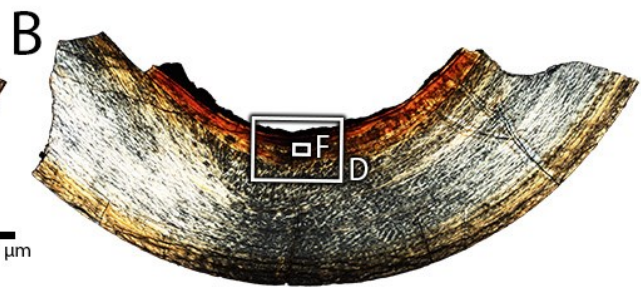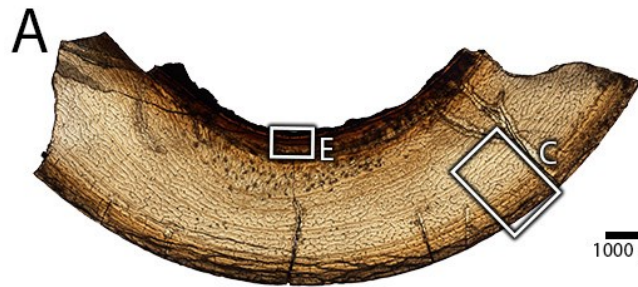
(Previous page)
Fig. 3.41. Osteohistology of the tibia of *Chirostenotes pergracilis* (UALVP 59400).

Transverse thin section of fragment of tibia from UALVP 59400 in plane-polarized (A) and cross-polarized (B) light. Detail (C) of cyclical growth marks (arrows) preserved in the cortex of the tibia in plane-polarized light. Detail (D) of multiple generations of endosteal lamellae with entrapped medullary bone at the endosteal surface of the tibia under cross-polarized light. Detail (E) of endosteal lamellae invaded by vascular canals as well as secondary remodeling of primary woven bone in between layers of endosteal lamellae on the endosteal surface of the tibia under plane-polarized light. Close-up (F) of woven medullary bone between layers of parallel-fibered endosteal lamellae under plane-polarized (left) and cross-polarized (right) light. **Abbreviations: el**, endosteal lamellae; **mb**, medullary bone; **pfb**, parallel-fibered bone; **so**, secondary osteon; **vasc**, vascular canal; **wb**, woven bone.
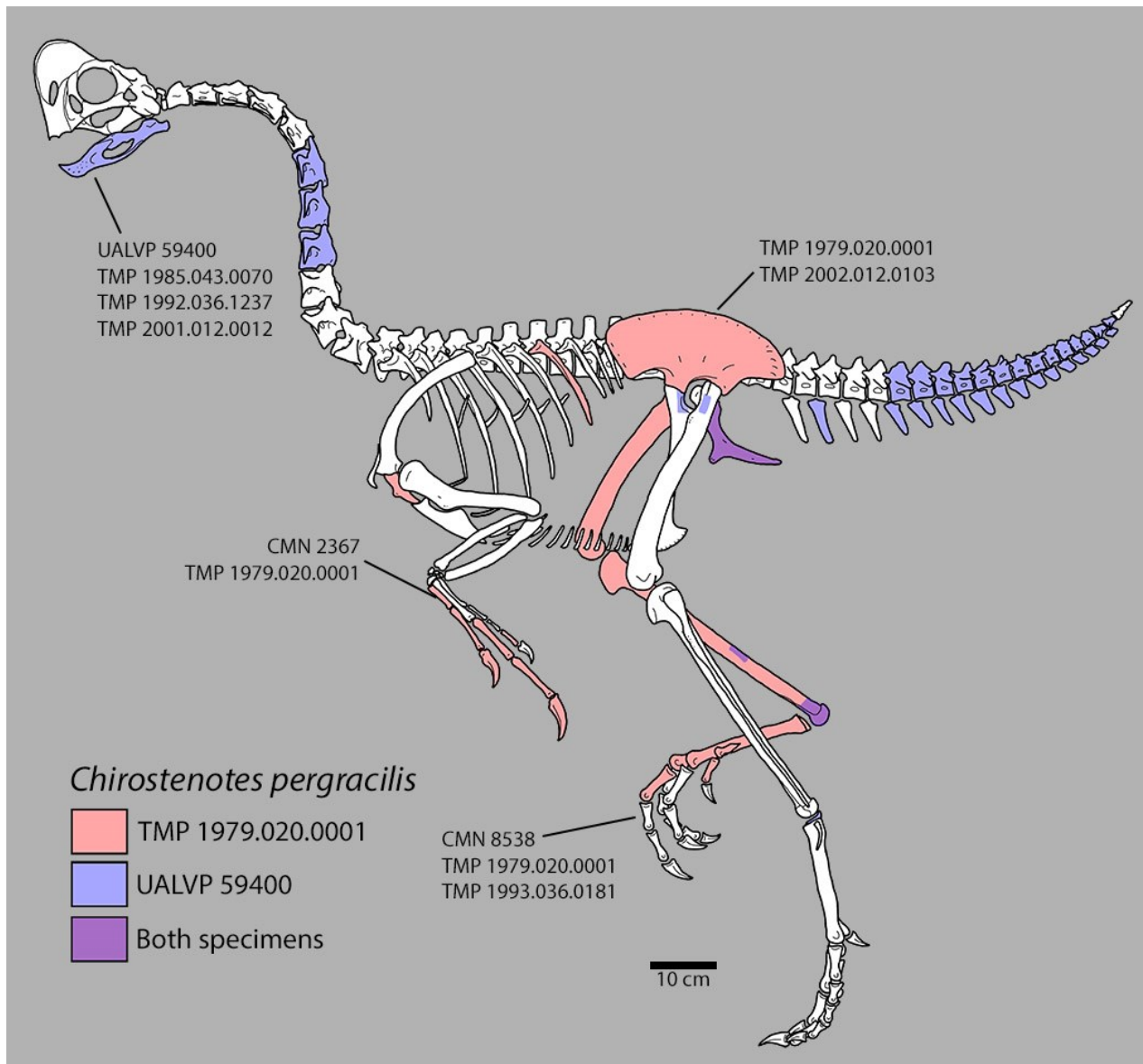
Fig. 3.42. Skeletal reconstruction of *Chirostenotes pergracilis*.

Skeletal reconstruction based on associated skeletons (CMN 2367, CMN 8538, TMP

1979.020.0001 and UALVP 59400), with other elements reconstructed from *Apatoraptor*

pennatus, *Nomingia gobiensis*, and ROM 65050.
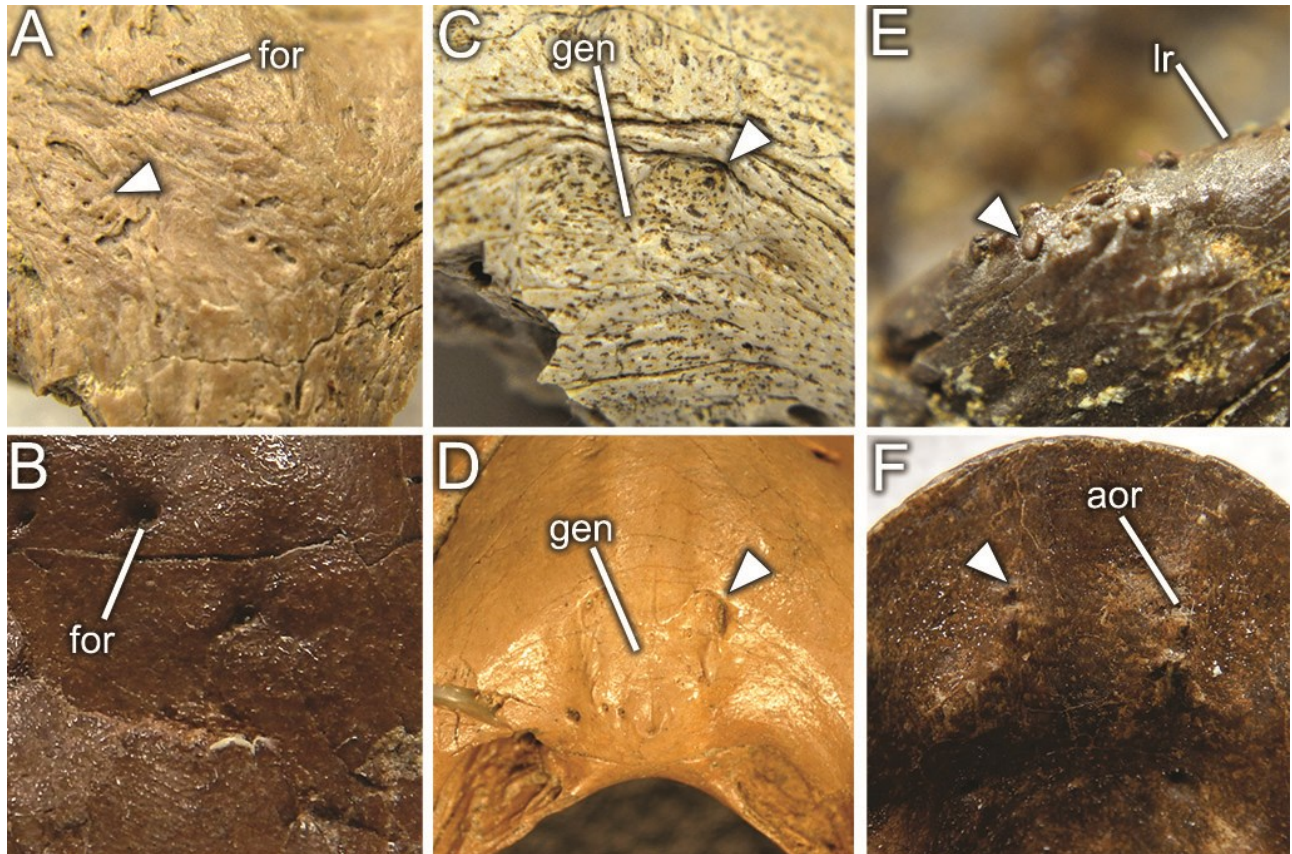
Fig. 3.43. Variation possibly related to ontogeny in caenagnathid dentaries.

Fibrous external bone texture (A, arrow) of TMP 1985.043.0070 versus finished bone texture (B) of TMP 1990.056.0006. Poorly formed M. genioglossus attachment (C, arrow) of TMP 1992.040.0044 versus well defined, lipped M. genioglossus attachment (D, arrow) of TMP 2001.012.0012. Nodule formation on the tubercle of the lingual ridge (E, arrow) of TMP 1992.036.1237 and the anterior occlusal ridges (F) of TMP 1992.036.0390. Images not to scale.

Abbreviations: aor, anterior occlusal ridge; **for**, foramen; **gen**, attachment of *m. genioglossus*; **lr**, lingual ridge.
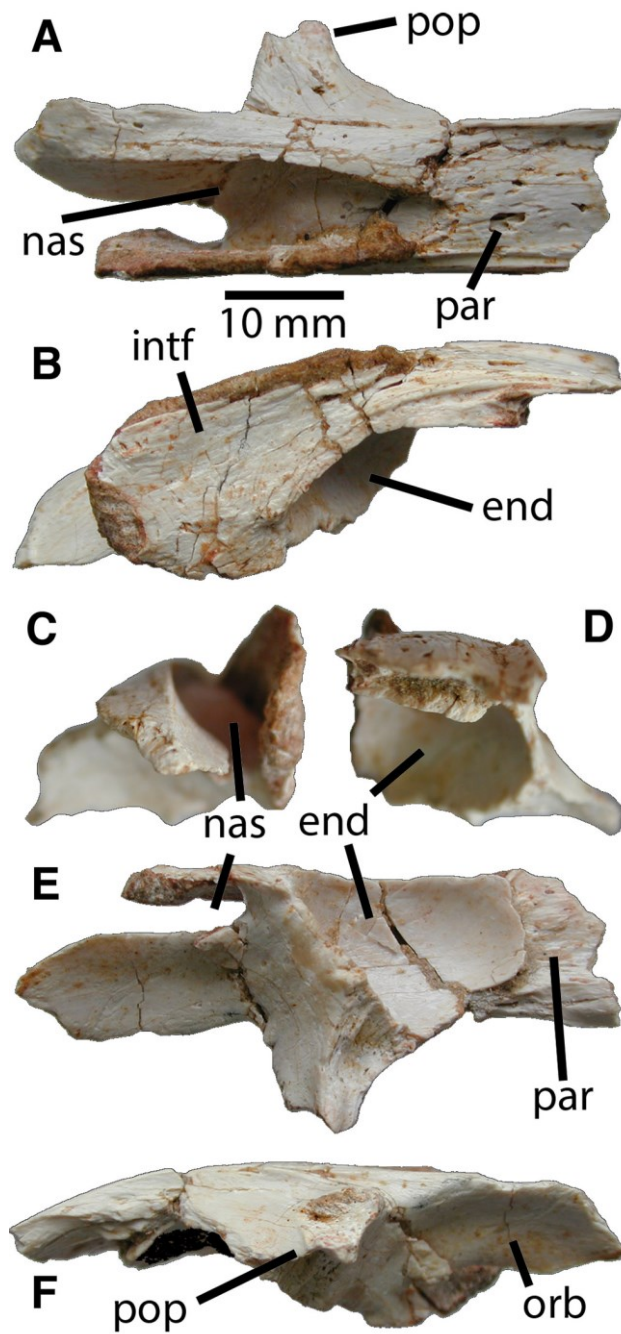
Fig. 3.44. Frontal of *Elmisaurus rarus*.

Frontal of MPC-D 102/007 in dorsal (A), medial (B), anterior (C), posterior (D), ventral (E), and

lateral (F) views. **Abbreviations: end**, endosteal cavity; **intf**, interfrontal contact; **nas**, slot for

nasal; **par**, parietal contact; **pop**, postorbital process.
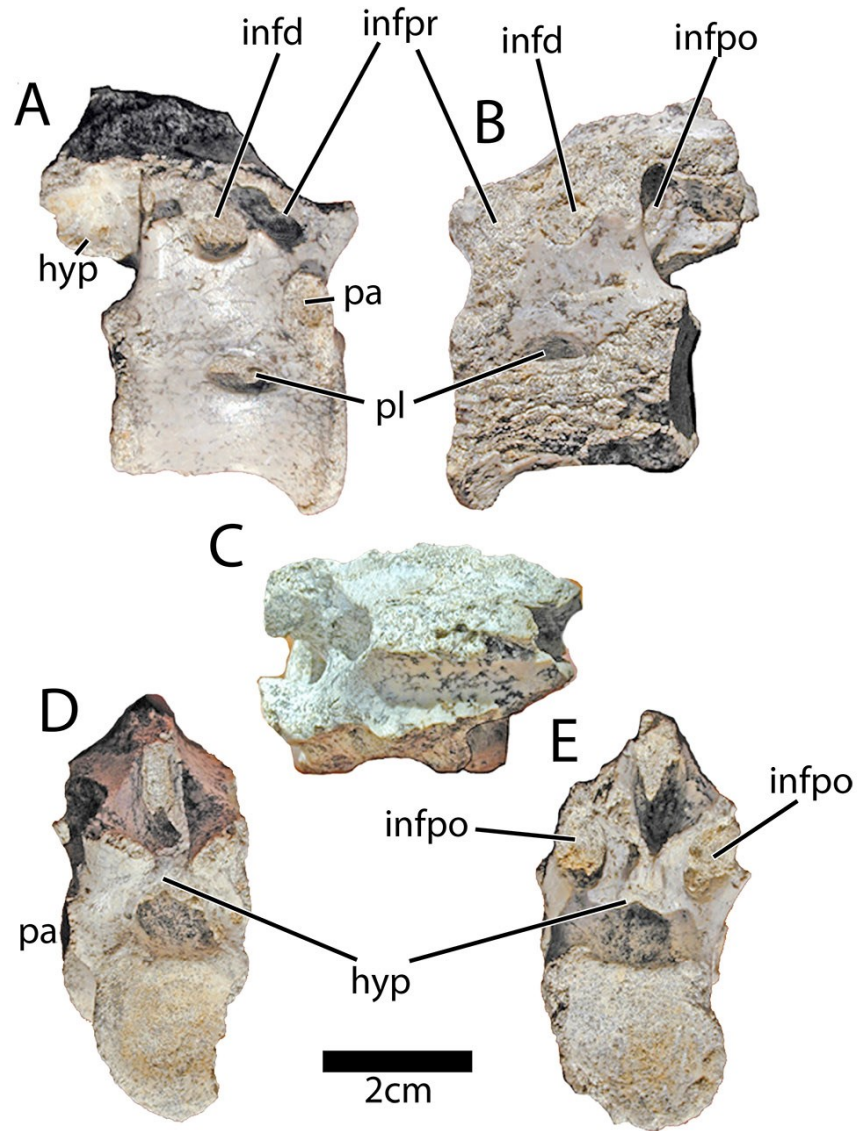
Fig. 3.45. Vertebra of *Elmisaurus rarus*.

Anterior dorsal vertebra of MPC-D 102/007 in right lateral (A), left lateral (B), dorsal (C), anterior (D), and posterior (E) views. **Abbreviations: hyp**, hypantrum; **infd**, infradiapophyseal fossa; **infpo**, infrapostzygapophyseal fossa; **infpr**, infraprezygapophyseal fossa; **pa**, parapophysis; **pl**, pleurocoel.
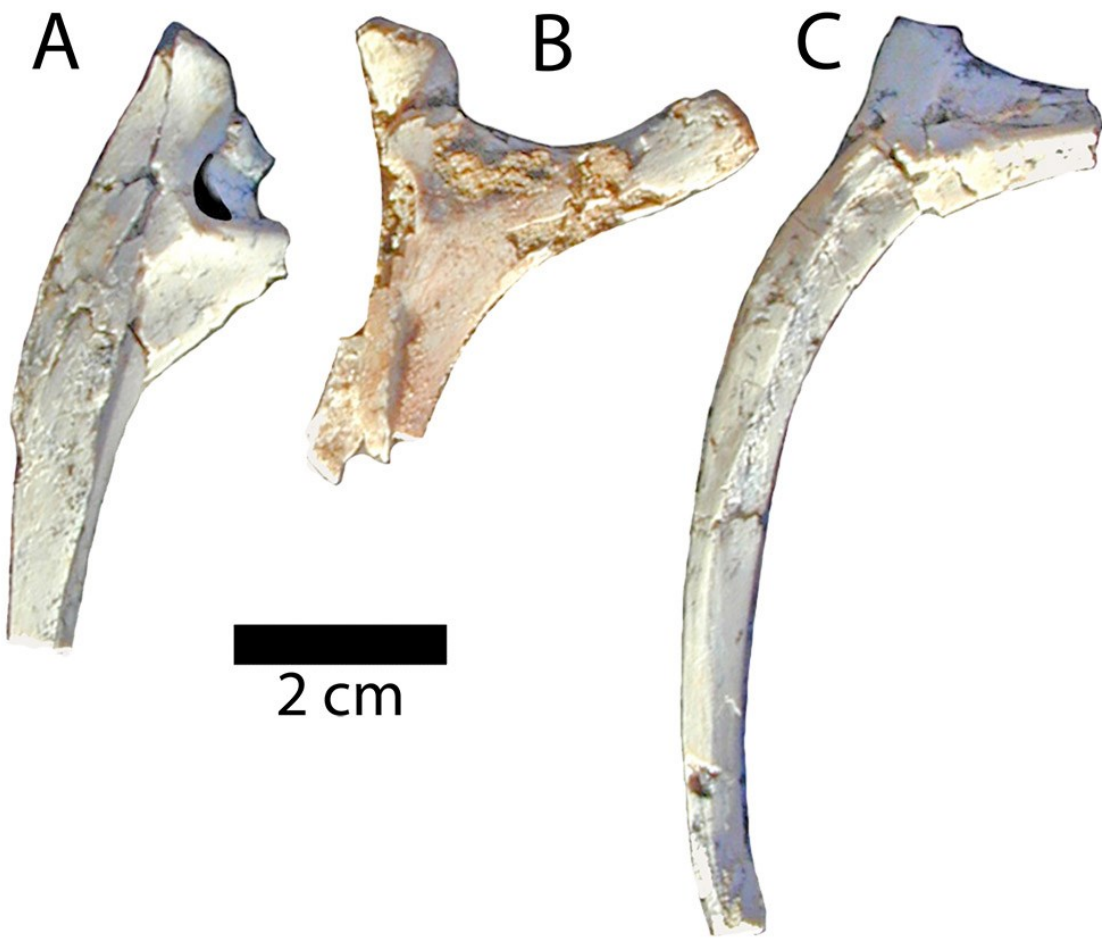
Fig. 3.46. Dorsal ribs of *Elmisaurus rarus*.

First dorsal rib (A), posterior dorsal rib (B), and anterior dorsal rib (C) of MPC-D 102/007 in anterior view.
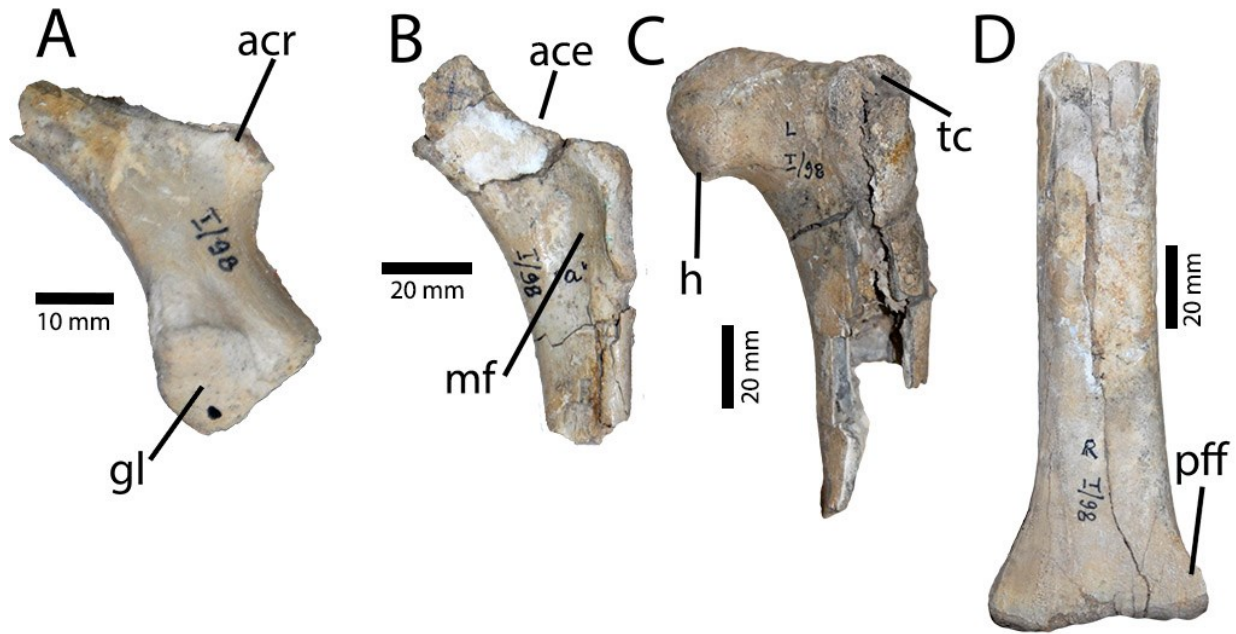
Fig. 3.47. Appendicular elements of *Elmisaurus rarus*.

Proximal portion of right scapula (A), proximal right pubis (B), proximal left femur (C), and distal right tibia (D) of ZPAL MgD-I/98. **Abbreviations: ace,** acetabulum; **acr**, acromion process; **gl**, glenoid; **h**, head; **mf**, medial fossa; **pff**, postfibular flange; **tc**, trochanteric crest.
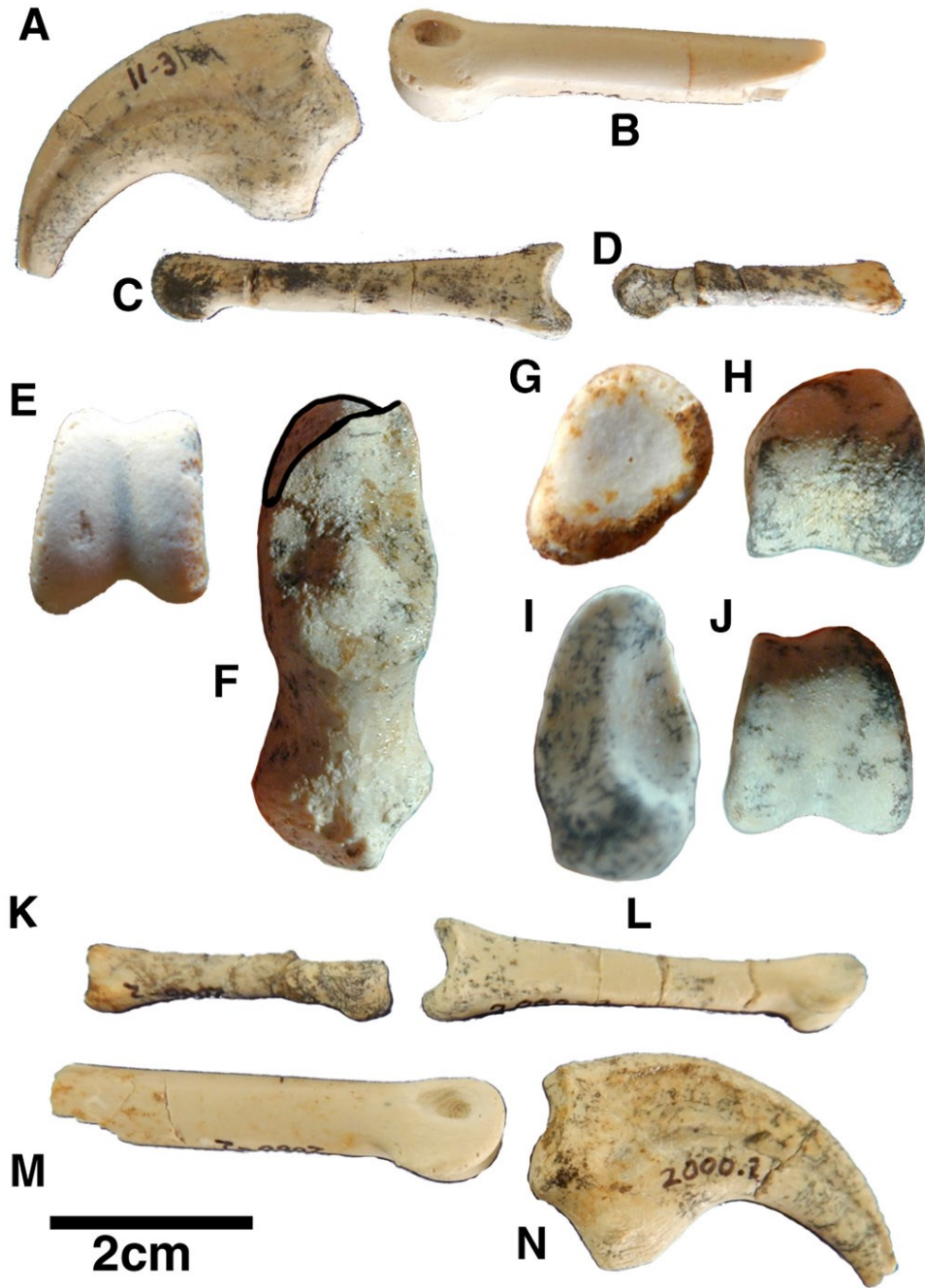
Fig. 3.48. Manual elements of *Elmisaurus rarus*.

Manual phalanges II-3 (A, F, N), II-2 (B, E, M), III-1 (D, G, H, K), and III-3 (C, I, J, L) of MPC-D 102/007 in lateral or medial (A–D; K–N), proximal (F, G, I), and distal (E, H, J) views.
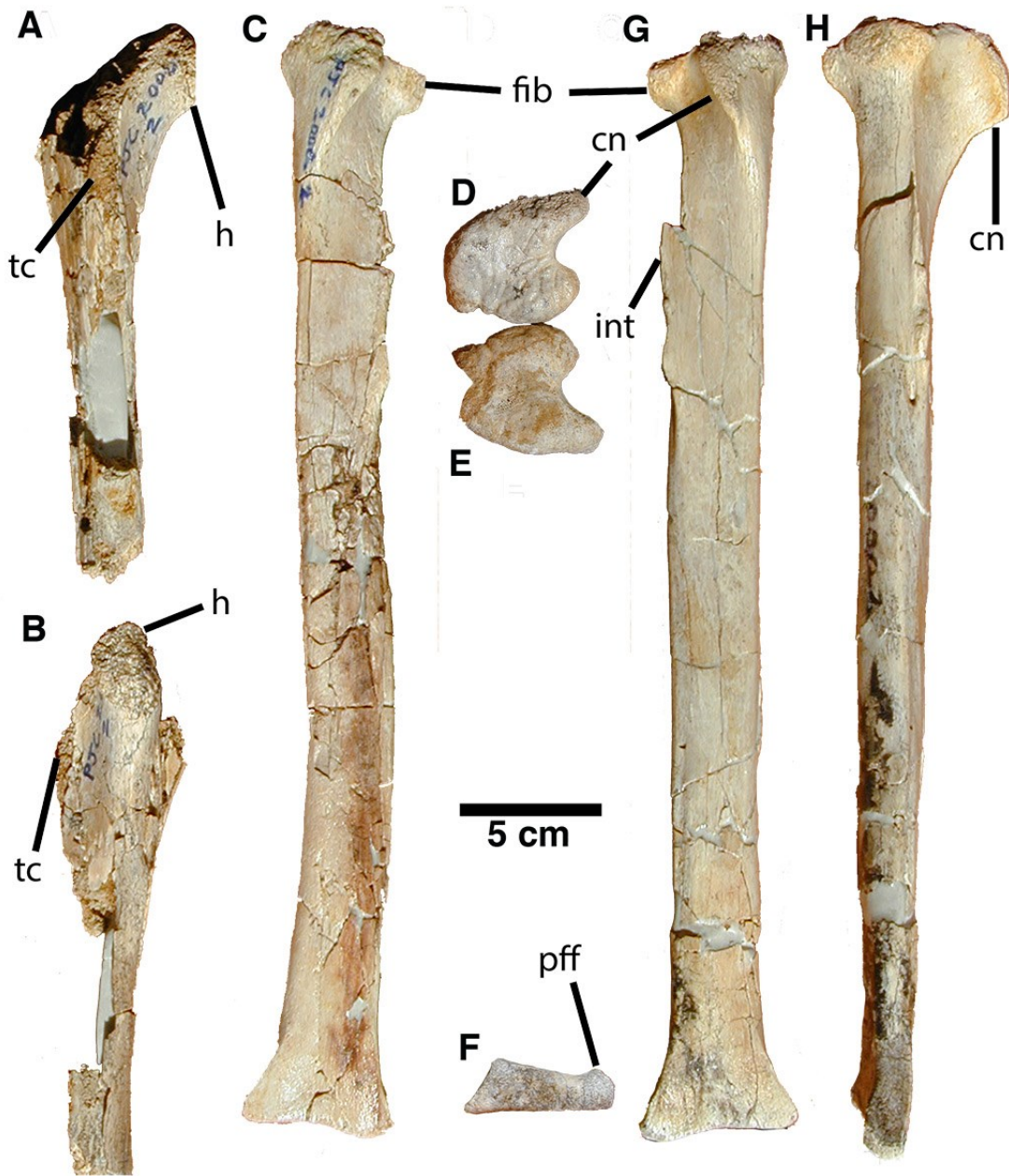
Fig. 3.49. Hindlimb elements of *Elmisaurus rarus*.

Proximal head of femur of MPC-D 102/007 in anterior (A) and medial (B) views. Tibiae of

MPC-D 102/007 in anterior (C, G), proximal (D, E), distal (F), and lateral (H) views.

Abbreviations: cn, cnemial crest; **fib**, fibular condyle; **h**, head; **int**, interosseum crest; **pff**,

postfibular flange; **tc**, trochanteric crest.
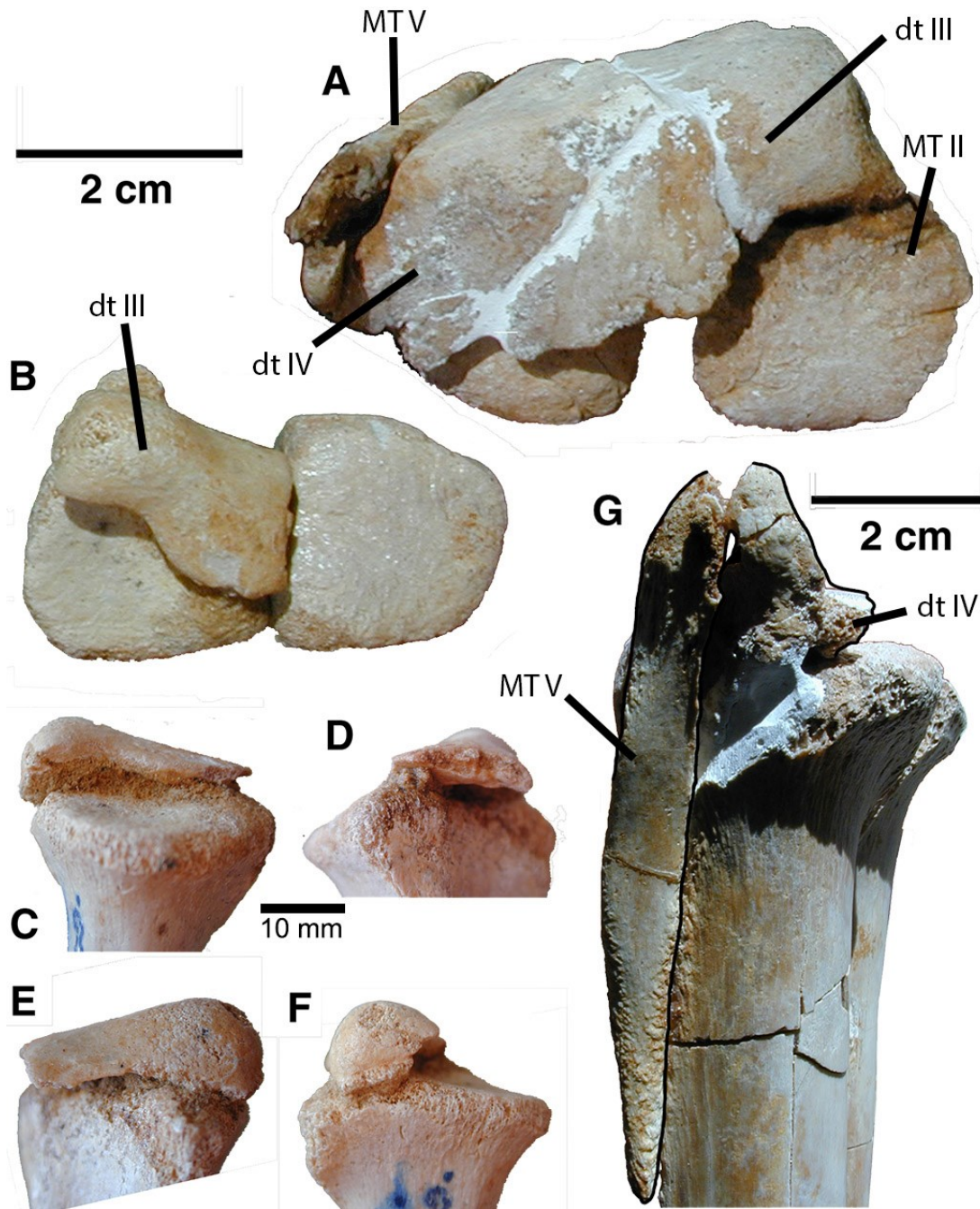
Fig. 3.50. Distal tarsals of *Elmisaurus rarus*.

Proximal tarsometatarsi of MPC-D 102/006 (B–F) and MPC-D 102/007 (A, G) in proximal (A, B), anterior (C), lateral (D, G), posterior (E), and medial (F) views. **Abbreviations: dt III,** distal tarsal III; **dt IV**, distal tarsal IV; **mt II**, metatarsal II; **mt V**, metatarsal V.

A

pdp

MT V

atp

dt III

B

5 cm

plr

cr

mtc

vs

pmr

C

D

F

mt IV

mt III

E

1 cm

G

H

5 cm
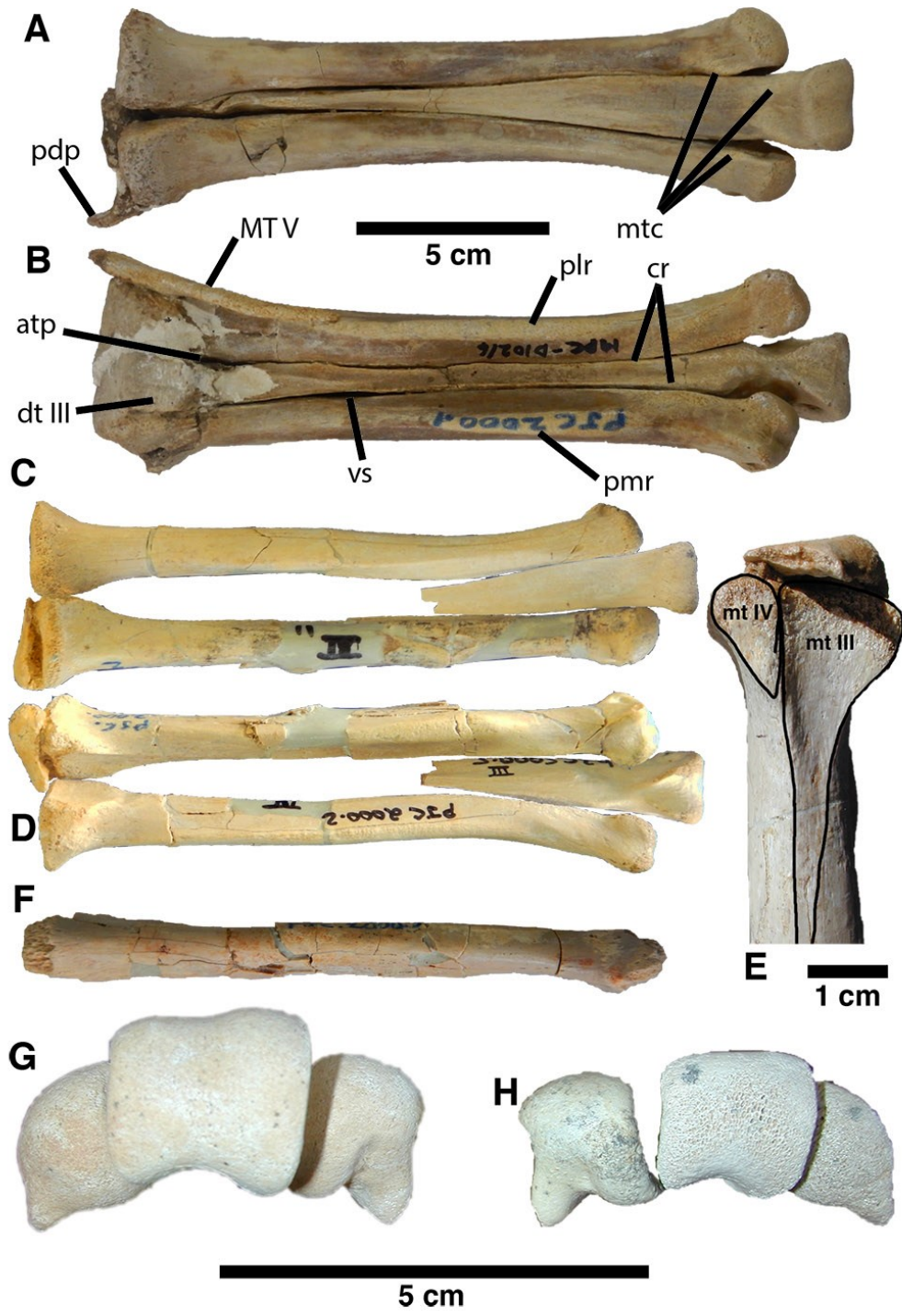
(Previous page)
Fig. 3.51. Tarsometatarsi of *Elmisaurus rarus*.

Tarsometatarsi of MPC-D 102/006 (A, B, G) and MPC-D 102/007 (C–E, H) and MPC-D 102/008 (F) in anterior (A, C, F), posterior (B, D), medial (E), and distal (G, H) views. Metatarsal III of MPC-D 102/007 (C, D) is reversed from the left side. **Abbreviations: atp**, slit for *a. tarsalis plantaris*; **cr**, cruciate ridges; **dt III**, distal tarsal III; **mtc**, insertion of *m. tibialis cranialis*; **MT V**, metatarsal V; **pdp**, proximodorsal process; **plr**, posterolateral ridge; **pmr**, posteromedial ridge; **vs**, vascular slit.
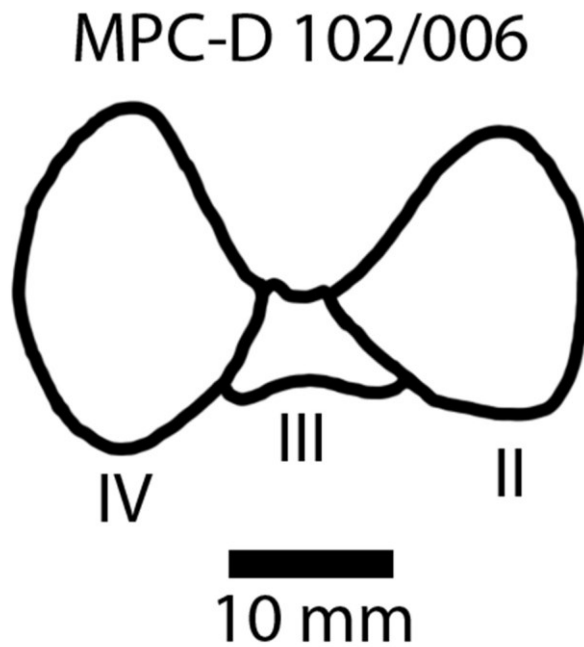
Fig. 3.52. Cross-sectional diagram of tarsometatarsus of *Elmisaurus rarus*.

Cross section taken approximately 1/3 of the length from the proximal end, showing deep posterior concavity of the foot (posterior is up, anterior is down). **Abbreviatons: II,** metatarsal II; **III**, metatarsal III; **IV**, metatarsal IV.
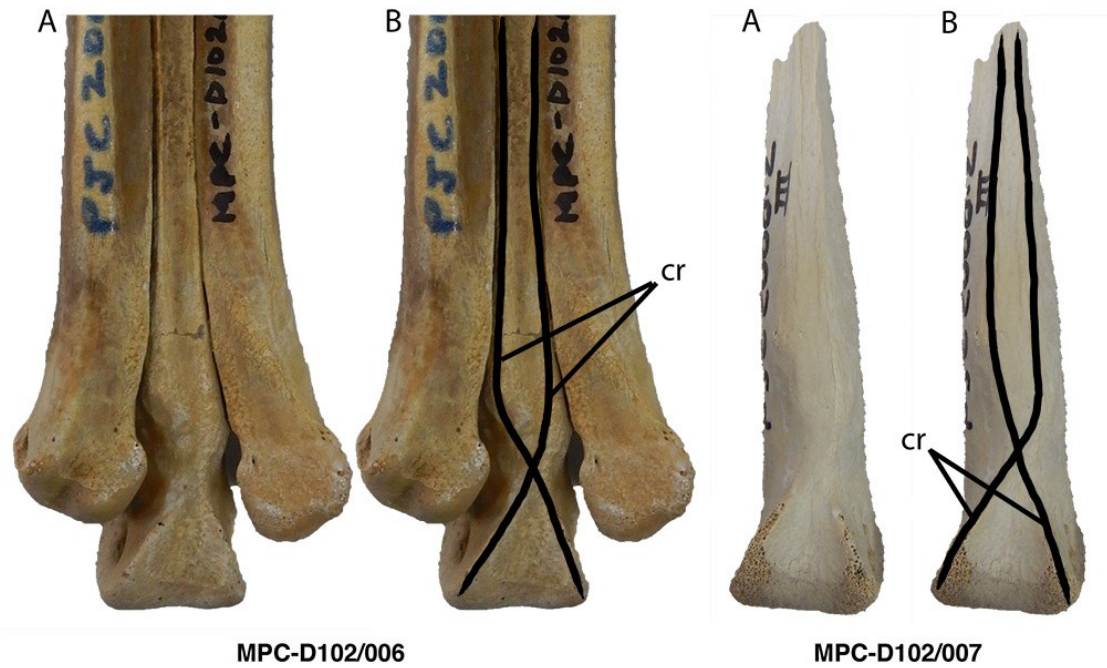
Fig. 3.53. Cruciate ridges of *Elmisaurus rarus*.

Distal tarsometatarsi of MPC-D 102/006 (left) and MPC-D 102/007 (right), annotated (B) to show cruciate ridges of metatarsal III. **Abbreviations: cr**, cruciate ridges.
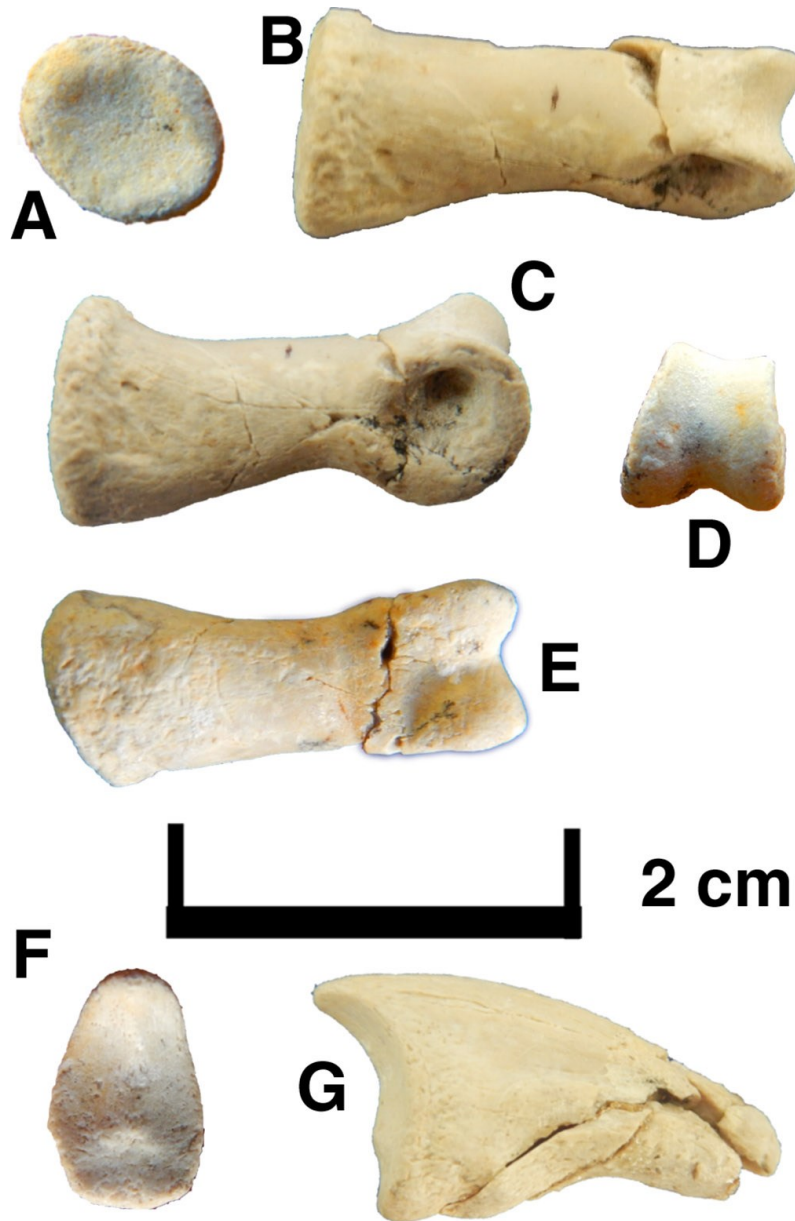
Fig. 3.54. Pedal elements of *Elmisaurus rarus*.

Pedal phalanges I-1 (A–E) and I-2 (F, G) of MPC-D 102/007 in proximal (A, F), dorsal (B), lateral (C, F), distal (D), and ventral (E) views.
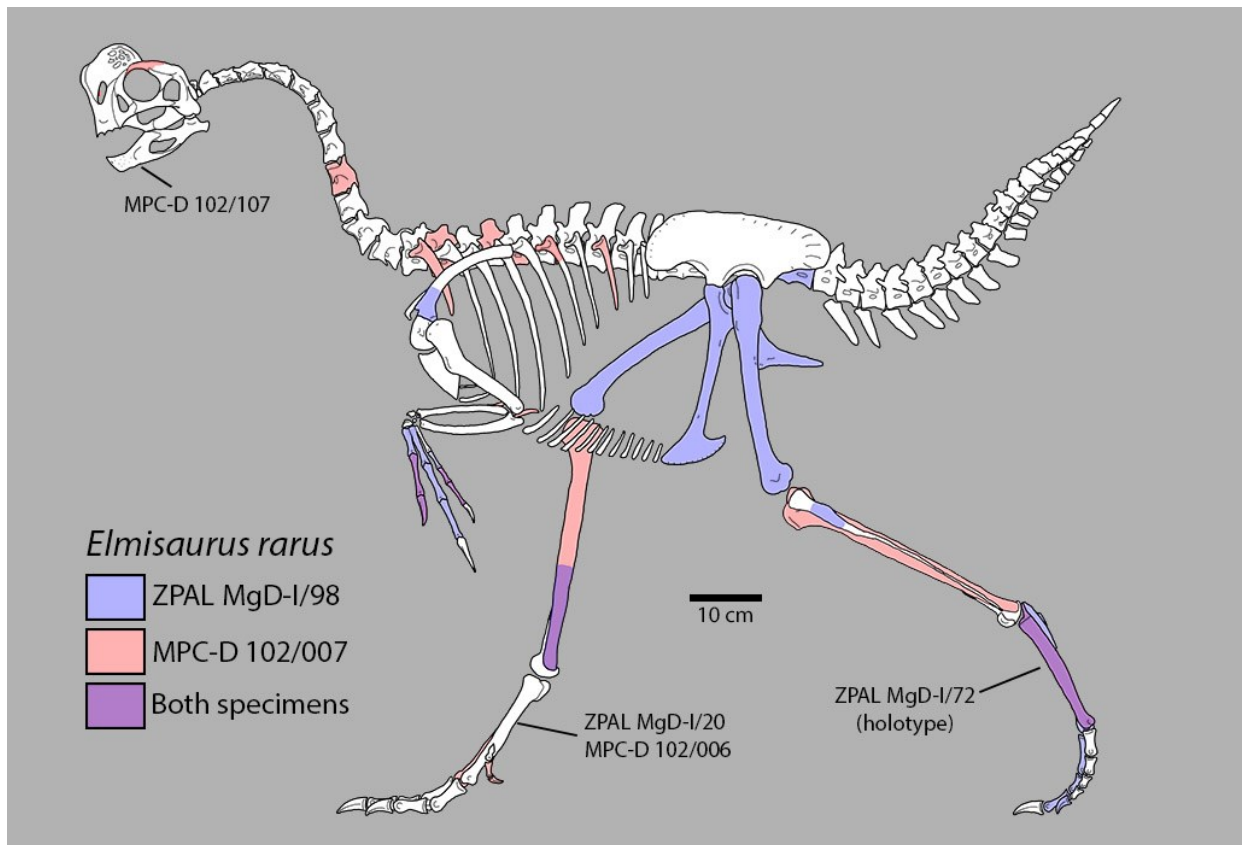
Fig. 3.55. Skeletal reconstruction of *Elmisaurus rarus*.

Skeletal reconstruction based on associated skeletons (MPC-D 102/007; ZPAL MgD-I/98), with

other elements reconstructed from *Apatoraptor pennatus* and *Nomingia gobiensis*.
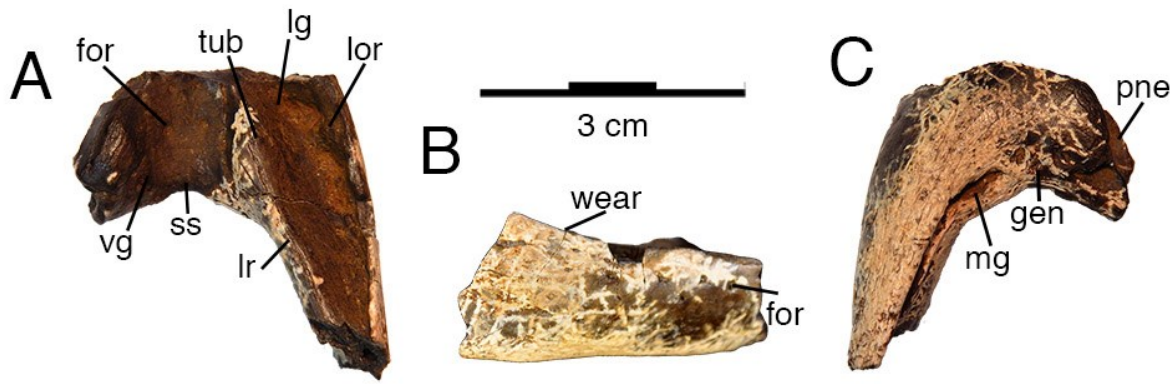
Fig. 3.56. Dentaries of *Leptorhynchos elegans*.

Partial dentaries of UALVP 55639 in dorsal (A), right lateral (B), and ventral (C) views.

Abbreviations: for, foramen; **gen**, attachment of *m. genioglossus*, **lg**, lingual groove; **lor**, lateral occlusal ridge; **lr**, lingual ridge; **mg**, Meckelian groove; **pne**, pneumatic space; **ss**, symphyseal sulcus; **tub**, tubercle; **vg**, vascular groove; **wear**, taphonomic wear of the occlusal margin.
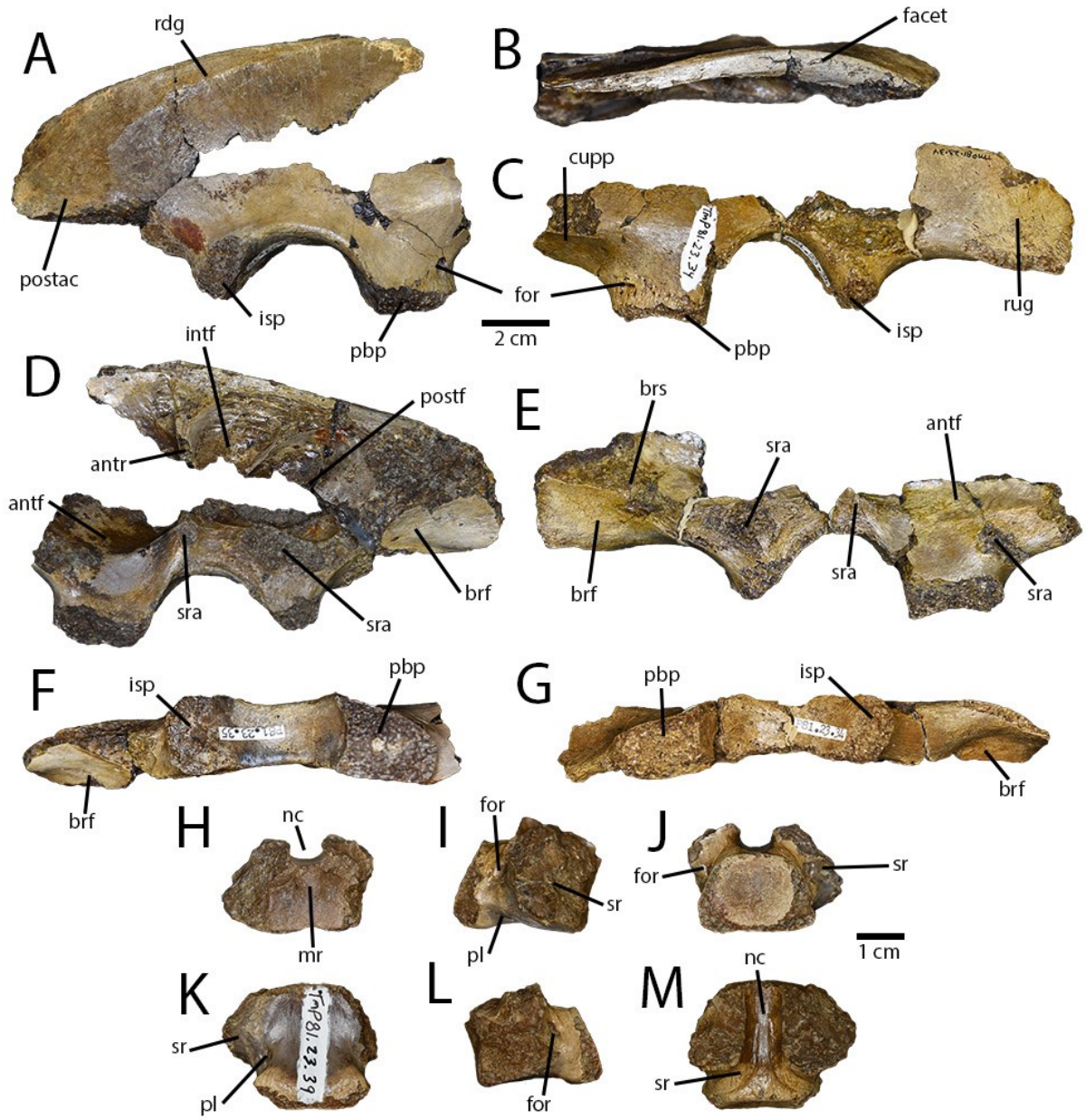
Fig. 3.57. Associated pelvic elements of *Leptorhynchos elegans*.

Associated ilia (A–G) and last sacral vertebra (H–M) of TMP 1981.023.0034 (C, E, G), TMP 1981.023.0035 (A, B, D, F), and TMP 1981.023.0039 (H–M). Ilia in lateral (A, C), dorsal (B), medial (D, E), and ventral (F, G) views. Last sacral vertebra in anterior (H), right lateral (I), posterior (J), ventral (K), left lateral (L), and dorsal (M) views. **Abbreviations: antf**, anterior fossa; **antr**, anterior ridge; **brf**, brevis fossa; **cupp**, cuppedicus fossa; **facet**, flattened dorsal facet; **for**, foramen; **intf**, intermediate fossa; **isp**, ischiadic peduncle; **mr**, median ridge; **nc**, neural canal; **pbp**, pubic peduncle; **pl**, pleurocoel; **postac**, postacetabular process; **postf**, posterior fossa; **rdg**, ridge; **sr**, sacral rib; **sra**, sacral rib attachment.
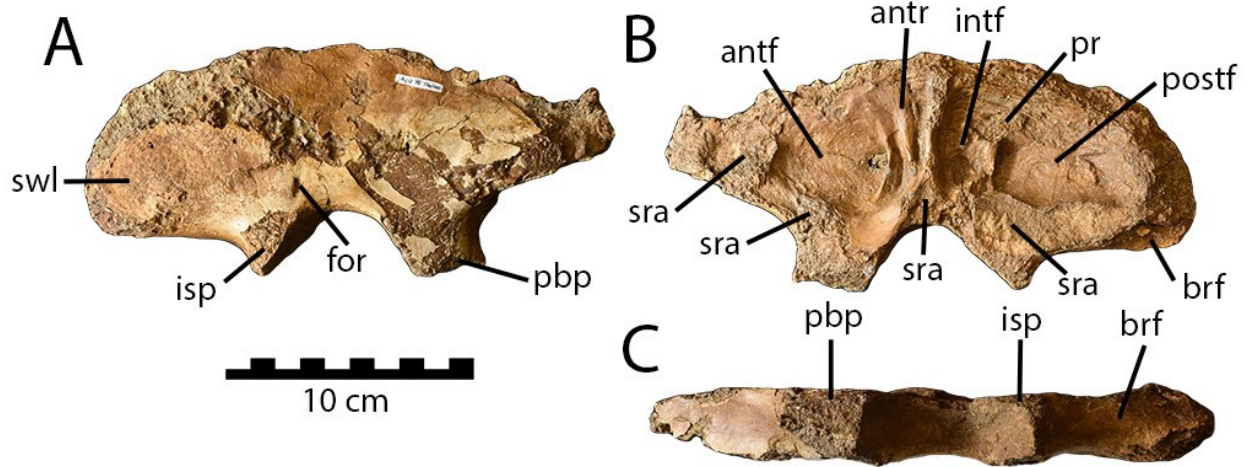
Fig. 3.58. Pathological ilium of *Leptorhynchos elegans*.

Right ilium of TMP 1992.036.0674 in lateral (A), medial (B), and ventral (C) views.

Abbreviations: antf, anterior fossa; **antr**, anterior ridge; **brf**, brevis fossa; **for**, foramen; **intf**, intermediate fossa; **isp**, ischiadic peduncle; **pbp**, pubic peduncle; **postf**, posterior fossa; **pr**, posterior ridge; **sra**, sacral rib attachment; **swl**, pathological swelling.

Fig. 3.59. Tibia of *Leptorhynchos elegans*.

Left tibia of TMP 1994.012.0880 in anterior (A), posterior (B), proximal (C), and distal (D)

views. **Abbreviations: cn**, cnemial crest; **fib**, fibular condyle; **int**, interosseum crest; **pff**,

postfibular flange.
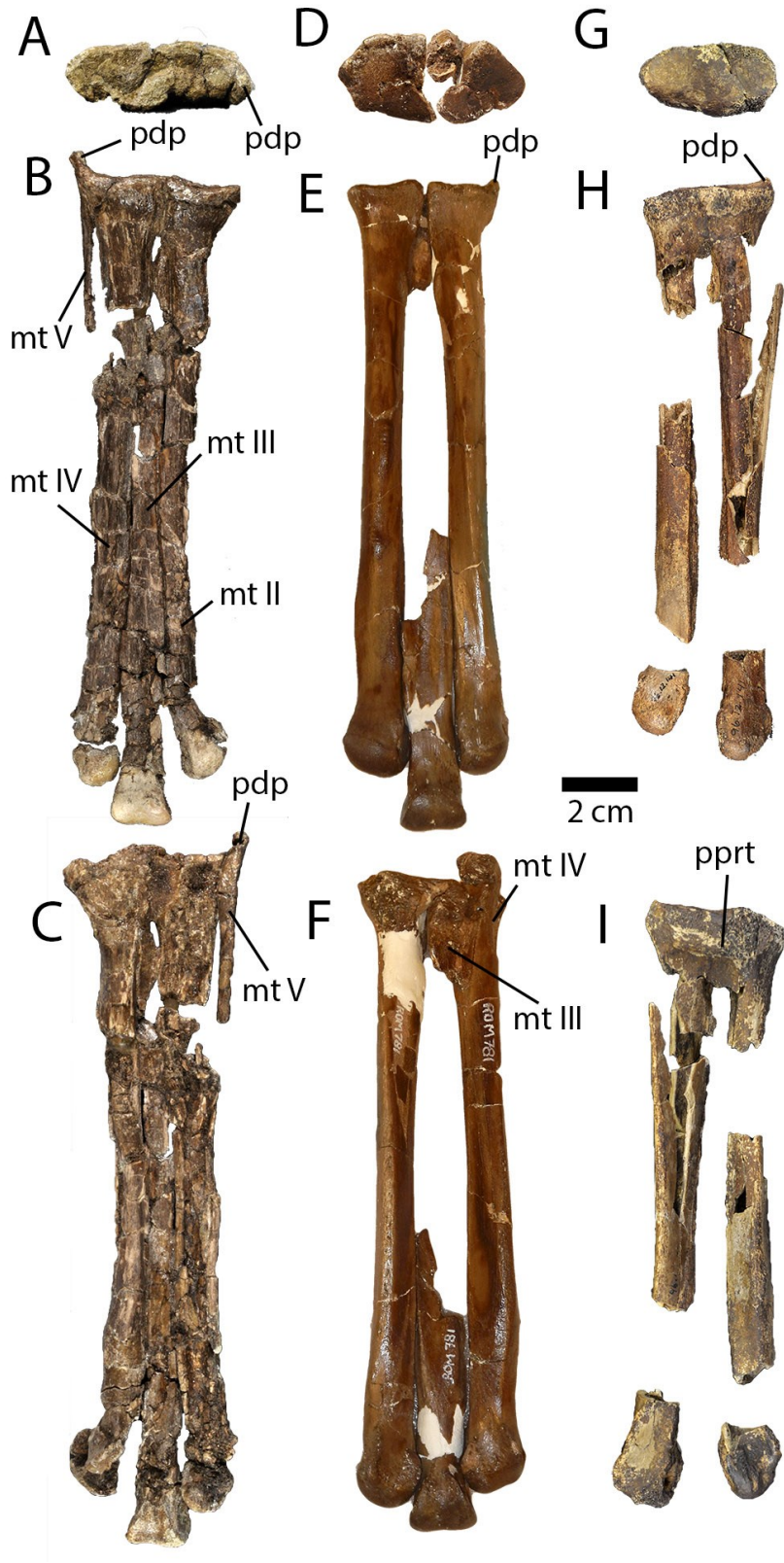
(Previous page)

Fig. 3.60. Tarsometatarsi of *Leptorhynchos elegans*.

Left tarsometatarsus of TMP 1982.016.0006 (A–C) in proximal (A), anterior (B), and posterior (C) views. Right tarsometatarsi of ROM 781 (D–F) and TMP 1996.012.0141 (G–I) in proximal (D, G), anterior (E, H), and posterior (F, I) views. **Abbreviations: mt II**, metatarsal II; **mt III**, metatarsal III; **mt IV**, metatarsal IV; **mt V**, metatarsal V; **pdp**, proximodorsal process; **pprt**, posterior protuberance.
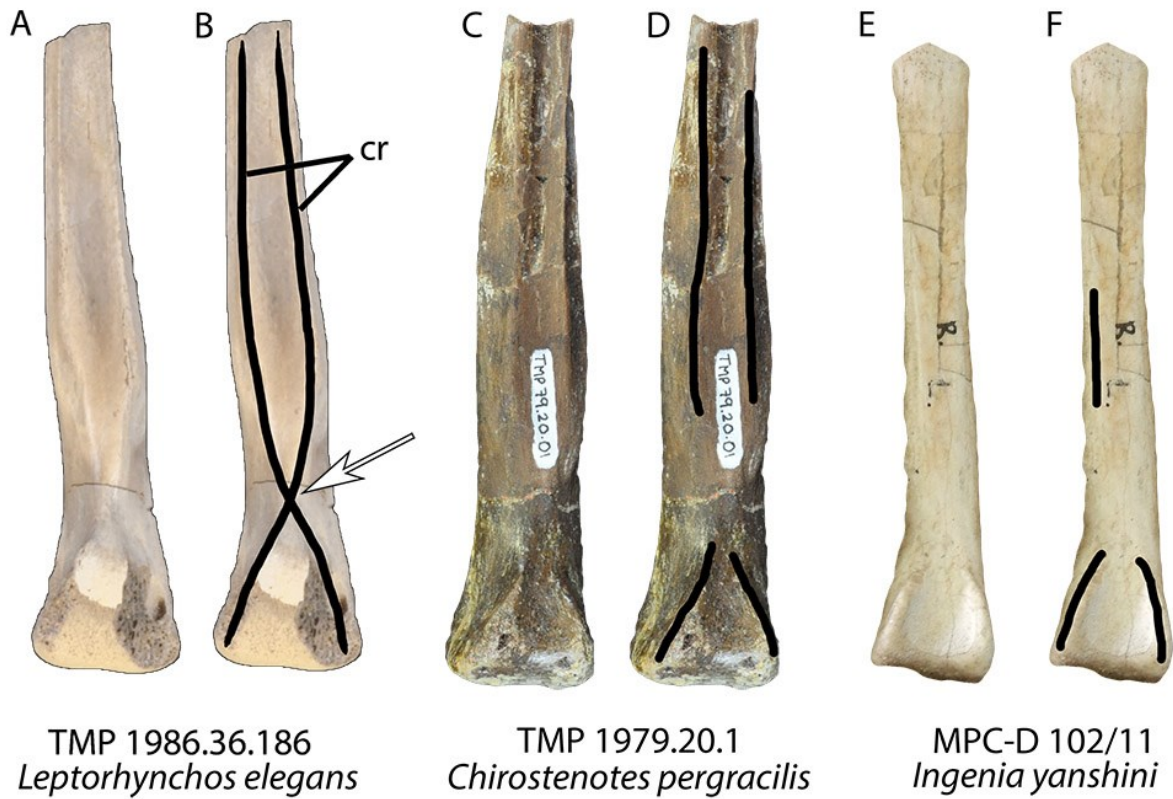
Fig. 3.61. Variable development of cruciate ridges in oviraptorosaurs.

Third metatarsals of *Leptorhynchos elegans* (A, B), *Chirostenotes pergracilis* (C, D) and an unnamed oviraptorid (E, F) in posterior view, showing development of intersecting (arrow) cruciate ridges (B, D, F). **Abbreviation: cr**, cruciate ridges.
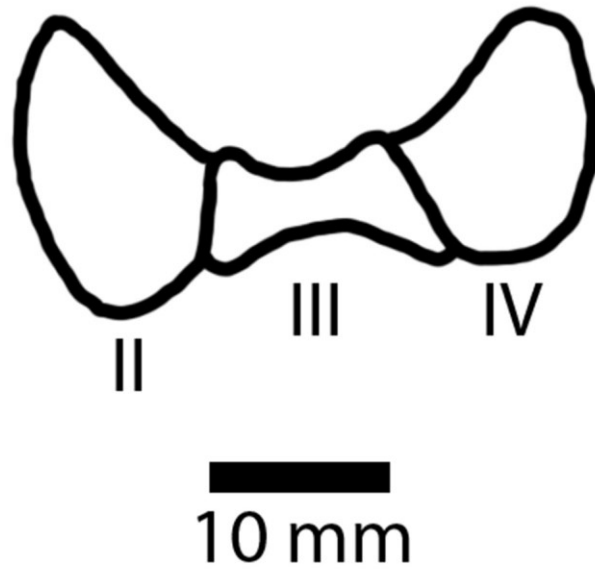
Fig. 3.62. Cross-sectional shape of the tarsometatarsus of *Leptorhynchos elegans*.

Diagram of cross-sectional shape approximately 1/3 of the length from the proximal end of the tarsometatarsus of ROM 781, showing deep plantar concavity. Posterior is up, anterior is down.

Abbreviations: II, metatarsal II; **III**, metatarsal III; **IV**, metatarsal IV.
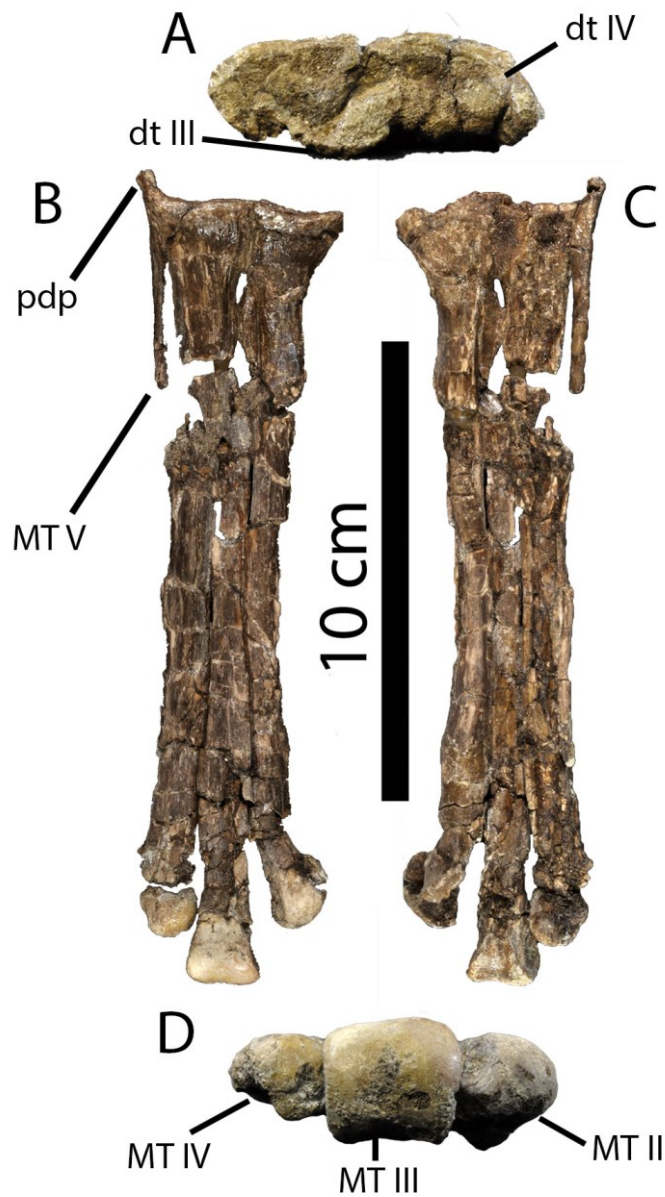
Fig. 3.63. Fused tarsometatarsus of *Leptorhynchos elegans*.

Fused right tarsometatarsus of TMP 1982.016.0006 in proximal (A) anterior (B), posterior (C) and distal (D) views. **Abbreviations: dt III**, distal tarsal III; **dt IV**, distal tarsal IV; **MT II**, metatarsal II; **MT III**, metatarsal III; **MT IV**, metatarsal IV; **MT V**, metatarsal V; **pdp**, proximodorsal process.
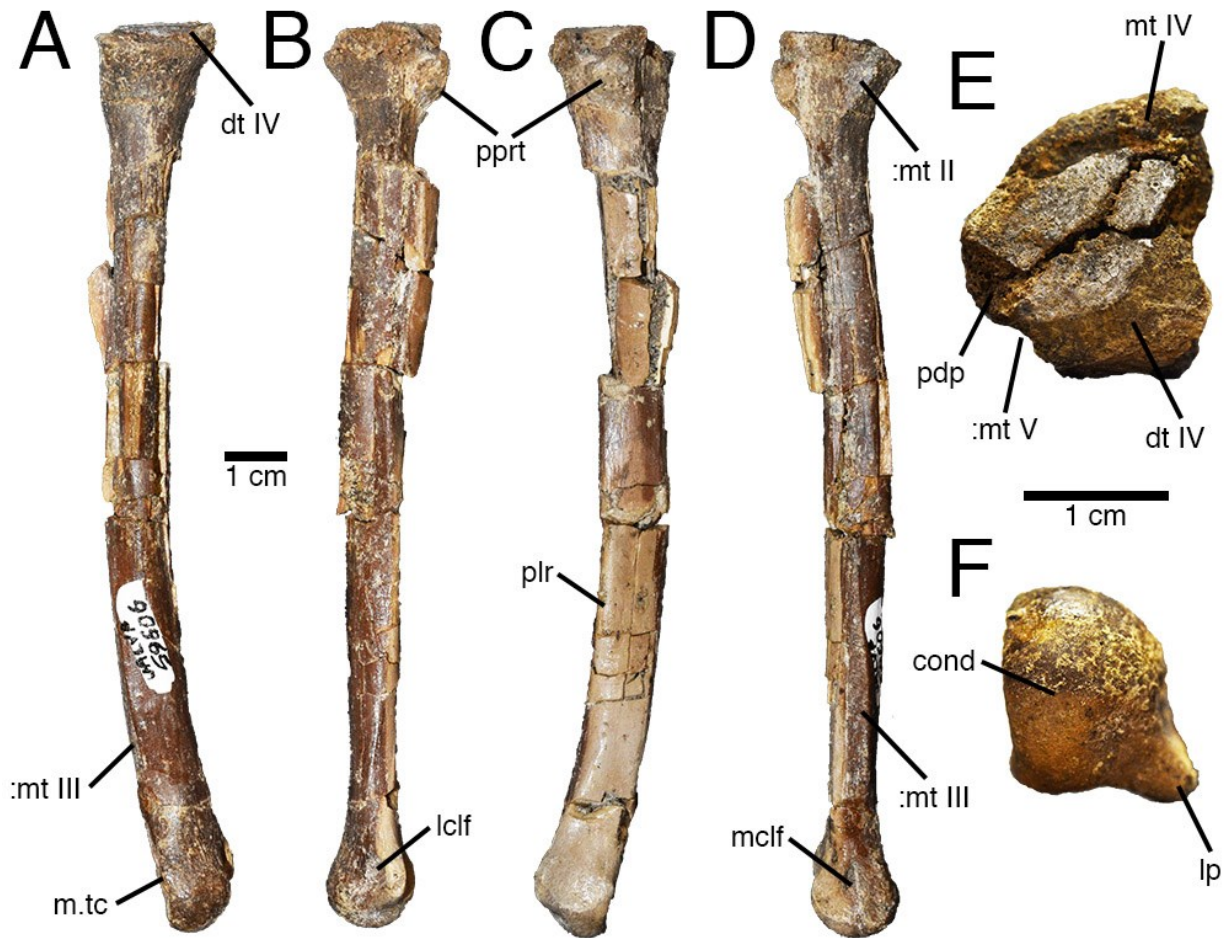
Fig. 3.64. Metatarsal IV of *Leptorhynchos elegans*.

Left metatarsal IV and fused distal tarsal IV of UALVP 59606 in anterior (A), lateral (B), posterior (C), medial (D), proximal (E) and distal (F) views. **Abbreviations: cond,** condyle; **dt IV**, distal tarsal IV; **lclf,** lateral collateral ligament fossa; **lp**, lateral process; **mclf**, medial collateral ligament fossa; **:mt II**, contact for metatarsal II; **:mt III**, contact for metatarsal III; **:mt V**, contact for metatarsal V; **mt IV**, metatarsal IV; **m.tc**, attachment for *m. tibialis cranialis*; **pdp**, proximodorsal process; **plr**, posterolateral ridge; **pprt**, posterior protuberance.
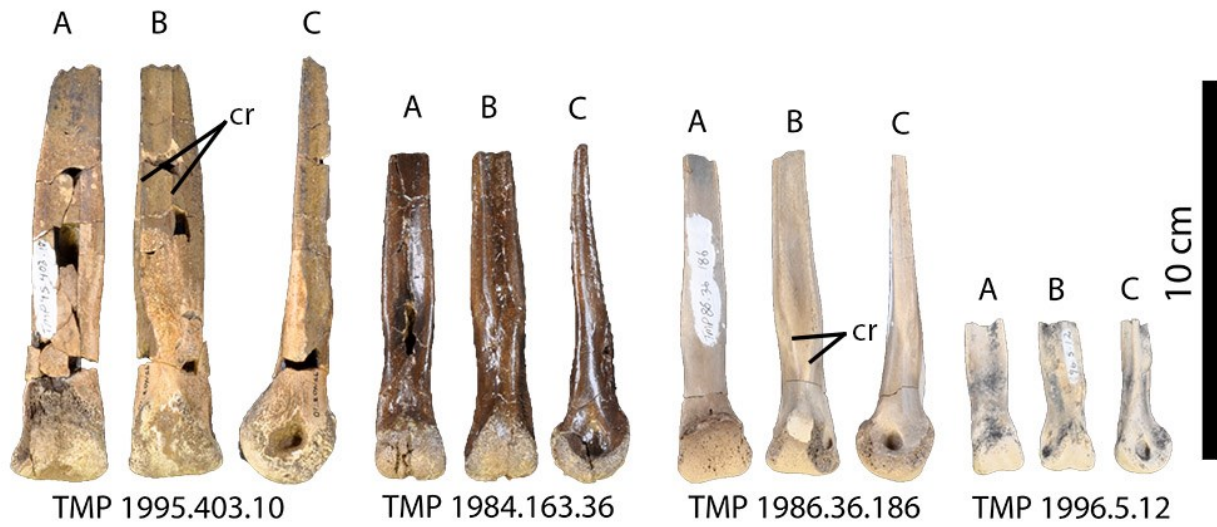
Fig. 3.65. Isolated distal ends of metatarsal III of *Leptorhynchos elegans*.

TMP 1995.403.0010 (left), TMP 1984.163.0036 (centre-left), TMP 1986.036.0186 (centre-right)

and TMP 1996.005.0012 (right) in anterior (A), posterior (B), and medial or lateral (C) views.

Abbreviation: cr, cruciate ridges.

Fig. 3.66. Metatarsal III of *Leptorhynchos elegans*.

Partial shaft of metatarsal III of UALVP 55585 in anterior (A), posterior (B), and proximal (C)

views. **Abbreviation: cr**, cruciate ridges.
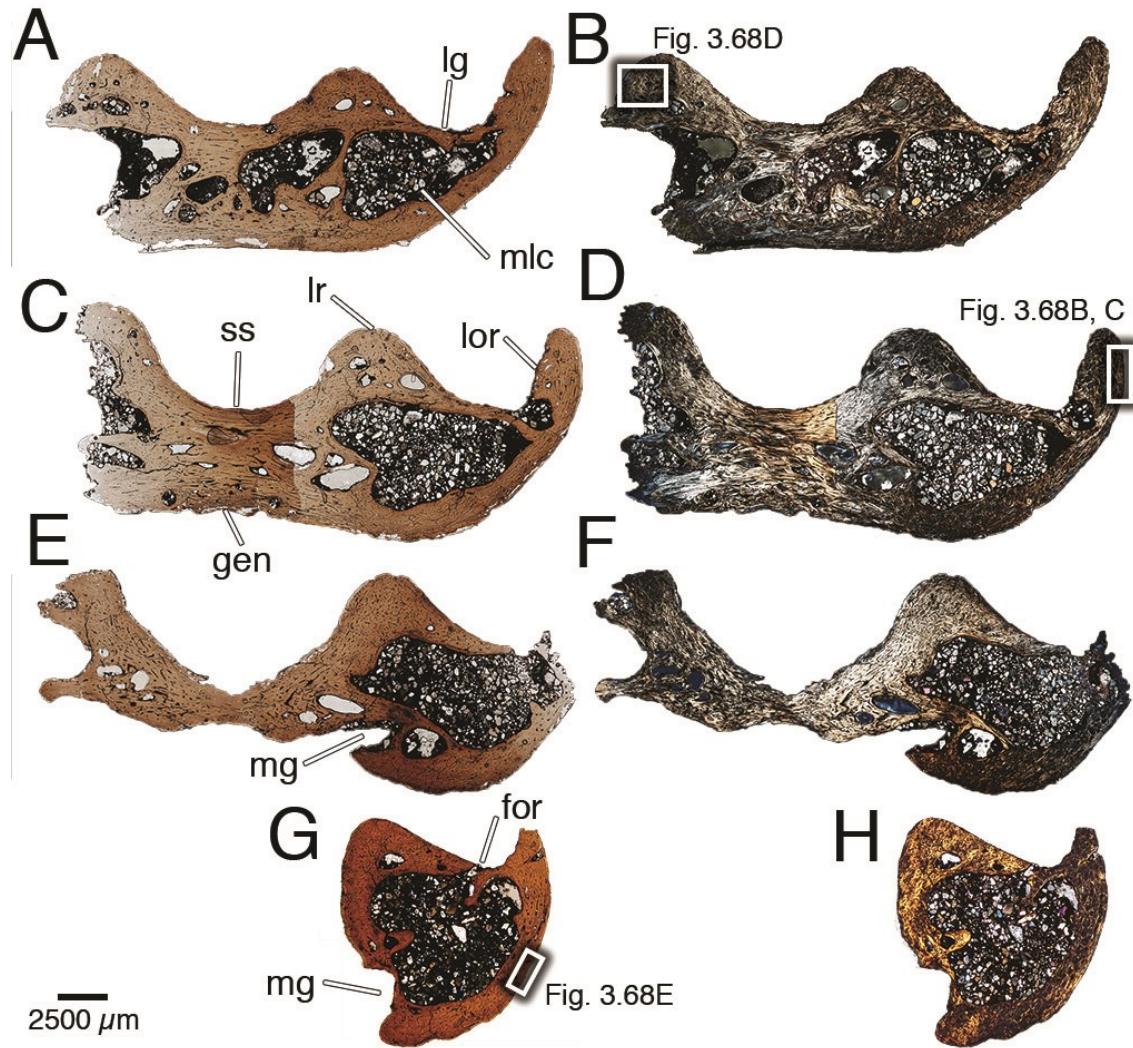
Fig. 3.67. Histological sections of the dentaries of *Leptorhynchos elegans*.

Thin sections of UALVP 55639 under normal (A, C, E, G) and cross-polarized (B, D, F, H) light.

Section A (A, B), showing asymmetrical internal cavities and highly remodeled Haversian bone.

Section B (C, D) showing lateral occlusal ridge and tubercles of lingual ridges. Section C (E, F)

showing Meckelian groove. Section D (G, H) showing caudal ramus of dentary and foramina

connecting major labial cavity and lingual groove. Boxes indicate locations of close-ups in Fig.

3.68. **Abbreviations: for**, foramen; **gen**, attachment of *m. genioglossus*; **lor**, lateral occlusal

ridge; **lr**, lingual ridge; **mg**, Meckelian groove; **mlc**, major lateral cavity; **ss**, symphyseal sulcus.

372
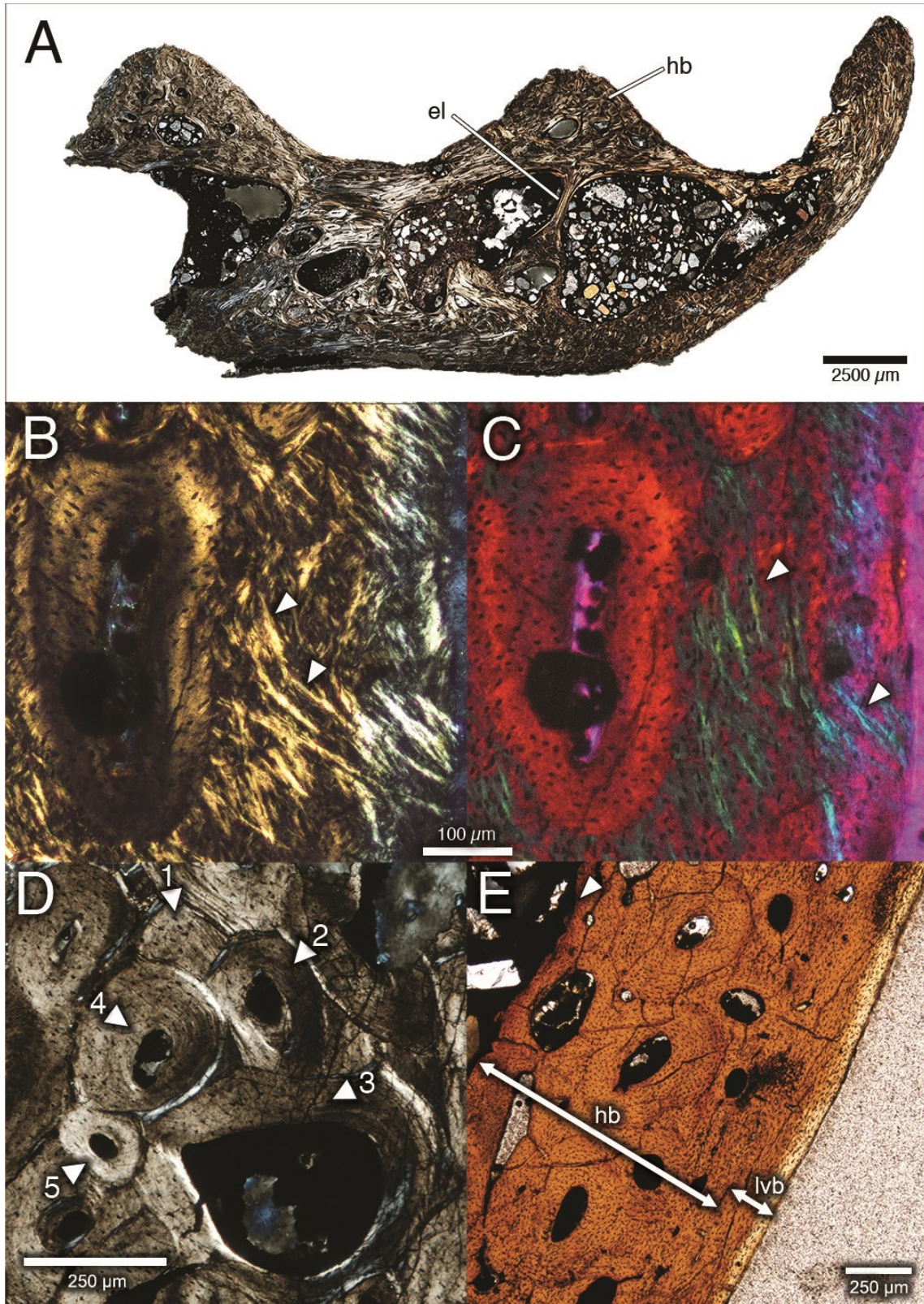
(Previous page)

Fig. 3.68. Histological details of the dentaries of *Leptorhynchos elegans*.

Overview of thin section of UALVP 55639 (A) in cross polarized light. Close-up (B, C) of well-developed Sharpey's fibers (arrows) near the periosteal surface of the occlusal margin under cross-polarized (B) and lambda-filtered cross-polarized (C) light. Close-up (D) of multiple generations of cross-cutting secondary osteons (numbered arrows indicate order of deposition) in the lingual ridge under cross-polarized light. Detail (E) of extensive remodeling and low-vascularity bone (arrows) near the periosteal surface under plane-polarized light. **Abbreviations: el**, endosteal lamellae; **hb**, Haversian bone; **lvb**, low vascularity bone.
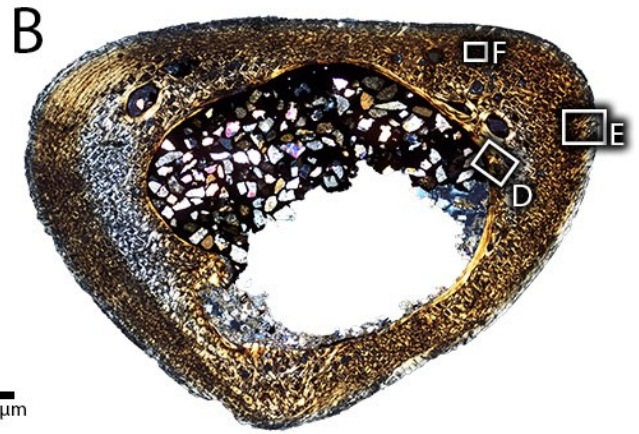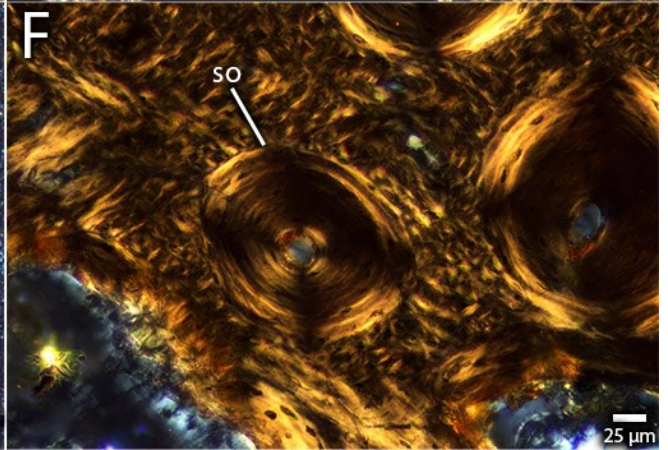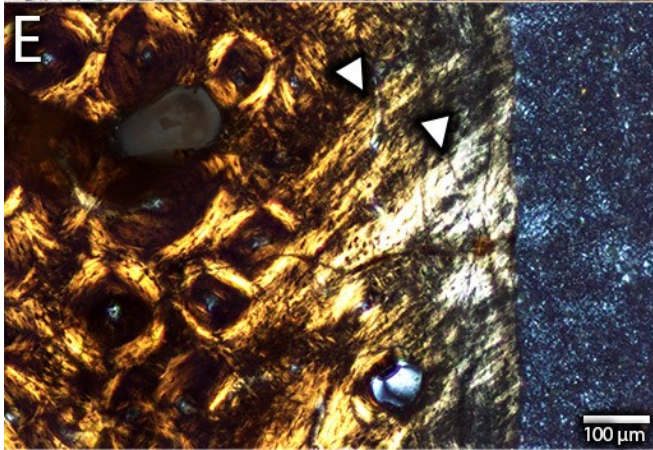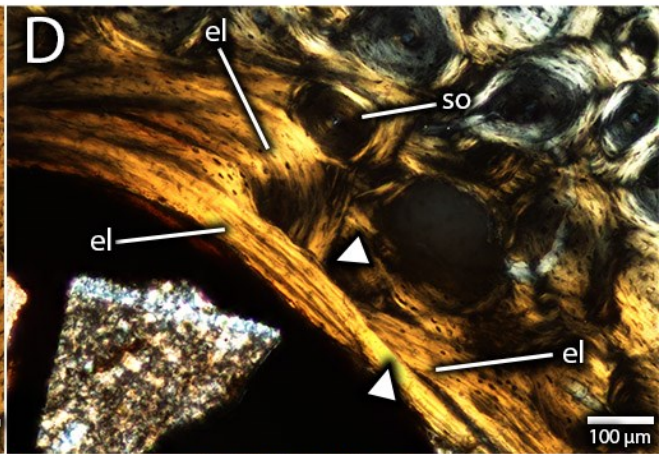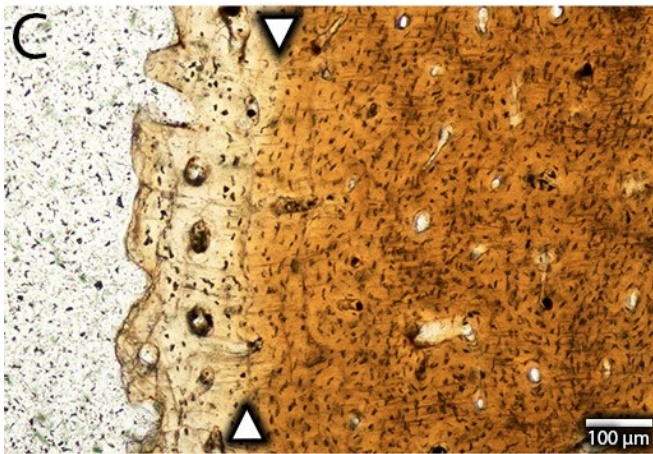
Fig. 3.69. Osteohistology of metatarsal III of *Leptorhynchos elegans*.

Overview of histological thin section of UALVP 55585 in plane-polarized (A) and cross-polarized (B) light, showing locations of close-up images. Detail (C) of transition to woven-fibered primary bone (arrows) towards the periosteal surface of the metatarsal, indicating rapid growth, under plane-polarized light. Close-up (D) of multiple generations of endosteal lamellae (arrows) and cross-cut secondary osteons near the medullary cavity under cross-polarized light. Detail (E) of well developed Sharpey's fibers (arrows) near the periosteal surface under cross-polarized light. Close-up (F) of well developed secondary osteons with multiple internal lamellae under cross-polarized light. **Abbreviations: el**, endosteal lamellae; **so**, secondary osteon.
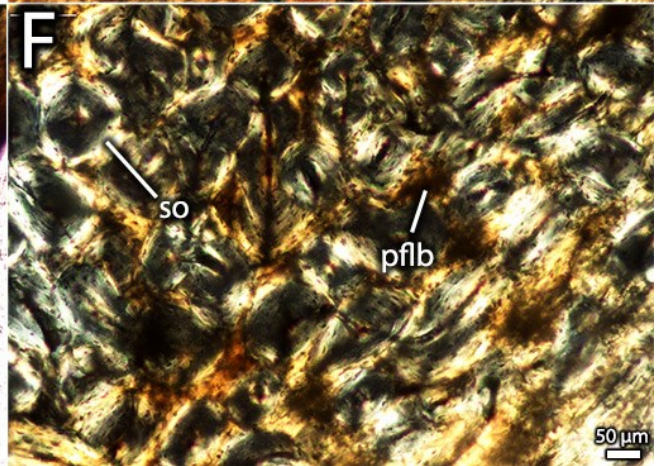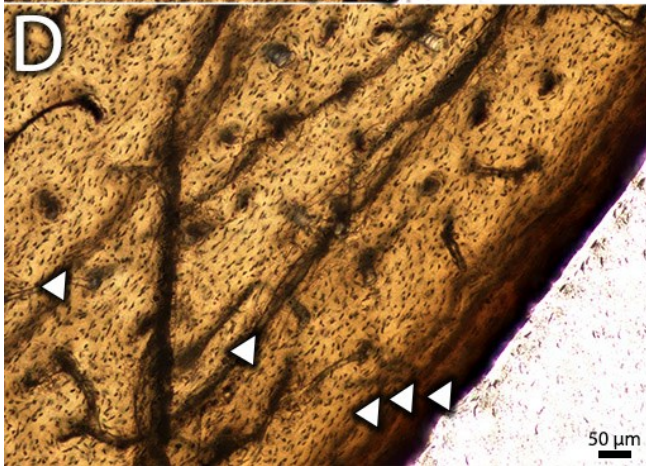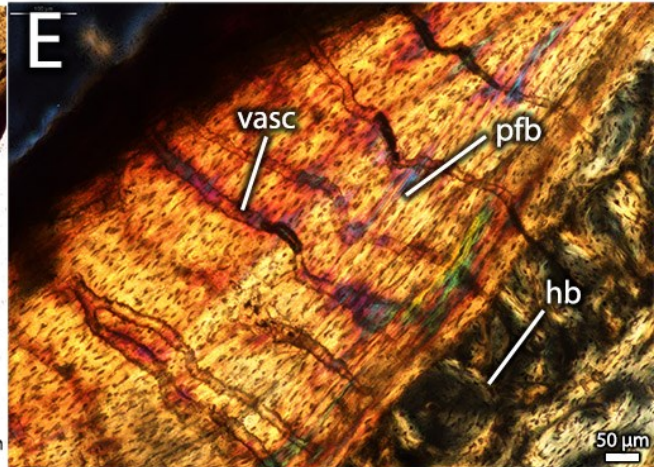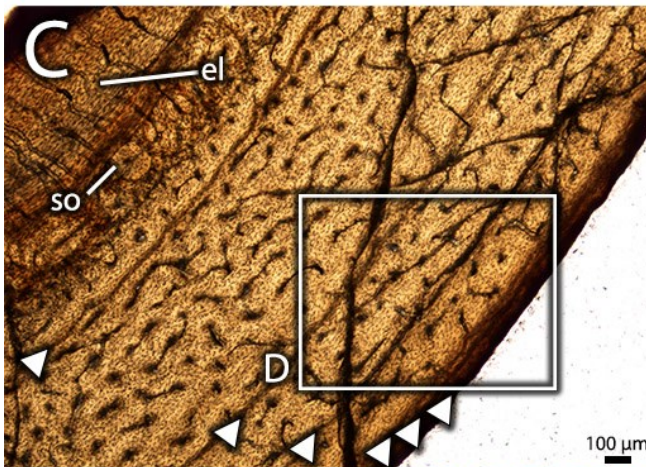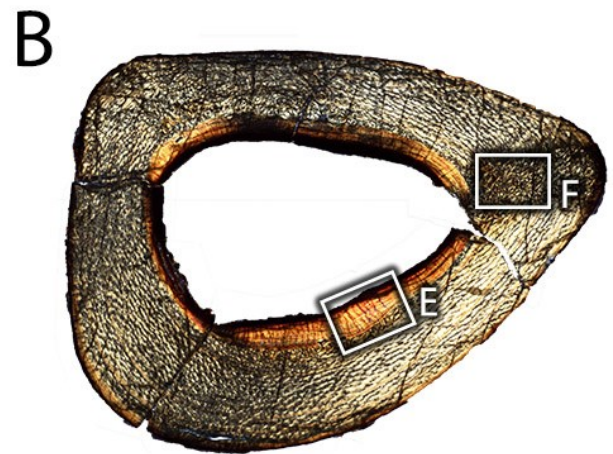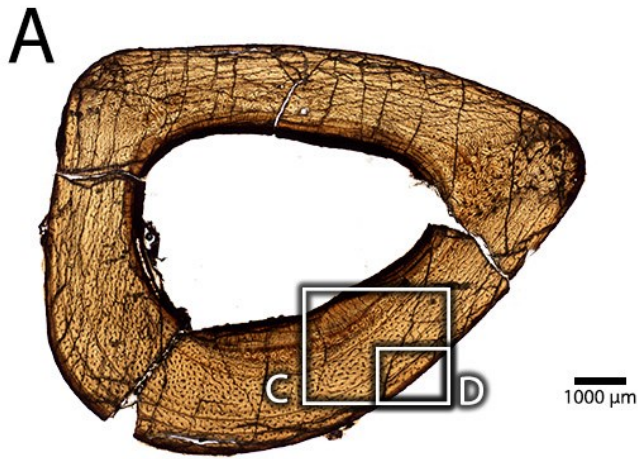
(Previous page)

Fig. 3.70. Osteohistology of metatarsal IV of *Leptorhynchos elegans*.

Overview of histological thin section of UALVP 59606 in plane-polarized (A) and cross-polarized (B) light, showing locations of close-up images. Detail (C) of cortex showing predominantly primary fibrolamellar bone with longitudinal-reticular vascularity, endosteal resorption, and cyclical growth marks (arrows), under plane-polarized light. Close-up (D) of tightly packed cyclical growth marks (arrows) near the periosteal surface of the cortex, under plane-polarized light. Close-up (E) of well developed endosteal lamellae on the medullary cavity, showing secondary excavation by simple vascular canals, under cross-polarized light. Close-up (F) of localized secondary remodeling in the posterolateral part of the cortex, under cross-polarized light. **Abbreviations: el,** endosteal lamellae; **hb**, Haversian bone; **pfb**, parallel-fibered bone; **pflb**, primary fibrolamellar bone; **so**, secondary osteon; **vasc**, vascular canal.
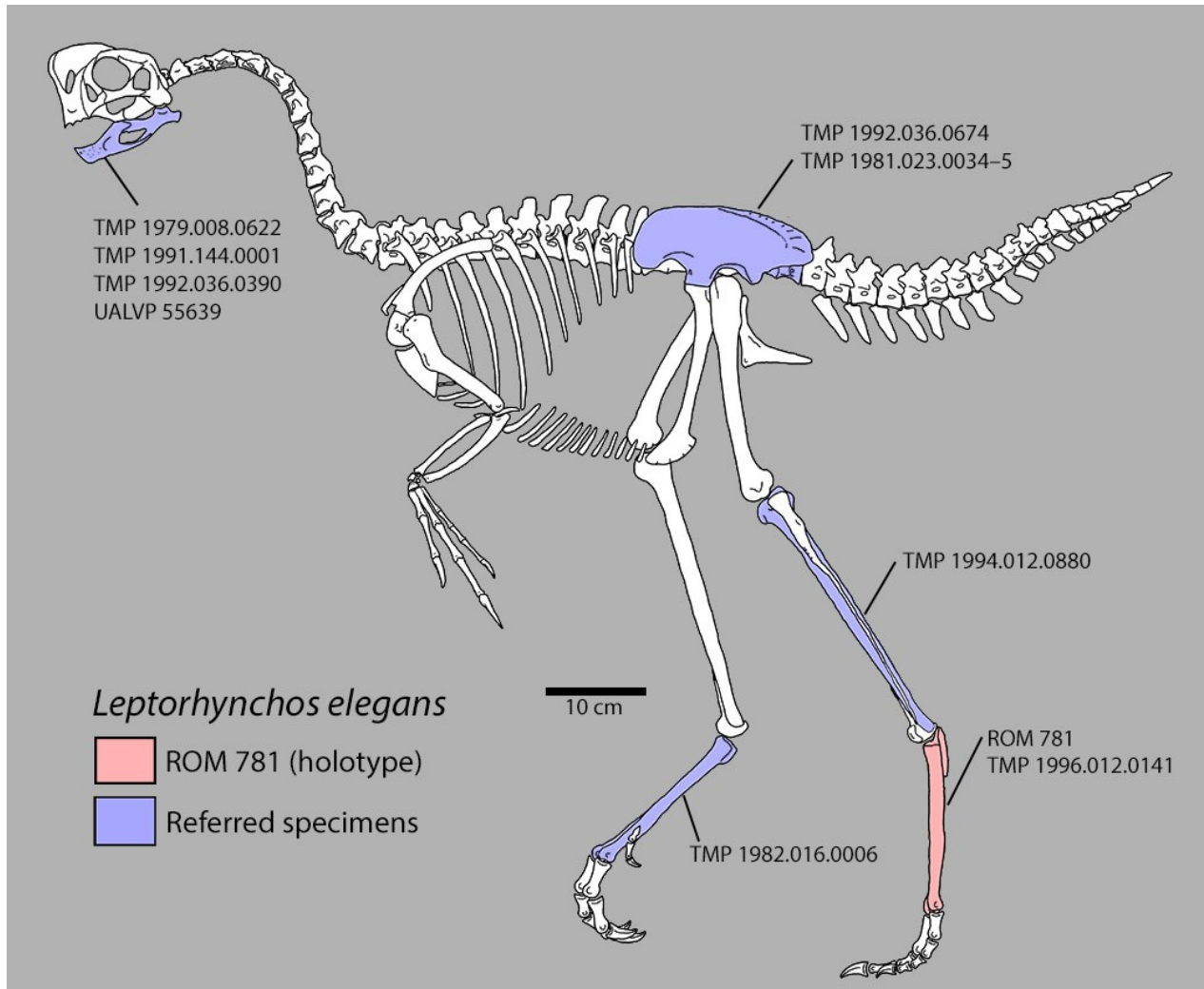
Fig. 3.71. Skeletal reconstruction of *Leptorhynchos elegans*.

Skeletal reconstruction based on known specimens of *Leptorhynchos elegans*, scaled assuming

fused hindlimb elements are representative of adults near maximum body size, with remaining

elements taken from *Apatoraptor pennatus*, *Elmisaurus rarus*, and *Nomingia gobiensis*.
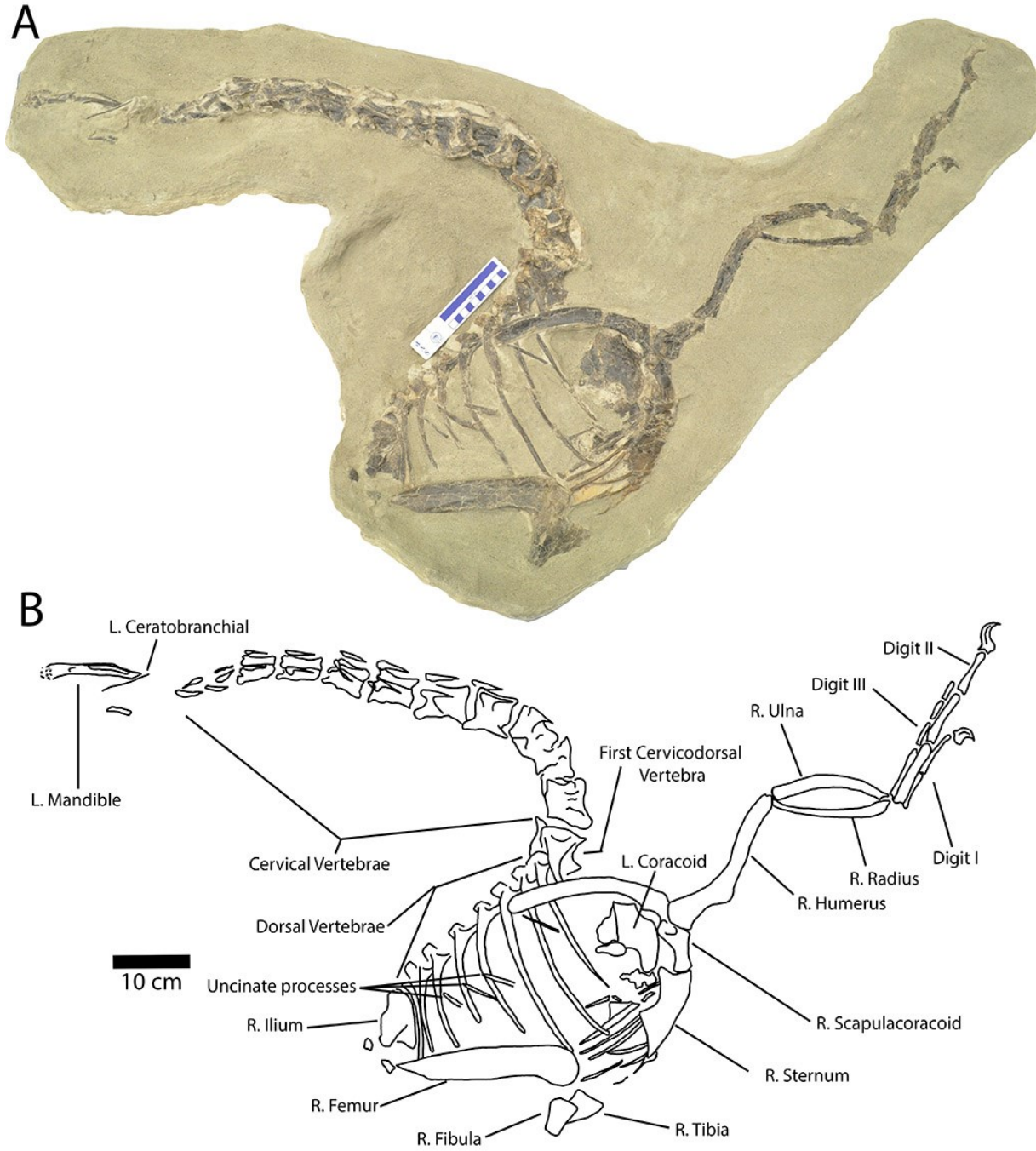
Fig. 3.72. Holotype specimen of *Apatoraptor pennatus*.

Photograph (A) of TMP 1993.051.0001 in right lateral view and illustration (B) of the same.
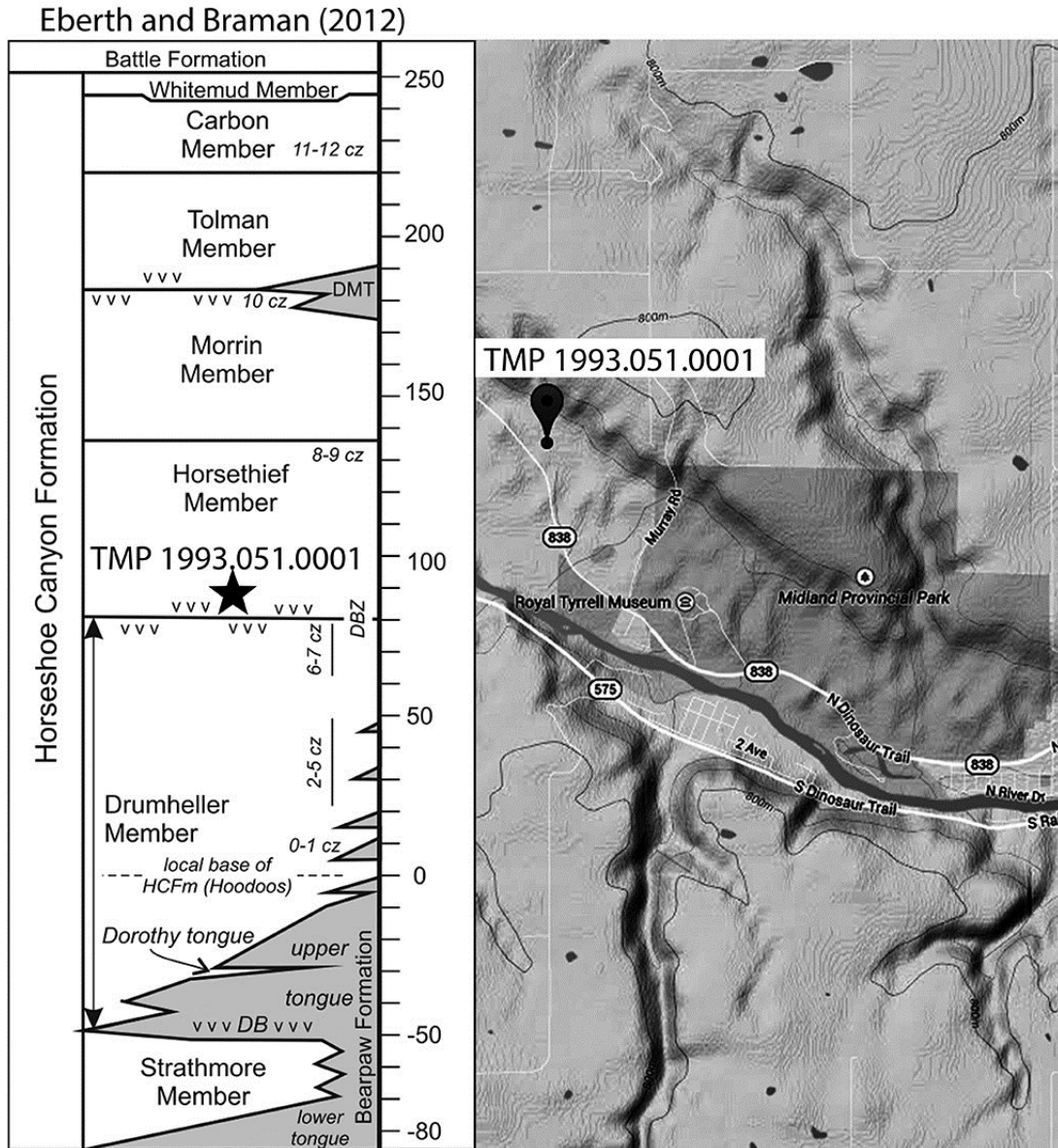
Fig. 3.73. Locality information for *Apatoraptor pennatus*.

Stratigraphic section (A) of the Horseshoe Canyon Formation, modified from Eberth and

Braman (2012). Star indicates stratigraphic level of TMP 1993.051.0001. Topographic map (B)

of region surrounding Midland Provincial Park, Alberta. Pointer indicates locality where TMP

1993.051.0001 was recovered.
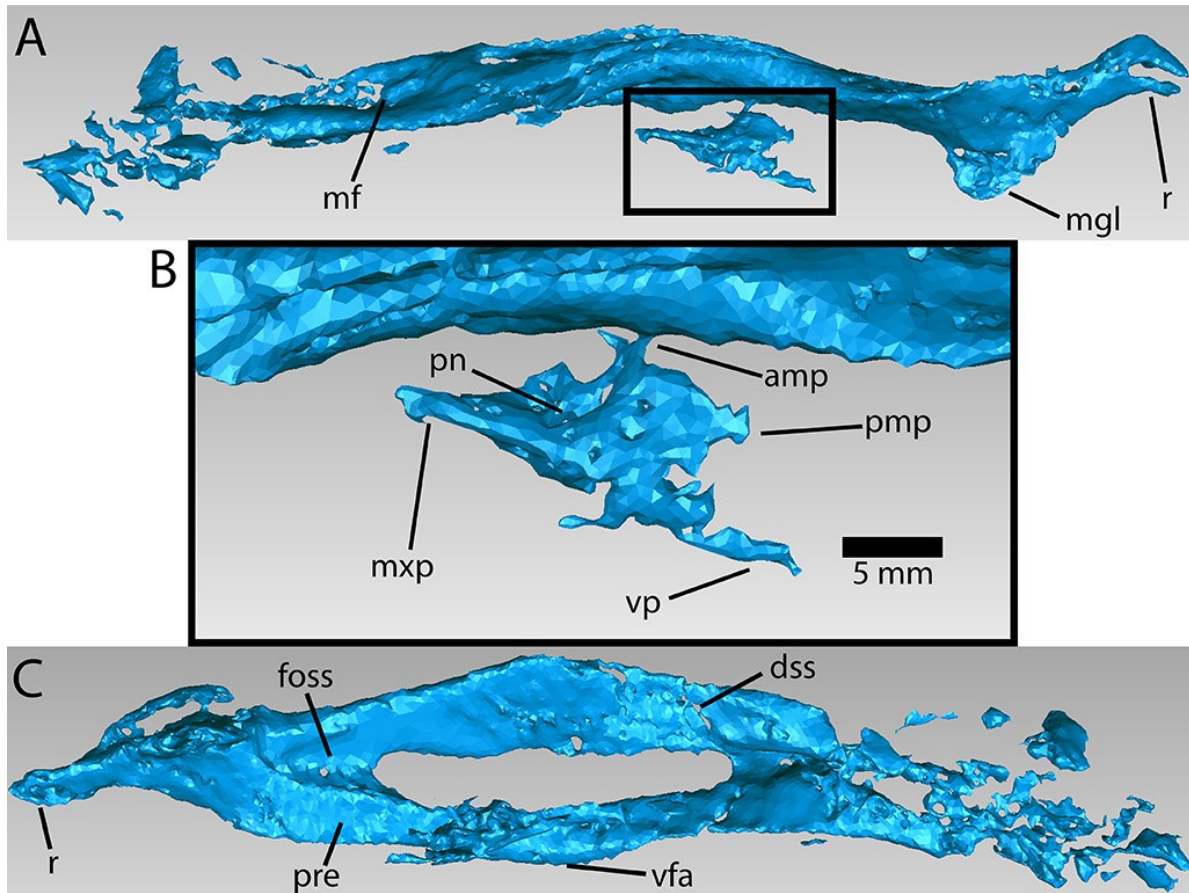
Fig. 3.74. Computed tomography of the mandible and palatine of *Apatoraptor pennatus*.
Computer tomography image (A) showing the left mandible and right palatine in ventral view. Detail (B) of right palatine. Computer tomography image (C) showing left mandible and right palatine in medial view. **Abbreviations**: **amp**, anterior medial process; **dss**, dentary-surangular suture; **foss**, medial fossa on articular-surangular-coronoid complex; **mf**, mandibular fossa; **mgl**, medial glenoid; **mxp**, maxillary process; **pmp**, posteromedial process; **pre**, prearticular **r**, retroarticular process; **vfa**, ventral flange of angular **vp**, vomeral process.
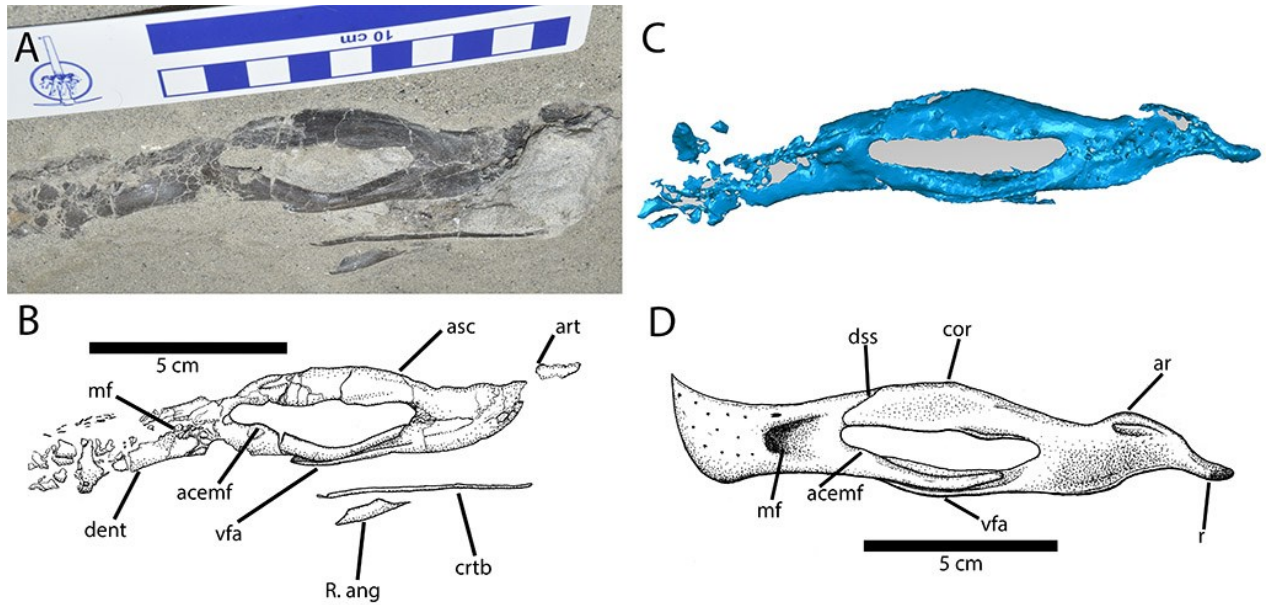
Fig. 3.75. Mandible of *Apatoraptor pennatus* (TMP 1993.051.0001).

Photograph (A) of mandible in left lateral view. Illustration (B) of mandible in left lateral view. Computer tomography reconstruction (C) of mandible in left lateral view; Hypothesized reconstruction (D) of mandible in left lateral view. **Abbreviations**: **acemf**, anterior constriction of external mandibular fenestra; **ar**, articular ridge; **art**, articular region; **asc**, articular-surangular-coronoid complex; **cor**, coronoid eminence; **crtb**, ceratobranchial; **dent**, dentary; **dss**, dentary-surangular suture; **mf**, mandibular fossa; **r**, retroarticular process; **R. ang**, right angular; **vfa**, ventral flange of angular.
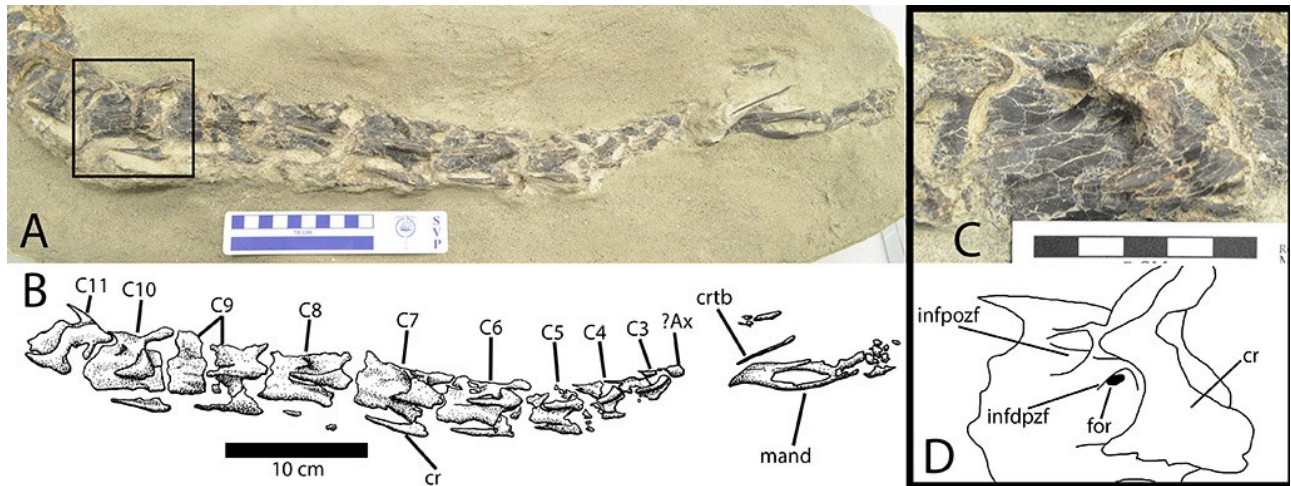
Fig. 3.76. Cervical series of *Apatoraptor pennatus* (TMP 1993.051.0001).

Photograph (A) and illustration (B) of cervical series in right lateral view. Detail (C) of cervical vertebra c10 in right lateral view. Illustration (D) of c10 in right lateral view. **Abbreviations**: **?Ax**: possible axis; **C3-C11**, cervical vertebrae c3 through c11; **cr**, cervical rib; **crtb**, ceratobranchial; **for**, foramen; **infdpzf**, infradiapophyseal fossa; **infpozf**, infrapostzygapophyseal fossa; **mand**, mandible.
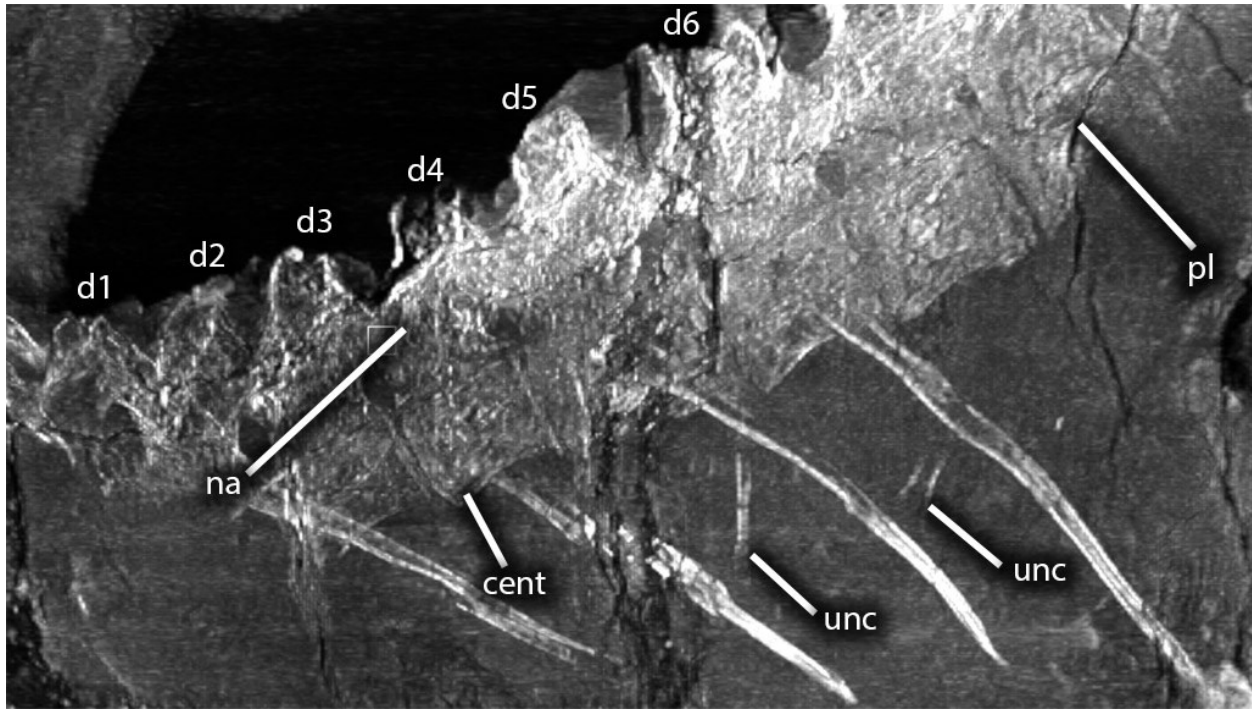
Fig. 3.77. Dorsal vertebrae of *Apatoraptor pennatus.*

X-Ray image of dorsal vertebrae of TMP 1993.051.0001 in left lateral view. Brighter areas

indicate regions of greater density. **Abbreviations: cent**, centrum; **d1–d6**, dorsal vertebrae 1 to

6; **na**, neural arch; **pl**, pleurocoel; **unc**, uncinate process.
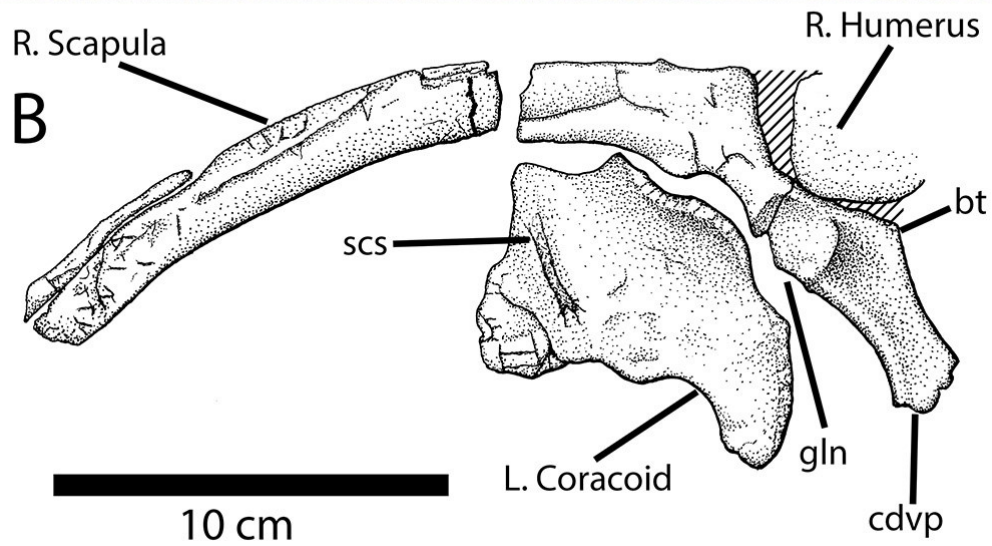
Fig. 3.78. Pectoral girdle of *Apatoraptor pennatus*.

Photograph (A) and illustration (B) of right and left scapulacoracoid of TMP 1993.053.0001 in right lateral view. **Abbreviations**: **bt**, biceps tubercle; **cdvp**, caudoventral process; **gln**, glenoid of the scapulocoracoid; **scs**, scapulocoracoid suture.
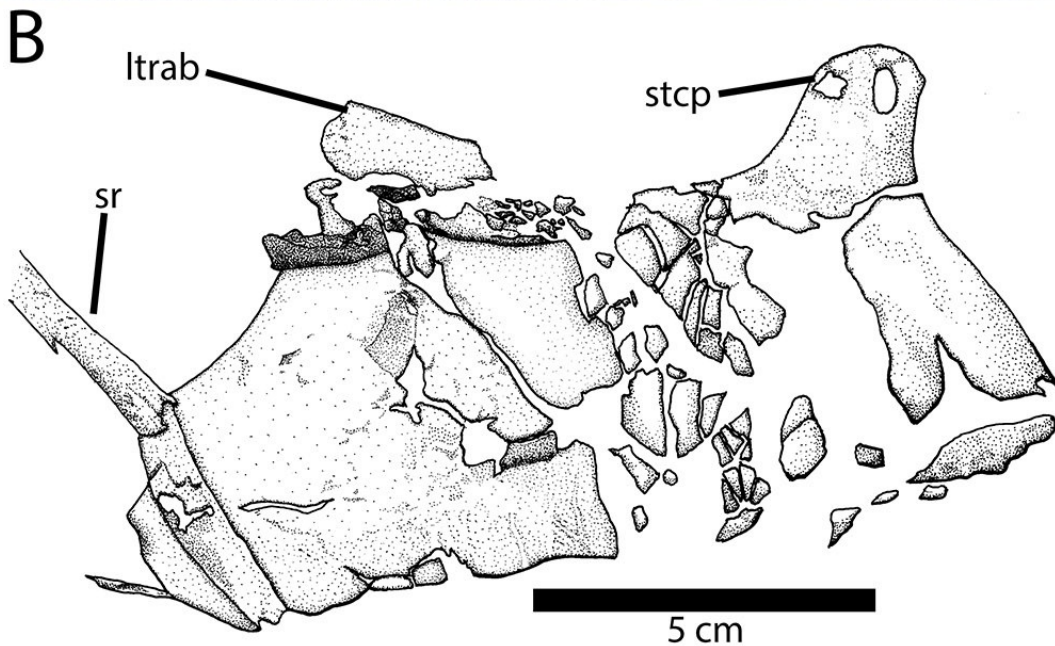
Fig. 3.79. Sternum of *Apatoraptor pennatus*.

Photograph (A) and illustration (B) of right sternal plate of TMP 1993.051.0001 in ventral view.

Abbreviations: **ltrab**, lateral trabecula; **sr**, sternal rib; **stcp**, sternocoracoidal process.

R. Humerus

dpc

R. Ulna

R. Manus

R. Radius

10 cm
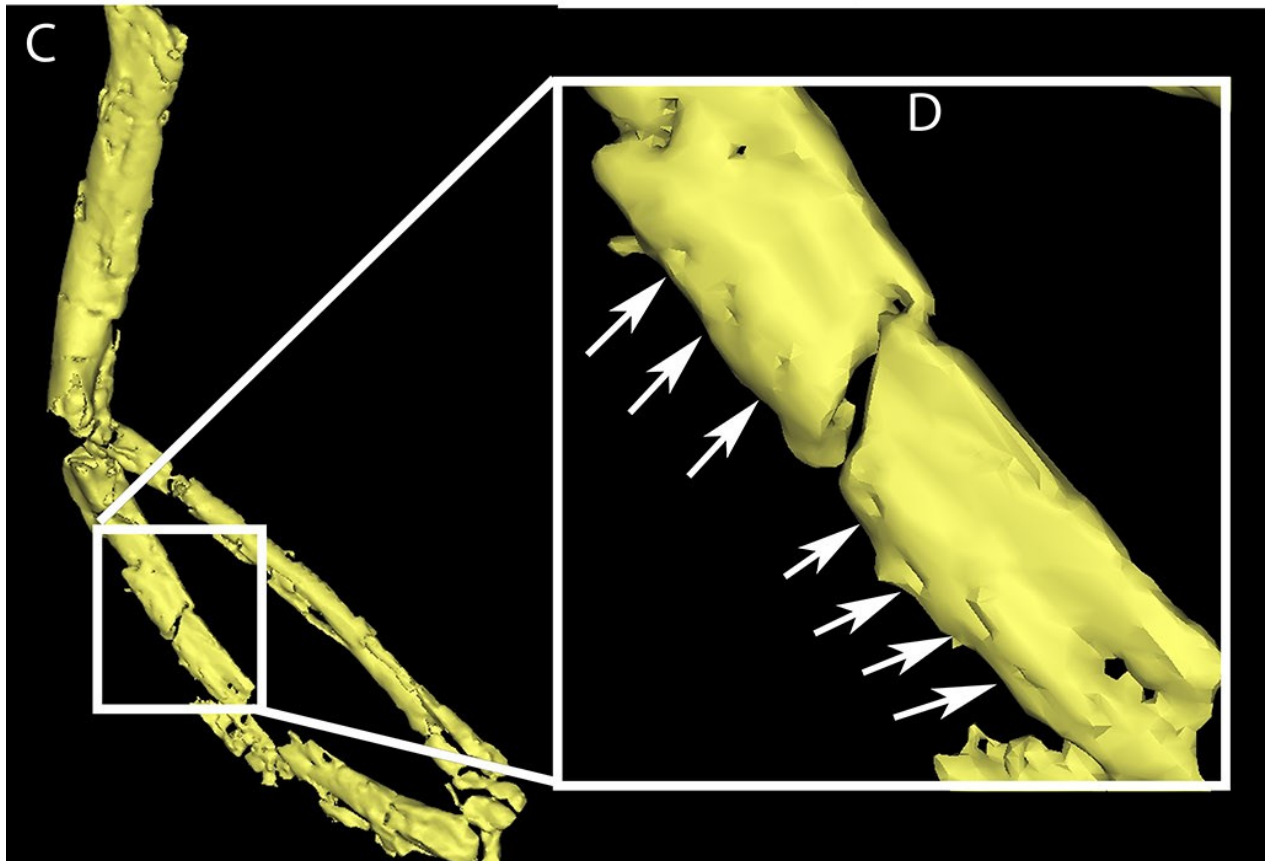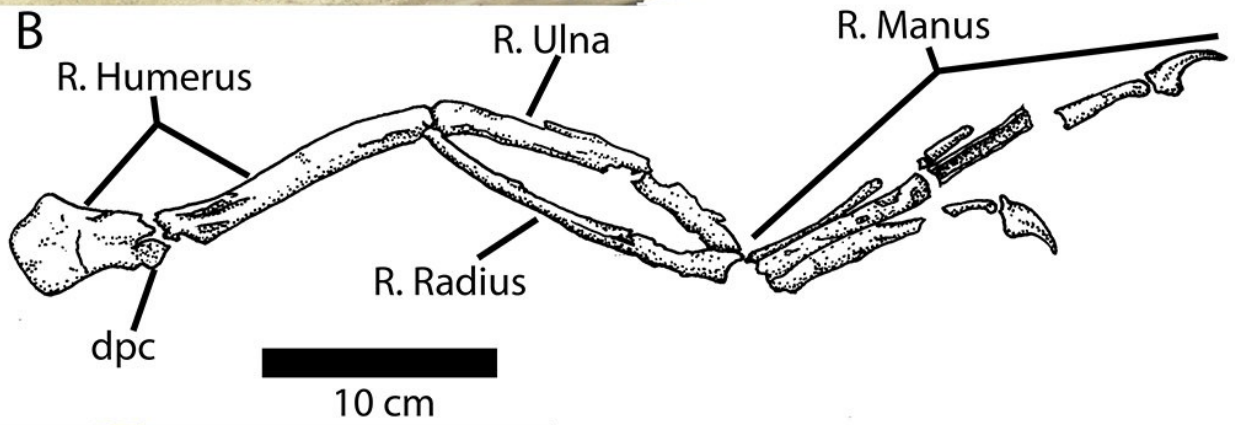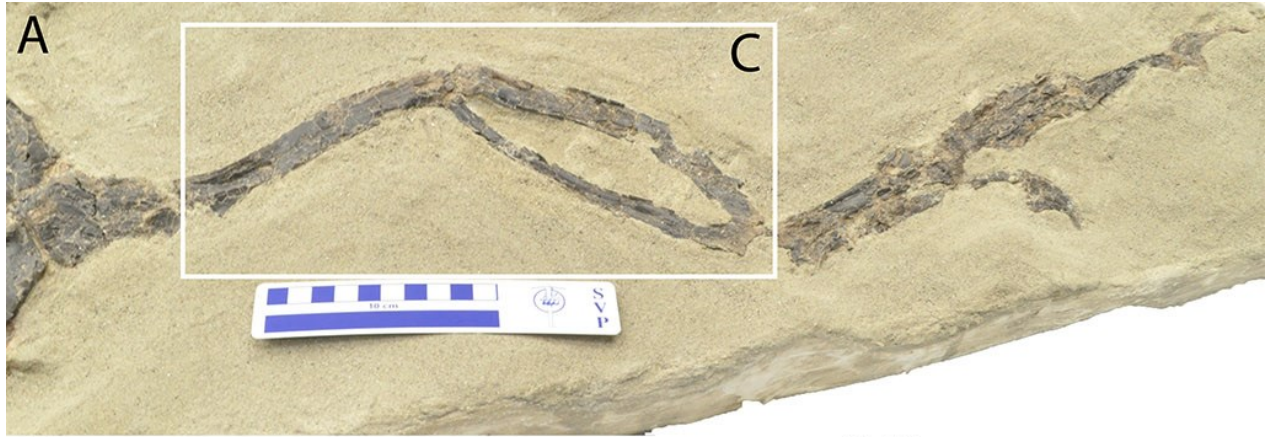
(Previous page)

Fig. 3.80. Forelimb of *Apatoraptor pennatus*.

Photograph (A) and illustration (B) of right arm of TMP 1993.051.0001 in medioventral view.

Computed tomography reconstruction (C) of right arm in lateral view. Detail (D) of right ulna in

lateral view, showing quill marks (arrows). **Abbreviation: dpc**, deltopectoral crest.
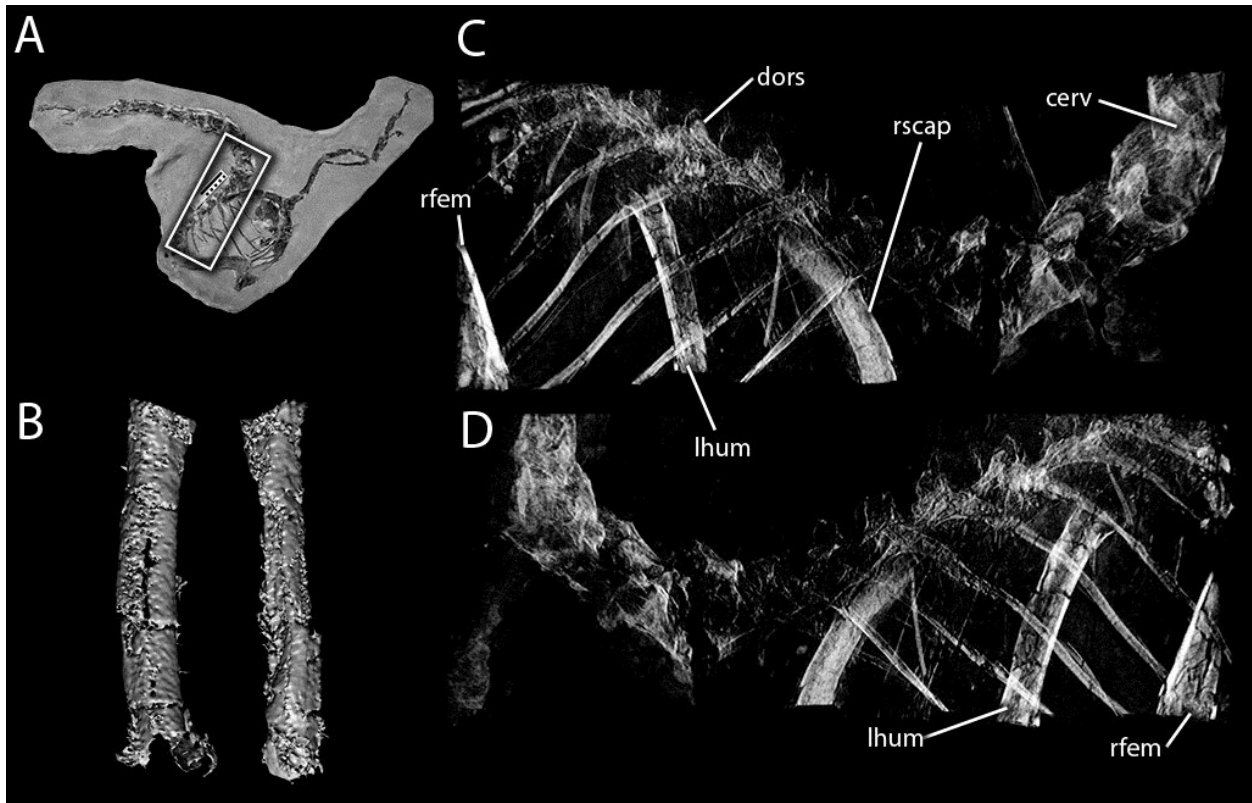
Fig. 3.81. Left side of the body of *Apatoraptor pennatus* as revealed by computed tomography.

Photograph (A) of TMP 1993.051.0001 in right lateral view, showing location of three-dimensional density visualizations. Three-dimensional reconstruction (B) of left humerus in posterior (left) and anterior (right) views. Three-dimensional density visualizations (C, D) of the thoracic region in right lateral (C) and left lateral (D) views. **Abbreviations: cerv**, cervical vertebra; **dors**, dorsal vertebra; **lhum**, left humerus; **rfem**, right femur; **rscap**, right scapula.
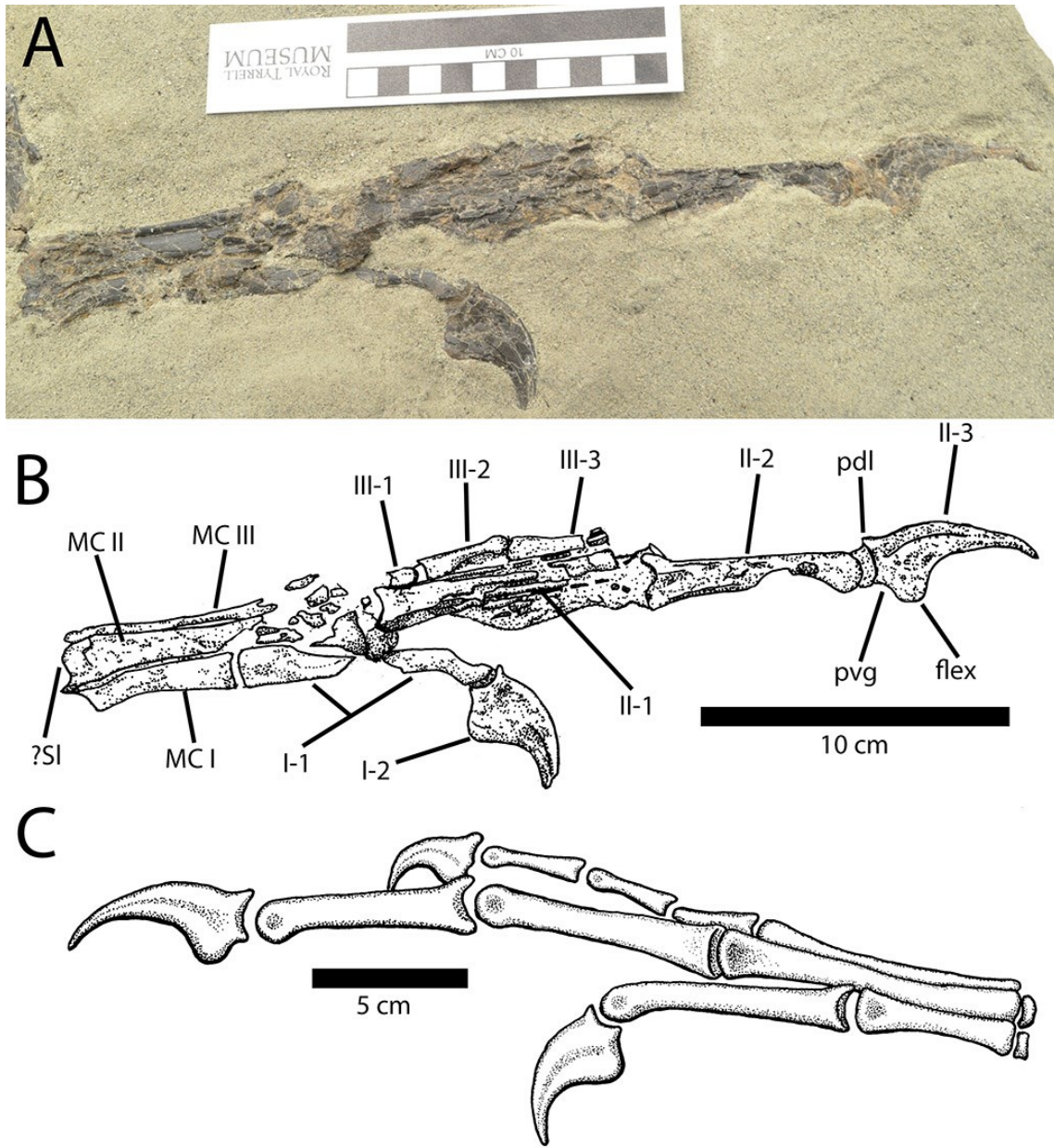
Fig. 3.82. Manus of *Apatoraptor pennatus*.

Photograph (A) and illustration (B) of right manus in palmar view. Reconstruction (C) of right

manus in medial view. **Abbreviations**: **flex**, flexor tubercle; **MC I**, metacarpal I; **MC II**,

metacarpal II; **MC III**, metacarpal III; **pdl**, proximodorsal lip; **pvg**, posteroventral groove; **?Sl**,

possible semilunate carpal.
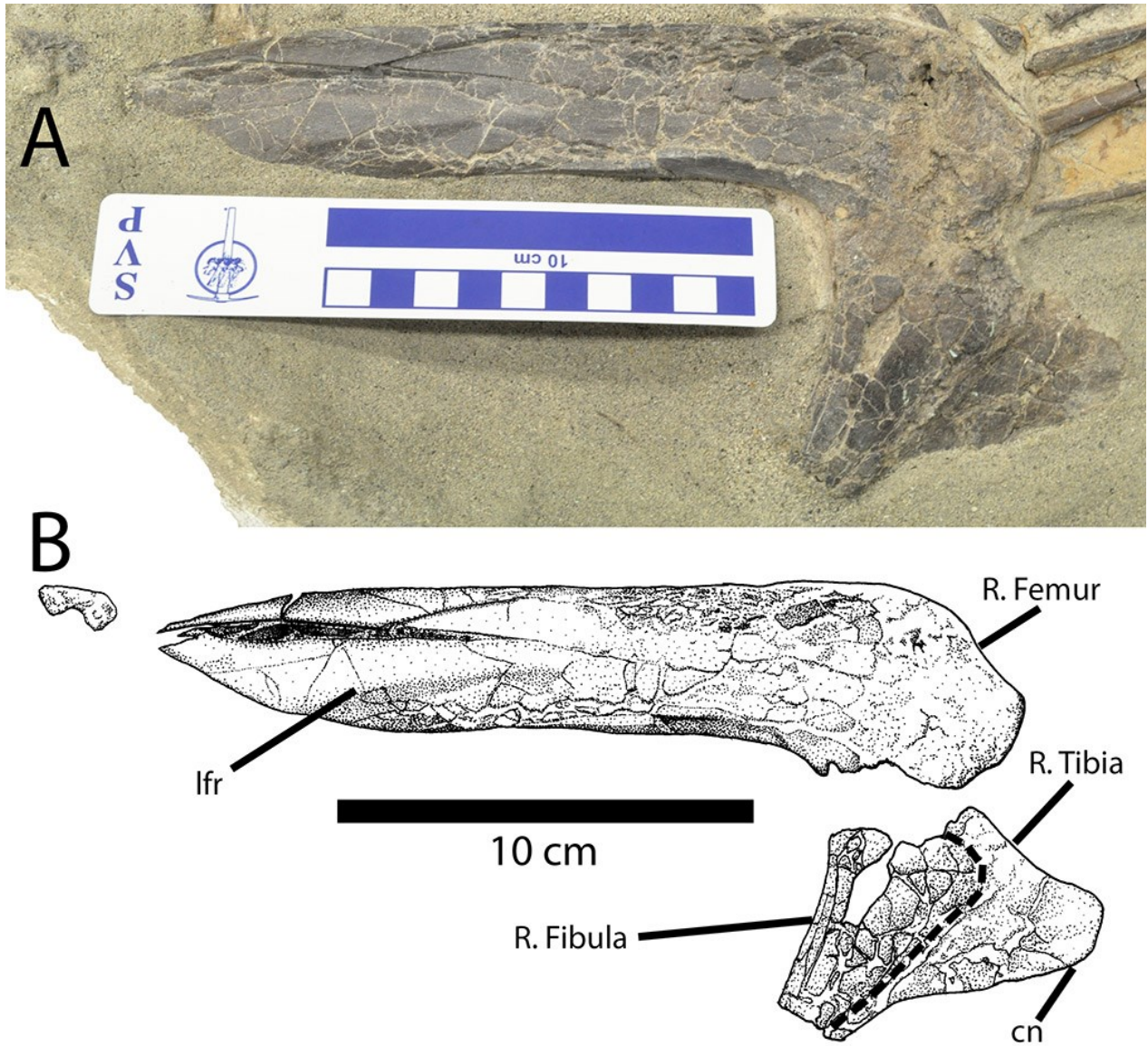
Fig. 3.83. Hindlimb of *Apatoraptor pennatus*.

Photograph (A) and illustration (B) of right distal femur and proximal tibia and fibula of TMP

1993.051.0001 in right lateral view. **Abbreviations**: **cn**, cnemial crest; **lfr**, lateral femoral ridge.

Fig. 3.84. Life reconstruction of *Apatoraptor pennatus*.

Artwork by Sydney Mohr.
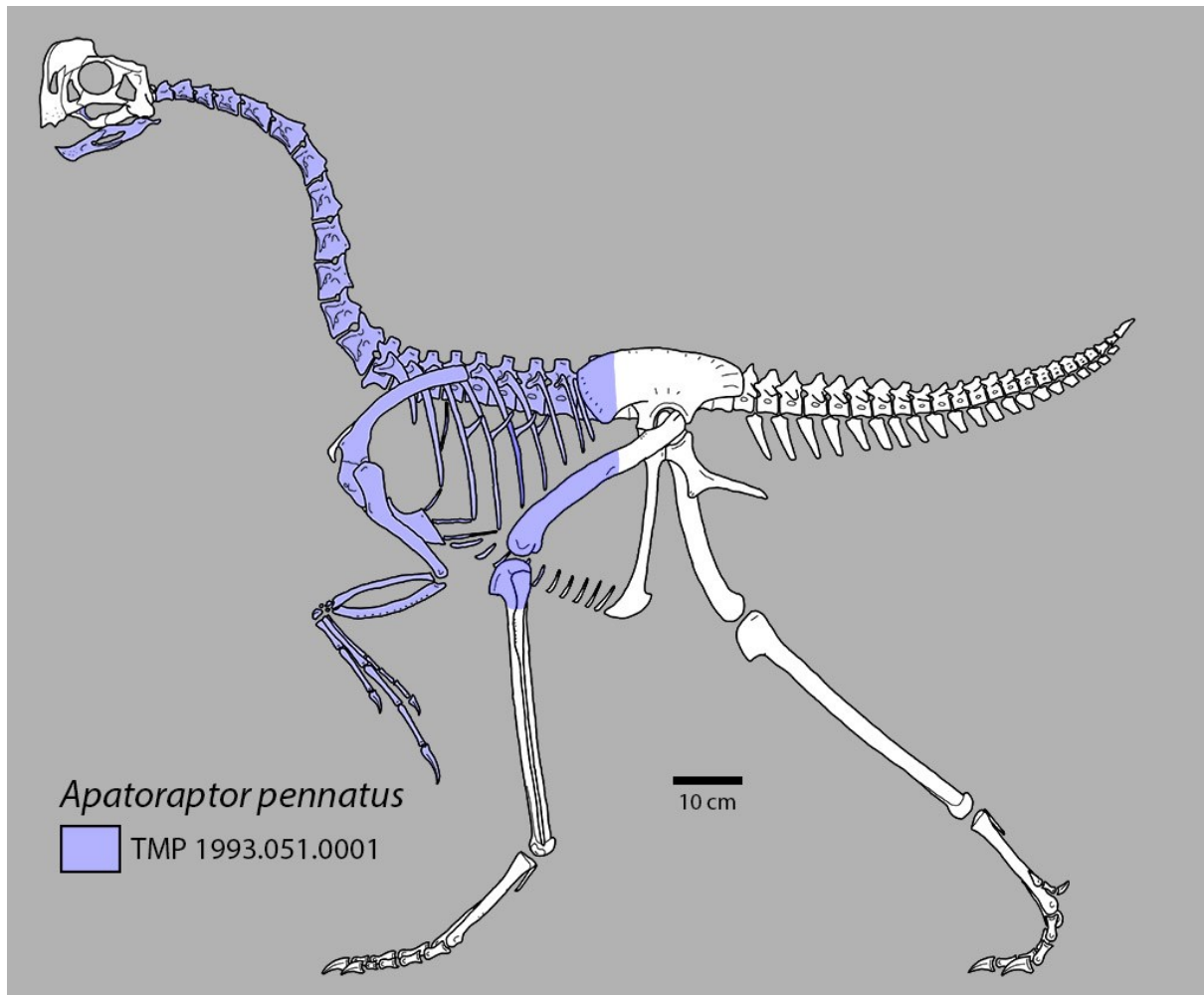
Fig. 3.85. Skeletal reconstruction of *Apatoraptor pennatus*.

Skeletal reconstruction based on TMP 1993.051.0001 with other elements based on

Chirostenotes pergracilis and *Elmisaurus rarus*.
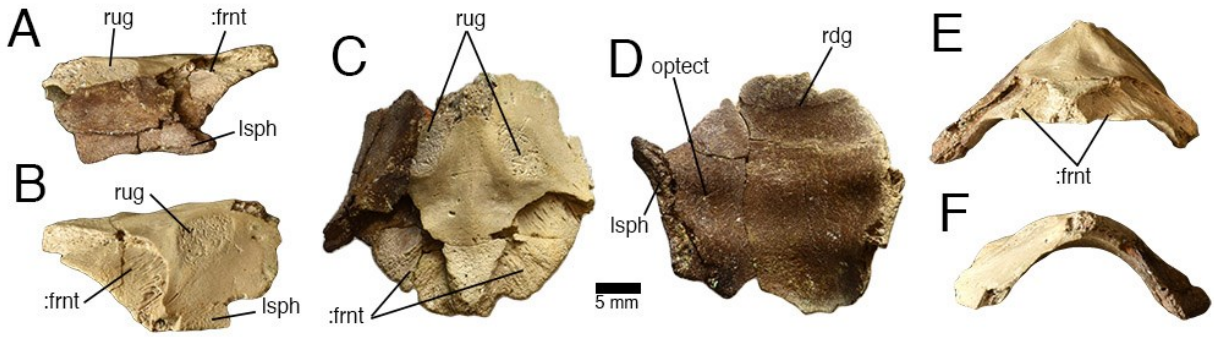
Fig. 3.86. Indeterminate caenagnathid parietals from the Dinosaur Park Formation.
Fused parietals of TMP 1981.019.0252 in right lateral (A), left lateral (B), dorsal (C), ventral (D), anterior (E), and posterior (F) views. **Abbreviations: :frnt**, contact surfaces for frontals; **lsph**, laterosphenoid; **optect**, fossa for optic tectum; **rdg**, ridge; **rug**, rugosity.
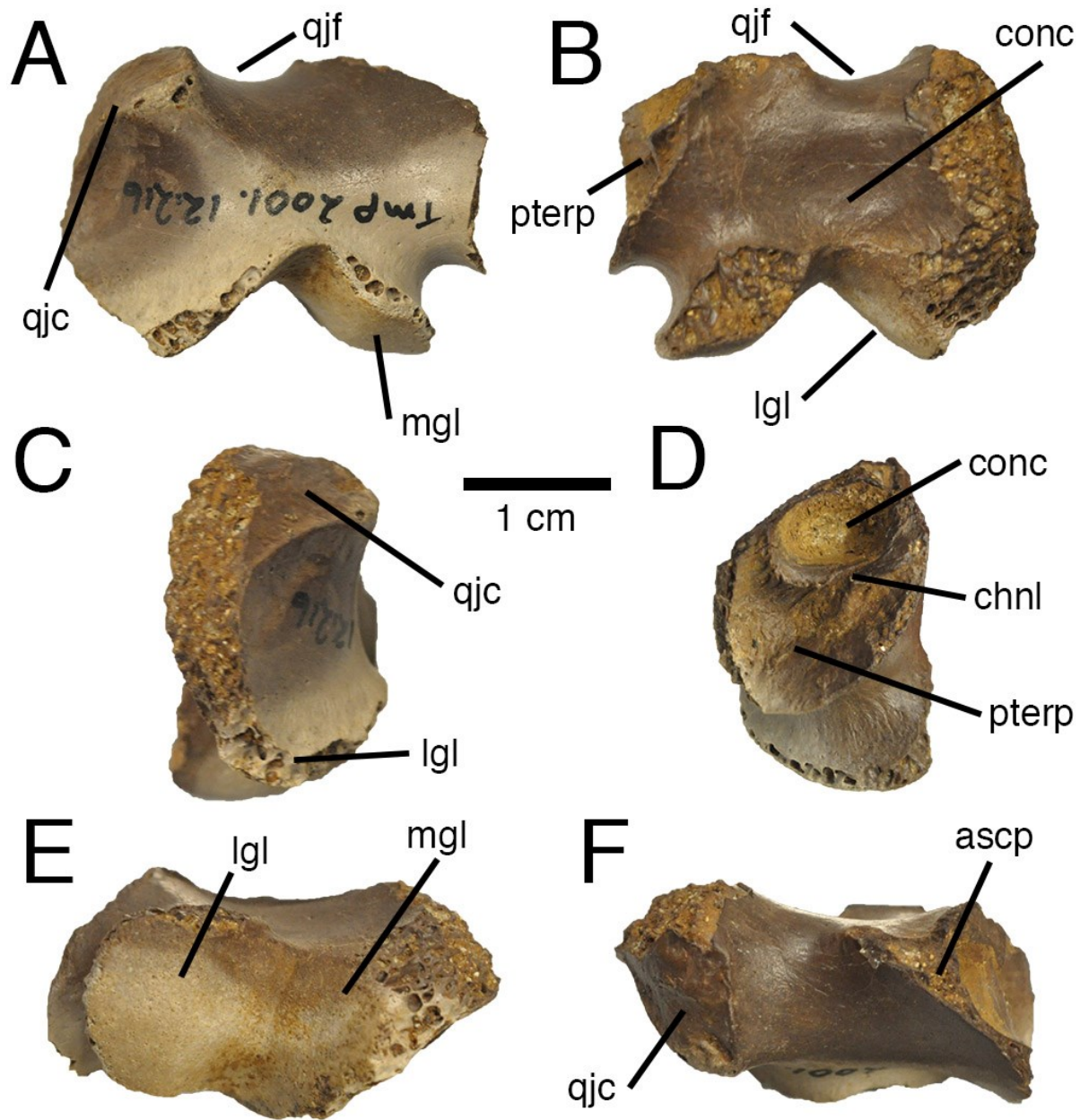
Fig. 3.87. Indeterminate caenagnathid quadrate from the Dinosaur Park Formation.
Right quadrate of TMP 2001.012.0216 in anterior (A), posterior (B), lateral (C), medial (D), ventral (E), and dorsal (F) views. **Abbreviations: ascp**, ascending process; **chnl**, channel; **conc**, concavity; **lgl**, lateral glenoid; **mgl**, medial glenoid; **pterp**, pterygoid process; **qjc**, quadratojugal contact.
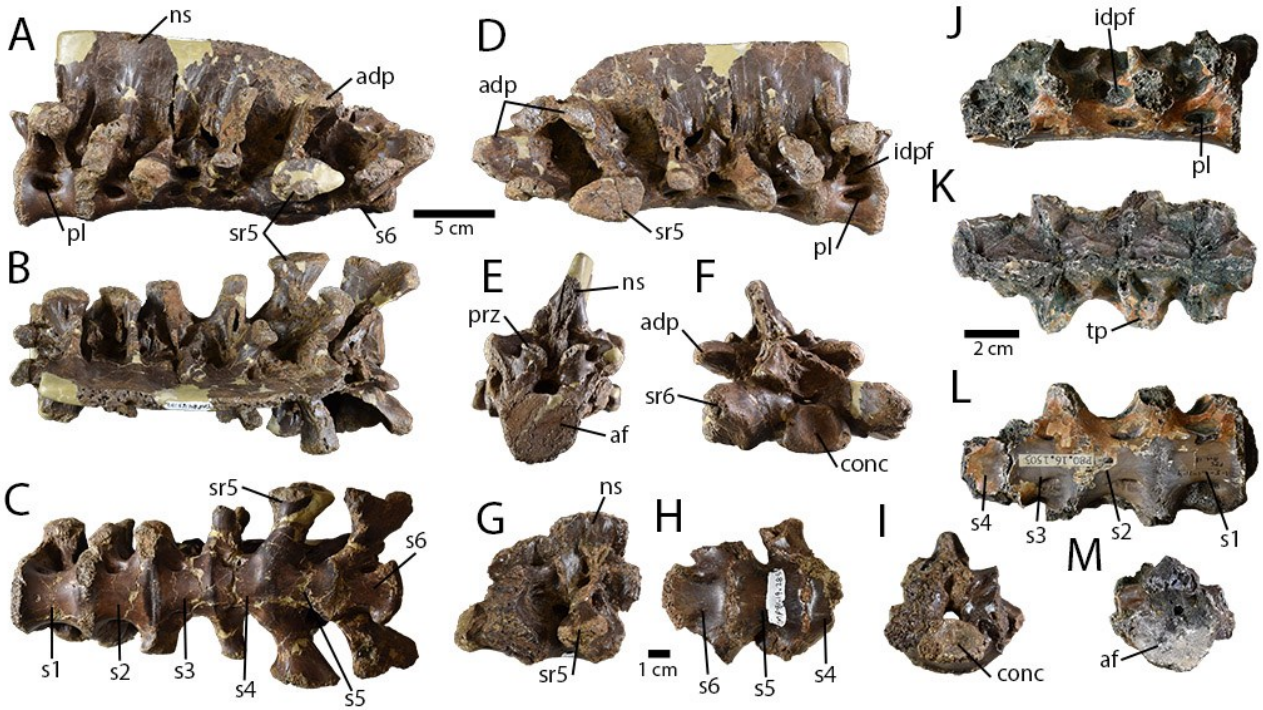
Fig. 3.88. Indeterminate caenagnathid sacra from the Dinosaur Park Formation.

Sacrum of TMP 1984.163.0102 (A–F) in left lateral (A), dorsal (B), ventral (C), right lateral (D), anterior (E) and posterior (F) views. Sacrum of TMP 1981.019.0285 (G–I) in right lateral (g), ventral (H), and posterior (I) views. Sacrum of TMO 1980.016.1503 (J–M) in right lateral (J), dorsal (K), ventral (L) and posterior (M) views. **Abbreviations: adp**, accessory dorsal process; **af**, articular face; **conc**, concavity; **idpf**, infradiapophyseal fossa; **ns**, neural spine; **pl**, pleurocoel; **prz**, prezygapophysis; **s1–s6**, sacral vertebrae 1 to 6; **sr5**, sacral rib 5; **tp**, tranverse process.
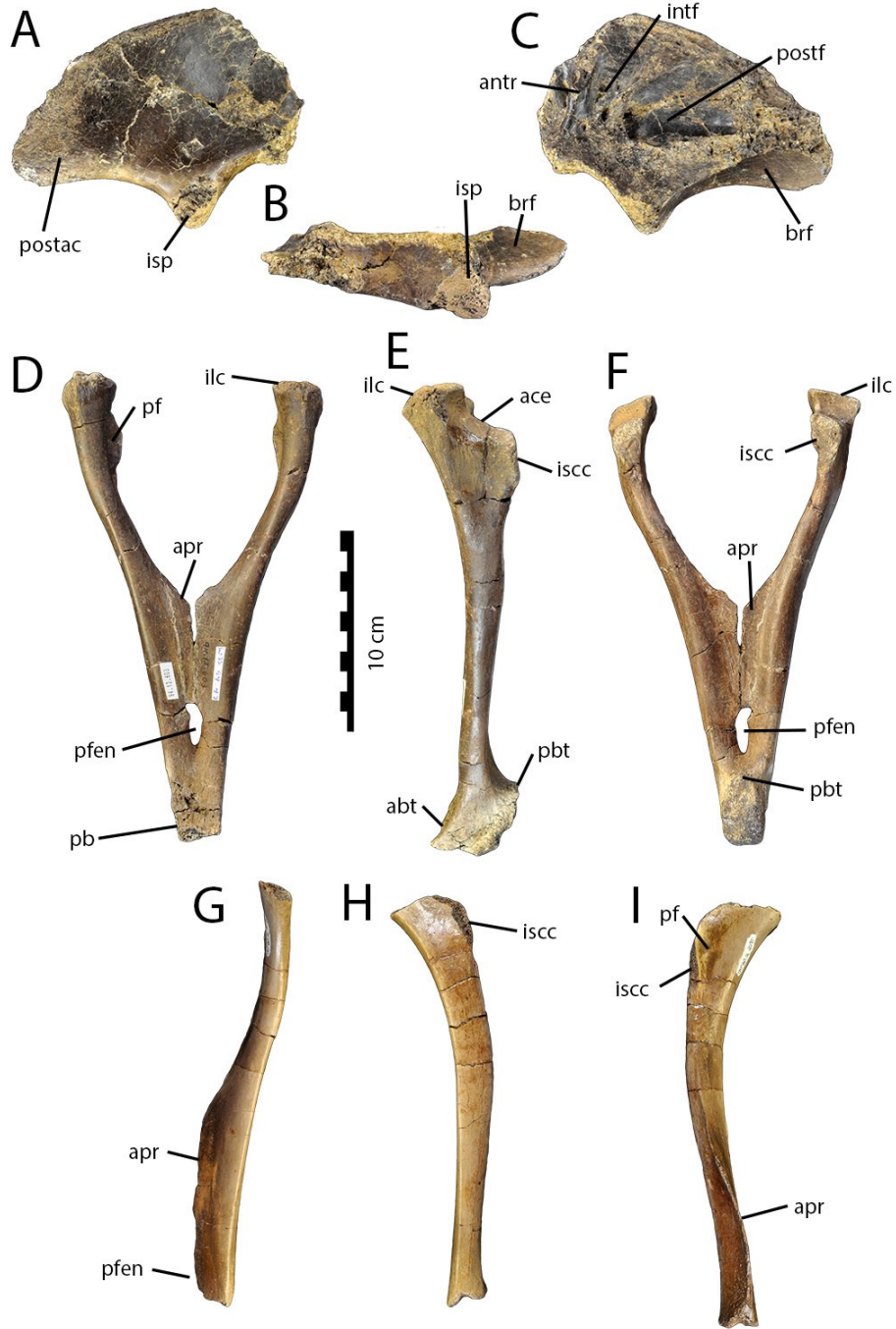
Fig. 3.89. Indeterminate caenagnathid pelvic elements from the Dinosaur Park Formation.

Partial right ilium (A–C) of TMP 1998.093.0013 in lateral (A), ventral (B), and medial (C) views. Pubes (D–F) of TMP 1994.012.0603 in anterior (D), left lateral (E), and posterior (F) views. Left pubis of TMP 1980.016.2095 (G–I) in anterior (G), lateral (H) and medial (I) views.

Abbreviations: abt, anterior process of pubic boot; **ace**, acetabulum; **antr**, anterior ridge; **apr**, pubic apron; **brf**, brevis fossa; **ilc**, iliac contact; **intf**, intermediate fossa; **iscc**, ischiadic contact; **isp**, ischiadic peduncle; **pb**, pubic boot; **pbt**, posterior process of pubic boot; **pfen**, pubic fenestra; **postac**, postacetabular blade; **postf**, posterior fossa.
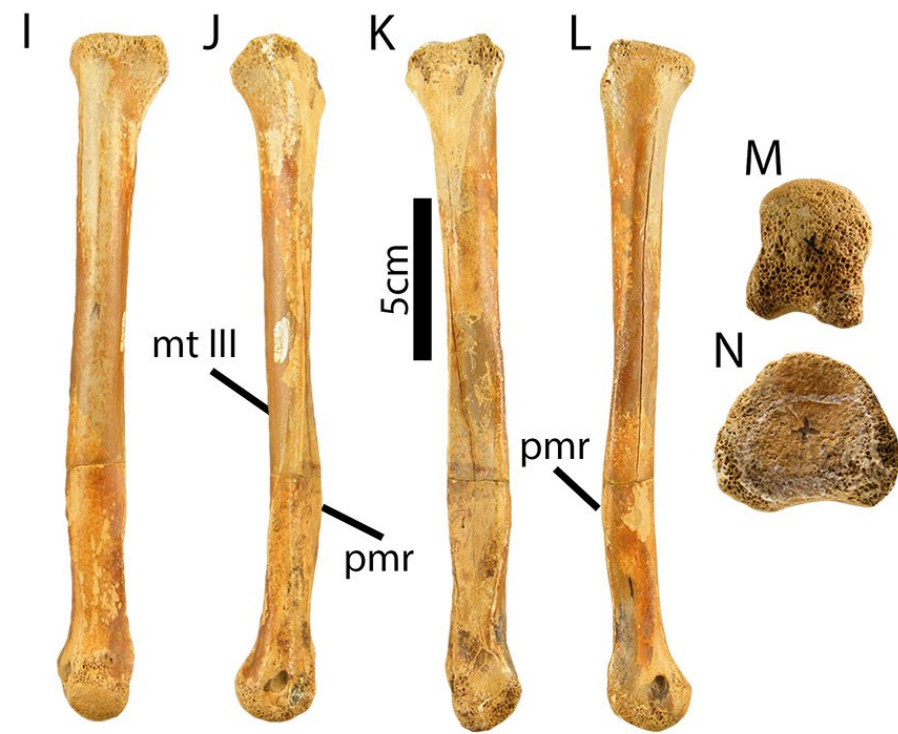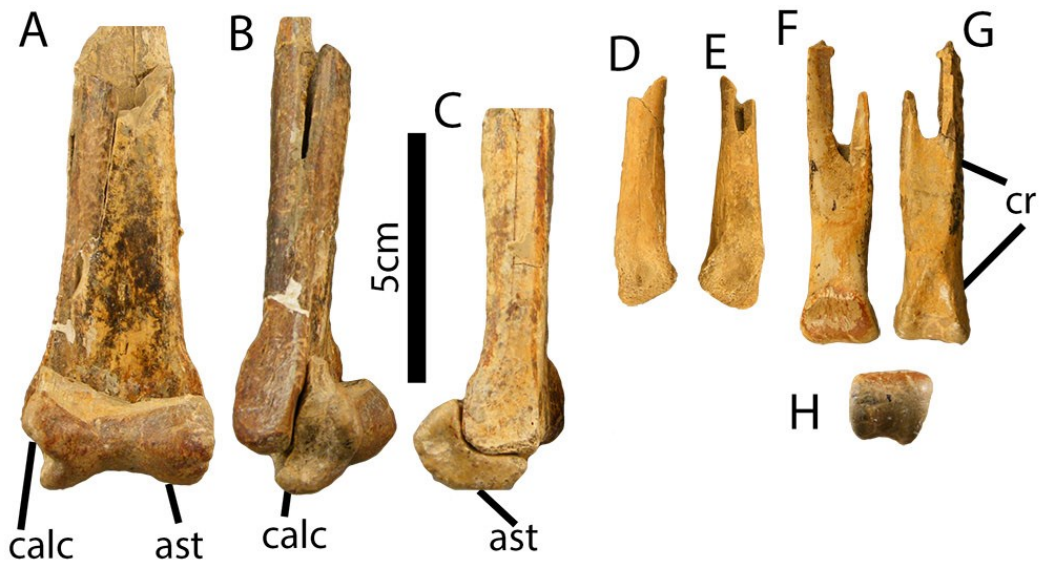
Fig. 3.90. Caenagnathid material from the Frenchman Formation.

Partial hindlimb of RSM P2600.1 (A–G). Right distal tibia and associated astragalus (A–C) in anterior (A), lateral (B), and medial (C) views. Right metatarsal II (D, E) in anterior (D) and posterior (E) views. Right metatarsal III (F–H) in anterior (F), posterior (G), and distal (H) views. Left second metatarsal (I–N) of RSM P2161.1 in anterior (I), lateral (J), posterior (K) medial (L), distal (M), and proximal (N) views. **Abbreviations: ast**, astragalus; **calc**, contact surface for calcaneum; **cr**, cruciate ridges; **mt III**, contact surface for metatarsal III; **pmr**, posteromedial ridge.
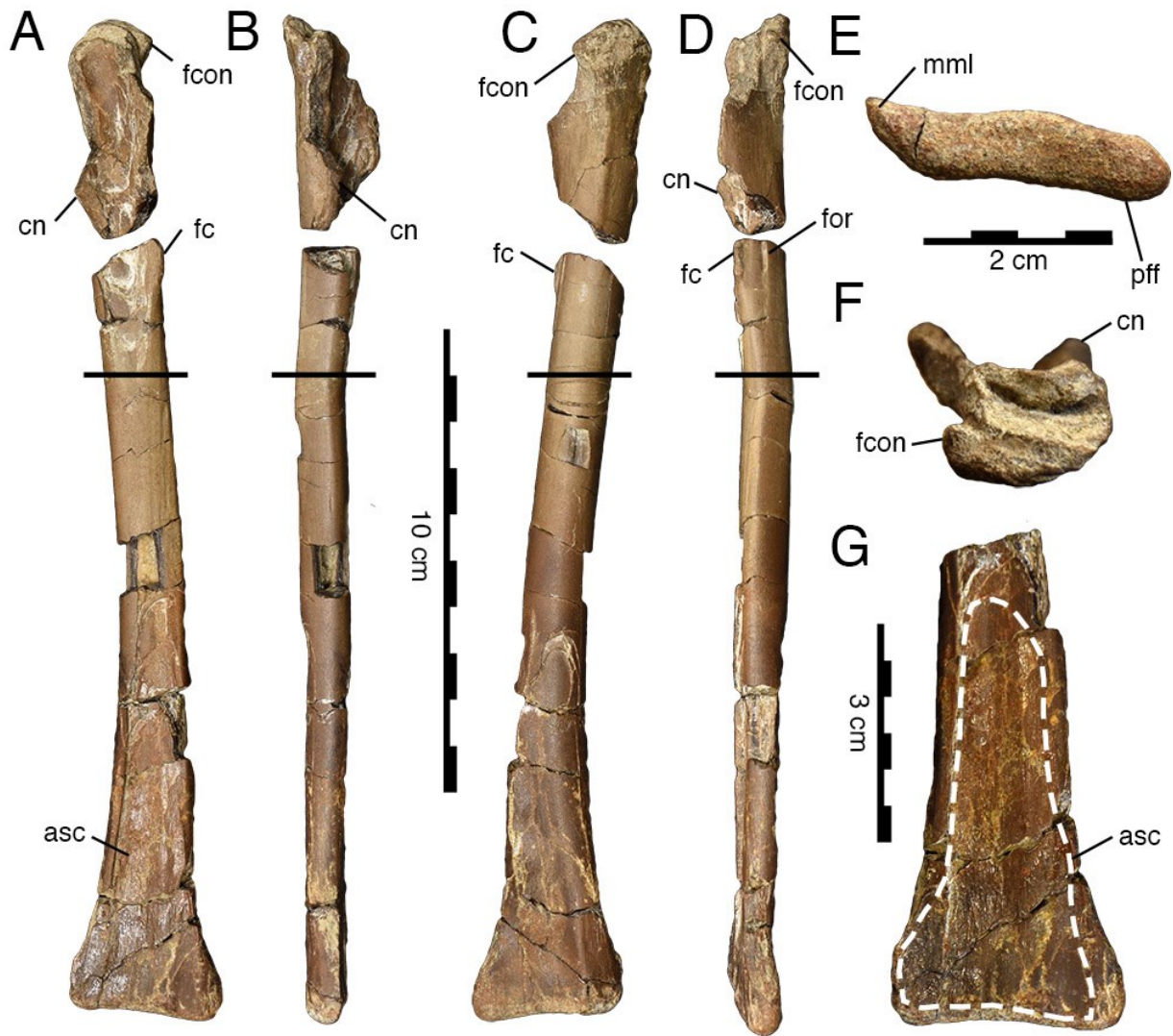
Fig. 3.91. Indeterminate caenagnathid tibia from the Horseshoe Canyon Formation.

Left tibia of UALVP 57349, in anterior (A), medial (B), posterior (C), lateral (D), distal (E), and proximal (F) views. White line indicates location of thin section in Figs. 3.92–3.93. Detail (G) of contact surface for the astragalus, highlighted by dashed line. **Abbreviations: asc,** contact surface for astragalus; **cn**, cnemial crest; **fc**, fibular crest; **fcon**, fibular condyle; **for**, foramen; **mml**, medial malleolus; **pff**, postfibular flange.
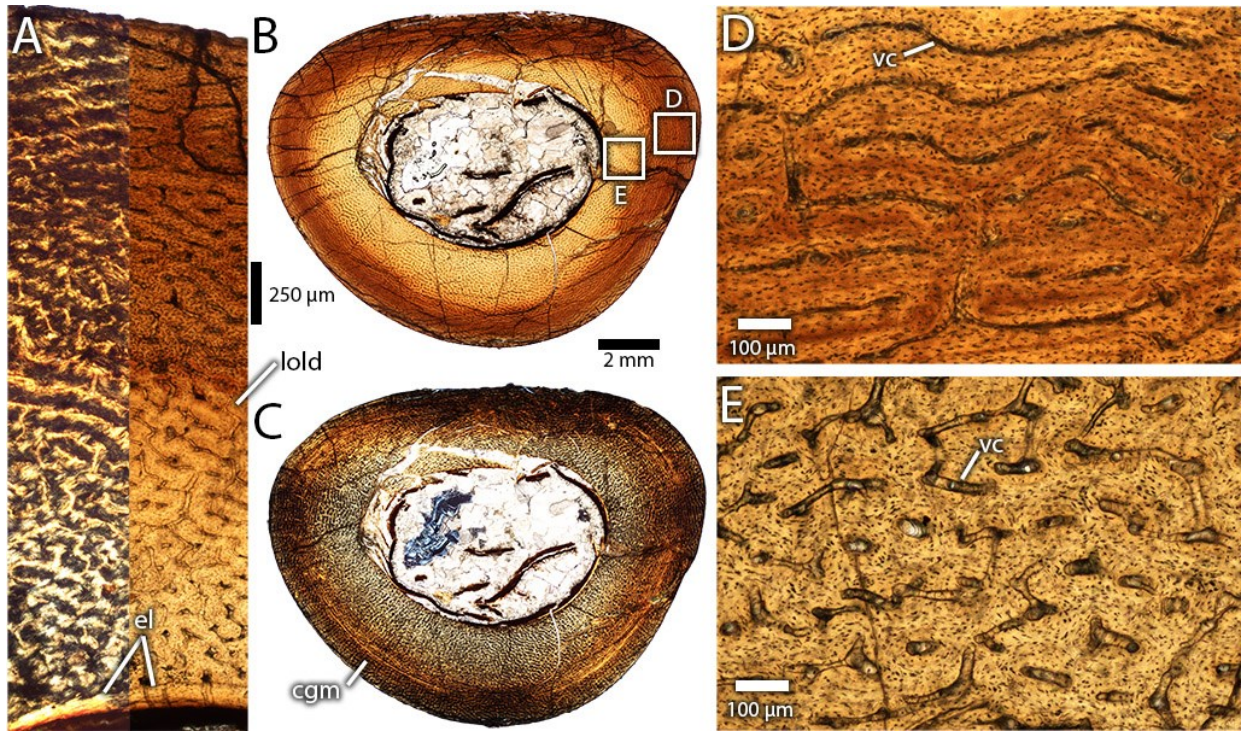
Fig. 3.92. Histological aspects of UALVP 57349.

Column (A) through entire cortex in cross-polarized (left) and normal light (right), showing

changes in vasculature and osteocyte lacunar density. Periosteal surface is at the top. Complete

cross-sections in normal (B) and cross-polarized light (C), showing cross-sectional shape, colour

change associated with increased osteocyte lacunar size, and cyclical growth mark. Boxes show

locations of images (D) and (E). Detail (D) of outer cortex, showing plexiform vasculature and

larger osteocyte lacunae. Detail (E) of inner cortex, showing reticular vasculature and smaller,

flatter osteocyte lacunae. **Abbreviations: cgm**, cyclical growth mark; **el,** endosteal lamellae;

lold, zone of low osteocyte lacunar density; **vc**, vascular canal.
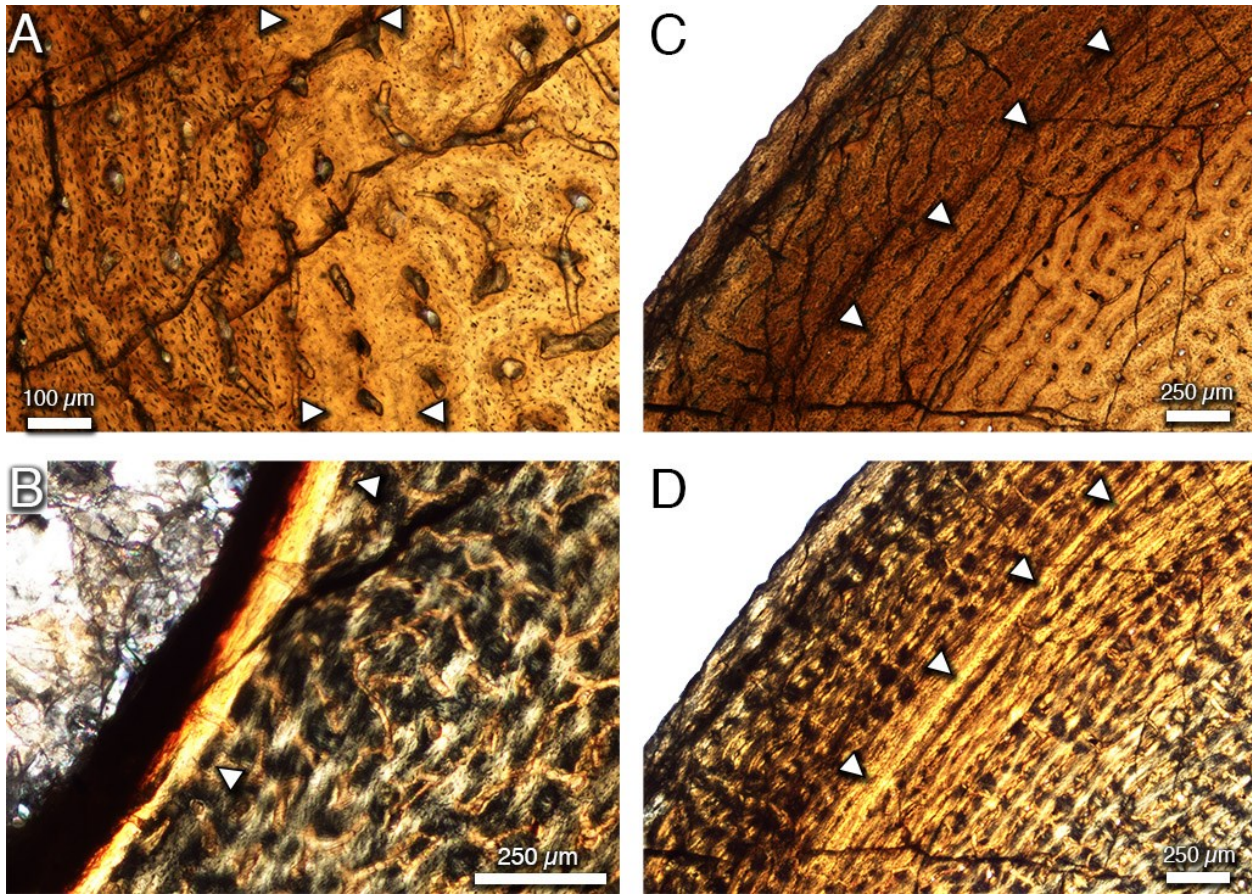
Fig. 3.93. Additional histological images of UALVP 57349.

Detail (A) of cortex, showing changes in osteocyte lacunar density and size, and zone of low osteocyte lacunar density (between white arrows). Detail (B) of endosteal surface, showing contact of endosteal lamellae with primary fibrolamellar bone of the cortex; arrows indicate primary osteons cross-cut by endosteal lamellae. Detail of outer cortex in normal light (C) and cross-polarized light (D), showing zone of parallel-fibered bone (white arrows) representing the first cyclical growth mark. Note alignment of vascular canals (white arrows) in (C).
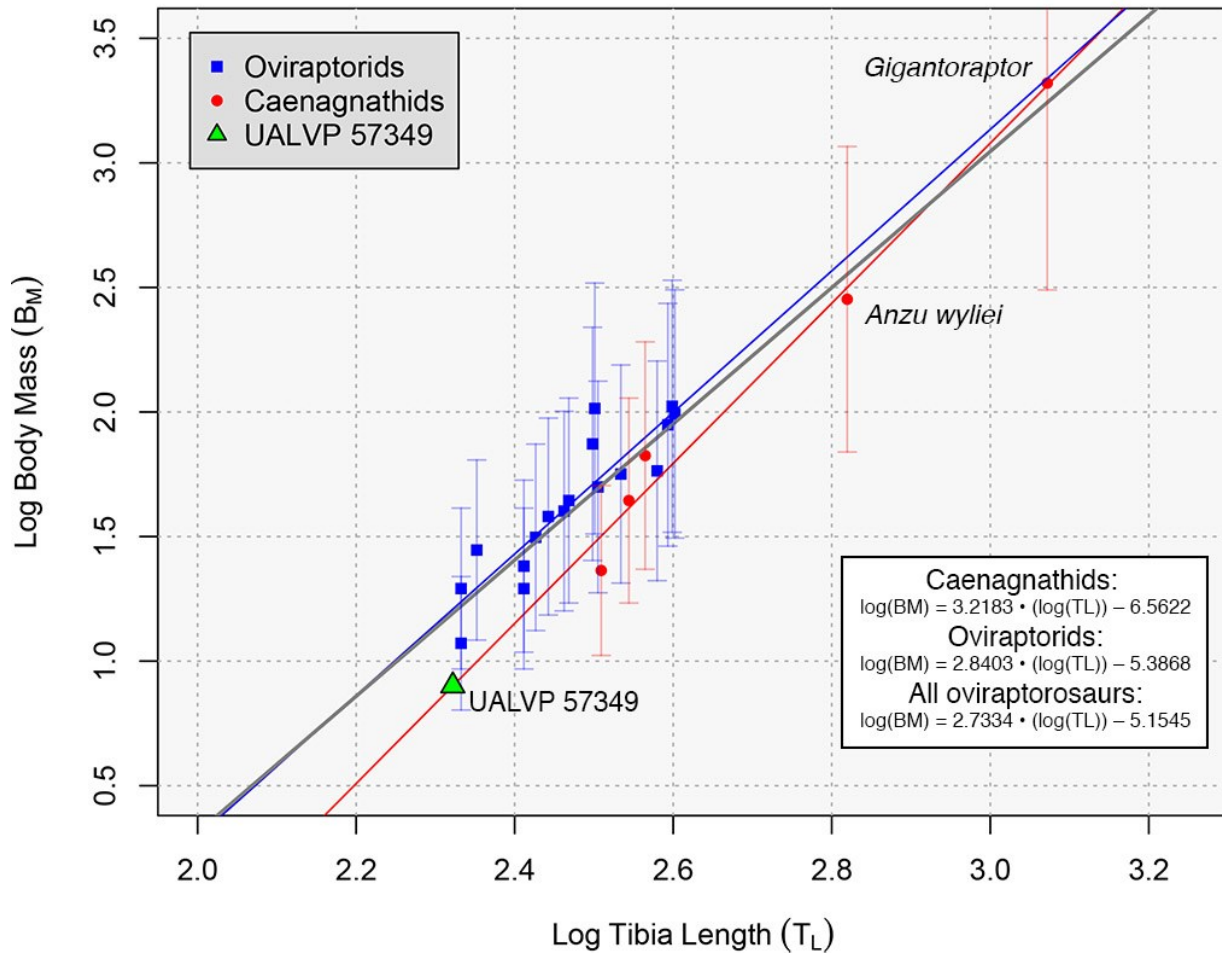
Fig. 3.94. Scatterplot of log-transformed Tibia Length against log-transformed hypothesized Body Mass.

Body mass estimated using the method of (Campione et al., 2014) for oviraptorids (blue squares), caenagnathids (red circles), and UALVP 57349 (green triangle). Error bars indicate 25% estimation error of body mass from (Campione et al., 2014). Lines represent least-squared regressions for oviraptorids (blue), caenagnathids (red), and all oviraptorosaurs (grey).
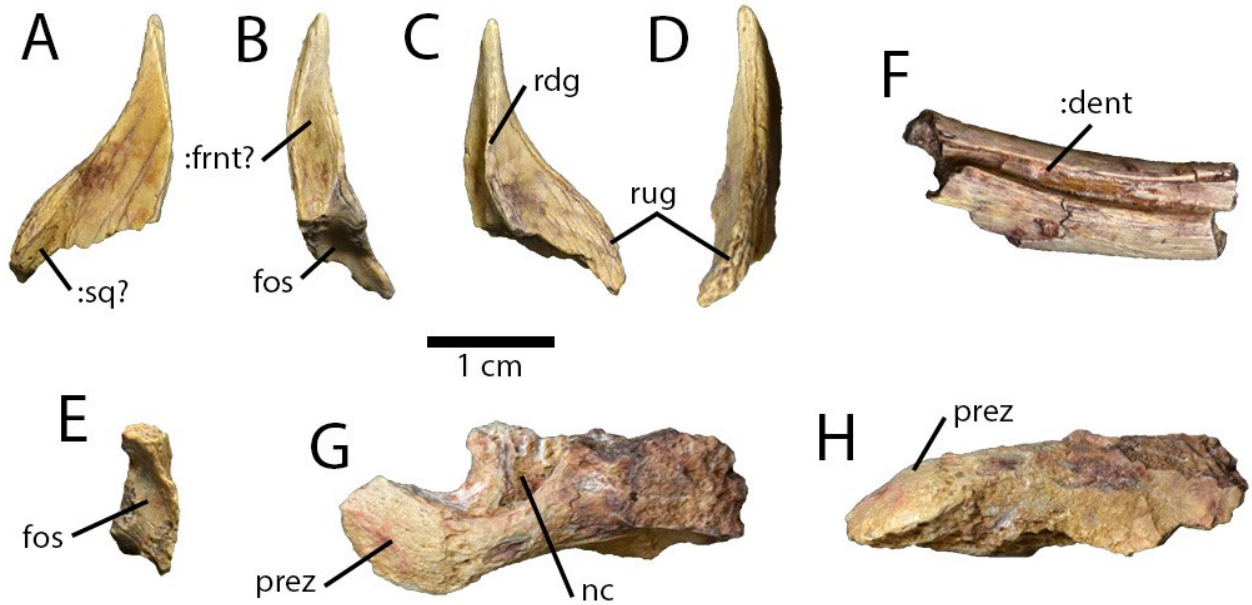
Fig. 3.95. Cranial and axial elements of an indeterminate caenagnathid skeleton (MPC-D NatGeo.2018.040) from the Nemegt Formation.

Possible right postorbital (A–E) in presumed lateral (A, anterior (B), medial (C), posterior (D), and ventral (E) views. Right angular (F) in lateral view. Partial cervical neural arch in dorsal (F) and left lateral (H) views. **Abbreviations: :dent**, contact groove for dentary; **fos**, fossa; **:frnt?**, presumed contact surface for frontal; **nc**, neural canal; **prez**, prezygapophysis; **rdg**, ridge; **rug**, rugosity; **:sq?** presumed contact surface for squamosal.
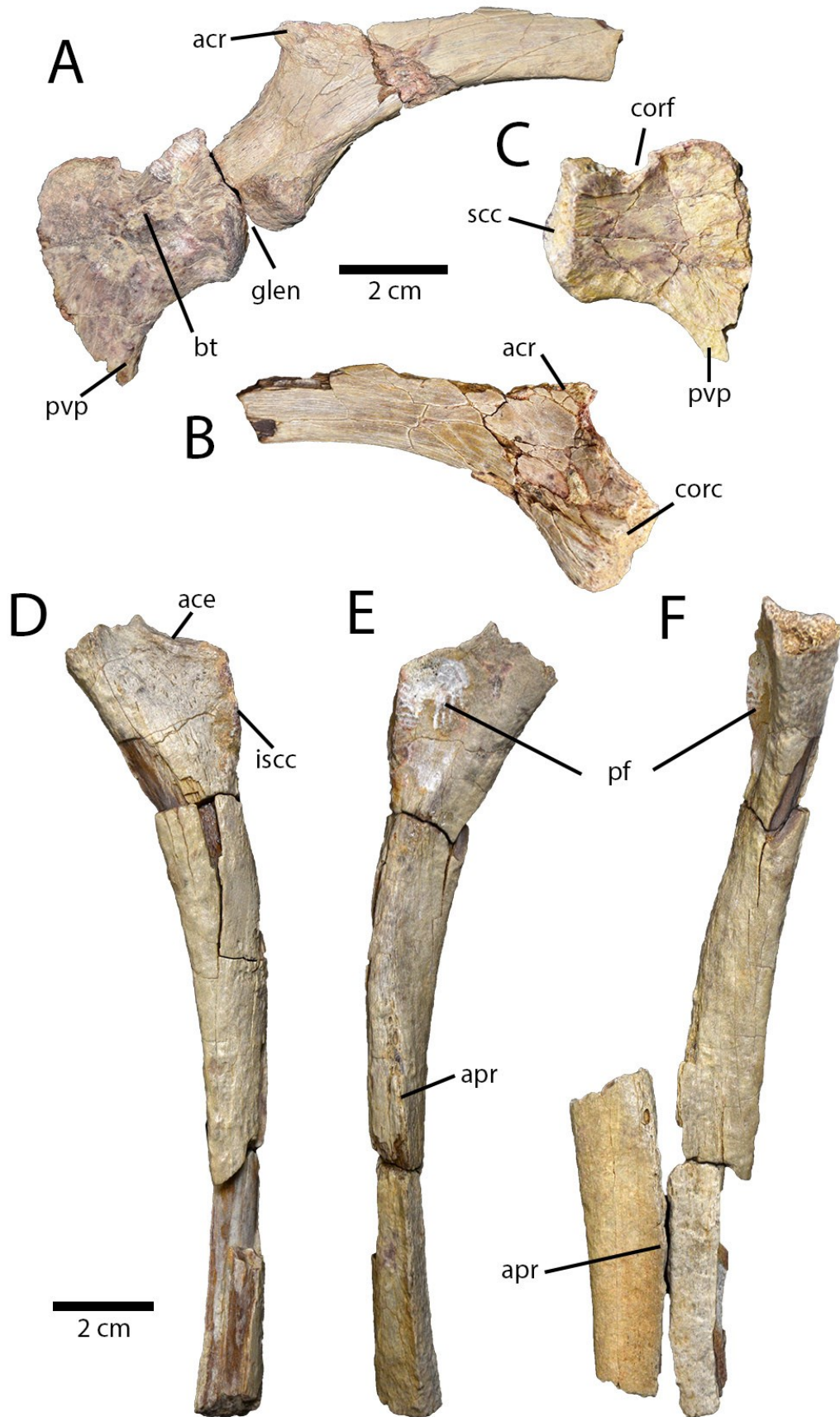
(Previous page)

Fig. 3.96. Appendicular girdle elements of an indeterminate caenagnathid skeleton (MPC-D NatGeo.2018.040) from the Nemegt Formation.

Left scapulacoracoid (A) in lateral view. Left scapula (B) in medial view. Left coracoid (C) in medial view. Left pubis in lateral (D) and medial (E) views. Left and right pubis (F) in anterior view. **Abbreviations: ace**, acetabulum; **acr**, acromion process; **apr**, pubic apron; **bt**, biceps tubercle; **corc**, coracoid conract; **corf**, coracoid foramen; **glen**, glenoid; **iscc**, ischiadic contact; **pf**, pubic fossa; **pvp**, posteroventral process; **scc**, scapular contact.
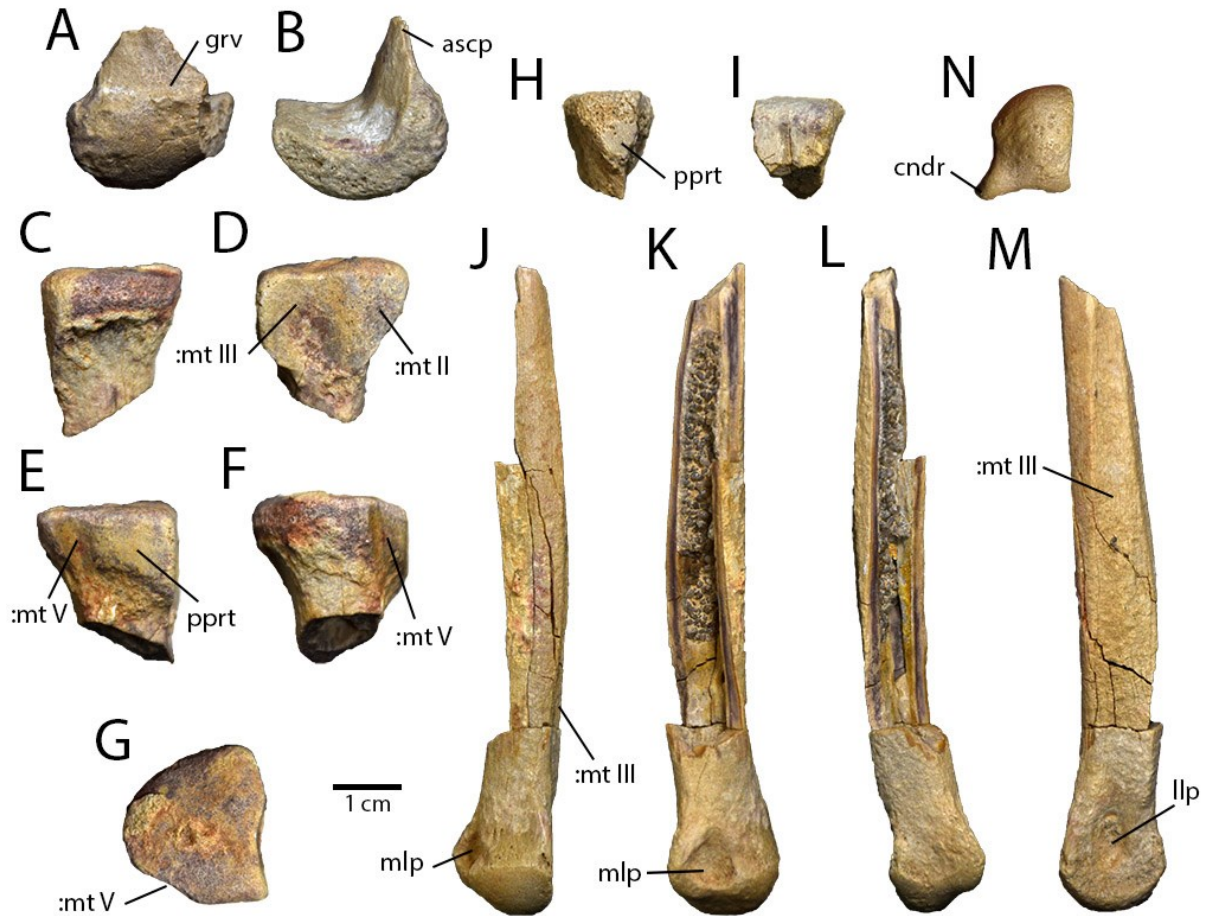
Fig. 3.97. Pedal elements of an indeterminate caenagnathid skeleton (MPC-D NatGeo.2018.040) from the Nemegt Formation.

Partial left astragalus in anterior (A) and medial (B) views. Proximal end of left metatarsal IV (C–G) in anterior (C), medial (D), posterior (E), lateral (F), and proximal (G) views. Proximal end of left metatarsal III (H-I) in posterior (H) and anterior (I) views. Distal end of right metatarsal II (J–N) in anterior (J), medial (K), posterior (L), lateral (M) and distal (N) views.
Abbreviations: ascp, ascending process; **cndr**, condylar ridge; **grv**, groove; **llp**, lateral ligament pit; **mlp**, medial ligament pit; :**mt II**, contact surface for metatarsal II; :**mt III**, contact surface for metatarsal III; :**mt V**, contact surface for metatarsal V; **pprt**, posterior protuberance.

408
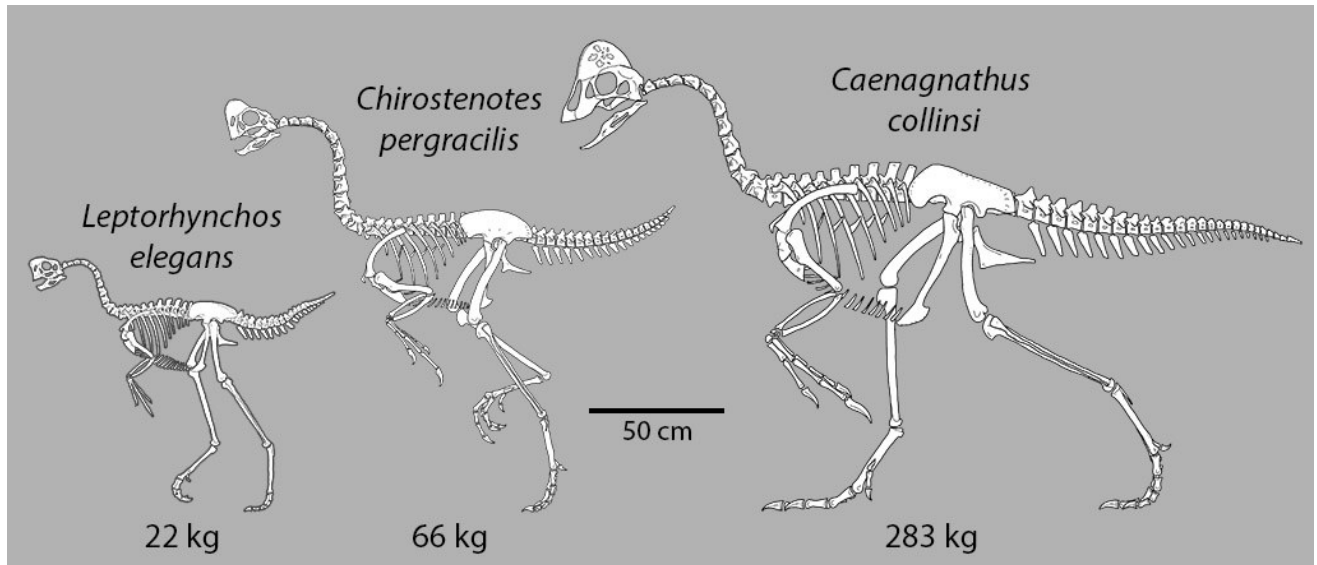
Fig. 3.98. Body size variation in caenagnathids from the Dinosaur Park Formation.

Skeletal reconstructions of *Leptorhynchos elegans* (left), *Chirostenotes pergracilis* (middle), and *Caenagnathus collinsi* (right) to scale, showing differences in body size. Body mass estimates (bottom) were generated for *Leptorhynchos elegans* based on the regression of tibia length to body mass of Funston and Currie (2018); for *Chirostenotes pergracilis* using the method of Campione et al. (2014) based on the femoral circumference of TMP 1979.020.0001; and for *Caenagnathus collinsi* based on the estimated body mass of CM 78000 (*Anzu wyliei*), which is equal in size to the individual represented by UALVP 56638.
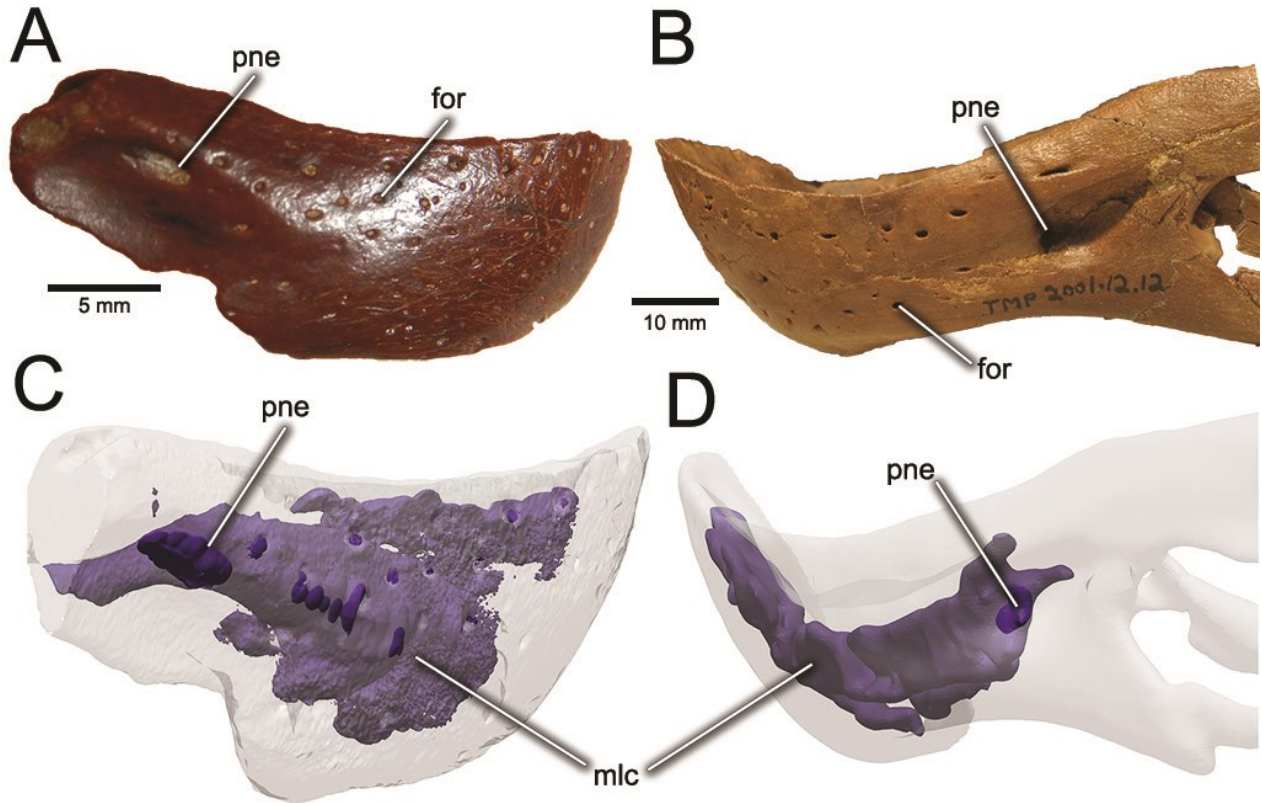
Fig. 3.99. Pneumaticity of caenagnathid dentaries.

Photograph (A) and CT reconstruction (C) of CCMGE 402/12457 (*Caenagnathasia martinsoni*) in right lateral and posterolateral views, respectively. Note connection of major lateral cavity to both external foramina and large pneumatopore housed in a depression. Photograph (B) and CT reconstruction (D) of TMP 2001.012.0012 (*Chirostenotes pergracilis*) in left lateral and posterolateral views, respectively. Note connection of major lateral cavity to pneumatopore housed in a depression. CT scan resolution was not sufficient to reconstruct connection of major lateral cavity to external foramina. Images C and D not to scale.
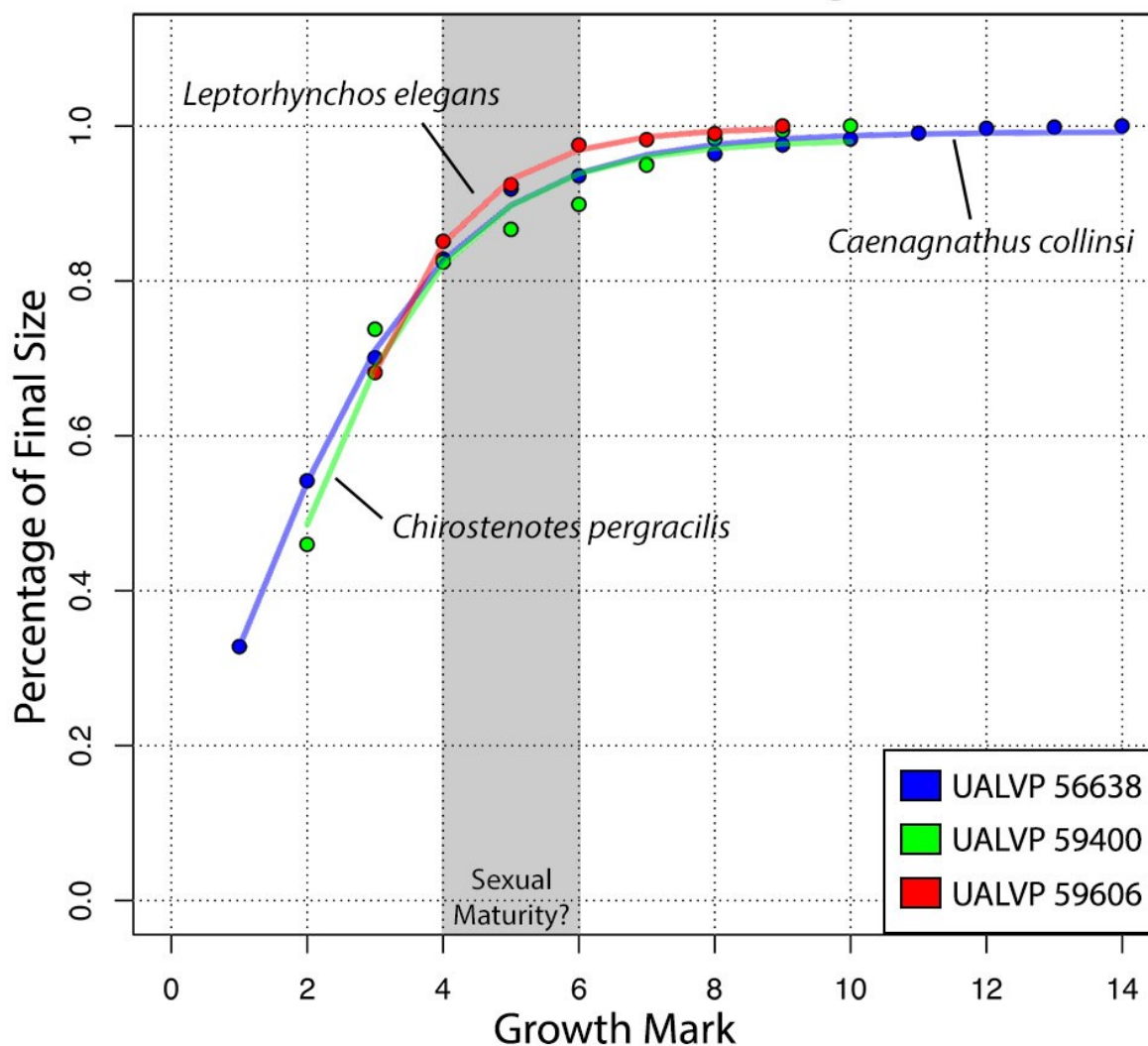
Fig. 3.100. Reconstructed growth curves for caenagnathids from the Dinosaur Park Formation.

Gompertz growth curves fit to line of arrested growth spacing data from UALVP 56638 (blue), UALVP 59400 (green), and UALVP 59606 (red), scaled to size at the final growth mark. Growth curves aligned at inflection point, and shaded area shows interval where sexual maturity is probably achieved, based on drastic reduction in growth rate.

Table 3.1: Measurements of caenagnathid mandibles.
[See supplementary electronic files]

Table 3.2: Body mass estimations of caenagnathids using the method of Campione et al. (2014).
[See supplementary electronic files]

Table 3.3: Taxonomic referral of caenagnathid material from the Dinosaur Park Formation described in Chapter 3.

Taxon	Specimen	Material	Reference
Caenagnathus collinsi	CMN 8776 (holotype)	Complete mandible	(Sternberg, 1940)
	TMP 1979.014.0001	Manual ungual I-2	(Funston et al., 2015)
	TMP 1982.019.0222	Manual ungual I-2	(Funston et al., 2015)
	TMP 1986.036.0323	Femur	(Funston et al., 2015)
	TMP 1993.036.0197	Metatarsal II	(Funston et al., 2015)
	TMP 1993.036.0198	Metatarsal II	(Funston et al., 2015)
	TMP 1993.036.0475	Manual ungual II-3	(Funston et al., 2015)
	TMP 1993.036.0631	Partial astragalocalcaneum	(Funston et al., 2015)
	TMP 1993.075.0049	Astragalocalcaneum	(Funston et al., 2015)
	TMP 2009.003.0029	Manual ungual I-2	(Funston et al., 2015)
	UALVP 55725	Partial caudal vertebra	(Funston et al., 2015)
	UALVP 56638	Pubes	This study
	UALVP 59791	Partial ilium	This study
Chirostenotes pergracilis	CMN 2367 (holotype)	Articulated manus	(Gilmore, 1924)
	CMN 8538	Articulated pes	(Sternberg, 1932)
	TMP 1979.020.0001	Partial skeleton	(Currie and Russell, 1988)
	TMP 1985.043.0070	Partial dentaries	(Funston et al. in press)
	TMP 1992.036.1237	Partial dentaries	(Funston et al. in press)
	TMP 1993.036.0181	Partial tarsometatarsus	(Funston et al., 2016); This study
	TMP 2001.012.0012	Complete mandible	(Funston and Currie, 2014)
	TMP 2002.012.0103	Partial ilium	This study
	UALVP 59400	Partial skeleton	This study
Leptorhynchos elegans	ROM 781 (holotype)	Tarsometatarsus	(Parks, 1933)
	TMP 1979.008.0622	Partial dentaries	(Currie et al., 1993)
	TMP 1981.023.0034	Partial ilium	This study
	TMP 1981.023.0035	Partial ilium	This study
	TMP 1981.023.0039	Sacral vertebra	This study
	TMP 1982.016.0006	Tarsometatarsus	(Funston et al., 2016)
	TMP 1982.039.0004	Tarsometatarsus	(Funston et al., 2016)
	TMP 1984.163.0036	Metatarsal III	(Funston et al., 2016)
	TMP 1986.036.0186	Metatarsal III	(Funston et al., 2016)
	TMP 1988.036.0104	Metatarsal II	(Funston et al., 2016)
	TMP 1992.036.0390	Dentaries	(Longrich et al., 2013)
	TMP 1992.036.0674	Ilium	This study
	TMP 1992.040.0044	Partial dentaries	(Currie et al., 1993)
	TMP 1993.036.0630	Metatarsal III	(Funston et al., 2016)
	TMP 1994.012.0880	Tibia	(Funston et al., 2016)
	TMP 1996.005.0012	Metatarsal III	(Funston et al., 2016)
	TMP 1996.012.0141	Tarsometatarsus	(Funston et al., 2016)
	TMP 2005.049.0190	Metatarsal III	(Funston et al., 2016)
	UALVP 55585	Partial metatarsal III	(Funston et al., 2016)
	UALVP 55639	Partial dentaries	(Funston et al. in press)
	UALVP 59606	Metatarsal IV	This study
Indeterminate	TMP 1980.016.1503	Sacrum	This study
	TMP 1980.016.2095	Pubes	This study
	TMP 1981.019.0252	Parietals	(Currie 1992); This study
	TMP 1981.019.0285	Sacrum	This study
	TMP 1984.163.0102	Sacrum	This study
	TMP 1994.012.0603	Pubes	This study
	TMP 1998.093.0012	Ilium	This study
	TMP 2001.012.0216	Quadrate	This study

413

4.1 INTRODUCTION

Oviraptorids were relatively small, edentulous theropod dinosaurs from the Late Cretaceous of Mongolia and China (Osmólska et al., 2004; Fig. 4.0). The first oviraptorid, named *Oviraptor philoceratops* Osborn 1924 by Osborn (1924), was recovered by the famed expeditions of Roy Chapman Andrews on behalf of the American Museum of Natural History (AMNH). Initially, the association of the holotype with a nest of eggs was interpreted as evidence of an egg-based diet in *Oviraptor.* Although it is now realized that this not the case (Norell et al., 1995; Dong and Currie, 1996), it has become popular in media portrayals of oviraptorids.

The unusual anatomy of *Oviraptor philoceratops* led to confusion about its relationship to other theropod dinosaurs, and Osborn (1924) believed it to be closely related to ornithomimids. Only with the description of new specimens by Barsbold (1976a, 1976b) and Osmólska (1976) did it become clear that oviraptorids were a separate family of edentulous coelurosaurs. The distinctive, unique bodyplans of oviraptorids led Barsbold to describe these new specimens as various species of *Oviraptor* (Barsbold, 1976a, 1981), but they have since been recognized as separate genera in a diverse family (Barsbold, 1981, 1986, 1997). This initial pulse of discovery led to widespread interest not only in oviraptorids, but also in the fossils of the Western Gobi Desert of Mongolia.

This renewed interest led the AMNH to launch a second set of expeditions in the early 1990s into the Western Gobi, focusing on the areas where Andrews had discovered Cretaceous dinosaurs. In 1993, the expedition discovered Ukhaa Tolgod, an exposure of the Djadokhta

Formation that has now produced dozens of skeletons of oviraptorids and other theropods—alongside mammals, lizards, protoceratopsians, and ankylosaurs. The well-preserved skeletons collected at Ukhaa Tolgod have since provided a wealth of information on oviraptorid anatomy, reproduction, and diversity. Most famous among these advances are the brooding *Citipati osmolskae* Clark et al. 2001, nicknamed 'Big Mama' and 'Big Auntie', preserved sitting atop their nests (Norell et al., 1995, 2018; Clark et al., 1999). *Citipati osmolskae* is now among the best known oviraptorids, represented by several specimens including a complete skeleton (Clark et al., 2002a) and an embryo within an egg (Norell et al., 1994, 2001). Another highlight of the expedition was the discovery of two associated skeletons of a new taxon, *Khaan mckennai* Clark et al. 2001 (Clark et al., 2001). These specimens are incredibly well-preserved and their anatomy has been described in detail (Balanoff and Norell, 2012a).

Beginning in the early 2000s, work by two research groups in China—led by Lü Junchang and Xu Xing—has led to the discovery of at least a dozen new oviraptorids. These new taxa reveal a radiation of oviraptorids in southern China during the latest Cretaceous, contrasting with the stable diversity of many other dinosaur groups. Oviraptorids are now among the most diverse theropod families, with more than 20 disparate genera. Unfortunately, their excellent fossil record has led to many issues with poaching and the illegal fossil market. Numerous oviraptorid skeletons have been illegally exported from Mongolia and circulated in black markets around the globe. Even some legitimately collected specimens (e.g. MPC-D 102/03) have been vandalized or stolen during preparation. Fortunately, a few of these specimens have been confiscated and returned to Mongolia, making them available for study, but in most cases they lack critical data on provenance and taphonomy. A further issue in the study of oviraptorids—and other oviraptorosaurs from Mongolia—is that the absolute ages of the

formations where they are found are unknown. Gobi sediments lack datable volcanics, and paleomagnetism studies have provided ambiguous results. On the basis of paleomagnetism, Dashzeveg et al. (2005) proposed a Campanian age for the Djadokhta Formation, and therefore overlying formations like the Baruungoyot and Nemegt Formations must be younger. The presence of *Saurolophus* Brown 1912 in both the Maastrichtian Horseshoe Canyon Formation of Alberta and the Nemegt Formation in Mongolia has led most authors to regard the latter as Maastrichtian in age (Averianov and Sues 2012; Eberth 2018). However, patchy outcrop makes correlation of individual localities challenging, so a comprehensive stratigraphic framework including all western Gobi sites still eludes us.

Thus, numerous problems still remain in the study of oviraptorids. One of the most challenging issues is that many of the seminal papers describing new oviraptorids are in Russian, and therefore difficult to access and reference by non-Russian researchers. Even when translated versions are available, the distinctiveness of oviraptorids led to poor descriptions, because there were few meaningful characters to compare to other theropod taxa. With our increased understanding of oviraptorid anatomy and how it varies, it is critical that the descriptions of historic specimens are updated. This is particularly important for evaluating species richness, as some studies have suggested that oviraptorids suffer from taxonomic inflation and that some of these taxa could be ontogenetic morphs (Lü et al. 2016). However, even with relatively complete growth series for several taxa (e.g. *Citipati osmolskae*, *Heyuannia huangi* Lü 2002), no study has yet examined ontogenetic change in oviraptorids. In this chapter, I test the hypothesis that oviraptorid species richness is overestimated by redescribing historic specimens and documenting newly discovered material. Using this data, I summarize the changes to the skeleton throughout ontogeny with the aim of evaluating whether ontogenetic change can

account for suspected taxonomic variation. Finally, using a growth series of a new taxon of oviraptorids, I assess whether oviraptorid growth styles were similar to those of other oviraptorosaurs. Together, these analyses improve our understanding of the anatomy, diversity, and ontogeny of oviraptorids in the Western Gobi Desert of Mongolia.

4.2 MATERIALS AND METHODS

Late Cretaceous oviraptorid material in the collections of the Institute of Paleontology and Geology, Mongolian Academy of Sciences, Ulaanbaatar (MPC-D) and the Central Museum of Mongolian Dinosaurs (CMMD) was examined firsthand. Some additional mechanical preparation of the left manus of MPC-D 102/110.a was undertaken using a pin vise and stabilised with Vinac or Paleobond Pre-Prep Consolidant. The material was measured using digital calipers to an accuracy of 0.5 mm or a fabric measuring tape to an accuracy of 1 mm (Appendix 1). Photographs were taken using a Nikon D5000, a Nikon D7200, or a Nikon Coolpix AW120 using conventional photographic techniques. Three-dimensional models of some material were generated using photogrammetric reconstruction in Agisoft Photoscan Standard v. 1.4.3. Histological thin-sections were made at the Hokkaido University Museum Petrographic Thin-Section Lab, using conventional petrographic techniques. They were imaged at the MPC-D using a polarizing microscope under plane-polarized light, cross-polarized light, and cross-polarized light with a lambda filter.

The growth curve of MPC-D 102/12 was created using osteohistological sections of the femur. Circumference of the femur was calculated at each growth mark, assuming a circular

cross-section, by measuring the distance from the growth mark to the center of the circle as determined by the intersection of two lines perpendicular to a tangent of the circle. Because the external circumference of the femur could be measured directly, the ratio of this measurement to the mathematically-derived value (approximately 1.2) was used to correct all of the measurements. These corrected circumference measurements were used to estimate body mass at each growth mark using the method of Campione et al. (2014). The same body mass estimation method was used to estimate the body masses of MPC-D 102/11 and MPC-D 102/110 based on the external circumference of the femur.

4.3 RESULTS

4.3.1 *Conchoraptor gracilis* Barsbold 1986

Dinosauria Owen, 1842

Saurischia Seeley, 1888

Theropoda Marsh, 1881

Coelurosauria Huene, 1914

Maniraptora Gauthier, 1986

Oviraptorosauria Barsbold, 1976

Oviraptoridae, Barsbold 1976

Conchoraptor gracilis Barsbold 1986

(Figs. 4.1–4.11)

Holotype: MPC-D 100/20, nearly complete skull.

Localities and horizons: Hermiin Tsav and Khulsan, Baruungoyot Formation (?early Maastrichtian); and Guriliin Tsav, Nemegt Formation (?Maastrichtian); Nemegt Basin, Western Gobi Desert, Mongolia.

Newly referred material: MPC-D 102/3, nearly complete skeleton lacking anterior portion of the skull; MPC-D NatGeo.2018.036a, skull and mandible separated from flock of articulated individuals.

Etymology: *Concho-* , clam, *-raptor*, thief; *gracilis*, slender.

Revised Diagnosis: Small oviraptorid oviraptorosaur diagnosed by the following features: cranium lacking a pronounced crest; premaxilla with vertical or nearly vertical anterior margin; maxilla with large accessory antorbital fenestra*; nasals with three dorsal fenestrae per side*; postorbital extending nearly to the bottom of the orbit*; frontal with elliptical fenestra posterior to nasal contact*; parietal with low sagittal crest; enlarged first digit of manus.

Description

MPC-D 100/20:

The holotype skull (MPC-D 100/20; Fig. 4.1) is relatively complete but distorted and poorly preserved. A coat of preservative lacquer now obscures many of the contacts between bones. A number of small, matrix-infilled perforations suggest that the skull may have been burrowed by insects before fossilization. The left side is more complete than the right, which is missing much of the lower temporal and suborbital bars. The supraoccipital, basioccipital, and the paroccipital processes are missing, which exposes the matrix-filled endocranial space.

The unfused premaxillae (Fig. 4.1) each have a foramen on the lateral surface and the tomium lacks obvious denticulation, but this may be because of poor preservation. The

supranarial process curves posteriorly and tapers dorsally. The naris is bisected transversely by a thin strut of bone, which is either a septum from the nasal or a part of the supranarial process of the premaxilla. The palatal surface has a shallow anterior mound and a posterior depression. The maxilla is not well preserved on either side. On the left, a small portion of the tomial margin is preserved, as is the bony strut separating the elliptical antorbital fenestra from the large accessory antorbital fenestra. The lateral surface of the maxilla has a low ridge that joins the tomium of the premaxilla anteriorly. The tooth-like projection on the palatal surface is composed mostly of the vomer, with a small contribution from the maxilla. The fused nasals form a short anterior midline process and have small lateral descending processes. The midline process slopes anteroventrally, instead of being raised into a crest as in some other oviraptorids (e.g. *Citipati osmolskae* and *Nemegtomaia barsboldi* Lü et al. (2004)). The body of the nasal is pierced dorsally by three symmetrical perforations on each side. The body of the lacrimal has an oblong nasopharyngeal canal below the nasopharyngeal duct. The anterior process of the lacrimal is rounded, which results in a circular antorbital fenestra. The preorbital ramus of the lacrimal has a laterally directed flange that blocks the orbit in anterior view. The jugal is slender, with a tall postorbital process that forms most of the anterior border of the supratemporal fenestra. The ventral border of the jugal is straight, as in *Citipati osmolskae* and *Rinchenia mongoliensis* Barsbold 1997. The postorbital is triradiate with an anteriorly directed frontal process. The jugal process extends far ventrally, excluding the jugal from nearly the entire orbital margin of the postorbital bar. The squamosal process is flattened in cross-section, tapers posteriorly, and inserts into a groove on the squamosal. It extends posteriorly past the midpoint of the elliptical supratemporal fenestra. The squamosals form the posterodorsal corner of the rectangular infratemporal fenestra. The lateral surface of the squamosal has a curved ridge that demarcates a

muscle origin, possibly an expanded head of the *M adductor mandibularis posterior*. The quadrate has a wide, thin pterygoid wing that is limited anteriorly. As a result, the prootic and laterosphenoid are visible in lateral view. The quadratojugal foramen is large and incises the quadrate. The ventral process that contacts the pterygoid is small and narrow. The mandibular condyles are shallow, but they are mostly obscured by the articulated mandible. Only a small, rod-like part of the jugal portion of the quadratojugal is preserved.

The frontal (Fig. 4.1C) has a flat dorsal surface with a shallow transverse arch. The frontals do not separate the posterior ends of the nasals. The frontoparietal suture is entirely obscured by a combination of insect burrows, matrix, and lacquer. The postorbital process of the frontal is relatively small and does not extend medially as a ridge, in contrast with the morphology seen in *Nemegtomaia barsboldi* and *Rinchenia mongoliensis*. The orbital margin is slightly thickened and rugose. A triangular process of the frontal underlies the lacrimal along the orbital rim. The parietals are fused and have a slight sagittal crest. Posteriorly the parietals flare laterally to contact the squamosals. They are slightly arched where they would have met the supraoccipital in a transversely straight contact. The prootics are preserved with their internal surfaces exposed dorsally because of the missing exoccipitals. The foramen magnum extends between them as a semi-circular canal, and expands anteriorly into the endocranial cavity. The lateral surfaces of the prootics are poorly preserved, and the only clear features are the foramen ovalis and another, more posterodorsal foramen on the right side. The ventral parts of the laterosphenoids are not well preserved, and only a small, ridge-bearing portion of the right side is present. The dorsal sheet extends onto the parietal and is visible through the supratemporal fenestra in lateral view.

The palate (Fig. 4.1D) is relatively well preserved. The vomer is short and stout, with a club-shaped anterior end. There is a slight ventral ridge along its midline. The palatines are poorly preserved, and are represented by small portions of bone fused to the pterygoids. The ectopterygoid is dorsally hooked to meet the maxilla just ventral to the lacrimal-jugal-maxilla junction. There is a small, rugose knob on the anterior margin of the ectopterygoid, where it may have occluded with the dentary. The robust pterygoid has a ventrally flaring contact with the ectopterygoid, and a deep groove on the ventral surface. Posteriorly, where it meets the quadrate, it is thin and cylindrical.

The preserved mandible includes the surangulars, the articular regions, and part of the posterodorsal ramus of the dentary. The left surangular is the more complete, and comprises the coronoid eminence, the base of the surangular prong, and the posterior adductor fossa. The coronoid eminence is medially everted and rugose. The articular has a small lateral glenoid, a thin, flat retroarticular process, and a well-developed medial glenoid.

MPC-D NatGeo.2018.036a:

Skull

A complete skull (Figs. 4.2, 4.3) was collected from a block of at least eight articulated individuals at Guriliin Tsav in 2018 (see Chapter 5: section 5.2). Both sides of the skull are well preserved, but each is damaged around the jugal-quadratojugal contact. Furthermore, the squamosals, postorbitals, and the frontoparietal suture are damaged.

Premaxilla—The premaxillae are unfused (Fig. 4.2E), but discerning the dorsal part of the suture is difficult because it is damaged. The premaxilla is tall and transversely narrow, with a well developed tomium and two processes surrounding the naris. There are numerous foramina

on the lateral surface that indicate that the premaxillae bore a keratinous beak. There is a lateral

depression just ventral to the naris, as in *Citipati osmolskae*, but not as pronounced. The palatal

surfaces of the premaxillae are well exposed (Fig. 4.2C) and there are several foramina that

pierce this area. Towards the midline, there is a longitudinal ridge that is continuous with the

medial ridge of the maxilla, as in *Citipati osmolskae* and *Khaan mckennai*. Lateral to this, there

is a shallow groove that tapers in transverse width towards its anterior end. The tomium

protrudes far below the palate and does not appear to be denticulated (Fig. 4.2B), in contrast to

Citipati osmolskae and *Khaan mckennai*. The subnarial process extends posterodorsally and

excludes the maxilla and the lacrimal from the border of the naris. The subnarial process is much

broader anteroposteriorly than the nasal process, although the latter may have sustained some

damage during collection, as it is relatively thicker in the holotype. Dividing the nasal and

subnarial processes of the premaxilla there is a small invagination of the naris that creates a

circular fenestra. In the type skull of *Conchoraptor gracilis*, the naris appears to be divided by a

septum near this region, and this may be the corresponding feature. Like in most oviraptorosaurs,

the nasal processes of the premaxillae surround the anterior midline process of the nasal.

   Maxilla—The maxilla is much better preserved on the left side (Fig. 4.2A) than on the

right, where it is missing all but the palatal portion. The body of the maxilla has a distinct lateral

shelf that demarcates the ventral margin of the antorbital fossa. This shelf inclines

posterodorsally, reflecting the anterior downturn of the maxilla relative to the long axis of the

skull. Ventral to this shelf, near the midpoint of the maxilla, there is a deep circular depression.

There is another pneumatic cavity near the anteroventral edge of the maxilla. Ventral to this

cavity is a roughly horizontal groove that separates the lateral face of the maxilla from the palatal

surface. There are two longitudinal ridges, one medial and one lateral, on the palatal surface of

the maxilla (Fig. 4.2C). Between the lateral and medial palatal ridges, there is a deep groove with a laterally scalloped edge. The medial palatal ridge is pronounced and curves ventrally towards its posterior end, where it also flattens transversely to become a tab-like process articulating with the vomer. The lateral palatal ridge also extends posteriorly and contacts the dorsal surface of the vomer. The body of the maxilla is underlain by the palatine and it contacts the ectopterygoid posteriorly. The lateral shelf of the maxilla contacts the lacrimal and this contact is transversely wide. The dorsal part of the maxilla is hidden completely by the premaxilla on the lateral surface of the skull. The antorbital fenestra is divided by a very narrow strut of bone that extends and tapers posteroventrally. This creates two fenestra, which are each nearly circular, but the posterior one is about double the size of the anterior one.

Lacrimal—The lacrimal is better preserved on the left (Fig. 4.2A). It contacts the maxilla ventrally and the premaxilla, nasal, and frontal dorsally. It presumably also contacted the jugal ventrally, but the nature of this contact is obscured by damage on both sides. The preorbital bar is posteriorly curved, which gives the orbit a rounded anterior edge. As in other oviraptorids, the preorbital bar is transversely wide and blocks the orbit in anterior view. The body of the lacrimal has a large circular fenestra and a smaller, oblong fossa that correspond to the naropharyngeal duct and canal, respectively. At its posterodorsal end, the lacrimal wedges between the frontal and nasal, producing a Z-shaped suture in left lateral view. A small portion of the frontal underlies the lacrimal along the dorsal edge of the orbit, excluding the lacrimal from the dorsal border of the orbit.

Nasal—The nasals (Fig. 4.2D, E) are poorly preserved, especially the central portion of the posterior plate. The lateral descending processes are roughly rectangular and do not taper posteriorly. They have a broad, flat sheet of bone at their lateral edges, and several pneumatic

fenestrae more medially. The lateral edge of the nasal is bilobed, and there is a small notch

separating these convexities. The anterior edge of the lateral descending process is concave, so

that the anterolateral corners are pointed anteriorly. The posterior edge is broken but appears to

have been transversely straight, similar to other oviraptorids. The anterior midline process of the

nasal is long and narrow, posteriorly it forms a ventral ridge between the lateral descending

processes. The nasal recesses are difficult to distinguish because of breakage. Anteriorly there

are two small fenestrae on each side separated by a cross-shaped region of bone. Posterior to this,

there is at least one large lateral fossa, but whether there is a medial one as well cannot be

determined. A facet on the frontal shows the posterior extent of the nasals, indicating that the

lateral descending processes were about as wide transversely as long anteroposteriorly.

Frontal—The frontals (Fig. 4.2D) contact the nasals and lacrimal anteriorly, the

postorbital laterally, the laterosphenoid and orbitosphenoid ventrally, and the parietal posteriorly.

The interfrontal suture is difficult to discern because of breakage, but it appears to be

interfingering towards its posterior end. Anteriorly, the medial surface of each frontal is

excavated by a circular opening (Fig. 4.2D: font), divided from each other along the midline by a

small sheet of bone. This arrangement is reminiscent of the slot in the frontal of *Elmisaurus*

rarus Osmólska 1981 (Currie et al., 2016), although it is transversely wider in MPC-D

NatGeo.2018.036a. It is possible that these fenestrae contribute to the pneumatic system of the

nasal, but their position on the frontal is unusual and contrasts with those of other oviraptorids.

Reexamination of the holotype skull of *Conchoraptor gracilis* (MPC-D 100/20) shows that this

area remains covered by matrix and that these holes were previously interpreted as taphonomic

damage. The same is true of ZPAL MgD I/95, where these holes were ignored by Osmólska

(1976) and interpreted as surface damage by Kundrát and Janáček (2007). In MPC-D

NatGeo.2018.036a, the frontals do not appear to contact each other anterior to these fenestrae, and they were likely separated by a broken portion of the nasals. In any case, a large void would have remained between the anterior ends of the frontals. The frontals are slightly longer than the parietals, which divide them posteriorly in a wedge-shaped contact. The frontals are only slightly arched dorsally. Anterior to the dorsal fenestra, the medial edge of the frontal is oriented oblique to the midline and has a flat face. Lateral to this, there is a small facet for the nasal. Dorsal to the anteroposterior midpoint of the orbit and just lateral to the dorsal fenestra, there is a large foramen on the dorsal surface of the frontal. There are also some small foramina posterior to this. The orbital margin is rugose, but not deeply incised as in some other oviraptorids. The postorbital process of the frontal appears to be flush to the posterior surface of the frontal, but the frontal contributes to the supratemporal fenestra nonetheless.

Parietal—The parietals (Fig. 4.2B, D) are well preserved, especially on the right side, where they are complete but the squamosal process has been separated. They are fused without a suture, and there is no sagittal crest. Together, the parietals for a posteriorly tapering tube with a flat ventral edge and an inclined anterior edge. They are very slightly transversely constricted towards their anteroposterior midpoint, so that they are saddle shaped in dorsal view. The dorsal surface of the parietal becomes posteroventrally inclined posteriorly so that the dorsal edge of the skull has a sloped appearance in lateral view. Despite this, the occiput is vertical, unlike the anterodorsally sloped occiput of *Citipati osmolskae*. This sloped area of the parietal is divided at the midline by the supraoccipital, and the parietal flares laterally here to contact the squamosal.

Jugal—The jugal (Fig. 4.2A, B) is triradiate, composed of three rami: the suborbital ramus, postorbital ramus, and quadratojugal ramus. The jugals are both incomplete, but the right one has the full suborbital bar. This process is delicate and narrow, tapering anteriorly in lateral

view to become a transversely widened ribbon. It has a slightly lipped dorsal edge, overlapping part of the orbit. The postorbital and quadratojugal rami are much broader than the suborbital bar in lateral view, and are about equal in size and length. The postorbital ramus is tall, forming at least two thirds of the infratemporal fenestra. It extends perpendicular to the other rami, which are parallel to each other except for a slight ventral bow in the suborbital ramus. The postorbital ramus has a long, anterodorsolaterally facing facet for the postorbital, which extends two thirds the length of the orbit. The quadratojugal ramus is dorsoventrally broad and tab like in lateral view. It tapers slightly towards its posterior end and has a small ventral notch on its lateral surface, which accommodates the quadratojugal.

Postorbital—The postorbital is badly damaged on both sides. Each has the jugal process adhered to the jugal, but the squamosal processes are missing. The left side (Fig. 4.2A) preserves the frontal process, which is short and tongue-like. It is directed anterodorsally and has a blunted dorsal end. It formed most of the supratemporal fenestra, but the frontal contributed a small portion of the anterior edge. The jugal process extends two thirds the length of the orbit, and overlaps the anterolateral surface of the jugal.

Squamosal—The squamosal is badly damaged on both sides, but the left side (Fig. 4.2A) is more complete. The postorbital process curves medially and tapers anteriorly. Its lateral surface has a groove along its ventral half that deepens posteriorly. The ridge demarcating the dorsal edge of the groove extends posteriorly and curves ventrally to create a dish-like depression on the lateral surface of the squamosal, likely to accommodate mandibular adductor musculature. The cotyle and descending portion of the squamosal are too badly damaged to provide much information.

Quadratojugal—The quadratojugal from the right side was disarticulated and preserved underneath the left jugal and postorbital, which is unusual considering that it had to traverse the braincase to reach that location. The quadratojugal is composed of a tongue-like tab that extends posteroventrally and two branching processes extending anteriorly and dorsally. The anterior process, for the jugal, expands anteriorly and twists so that its lateral face becomes flat where it contacts the jugal. It bows slightly laterally. The dorsal process curves posteriorly to follow the outline of the quadrate. Its distal end is quadrangular and has medial and lateral longitudinal grooves.

Quadrate—Both quadrates (Fig. 4.2C, F) are relatively well preserved, but they seem to be slightly deformed and have shifted relative to each other. The medial mandibular condyle is larger and positioned further anteriorly. It is convex and separated from the thinner, sheetlike lateral condyle by a deep, slightly anterolaterally directed groove. The lateral surface of the quadrate has an anterodorsally inclined protrusion for the quadratojugal, like in *Nemegtomaia barsboldi* (Lü et al., 2004). However, when this is articulated with the quadratojugal, which has a corresponding depression, the contact superficially appears flat. The ascending wing of the quadrate has a lateral notch that forms the entirety of the quadratojugal foramen, and the wing curves posterodorsally. The posterior face of the condyle has two depressions on the right side. The anterior wing of the quadrate, lying lateral to the braincase, is preserved on the left but not the right side. It tapers dorsally and has a small notch in its anteroventral edge.

Pterygoid—The palate (Fig. 4.2C) is well preserved but slightly comminuted and deformed. Regardless, all of the bones are present and identifiable. The pterygoid is massive and robust. Posteriorly it lies medial to the quadrate and forms a square, faceted wing. It appears to contact the basipterygoid processes but this area is broken and deformed so this is unclear. The

pterygoid wing also contacts the parasphenoid where it laps onto its lateral surface. Anteriorly, the pterygoid becomes cylindrical near its midpoint and then platelike and transversely wide at its anterior end. The lateral edge extends ventrally, producing a cup-like, ventrally opening facet into which the ectopterygoid inserts. In lateral view, this creates the crescentic contact typical of oviraptorids. The medial part of the pterygoid extends far anteriorly and tapers, eventually overlying the vomer and its contact with the palatine. A ventromedial process underlies the palatine and supports its contact with the vomer. Thus, the pterygoid is complex and cradles the entire palate, quadrate, and braincase.

Ectopterygoid—The ectopterygoid is dorsally hooked as in other oviraptorids. It is fairly robust, and is broad both dorsoventrally and transversely at its posterior end. Its contact with the pterygoid (Fig. 4.2A, B) is onlapping, which would have allowed these bones to rotate relative to each other.

Palatine—The palatine is not well preserved but its maxillary process remains attached to the maxilla, where it curves sinuously in lateral view (Fig. 4.2A). There is a suborbital fenestra between the palatine and the ectopterygoid, as in some but not all oviraptorids. Part of the body of the palatine is present where it contacts the vomer and pterygoid, but this area does not provide much morphological information.

Vomer—The vomer is well preserved (Fig. 4.2A, C). It expands transversely at both ends and it is compressed at its midpoint. Posteriorly, there are two posteroventrally facing facets for the palatines, separated by a shallow ventral groove. This groove transitions into the sharp ventral edge of the vomer anteriorly, and extends ventrally into the maxillovomeral process at its anterior end. Dorsally, there is a cleft between the two halves of the vomer, which is fused without a suture on its ventral surface.

429

Basioccipital—The braincase is not particularly well preserved (Fig. 4.2F), but the lack of osteological description of other *Conchoraptor gracilis* braincases necessitates its description here. Only the right half of the basioccipital is preserved. The occipital condyle has small contributions from the exoccipitals, evident because these dorsolateral portions have separated taphonomically. The shape of the condyle cannot be determined, but it does project far posteriorly and has a constricted neck. The basal tubera are about equal in size to the occipital condyle and are positioned anterior to it. They are divided ventrally by a deep groove that lacked a pneumatic pit, in constrast to some oviraptorosaurs.

Basisphenoid—The basisphenoid appears to have been disarticulated and has shifted anteriorly, or the quadrate, basioccipital and exoccipital have shifted posteroventrally. Regardless, the basisphenoid would have been anterior to the basioccipital in life, rather than directly ventral to it, which is the case in some caenagnathids (Sues, 1997; Lamanna et al., 2014). The basisphenoid is visible in lateral view on the right side (Fig. 4.2B), but is not exposed ventrally or on the left. The basipterygoid processes are large and face anteroventrally about 45° from the long axis of the skull. They are slightly everted laterally and appear to be contacted directly by the pterygoids.

Exoccipital—The right exoccipital is better preserved, but lacks most of the paroccipital process, the ventral end of which is preserved on the left side (Fig. 4.2F). The exoccipital contributes a small process to the occipital condyle, lateral to which there is a posteriorly opening jugular foramen. On the internal side, there is at least one small foramen at the ventrolateral corner. It is likely that more are present, but this area is obscured. On the lateral side of the exoccipital, anterior to the paroccipital process, there are several small depressions

posterior to a large metotic fissure. The metotic fissure is open and roughly circular in lateral view.

Supraoccipital—The supraoccipital is damaged on the left side and complete but crushed on the right (Fig. 4.2F). It tapers transversely towards its anterior end, where it is also dorsoventrally thicker and has a midline ridge. Posterior to this thickened area, marking its posterior border, are two anterolaterally inclined depressions that are probably for muscular attachment. Their positions and shape give the thickened area a wedgelike outline in dorsal view. Posteriorly the supraoccipital is transversely wide, and a flat facet on its posterior edge shows that it formed a large portion of the foramen magnum.

Prootic—The right prootic is well exposed on the lateral side of the braincase (Fig. 4.4), where it lies anterior to the metotic fissure. The fenestra ovalis is tucked into a vertical pocket in the prootic just anterior to the metotic fissure. Anteroventral to this, there is a large, oval opening for CN V. Ventral to this, there are two openings, the posterior of which probably conducted CN VII, and the anterior one was probably for CN VI. A large depression separates the prootic from the laterosphenoid, but they appear to have contacted dorsally. This contact consists of two laterally lipped faces, which are separated by a wide dorsoventrally oriented gap, which may be taphonomic.

Laterosphenoid—The right laterosphenoid is well preserved and essentially complete (Fig. 4.4). The posterior edge is transversely thick and projects laterally where it contacts the prootic. Ventrally, there is a lateral depression that houses a cleft for CN III. Posterior to this is a miniscule foramen that probably conducted the deep ophthalmic nerve. Dorsally the laterosphenoid laps onto the lateral surface of the parietal. The capitate process is large and relatively robust. It extends laterally to underlie the postorbital and has a flat dorsal surface and a

groove anterior surface. The ventral surface extends as a ridge to the region that lies anterior to the opening for CN III.

Orbitosphenoid—The orbitosphenoid (Fig. 4.4) is much smaller than that of *Citipati osmolskae* (Clark et al., 2002a), and lies flush to the laterosphenoid instead of projecting ventrally into a hatchet-shaped process. Separating its ventral edge from the laterosphenoid is an opening for CN II. This opening consists of a gap between the two bones, rather than a distinct foramen. Towards the anterodorsal edge of the orbitosphenoid there is another gap between it and the laterosphenoid that probably accommodated CN IV. Cranial Nerve I would have extended anteriorly between the orbitosphenoids.

Parabasisphenoid—The parabasisphenoid (Fig. 4.4) has a long, anteroventrally directed rostrum that tapers in dorsoventral breadth towards its anterior end. There is a slight ventral protuberance at about its midpoint. The dorsal flange of the parabasisphenoid for insertion of eye retractor musculature is large, laterally concave, and square at its dorsal edge. The posterior end of the parabasisphenoid is covered by the small, narrow epipterygoid.

Epipterygoid—The epipterygoid is a small sheet of bone adhered to the lateral side of the braincase (Fig. 4.4). Its posterodorsal end is rounded and curves slightly anteriorly. The ventral edge is difficult to interpret because of breakage but appears to have been a simple, platelike sheet of bone.

Mandible

The mandibles (Fig. 4.5) are nearly complete, but the dentaries were taphonomically separated from the postdentary bones. However, these bones were disarticulated when discovered, so it is likely that the dentary-surangular contact was highly mobile and unfused.

Dentary—The dentaries (Fig. 4.5A–F) are unfused and they have shifted slightly relative to each other. The suture is wide but does not interdigitate, contrasting with those of other oviraptorids. The beak is deep, with a distinct ventral chin resulting from the downturn of the dentary relative to the long axis of the mandible. The dorsal ramus extends dorsally at an angle of about 85° from the long axis of the mandible, nearly perpendicular to the jugal when articulated. There is a small channel in the dorsal surface that accommodated an anterior extension of the surangular. The external mandibular fenestra is round anteriorly and heart-shaped posteriorly, separated by the surangular process, which is more tablike than spinous, contrasting with other oviraptorids. The lateral surface of the dentary is pierced by numerous small foramina, which are not arranged in rows but rather randomly distributed. A vertical slit on the anterolateral surface of each dentary is for the inferior alveolar nerve. Unlike caenagnathids, there is no lateral mandibular fossa, nor any obvious pneumatopores on the dentary. On the ventral surface, there are 3 small foramina that flank a small ridge (Fig. 4.5D), and together these may represent the attachment of *M. genioglossus*. The posterior side of the dentary is highly complex, with several facets and fossae (Fig. 4.5C). The most dorsal of these is the largest, and it forms a deep concavity under the dorsal ramus of the dentary anterior to the external mandibular fenestra. As a result, the ventral surface of the dorsal ramus is concave. This concavity extends anteriorly into the dentary where it produces a hollow space, similar to the condition in caenagnathids. This hollow space is exposed dorsally where there is a crack in the dentary, indicating that it extended far anteriorly. Ventral to this space, there is a facet on the medial surface of the dentary where the angular and possibly splenial inserted. Anterior to this facet and extending anterodorsally is a slit-like pocket for the Meckelian cartilage, separate from the large hollow concavity. Medial to the Meckelian groove, the posterior edge of the occlusal surface is

rounded and striated, which may reflect an attachment for tongue musculature or other symphyseal soft tissue. The occlusal surface of the dentary (Fig. 4.5E, F) is relatively large for an oviraptorid and could be described as an extended caudal shelf similar to those of caenagnathids. In this respect, it is identical to that described as autapomorphic for *Gobiraptor minutus* Lee et al. 2019 (Lee et al., 2019). There are some small foramina, but like on the lateral surface of the dentary, these appear to be randomly distributed. The occlusal surface is not highly ornamented, but there are some features that contrast with the smooth occlusal surfaces of oviraptorids and are more similar to those of caenagnathids. Most obvious is an occlusal cleft and a rudimentary lingual ridge just medial to the tomium, which generally resemble the lingual groove and ridge of caenagnathid dentaries. On the left side (Fig. 4.5F), which is better preserved, the occlusal cleft is divided into three: the anterior and posterior pockets are small, whereas the middle one is much larger (Fig. 4.5F: ocp). Anterior to this, the internal surface of the tomium is scalloped, similar to the anterior or lateral occlusal ridges of caenagnathids. These features are identical to those described in *Gobiraptor minutus* (Lee et al., 2019). While it is unlikely based on oviraptorosaur phylogeny (see Chapter 5) that these features are indeed homologous to those in caenagnathids, they probably served similar functions for food processing.

Surangular—Both surangulars and the remainders of the ASC complexes are preserved to some degree (Fig. 4.5G–J), but each is incomplete anteriorly where it would have contact the dentary. A small splint of bone underlies the coronoid process on the medial surface of the surangular (Fig. 4.5I). This was described as the remnant of the coronoid bone by Lee et al. (2019) and reexamination of MPC-D 100/20 shows that it is present in the type of *Conchoraptor gracilis* as well. The coronoid process is well pronounced but is not medially inflected. It is tab-like and rounded at its apex rather than square. The apex and the medial side of the coronoid

process are both rugose. There is no sign of a coronoid bone, either it was absent or it has fused indistinguishably to the surangular. Below the coronoid process, the surangular is thin and platelike. The dorsal edge is rounded and thickened medially, which produces a medial concavity. The surangular spine is not well preserved but was apparently tablike rather than extended into a spine. There is a small, circular surangular foramen just anterior to the articular, within the medial concavity.

Angular—The angular is relatively complete on the left (Fig. 4.5G), missing just a small portion of the anterior end. It is plate-like dorsally, where it cups the lateral side of the surangular. Ventrally it is more robust, and it extends anteriorly into a solid, grooved arm that contacted the posteroventral ramus of the dentary. This portion of the dentary is accommodated by a lateral groove, which extends just ventral to the posterior edge of the coronoid process. The angular tapers posteriorly into a rod-like splint that extends only to the base of the retroarticular process, not contributing significantly to that structure.

Prearticular—The body of the prearticular is a tall sheet of bone that lies anteroventral to the medial condyle of the mandible (Fig. 4.5I, J). Anteriorly, it tapers and extends as a thin splint of bone medial to the angular, as is the case in caenagnathids. Here, it inserts between the splenial and the angular, although most of this region is damaged. Posteriorly, the prearticular forms a thin ribbon of bone that contributes to the medial surface of the retroarticular process.

Articular—The articular forms a distinct convex ridge (Fig. 4.5G, I) and slopes posteroventrally to form the majority of the retroarticular process. The medial glenoid is the larger of the two, and it is broad and tongue-like in dorsal view. Its medial edge is flattened, forming a lens-shaped facet in medial view, rather than tapering to a crest. The articular ridge is shallow, but is offset from the dorsal edge of the surangular. Unlike in *Heyuannia yanshini*

435

Barsbold (1981), the lateral glenoid is well developed and projects laterally from the lateral surface of the mandible. In other oviraptorids, the lateral glenoid is flush with the lateral surface of the mandible.

MPC-D 102/3:

Two skeletons of *Conchoraptor gracilis* were recovered at Hermiin Tsav in 2002. One of the skeletons is nearly complete (Fig. 4.6), missing only the distal caudal vertebrae and the anterior portion of the skull. The second individual, collected in the same jacket, consists of the mid-caudal vertebrae and a foot. Unfortunately, the specimen was vandalized during preparation and the hands and feet were removed from the skeletons after they were flipped. Luckily, a cast had been made of the ventral part of the body before it was flipped, allowing these elements to be described. The more complete skeleton is preserved with its legs crouched under the body and the arms tucked in towards the torso (Fig. 4.6). The skull is anterior to the rest of the body, oriented dorsal-up rather than lying on its side. The neck is disarticulated and cervical vertebrae are in differing orientations, but it is likely that the neck was twisted on itself before preservation. The pelvic elements have been disarticulated from their natural positions, but their orientations can be explained by vertical compaction of the skeleton displacing acetabula laterally.

Skull—The skull (Fig. 4.7) is missing the preorbital bar, maxillae, premaxillae, and nasals. These elements were destroyed during pedestalling while the specimen was being excavated (P. Currie, pers. comm.). The palatal skeleton (Fig. 4.7C, D) is mostly present, but obscured by the overlying mandibles. The left side of the skull is exposed (Fig. 4.7A, B). The jugal is T-shaped and the postorbital ramus extends slightly posteriorly. It extends far dorsally,

nearly to the top of the infratemporal fenestra, but it is likely that this has been exaggerated by dorsoventral compaction of the skeleton. The ventral edge of the jugal is flat, rather than being concave. The postorbital has a longer frontal process than squamosal process, and these are each longer than the jugal process. The frontal process curves dorsally towards its anterior end, which is rounded. The frontal contributes to the supratemporal fenestra and forms most of the dorsal margin of the orbit. The superciliary lip is neither thickened nor rugose. Just anteroventral to the tip of the postorbital, the frontal is pierced by a small foramen. On the orbital surface, the frontal has a small groove posteriorly that curves parallel to the anterior margin of the supratemporal fenestra. The squamosal has a well defined, curved ridge at its posterodorsal corner that extends anteriorly and ventrally. The occipital process extends about halfway down the length of the infratemporal fenestra, even with the quadrate process. The parietal is low and appears slightly lipped above the supratemporal fenestra, although a distinct sagittal crest is absent. Posteriorly, it flares widely to contact the squamosals. The quadrate has a large optical wing, which does not appear to have a concave dorsal edge, and therefore covers most of the prootic in lateral view. The quadratojugal foramen is large and opens anteriorly. The condyles are obscured by the overlying mandible. The quadratojugal is tall and has a relatively large, tablike posteroventral process. The anterior jugal process bows laterally. The pterygoids and ectopterygoids are preserved but not well exposed. Their contact forms a distinct crescentic suture as in other oviraptorids, and their ventral edges protrude to form a slight ventral process.

Mandible—The surangular (Fig. 4.7A, B) is tall and thin, although its dorsal edge is obscured by the overlying jugal. There is a small surangular foramen posteriorly and the surangular spine was apparently small. The mandible has a flat ventral edge extending from the retroarticular process anteriorly, which contrasts with the ventrally bowed mandible of

Heyuannia yanshini. The prearticular expands transversely towards its posterior end, and forms the ventral surface of the retroarticular process, excluding the angular. The medial glenoid of the articular is large and the articular ridge is tall. The retroarticular process is short and peg-like. The ceratobranchial is dorsally bowed and rodlike, with no anterior expansion.

Vertebrae and ribs—The cervical vertebrae (Fig. 4.8) are disarticulated and oriented differently, so it is difficult to establish a total vertebral count. The anterior cervical vertebrae have lateral pleurocoels and large, deep infrapostzygapophyseal fossae. A lamina connects the neural spine, transverse process, and prezygapophysis, and it is roughly triangular, covering the anterior part of the centrum. The parapophyses are strongly deflected ventrolaterally, and appear large on the exposed ventral surfaces of the anterior cervical vertebrae (Fig. 4.8C, E). The cervical ribs are unfused and, in most cases, disarticulated from their respective vertebrae. The posterior cervical vertebrae have relatively larger lateral pleurocoels on the centra and develop infradiapophyseal fossae in addition to a small infraprezygapophyseal fossae and large infrapostzygapophyseal fossae. The neural spines remain small and knobby throughout the cervical vertebral series. The centra become taller towards the posterior part of the cervical vertebral series and develop deeper concavities on their anterior articular faces. At least one cervicodorsal vertebra is present, bearing a large hypapophysis. This vertebra has a lateral pleurocoel and a large parapophysis, but no infradiapophyseal fossa. The centra of the dorsal vertebrae are barrel shaped and have large lateral pleurocoels (Fig. 4.8A, B). The dorsal vertebrae have equally deep infraprezygapophyseal and infrapostzygapophyseal fossae, but the infradiapophyseal fossae are much smaller. However, these fossae become larger and deeper in more posterior vertebrae along the series. There are probably six sacral vertebrae, but the middle ones are obscured by the overlying ischium. The sacral ribs are wider anteroposteriorly than long

transversely (Fig. 4.8G, H), and the fifth sacral rib appears to have a foramen on its posterior side near the base. Only the anterior caudal vertebrae are preserved, and each bears a lateral pleurocoel. The caudal vertebrae become slightly more elongate posteriorly along the series, and have wide, anteriorly curving transverse processes. The anterior chevrons are long and slender, and have small anterior processes at their proximal ends that become larger in more posterior chevrons.

Dorsal ribs lack laminae between the capitulum and tuberculum (Fig. 4.8D, F), indicating that they were unlikely to be pneumatized, unlike the condition in caenagnathids. Each rib has a strong lateral ridge, and uncinate processes were present, but their number cannot be determined. The gastral basket is complete, but it has become slightly disarticulated by dorsoventral compaction. Gastralia are gracile and the right ones are anterior to the corresponding left gastralia.

Pectoral girdle and forelimb—The right side of the furcula is preserved, and it has a relatively straight ramus. The distal end is flattened dorsoventrally but not expanded transversely. The hypocleidium is relatively small. The scapula is long and straplike (Fig. 4.9A, B). The distal end is not expanded, and the acromion is laterally everted but relatively small. The partial disarticulation of the scapulae and coracoids suggests that these bones were not fused. The coracoid has a strongly curved posteroventral process and a large biceps tubercle. The anteromedial edge of the coracoid is curved and traces a nearly circular outline. The sternal plates are damaged, but each was wider transversely than long anteroposteriorly. The sternal plates were not fused to each other, and each has a well developed lateral trabecula that is transversely wider than the sternocoracoidal process.

The humerus has a well-developed medial head and a large deltopectoral crest that extends about one third of the length of the shaft (Fig. 4.9A, B). Its apex is rounded, rather than square, unlike the condition in *Heyuannia yanshini*. The distal end of the humerus lacked a prominent ectepicondyle, which also contrasts with that of *Heyuannia yanshini*. The ulna has a poorly developed olecranon and the proximal head is relatively unexpanded compared to the shaft (Fig. 4.9A–D). The shaft does not bow strongly posteriorly, but is transversely expanded distally. The proximal end of the radius is slightly expanded but generally cylindrical. The shaft is slightly curved.

The metacarpals are not well exposed along their full lengths, except for metacarpal I, which is more robust than metacarpals II and III (Fig. 4.9C–F). Its transverse width exceeds the combined width of metacarpals II and III, although it is less than half as long proximodistally as metacarpal II. Phalanx I-1 is longer than metacarpal I but comparably broad, and ungual I-2 is trenchant with a large flexor tubercle. However, it lacks a proximodorsal lip, and the proximal articular surface is flush with the proximal surface of the flexor tubercle, rather than being offset by a groove. Metacarpal II is long and slender, about a quarter the width of metacarpal I and subequal in width to metacarpal III. Phalanx II-1 is longer than phalanx II-2, and together their length is about equal to phalanx I-1. Ungual II-3 is small and straight, with a poorly developed flexor tubercle. Metacarpal III is as long as metacarpal II and its proximal end is expanded, contrasting with the condition in the Guriliin Tsav oviraptorid. Most of the third digit is obscured by the overlying first and second digits, but phalanx III-3 and ungual III-4 are visible. III-3 is longer than digit III-2, but much smaller than the phalanges of the other digits. Ungual III-4 is very small, only one third the length of ungual I-2 and half the length of ungual II-3. Like the latter, it is straight and slender, lacking a flexor tubercle.

Pelvic girdle and hindlimb—Both legs were well preserved and naturally articulated, but the entire right limb was poached during preparation. The ilium has a slightly shorter preacetabular process than postacetabular process (Fig. 4.10 A, B), contrasting with those of most oviraptorosaurs. The preacetabular blade is downturned and its posteroventral corner is square, despite the anterior edge being distinctly rounded. The downturned portion of the preacetabular blade does not extend as far ventrally as the pubic peduncle. The dorsal edge of the ilium is slightly convex, and posterior to the ischiadic peduncle it tapers to a blunt point. The pubic peduncle is level with the ischiadic peduncle and projects anteroventrally. Its anterior edge is square, but the ventral edge is inclined anterodorsally rather than parallel to the long axis of the bone. The ischiadic peduncle is triangular and slightly everted laterally. The pubes are visible only in ventral view (Fig. 4.10C, D). Each pubis is anteriorly concave, and the maximum curvature of the shaft is towards the proximal end. The pubic apron begins just ventral to the maximum curvature of the shaft and extends to about a quarter of the length of the shaft from the pubic boot. The boot is fused and has a much larger anterior process than posterior process. The ischium has an expanded proximal end and a moderately constricted neck (Fig. 4.10E, F). The obturator process is large, pointed, and situated close to the midpoint of the ischium. The dorsal edge of the ischium is distinctly concave, but not to the same degree as in caenagnathids, and the proximal and distal ends form an obtuse angle.

The femur (230 mm) is shorter than the tibia (280 mm), and the metatarsus (130 mm) is less than half the length of the tibia. When the pedal digits are included, the foot (237 mm) is just slightly longer than the femur, but still shorter than the tibia. The toes on the left side are strongly flexed, whereas those on the right side are extended (Fig. 4.11). The upper hindlimb bones are not well exposed because of the overlying feet. The femur has a well developed medial head and

a shallow depression separating it from the greater trochanter. The anterior trochanter extends just shy of the level of the greater trochanter. It is narrow and appressed to the anterior edge of the greater trochanter, from which it is separated by a groove as in all oviraptorids. The shaft of the femur is relatively straight and lacks a fourth trochanter. The lateral condyle extends further ventrally than the medial condyle and is separated from the fibular trochlea by a deep groove. The medial condyle slightly overhangs the popliteal fossa, similar to the condition in *Rinchenia mongoliensis*, but not to the same degree. The tibia has a laterally deflected cnemial crest that is restricted in proximodistal length. The fibular condyle is large and separated from the cnemial crest by a deep incisura tibialis. The fibular crest is not exposed, nor is the anterior surface of the tibia. The postfibular flange is small and rounded, rather than attenuated into a crest. The distal end of the tibia is not greatly expanded relative to the transverse width of the shaft. The fibula is broken at its midpoint, but it has a medially concave head and a low lateral crest. It does not contact the calcaneum (Fig. 4.11), and these bones are separated by a gap of several millimetres. The bones of the astragalocalcaneum are not fused to each other or the tibia. The articular surface covers only the distal end of the tibia, and does not wrap onto the posterior surface of the tibia as in some caenagnathids. The base of the ascending process has a pit excavating the middle of a shallow transverse groove. The height of the ascending process cannot be determined, but it is clear that it covered the entire transverse breadth of the tibia. The calcaneum is small and kidney-shaped, and it sits in a pocket on the astragalus, which has a small dorsolateral process extending to the lateral margin of the tarsus.

Distal tarsals III and IV are restricted to the proximal surfaces of the metatarsals, not extending onto their posterior surfaces (Fig. 4.11). Together, they cover the entire proximal surfaces of metatarsals III and IV. Distal tarsal III has a small lateral process that covers the

medial portion of metatarsal IV, rather than being restricted solely to metatarsals II and III. The metatarsals are only exposed in posterior view (Fig. 4.11). Metatarsal III is the longest and transversely widest at both ends, in stark contrast to the arctometatarsalian pedes of avimimids and caenagnathids. Metatarsal IV is longer and more robust than metatarsal II, but it lacks a lateral flange posterior to the lateral ligament pit. Metatarsal I is small and teardrop shaped, whereas metatarsal V is an anteriorly curving splint of bone. Digit III is the longest, and digits II and IV are subequal in length. The phalanges of each digit are short and broad, and they become successively shorter towards the ungual. This contrasts with the condition in caenagnathids, where the penultimate pedal phalanx is longer than the preceding one. The unguals are recurved and have small flexor tubercles. Unguals II-3 and III-4 are about equal in size, whereas ungual IV-5 is smaller and I-2 is the smallest.

Remarks

Specimens of *Conchoraptor gracilis* are abundant in the Baruungoyot beds of Hermiin Tsav and Khulsan, but had not been recovered from the Nemegt Formation until the discovery of MPC-D NatGeo.2018.036. *Conchoraptor gracilis* is paradoxical in that, despite an abundance of specimens, few of them have been described in the literature. The exceptions are two partial skulls, MPC-D 100/3006 and ZPal Mg-D I/95 (Osmólska, 1976; Kundrát, 2007; Kundrát and Janáček, 2007; Balanoff et al., 2013), but even these are only described in terms of endocranial or palatal anatomy. In addition to legitimately collected specimens, casts of several poached specimens have been circulated (e.g. UALVP 49391-2, UALVP 53348), although their provenance and identity cannot be confirmed. Barsbold (1986) described a hand for the holotype specimen (MPC-D 100/20), which was separated from the skull sometime after the latter was

mounted on the postcrania of *Heyuannia yanshini*. Accordingly, only the skull of *Conchoraptor gracilis* is well documented in the literature, and many features of the type specimen are obscured by protective lacquer.

The new specimens described here, therefore, drastically improve our knowledge of the anatomy of *Conchoraptor gracilis* (Fig. 4.12). The juvenile skull (MPC-D NatGeo.2018.036a) shows considerably more detail of the fine anatomy of the skull, especially the braincase, which is missing from MPC-D 100/20. It also reveals unusual fenestrae in the frontals, which were initially interpreted in the type specimen to be dermestid borings (Funston et al., 2018a). These fenestrae are also present in ZPAL MgD-I/95, but were not described by Osmólska (1976), nor by Kundrát and Janáček (2007). Osmólska (1976) ignored them in her reconstruction of the dorsal surface of the skull, and Kundrát and Janáček (2007) described them as 'surface irregularities'. The function of these fenestrae is currently unknown, as there is no analogue in any other theropod. Although it is possible that they are associated with respiration or olfaction, this seems unlikely based on their position, and CT scans would be necessary to establish their connection to the airway. It is possible that they are related to the extensive pneumatization of the nasals, and served a display purpose. In this case, the top of the head may have hosted a snood-like soft-tissue structure instead of an osseous crest. Further investigation and comparison to extant analogues is necessary to determine the function of these fenestrae.

MPC-D NatGeo.2018.036a and MPC-D 102/03 also have ramifications for the diversity of Nemegt Basin oviraptorids. The mandible of MPC-D NatGeo.2018.036a (Fig. 4.5) shows that same expanded symphysis and occlusal features that were recently described as a autapomorphies of a new taxon, *Gobiraptor minutus* (Lee et al., 2019). Similarly, reexamination of MPC-D 100/20 shows that all three of these specimens retain a coronoid bone. Comparison of

444

the cranial and postcranial material to that described here shows few differences, and these can be attributed to individual variation or ontogeny. The fusion of the palatine and pterygoid in MPC-D 100/20 likely progressed through ontogeny, because they are not fused in MPC-D NatGeo.2018.036a. Lee et al. (2019) suggest that *Conchoraptor gracilis* lacks a posterior process of the vomer that contacts the pterygoids, but this is untrue, and both MPC-D 100/20 and MPC-D NatGeo.2018.036a preserve this contact. The quadrate–quadratojugal contact was described as differing between MPC-D 100/20 and MPC-D 102/111 (*Gobiraptor minutus*), but this contact is poorly preserved in the former specimen and MPC-D NatGeo.2018.036a shows a condition identical to MPC-D 102/111. The pelvic girdle of MPC-D 102/03 is identical to that of MPC-D 102/111, including the shape of the ilium, which is highly variable and relatively diagnostic for oviraptorosaurs. The furrow between the lesser and greater trochanters in *Gobiraptor minutus* is likely a result of its young ontogenetic stage, as this contact becomes more extensive and fuses through ontogeny in other oviraptorids (see section 4.3.5 and 4.4). Indeed, the femora in the blocks of MPC-D NatGeo.2018.036 show less fusion between the lesser and greater trochanters than do those of MPC-D 102/03. Based on these observations and the new material described here, I consider *Gobiraptor minutus* a junior synonym of *Conchoraptor gracilis*.

4.3.2 An oviraptorid skull from Dzamyn Khondt

Oviraptoridae Barsbold 1976

Gen. et sp. nov.

(Figs. 4.13–4.15)

Holotype: MPC-D 100/79-D, partial skull, complete mandible, and atlas-axis complex.

Locality and Horizon: Djadokhta Formation, Dzamyn Khondt, Omnogov Province, Mongolia.

Diagnosis: Large oviraptorid oviraptorosaur diagnosed by the following features (autapomorphies indicated by an asterisk): Premaxillo-nasal crest (shared with *Citipati* and *Nemegtomaia*); Posterodorsally sloping premaxilla (shared with *Conchoraptor* and *Khaan*); subnarial process of premaxilla short, not overlying entire antorbital fenestra, and separated from lacrimal by maxilla*; large trapezoidal antorbital fenestra*; quadrate with large medial fossa*; anterodorsally sloped occiput (shared with *Citipati*).

Description

Skull:

The skull (Fig. 4.13) is missing the lateral portions surrounding the infratemporal fenestra, including most of the jugal, the postorbital, the squamosal, and most of the quadratojugal. The specimen has been transversely compressed and the right side has been displaced anterior to the left side. The left side is better preserved overall, although certain elements like the ectopterygoid, palatine, and basisphenoid are better viewed on the right.

Premaxilla—As in all oviraptorids (Osmólska et al., 2004a), the premaxillae are tall and dorsally bifurcated where they form the anterior margin of the naris (Fig. 4.13B). The

premaxillae are fused, but there is still a midline suture (Fig. 4.13A). The premaxilla contacts the nasals dorsally and posteriorly, and the maxilla posteroventrally. Unusually for an oviraptorid (Osmólska et al., 2004a; Funston et al., 2018a), the premaxilla does not contact the lacrimal, from which it is separated by a small portion of the maxilla. The premaxilla laterally overlies the maxilla where they contact, and it therefore forms the anterodorsal border of the antorbital fossa in lateral view. Ventral to the naris, there is a depression similar to that of *Citipati osmolskae* (Clark et al., 2002a). The subnarial process of the premaxilla meets the lateral descending portion of the nasal, separating the maxilla from the naris on the lateral surface of the skull. On the better-preserved left side (Fig. 4.13B), there is a pit at the base of the supranarial process of the premaxilla, where it contacts the anterior midline process of the fused nasals. The tomium of the premaxilla has three denticulations along its ventral edge. The tomium does not extend posteriorly past the premaxilla, unlike in *Citipati osmolskae*, where the maxilla contributes a small portion of the beak. The palatal surface of the premaxilla has a groove medial to the tomium and a ridge separating the groove from the midline. The anterior edge of the premaxilla is not vertical as in *Citipati osmolskae* (Clark et al., 2002a), *Citipati sp.* (MPC-D 100/42; Barsbold, 1983) and *Nemegtomaia barsboldi* (Lü et al., 2004; Fanti et al., 2012), and instead forms a posterodorsal slope with the nasal, similar to that of *Khaan mckennai* (Balanoff and Norell, 2012a). As a result, the snout of MPC-D 100/79-D is considerably less foreshortened than *Citipati*, and the pre- and post-orbital portions of the skull are about equal in length (Fig. 4.14).

Maxilla—The maxilla (Fig. 4.13) is large and long, and appears to be less anteriorly downturned than most other oviraptorids (Osmólska et al., 2004a; Balanoff and Norell, 2012a). The antorbital fenestra is exceptionally large for an oviraptorid and is trapezoidal in shape. The

posterodorsal corner of the antorbital fenestra is far dorsal to the ventral margin of the naris, producing an extensive overlap of the two fenestrae. This is similar to the conditions in *Banji* Xu and Han 2010, *Conchoraptor*, *Huanansaurus* Lü et al. 2015, *Wulatelong* Xu et al. 2013, and *Yulong* Lü et al. 2013 (Lü et al., 2016). Anterior to the antorbital fenestra is an accessory antorbital fenestra, which excavates the maxilla anteroventrally. Unlike in *Citipati* and *Khaan*, this accessory antorbital fenestra is considerably smaller than the true antorbital fenestra. Lateral to the accessory antorbital fenestra, on the lateral surface of the maxilla, there are three or four asymmetrical openings that communicate with the antorbital fossa. The lateral surface of the maxilla below the antorbital fossa is raised into a shallow ridge, which demarcates the edge of the oral cavity. The maxilla contacts the premaxilla and lacrimal along its dorsal edge, and the jugal, lacrimal, palatine, and ectopterygoid at the anteroventral corner of the orbit. It contacts the vomer ventromedially, and both bones protrude ventrally in this region to produce a small maxillovomeral process or 'tooth'. This process is ventral to the anterior edge of the naris, rather than posterior to the naris like in *Citipati osmolskae* (Clark et al., 2002a).

Lacrimal—The lacrimal (Fig. 4.13) forms the posterodorsal corner of the antorbital fenestra, and the anterodorsal margin of the orbit. The body of the lacrimal is triangular in lateral view, and is pierced by a large lacrimal duct. Anteroventral to this foramen is a horizontal sulcus that would have accommodated the nasopharyngeal canal. The orbital margin of the lacrimal is rounded and thickened, and its lateral surface is rugose. The preorbital ramus of the lacrimal is transversely flattened, and has a lateral flange that blocks the orbit in anterior view. The preorbital ramus is marked on its anterior surface by a pneumatic fossa. On the left side, it is simple, but on the right side it is bisected by a horizontal lamina. The lacrimal contacts the

frontal posteriorly, the nasal dorsally, the maxilla anterodorsally, and the jugal, ectopterygoid, and maxilla ventrally.

Nasal—The nasals (Fig. 4.13) are fused, and the anterior midline process is transversely flattened into a sheet-like crest. This crest is invaded by several asymmetrical openings. The lateral descending processes are also penetrated by numerous openings, but these lie within a deep anterior fossa. In life, these fossae would probably have been separated by a dorsal midline septum, but this structure has been broken. The nares are elliptical, but with a more pointed posterodorsal apex and a rounded anteroventral apex. The nasals contact the lacrimals ventrally, the frontals posteriorly, and the premaxilla anterodorsally and anteroventrally. Their anteroventral contact with the premaxillae serves to exclude the maxilla from forming the narial border, as in all oviraptorids (Osmólska et al., 2004a).

Frontal—The frontals (Fig. 4.13) are fused along the midline, and they have tapered anterior ends that separate the nasals posteriorly. The frontal is tall and has a flattened dorsal surface. The postorbital process is a low ridge, with a flattened triangular facet for the postorbital. The supraciliary rim is thickened and rugose, like orbital margin of the lacrimal. The frontal contacts the orbitosphenoid medially and the laterosphenoid posteroventrally. There is a groove between the frontal and laterosphenoid. The frontals are separated posteriorly by a triangular process from the parietals.

Parietal—The parietals (Fig. 4.13) are badly damaged and not much detail can be discerned. There is a posterodorsally inclined rugosity near the contact with the laterosphenoid and prootic. A sagittal crest is present, although its size may be overemphasized by mediolateral compression. Posteriorly, there is a small nuchal crest, and anteroventral to this there is a deep fossa, best seen on the left side. The parietal does not slope posteroventrally like it does in

Citipati osmolskae (Clark et al., 2002a), so the nuchal crest forms the posterodorsal corner of the skull.

Braincase—Because the jugals, postorbitals, and squamosals are missing, the bones forming the coossified braincase are well exposed (Fig. 4.13B, E). Except for the epipterygoid, these bones are fused to each other and the skull roof, so observing the contacts between elements is difficult. The orbitosphenoid is triangular and its anteroventral edge forms a ridge that projects into the orbit. The laterosphenoid underlies the postorbital process of the frontal and forms the medial part of the orbit. On the midline, there is an anterior process and a large lateral foramen, probably for CN II. Posterior to this, there is another fossa situated anteromedial to the contact with the epipterygoid. The epipterygoid is triangular and sheetlike. Dorsally, it is laterally everted, and has two small tubercles on its thickened edges. The posterior edge has a tab-like flange that contacts a similar projection from the prootic. Like in *Citipati*, the capitate process is transversely expanded, and forms a continuous ridge with the laterosphenoid. The prootic is well exposed and has a complexly relieved lateral surface. There is a rounded ridge where it meets the supraoccipital, and this is separated from a rounded bump by a posterodorsally inclined groove. This bump is just dorsal to the foramen ovalis, the dorsal border of which is rugose. Ventral to the foramen ovalis, there is another small foramen. Anteroventral to this, there is a deep fossa, and a horizontal groove that extends posteriorly from the fossa. The parasphenoid rostrum is broken, but the base is preserved anterior to the basisphenoid and medial to the epipterygoid. The occiput faces vertically (Fig. 4.13C), unlike the posteroventrally inclined occiput of *Citipati*. The supraoccipital is badly damaged, but appears to have contributed significantly to the dorsal margin of the foramen magnum. The exoccipitals have very small paroccipital processes, which protrude ventrolaterally. It is possible that they have been broken,

but the left paroccipital process appears mostly intact. The foramen magnum would have been circular, but it has been distorted by transverse crushing. It is much wider than the occipital condyle, which lacks a constricted neck and would have been kidney shaped. There is a foramen form CN XII on the lateral side of the basioccipital, and anterior to this there is a small fossa dorsal to the basal tubera. The basal tubera are large and, ventrally, there is a deep basisphenoid recess between them. They are positioned far anterior to the occipital condyle, rather than ventral to it. This contrasts with the conditions in *Citipati,* where they are directly ventral to the condyle, and is more similar to *Khaan* and *Incisivosaurus* Xu et al 2002 (Balanoff et al., 2009; Balanoff and Norell, 2012a). The basisphenoid has well-developed basipterygoid processes that contact the pterygoids, although there is a wide suture between them.

Palate— The palate is well preserved and all of the bones are visible (Fig. 4.13B, E, F). The vomers are completely fused into a straplike rod that is taller than wide. It is relatively long, and demarcates a similarly long choana. Posteriorly it contacts the palatines in dorsoventrally sinuous sutures. Anteriorly it contacts the maxilla, where it contributes to the maxillovomeral process. The ectopterygoid curves anterodorsally to contact the lacrimal, jugal, and maxilla. The anterior and posterior ends are expanded dorsoventrally, but the middle portion of the shaft is thin and cylindrical. Whereas in other oviraptorids, the posterior contact with the pterygoid is crescentic, in MPC-D 100/79-D this contact is sinuous. Dorsally, it is convex anteriorly, but ventrally it is convex posteriorly. The palatine is mostly missing, despite excellent preservation of the rest of the palate. A small portion is preserved on the right-hand side, where it lies medial to the ectopterygoid. The pterygoids are relatively long and robust, but they are not as wide posteriorly as those of *Citipati*. The lateral edge protrudes ventrally where it meets the

451

ectopterygoid, to produce a distinct palatal ridge. The pterygoid contacts the ectopterygoid and palatine anteriorly, the basisphenoid and quadrate posteriorly, and the epipterygoid dorsally.

Mandible:

The mandible (Fig. 4.15) is nearly complete, except that it is missing small parts of the retroarticular processes and the left surangular prong. The retroarticular process is slender and taller dorsoventrally than wide mediolaterally. The medial side has a ridge extending posterior to the medial glenoid that becomes rugose posteriorly.

Dentary—The dentary (Fig. 4.15) has a short, sharply upturned beak, and rises steeply to the coronoid process. There is a distinct notch on the tomial margin that probably occluded against the posterior denticulation of the premaxilla. The dentary itself has one lateral denticulation and one midline denticulation, which appear to oppose those of the premaxilla. The dentaries are fused, but there is a small suture on the external surface. The lateral surface of the dentary is pierced by numerous foramina, which are denser ventrally. The internal surface of the dentary is simple (Fig. 4.15C), and is marked only by the Meckelian groove and a faint ridge dorsal to this groove. On the tomial surface there is a small tubercle on the midline. On the right side, the Meckelian groove is more deeply excavated, and there is a small posteroventral flange overlying it ventrally. This flange is in contact with the floor of the Meckelian groove on the left side, but this may be an artifact of preparation. The dorsal ramus of the dentary is tall and straplike, with a ventral ridge demarcating the Meckelian groove. There is a clear inflection point that roughly corresponds to the start of the lateral ridge on the maxilla. Posterior to this inflection, the dorsal edge of the dentary thickens, and the dentary extends more or less horizontally to the coronoid. The delicate ventral ramus of the dentary is not well preserved, so I

is difficult to determine how far the dentary extended posteriorly. The ventral ramus lies lateral to the angular and splenial. Its ventral surface is curved dorsally, producing a distinct 'chin' anteriorly. Its dorsal surface forms the ventral edge of the external mandibular fenestra, and is widely curved, making a circular outline instead of the more pointed one of *Khaan*, and closer in shape to *Citipati*, but relatively larger.

Splenial—The splenial is not well preserved, but what is preserved is a small, anteriorly expanding sheet of bone. Its position in MPC-D 100/79-D and other oviraptorids suggests that the anterior expansion of the 'prearticular' in caenagnathids is in fact a dorsally expanded splenial that is fused posteriorly to the prearticular. The posterior end of the splenial extends to the midpoint of the mandible, and meets the prearticular dorsally and the angular ventrally.

Surangular—The surangular (Fig. 4.15A, B) appears to be fused to the dentary, although on the left side there is a small suture between the two bones. There is no evidence for a separate coronoid bone, but this region is not well preserved on either side. The coronoid eminence is well developed and medially inset (Fig. 4.15C). At its apex, there is a small lateral ridge that is rugose. The dorsal edge of the surangular posterior to the coronoid eminence is thickened medially and overhangs the medial surface of the rest of the surangular. The body of the surangular is tall anteriorly and tapers posteriorly. Posterior to the external mandibular fenestra, the surangular is a thin sheet, and its medial surface is depressed relative to its own dorsal edge, the angular, and the prearticular. The surangular prong tapers anteriorly to a sharp point and extends about halfway the length of the external mandibular fenestra. Posteriorly, there is a deep depression on the lateral surface of the surangular. The surangular is fused to the angular, articular, and coronoid—if it is present—but is divided from the prearticular by a suture.

Angular—The angular (Fig. 4.15A) tapers anteriorly; it has a flat medial surface for the splenial and a lateral groove for the dentary. Dorsally, it has a posterior groove into which the prearticular inserts but does not fuse. Posteriorly, the angular tapers transversely where it forms the lateral half of the retroarticular process.

Prearticular—The prearticular tapers transversely anteriorly and expands dorsally to form the medial half of the retroarticular process and the base of the medial glenoid.

Articular—The articular has a low, laterally deflected articular ridge, a well-developed medial glenoid, and a small lateral glenoid. The articular surface slopes posteroventrally, and is confluent with the retroarticular process.

Vertebrae:

Atlas—The atlas (Fig. 4.13C) is preserved in articulation with the axis and occipital condyle. Together, the portions of the atlas form an unclosed ring of bone. The centrum is featureless besides a foramen on the ventral surface. Where the neural arches articulate, there are two rugose knobs, one on either side. These tuberosities pinch the odontoid process of the axis and overlie articular fingers on the centrum of the axis.

Axis—The axis (Fig. 4.13C) is incomplete posteriorly. It has a triangular and dorsally flattened odontoid process. Ventrolateral to the odontoid there is an articular finger on the centrum that extends to contact the atlas.

Remarks

The Dzamyn Khondt locality (=Dzamin Khondt; =Zamyn Khondt) has produced excellent theropod material, despite its small size (approximately 0.36 km^2). In addition to the

more famous Dzamyn Khondt oviraptorid (MPC-D 100/42), which is a relatively complete skeleton usually allied with *Citipati*, the type of *Gobivenator* Tsuihiji et al. 2014 was also found at the site. In comparison, MPC-D 100/79-D is less complete but also excellently preserved. Despite these excellent discoveries, the site is generally understudied and its remote location makes it difficult to correlate to other localities. It is generally accepted as an exposure of the Djadokhta Formation (Jerzykiewicz and Russell, 1991), although whether it can be considered contemporaneous to other Djadokhta Formation localities is unknown (Makovicky, 2008). Indeed, the disparity between the theropod fossils from Dzamyn Khondt and those of other Djadokhta Formation localities suggests that it represents either a separate environment or a separate stratigraphic interval.

The morphology of the skull of MPC-D 100/79-D differs considerably from MPC-D 100/42 and other oviraptorids in the elongated snout with a broad premaxilla and a long, shallowly inclined maxilla. In other oviraptorids, the maxilla is steeply inclined, which results in a characteristically arched buccal margin. Although this is still the case in MPC-D 100/79-D, the curvature of this arch is significantly less than other forms like *Citipati osmolskae* or *Nemegtomaia barsboldi*. Unlike other oviraptorids, the preorbital portion of the skull is significantly longer anteroposteriorly than the postorbital portion, and the orbit is therefore positioned far posteriorly, rather than close to the midpoint of the skull. The mandible is also unusual in its exceptionally deep and robust dentary. This is accompanied by a deeply depressed adductor fossa on the lateral surface of the surangular, and together these features suggest a powerful crushing bite.

4.3.3 *Heyuannia yanshini* (Barsbold 1981)

Heyuannia yanshini (Barsbold 1981), nov. comb.

(Fig. 4.16)

Holotype

MPC-D 100/30; partial skeleton including mandible, cervical, sacral, and caudal vertebrae, pectoral girdle, partial arms and hands, tibiae, and metatarsus; Baruungoyot Formation, Hermiin Tsav, Mongolia.

Referred material

MPC-D 100/31, partial skeleton; MPC-D 100/32, partial skeleton.

Etymology: *Heyuan*, Heyuan Province in China, where the type species was found; *yanshini*, named in honour of A.L. Yanshin.

Revised diagnosis: Small oviraptorid oviraptorosaur diagnosed by the following features: low ridge on medial side of surangular*; angular contributing to retroarticular process; fused axis intercentrum; relatively large epipophyses on anterior cervical vertebrae; accessory foramen anteroventral to lateral pleurocoel of posterior cervical vertebrae; eight sacral vertebrae* (shared with *Nemegtomaia barsboldi*); 30 caudal vertebrae with hatchet-shaped transverse processes; chevrons with distal bulb*; unfused scapulacoracoid with unexpanded posterior blade, laterally-facing glenoid, and small biceps tubercle; humerus with large deltopectoral crest occupying nearly half of humeral length and large ectepicondyle; ulna with large lateral distal process*; metacarpal I short (two-thirds length of metacarpus) and broad; metacarpal II and III subequal in length; ungual I-2 longer than metacarpal I*; fibula contacting calcaneum; metatarsal I spade-shaped; metatarsal II longer than metatarsal IV.

Description

The holotype material (MPC-D 100/30) of *Heyuannia yanshini* is displayed in a mount at the Institute of Paleontology and Geology in Ulaanbaatar, Mongolia. To fill in gaps in the holotype material, the mount also includes material from MPC-D 100/31 and MPC-D 100/32, and is mounted with the holotype skull of *Conchoraptor gracilis* (Fig. 4.16). Taken together, as is often the case (e.g. Easter 2013), the mount is misleading in terms of skeletal representation and proportions of the type material. The following description includes only the holotype, to avoid further confusion.

MPC-D 100/30:

The holotype of *Heyuannia yanshini* (Fig. 4.16) includes a partial mandible, nine cervical vertebrae, some of the dorsal ribs, all eight sacral vertebrae, 30 caudal vertebrae, 12 chevrons, a complete pectoral girdle including fused sternal plates, left and right humeri, left and right ulnae, a right manus missing phalanx I-1, left and right tibiae, left and right fibulae, and the left metatarsus. Barsbold (1983, fig. 9) figures a partial skull he refers to as MPC-D 100/30, which appears to include a basioccipital, laterosphenoid, orbitosphenoid, partial parietals, possibly a lacrimal, and some other indeterminate bones. Osmólska (2004) further describes the partial parietals, but refers to them as MPC-D 100/31. Regardless of which specimen these elements belonged to, they have now been lost, and so cannot inform us further than the existing figures.

Mandible—The left mandible (Fig. 4.16A) is missing the dentary and the anterior part of the splenial as well as the delicate surangular spine. The coronoid eminence is large, medially inset, and rugose distally. It is thickened dorsally, so that it is more knoblike than tab-like. The surangular is convex laterally and its dorsal margin is thickened along its whole length. There is a low ridge running diagonally from the posteroventral corner of the external mandibular

fenestra towards the dorsal margin of the surangular on the medial side of the mandible. At the posterior end of this ridge there is a shallow circular depression. The lateral surface of the surangular has a deep posterior depression that surrounds the surangular foramen. The splenial extends far posteriorly, separating the angular and prearticular just anterior to the articular condyle. The angular is relatively thick posteriorly and forms the lateral half of the retroarticular process. It forms the posteroventral surface of the mandible with the prearticular, which tapers anteriorly and forms the base of the medial articular glenoid. The articular has a low ridge, which is barely offset from the medial and lateral glenoids. The medial glenoid is large and tongue-like, and the lateral glenoid is a small wedge flush with the lateral surface of the mandible.

Axial skeleton—The atlas (Fig. 4.16) is a dorsally-open ring of bone with a kidney-shaped facet for the occipital condyle on the anterior surface of the intercentrum. There is a small lateral tubercle just ventral to the fused contact with the wing-like neural arch. The axis intercentrum is fused to the cylindrical odontoid process and has a pleurocoel. Each of the preserved postaxial cervical vertebrae has lateral pleurocoels, and all have inclined articular surfaces that become more vertical posteriorly along the cervical vertebral series. The first postaxial cervical vertebra (C3) has a wide, flat centrum, and large, rugose epipophyses. C4 has fused cervical ribs, which are otherwise missing on all vertebrae except C9, its centrum is procoelous, unlike the other vertebrae, and the neural arch is low. Towards the posterior end of the neck, the vertebrae become relatively taller and the epipophyses become less pronounced. Posterior to C5, there is a small accessory pneumatic foramen anteroventral to the lateral pleurocoel on each vertebra. Starting at C7, the posterior cervical vertebrae have infraprezygapophyseal and infrapostzygapophyseal fossae, which become deeper along the series. There are eight sacral vertebrae (labeled MPC-D 100/30), which appear to be fused with

the ilia (labeled MPC-D 100/31). It is possible that these elements were artificially connected during the creation of the mount, or that the labels are incorrect. The first sacral vertebra is ventrally keeled, and sacral vertebrae 4-6 have a ventral longitudinal groove. The anterior five sacral vertebrae have pleurocoels, and the transverse processes of the sacral vertebrae descend from the first to sixth vertebrae, concomitant with the decreasing height of the centra. The posterior three sacral vertebrae do not have lateral pleurocoels, which suggests they are apneumatic. This may reflect separate developmental origins for pneumatic invasion of the sacral and caudal vertebrae. The last two vertebrae are taller, but their transverse processes are broken. There are 30 caudal vertebrae, and 12 chevrons. The first 11 vertebrae have pleurocoels, and all but the five distal caudal vertebrae have caudal ribs. The caudal ribs of the mid-caudal vertebrae each have a distal bulb, which becomes successively more emphasized until the caudal ribs of the distal caudal vertebrae are hatchet-shaped. The final caudal vertebrae are small and tapered, but are not fused into a pygostyle. The chevrons are elongate and do not become platelike posteriorly, as they do in *Citipati osmolskae* and *Rinchenia mongoliensis*.

Forelimb—The scapular blade (Fig. 4.16) is long and narrow, without a posterior expansion. The scapulacoracoid is not fused, and has a laterally-deflected acromion process for the furcula. The glenoid is strongly excavated and faces laterally. The coracoid has a relatively straight posteroventral process and a small coracoid tubercle. The furcula is U-shaped and there is a robust hypocleidium. Its epicleidal ends are flattened where they insert onto the acromion processes. The sternal plates of MPC-D 100/30 are fused and do not diverge posteriorly. The coracoid sulcus is a wide shelf and a ventral lip projects anterolaterally from the ventral sternal surface to embrace the coracoid. The sternocoracoidal process and the posterolateral process are relatively close, separated by a semicircular notch. The humerus (Fig. 4.16G; 141 mm) has a

wide articular surface with a modestly developed medial margin of the head. The deltopectoral crest is exceptionally large and extends almost halfway down the shaft, creating a rectangular outline for the humerus in medial view. The edge of the deltopectoral crest is thickened and its apex is pointed. The distal condyles of the humerus are transversely widened, with an anteriorly deflected ectepicondylar tuber. The ulna (116 mm) has a well-developed coronoid process and a modestly developed olecranon process, which bound a saddle-shaped proximal articulation. The distal end of the ulna has a large, curved lateral process that is absent in most other oviraptorids. The right metacarpus, radiale, and semilunate carpal are rugose and coossified (Fig. 4.16E). Metacarpal I is short and broad—63% of the length of metacarpal II, but 150% of the diameter. Metacarpal III (46.5 mm) is slightly shorter than metacarpal II (50.3 mm). Phalanx I-1 is not preserved in the holotype, so the length of digit 1 cannot be determined. Ungual I-2 (49.2 mm) is larger than metacarpal I (31.6 mm), and is larger than the combined lengths of II-1 (21.3 mm) and II-2 (19.8 mm). Digit II is complete, except for the tip of II-3, and is approximately 67 mm long. Digit III is missing the final two phalanges.

Hindlimb—The tibia (Fig. 4.16H) has a laterally deflected cnemial crest, which is hooked ventrally at its distal apex. The shaft of the tibia has a flattened anterior face is semicircular in cross section. The fibular crest is poorly developed. The distal end of the tibia has a large, rugose post-fibular flange (*sensu* Funston et al. 2016). The fibula has a posterodorsally expanded, medially concave proximal head. The astragalocalcaneum is fused with no sign of a suture, and the ascending process is relatively short. The fibula contacts the calcaneum, which is laterally concave. The base of the ascending process has a shallow median depression and a shelf-like ridge that outlines the transverse groove. The third distal tarsal is roughly circular and flat. Metatarsal I is small and triangular, with a constricted proximal neck that results in a spade-

like outline. Metatarsal II is longer than metatarsal IV, but shorter than the non-arctometatarsalian metatarsal III. The plantar surface of the metatarsus is slightly concave, and this is exaggerated by a shallow posteromedial ridge on metatarsal II. The distal condyle of metatarsal IV has a well-developed posterolateral flange.

Remarks

Barsbold (1981) originally described this oviraptorid as *"Ingenia" yanshini*, but the genus was preoccupied by a nematode. Despite recognition of the taxonomic issue, it was not resolved until Easter (2013) coined "*Ajancingenia"* Easter 2013. There are, however, several ethical problems with the study of Easter (2013), including the plagiarism of text and a figure. Hence, despite the validity of '*Ajancingenia'* under the ICZN, we propose synonymizing *Ajancingenia* and *Heyuannia* to avoid an ethical dilemma. This synonymy is supported by recent oviraptorosaur phylogenies (Lamanna et al., 2014; Funston and Currie, 2016; Lü et al., 2016), which find *"Ingenia" yanshini* and *Heyuannia huangi* as sister taxa. Although the holotype material has often been described as a nearly complete postcranial skeleton, the mounted skeleton to which most authors refer (Osmólska et al., 2004) is in fact a chimera of four specimens (Fig. 4.16). Gaps in the holotype material were filled by the radii, left metacarpus, complete pelvis, femora, right metatarsus, and toes of MPC-D 100/31, and by the manual digits of MPC-D 100/32. In addition, the skeleton is mounted with a skull, MPC-D 100/20 (labeled MPC-D 100/80-1), which is the holotype of *Conchoraptor gracilis*. Based on the anatomy of the holotype as described here, it is unlikely that the paratype MPC-D 100/33 is in fact referable to *Heyuannia yanshini*. MPC-D 100/33 has six sacral vertebrae, lacks extensive contact between the fibula and calcaneum, and has unfused sternal plates. It also differs in the proportions of the

461

metacarpals, as its third metacarpal is greatly reduced compared to MPC-D 100/30, MPC-D

100/31, and MPC-D 100/32. In these qualities, it is similar to the unnamed Guriliin Tsav

oviraptorid. Indeed, MPC-D 100/33 is from Bugiin Tsav, distant in both geography and

stratigraphy from Hermiin Tsav, where the other specimens of *Heyuannia yanshini* were found.

4.3.4 *Rinchenia mongoliensis* Barsbold 1997

Rinchenia mongoliensis Barsbold 1997

(Figs. 4.17–4.24)

Holotype: MPC-D 100/32-A, nearly complete skeleton including skull; mandible; complete vertebral series except distalmost caudal vertebrae; gastralia; scapulae; right coracoid; right humerus; right ulna and radius; right ilium; proximal pubis and ischium; right femur and partial left femur; right tibia and partial fibula; partial right pes.

Locality and Horizon: MPC-D 100/32-A was collected in 1984 from the Nemegt Formation of Altan Ula II, Omnogovi, Mongolia. The Nemegt Formation is typically interpreted as earliest Maastrichtian (Averianov and Sues, 2012).

Etymology: *Rinchen*, in honour of Byambyn Rinchen, Mongolian linguist and father of Barsbold Rinchen; *mongoliensis*, from Mongolia.

Revised Diagnosis: Oviraptorid oviraptorosaur diagnosed by the following features (autapomorphies marked by an asterisk): tall, domed cranial crest composed primarily of nasals*; frontal taller than anteroposteriorly long* (shared with unnamed Guriliin Tsav oviraptorid); postorbital with vertical frontal process parallel to jugal process* (shared with unnamed Guriliin Tsav oviraptorid); interfingering jugal-quadratojugal contact*; ventral ramus of dentary extending posterior to external mandibular fenestra* (shared with *Citipati osmolskae*); angular not con- tributing to retroarticular process* (shared with *Citipati osmolskae*); rounded hypapophyses on anterior dorsals; six sacral vertebrae; plate-like distal chevrons; unfused scapulocoracoid with straight posteroventral process of coracoid; deltopectoral crest of humerus ventrally tapering; ilium anterodorsally expanded*; preacetabular process of ilium ventrally

hooked and pointed; tall but anteroposteriorly restricted brevis fossa; low syntrochanteric crest (fused lesser and greater trochanters) of femur (shared with unnamed Guriliin Tsav oviraptorid); popliteal fossa of femur overhung by medial distal condyle*.

Description

The skeleton is nearly complete, missing the manus, most of the pubes and ischia, parts of the hindlimbs, and the distalmost caudal vertebrae. The skull is well preserved on the right side, but on the left side the delicate nature of the bone has necessitated incomplete preparation of the crest and internal parts of the skull. The postcranial bones are generally well preserved, but are comminuted, which may have slightly changed their proportions.

Skull:

Premaxilla—The premaxillae (Fig. 4.17) are unfused, unlike some oviraptorids (Clark et al., 2002a), and have a nearly vertical anterior surface that slopes posterodorsally, similar to *Citipati osmolskae*. The premaxilla has a tall anterior nasal process and a wider, posteriorly tapering subnarial process. The nasal process is long, slender and tapers dorsally. It extends dorsally above the top of the naris, and lies anterior to the relatively short anterior midline process of the nasal. The lateral surface of the nasal process of the premaxilla bears a ridge that anteriorly bounds a grooved facet, which probably received the nasal. The subnarial process tapers as it extends posterodorsally, separating the nasal and lacrimal anteriorly, and preventing the maxilla from contacting the nasal, as in all other oviraptorids. Ventral to the naris, at the

junction of the nasal and subnarial processes, there is a lateral depression on the premaxilla, similar to *Citipati osmolskae* but without an accessory opening (Clark et al. 2002). Ventral and slightly posterior to this depression there is a posteriorly opening foramen, probably for innervation or vascularization of the premaxillary beak. The tomial margin of the premaxilla has a single midline denticulation, and at least one lateral denticulation preserved on the left side. The maxillae separate the small palatal portions of the premaxillae, resulting in a U-shaped premaxillary contribution to the palate in ventral view. The palatal portion of the premaxilla does not contribute to the maxillary ridges, as opposed to the condition in *Citipati osmolskae* (Clark et al. 2002) and *Khaan mckennai* (Balanoff and Norell 2012).

Maxilla—The maxilla (Fig. 4.17) is damaged so the shape and relative sizes of the antorbital fenestra and maxillary fenestra cannot be seen. The lateral ridge that forms the buccal margin of the maxilla is broken anteriorly, but is well developed posteriorly, forming a shelf separating the facial and palatal parts of the maxilla. Posteriorly, this shelf is dorsally upturned, and covers the ventral margin of the antorbital fenestra in lateral view. On the anterior part of the buccal portion of the maxilla, there is a shallow ridge, dorsolateral to the palatal ridge, bordered on each side by a groove. This ridge ends posteriorly in a small tubercle, which would have acted as a second, lateral maxillary 'tooth'. Ventral to the maxillary fenestra, there is a lateral hump on the maxilla, most pronounced anteriorly where it meets the premaxilla. The palatal surface of the maxilla has a tall, blunt, longitudinal ridge with a pronounced tubercle where it meets the vomer, forming the distinctive maxillovomeral process present in all oviraptorids.

Lacrimal—The body of the lacrimal (Fig. 4.17) has a large lacrimal duct, but in place of the horizontal groove typical of oviraptorids, there is an anteriorly-facing pocket. The preorbital bar of the lacrimal does not have any of the anterior openings seen in *Citipati*, but it is laterally

flared to block the orbit in anterior view. The lacrimal abuts against the frontal in a simple contact, unlike the tongue-and-groove contact of *Citipati osmolskae*, where a finger of the frontal underlies the lacrimal on the orbital margin. The lacrimal, with the frontal, forms a supraorbital shelf that underlies the base of the nasal crest. This shelf extends posterodorsally along the contact of the frontal and nasal, creating a distinct transition between the wide circumorbital skull and the narrower nasal crest.

Nasal—The nasal (Figs. 4.17, 4.18) is by far the largest bone of the skull, almost equal in size to the circumorbital and circumotic parts of the skull combined. Its great size, however, comes only from the lateral descending processes, which have been hypertrophied into a honeycomb-like, dorsally rounded, robust crest. The midline process of the nasal is not enlarged relative to the rest of the skull, and contacts the premaxilla around a normally sized subcircular naris, about equal in size to the antorbital fenestra. The height of the crest is formed mostly by the convexity of the dorsal surface of the nasal, which is not lipped and therefore does not encompass a lateral depression. Directly dorsal to the lacrimal there is a large ovoid cavity that accompanies dozens of smaller pneumatic openings. The hypertrophication of the lateral descending process results in a reorientation of the nasal. The anterior midline bar is vertical, rather than subhorizontal as in all other oviraptorids. The lateral descending process of the nasal has a posteroventrally convex, curved contact with the frontal, rather than the usual dorsoventral contact of other oviraptorids. The result is that the nasal appears to have rotated 90° anteroventrally from its normal orientation.

Frontal—The frontal (Fig. 4.17) is much taller dorsoventrally than long anteroposteriorly and is inclined posterodorsally from the orbit. The anterior margin of the frontal is concave, to accommodate the large nasal. The postorbital process is directed slightly posteriorly, and is

situated at roughly the midpoint of the frontal. The postorbital process continues dorsally as a lateral ridge that extends to the dorsal edge of the frontal, dividing it into orbital and supratemporal portions. The orbital margin of the frontal is relatively flat and horizontal, rather than strongly concave as in *Citpati osmolskae*. The orbital rim is rounded and slightly rugose, but it is not lipped nor laterally everted. The frontal contributes to at least half of the supratemporal fenestra, above which it seems to bear a circular depression, though this may be an artifact of crushing.

Parietal—The parietal (Fig. 4.17) has a large sagittal crest that becomes taller anteriorly and forms the posterior part of the cranial crest. The dorsal edge of the sagittal crest is transversely expanded and diverges posteriorly into a strong nuchal crest. The parietal is otherwise too badly crushed to see any details.

Postorbital—The postorbital (Fig. 4.17) is distinctive, with a vertical frontal process subparallel to the jugal process. The reorientation of the frontal process gives the postorbital a sinuous anterior margin, as opposed to the concave margins of other oviraptorids. The frontal process is about as long as the jugal process, and both are longer than the short and squat squamosal process. It is likely that the vertical orientation of the frontal process is tied to the development of the lateral ridge of the frontal. These features may be linked to either dorsal expansion of the adductor musculature, the development of the cranial crest, or both. The position of the postorbital in MPC-D 100/32-A is reconstructed improperly, with the postorbital medial to the jugal, but facets on both elements indicate that the postorbital would indeed lie lateral to the jugal, as in all other oviraptorids.

Jugal—The jugal (Fig. 4.17) is triradiate and has a small body where the three processes meet perpendicularly. The postorbital process is expanded slightly anteroposteriorly, and the

lateral facet for the postorbital extends just less than one-third of the way up the orbit. The maxillary process is long, and expands transversely anteriorly. At its anterior end, it curves ventrally slightly. The quadratojugal process is long and slender, extending about three-quarters of the length of the trapezoidal infratemporal fenestra. The quadratojugal process is unique amongst oviraptorosaurs in that it bifurcates dorsoventrally to interfinger with the quadratojugal, which is also bifurcated. This feature is similar to the bifurcated posterior end of the jugal of *Anzu wyliei* Lamanna et al 2014, but in *Rinchenia mongoliensis* the bifurcation is not accompanied by dorsoventral expansion of the jugal. Rather, in *Rinchenia mongoliensis*, the jugal continues to taper posteriorly as it divides.

Quadratojugal—The quadratojugal (Fig. 4.17) has a short jugal process that bifurcates laterally to interlock with the jugal. It extends only half the length of the infratemporal fenestra. The body of the quadratojugal has not fused to the quadrate, and is pointed ventrally, instead of rounded or squared off, as in most other oviraptorids. The posteroventral apex of the quadratojugal is not rugose. The squamosal process of the quadratojugal is broken, but seems to have been short, as there is a triangular facet on the squamosal that probably would have received the squamosal process. Because of the transverse crushing of the skull, the quadratojugal has collapsed into the quadratojugal foramen, which would have been a relatively tall, vertical ellipse.

Quadrate—The quadrate (Fig. 4.17) has a large, anterodorsally concave optic wing that curves ventrally from the squamosal to the epipterygoid, exposing the prootic in lateral view. The mandibular condyles of the quadrate are shallow, not extending ventrally beyond the pterygoids or the maxillovomeral process. On the medial side of the optic wing, dorsal to the

condyles, there is a small pocket, which is also present in *Citipati osmolskae*, and both Dzamyn Khondt oviraptorids.

Squamosal—The squamosal (Fig. 4.17) has a small adductor ridge that is poorly pronounced at the corner of the infratemporal fenestra, where the squamosal meets the parietal. This ridge expands anteriorly along the length of the postorbital process, and splits to surround the postorbital. The contact between the squamosal and parietal is wide. The occipital process of MPC-D 100/32-A has been broken, but early photographs show that it was long.

Braincase—The occiput (Fig. 4.17C) is either missing or crushed, and no good information can be discerned. The prootic is broken and difficult to interpret, but it is clear that there is a dorsal tympanic recess. Ventral to this there is a shallow ridge that forms the dorsal margin of a lateral fossa. This fossa is divided into an anteroventral part and a posterodorsal part by a ridge with a circular tubercle. The parasphenoid has a tall posterior base and the rostrum is directed anteroventrally. The distal end of the parasphenoid rostrum is broken, but seems to be tapering, rather than expanded into a boot, as is the case in some oviraptorids (MPC-D 102/11). The laterosphenoid and orbitosphenoid are too badly crushed and poorly exposed to discern any useful information.

Palatal skeleton—The palatal skeleton is excellently preserved (Fig. 4.17A, D, E). Anteriorly the vomer is cylindrical, but it becomes a dorsoventrally oriented sheet posteriorly. It is ventrally expanded at its anterior end where it meets the maxilla, and it contributes to the maxillovomeral process. Posteriorly, the vomer has a ventral groove that separates the ventrolaterally oriented facets for the palatines. The palatine has a short, triangular pterygoid process; a thin, pointed vomeral process; and a long, anterodorsally curving maxillary process. The maxillary process of the palatine is separated from the ectopterygoid by a foramen ventral to

where they contact the maxilla. The ectopterygoid curves anterodorsally and is bowtie-shaped, with a constricted neck and expanded ends. The pterygoid-ectopterygoid contact is crescentic, and is dorsoventrally expanded to form a ventral process as in *Citipati osmolskae*. The anterior ramus of the pterygoid is short in length but tall dorsoventrally. The posterior part of the pterygoid is a large dorsoventral wing that contacts the quadrate laterally and expands posteriorly.

Mandible:

    Dentary—The dentary (Fig. 4.17G–K) has a downturned beak and is sutured at the midline. It is thickened along the midline, producing a shallow midline lingual ridge extending ventrally to a pronounced ventral chin. There is a transverse ridge close to the ventral edge of the dentary that produces a small symphyseal shelf. This symphyseal shelf, with the midline lingual ridge, demarcates a shallow Meckelian fossa on each side. The tomial margin of the dentary has a raised lateral tab that protrudes above the occlusal margin of the anterior part of the dentary. The contact between the dentary and surangular is Z-shaped, as in caenagnathids, and is close to the coronoid eminence. The posteroventral ramus is long, and extends far past the external mandibular fenestra. The posteroventral ramus of the dentary is straight and tapers posteriorly where it underlies the angular.

    Splenial—The splenial is a long triangular splint that separates the anterior parts of the angular and prearticular. Its position and shape suggest that the 'prearticular' of caenagnathids (Sternberg, 1940; Funston and Currie, 2014) is in fact the splenial. In MPC-D 100/32-A, the splenial is not fused posteriorly to the prearticular, though they do contact extensively to form a long splint of bone dorsal to the angular on the medial surface of the mandible. Fusion of the

splenial and prearticular in caenagnathids probably explains the misidentification of this element in those animals.

Surangular—The surangular (Fig. 4.17) is tall anteriorly, but tapers dorsoventrally posterior to the coronoid process. The coronoid process protrudes dorsally and is medially inturned. The surangular spine that usually divides the external mandibular fenestra of oviraptorids is broken on both sides. Posteroventral to the coronoid process the surangular has a lateral depression, where the sheet-like bone is broken on both sides. The sutures between all of the post-dentary bones are open and distinct, suggesting that—at least at this developmental stage—the ASC complex typical of caenagnathoids had not fused in this individual.

Angular—The angular (Fig. 4.17) is dorsally expanded at its midpoint but tapers anteriorly and posteriorly. It extends posteriorly to the base of the retroarticular process, but does not contribute at all to the process, unlike all other oviraptorosaurs. Instead, the retroarticular process is clearly composed of the surangular laterally, the prearticular medially, with a small dorsal portion from the articular.

Prearticular—The prearticular (Fig. 4.17) is a narrow splint anteriorly, where it lies dorsal to the splenial and angular on the medial surface of the mandible. It expands posteriorly to form the base of the medial glenoid of the mandible, and the medial half of the retroarticular process.

Articular—The articular (Fig. 4.17) has a moderate longitudinal articular ridge and a well developed lateral glenoid that is strongly offset from the lateral surface of the surangular. This is unlike in *Heyuannia*, where the lateral glenoid is flush with the face of the dorsally thickened surangular. There is a faint suture separating the articular from the surangular and prearticular.

Axial series:

Cervical vertebrae—The complete cervical vertebral series is preserved (Fig. 4.19A), including the atlas, axis, and nine postaxial cervical vertebrae. The atlas is composed of three unfused parts: each neuropophysis and the intercentrum (Fig. 4.19B, C). The neural arches are spade shaped, but with blunted dorsal apices that curve medially. The neural arches and intercentrum contact around a diamond-shaped hole for the odontoid of the axis. The axis intercentrum is not fused to the axis, and has broken into two pieces along its midline. The lateral surfaces of the axis are broken, but each bore a depression that may have housed a pleurocoel. The odontoid is relatively long for an oviraptorosaur, but crushed so that its shape cannot be determined accurately. The neural spine of the axis is low and humped. The anterior cervical vertebrae (Fig. 4.19H–M) have elongate centra with anteroventrally inclined articular surfaces, nearly 45° from vertical in the anteriormost vertebrae. The lateral surface of each postaxial cervical vertebra has a pleurocoel, housed in a lateral depression. The infrapostzygapophyseal fossa is deep, but the infradia- and infraprezyga-pophyseal fossae, if present at all, would have been shallow. On each anterior cervical vertebra, the lamina connecting the prezygapophysis, postzygapophysis and transverse process is wide anteriorly, and descends far ventrally, covering the side of the centrum in lateral view. This lamina becomes smaller posteriorly along the cervical vertebral series, and extends less far ventrally, revealing the centrum in lateral view. The flat faces of the zygapophyses change in orientation from dorsoventrally facing to mediolaterally facing posteriorly in the cervical vertebral series. The epipophyses are small anteriorly and essentially absent posteriorly, retained solely as small rugosities. The neural spine is low, anteroposteriorly broad, and square anteriorly, but becomes taller and more slender posteriorly in

the cervical vertebral series. The articular facets of the centra—especially after the fifth postaxial cervical (C7)—become more vertical successively along the neck (Fig. 4.19A). The posterior cervical vertebrae are similar to the dorsal vertebrae in proportions, though they are relatively longer, have larger pleurocoels, and have lower neural spines.

Dorsal vertebrae—There are 11 dorsal vertebrae (Fig. 4.20A), one of which was kept in articulation with the sacrum. The three anteriormost dorsal vertebrae have hypapophyses, though it is broken on the first one. The second dorsal vertebra has the largest hypapophyses, and in all three the hypapophysis is a blunted tongue-like triangle with a posteroventrally directed apex. The hypapophysis extends along the ventral surface of the centrum more than half of the length of the centrum. The pleurocoel in the anterior dorsal vertebrae is nearly circular, and posteriorly it becomes elliptical anteroposteriorly. The infradiapophyseal fossa is positioned far dorsally on the neural arch relative to other oviraptorids, and is circular. The infrapre- and infrapost-zygapophyseal fossae are equal in size to each other and the infradiapophyseal fossa. The faces of the zygapophyses are vertical, as is typical of oviraptorosaur dorsal vertebrae, and do not extend far past their respective centra. The neural spines are directed slightly posteriorly, and are triangular anteriorly but become square posteriorly along the dorsal vertebral series. The ventral surfaces of the dorsal centra are keeled, but this may be partially due to mediolateral crushing of the vertebrae. Though the vertebrae appear well fused, the neurocentral sutures are not closed.

Sacral vertebrae—There are six sacral vertebrae (Fig. 4.21A, B), which are completely fused. The anterior sacral vertebrae—and probably all of the badly crushed posterior sacral vertebrae—have pleurocoels. On the posteriormost vertebra, the pleurocoel is positioned posterodorsally on the centrum, nearly at the junction of the neurocentral suture with the posterior edge of the centrum. Each of the sacral vertebrae has a flat ventral surface, with no

ventral midline groove or ridge. The neural spines of the sacral vertebrae are tall and fused into a single sheet (Fig. 4.21A), though there is a small gap between the bases of the neural spines of the first and second sacral vertebrae. The neural spines become shorter posteriorly, to follow the sloping postacetabular blade of the ilium. Five sacral ribs are preserved and, except for the last, they become wider posteriorly along the sacral vertebral series. The fourth sacral rib is wide and has a tall dorsal process with a lamina connecting it to the piston-shaped iliac process.

Caudal vertebrae—There are 27 caudal vertebrae preserved (Fig. 4.21C). The first eight caudal vertebrae have slightly anteroventrally inclined articular faces, but the rest have vertical faces. The centra are nearly identical to each other in the first fifteen vertebrae, each only slightly smaller than its predecessor. The centra are barrel-shaped and have only a slighy ventral concavity in lateral view (Fig. 4.21). The centra do not become more elongate posteriorly, rather they are uniform in proportion until the distal-most vertebrae. In the anterior caudal vertebrae, the neural arches lack infrapostzygapophyseal fossae, but have infradiapophyseal and infraprezygapophyseal fossae. The neural spines are square and vertical, and project from the posterior half of the vertebra. The transverse processes are posterolaterally directed and persist until the third-last preserved vertebra, inclusive. Posteriorly along the caudal vertebral series, the transverse processes occupy more of the centrum but develop a constriction around their midlength. They shorten transversely to become lateral sheets that are as long as the centra. The distal caudal vertebrae become flatter and more elongate, and lose their pleurocoels after the seventeenth vertebra (Fig. 4.21C). Also on the seventeenth caudal vertebra, the neural arch becomes small and tab-like, and the transverse processes develop supradiapophyseal depressions. The last preserved vertebra has a posterior articular face, and so does not appear to be the distalmost caudal vertebra. This suggests that the previously indicated absence of a pygostyle in

Rinchenia mongoliensis is uncertain. The anterior chevrons are missing, but the posterior ones are short and broad, with expanded distal ends. Posteriorly they develop greatly expanded anterior distal processes, and become anteriorly directed. The chevrons persist on the tail as far as the transverse processes. Posteriorly, they are leaf-like splints that extend anteriorly from the intervertebral joints.

Appendicular skeleton:

    Scapulocoracoid—The scapula and coracoid are not fused (Fig. 4.22A, B). The scapula is long and flat, with a slight distal expansion. The acromion is large and protrudes anteroventrally. The facet on the acromion for the flattened furcula faces anterodorsally. The contact of the acromion with the distally triangular furcula creates and anteromedial pocket. The glenoid of the scapulocoracoid faces posteroventrally, rather than being laterally everted as in some caenagnathids (Currie et al. 2016; Funston and Currie 2016). The coracoid is broken but the base of the caudoventral process is relatively straight.

    Sternum—A crushed plate of bone appears to be the sternal plates (Fig. 4.22C), which have been transversely flattened. Their margins are broken and incomplete, so little can be said of their morphology or shape compared to other oviraptorids. At least four sternal ribs are articulated with the sternal plates, but whether more contacted it in life cannot be determined.

    Humerus—The humerus (Fig. 4.22D–I) has a transversely wide proximal head that is compressed anteroposteriorly. The head is well developed medially, and projects from the shaft. The deltopectoral crest is directed mostly anteriorly, and only at the rounded tip is it slightly inflected medially. The deltopectoral crest is short and tapered ventrally, rather than square, so the proximal humerus is not rectangular as it is in other oviraptorids. The apex of the

deltopectoral crest is situated just over one-quarter the length of the humerus from the proximal end. The shaft of the humerus bends slightly posterolaterally, but not considerably so, and it is not twisted to the same degree as in caenagnathids (*Anzu, Apatoraptor* Funston and Currie 2016). The distal end of the humerus has poorly divided facets and bears a small lateral ectepicondylar knob.

Ulna and Radius—The ulna and radius are missing the distal ends (Fig. 4.22J, K). The ulna has a poorly developed olecranon process and an almost absent coronoid process, resulting in a poorly defined glenoid for the humerus. There is an anteroposterior ridge on the medial side of the articular surface of the ulna, which itself is not greatly expanded transversely from the shaft. The radius has a proximomedial process and a small longitudinal groove on the posterior side.

Pelvis—The pelvis (Fig. 4.23A) is represented by a complete right ilium and the proximal parts of the right pubis and ischium. The ilium is unique among oviraptorosaurs. The preacetabular blade is greatly expanded dorsally, hooked ventrally, and tapered to a sharp point. The postacetabular process is small and rounded, giving the ilium an overall tall and anteroposteriorly short shape. The preacetabular process does not extend as far as the pubic peduncle, which is pointed at its anteroventral corner. The supracetabular rim extends onto the pubic peduncle as a lateral crest. The cuppedicus fossa is transversely narrow. The ischiadic peduncle is triangular and the antitrochanter is small, resulting in a transversely narrow ischiadic peduncle. The narrow brevis shelf borders a dorsoventrally tall brevis fossa that is restricted to the posterior half of the postacetabular process. The pre- and post-acetabular processes are subequal in length, but each is shorter in length than the height of the ilium over the acetabulum. Only a small proximal portion of the pubis is preserved (Fig. 4.23A). The proximal end has an

anterior process, and a thickened edge posterior to the shallow medial fossa. The ischium is also represented by only the proximal part. It bears a convex facet for the pubis, separated from the acetabular rim by an oblique ridge.

Femur—The femur (Fig. 4.23B–G) has a large medial head with a posterior flange. The proximal head is directed slightly dorsally, rather than perpendicular to the shaft of the femur. The greater trochanter is small and rounded, and does not extend far above the shaft, resulting in only a shallow groove between it and the femoral head. The anterior trochanter is fingerlike and tapers proximally where it is level with the greater trochanter. Together, these two trochanters form a syntrochanteric crest, which in *Rinchenia* is low compared to other oviraptorids. The shaft of the femur is robust and curves slightly anteriorly. The distal condyles are separated by a deep popliteal fossa, which is deeper than those of other oviraptorids. The medial distal condyle of the femur overhangs this popliteal fossa posteriorly, creating an open tunnel. The lateral condyle has a large posterior flange and a round, bulbous ectocondylar tuber. There is a wide, shallow groove separating the lateral condyle from the fibular trochlea.

Tibia—The tibia (Fig. 4.23H–M) is only slightly longer (~20 mm) than the femur. The cnemial crest is broken, but would have been restricted to a proximal position. The fibular condyle is separated from the rest of the articular surface by a posterior groove, and seems anteroposteriorly long, even if not well pronounced laterally. The fibular crest on the shaft of the tibia is not well pronounced. The shaft and distal end of the tibia are mostly shattered, so little can be said about their morphology.

Fibula—The fibula has a large posterior expansion at its proximal end. The medial surface of the head is strongly concave, but is not excavated as in ornithomimids. The shaft of the fibula bears an anterolateral crest, with a small anterior tubercle.

Pes—The astragalocalcaneum and distal tarsals are missing. The foot (Fig. 4.23N–S) is incomplete, though the ends of the metatarsals and several phalanges are preserved. Metatarsal III and IV are preserved, but only the proximal and distal ends. Metatarsal III is roughly triangular in cross-section proximally, tapering anteriorly, and has a larger facet for metatarsal II than for metatarsal IV. Distally metatarsal III is narrow, with a ventral articular surface that is restricted to the distal part of the condyle. Metatarsal IV is larger than Metatarsal III proximally, and its proximal face is teardrop-shaped, with a flattened facet for metatarsal III. The distal end of Metatarsal IV is anteriorly bulbous and has a small lateral wing projecting from the condyle. The pedal phalanges are short and broad relative to other oviraptorosaurs, especially caenagnathids and larger oviraptorids like *Citipati osmolskae*. The unguals are also relatively short in length and are strongly recurved, rather than flat.

Remarks

Originally described as *Oviraptor mongoliensis* (Barsbold 1986), the specimen was renamed *Rinchenia mongoliensis* (Barsbold, 1997) without a diagnosis. The genus *Rinchenia*, despite being rendered valid when equated by (Osmólska et al., 2004) to "*Oviraptor*" *mongoliensis*, has since lacked proper description and diagnosis. It was diagnosed by Funston et al. (2018a) on the basis of several autapomorphies of the skull, mandible, and pelvis. The holotype is from Altan Uul II, although the precise site and horizon in that locality is unknown. This skeleton is relatively complete (Fig. 4.24) and provides information on all parts of the anatomy except the hand. No other material from *Rinchenia mongoliensis* has yet been reported, despite its distinctiveness—both cranial and postcranially—from other oviraptorids in the Nemegt and Baruungoyot Formations. *Rinchenia mongoliensis* tends to be grouped

phylogenetically with *Citipati osmolskae*, partly because of its sacral vertebral count and the morphology of the chevrons. Interestingly, *Citipati osmolskae* also shares some unusual aspects of the mandible with *Rinchenia mongoliensis,* specifically the extended ventral ramus of the dentary and the lack of angular contribution to the retroarticular process. Incorporation of these characters into phylogenies may strengthen the relationship between *Citipati osmolskae* and *Rinchenia mongoliensis*. In any case, *Rinchenia mongoliensis* appears to be the only representative of Citipatinae in the Nemegt Basin—all other taxa are heyuannine (see Chapter 5: section 5.4). This is likely the result of dispersal into the region (see Chapter 5: section 5.4).

4.3.5 A new oviraptorid from Guriliin Tsav

Oviraptoridae Barsbold 1976

Gen. et sp. nov.

(Figs. 4.25–4.49)

Localities and Horizon

Guriliin Tsav (MPC-D 102/12), Bugiin Tsav (MPC-D 100/33) and unknown (MPC-D 102/11;

MPC-D 102/110), Nemegt Formation, Western Gobi Desert, Mongolia.

Referred specimens

MPC-D 102/110.a, a block confiscated by the Mongolian Government, containing three

individuals (Fig. 4.25). Individual 'a' is the holotype and includes complete skull and mandible;

anterior cervical vertebrae, dorsal vertebrae; three sacral vertebrae; anterior caudal vertebrae and

chevrons; gastralia; right ulna and radius, complete manus, pubes; ischia; femora; tibiae; fibulae;

and pedes. Individual 'b' includes complete skull and mandible; anterior cervical vertebrae;

sacrum; anterior caudal vertebrae; dorsal ribs; right manus; partial pubes; ischia; partial right

femur, tibia and fibula; and pedes. Individual 'c' includes three sacral vertebrae, four anterior

caudal vertebrae and chevrons; a partial ilium; a distal tibia; and an astragalocalcaneum.

MPC-D 100/33 (Fig. 4.26), partial postcranial skeleton including complete pectoral girdle

and nearly complete forelimbs, sacrum, pubes, ischia, complete hindlimbs, and complete tail.

MPC-D 102/11.a–b (Fig. 4.26), confiscated partial skeleton including partial skull and

mandible, anterior cervical vertebrae, posterior dorsal vertebrae, sacrum, complete caudal series,

complete pelvis and nearly complete hindlimbs. The specimen includes an isolated postorbital,

quadrate and quadratojugal that are identical in anatomy to the skull, but must be from a different

individual.

MPC-D 102/12 (Fig. 4.26), partial postcranial skeleton including nearly complete axial series except for sacrum, partial right ilium and ischium, and partial right hindlimb including femur, tibia, fibula, and metatarsus. Collected in 1998 by the Hiyashibara Museum in Guriliin Tsav, Nemegt Basin.

Diagnosis: A medium-sized oviraptorid oviraptorosaur distinguished from other oviraptorosaurs by the following autapomorphies (asterisks) and suite of characters: apically thickened, dome-shaped cranial crest composed equally of nasals and frontals*; nasal recesses housed in a depression; postorbital with dorsally directed frontal process; cervical vertebrae with large epipophyses; didactyl manus*; accessory ridge of brevis fossa of ilium*, anteriorly curving pubis; large proximodorsal process of distal tarsal IV; and non-arctometatarsalian pes.

Description

Between the six skeletons represented by the specimens, nearly every bone of this oviraptorid is known (Fig. 4.27). They reveal an oviraptorid with a short forelimb, elongate hindlimbs that shorten through ontogeny (see section 4.4.2), and a relatively short tail (Fig. 4.27).

Cranial Skeleton:

The skulls of MPC-D 102/110.a and MPC-D 102/110.b are complete (Fig. 4.28), but are crushed mediolaterally. The skull of MPC-D 102/11.a is relatively complete, but is missing most of the anterior parts of the face, palate, and mandible. The left side of the skull is roughly articulated and is well preserved. The right and posterior sides have been crushed and lie on a single plane parallel to the left side of the skull. Three skull bones are preserved from MPC-D 102/11.b: the postorbital, quadratojugal, and quadrate. The other specimens lack cranial elements.

Premaxilla—The premaxilla (Fig. 4.28A) is preserved in MPC-D 102/110.a and MPC-D 102/110.b, but not MPC-D 102/11. It is tall dorsoventrally and constricted anteroposteriorly. Dorsally, it is divided by the naris into two processes: the nasal process extending dorsally, and the subnarial process directed posterodorsally. The nasal process is much narrower than the subnarial process in lateral view, unlike in *Citipati*, *Khaan*, *Nemegtomaia*, and *Rinchenia*, where these processes are subequal in width. The nasal process curves posterodorsally so that it forms a small part of the continuous semicircular crest with the nasals, frontals, and parietals. It extends dorsally to the ventral third of the naris, whereas in *Rinchenia* the premaxilla extends far above the naris. The subnarial process of the premaxilla is broad and tapers posteriorly. Posteriorly, it separates the lacrimal and nasal anteriorly and prevents the maxilla from contacting the nasal on the lateral surface of the skull. The lateral surface of the body of the premaxilla is pierced by multiple small foramina. Ventral to the small, oval naris, there is a lateral depression in the premaxilla similar to that of *Citipati osmoslkae* (Clark et al. 2002). The occlusal margin of the premaxilla has at least two denticulations, but this area is broken in both individuals and there may have been more. The palatal surface cannot be seen on any of the specimens.

Maxilla—The maxilla (Fig. 4.28A) is missing in MPC-D 102/11 and poorly preserved in both individuals of MPC-D 102/110. The antorbital fossa is small and the antorbital fenestra is divided in two by a dorsally-expanding strut of bone. The jugal process is relatively short and extends only partway under the orbit. Labial-buccal transition on the lateral side of the maxilla is marked by a ridge, ventral to which there is a pronounced lateral tubercle, as in *Rinchenia mongoliensis*. The maxillovomeral tubercle (=palatal 'tooth'), which is present in all oviraptorids, is obscured by matrix in MPC-D 102/110, so the contribution of the maxilla cannot be determined.

Nasals—The fused nasals (Fig. 4.28) are complete but crushed in both individuals of MPC-D 102/110. Only the posterolateral wings of the nasals are preserved in MPC-D 102/11. In this individual, the nasals are fused along the midline, but posteriorly a suture is still visible. Like *Rinchenia mongoliensis*, the great size of the nasals is mostly due to expansion of the lateral descending processes. Like in *Citipati osmolskae* (Clark et al. 2002) and *Khaan mckennai* (Balanoff and Norell 2012), the posterodorsal part of the premaxilla excludes the maxilla from contributing to the naris and from contacting the nasal. The elliptical naris is displaced far dorsally and overlies the antorbital fenestra, similar to *Citipati osmolskae* (Clark et al. 2002). It extends above the dorsal margin of the orbit; posteriorly its ventral margin is level with the top of the orbit. The anterior midline process forms less than half the length of the nasal, and curves anteroventrally to meet the posterodorsal process of the premaxilla. In lateral view (Fig. 4.28A), it is broad dorsoventrally, the result of a septal ridge on its ventral surface. The lateral descending processes host several pneumatic cavities, which vary in position between each specimen. In the better-preserved MPC-D 102/11 (Fig. 4.28C–F), the midline rami of the fused nasals are thickened and rounded dorsally, delimiting a lateral recess in which the pneumatic cavities lie. These complex asymmetric pneumatic pockets are similar to those of MPC-D 100/42 and *Citipati osmolskae*, and appear to fully penetrate the nasal and open into the nasal passage. The buttress formed by the fused nasals above the pneumatic pockets is confluent with the similarly thickened dorsal parts of the frontals and parietals. Together, they form a raised rim on the dorsal margin of the cranial crest. The posterior suture with the frontal is simple and straight, like in *Citipati osmolskae* (Clark et al. 2002), and does not have the interdigitating irregularity present in *Khaan mckennai* (Balanoff and Norell 2012). The fused nasals are arched transversely so that their wing-like posterolateral processes are nearly vertically oriented, as in *Rinchenia*

mongoliensis. Although this may be exaggerated by transverse crushing of the skulls in MPC-D 102/110, a similar arched morphology is present in *Citipati osmolskae* (Clark et al. 2002), where the nasals contribute to a cranial crest.

Lacrimal—The lacrimal (Fig. 4.28) is well preserved in all three skulls. The lacrimal contacts the nasal dorsally, the maxilla and premaxilla anteriorly, and the frontal posteriorly above the orbit. Like other oviraptorids, the lacrimal has a poorly developed anterior nasal process, and lacks the T-shape present in *Caudipteryx zoui* Qiang et al. 1998 (Qiang et al. 1998) and deinonychosaurs. The foramen for the lacrimal duct faces anteriorly and opens into a shallow subhorizontal channel on the lateral surface of the lacrimal. The pneumatic pockets seen on *Citipati osmolskae* (Clark et al. 2002) and *Khaan mckennai* (Balanoff and Norell, 2012) are present on only one individual, MPC-D 102/110.b. The frontal process is long, but does not extend posteriorly past the nasal. A triangular process of the frontal separates the lacrimal from the dorsal edge of the orbit, creating a Z-shaped suture in lateral view. The jugal process curves posteroventrally to meet the jugal, forming an inclined posterodorsal margin to the antorbital fenestra. The preorbital bar of the lacrimal is anteriorly pierced at its midlength by a small, vertical slit that communicates with the orbit. The preorbital bar is flared slightly laterally, its posterior margin is broadly concave, and it forms the entire anterior margin of the orbit.

Frontal—The frontal (Fig. 4.28) is well preserved in each skull. It is taller dorsoventrally than long anteroposteriorly, which is unusual for a theropod. It forms most of the dorsal part of the orbit, with the postorbital, and contributes to the supratemporal fenestra posteriorly. It tapers dorsally, so that it is longer anteroposteriorly above the orbit than on the dorsal margin of the cranial crest. It contacts the lacrimal and nasal anteriorly, the postorbital laterally, the parietal posteriorly, and the laterosphenoid posterolaterally. The postorbital process is elongated

dorsoventrally to accommodate the tall frontal process of the postorbital, and continues dorsally as a distinct ridge separating the supraorbital and supratemporal portions of the frontal. The supraorbital part of the frontal is concave laterally, and has a dorsoventrally oriented pneumatic depression on most of its lateral surface. The supratemporal part of the frontal is not pierced by pneumatic openings, but the breakage pattern on the left side of MPC-D 102/11 suggests that it may have been hollow above the braincase, as in *Citipati osmolskae* (Clark et al. 2002). Unlike MPC-D 102/110, the frontals of MPC-D 102/11 are not fused, but all three individuals have a simple, straight contact. The frontals are separated only slightly posteriorly by the parietals, with which they have a simple, obtusely angled contact. The supraorbital rim lacks a supraciliary lip, which is the case in *Citipati osmolskae* (Clark et al. 2002), but not in *Khaan mckennai* (Balanoff and Norell, 2012). The dorsal surface of the orbit is badly crushed in all individuals, but appears to have a groove posteriorly.

Parietal—The parietal (Fig. 4.28) is preserved in each skull. It is tall dorsoventrally, which has probably been slightly exaggerated by transverse crushing in each individual. The parietals of MPC-D 102/11 are fused completely, though a furrow is still visible on the dorsal midline. The lateral surface of the parietal is deeply concave, to accommodate mandibular adductor musculature. The sagittal crest is tall, extending about 20 mm above the apex of the nuchal crest in MPC-D 102/11, and is transversely expanded, tapering posteriorly. The nuchal crest is pronounced and merges at the midline with the sagittal crest. The posterior end of the sagittal crest is near the apex of the cranial crest, posterior to which the skull roof descends steeply (Fig. 4.28A). A similarly sloped skull roof is present in most oviraptorids, except *Conchoraptor gracilis* (Funston et al., 2018a), (*Khaan mckennai* (Balanoff and Norell 2012), and *Yulong mini* (Lu et al. 2013). The parietal contributes only to the posterior half of the medial

surface of the supratemporal fenestra, contrasting with *Khaan mckennai* (Balanoff and Norell 2012), where it forms the majority of this surface. The transversely straight but dorsally arched occipital margin of the parietal is the widest point of the bone. In MPC-D 102/110.a–b, the arched margin of the parietal contacts the supraoccipital and exoccipital posteriorly and the squamosal laterally.

Jugal—The jugal (Fig. 4.28) is best observed in MPC-D 102/110.a and MPC-D 102/11. It is triradiate and relatively robust compared to other oviraptorids. Unlike most oviraptorids where the ventral margin of the jugal is straight or dorsally arched, in this taxon it is slightly sinuous. The maxillary process is dorsoventrally broad towards its posterior base and tapers anteriorly where it meets the lacrimal and maxilla. The postorbital process is wide in lateral view, and has an anterior facet for the postorbital that extends ventrally only a third of the length of the postorbital process. In *Citipati osmolskae* (Clark et al. 2002) and *Khaan mckennai* (Balanoff and Norell 2012), this facet extends much further ventrally, almost to the junction of the postorbital process and the other two processes of the jugal. The quadratojugal process of the jugal is short and laterally overlies the quadratojugal. It is much shorter and more robust than that of *Rinchenia mongoliensis*, where it is bifurcated posteriorly to interfinger with the quadratojugal.

Postorbital—The postorbital (Fig. 4.28) is preserved in all of the articulated skulls and an isolated postorbital is present with MPC-D 102/11.b. The postorbital is tall and its frontal process is vertical, which distinguishes this taxon from all other oviraptorids except *Rinchenia mongoliensis*. In other oviraptorids, the frontal process is oriented anterodorsally, and is typically shorter than the jugal process. In MPC-D 102/11 (Fig. 4.28C, D) and MPC-D 102/110.b, the jugal process is shorter than the frontal process, and only forms half of the posterior orbital

margin. It is slightly longer in MPC-D 102/110.a (Fig. 4.28A, B), where it forms almost two-thirds of the orbital margin. The anterior (orbital) margin of the postorbital is strongly sinuous, with a concave orbital portion and a convex frontal portion. In most oviraptorids, the anterior margin of the postorbital is smoothly concave. The squamosal process is unbroken only in MPC-D 102/110.b, where it is dorsoventrally broad and anteroposteriorly short.

Squamosal—The squamosal (Fig. 4.28) forms the posterodorsal corner and upper margin of the subrectangular infratemporal fenestra. The postorbital process has a lateral rugosity and a dorsolateral groove for the postorbital. The lateral surface of the squamosal has a curved ridge posterodorsally that would have anchored adductor musculature. Medially the squamosal has an anteroposteriorly wide contact with the parietal, best observed in MPC-D 102/110.b. The squamosal bifurcates ventrally, as in all oviraptorids. The posterior process contacts the paroccipital process of the exoccipital and encapsulates the external auditory meatus. Ventromedially, the squamosal contacts and fuses to the quadrate, and ventrolaterally it contacts the quadratojugal, where it borders the external auditory meatus.

Quadratojugal—The triradiate quadratojugal (Fig. 4.28) is not fused to the quadrate, even in the large isolated individual (MPC-D 102/11.b) associated with MPC-D 102/11.a. The anterior process lies medial to the jugal, and forms about two-thirds of the ventral margin of the infratemporal fenestra. Dorsally, the ascending process forms at least half of the posterior border of the infratemporal fenestra, though its full extent is obscured by fusion to the squamosal. The ascending process contacts the quadrate along most of its length, but is separated ventrally by a quadrate foramen. The posterior process of the quadratojugal forms a cap on the lateral surface of the quadrate, and has a tab-like posteroventral extension. The posterior process is relatively

long, comparable to *Banji long* (Xu and Han 2010), *Citipati osmolskae* (Clark et al. 2002), and *Nemegtomaia barsboldi* (Fanti et al. 2012).

Quadrate—The quadrate (Fig. 4.28) is poorly exposed in MPC-D 102/110, and in MPC-D 102/11.a it is badly damaged on the left and preserved only in posterior view on the right. The isolated quadrate from MPC-D 102/11.b is incomplete, but useful for determining morphology. Medially, the quadrate contacts the parasphenoid, prootic, and pterygoid; laterally, the quadratojugal; and dorsally the squamosal. It does not appear to contact the exoccipital/opisthotic extensively, though on both sides of MPC-D 102/11 these bones are disarticulated and this area is not visible in the skulls of MPC-D 102/110. The optic wing of the quadrate is oblique to the midline, and covers most of the lateral surface of the braincase. Anteriorly, the optic wing of the quadrate contacts the epipterygoid. At this point, it also contacts the pterygoid ventrally. The condyles of the quadrate are saddle-shaped as in other oviraptorosaurs. There is a large, vertically-oriented, oval quadratojugal foramen, formed entirely by excavation of the quadrate. Just medial to this, on the anterior side of the quadrate, there is a deep depression. There is a vertical ridge on the anterior surface of the quadrate, just lateral to the optic wing. The lateral surface of the quadrate contacts—but is not fused with—the quadratojugal.

Palatal skeleton—The palatal skeleton is incomplete in MPC-D 102/11.a (Fig. 4.28C, D), with only the pterygoids, ectopterygoids, and a small part of the right palatine preserved. In MPC-D 102/110, the palatal skeleton is mostly obscured by the overlying mandible. The ectopterygoid has a dorsally curved maxillary process, which would have contacted the maxilla dorsally and the palatine anteriorly. Anteriorly, the pterygoid has a crescentic contact with the ectopterygoid in lateral view, as in almost all oviraptorids. The ramus of the pterygoid is short

anteroposteriorly and tall dorsoventrally. The pterygoids are separated by an interpterygoid vacuity. The pterygoid has a broad posterodorsally-facing contact with the quadrate, from which it tapers anteriorly. Posteriorly, it underlies the optic wing of the quadrate, and is mostly obscured by crushing. At its posterior end, it is dorsoventrally tall and transversely thin. At this point, it contacts the basipterygoid process of the basisphenoid medially.

Occiput—The occiput is not visible on either skull of MPC-D 102/110. In MPC-D 102/11.a (Fig. 4.29) it is well preserved and none of the bones of the occiput are fused, although the basioccipital and basisphenoid have begun to coossify. The trapezoidal supraoccipital is disarticulated from the rest of the occiput. The facets for the exoccipitals on the supraoccipital are separated by a groove, indicating that the supraoccipital contributed to the foramen magnum. The supraoccipital tapers anterodorsally, where it would have fit between the squamosal processes of the fused parietals. The dorsal surface of the supraoccipital bears two longitudinal, shallow elliptical depressions. The ventral surface of the supraoccipital has a lateral lamina on each side, which would have formed the walls of the foramen magnum. The exoccipitals have been rotated anterolaterally from life position, which exposes the medial sides (Fig. 4.29). A medioventral process indicates that the exoccipital formed only the dorsolateral corner of the occipital condyle. The exoccipital is thickened dorsomedially where it contacts the supraoccipital, and tapers laterally towards the dorsal border of the paroccipital process. The paroccipital process curves ventrally, and has a raised, undulating lateral edge. Medially, the base of the paroccipital process has a depression, which is bordered laterally by a rounded ridge that extends along the long axis of the paroccipital process. On the medial surface, which forms the posterior wall of the foramen magnum, there are multiple foramina (Fig. 4.29B). The posteriormost of these is for Cranial Nerve XII, which exits on the exterior surface of the

exoccipital ventrolateral to the occipital condyle. The basioccipital is articulated with the basisphenoid, and though they have begun to coossify in this individual, they were not yet fully fused. The occipital condyle is kidney shaped, and has a ventrally constricted neck. The basal tubera are situated ventral to the occipital condyle in posterior view (Fig. 4.29), rather than level with it as in *Citpati osmolskae* (Clark et al. 2002 fig. 6). The basal tubera are not widely spaced and are relatively small, which may be a consequence of the early developmental stage of MPC-D 102/11.a. The basisphenoid is not well exposed in MPC-D 102/11.a, but several features can be discerned. It has begun to coossify with the basioccipital, but there is still a suture. The basipterygoid processes face ventrolaterally, and are separated by a dorsoventrally oriented groove. This groove extends dorsally to the basisphenoid recess. Lateral wings of the basisphenoid extend dorsally to encapsulate the basioccipital, and contact the exoccipital and probably prootic.

Braincase—Most of the braincase is obscured by the overlying bones in MPC-D 102/110, but on the left side of MPC-D 102/11.a parts of the laterosphenoid and parasphenoid are exposed (Fig. 4.28C, D). The laterosphenoid extends dorsally into the supratemporal fenestra, terminating just dorsal to the supratemporal bar in lateral view. Only the anterior part of the prootic is exposed, where it is pierced by the large foramen ovale. For such a delicate element, the parasphenoid rostrum is exceptionally preserved in MPC-D 102/11.a. It occupies the space dorsal to the interpterygoid vacuities, and has been taphonomically shifted dorsally so that it lies at the center of the orbit. It is transversely narrow but dorsoventrally tall and straplike. The anterior end is modified into a 'boot', superficially similar in shape to the pubic boot of most oviraptorosaurs. At its posterior end, it is pierced by two small foramina.

Scleral ossicles—Dozens of small, crushed plates of bone are present in the orbits of both MPC-D 102/110.a–b (Fig. 4.28A, B). The more complete plates are roughly square, with rounded corners. The largest is 6.5 mm in height and 9 mm in length, about 20% the anteroposterior length of the orbit.

Mandible—The lateral surface of the mandible is well preserved in MPC-D 102/110.a (Fig. 4.28A, B), but is mostly missing from MPC-D 102/11.a. The dentary is tall and downturned anteriorly, with a pronounced ventral chin. The occlusal margin is concave anterodorsally and the labial surface is marked by minute foramina. The posterodorsal ramus is broad and strap-like, tapering posteriorly where it contacts the surangular above the heart-shaped external mandibular fenestra. The posteroventral ramus is long, extending as far as the surangular fossa on the lateral side of the surangular, and tapers where it underlies the angular. The coronoid process is tall and protrudes far above the rest of the mandible. The surangular prong is broken in MPC-D 102/110.a, but appears to be present in MPC-D 102/110.b. The angular straplike and extends to the anterior end of the external mandibular fenestra. The surangular has a deep recess, which may have housed a surangular foramen, but this region is broken. The articular has a tall, convex articular ridge and a small, posteriorly directed retroarticular process. As in *Rinchenia mongoliensis* and unlike all other oviraptorosaurs, the retroarticular process of MPC-D 102/110.a is composed predominantly of the surangular, rather than including a contribution from the angular.

Ceratobranchial—A long, rod-shaped ceratobranchial is preserved just lateral to the mandible of MPC-D 102/110.a (Fig. 4.28A, B). The anterior end of the element is expanded dorsoventrally. The shaft is straight and cylindrical, unlike the curved ceratobranchial of *Citipati*

osmolskae. The ceratobranchial is nearly half the length of the mandible, and about one-third the length of the skull.

Axial Skeleton:

Alongside the anteriormost cervical vertebrae, only the posterior sacral vertebrae and the ventral surfaces of the caudal vertebrae are exposed in MPC-D 102/110 (Fig. 4.30). The axial skeleton of MPC-D 102/11 is represented by an incomplete atlas, a partial axis, two anterior cervical vertebrae, four posterior dorsal vertebrae, a sacrum composed of three coossified vertebrae, and a complete caudal series. A nearly complete vertebral column is known from MPC-D 102/12, although it is missing the sacrum and the anterior cervical vertebrae. Only the sacrum and caudal vertebrae are mounted with MPC-D 100/33, but photographs taken in September 2001 show a nearly complete axial series including the atlas-axis, anterior cervical vertebrae, dorsal vertebrae, a sacrum, and caudal vertebrae. Together, the vertebrae from all specimens represent the entire axial column, and most positions are represented by multiple individuals.

Cervical Vertebrae—The anterior cervical vertebrae of MPC-D 102/11 (Fig. 4.28C–F) are incompletely ossified, and their articulation with the base of the skull obscures the morphology of the centra. The neural arches are not fused to the centra, and have low neural spines. The right side of the neural arch of the atlas is exposed and is separate from the left, though the two halves would probably have fused later in life. The atlas intercentrum and the odontoid process of the axis are missing, so their morphology cannot be discerned. The axis has an anteroposteriorly long neural spine, which is transversely thickened distally and extends posteriorly past the centrum. The first postaxial cervical vertebra has a relatively tall and

fingerlike neural spine, though the rest of the neural arch is broad and dorsoventrally flattened, typical of oviraptorosaurs (Balanoff and Norell, 2012). MPC-D 102/12 and MPC-D 100/33 provide more information on the entire cervical vertebral series (Fig. 4.30). The atlas-axis (Fig. 4.30C) of MPC-D 100/33 is tightly adhered, but sutures are still visible between the atlas intercentrum and the axis. The neuropophyses of the atlas are fused to each other along the midline and have begun to coossify with the intercentrum. The neural spine of the axis is missing, but its morphology is bulbous in MPC-D 102/110 and MPC-D 102/11 (Fig. 4.28F). In contrast, the neural spine of the third cervical is peglike (Fig. 4.28F). The centra of the anterior cervical vertebrae have steeply inclined articular faces and widely spaced parapophyses, resulting in a triradiate appearance in ventral view (Fig. 4.30F). Each has a deep lateral pleurocoel and a concave posterior articular surface. The neural arches are as wide as they are long and have large, circular, anteriorly-facing prezygapophyses. These are connected to the postzygapophyses by a broad lamina, from which the transverse processes barely protrude. Large, moundlike epipophyses (Fig. 4.30E) sit on the dorsal surfaces of the postzygapophyses, and these appear to become larger in more posterior vertebrae. The neural spines are low and square. Based on their absence, the cervical ribs had not yet fused in MPC-D 100/33, but in MPC-D 102/12, some appear to have fused to the parapophyses. MPC-D 102/12 is missing the anterior cervical vertebrae but preserves the mid and posterior cervical vertebrae. The centra become relatively taller posteriorly along the cervical vertebral series (Fig. 4.30B), and this is accompanied by broadening of the neural arches so that they are wider than they are long. The centra retain large pleurocoels, but the articular faces become less inclined posteriorly along the series. Regardless, the posterior articular face remains concave throughout the series. The transverse processes become better developed and fuse to the cervical ribs, which decrease in

relative length successively. The epipophyses are large until about postaxial cervical vertebra 8, posterior to which they decrease in size.

Dorsal Vertebrae—The posterior dorsal vertebrae, the sacral vertebrae, and four of the anterior caudal vertebrae are articulated with the right ilium of MPC-D 102/11 (Fig. 4.27I, M). A complete dorsal vertebral series is preserved with each of MPC-D 102/12 and MPC-D 100/33, although they are better preserved in MPC-D 102/12 (Fig. 4.31). The dorsal vertebral series comprises 10 vertebrae, which increase in size successively. The anterior three vertebrae have hypapophyses, which are largest on the anterior one and smallest on the posterior one. The centra are barrel shaped with a ventral keel and develop a ventral curve in lateral view towards the posterior end of the series. This is accompanied by an increase in the size of the lateral pleurocoel—which is present on all dorsal vertebrae—and a transverse broadening of the centrum. In MPC-D 102/12, the neural arches are fused to the centra, and in most cases the suture is closed (Fig. 4.31). This is not the case in MPC-D 100/33, where the neural arches are not fused and in many cases have become disarticulated. The parapophyses of MPC-D 102/12 are large and concave. They become more dorsally positioned posteriorly along the dorsal vertebral series, transitioning from a location exclusively on the centrum (D1–D5), to bridging the neurocentral suture (D6–D8), to exclusively on the neural arch (D9, D10). The neural arches are deeply excavated by infraprezygapophyseal, infradiapophyseal, and infrapostzygapophyseal fossae, which in some cases have merged, leaving a strut of bone remaining (Fig. 4.31H). The infraprezygapophyseal fossae become shallower in more posterior vertebrae, whereas the infradiapophyseal and infrapostzygapophyseal fossae remain deep throughout. The neural spines become taller until D8, after which they are slightly shorter.

Sacral Vertebrae—There are six sacral vertebrae (Fig. 4.32), which are all fused in MPC-D 100/33. In contrast, only three vertebrae have been coossified to form the sacrum in MPC-D 102/11 (Fig. 4.32B), which is likely attributable to ontogeny rather than taxonomy. Like all oviraptorosaurs, the centra of the sacrum have large lateral pleurocoels, and are flattened ventrally. However, they are not flattened to the same degree as in caenagnathids, and the pleurocoels sit above the ventral surface of the sacrum. The second sacral vertebra shows an incipient ventral keel, whereas sacral vertebrae 3–6 have a midline groove. The anterior sacral neural arches of MPC-D 100/33 are missing, but the posterior ones have fused together into a fan-like sheet of bone. In MPC-D 102/11, the neural spines remain separate dorsally (Fig. 4.32A), but their ventral bases have begun to fuse. Unlike in caenagnathids, the transverse processes and their accompanying sacral ribs do not vary in position along the sacral series. Rather, in each vertebra they are consistently located at the level of the neurocentral suture. As in caenagnathids, however, the transverse process and sacral rib of sacral vertebra 5 appear to be the largest, although not forming the same hatchet-shaped process. The lack of sacral fusion in MPC-D 102/11 provides insight into the somitic origin of the sacral series. The three fused sacral vertebrae likely represent the primordial sacral vertebrae, based on the extent of their fusion early in life. Indeed, three sacral vertebrae are fused even before hatching in oviraptorids (Norell et al. 2001). Accordingly, the anteriormost sacral vertebra must have been recruited from the dorsal series and two caudosacral vertebrae must have been incorporated from the tail (Fig. 4.32A). This is supported by the morphology of these vertebrae, which most closely resemble the dorsal and caudal vertebrae, respectively.

Caudal Vertebrae—The complete caudal vertebral series of the Guriliin Tsav oviraptorid would have had 29 caudal vertebrae, the last three of which fuse into a pygostyle

later in life. MPC-D 102/11 preserves 27 of the 29 caudal vertebrae (Fig. 4.33B), and is missing only the last two pygal vertebrae. MPC-D 102/12 has the complete pygal series, but is missing the proximal caudal vertebrae (Fig. 4.33C), which were presumably lost at the same time as the sacral vertebrae, resulting in a total of 26 vertebrae. MPC-D 100/33 has 23 caudal vertebrae from the middle part of the tail, missing both the proximal and distal vertebrae. MPC-D 102/110.a–c preserve seven, four, and seven caudal vertebrae, respectively, from the base of the tail, but are missing the distal parts of the tail. The centra of the caudal vertebrae have pleurocoels, though they are reduced in size relative to the dorsal and sacral vertebrae, and become absent in the eleventh vertebra from the tip of the tail. In MPC-D 102/12, some of these pleurocoels have become infilled with bone, but their borders can still be discerned (Fig. 4.33D). The centra of the caudal vertebrae are barrel-shaped and not elongated anteroposteriorly as in many theropods. Posteriorly, they become slightly more elongate relative to their height (Fig. 4.33H–J), though still not to the degree seen in theropods like deinonychosaurs, tyrannosaurs, and ornithomimids. In MPC-D 102/11, the anterior neural arches are not fused to the caudal vertebrae, but the seventeen posteriormost vertebrae have neural arches that are fused with a closed suture. In contrast, all of the caudal vertebrae of MPC-D 102/12 have fused neurocentral sutures. The neurocentral fusion of the posterior caudal vertebrae and the lack of fusion in all the other vertebrae of MPC-D 102/11 suggests that closure of the neurocentral sutures proceeds posterior to anterior, as in crocodiles (Brochu, 1996). This lends support to previous suggestions that closure of the neurocentral sutures in the cervical vertebrae is evidence of maturity (Funston and Currie, 2016). There is a relatively large infradiapophyseal fossa below the high transverse process on the anterior caudal vertebrae. In MPC-D 102/12, this is accompanied by a supradiapophyseal fossa on the anterior two caudal vertebrae. The transverse processes descend

progressively towards the lateral surface of the centra posteriorly and become shorter

mediolaterally. Their orientation also changes from being directed posteroventrally to more

directly laterally. In MPC-D 102/11, the transverse processes persist until the eighth last

vertebra, whereas in MPC-D 102/12 they persist until the last vertebra preceding the pygostyle.

However, these distal transverse processes are anteroposteriorly elongate and hatchet-shaped in

dorsal view (Fig. 4.33I), barely protruding from the centrum. Similar transverse processes are

present in MPC-D 100/33, but they do not extend as far down the tail, likely representing an

intermediate ontogenetic stage of development.

Ribs and Gastralia—The dorsal ribs are poorly preserved in MPC-D 102/110 and are

missing in MPC-D 102/11. Only the distal portions of the shafts of the dorsal ribs are preserved

in MPC-D 102/110.a, where they are articulated with the gastral basket. Four partial ribs are

preserved with MPC-D 102/12 (Fig. 4.34). The head of the ribs are relatively simple, lacking the

pneumatization present in caenagnathids like *Apatoraptor pennatus*. The largest of the four ribs

has a broad capitulum, suggesting it is from the middle part of the dorsal series. On the

posterolateral surface of the shaft, there is a facet for the attachment of an uncinate process (Fig.

4.34D). However, the uncinate process was not recovered with the skeleton. The gastralia are

well preserved and articulated in MPC-D 102/110, but not the other specimens. There are at least

12 rows of medial gastralia, and lateral gastralia are associated with most of these rows. The

right medial gastralia are offset anteriorly from the left gastralia, and anteriorly some of the

medial gastralia fuse.

Chevrons—The anterior chevrons are preserved in MPC-D 102/110.a–c (Fig. 4.35A, B),

and relatively complete series of chevrons are preserved with MPC-D 100/33, MPC-D 102/11,

and MPC-D 102/12. The anterior chevrons of MPC-D 102/110.a, MPC-D 102/110.c, MPC-D

102/11, MPC-D 100/33, and MPC-D 102/12 are elongate and taper distally to a bulbous process (Fig. 4.35C), similar to *Heyuannia yanshini*. However, the first chevron of MPC-D 102/110.b are unusual and extremely small compared to the other specimens (Fig. 4.35B), despite similarity in the size of the associated caudal vertebrae. Indeed, the first chevrons of MPC-D 102/110.a,c are more than twice the size of MPC-D 102/110.b. This condition is reminiscent of the dimorphism in chevrons in *Khaan mckennai*, although to a greater degree. Without a larger sample size, the cause of this dimorphism cannot be determined, but it is in any case notable and worthy of future study. Some of the distal chevrons are preserved with MPC-D 102/11 and MPC-D 100/33. These remain elongate dorsoventrally, rather than becoming platelike as is the case in caenagnathids and MPC-D 100/42, the Dzamyn Khondt oviraptorid.

Pectoral Girdle:

The complete pectoral girdle of MPC-D 100/33 is preserved and was disarticulated during preparation, allowing for detailed description. Both halves of the pectoral girdle are present but the left scapula is missing its distal end and the right coracoid is slightly damaged. The pectoral girdles of MPC-D 102/110.a–b are likely complete, but are mostly obscured by the overlying bodies. The pectoral girdles of MPC-D 102/11 and MPC-D 102/12 are unknown.

Scapula—The scapula is long and gracile (Fig. 4.36A–E). The distal end is slightly expanded and has a rounded end. In cross-section, the lateral surface of the scapula is flat, whereas the medial side is rounded, which produces a lens-shaped outline. The ventral edge of the scapula is sharp, but the dorsal edge is rounded. The scapular blade thickens transversely and curves medially towards the glenoid. About 30 mm distal to the glenoid, there is a small protrusion on the ventral edge of the blade that may have anchored musculature. Just anterior to

this, on the dorsal edge of the blade, there is a shallow groove. The acromion process is small and rounded in dorsal view (Fig. 4.36E). Its dorsal surface is flat, but this flattened area does not extend far posteriorly. The lateral edge is dorsally upturned and has a rounded, thickened edge. The anterior edge is thick and barely protrudes from the region where it connects medially to the body of the scapula. The acromion does not extend anteriorly past the contact of the scapula and coracoid. The glenoid of the scapula is approximately rectangular in articular view. Its lateral edge extends anterodorsally, whereas its medial edge is parallel to the scapular blade. As a result, the anterior part of the articular surface is exposed laterally (Fig. 4.36D). The articular surface is slightly concave and tapers transversely towards the posterior side. The unfused contact between the scapula and coracoid is crescentic (Fig. 4.36B). The anterior surface of the scapula is convex, whereas the posterior side of the coracoid is concave. Accordingly, the scapula has a relatively large dorsal flange anterior to both the glenoid and acromion, which differs from other oviraptorids like *Heyuannia yanshini*, where the acromion is the most anterior part of the scapula. On the medial side of the head of the scapula, there is a proximodistal groove that extends to the same level as the glenoid. This groove is continuous with a groove leading to the coracoid foramen, so it probably accommodated vasculature and nerves.

Coracoid—The coracoid is long dorsoventrally (Fig. 4.36B, D). The contact for the scapula is concave and tapers in transverse thickness dorsally. The glenoid is approximately square and faces completely posteriorly, with a slight lateral exposure. The coracoid foramen is oval and oriented with its long axis anteroventrally to posterodorsally. On the medial surface, it is connected to a deep groove that extends to the scapulacoracoid contact. The biceps tubercle is relatively large and circular. Its apex is rounded, rather than rugose, and there are no other ridges on the lateral surface of the coracoid. On the medial surface there are two fossae separated by a

trabecula that correspond in position to the biceps tubercle (Fig. 4.36B). The body of the coracoid has two main processes: the posteroventral process and an anteriorly projecting flange—the acrocoracoid process. The latter process is rounded in profile and its apex is thickened. There is a concavity in the edge of the coracoid separating this process from the posteroventral process. This notch is shallower than a similar feature present in the coracoid of *Heyuannia yanshini*. The posteroventral process curves strongly posteriorly. It tapers in transverse thickness towards all edges and the apex, except that the apex itself is thickened and bulbous.

Furcula—The furcula is excellently preserved (Fig. 4.36F–J), and is missing only the very distal ends. The hypocleidium is long and pointed, but is relatively gracile, especially compared to the robust hypocleidium of *Citipati osmolskae*. The entire furcula is gracile and its curvature follows a rounded V-shape (i.e. the epicleidal processes are not parallel). Each epicleidal process expands transversely to its midpoint, and then tapers again distally. At the midpoint, there is a ventral facet where the furcula contacts and rests upon the acromion process of the scapula (Fig. 4.36G, H). In lateral view, this facet invades the lateral edge of the bone, which accommodates the upturned lateral edge of the acromion. In articulation, the hypocleidium of the furcula extends nearly to the acrocoracoid process of the coracoid, but a relatively large, lens-shaped triosseal fenestra remains.

Sternum—Both sternal plates are partly exposed in MPC-D 102/110.a, but not in the other individuals of MPC-D 102/110. The sternals are well preserved in MPC-D 100/33 (Fig. 4.36K, L), but were difficult to observe because they were mounted behind glass at the time of observation. The sternal plates are not fused along the midline and their posterior ends are separated. The sternocoracoidal process and lateral trabecula are both well-developed and are

separated by an incised notch. Whereas the sternocoracoidal process is pointed in MPC-D 102/110.a, it is rounded and bulbous in MPC-D 100/33, possibly the result of older age and increased ossification. At least one foramen consistently pierces the sternal plate, but its position varies. In MPC-D 100/33, it is closer to the sternocoracoidal process (Fig. 4.36K, L), whereas in MPC-D 102/110.a, it is further medially, near the midline, and consists of two foramina. The right sternal of MPC-D 100/33 has a large fenestra near the center of the plate (Fig. 4.36K). It is possible that this is pathological, but it could also be the result of variable ossification of the plates. Unfortunately, the detailed examination necessary to support these hypotheses was not possible.

Forelimb:

The right forelimb of MPC-D 100/33 is completely preserved, although it appears to be either missing phalanx III-1 or this element had not ossified. The left forelimb is represented by the humerus, ulna, and radius, but the carpals, metacarpals and ungual II-3 are missing. The right humerus, ulna, radius, and manus of MPC-D 102/110.a are exposed, as is the left manus. Only the left ulna, radius, and manus of MPC-D 102/110.b are visible, although it is likely that the right forelimb is preserved under the body of MPC-D 102/110.a. The quarry of MPC-D 102/12 was revisited in 2018 and a manual ungual I-2 was recovered, but otherwise the forelimb of that individual is unknown.

Humerus—Both humeri of MPC-D 100/33 are well preserved and identical in size and shape. The humeral head is modestly developed (Fig. 4.37A, C), but does protrude slightly from the shaft. It is anteroposteriorly thin and appears more like a crest than a condyle. The proximal end is roughly parallelogram-shaped in proximal view (Fig 4.37E). On the posterior side of the

humerus, the articular surface overhangs the surface of the rest of the bone. The deltopectoral crest extends distally from the lateral side of the head, which is anteriorly deflected. The crest thickens towards its apex, which is not downturned like in *Heyuannia yanshini*. The edge of the crest is rounded and slightly rugose on either side. The apex of the crest is just under half the length of the humerus (47%) from the proximal end. The anterior surface of the crest is concave, whereas the posterior surface has a plateau with a slightly depressed surface. The ridge outlining its anterior side has faint striations for muscle attachment, but there is no rugose mound like the one in *Heyuannia yanshini*. The depression is slightly triangular, tapering distally. The shaft of the humerus is almost perfectly cylindrical, but the anterior face is slightly flattened. There are no ridges of features on the shaft, which has less torsion and is more gracile than that of *Heyuannia yanshini*. The distal end is about as wide as the head and is roughly rectangular in distal view. The entepicondylar tuber is larger than the ectepicondylar tuber (Fig. 4.37A, F), but both are small compared to the large, anteriorly curving ones of *Heyuannia yanshini*. In MPC-D 100/33, the entepicondylar tuber is dorsally hooked but does not protrude more than the ectepicondylar tuber, which itself extends proximally as a rounded ridge. In *Heyuannia yanshini*, this ridge is large and extends far anteriorly to become wing-like. In MPC-D 100/33, the medial side of the condyle is swollen and larger than the lateral side; the opposite is true in *Heyuannia yanshini*.

Ulna—The ulnae and radii of MPC-D 100/33 and MPC-D 100/110.a,b (Fig. 4.37G, H) are preserved, but those of MPC-D 100/33 were mounted and unavailable for detailed examination. The ulna is robust, expanding towards both the proximal and distal ends. The proximal end has a tall, bulbous coronoid process but a poorly developed olecranon, so that the socket for the humerus is poorly pronounced. The shaft tapers in dorsoventral thickness to the

distal end, where it instead becomes transversely broad. The distal end of the ulna is crescentic in outline, with a distinct medial process, similar to the one in *Heyuannia yanshini*.

Radius—The radius is also robust (Fig. 4.37G, H), but is only half the thickness of the ulna throughout the shaft. Its proximal end is square and about the same dimensions as the shaft. A slight ridge extends distally from the ventromedial edge, probably to accommodate the interosseum membrane. The distal end is expanded but does not appear to have a styloid process; however, this region is broken in MPC-D 100/33 and not visible in MPC-D 102/110.

Carpals—The carpals (Fig. 4.38) of the left hand of MPC-D 102/110.a are incredibly well preserved, and provide considerable information on the homology and development of the oviraptorid carpals. The radiale is the most proximal carpal (Fig. 4.37G, H), but it differs in shape from the angular, trapezoidal radiales of most theropods. Instead, it is more rounded and essentially featureless, although it is slightly wedged dorsally (Fig. 4.38H–M). The semilunate carpal (Fig. 4.38A–G) is the largest of the wrist and it covers the proximal ends of metacarpals I and II. It is roughly dumbbell-shaped, with a flat distal surface and a rounded proximal surface. Its proximal surface forms a distinct trochlea, with which the radiale and the crescentic distal end of the ulna articulate. The dorsal side of the trochlea is slightly smaller than the ventral side, but both are semicircular in lateral view. The flat distal side of the semilunate carpal is divided into two distinct faces separated by a shallow ridge (Fig. 4.38F). The medial face would have articulated with metacarpal I, although it did not overlie its entire proximal surface (Fig. 4.38B, D, E). The lateral facet for metacarpal II is concave, and in this depression sit two miniscule carpals, which are closely appressed if not fused (Fig. 4.38F, G). The larger of these is roughly triangular, and the smaller one is spherical. These carpals would have separated the proximal ends of the metacarpal I and metacarpal II in life (Fig. 4.38B). It is likely that these two minute

carpals represent the vestiges of the intermedium and ulnare, which typically lie lateral to the semilunate carpal and cover the proximal ends of metacarpals II and III. In this case, the larger element is more likely to be the intermedium, whereas the smaller element is the ulnare (Fig. 4.38F, G). It is likely that as the third digit was reduced and the carpal region simplified by expansion of the semilunate carpal, these carpals migrated to their present position and were reduced. Whereas previous work has suggested that one or more of these carpals are missing in oviraptorids (Osmólska et al., 2004a; Balanoff and Norell, 2012a) but present in caenagnathids (Zanno and Sampson, 2005), their presence in MPC-D 102/110.a suggests they may not be detectable unless the wrist is entirely disarticulated.

Manus—The manus of MPC-D 100/33 and MPC-D 102/110 are well preserved. The compete left hand of the latter specimen was disarticulated and provides detailed information on the elements (Fig. 4.39). Metacarpal I is roughly rectangular (Fig. 4.39A–F). The proximal end is kidney-shaped in proximal view (Fig. 4.39E), with a convex medial side and a concave lateral side. It is inclined so that the medial side reaches further proximally. The lateral side of the metacarpal has a concavity (Fig. 4.39E), which is deeper proximally, to accommodate metacarpal II. The edge of this concavity prevents metacarpal II from reaching the ventral surface of the metacarpus in life. In distal view, the distal end of the metacarpal is roughly rectangular, but with a deep notch in its medial side. The lateral condyle is larger than the medial one, and both are transversely constricted about halfway up their height (Fig. 4.39F). The condyles are only weakly ginglymoid and almost straight in mediolateral view. Manipulation of phalanx I-1 with the condyles of metacarpal I results in a restricted range of motion when the condyles are kept in full contact. Phalanx I-1 is the largest of the hand (Fig. 4.39T) and exceeds metacarpal I in length. Its proximal articular surface is relatively flat, rather than deeply

excavated, which contrasts with most theropod manual phalanges. In dorsal view (Fig. 4.39B), the shaft curves slightly medially. The collateral ligament pits are relatively shallow but the medial one is deeper, and the medial condyle is larger than the lateral one. The ungual I-2 is strongly recurved and has a well-developed flexor tubercle (Fig. 4.39A, D). The proximal articular surface lacks a proximodorsal lip, and there is no groove between it and the rounded flexor tubercle. The vascular grooves are shallow and the lateral one is positioned further dorsally.

Metacarpal II is the longest of the hand (Fig. 4.39T), but is about half the transverse width of metacarpal I. Its proximal end is strongly compressed mediolaterally, and sits entirely within the concavity on metacarpal I. The shaft is straight and cylindrical, lacking any ridges or grooves. The medial condyle is slightly larger than the lateral one (Fig. 4.39L), but this disparity is not as great as in metacarpal I. When articulated with the first metacarpal, metacarpal II is deflected laterally (Fig. 4.39T). Phalanx II-1 is small, about half the length of phalanx I-1, but subequal in length to II-2. It is transversely compressed and minimally ginglymoid. The collateral ligament pits are shallow. Phalanx II-2 is more gracile than phalanx II-1, but overall similar in shape and size. Ungual II-3 is relatively straight and has a poorly developed flexor tubercle. Like ungual I-2, it lacks a proximodorsal lip, but it has a more poorly developed proximal articular surface. The flexor tubercle is small and just dorsal to it there is a foramen on the lateral side.

Metacarpal III is diminutive and unusual in morphology (Fig. 4.39M). Its proximal end is tongue-like and deflected laterally. In articulation, it does not reach the carpus (Fig. 4.39T). The shaft is transversely compressed and less than half the transverse diameter of metacarpal II. The distal end is unusual for an oviraptorosaur, and indeed any theropod. The condyle is bulbous and

spherical, rather than being divided into a true trochlea, and is overhung by a dorsal process (Fig. 4.39M). In articulation, this restricts the mobility of phalanx III-1 to mild flexion. Phalanx III-1 is also unusual. It is exceptionally small, less than 1 cm in length, and has poorly developed articular surfaces (Fig. 4.39M–S). Whereas the proximal articular surface is conventional, the distal end is blunted and transversely convex (Fig. 4.39S). As a result, there is no distal articular surface, which starkly contrasts with the condition in all other oviraptorids. This suggests that digit III of the manus was comprised only of the metacarpal and a single phalanx. This is supported by the absence of any more distal phalanges in all three hands visible in MPC-D 102/110, despite preparation from fresh matrix and the preservation of delicate elements like sclerotic plates. The combined length of metacarpal III and phalanx III-1 in articulation does not exceed the length of metacarpal II (Fig. 4.39T), so it is unlikely that the third digit would have protruded from the manus in life.

Pelvic Girdle:

The pubes, ischia, and some parts of the ilium are visible on MPC-D 102/110, but are best seen in MPC-D 102.11, where they are exquisitely preserved (Fig. 4.40). All six bones of the pelvis are complete in MPC-D 102/11 (Fig. 4.27I), but the right ischium is broken into two pieces. The pubes and ischia of MPC-D 100/33 are preserved, but the ilia are missing. The right ilium and left ischium of MPC-D 102/12 are known.

Ilium—The ilium (Fig. 4.40) is dolichoiliac and the preacetabular and postacetabular blades are nearly equal in length, thought the postacetabular blade is slightly longer. The two ilia diverge posteriorly, and do not contact dorsally, as the neural spines of the sacrum extend past the dorsal margins of the ilia (Fig. 4.40A). The preacetabular blade has a rounded anterior

margin, and is expanded anteroventrally anterior to the cuppedicus fossa. This anteroventral

process is rounded and extends ventrally level with the dorsal margin of the acetabulum. The

cuppedicus fossa is shallow, though posteriorly its medial border is demarcated by a sharp dorsal

ridge. The pubic peduncle extends slightly further ventrally than the ischial peduncle, though it is

equal in length anteroposteriorly to the narrow ischial peduncle. The pubic peduncle has a

flattened ventrally-facing surface where it meets the pubis, to which was not fused or coossified

in MPC-D 102/11 or MPC-D 102/12. There is no supracetabular crest, but there is a bulge above

the ischiadic peduncle, which probably represents a poorly developed antitrochanter. The

ischiadic peduncle is triangular in lateral view and projects laterally past the lateral surface of the

iliac blade. The brevis fossa is modestly developed and short, extending anteriorly about halfway

as far as the base of the ischial peduncle. The brevis shelf is unique amongst oviraptorosaurs in

that it is not continuous with the ischiadic peduncle (Fig. 4.40E, G). Instead, the brevis shelf is

short and the postacetabular blade has an extra posterodorsally inclined ridge, separated from the

brevis shelf by a groove (Fig. 4.40E, G). This unique morphology is clearly demonstrated in

MPC-D 102/11 and MPC-D 102/12, but is absent in all other oviraptorosaurs. The dorsal margin

of the ilium is nearly flat from the preacetabular blade to the anterior margin of the brevis fossa,

where it tapers dorsoventrally. The postacetabular blade is squared off posteriorly, as in most

oviraptorids.

Pubis—The pubis (Fig. 4.41) is strongly curved anteriorly, a feature shared with all other

oviraptorids. When articulated (Fig. 4.27I), the pubis extends anteriorly far past the anterior

margin of the ilium. The iliac and ischiadic contacts of the pubis are widely separated by the

rounded margin of the acetabulum. The iliac contact is long anteroposteriorly, with an anterior

process, and wide transversely. The ischiadic contact is oriented vertically, and is tall

dorsoventrally but very narrow transversely. It protrudes posteriorly from the shaft of the pubis, and is offset ventrally from the shaft by a square notch. Medial to the ischiadic contact, there is a shallow concavity that lacks the posterior circumscription of caenagnathids (Sullivan et al., 2011). The shafts of the pubes are separated by a transversely narrow pubic apron (Fig. 4.41A, B). Ventral to the pubic apron there is a long oval fenestra separating the shafts of the pubes before they converge again at the symphysis. Even in MPC-D 102/11, the pubic symphysis is fused, but there are grooves both dorsally and ventrally where the pubes meet and a wide anterior cleft separating the pubes. The pubic boot is longer anteriorly than posteriorly (Fig. 4.41C, F).

Ischium—The ischium is long, gracile, and concave posterodorsally (Fig. 4.42). There is a proximal groove that separates the pubic and iliac contacts, which represents the minimal involvement of the ischium in the acetabulum. The pubic contact is pitted and rugose, indicative of a cartilaginous element separating it from the pubis. The anterior margin of the obturator process is gently convex, curving towards the apex. This contrasts with the concave anterior edges of the ischium in caenagnathids. The obturator process is more than halfway down the shaft of the ischium, and forms a square point. The obturator process is thin and delicate, and is broken in both MPC-D 102/11 and MPC-D 102/12, although it is completely represented in the former. The ischia of both individuals of MPC-D 102/110 are excellently preserved, but they differ slightly in morphology. Whereas the shapes of the ischia of MPC-D 102/110.a are identical to those of MPC-D 102/11, MPC-D 102/12, and MPC-D 100/33, those of MPC-D 102/110.b differ. This individual has a deep notch in the ventral edge of the ischium (Fig. 4.42B), separating the obturator from the distal end. Although this is incipiently developed in the other specimens, in MPC-D 102/110.b it is about three times as deep. It is important to note that

this individual also has dimorphic chevrons, and therefore these elements may differ for the same reasons.

Hindlimb:

Femur— The femora are complete in MPC-D 102/110, but are not fully exposed. Both femora are preserved in MPC-D 102/11, but the right femur (Fig. 4.43A–E) is more complete than the left, which is represented by only the proximal half. The right femur lacks the medial side of the distal end, though the lateral condyle is present, so length can be estimated. The femur of MPC-D 102/12 is complete but badly damaged and communited (Fig. 4.43F–K). The femora of MPC-D 100/33 are both well preserved but could not be observed because they were mounted. The femoral head is directed medially and has only a slightly constricted neck. The anterior face of the head is continuous with the neck, but the posterior edge projects posteriorly past the surface of the neck. In medial view (Fig. 4.43C, H), the posterodorsal corner of the femoral head is depressed and the anterodorsal corner is more bulbous. There is no rugosity for the capitate ligament, although this area is damaged in the larger MPC-D 102/12. The greater trochanter is broadly curved, but does not extend far above the neck of the head. It does not form a crest, but rather a rounded mound. The lesser trochanter is narrow and fingerlike, appressed to the anterior surface of the greater trochanter throughout its length (Fig. 4.43A, F). However, there is a small cleft between these structures proximally, which continues into a short groove distally. The shaft of the femur is cylindrical and curved anteriorly. It lacks a fourth trochanter and instead there is a posteromedially located patch of rugose bone for *m. caudofemoralis*. Distal and lateral to this, there is a dorsolateral to ventromedially inclined muscle scar just above the popliteal fossa. The lateral surface of the femur has no obvious muscle scars, but there is a slight

mound just ventral to the greater trochanter, which continues distally as a posterolateral ridge. The anterior surface of the shaft has a long muscle scar that extends distally from the lateral groove of the lesser trochanter to just distal to the level of the insertion of *m. caudofemoralis*. This scar twists from the lateral side of the shaft to the medial side. On the distolateral part of the anterior surface, there is a pronounced rugosity with a mounded border. The popliteal fossa is very deep compared to most oviraptorids (Fig. 4.43I), but is not overhung by the crista tibiofibularis, which is the case in *Rinchenia mongoliensis*. The crista tibiofibularis is divided by a deep notch, separating the more bulbous fibular condyle from the larger tibial condyle. The ectocondylar tuber is mounded and rugose, and appears to become larger through ontogeny.

Tibia—Like the femora, the tibiae of MPC-D 102/110 are intact but not completely visible. The left tibia of MPC-D 102/11 (Fig. 4.44J, K) is missing its proximal end, but the right tibia is completely preserved in articulation with the fibula, tarsals, and complete foot (Fig. 4.26H). The right tibia and fused astragalocalcaneum are preserved with MPC-D 102/12 (Fig. 4.44), and both tibiae were recovered for MPC-D 100/33, but were not available for examination. The cnemial crest is proximodistally short but is relatively well pronounced. It is only slightly everted laterally, and its apex is at its ventral end, rather than the dorsal edge as in ornithomimids. The fibular condyle has two main lobes, separated by a narrow groove into which the fibula inserts. The posterior lobe is larger than the anterior one. These two lobes are separated from the posterior surface of the femoral condyle by a notch. In MPC-D 102/12, the fibular condyle and femoral condyle coalesce external to this notch, leaving a circular tunnel (Fig. 4.44B). The main portion of the femoral condyle is kidney shaped in proximal view, and extends further proximally than the fibular condyle. The fibular crest is poorly defined but is thick and rugose, rather than platelike (Fig. 4.44A, D). Posterior to the fibular crest there is a

shallow groove, but it is not continuous with the large nutrient foramen that opens dorsally. The shaft of the tibia has a flat anterior surface, but there is a slight ridge at the distal end of the shaft, near the ascending process of the astragalus. The posterior surface of the tibia is rounded but the apex of the curvature is more medially located. The result is that the anteromedial corner of the tibia is sharp, whereas the lateral corner is more rounded. There is no facet or groove for the fibula, instead it rests upon the rounded lateral corner of the tibia. The anterior side of the distal end is obscured by the overlying astragalocalcaneum in each specimen, but it is clear that the medial malleolus protrudes anteromedially to create a bowl into which the astragalus fits (Fig. 4.44C). The lateral malleolus is posteriorly deflected and has a modest postfibular flange that does not extend far proximally.

Fibula—Fibulae (Fig. 4.44E–G) from each specimen are preserved. Unlike conventional reconstructions, each of the articulated fibulae is oriented with the broadest portion of the head oriented transversely, rather than anteroposteriorly. The head is concavoconvex and crescentic in dorsal view, with a larger lateral portion than medial portion. The medial part of the head is fingerlike in proximal view, whereas the lateral side is bulbous, which results in a central groove extending to a fossa on the posterior face. The lateral edge of the fibula distal to the head is sharply attenuated to a ridge (Fig. 4.44G), and this continues distally to become the lateral edge of the shaft. Distal to the head, the shaft thickens and has a thick, rugose anteromedial ridge. This ridge lies adjacent to the fibular crest on the tibia, and likely accommodated the interosseum membrane. The remainder of the fibular shaft is slender and concavoconvex, with the concavity oriented towards the tibia. The distal end has a bulbous head and curves slightly posteriorly. It appears to be separated from the calcaneum in each specimen, although this may vary depending on the position of the leg.

Astragalocalcaneum—The astragalus (Fig. 4.44H, I) is obscured in MPC-D 102/110 and the right foot of MPC-D 102/11 by the overlying feet, but is exposed in MPC-D 100/33 and MPC-D 102/12. The medial condyle is much larger than the lateral one, and its medial surface is inclined to fit onto the medial malleolus of the tibia. The condyle is anteroposteriorly thin, which contrasts with the robust condyles of caenagnathids and some other oviraptorids. There is a concavity at the base of the ascending process that has a pronounced anterior lip (Fig. 4.44I). Distal to this, there is a fossa in the anterolateral part of the intercondylar space. On the distal surface of the astragalus, there is another depression in the intercondylar sulcus. The posterior edge of the astragalus is relatively straight, rather than curved. The lateral condyle has a sinuous anterolateral edge, which overhands the calcaneum dorsally but is excavated by it ventrally. The ascending process covers the entire surface of the tibia at its base, and extends at least 30% of the length of the tibia. The lateral edge of the ascending process is vertical, whereas the medial edge inclines proximolaterally to give the ascending process its taper. The calcaneum is unfused in the smaller specimens (MPC-D 102/11, MPC-D 102/110, and MPC-D 100/33), but it is fused in MPC-D 102/12 (Fig. 4.44H), which suggests that it fuses through ontogeny (see section 4.4.2). The calcaneum is kidney-shaped, with the convex side facing anteriorly. Its lateral surface is concave, surrounded by a transversely thickened circumferential lip. The calcaneum is thicker at its anterior end than its posterior side.

Distal tarsals—Distal tarsals III and IV (Fig. 4.45) are preserved with each specimen. Distal tarsal III is roughly trapezoidal, and, as in all oviraptorosaurs, thickens towards its posterior side. It covers the posterior half of metatarsal III in proximal view (Fig. 4.45A, B), but even in the mature MPC-D 102/12, it does not expand anteriorly. However, although it covers only metatarsal III in MPC-D 102/11 and MPC-D 102/110, it has expanded medially in MPC-D

512

102/12 to cover the posterolateral corner of metatarsal II. In MPC-D 102/11, the posterior edge of distal tarsal III is rounded, whereas it becomes more square and much thicker through ontogeny in MPC-D 102/12 (Fig. 4.45A, B). In this individual, it has also begun to fuse to metatarsal III (Fig. 4.45C), which resembles the condition in some derived caenagnathids (*Elmisaurus rarus* and *Leptorhynchos elegans* Parks (1933)). The medial side of distal tarsal III is rounded and bulbous. Although this is also the case for the lateral side in MPC-D 102/11, in the older MPC-D 102/12, the lateral edge is straight where it abuts—but does not fuse to—distal tarsal IV.

Distal tarsal IV is circular except for a rounded process extending from the lateral side (Fig. 4.45A, B). This process is likely homologous with the proximodorsal process of caenagnathids. Although oviraptorids generally lack a well-developed process here, the distal tarsals are typically poorly described, and so this feature may be more prevalent. The distal tarsal is disc-shaped and both sides are equal in thickness, but it tapers in thickness towards each edge. The lateral process is bulbous and thicker than the neck leading to it. In MPC-D 102/12, this process has become greatly enlarged and projects dorsolaterally (Fig. 4.45B, D), more closely resembling the proximodorsal process of caenagnathids. Furthermore, instead of remaining circular and disc-like, the fourth distal tarsal of MPC-D 102/12 is thickened posteriorly and has a straight medial edge where it meets distal tarsal III (Fig. 4.45B).

Pes—Both feet (Fig. 4.46) are preserved in their entirety in all specimens except MPC-D 102/12, which preserves only the right metatarsus, metatarsal III from the left side, and a single phalanx III-1 from the right. All five metatarsals are represented in most specimens, but the feet of MPC-D 102/11 appear to lack metatarsal V. It is possible it was disarticulated during

preparation and is represented by indeterminate splint-like bones accessioned with the specimen. Alternatively, metatarsal V may not have ossified yet in this individual.

Metatarsal I has a flat shaft and a small condyle (Fig. 4.46B, D, G). The shaft has a triangular proximal process and a tablike posterior process. The lateral side is flat, whereas the medial side is rounded. The condyle is roughly triangular in distal view, with a narrower anterior side. The medial ligament pit is shallow and small, and the lateral one is large and deep. The posterior side of the condyles each have a small ridge, separated by a small depression. Phalanx I-1 is about the same length as the metatarsal and ungual. The proximal articular surface is inclined to face dorsomedially and is deeply concave. The shaft of the phalanx twists laterally and slightly dorsally. The condyle is narrow and the medial ligament pit is shallow but equal in size to the lateral one. Ungual I-2 is small and relatively straight, except for a slightly hooked tip. The proximal surface is crescentic and there is only a slight transverse constriction distal to it. The flexor tubercle is poorly developed. The medial and lateral grooves are poorly developed but the lateral one is deeper and slightly further dorsal.

Metatarsal II (Fig. 4.46) is the shortest of the weight-bearing metatarsals, but has a large proximal end. The proximal end is trapezoidal in proximal view, with the wider side facing metatarsal III and inclined about 50° mediolaterally. The shaft tapers from the proximal end but is consistent in thickness throughout most of its length. It is thicker than the other metatarsals anterioposteriorly but equal to metatarsal IV in transverse breadth. There is an incipient posteromedial ridge, but it is not well developed in the smaller specimens. In MPC-D 102/12, this ridge becomes larger and has a rugose surface. The proximal end of II-1 is inclined dorsomedially in proximal view. There are two ridges on either side of its ventral edge. The shaft of the phalanx is slightly curved laterally. The condyle is not ginglymoid and there is a large

depression on the dorsal surface. The medial ligament pit is shallow, but the lateral one is deep. Phalanx II-2 is relatively symmetrical, but the proximal end is slightly skewed laterally. The phalanx is about half the length of phalanx II-1. Ungual II-3 is the largest ungual of the foot, but is only slightly larger than ungual III-4. The former is dorsoventrally deeper but slightly shorter in length. The flexor tubercle is weak and the claw is modestly recurved.

Metatarsal III is the longest of the foot (Fig. 4.46B, G) and the widest at its distal end. Its proximal end is wider than the other two metatarsals posteriorly, but it is anteriorly pinched— albeit not to the same degree as in caenagnathids. The proximal end is therefore triangular in proximal view, with a flat posterior edge. There is a flattened shelf on the posterior surface of the head (Fig. 4.46B, H) reminiscent of the posterior protuberance of *Elmisaurus rarus,* but much smaller. This raised area is continuous with similar platforms on metatarsals II and IV. The shaft of metatarsal III is square in cross section, with sharp posterior corners and flat sides. The distal condyle is asymmetrical, with a larger medial condyle than lateral condyle. The postcondylar ridges are well developed but end abruptly, rather than continuing proximally. Digit III is the longest and widest (Fig. 4.46B, G). Phalanx III-1 has a semicircular proximal face with two poorly developed ventral ridges. The shaft and condyle are symmetrical. The condyle is more ginglymoid than the phalanges of digit II and the collateral ligament pits are equal in depth. The more distal phalanges are virtually identical to phalanx III-1 in morphology, but they are each about 30% shorter than the previous one. Ungual III-4 is the longest of the foot but is more gracile than II-3. It is nearly perfectly symmetrical, including equally deep vascular grooves positioned equally far dorsally. The flexor tubercle is small, but larger than that of ungual II-3, and the claw is slightly more recurved than the latter.

Metatarsal IV (Fig. 4.46) has a large, semicircular proximal end in proximal view, with the flat edge against metatarsal III. The raised posterior area is triangular with a 45° inclination to the dorsal edge. The shaft of the metatarsal is compressed anteroposteriorly so that it is wider than deep. There is no sign of a posterolateral ridge in the smaller specimens, but in MPC-D 102/12 there is a rugose patch on the posteromedial side. The condyle of is not deflected laterally and the lateral condylar ridge is small. The lateral ligament pit is relatively shallow. Digit IV is about equal in length to digit II, including the unguals. Phalanx IV-1 is wider distally than proximally. It has a deeply concave, triangular proximal end. The shaft is directed slightly medially. The other phalanges are short, with barely any shaft separating the proximal and distal condyles. These phalanges are symmetrical except for a slight lateral skew to the proximal articular surfaces. Ungual IV-5 is small and straight with a weak flexor tubercle and greater transverse constriction than the other unguals. The medial vascular groove is deeper and more dorsally positioned.

Metatarsal V is missing in MPC-D 102/11 (Fig. 4.46), either as a result of preparation or poor ossification, and in MPC-D 102/12, likely because it was lost before collection. In the other specimens, it is a tapering splint tightly appressed to the posterolateral surface of metatarsal IV. Its proximal end is expanded and rounded. The shaft curves slightly anteriorly, but not to the same degree as in caenagnathids like *Chirostenotes pergracilis* Gilmore 1924. The distal end has a small bulb at its apex, but is otherwise simple. Its absence in MPC-D 102/12 suggests that it never fused throughout ontogeny, unlike in derived caenagnathids (*Elmisaurus rarus* and *Leptorhynchos elegans*), where it fuses to the proximodorsal process of distal tarsal IV.

Osteohistology:

MPC-D 102/11—The femur and fibula of MPC-D 102/11 differ in the degrees of secondary remodeling, but both lack any lines of arrested growth. The femur (Fig. 4.47E, F) is entirely composed of primary fibrolamellar bone with no secondary osteons. Vasculature is primarily arranged longitudinally, although there are some regions of reticular vasculature. A zone of parallel-fibered bone occurs towards the periosteal surface of the bone. This zone is similar to a growth mark described in a caenagnathid tibia from the Horseshoe Canyon Formation of Alberta (Funston and Currie, 2018), and likely represents the same phenomenon. The fibula has considerably more secondary remodeling than the femur, but it is still predominantly primary bone. On the lateral side, the cortex is mostly remodeled, except for a region of primary bone near the periosteal surface that has numerous Sharpey's fibers. On the medial side, there is primary osteonal bone towards the endosteal surface and avascular parallel-fibered bone near the periosteal surface. The medullary cavity and endosteal lamellae are both well developed. Like the femur, there is an annulus developed towards the periosteal surface that probably represents the first growth mark. Based on these data, MPC-D 102/11 is best regarded as a young juvenile approximately one year of age.

MPC-D 102/110.a—The fibula of MPC-D 102/110.a (Fig. 4.47A, B) is composed mostly of primary fibrolamellar bone, but there are some secondary osteons on the medial side. The medullary cavity is small but has defined edges and in some places there are endosteal lamellae. There are no obvious zones of parallel-fibered bone or lines of arrested growth. Towards the periosteal surface on the anterior side of the fibula there is a region of reduced vasculature, but no obvious annulus is present and this zone cannot be traced around the entire cortex. It is unlikely that a growth mark has been obscured by secondary remodeling because secondary osteons are sparse and primary bone is visible between them. The predominance of

primary bone and absence of a growth mark suggest this individual is a young juvenile, but no age assessment can be made.

MPC-D 102/110.b—Two fragments of the fibula of MPC-D 102/110.b (Fig. 4.47C, D) were sectioned and both have similar histological texture. Neither fragment shows the medullary cavity. Both are composed predominantly of primary fibrolamellar bone, but each has some secondary osteons endosteally. Vasculature is mostly longitudinal, but there are some small zones of reticular canals. Near the periosteal surface there is a zone of avascular, parallel-fibered bone similar to MPC-D 102/11. It likely represents the first growth mark, although no distinct rest line is visible. Like MPC-D 102/11, this specimen was likely a young juvenile approximately one year of age.

MPC-D 102/12—The fibula and a fragment of the femur (Fig. 4.47G, H) were sectioned. The fibula has more secondary remodeling, and therefore some of the growth record has been erased. The medullary cavity is well formed and lined by multiple generations of endosteal lamellae. Several other cavities also excavate the cortex; these are separated by trabeculae or endosteal lamellae. Vasculature is longitudinally oriented, and towards the medial surface these canals are arranged into circumferential rows. At least three lines of arrested growth are recorded on the medial surface, but it is likely that more have been obscured by secondary remodeling and expansion of the medullary cavity.

The femur (Fig. 4.47G, H) exhibits less secondary remodeling, all of which is concentrated in a vertical column extending perpendicular to the periosteal surface. The primary bone in this column contains larger, more densely packed osteocyte lacunae, and well-developed Sharpey's fibers towards the periosteal surface. Accordingly, it likely represents a zone of muscle insertion. A small strip of endosteal lamellae marks the edge of the medullary cavity,

518

indicating that the entire cortex is preserved. Vasculature changes from predominantly reticular endosteally through plexiform towards a zone of parallel-fibered bone about halfway through the cortex. A faint cement line is visible within this zone of parallel-fibered bone, indicating that it represents a growth mark in the form of an annulus. External to this annulus, vasculature is laminar and decreases towards the periosteal surface. At least four more annuli are visible in the external part of the cortex, decreasing in spacing periosteally. Whereas a zone of fibrolamellar osteonal bone separates the first, second, and third annuli, the spaces between the third, fourth, and fifth annuli are composed of parallel-fibered bone. This forms a continuous band of parallel-fibered bone on the periosteal surface of the cortex. Although no distinct lines of arrested growth can be distinguished in this area, it is likely that it represents an incipient external fundamental system. In any case, the dominance of parallel-fibered bone at the periosteal surface indicates that this individual was growing slowly. The presence of five annuli and the low growth rate suggest that this individual was an adult at least five years old and was approaching maximum body size.

Remarks

The specimens of this new taxon provide a wealth of information about the anatomy, behaviour (see Chapter 5: section 5.2), and ontogeny (see section 4.4.2) of oviraptorids. The assemblage of at least three skeletons indicates that this taxon was gregarious (Fig. 4.48), which has not been previously reported in oviraptorids (see Chapter 5: section 5.2).

Although the skull and cranial crest superficially resemble those of *Rinchenia mongoliensis*, the details of their composition and morphology differ considerably. For example, the cranial crest of *Rinchenia mongoliensis* lacks the apical thickening of the Guriliin Tsav

519

oviraptorid, which itself lacks the interfingering contact of the jugal and quadratojugal, and has a greater contribution of the premaxilla to the palate. The skull of the Guriliin Tsav oviraptorid has a much smaller infratemporal fenestra, so that the region of the skull posterior to the orbit is shorter anteroposteriorly than the preorbital region. This is not the case in *Rinchenia mongoliensis*, where the preorbital region of the skull is shorter than the postorbital region. The postcrania of the Guriliin Tsav oviraptorid also contrast with the morphology of other oviraptorids. The arm is reduced in length compared to the femur, and the manus is distinctive in the highly disparate sizes of the metacarpals and digits. The extreme reduction of the third digit contrasts with other oviraptorids, which retain all three phalanges of this digit and the ungual. The pelvic girdle is fairly typical for an oviraptorid, but the ilia have an accessory ridge anterior to the brevis fossa, unlike other oviraptorids where the brevis shelf is continuous with the ischiadic peduncle. The ischium itself is elongate and relatively straight, which contrasts with the more curved ischia of *Citipati, Conchoraptor,* and *Heyuannia.* The fourth distal tarsal has a distinctive lateral bulb that, through ontogeny, becomes upturned into a small proximodorsal process. This structure has not been reported in other oviraptorids, although distal tarsals are rarely described in detail.

Some new insights about the homology of the carpals can be made from the new specimens. The discovery of small ossifications distal to the semilunate carpal reveal that the homologues of the ulnare and intermedium were preserved in oviraptorids, but may have been highly reduced. The radiale is retained but simplified in the Guriliin Tsav oviraptorid, appearing closer to spherical than the triangular or trapezoidal radiales of other oviraptorosaurs. These simplifications of the carpal region may have been adaptations for enhanced flexibility, as they create a ball-and-saddle joint between the semilunate carpal and radiale that would allow

considerable flexion of the wrist. Alternatively, they may have been the result of general reduction of the forelimb, indicating reduced reliance on its functionality. The latter hypothesis may also be supported by reduction of the lateral digits in heyuannines (see Chapter 5: section 5.4), resulting in greater disparity of the digits and eventual loss of the third digit (as is the case in the Guriliin Tsav oviraptorid). However, most heyuannines retain and even expand the deltopectoral crest, indicating strong musculature of the forelimb, which conflicts with this hypothesis. It is possible that these changes reflect a change to a function of the forelimb less reliant on manipulation with the digits and more focused on powerful retraction of the arm. One possibility is scratch-digging, either for foraging or nest-building, which might explain the shorter, more robust digit I with a trenchant ungual.

The osteohistological results allow the ontogeny of this new oviraptorid to be tied to particular developmental stages. Most of the specimens are juveniles, and although histological sections for MPC-D 100/33 are not available, its intermediate size and degrees of vertebral fusion suggest an intermediate ontogenetic stage between MPC-D 102/110 and MPC-D 102/12. The zone of parallel-fibered bone surrounding the femoral cortex of MPC-D 102/12 suggests that this individual had slowed its growth considerably and can be considered mature (Fig. 4.49). This supports fusion of the neurocentral sutures and pygostyle as external evidence of skeletal maturity. Expansion of the distal tarsals and their fusion to the proximal metatarsals may also be features of advanced age, but the absence of these characters in other large, presumably adult oviraptorids may indicate that they are diagnostic to this taxon.

<center>4.4 DISCUSSION</center>

4.4.1 Taxonomy and diversity of oviraptorids

  Taxonomy—The specimens described here clarify the taxonomy of Mongolian

oviraptorids, especially *Conchoraptor gracilis* and *Heyuannia yanshini*, the representative

specimens of which have been unclear in the past. In particular, the chimaeric museum mount of

the skull of *Conchoraptor gracilis* united with the skeletons of MPC-D 100/30–32 (*Heyuannia*

yanshini) led to confusion as to whether the skull pertained to *Heyuannia yanshini*, and what

elements were recovered with the type specimen of *Heyuannia yanshini*. The description here

clarifies which bones belong to which taxon and skeleton, and show that based on this

information MPC-D 100/33 is not a representative of *Heyuannia yanshini*, rather, it is the same

taxon as the Guriliin Tsav oviraptorid. This new taxon, as well as taxon represented by the skull

MPC-D 100/79-D, will be formally named and described in a future, more accessible

publication. The referral of these complicated specimens to their respective taxa is summarized

in Table 4.1.

  The description of postcrania for *Conchoraptor gracilis* should improve the identifiability

of more incomplete specimens, particularly with regards to discerning between *Conchoraptor*

gracilis and *Heyuannia yanshini*. Those taxa are distinguished by the manual proportions as well

as by features of the mandible and vertebrae. Description of the unusual postcrania of *Rinchenia*

mongoliensis should also improve its recognition in the future. These specimens reveal the

stereotypical anatomy of oviraptorids, which can be characterized by their tall mandibles with a

downturned dentary; a strongly curved pubis; a straighter ischium than caenagnathids; and a tail

<div align="right">522</div>

of more than 25 vertebrae tipped, at maturity, by a fused pygostyle of three unmodified vertebrae.

Diversity—Oviraptorids were diverse in the Late Cretaceous of the Nemegt Basin, and at least ten taxa (including the two unnamed taxa described here) are known from the Djadokhta, Baruungoyot, and Nemegt Formations. All of these taxa are distinguished by numerous characters of both the crania and postcrania, which makes it unlikely that they are the result of individual variation or ontogeny. The stratigraphic intervals represented by these formations are unclear, and some evidence suggests that they may overlap or grade into each other at certain localities. Although it is therefore possible that some of these taxa are anagenetic series, little evidence is available to test this hypothesis. One possible instance of anagenesis may be *Khaan mckennai* and *Conchoraptor gracilis*. However, some stratigraphic analyses find Ukhaa Tolgod, where *Khaan mckennai* is found, equivalent to the Baruungoyot Formation (Makovicky, 2008), where *Conchoraptor gracilis* is found, which does not support this conclusion. Another possible example may be *Citipati osmolskae* and the unnamed Dzamyn Khondt oviraptorid (MPC-D 100/42), which have consistently been recovered as sister taxa. However, whether Ukhaa Tolgod and Dzamyn Khondt are stratigraphically equivalent has not yet been determined, and it is possible that they are vicariant or peripatric species because they are in separate depositional basins.

In any case, the diversity of oviraptorids was much higher than other theropod families in their communities, and they were clearly successful components of these ecosystems. Some evidence suggests that oviraptorids preferred xeric conditions (see Chapter 5: section 5.3), but they were clearly abundant and diverse in the mesic environments of the Nemegt Formation. Four taxa are known from the Nemegt Formation (*Conchoraptor gracilis*, the Guriliin Tsav

oviraptorid, *Nemegtomaia barsboldi* and *Rinchenia mongoliensis*), compared to two in the

Baruungoyot Formation (*Conchoraptor gracilis* and *Heyuannia yanshini*). Whether the four taxa

in the Djadokhta Formation coexisted is unclear (Jerzykiewicz and Russell, 1991; Makovicky,

2008). How coexisting oviraptorids partitioned resources is unclear, as there is little variation in

their body sizes, mandible morphology, or other functional traits. It is possible that they were

spatially partitioned, because few taxa coexist at each locality, or that their limited distribution

reflects rapid species turnover (see Chapter 5: section 5.3 for more discussion).

4.4.2 Ontogenetic change in oviraptorids

The new specimens of *Conchoraptor gracilis* and the Guriliin Tsav oviraptorid provide

two growth series from which ontogenetic changes in the skeleton can be assessed. Whereas the

Conchoraptor gracilis specimens reveal changes in the proportions and structure of the skull, the

Guriliin Tsav specimens primarily show changes in the postcrania, especially the hindlimbs,

although they do reveal some aspects of cranial crest development.

Cranial ontogeny—The new juvenile skull (MPC-D NatGeo.2018.036a) is slightly

smaller than the material Lee et al. (2019) described as *Gobiraptor minutus* (= *Conchoraptor*

gracilis), and together they reveal the early ontogeny of *Conchoraptor*. In general, the

proportions of the skull change very little throughout ontogeny. In particular, the preorbital and

postorbital portions of the skull remain approximately equal throughout ontogeny when

measured along the base of the skull. However, the nasal process of the premaxilla expands

anteroposteriorly, resulting in a more vertical orientation of the anterior edge of the premaxilla.

This is accompanied by lengthening of the anterior midline process of the nasal, to form a more

distinct anterodorsal corner of the skull in lateral view. Another significant change in proportion

is that the skulls of MPC-D 100/20 and MPC-D 102/03 are much broader transversely than MPC-D NatGeo.2018.036a. This appears to be accomplished mostly by transverse expansion of the frontals and parietals, as the parietals change from tapering posteriorly to being uniform in thickness throughout their length. Furthermore, the nasals do not appear to expand transversely at the same rate as the frontals, and so they are narrower than the frontals in MPC-D 100/20, whereas they are about equal in transverse length to the frontals in MPC-D NatGeo.2018.036a. The sagittal crest becomes better developed through ontogeny, as it is absent in MPC-D NatGeo.2018.036a and present in the two larger specimens. However, in these latter specimens, it remains small and rounded, rather than becoming a sharp crest.

The juvenile specimens of the Guriliin Tsav oviraptorid (MPC-D 102/11 and MPC-D 102/110) show that cranial crests are developed early in ontogeny. This contrasts with interpretations by previous authors that cranial crests may have developed later in life (Wang et al., 2016). Although the adult morphology of the crest is unknown in the Guriliin Tsav oviraptorid, it is unlikely based on the observations in *Conchoraptor gracilis* that it would be considerably different in shape from those of MPC-D 102/11 and MPC-D 102/110.

Postcranial ontogeny—Ontogenetic changes in the forelimbs cannot be established for *Conchoraptor gracilis* because forelimbs of MPC-D NatGeo.2018.36 were only observable in the field, where they were not completely exposed. Some changes in the forelimb of the Guriliin Tsav oviraptorid can be noted between MPC-D 102/110 and MPC-D 100/33, although what ontogenetic interval this represents is uncertain. The humerus of MPC-D 100/33 is slightly longer relative to the femur than that of MPC-D 102/110.b, and the deltopectoral crest is longer relative to the humerus. The radius and ulna are consistent in relative length between the specimens, however. The proportions of the manus remain the same, except that manual ungual

I-2 is strongly positively allometric, increasing from 13% (MPC-D 102/110.a) through 17% (MPC-D 100/33) to 22% (MPC-D 102/12) of the length of the femur.

The excellent hindlimb material of the Guriliin Tsav oviraptorid allows for excellent quantification of ontogenetic trends. MPC-D 102/11 and MPC-D 102/12 are ontogenetic endpoints for this taxon, and their hindlimb proportions differ, both between the hindlimb segments and the bones themselves. The femur increases in relative minimum anteroposterior diameter throughout ontogeny, from 94% of the minimum mediolateral diameter in MPC-D 102/11 to 108% of the minimum mediolateral diameter in MPC-D 102/12—an increase of 14%. The same is true for the tibia and metatarsus, although these relative increases are much smaller (5.5% and 3%, respectively). In the femur and tibia, these changes are caused solely by an increase in minimum anteroposterior diameter through ontogeny, because minimum mediolateral diameter remains constant relative to the lengths of the femur and tibia. However, this is not true of the metatarsus, which increases in relative minimum width throughout ontogeny (by 2.5% of its length). This suggests that the anteroposterior expansion of the metatarsus is stronger than initially suspected, roughly equal to the change in the tibia. The proportions of the hindlimb bones to each other change throughout ontogeny as well. The tibia is reduced in length from 124% of the length of the femur to 117% the length of the femur, a reduction of 7%. The metatarsals also decrease in relation to the femur (59% to 56%), but not relative to the tibia. It appears, therefore, that the change in proportions of the metatarsus and tibia are more strongly linked to each other, and that the distal hindlimb segments change as a single unit relative to the femur throughout ontogeny. This may reflect constraints on limb morphology related to tail-driven locomotion (Benson and Choiniere 2013).

Other qualitative changes occur in the hindlimb throughout ontogeny, particularly relating to fusion of various elements. The astragalocalcaneum fuses throughout ontogeny, although the onset of this fusion cannot be determined because the astragalocalcaneum of MPC-D 100/33 is still unfused. In MPC-D 102/12, however, this fusion is relatively extensive and these bones are separated by only a few small gaps. However, the astragalocalcaneum and the tibia remain unfused throughout life, contrasting with the condition in avimimids. Similarly, the distal tarsals expand posteriorly and the lateral process of distal tarsal IV thickens proximodistally into a proximodorsal process. This process had begun in MPC-D 100/33, but it was not as advanced as in MPC-D 102/12. Regardless of their expansion and eventually extensive contact, the distal tarsals do not fuse to each other, unlike in *Elmisaurus rarus* (Currie et al., 2016) and *Leptorhynchos elegans* (Funston et al., 2016a). They do, however, begin to fuse to the proximal ends of the metatarsals, although even in MPC-D 102/12, a suture is visible between these bones. This condition has not been reported in any other oviraptorids, so it is unclear whether it is related to senescence in MPC-D 102/12, or if it is a unique feature of this taxon. The articular parts of the metatarsus increase in size throughout ontogeny, especially the distal condyle of metatarsal II. Muscle insertions on all of the hindlimb bones, especially the metatarsals, become more defined and rugose, but these apparently do not expand in size throughout ontogeny.

These results suggest that there is relatively little ontogenetic character change in oviraptorids, besides states of fusion, but that their proportions change throughout life. In contrast to the findings of Lü et al. (2013) that oviraptorid hindlimbs are isometric to body size, these ontogenetic series show that the hindlimbs do become relatively shorter and stockier throughout life. Regardless, this negative ontogenetic trend is not as pronounced as carnivorous

theropods (Currie, 2003), and, as suggested by Lü et al. (2013), supports other evidence of herbivory in oviraptorids.

4.4.3 Growth styles in oviraptorids

Osteohistological samples of the Guriliin Tsav oviraptorid provide information on the growth of this taxon and probably oviraptorids in general. The most complete growth record is preserved in the femur MPC-D 102/12 (Fig. 4.49), where at least five growth marks are preserved. The growth marks decrease in spacing towards the outside of the cortex, indicating a decrease in growth rate throughout life. Like in caenagnathids (see Chapter 3: section 3.4.3), there is a distinct inflection point after which growth is markedly slowed (Fig. 4.49). However, MPC-D 102/12 is unusual in that this inflection point occurs after just the second recorded growth mark. Although it is likely that expansion of the medullary cavity has erased some of the growth record, the earliest recorded growth mark occurs halfway through the cortex, which suggests that the previous growth interval was large. Measuring from the earliest growth mark to the edge of the medullary cavity, this growth interval would account for a femoral circumference increase of more than 2 cm, or approximately 24 kg. Considering that the final body mass of this individual was approximately 74 kg, a growth rate of at least 30% of adult body size in a single year is considerable. This pattern is more unusual when the growth records of MPC-D 102/11 and MPC-D 102/110 are considered. The femoral circumferences of these individuals are similar to the circumference estimated at the earliest recorded growth mark of MPC-D 102/12—between 35 and 45 kg. Regardless, these specimens do not show any growth marks in the interior of the cortex, although some do have a zone of parallel-fibered bone towards the periosteal surface. This zone of parallel-fibered bone probably records the same event as the zone of parallel-fibered

bone that precedes the first growth mark in MPC-D 102/12. This suggests that the large growth interval recorded in MPC-D 102/12 is a real phenomenon, also recorded in these other individuals. Without additional smaller specimens, the timing of this growth interval and the succeeding growth mark is uncertain. In any case, it is unlikely that this mark represents the first year of growth, and it is more likely that it is the second or third growth mark.

In light of this, the external signs of immaturity in MPC-D 102/11 and MPC-D 102/110 may provide useful milestones for assessing maturity in other oviraptorids. Each of these specimens lacks complete fusion of the sacral vertebrae, and only the three primordial sacral vertebrae are fused (Fig. 4.32). The sacrum of the similarly-sized MPC-D 100/33 has a fused dorsosacral vertebra, but the two caudosacral vertebrae remain unfused (Fig. 4.32). Consolidation of the sacrum may therefore begin with the dorsosacral vertebra at about 50% of maximum body mass and proceed to the caudosacral vertebrae later in ontogeny. The neurocentral sutures of all but the most distal fifteen caudal vertebrae of MPC-D 102/11 are open, whereas some of the more proximal caudal vertebrae of MPC-D 100/33 have begun to fuse the neurocentral suture (although their exact positions cannot be determined). This suggests that neurocentral suture closure of the presacral vertebrae occurs relatively late in ontogeny, after at least 50% of maximum body mass has been attained. In turn, while absence of neurocentral suture fusion is an ambiguous indicator of immaturity, its presence may be a relatively good indicator that the individual is in the later stages of ontogeny.

The new specimens described here provide information on the anatomy, taxonomy, diversity, and growth of Mongolian oviraptorids. New specimens of *Conchoraptor gracilis* reveal its postcranial anatomy in more detail and show that *Gobiraptor minutus* is its junior synonym. An isolated skull and mandible from Dzamyn Khondt likely represent a new taxon from the Djadokhta Formation, characterized by a long snout and a deep beak. Redescription of the type specimens of *Heyuannia yanshini* and *Rinchenia mongoliensis* provide a new source of information for future comparisons with other oviraptorids. A new taxon represented by poached and legitimately-collected specimens is described here as the Guriliin Tsav oviraptorid. The exceptionally preserved skeletons show that this new taxon has a domed cranial crest and a reduced arm with two functional digits. Osteohistology of these specimens shows that they represent a growth series, providing information on the growth styles of oviraptorids and the changes in the skeleton throughout ontogeny.

4.6 LITERATURE CITED

Averianov, A. O., and H.-D. Sues. 2012. Correlation of Late Cretaceous continental vertebrate assemblages in Middle and Central Asia. Journal of Stratigraphy 36:462–485.

Balanoff, A. M., and M. A. Norell. 2012. Osteology of *Khaan mckennai* (Oviraptorosauria: Theropoda). Bulletin of the American Museum of Natural History 372:1–77.

Balanoff, A. M., G. S. Bever, T. B. Rowe, and M. A. Norell. 2013. Evolutionary origins of the avian brain. Nature 501:93–96.

Balanoff, A. M., X. Xu, Y. Kobayashi, Y. Matsufune, and M. A. Norell. 2009. Cranial Osteology of the Theropod Dinosaur *Incisivosaurus gauthieri* (Theropoda: Oviraptorosauria). American Museum Novitates 3651:1–35.

Barsbold, R. 1976a. A new Late Cretaceous Family of Small Theropods (Oviraptoridae n. fam.) in Mongolia. Doklady Akademii Nauk SSSR 226:685–688.

Barsbold, R. 1976b. On the evolution and systematics of the late Mesozoic carnivorous dinosaurs [in Russian]. Paleontologiâ i biostratigrafiâ Mongolii. Trudy, Sovmestnaâ Sovetsko−Mongol'skaâ paleontologičeskaâ èkspediciâ 3:68–75.

Barsbold, R. 1981. Toothless Dinosaurs of Mongolia. Transactions of the Joint Soviet Mongolian Paleontological Expedition 15:28–39.

Barsbold, R. 1983. Carnivorous dinosaurs from the Cretaceous of Mongolia. Transactions of the Joint Soviet Mongolian Paleontological Expedition 19:5–117.

Barsbold, R. 1986. The predatory dinosaurs - Oviraptors; pp. 210–223 in Herpetologische Untersuchungen in der Mongolischen Volksrepublik. Academia Nauk SSSR.

Barsbold, R. 1997. Oviraptorosauria; pp. 505–508 in P. J. Currie and K. Padian (eds.), Encyclopedia of Dinosaurs. Academic Press, Oxford, UK.

Benson, R. B. J., and J. N. Choiniere. 2013. Rates of dinosaur limb evolution provide evidence for exceptional radiation in Mesozoic birds. Proceedings of the Royal Society B: Biological Sciences 280:20131780.

Campione, N. E., D. C. Evans, C. M. Brown, and M. T. Carrano. 2014. Body mass estimation in non-avian bipeds using a theoretical conversion to quadruped stylopodial proportions. Methods in Ecology and Evolution 5:913–923.

Clark, J. M., M. Norell, and L. M. Chiappe. 1999. An oviraptorid skeleton from the late Cretaceous of Ukhaa Tolgod, Mongolia, preserved in an avianlike brooding position over an oviraptorid nest. American Museum Novitates 3265:1–36.

Clark, J. M., M. A. Norell, and R. Barsbold. 2001. Two new oviraptorids (Theropoda: Oviraptorosauria), Upper Cretaceous Djadokhta Formation, Ukhaa Tolgod, Mongolia. Journal of Vertebrate Paleontology 21:209–213.

Clark, J. M., M. A. Norell, and T. Rowe. 2002. Cranial anatomy of *Citipati osmolskae* (Theropoda, Oviraptorosauria), and a reinterpretation of the holotype of *Oviraptor philoceratops*. American Museum Novitates 1–24.

Currie, P., G. Funston, and H. Osmolska. 2016. New specimens of the crested theropod dinosaur *Elmisaurus rarus* from Mongolia. Acta Palaeontologica Polonica 61:143–157.

Currie, P. J. 2003. Allometric growth in tyrannosaurids (Dinosauria: Theropoda) from the Upper Cretaceous of North America and Asia. Canadian Journal of Earth Sciences 40:651–665.

Dashzeveg, D., L. Dingus, D. B. Loope, C. C. SWISHER III, T. Dulam, and M. R. Sweeney. 2005. New stratigraphic subdivision, depositional environment, and age estimate for the Upper Cretaceous Djadokhta Formation, southern Ulan Nur Basin, Mongolia. American Museum Novitates 1–31.

Dong, Z.-M., and P. J. Currie. 1996. On the discovery of an oviraptorid skeleton on a nest of eggs at Bayan Mandahu, Inner Mongolia, People's Republic of China. Canadian Journal of Earth Sciences 33:631–636.

Easter, J. 2013. A new name for the oviraptorid dinosaur *"Ingenia yanshini"* (Barsbold, 1981; preoccupied by Gerlach, 1957). Zootaxa 3737:184–190.

Eberth, D. A. 2018. Stratigraphy and paleoenvironmental evolution of the dinosaur-rich Baruungoyot-Nemegt succession (Upper Cretaceous), Nemegt Basin, southern Mongolia. Palaeogeography, Palaeoclimatology, Palaeoecology 494:29–50.

Fanti, F., P. J. Currie, and D. Badamgarav. 2012. New Specimens of *Nemegtomaia* from the Baruungoyot and Nemegt Formations (Late Cretaceous) of Mongolia. PLoS ONE 7:e31330.

Funston, G. F., and P. J. Currie. 2016. A new caenagnathid (Dinosauria: Oviraptorosauria) from the Horseshoe Canyon Formation of Alberta, Canada, and a reevaluation of the relationships of Caenagnathidae. Journal of Vertebrate Paleontology 36:e1160910.

Funston, G. F., and P. J. Currie. 2018. A small caenagnathid tibia from the Horseshoe Canyon Formation (Maastrichtian): Implications for growth and lifestyle in oviraptorosaurs. Cretaceous Research 92:220–230.

Funston, G. F., P. J. Currie, and M. Burns. 2016. New elmisaurine specimens from North America and their relationship to the Mongolian *Elmisaurus rarus*. Acta Palaeontologica Polonica 61:159–173.

Funston, G. F., S. E. Mendonca, P. J. Currie, and R. Barsbold. 2018. Oviraptorosaur anatomy, diversity and ecology in the Nemegt Basin. Palaeogeography, Palaeoclimatology, Palaeoecology.

Jerzykiewicz, T., and D. A. Russell. 1991. Late Mesozoic stratigraphy and vertebrates of the Gobi Basin. Cretaceous Research 12:345–377.

Kundrát, M. 2007. Avian-like attributes of a virtual brain model of the oviraptorid theropod Conchoraptor gracilis. Naturwissenschaften 94:499–504.

Kundrát, M., and J. Janáček. 2007. Cranial pneumatization and auditory perceptions of the oviraptorid dinosaur *Conchoraptor gracilis* (Theropoda, Maniraptora) from the Late Cretaceous of Mongolia. Naturwissenschaften 94:769–778.

Lamanna, M. C., H.-D. Sues, E. R. Schachner, and T. R. Lyson. 2014. A New Large-Bodied Oviraptorosaurian Theropod Dinosaur from the Latest Cretaceous of Western North America. PLoS ONE 9:e92022.

Lee, S., Y.-N. Lee, A. Chinsamy, J. Lü, R. Barsbold, and K. Tsogtbaatar. 2019. A new baby oviraptorid dinosaur (Dinosauria: Theropoda) from the Upper Cretaceous Nemegt Formation of Mongolia. PLOS ONE 14:e0210867.

Lü, J., Y. Tomida, Y. Azuma, Z.-M. Dong, and Y.-N. Lee. 2004. New oviraptorid dinosaur (Dinosauria: Oviraptorosauria) from the Nemegt Formation of Southwestern Mongolia. Bulletin of the National Science Museum of Tokyo Series C 30:95–130.

Lü, J., R. Chen, S. L. Brusatte, Y. Zhu, and C. Shen. 2016. A Late Cretaceous diversification of Asian oviraptorid dinosaurs: evidence from a new species preserved in an unusual posture. Scientific Reports 6:35780.

Lü, J., P. J. Currie, L. Xu, X. Zhang, H. Pu, and S. Jia. 2013. Chicken-sized oviraptorid dinosaurs from central China and their ontogenetic implications. Naturwissenschaften 100:165–175.

Makovicky, P. J. 2008. Telling time from fossils: a phylogeny-based approach to chronological ordering of paleobiotas. Cladistics 24:350–371.

Norell, M. A., J. M. Clark, and L. M. Chiappe. 2001. An Embryonic Oviraptorid (Dinosauria: Theropoda) from the Upper Cretaceous of Mongolia. American Museum Novitates 3315:1–20.

Norell, M. A., J. M. Clark, L. M. Chiappe, and D. Dashzeveg. 1995. A nesting dinosaur. Nature 378:774–776.

Norell, M. A., A. M. Balanoff, D. E. Barta, and G. M. Erickson. 2018. A Second Specimen of *Citipati Osmolskae* Associated With a Nest of Eggs from Ukhaa Tolgod, Omnogov Aimag, Mongolia. American Museum Novitates 3899:1–44.

Norell, M. A., J. M. Clark, D. Demberelyin, B. Rhinchen, L. M. Chiappe, A. R. Davidson, M. C. McKenna, P. Altangerel, and M. J. Novacek. 1994. A Theropod Dinosaur Embryo and the Affnities of the Flaming Cliffs Dinosaur Eggs. Science, New Series 266:779–782.

Osborn, H. F. 1924. Three new theropoda, *Protoceratops* zone, central Mongolia. American Museum Novitates 144:1–12.

Osmólska, H. 1976. New light on the skull anatomy and systematic position of *Oviraptor*. Nature 262:683–684.

Osmólska, H., P. J. Currie, and R. Barsbold. 2004. Oviraptorosauria; pp. 165–183 in D. B. Weishampel, P. Dodson, and H. Osmólska (eds.), The Dinosauria, 2nd ed. University of California Press, Berkeley, California.

Sues, H.-D. 1997. On *Chirostenotes*, a Late Cretaceous oviraptorosaur (Dinosauria: Theropoda) from western North America. Journal of Vertebrate Paleontology 17:698–716.

Sullivan, R. M., S. E. Jasinski, and M. P. A. Van Tomme. 2011. A new caenagnathid *Ojoraptorsaurus boerei*, n. gen., n. sp (Dinosauria, Oviraptorosauria), from the Upper Ojo Alamo Formation (Naashoibito Member), San Juan Basin, New Mexico. New Mexico Museum of Natural History and Science Bulletin 53:418–428.

Wang, S., S. Zhang, C. Sullivan, and X. Xu. 2016. Elongatoolithid eggs containing oviraptorid (Theropoda, Oviraptorosauria) embryos from the Upper Cretaceous of Southern China. BMC Evolutionary Biology 16.

Zanno, L. E., and S. D. Sampson. 2005. A new oviraptorosaur (Theropoda, Maniraptora) from the Late Cretaceous (Campanian) of Utah. Journal of Vertebrate Paleontology 25:897–904.

4.7 FIGURES & TABLES
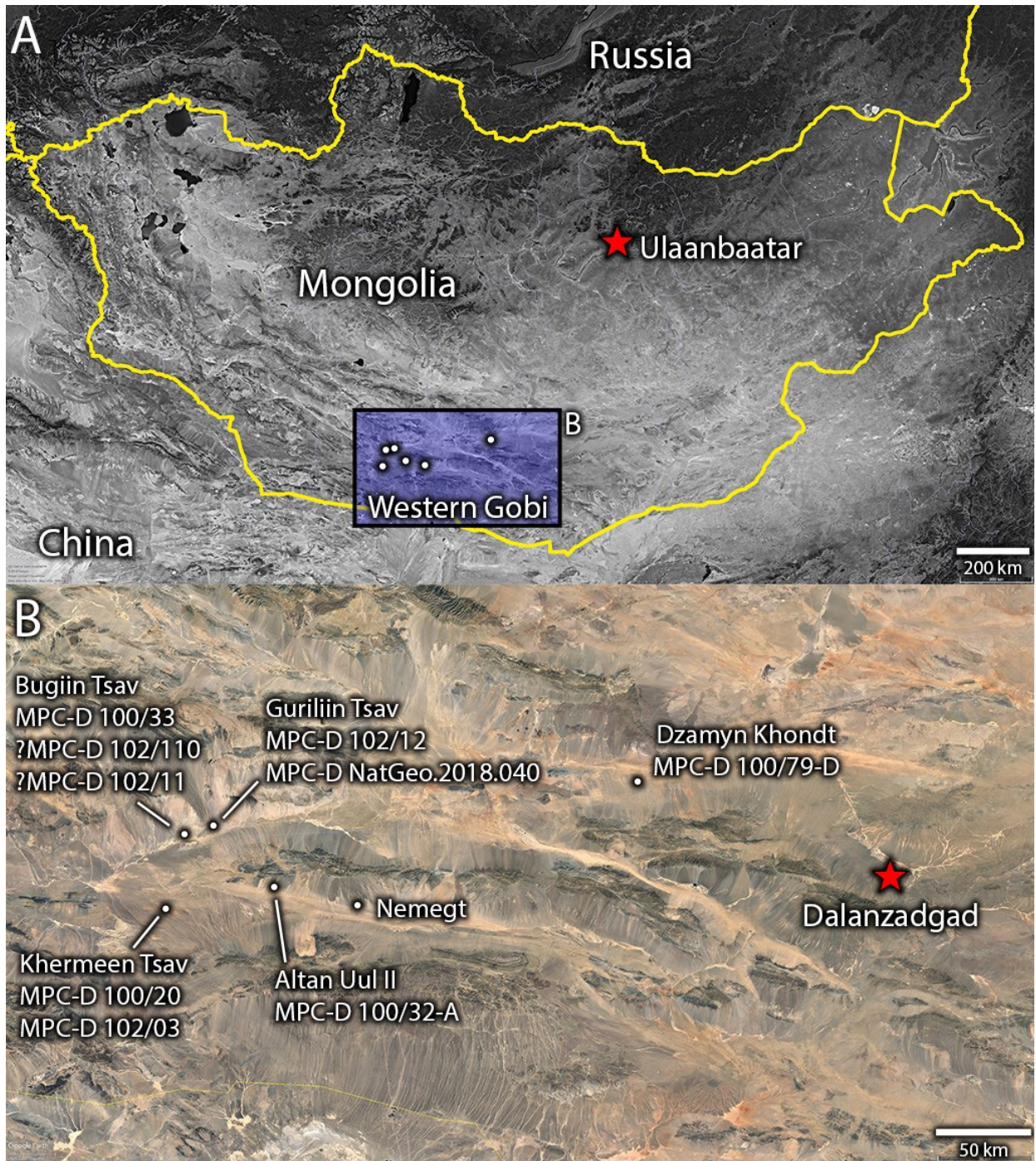
Fig. 4.0. Map of oviraptorid occurrences in Mongolia.

Satellite images (A, B) of Mongolia, showing locations of oviraptorid specimens described. Blue

box in (A) shows region of image (B), dots represent localities where oviraptorids are known.
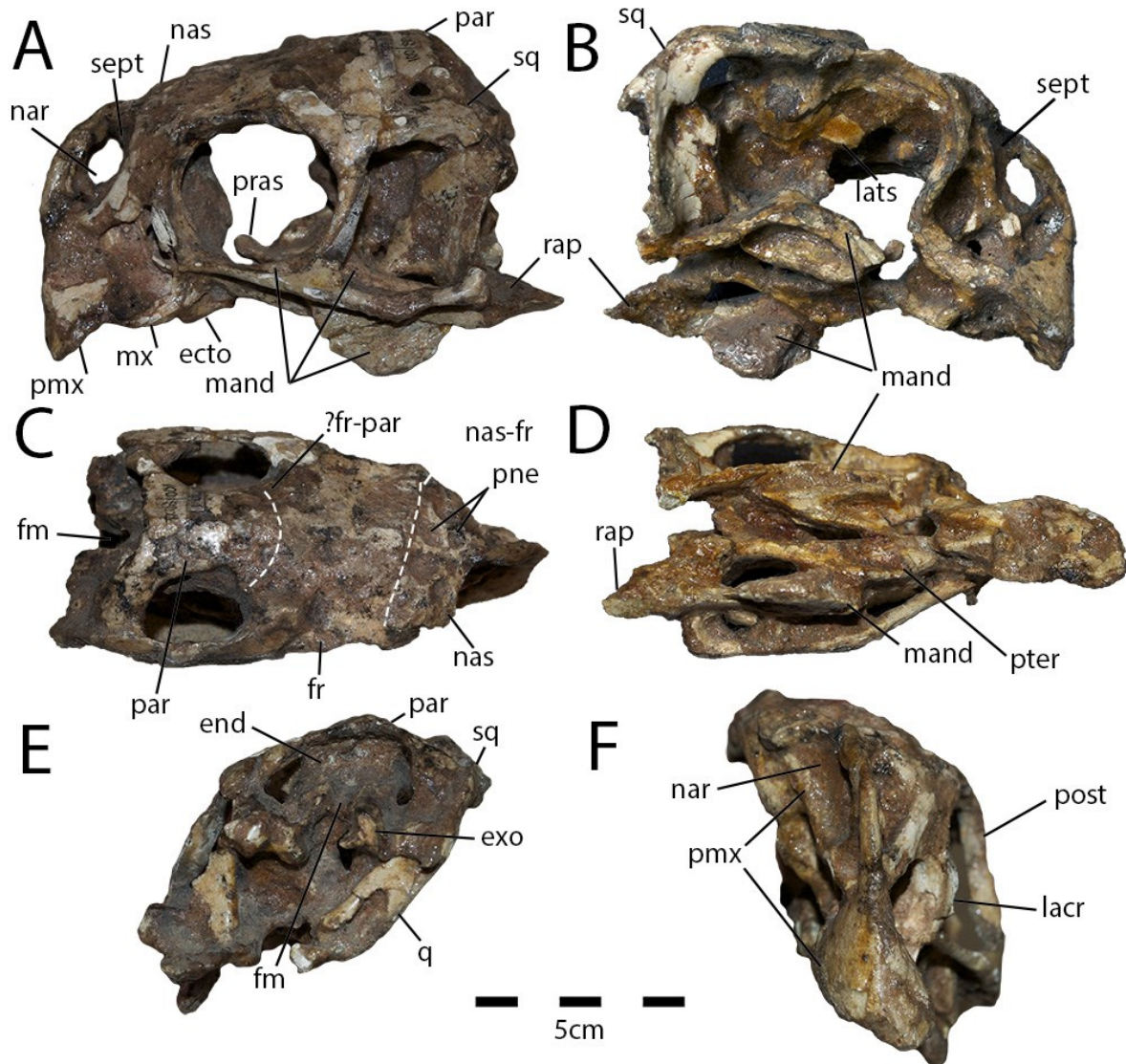
Fig. 4.1. Type specimen of *Conchoraptor gracilis*.

MPC-D 100/20 in left lateral (A), right lateral (B), dorsal (C), ventral (D), posterior (E), and anterior (F) views. **Abbreviations**: **ecto**, ectopterygoid; **end**, endocranial space; **exo**, exoccipital; **fm**, foramen magnum; **fr**, frontal; **?fr-par**, interpreted frontoparietal suture; **lacr**, lacrimal; **mand**, mandible; **mx**, maxilla; **nar**, naris; **nas**, nasal; **nas-fr**, nasofrontal contact; **par**, parietal; **pmx**, premaxilla; **pne**, pneumatic foramina; **post**, postorbital; **pras**, parasphenoid; **pter**, pterygoid; **q**, quadrate; **rap**, retroarticular process; **sept**, narial septum; **sq**, squamosal.
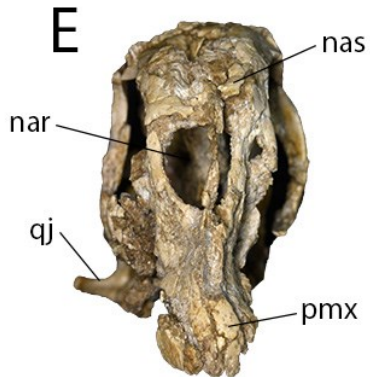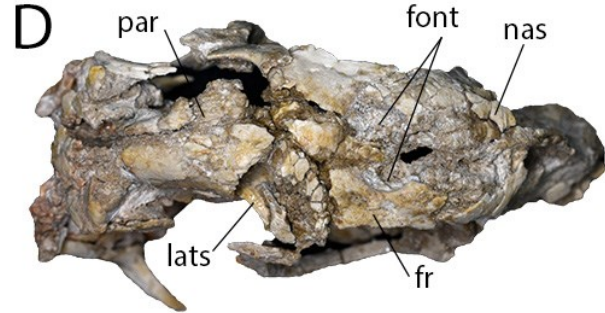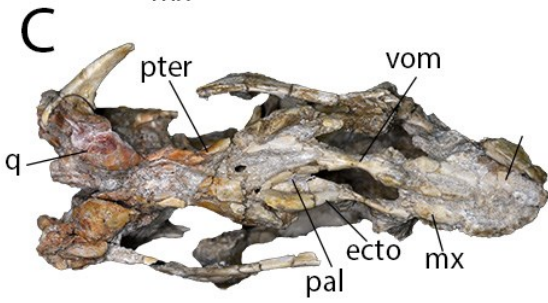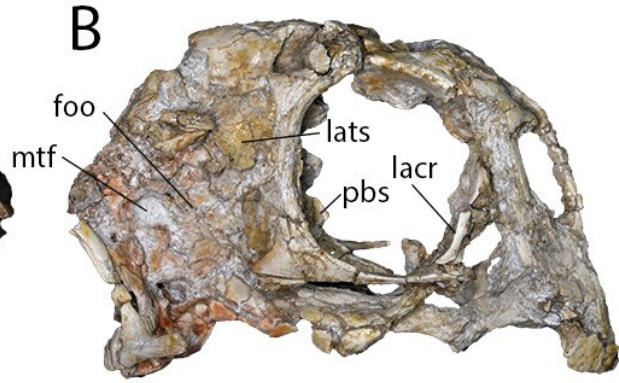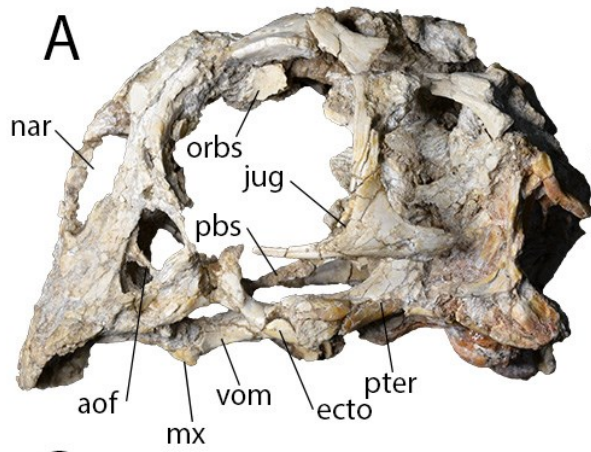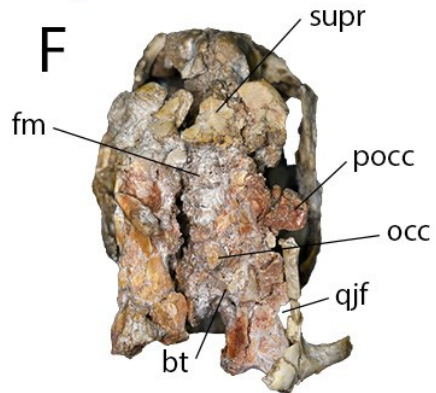
Fig. 4.2. Juvenile skull of *Conchoraptor gracilis* from Guriliin Tsav.

MPC-D NatGeo.2018.036a in left lateral (A), right lateral (B), ventral (C), dorsal (D), anterior (E) and posterior (F) views. **Abbreviations: aof**, antorbital fenestra; **bt**, basal tuber; **ecto**, ectopterygoid; **fm**, foramen magnum; **font**, frontal fenestrae; **foo**, foramen ovalis; **fr**, frontal; **jug**, jugal; **lacr**, lacrimal; **lats**, laterosphenoid; **mtf**, metopic fissure; **mx**, maxilla; **nar**, naris; **nas**, nasal; **occ**, occipital condyle; **orbs**, orbitosphenoid; **pal,** palatine; **par**, parietal; **pbs**, parabasisphenoid; **pmx**, premaxilla; **pocc**, paroccipital process; **pter**, pterygoid; **q**, quadrate; **qj**, quadratojugal; **qjf**, quadratojugal foramen; **supr**, supraoccipital; **vom**, vomer.
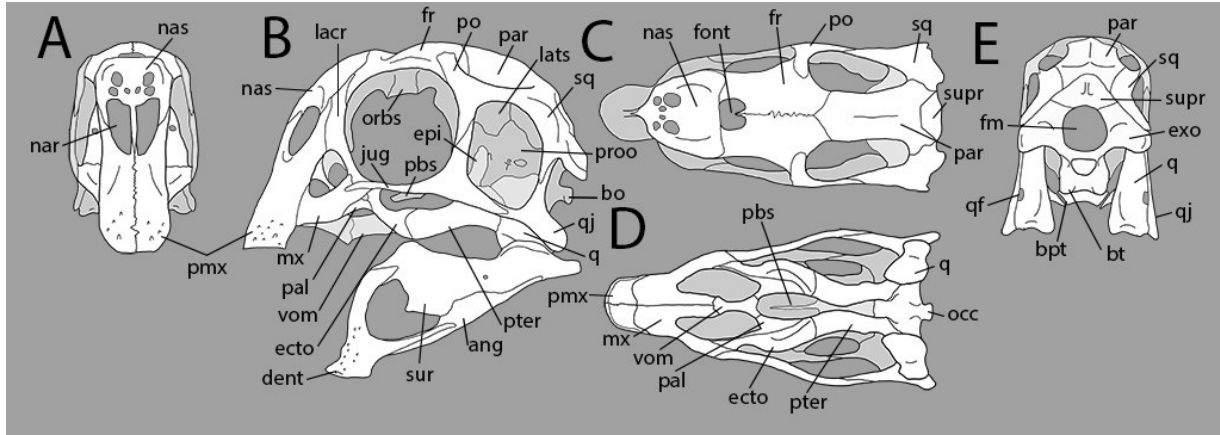
Fig. 4.3. Reconstruction of the skull of *Conchoraptor gracilis*.

Reconstruction based on MPC-D NatGeo.2018.036a in anterior (A), left lateral with mandible (B), dorsal (C), ventral (D) and posterior (E) views. **Abbreviations: ang**, angular; **bo**, basioccipital; **bpt**, basipterygoid process; **bt**, basal tuber; **dent**, dentary; **ecto**, ectopterygoid; **epi**, epipterygoid; **exo**, exoccipital; **fm**, foramen magnum; **font**, frontal fenestrae; **foo**, foramen ovalis; **fr**, frontal; **jug**, jugal; **lacr**, lacrimal; **lats**, laterosphenoid; **mtf**, metopic fissure; **mx**, maxilla; **nar**, naris; **nas**, nasal; **occ**, occipital condyle; **orbs**, orbitosphenoid; **pal,** palatine; **par**, parietal; **pbs**, parabasisphenoid; **pmx**, premaxilla; **po**, postorbital; **pocc**, paroccipital process; **proo**, prootic; **pter**, pterygoid; **q**, quadrate; **qj**, quadratojugal; **qjf**, quadratojugal foramen; **sq**, squamosal; **supr**, supraoccipital; **sur**, surangular; **vom**, vomer.
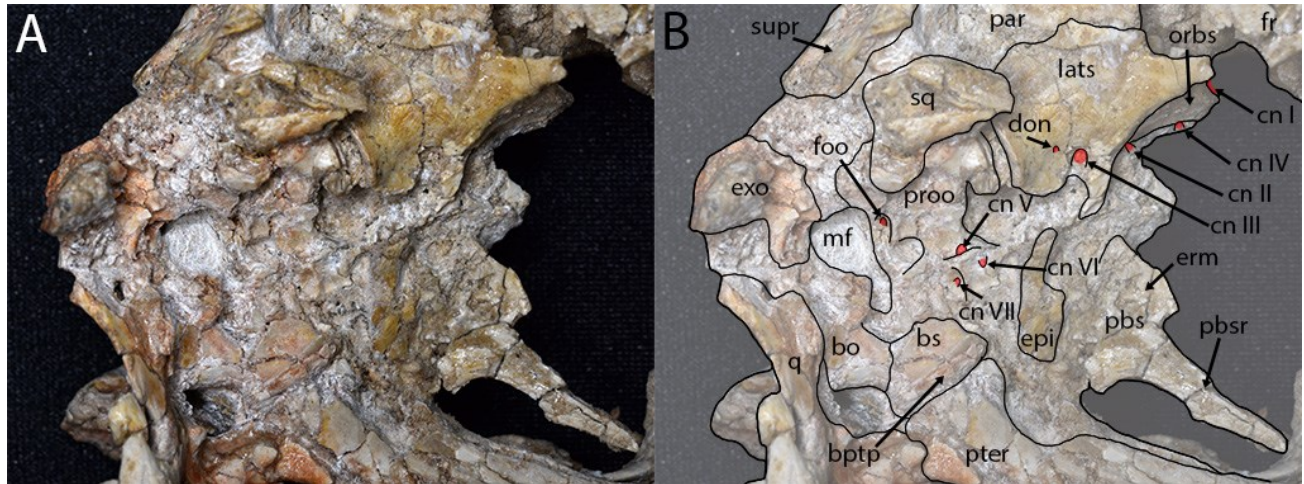
Fig. 4.4. Braincase of *Conchoraptor gracilis*.

Photograph (A) and annotated photograph (B) of the lateral wall of the braincase as exposed in MPC-D NatGeo.2018.036a. **Abbreviations: bo**, basioccipital; **bptp**, basipterygoid process; **bs**, basisphenoid; **cn I**, foramen for cranial nerve I; **cn II**, foramen for cranial nerve II; **cn III**, foramen for cranial nerve III; **cn IV**, foramen for cranial nerve IV; **cn V**, foramen for cranial nerve V; **cn VI**, foramen for cranial nerve VI; **cn VII**, foramen for cranial nerve VII; **don**, foramen for deep ophthalmic nerve; **epi**, epipterygoid; **erm**, origin of eye retractor musculature; **exo**, exoccipital; **foo**, foramen ovalis; **fr**, frontal; **lats**, laterosphenoid; **mf**, metopic fissure; **orbs**, orbitosphenoid; **par**, parietal; **pbs**, parabasisphenoid; **pbsr**, parabasisphenoid rostrum; **proo**, prootic; **pter**, pterygoid; **q**, quadrate; **sq**, squamosal; **supr**, supraoccipital.
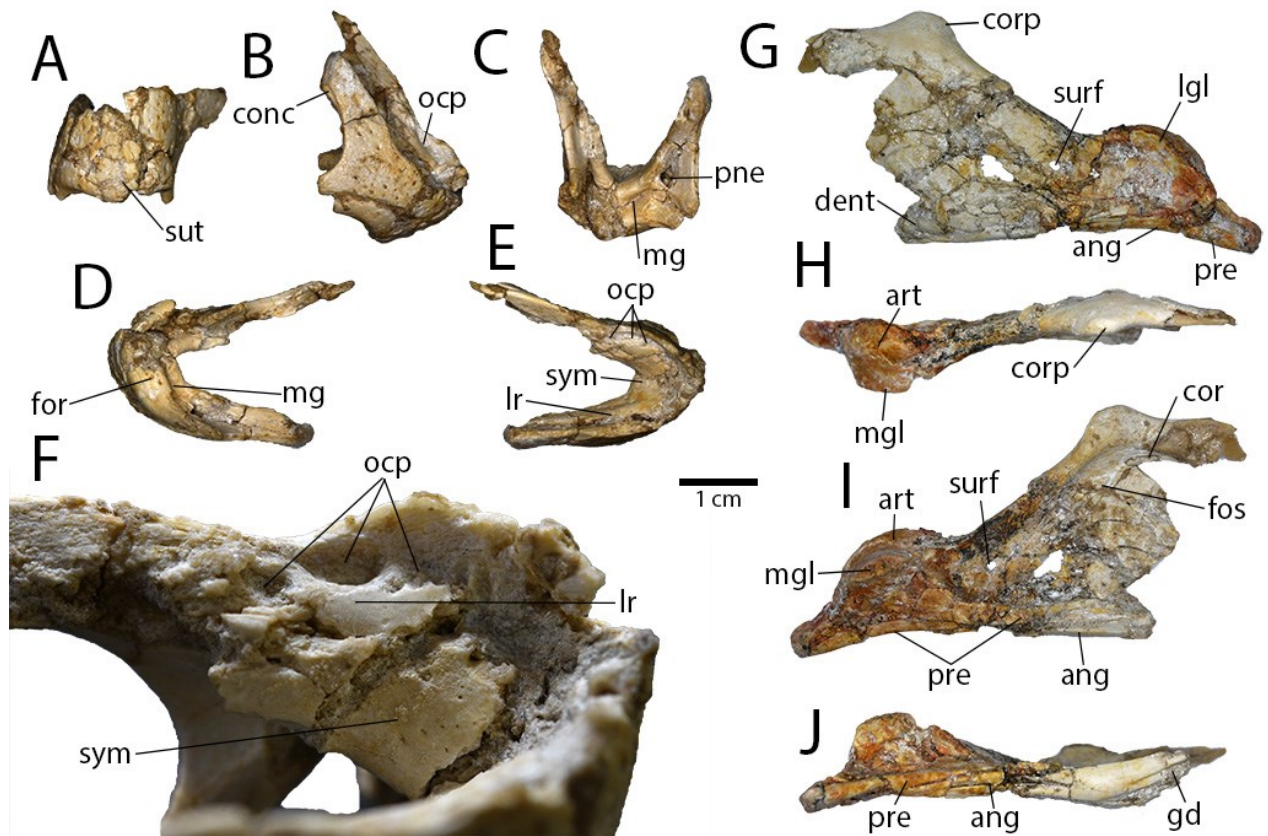
Fig. 4.5. Mandible of *Conchoraptor gracilis*.

Dentaries of MPC-D NatGeo.2018.036a in anterior (A), right lateral (B), posterior (C), ventral (D), and dorsal (E) views. Detail (F) of occlusal surface of left dentary in dorsomedial view. Left articular-surangular-coronoid complex in lateral (G), dorsal (H), medial (I) and ventral (J) views.

Abbreviations: ang, angular; **art**, articular; **conc**, concavity; **cor**, coronoid; **corp**, coronoid process; **dent**, dentary; **for**, foramen; **fos**, fossa; **gd**, groove for dentary; **lgl**, lateral glenoid; **lr**, lingual ridge; **mg**, Meckelian groove; **mgl**, medial glenoid; **ocp**, occlusal pits; **pne**, pneumatic cavity; **pre**, prearticular; **surf**, surangular foramen; **sut**, suture; **sym,** symphyseal shelf.
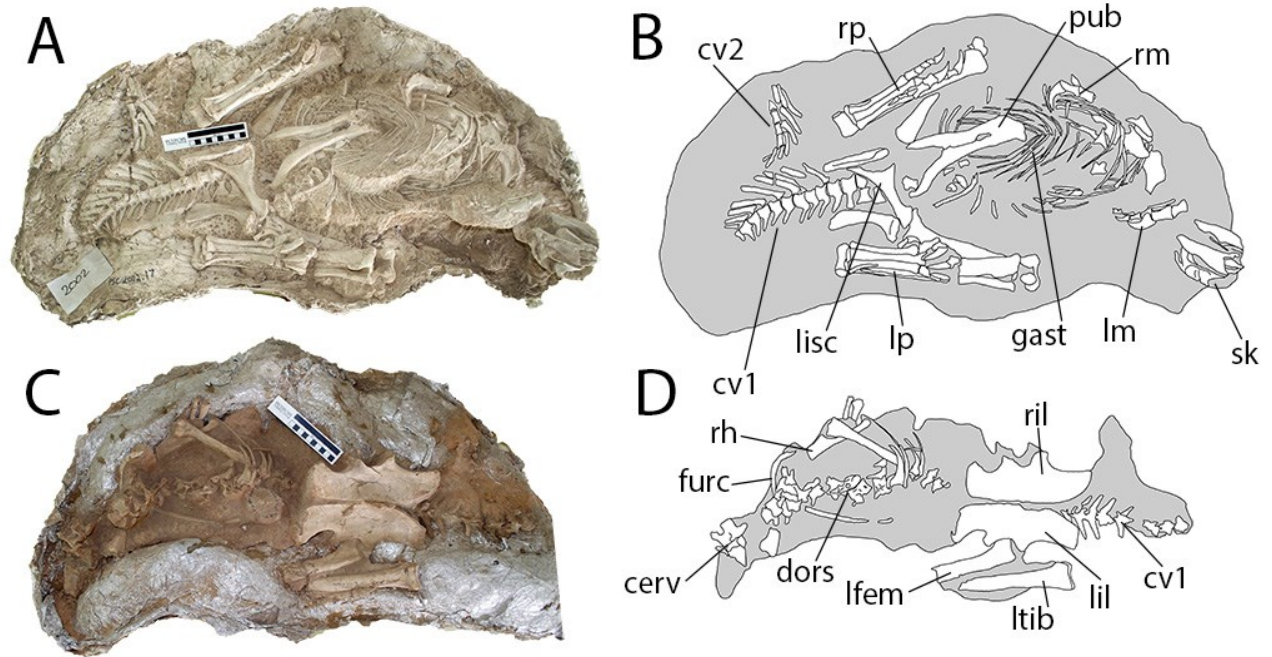
Fig. 4.6. Postcranial skeleton of *Conchoraptor gracilis*.

Cast (A) and illustration (B) of MPC-D 102/03 in ventral view. Photograph (C) and illustration (D) of MPC-D 102/03 in dorsal view. **Abbreviations: cerv**, cervical vertebrae; **cv1**, caudal vertebrae of individual 1; **cv2**, caudal vertebrae of individual 2; **dors**, dorsal vertebrae; **furc**, furcula; **gast**, gastralia; **lfem**, left femur; **lil**, left ilium; **lisc**, left ischium; **lm**, left manus; **lp**, left pes; **ltib**, left tibia; **pub,** pubes; **rh**, right humerus; **ril**, right ilium; **rm**, right manus; **rp**, right pes; **sk**, skull.
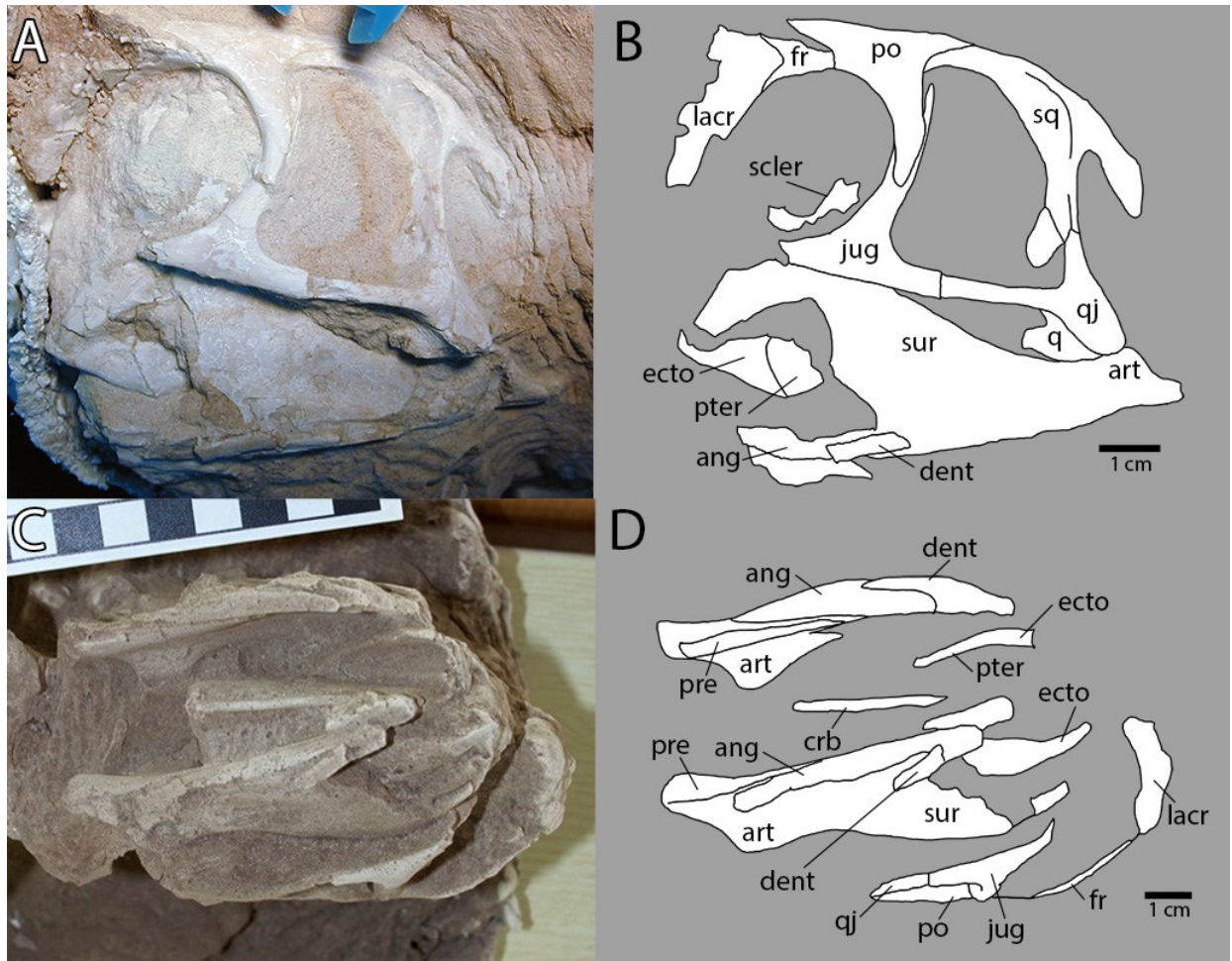
Fig. 4.7. Partial skull of adult *Conchoraptor gracilis*.

Photograph (A) and illustration (B) of skull of MPC-D 102/03 in left lateral view before final preparation. Cast (C) and illustration (D) of skull of MPC-D 102/03 in ventral view.

Abbreviations: ang, angular; **art**, articular; **crb**, ceratobranchial; **dent**, dentary; **ecto**, ectopterygoid; **fr**, frontal; **jug**, jugal; **lacr**, lacrimal; **po**, postorbital; **pre**, prearticular; **pter**, pterygoid; **q**, quadrate; **qj**, quadratojugal; **scler**, scleral ossicles; **sq**, squamosal; **sur**, surangular.
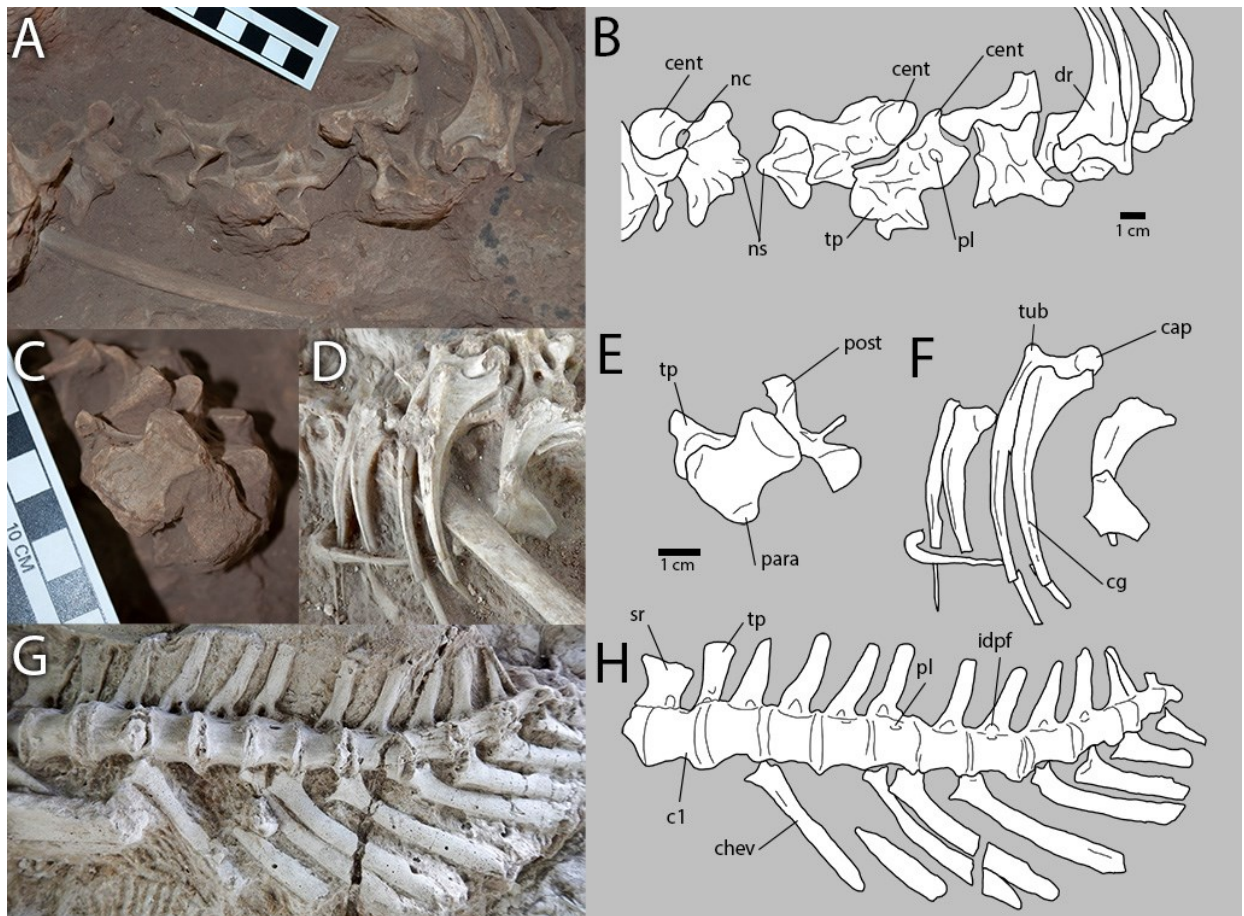
Fig. 4.8. Axial skeleton of *Conchoraptor gracilis*.

Photographs (A, C), casts (D, G), and illustrations (B, E, F, H) of MPC-D 102/03. Dorsal vertebrae (A, B) in various views, anterior is to the left. Mid-cervical vertebra (C, E) in ventral view, anterior is to the bottom left. Dorsal ribs (D, F) in anterolateral view. Proximal caudal vertebrae and chevrons (G, H) in ventral view, anterior is to the left. **Abbreviations**: **c1**, first caudal vertebra; **cap**, capitulum; **cent**, centrum; **cg**, costal groove; **chev**, chevron; **dr**, dorsal rib; **idpf**, infradiapophyseal fossa; **nc**, neural canal; **ns**, neural spine; **para**, parapophysis; **pl**, pleurocoel; **post**, postzygapophysis; **sr**, sacral rib; **tp**, transverse process; **tub**, tuberculum.
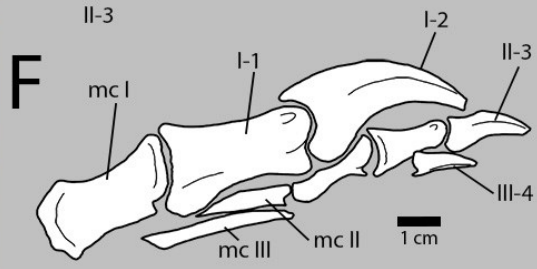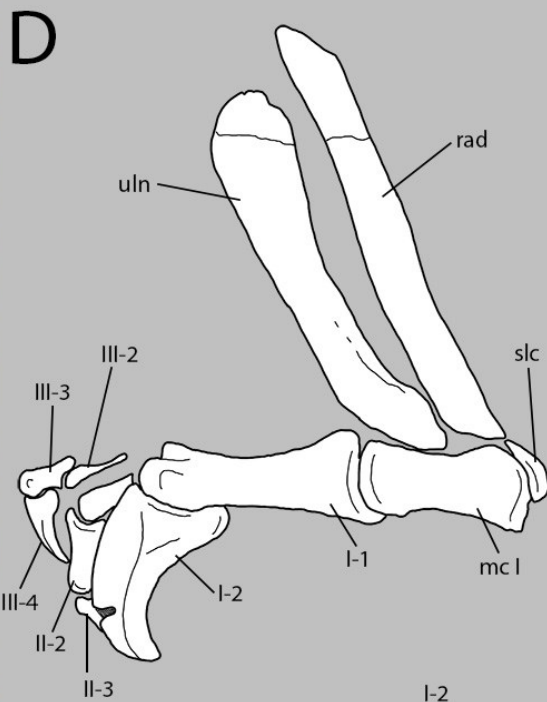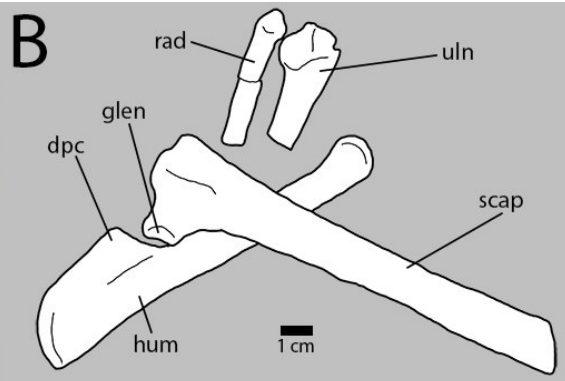
(Previous page)
Fig. 4.9. Forelimb of *Conchoraptor gracilis*.

Photograph (A), casts (C, E), and illustrations (B, D, F) of forelimb elements of MPC-D 102/03.

Right scapula, humerus, and proximal antebrachium (A, B) in dorsal view. Right antebrachium

and manus (C, D) in ventral view. Left manus (E, F) in medial view. **Abbreviations: dpc**,

deltopectoral crest; **glen**, glenoid; **hum**, humerus; **I-1**, manual phalanx I-1; **I-2**, manual ungual I-

2; **II-2**, manual phalanx II-2; **II-3**, manual ungual II-3; **III-2**, manual phalanx III-2; **III-3**, manual

phalanx III-3; **III-4**, manual ungual III-4; **mc I**, metacarpal I; **mc II**, metacarpal II; **mc III;**

metacarpal III; **rad**, radius; **scap**, scapula; **slc**, semilunate carpal; **uln**, ulna.
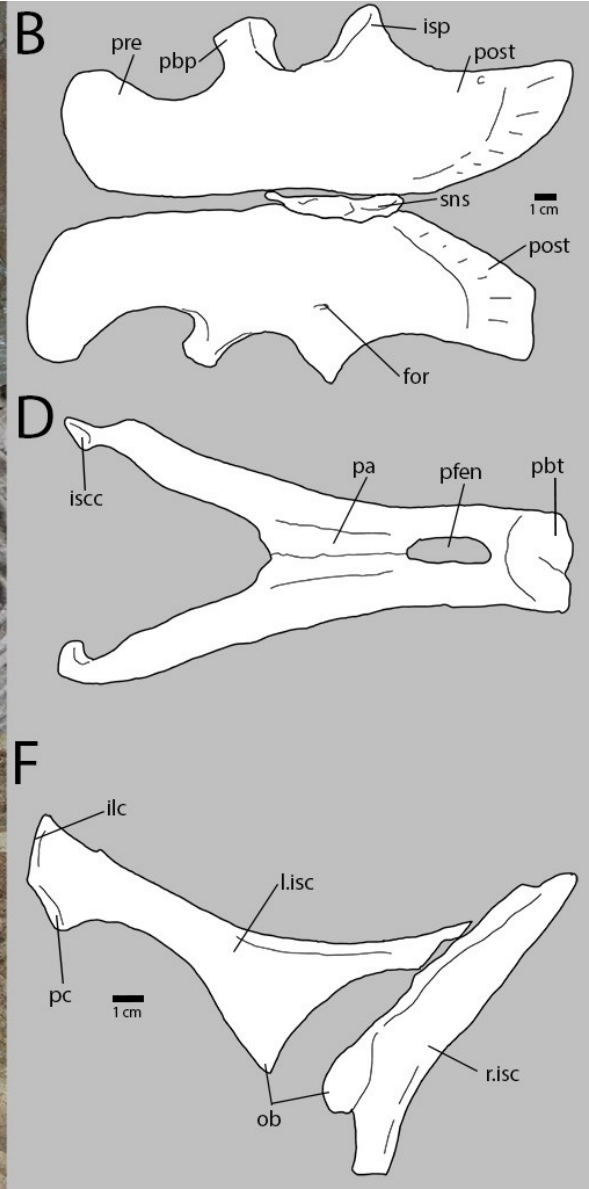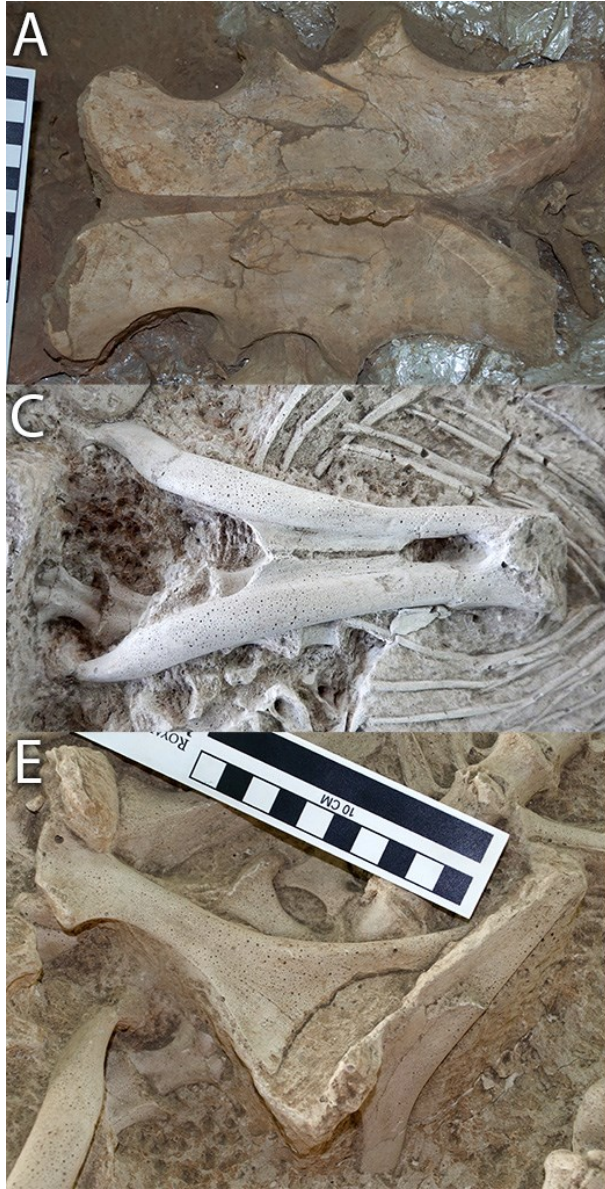
(Previous page)
Fig. 4.10. Pelvic elements of *Conchoraptor gracilis*.

Photographs (A, E), cast (C), and illustrations (B, D, F) of pelvic elements of MPC-D 102/03.

Ilia (A, B) in dorsal view. Pubes (C, D) in ventral view. Ischia (E, F) in lateral (left) and ventral

(right) views. **Abbreviations: for**, foramen; **ilc**, iliac contact; **iscc**, ischiadic contact; **isp**,

ischiadic peduncle; **l.isc**, left ischium; **ob**, obturator process; **pa**, pubic apron; **pbp**, pubic

peduncle; **pbt**, pubic boot; **pc**, pubic contact; **pfen**, pubic fenestra; **post**, postacetabular blade;

pre, preacetabular blade; **r.isc**, right ischium; **sns**, sacral neural spines.
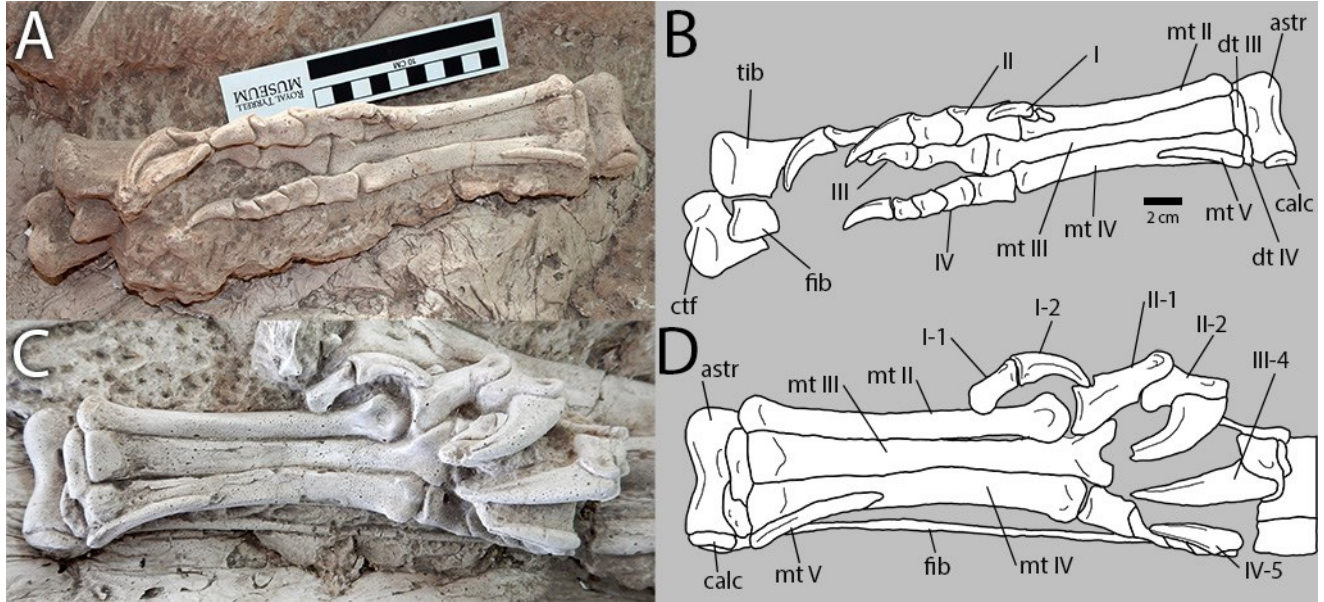
Fig. 4.11. Hindlimbs of *Conchoraptor gracilis*.

Casts (A, C), and illustrations (B, D) of feet and distal hindlimbs. Right foot (A, B) in ventral view. Left foot (C, D) in ventral view. **Abbreviations: astr**, astragalus; **calc**, calcaneum; **ctf**, crista tibiofibularis; **dt III**, distal tarsal III; **dt IV**, distal tarsal IV; **fib**, fibula; **I**, digit I; **I-1**, pedal phalanx I-1; **I-2**, pedal ungual I-2; **II**, digit II; **II-1**, pedal phalanx II-1; **II-2**, pedal phalanx II-2; **III**, digit III; **III-4**, pedal ungual III-4; **IV**, digit IV; **IV-5**, pedal ungual IV-5; **mt II**, metatarsal II; **mt III**, metatarsal III; **mt IV**, metatarsal IV; **mt V**, metatarsal V; **tib**, tibia.
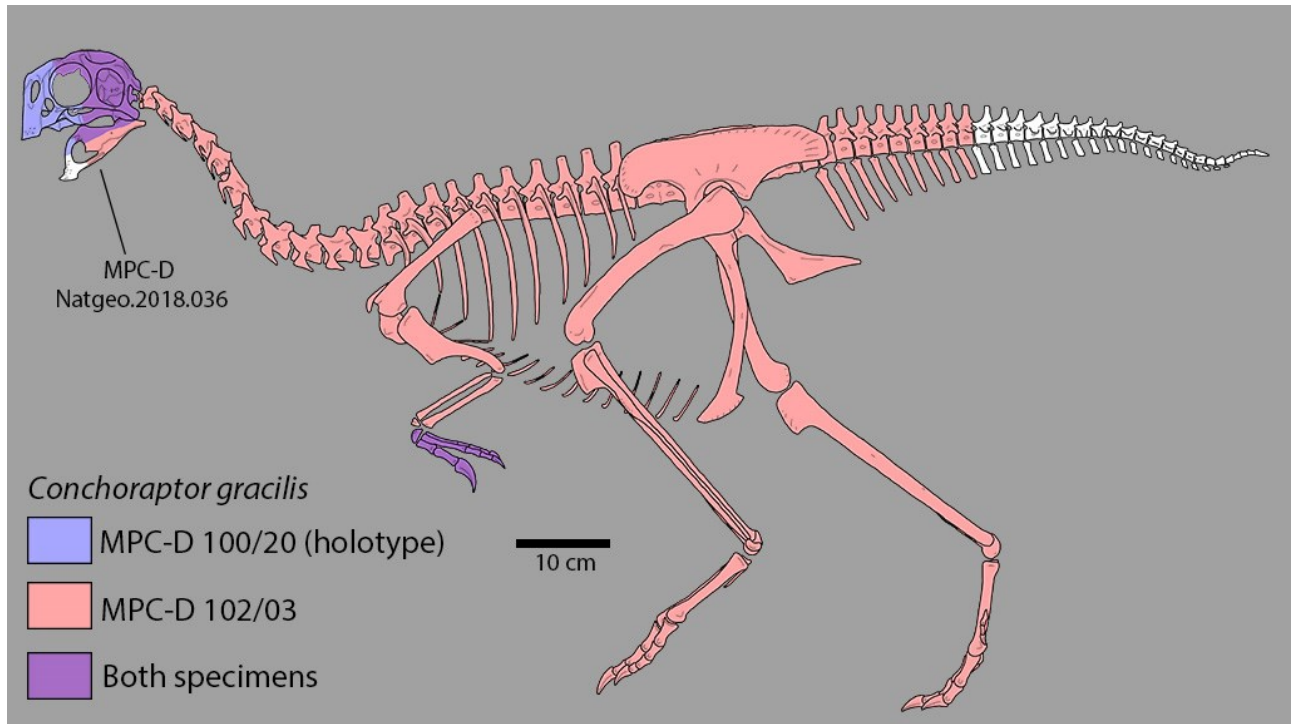
Fig. 4.12. Skeletal reconstruction of *Conchoraptor gracilis*.

Reconstruction of *Conchoraptor gracilis* based on MPC-D 100/20, MPC-D 102/03, and MPC-D NatGeo.2018.036a.
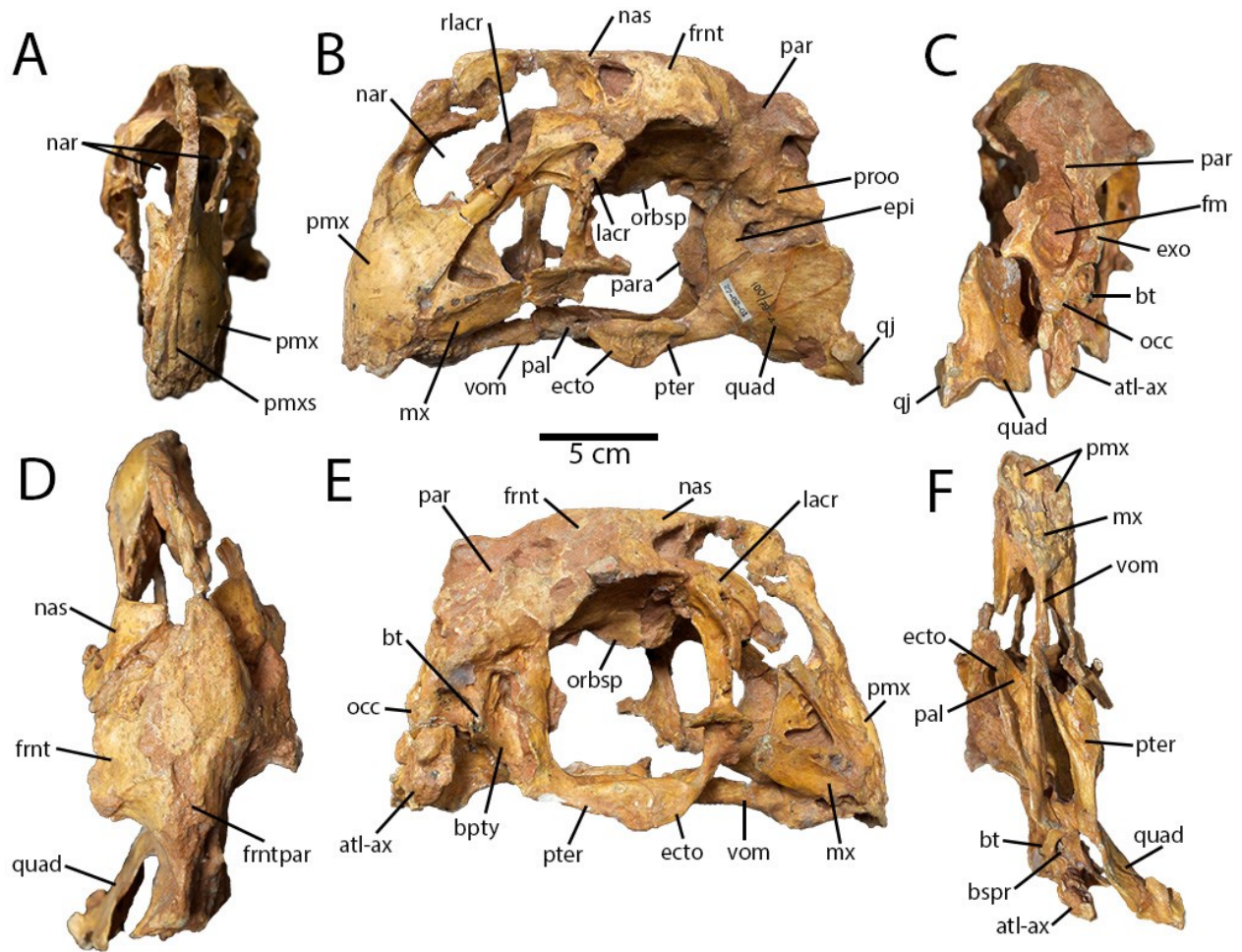
Fig. 4.13. An oviraptorid skull from Dzamyn Khondt.

Skull of MPC-D 100/79-D in anterior (A), left lateral (B), posterior (C), dorsal (D), right lateral (E), and ventral (F) views. **Abbreviations**: **atl-ax**, atlas-axis complex; **bpty**, basipterygoid process; **bspr**, basisphenoid recess; **bt**, basal tuber; **ecto**, ectopterygoid; **epi**, epipterygoid; **exo**, exoccipital; **fm**, foramen magnum; **frnt**, frontal; **frntpar**, frontoparietal suture; **lacr**, lacrimal; **mx**, maxilla; **nar**, naris; **nas**, nasal; **occ**, occipital condyle; **orbs**, orbitosphenoid; **pal**, palatine; **par**, parietal; **para**, parabasisphenoid; **pmx**, premaxilla; **pmxs**, premaxillary suture; **proo**, prootic; **pter**, pterygoid; **quad**, quadrate; **qj**, quadratojugal; **rlacr**, right lacrimal; **vom**, vomer.

Fig. 4.14. Reconstruction of an oviraptorid skull from Dzamyn Khondt.

Reconstruction of skull and mandible of MPC-D 100/79-D, showing long preorbital portion of

the skull and deep beak.
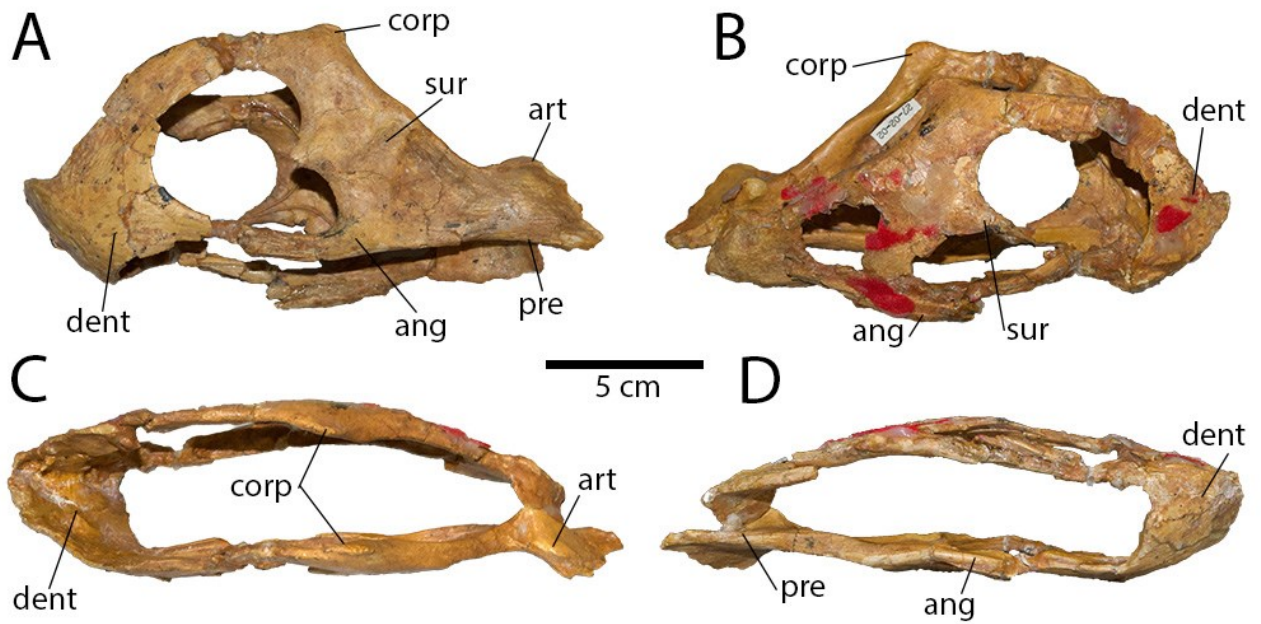
Fig. 4.15. Mandibles of an oviraptorid from Dzamyn Khondt.

Mandibles of MPC-D 100/79-D in left lateral (A), right lateral (b), dorsal (C), and ventral (D)

views. **Abbreviations: ang**, angular; **art**, articular; **corp**, coronoid process; **dent**, dentary; **pre**,

prearticular; **sur**, surangular.
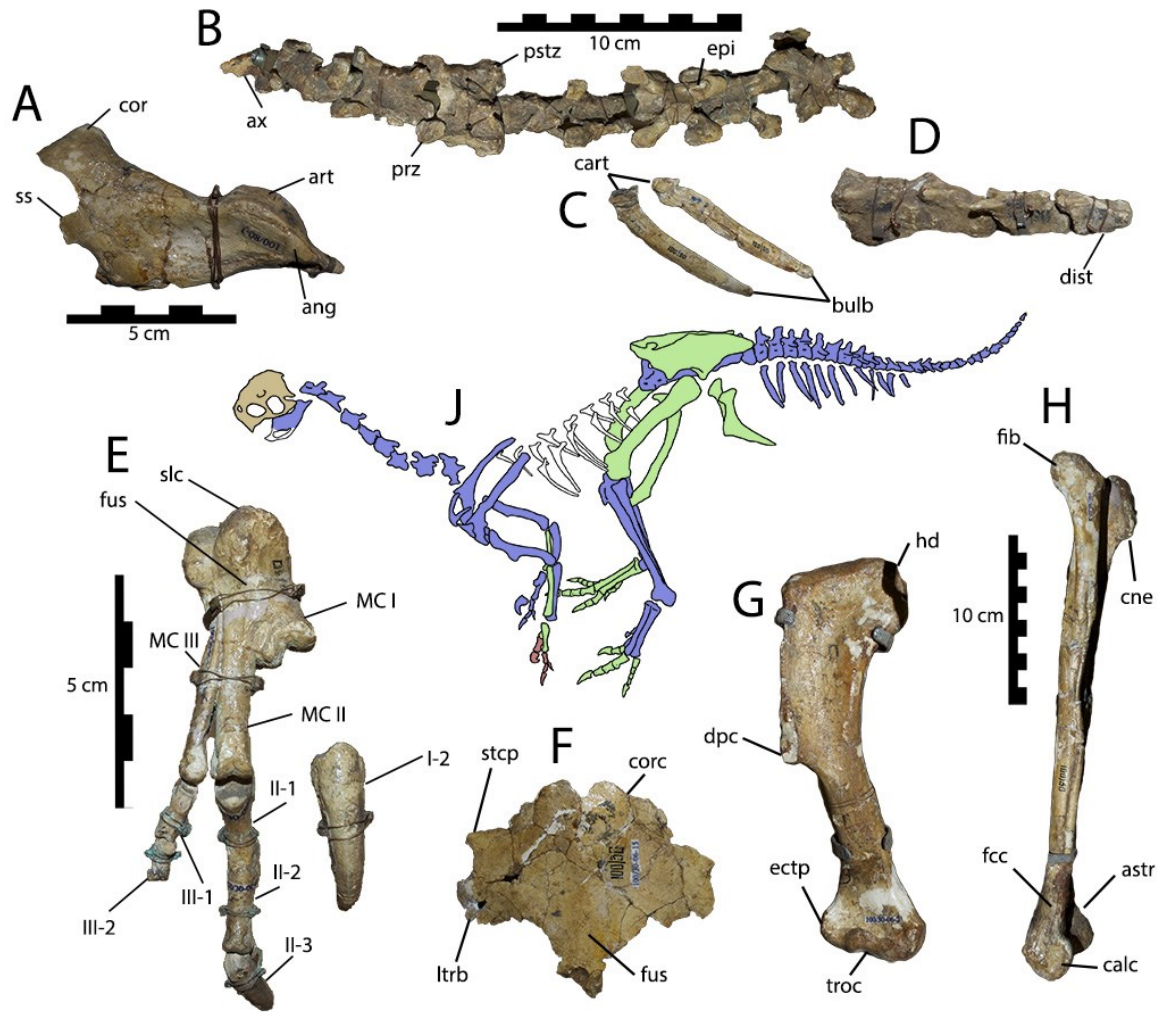
(Previous page)
Fig. 4.16. Type skeleton of *Heyuannia yanshini*.

Elements of MPC-D 100/30 from a chimaeric mount. Posterior portion of left mandible in lateral view (A); articulated cervical vertebrae in dorsal view (B); proximal chevrons in left lateral view (C); distal caudal vertebrae (reversed) in lateral view (D); right hand in anterior view (E); sternum in anterior view (F); right humerus in anterior view (G); right tibia and fibula in lateral view (H); and illustration (J) of holotype mount showing composition: blue—MPC-D 100/30, green—MPC-D 100/31, red—MPC-D 100/32, tan—MPC-D 100/20 (holotype of *Conchoraptor gracilis*). **Abbreviations**: **ang**, angular; **art**, articular; **astr**, astragalus; **ax**, axis; **bulb**, distal bulb of chevrons; **calc**, calcaneum; **cart**, caudal articulation; **cne**, cnemial crest; **cor**, coronoid process; **corc**, coracoid contact; **dist**, distal caudal; **dpc**, deltopectoral crest; **ectp**, ectepicondylar tuber; **epi**, epipophysis; **fcc**, fibulocalcaneal contact; **fib**, fibula; **fus**, fusion; **hd**, humeral head; I-**2**; Manual ungual I-2; **II-1**, manual phalanx II-1; **II-2**, manual phalanx II-2; **II-3**, manual phalanx II-3; **III-1**, manual phalanx III-1; **III-2**, manual phalanx III-2; **ltrb**, lateral trabecula; **MC I**, metacarpal I; **MC II**, metacarpal II; **MC III**, metacarpal III; **prz**, prezygapophysis; **pstz**, postzygapophysis; **slc**, semilunate carpal; **ss**, surangular spine; **stcp**, sternocoracoidal process.
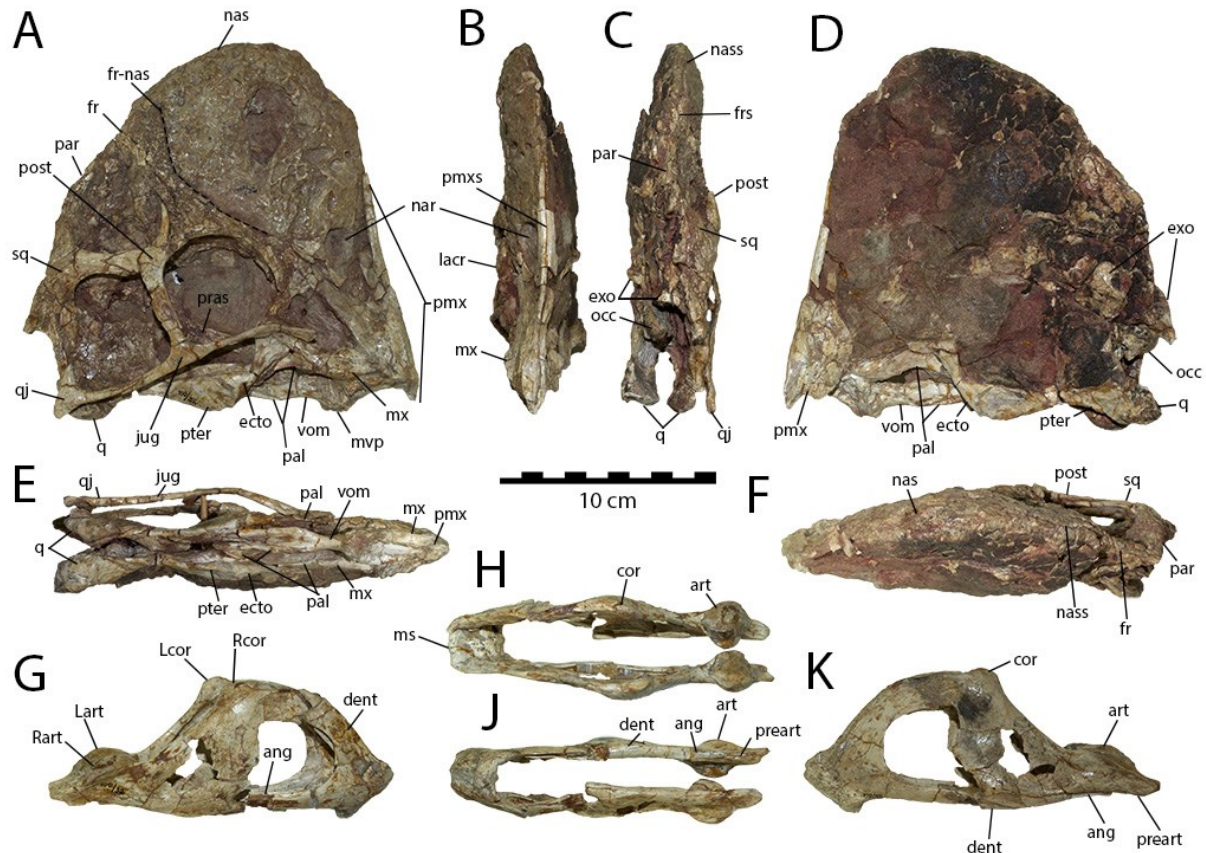
Fig. 4.17. Skull and mandible of *Rinchenia mongoliensis*.

Skull (A-F) and mandible (G-K) of MPC-D 100/32-A. Skull in right lateral (A), anterior (B), posterior (C), right lateral (D), ventral (E), and dorsal (F) views. Mandible in right lateral (G), dorsal (H), ventral (J), and left lateral (K) views. **Abbreviations**: **ang**, angular; **art**, articular; **cor**, coronoid process; **dent**, dentary; **ecto**, ectopterygoid; **exo**, exoccipital; **fr**, frontal; **frs**, interfrontal suture; **fr-nas**, nasofrontal suture; **jug**, jugal; **lacr**, lacrimal; **Lart**, left articular; **Lcor**, left coronoid process; **ms**, intermandibular suture; **mvp**, maxillovomeral process; **mx**, maxilla; **nar**, naris; **nas**, nasal; **nass**, internasal suture; **occ**, occipital condyle; **pal**, palatine; **par**, parietal; **pmx**, premaxilla; **pmxs**, interpremaxillary suture; **pne**, pneumatic foramina; **post**, postorbital; **pras**, parasphenoid; **preart**, prearticular; **pter**, pterygoid; **q**, quadrate; **qj**, quadratojugal; **Rart**, right aticular; **Rcor**, right coronoid process; **sq**, squamosal; **vom**, vomer.

559
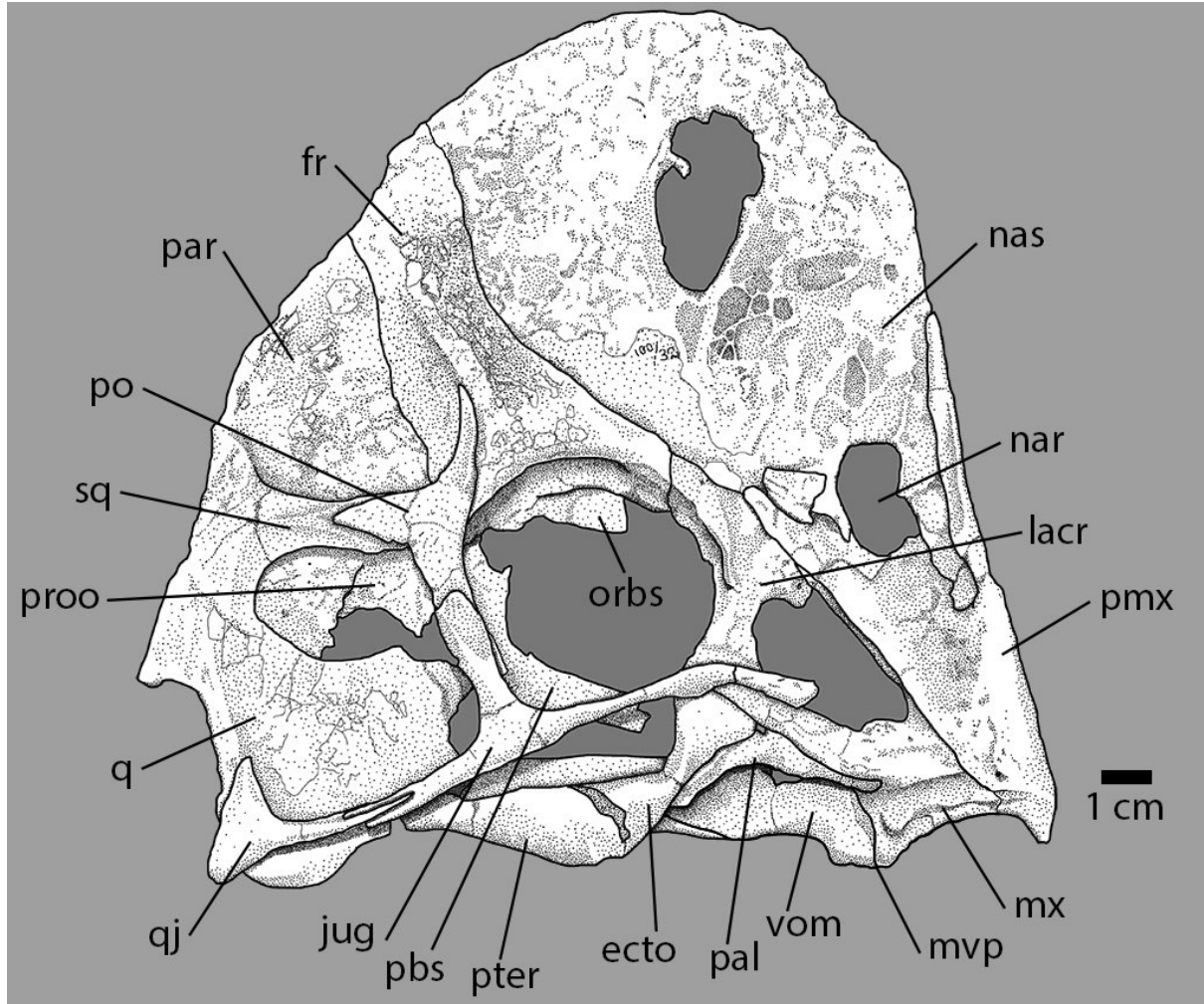
Fig. 4.18. Skull of *Rinchenia mongoliensis*.

Illustration of the skull of MPC-D 100/32-A in right lateral view. **Abbreviations: ecto**,

ectopterygoid; **fr**, frontal; **jug**, jugal; **lacr**, lacrimal; **mvp**, maxillovomeral process; **mx**, maxilla;

nar, naris; **nas**, nasal; **orbs**, orbitosphenoid; **pal**, palatine; **par**, parietal; **pbs**, parabasisphenoid;

pmx, premaxilla; **po**, postorbital; **proo**, prootic; **pter**, pterygoid; **q**, quadrate; **qj**, quadratojugal;

sq, squamosal; **vom**, vomer.
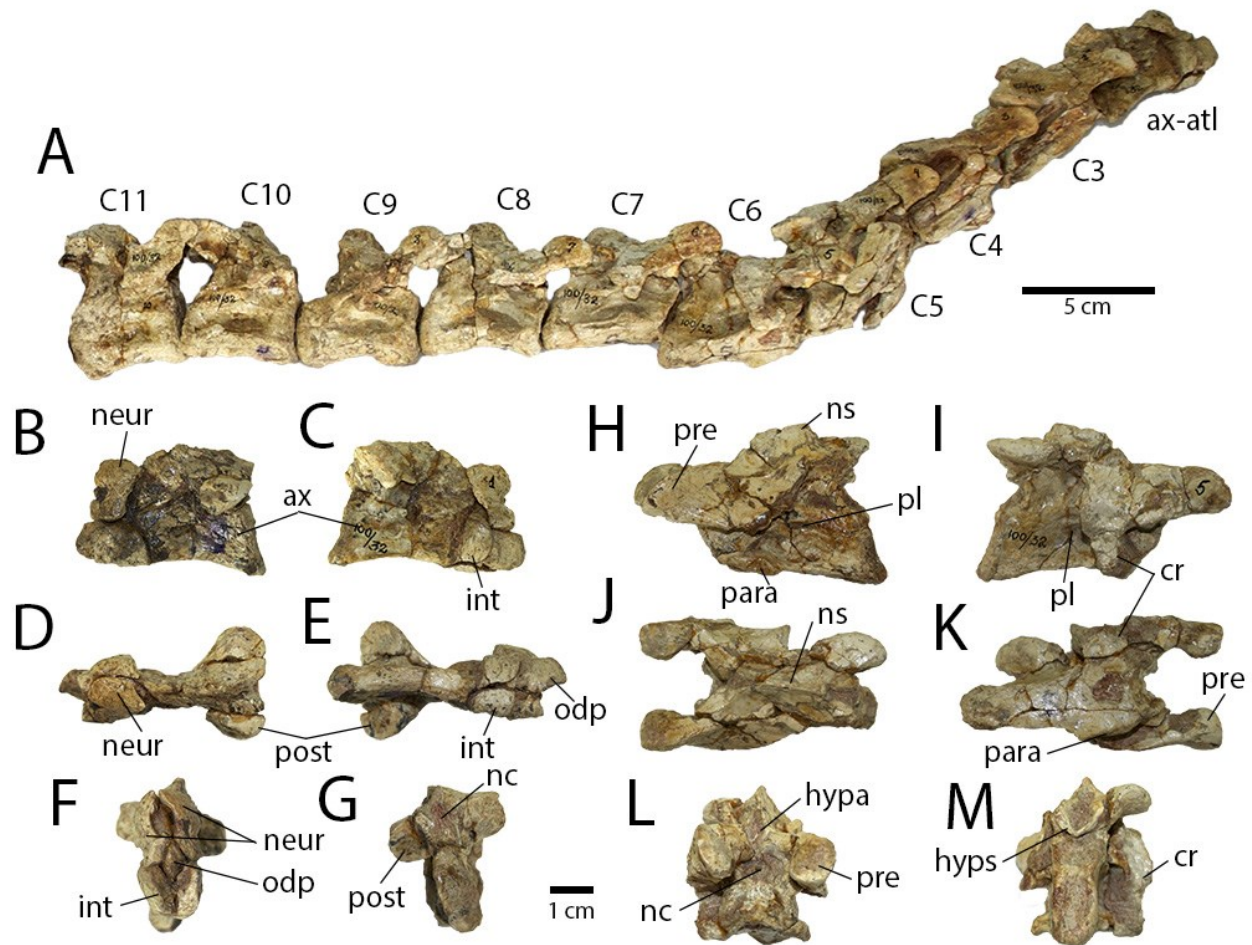
Fig. 4.19. Cervical vertebrae of *Rinchenia mongoliensis*.

Articulated cervical series of MPC-D 100/32 in right lateral view (A). Atlas-axis complex in left lateral (B), right lateral (C), dorsal (D), ventral (E), anterior (F), and posterior (G) views. Mid-cervical vertebra in left lateral (H), right lateral (I), dorsal (J), ventral (K), anterior (L) and posterior (M) views. **Abbreviations: ax**, axis; **ax-atl**, axis-atlas complex; **C3–C11**, third to eleventh cervical vertebrae; **cr**, cervical rib; **hypa**, hypantrum; **hyps**, hyposphene; **int**, atlas intercentrum; **nc**, neural canal; **neur**, neuropophysis; **ns**, neural spine; **odp**, odontoid process; **para**, parapophysis; **pl**, pleurocoel; **post**, postzygapophysis; **pre**, prezygapophysis.

A

D10 D9 D8 D7 D6 D5 D4 D3 D2 D1

1 cm

B — ns, pl, hypp
C — idpf, hypp
H — post, ncs, pl
I — post, idpf, pl
D — post
E — hypp
J — ns, nc
K — k
F — hypa, hypp
G — post, hyps, nc
L — hypa, nc
M — nc
N — lg, mg, cg, str

5 cm
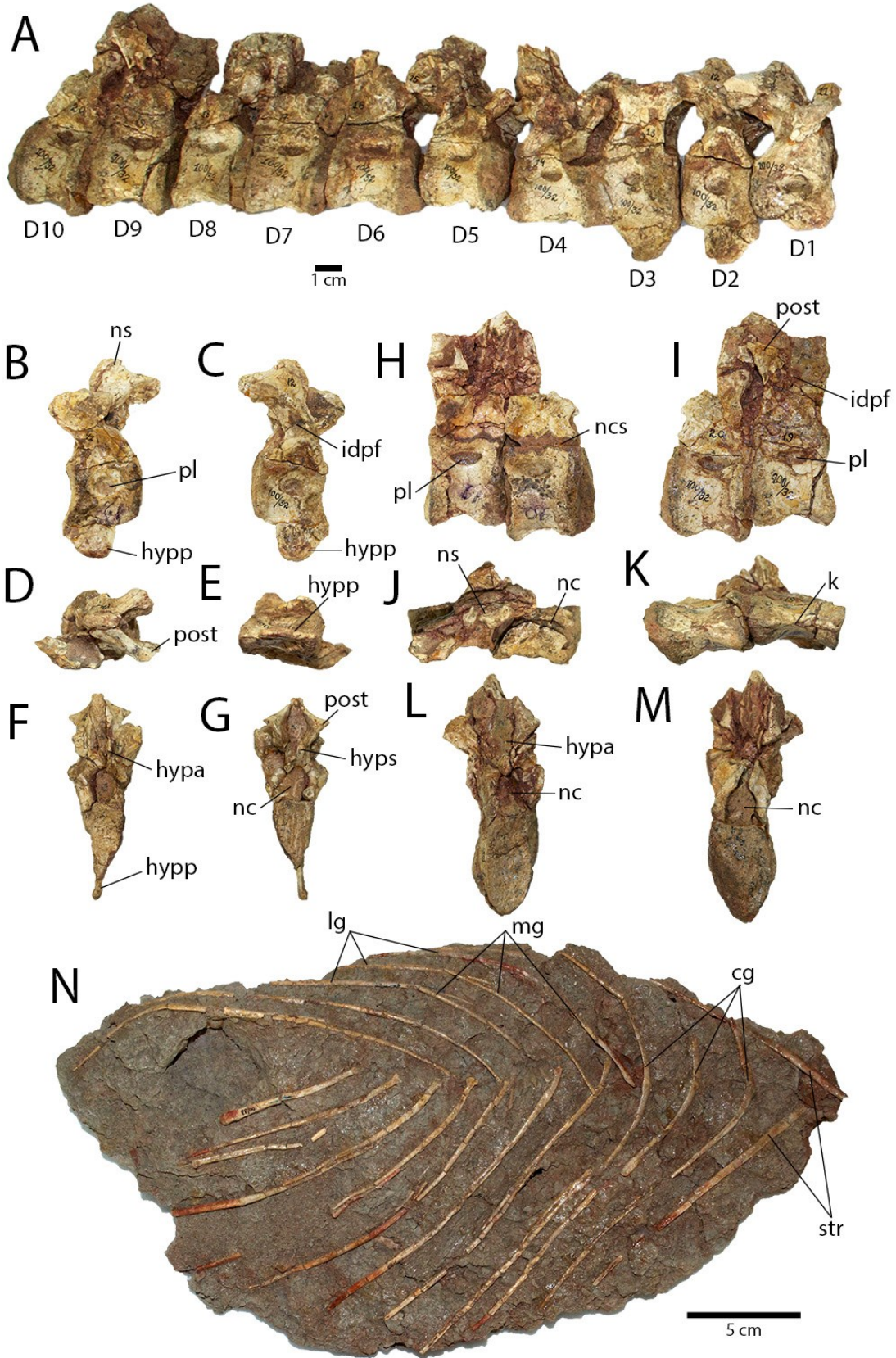
Fig. 4.20. Dorsal vertebrae and gastralia of *Rinchenia mongoliensis*.

Articulated dorsal series of MPC-D 100/32-A in right lateral view (A). Second cervicodorsal vertebra in left lateral (B), right lateral (C), dorsal (D), ventral (E), anterior (F), and posterior (G) views. Two articulated posterior dorsal vertebrae in left lateral (H), right lateral (I), dorsal (J), ventral (K), anterior (L) and posterior (M) views. Articulated gastralia in ventral view (N).

Abbreviations: cg, chevron-like anterior gastralia; **D1–D10**, first to tenth dorsal vertebrae; **hypa**, hypantrum; **hypp**, hypapophysis; **hyps**, hyposphene; **idpf**, infradiapophyseal fossa; **k**, keel; **lg**, lateral gastralia; **mg**, medial gastralia; **nc**, neural canal; **ncs**, neurocentral suture; **ns**, neural spine; **pl**, pleurocoel; **post**, postzygapophysis; **str**, sternal ribs.
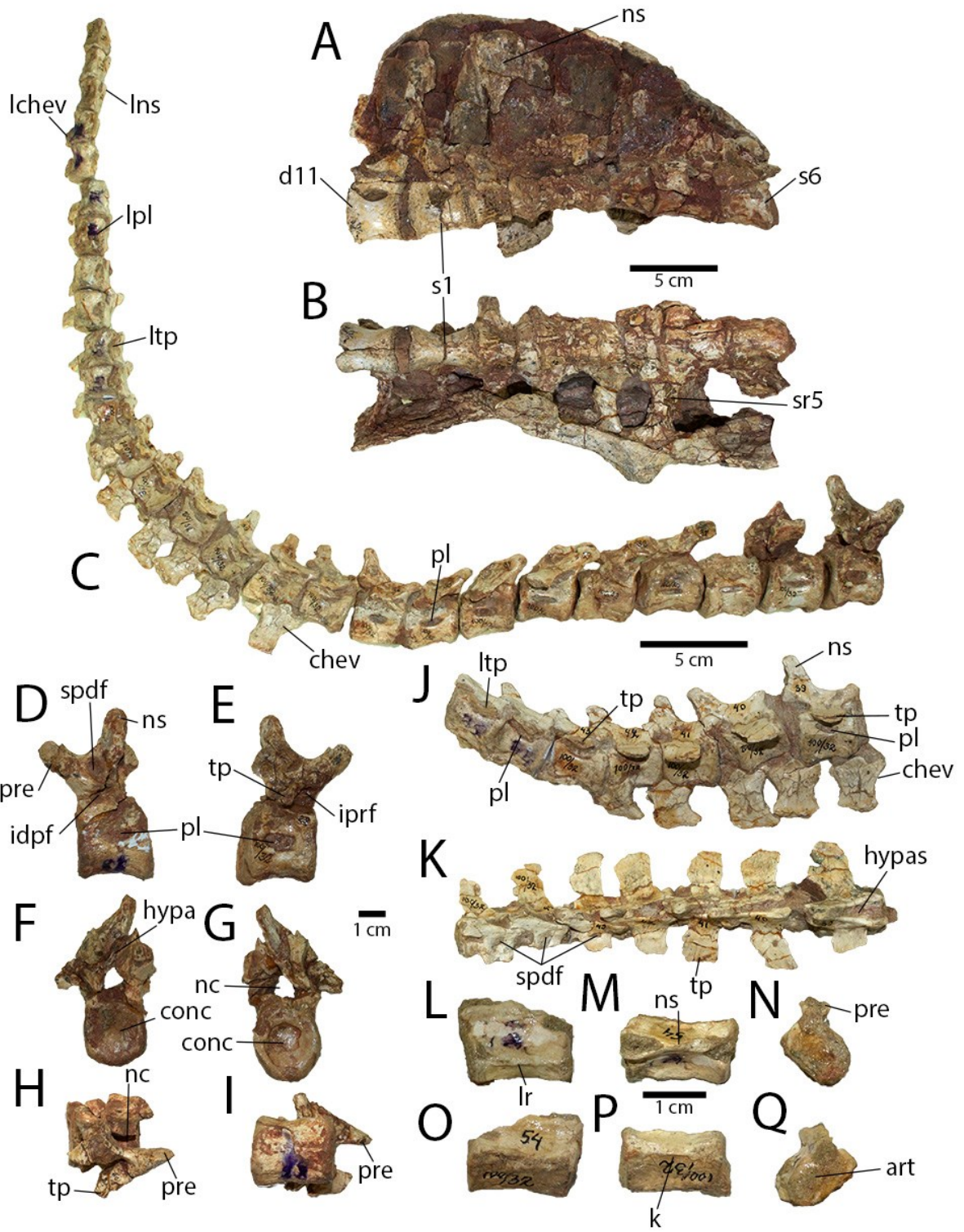
(Previous page)
Fig. 4.21. Sacral and caudal vertebrae of *Rinchenia mongoliensis*.

Sacrum and articulated right ilium of MPC-D 100/32-A in left lateral (A) and ventral (B) views.

Articulated caudal series in right lateral view (C). Proximal caudal vertebra in left lateral (D),

right lateral (E), anterior (F), posterior (G), dorsal (H), and ventral (I) views. Articulated block of

mid-caudal vertebrae in right lateral (J) and dorsal (K) views. Distal caudal in left lateral (L),

dorsal (M), anterior (N), right lateral (O), ventral (P), and posterior (Q) views. **Abbreviations:**

art, articular face; **chev**, chevron; **conc**, concavity; **d11**, eleventh dorsal vertebra; **hypa**,

hypantrum; **hypas**, hypantral slot; **idpf**, infradiapophyseal fossa; **iprf**, infraprezygapophyseal

fossa; **k**, keel; **lchev**, last chevron; **lns**, last neural spine; **lpl**, last pleurocoel; **lr**, lateral ridge; **ltp**,

last transverse process; **nc**, neural canal; **ns**, neural spine; **pl**, pleurocoel; **pre**, prezygapophysis;

s1, first sacral vertebral; **s6**, sixth sacral vertebra; **spdf**, supradiapophyseal fossa; **sr5**, fifth sacral

rib; **tp**, transverse process.
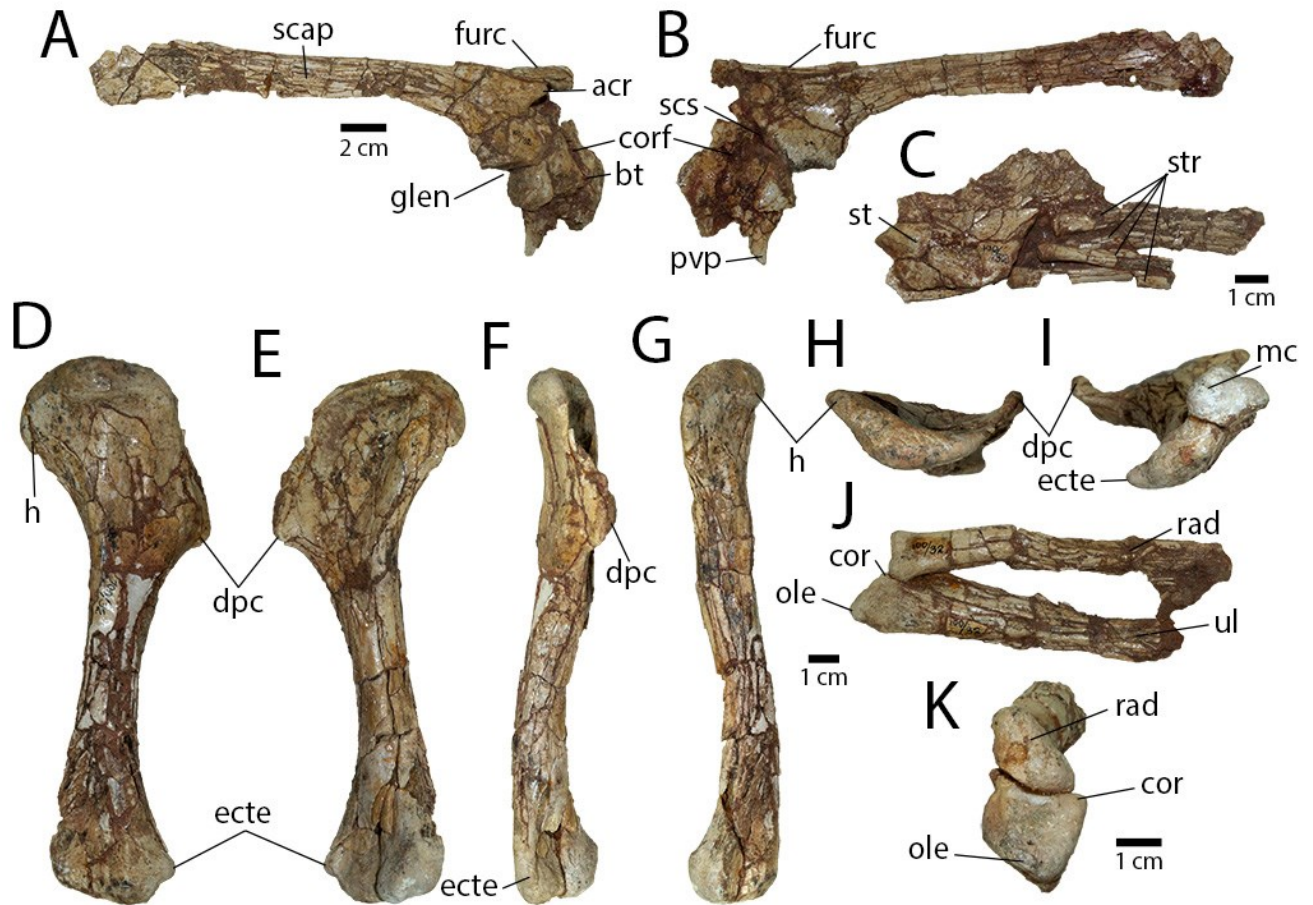
Fig. 4.22. Forelimb elements of *Rinchenia mongoliensis*.

Right scapulacoracoid of MPC-D 100/32-A in lateral (A) and medial (B) views. Sternal plates in ?right lateral view (C). Right humerus in posterior (D), anterior (E), lateral (F), medial (G), proximal (H), and distal (I) views. Right ulna and radius in lateral (J) and proximal (K) views.

Abbreviations: acr, acromion process; **bt**, biceps tubercle; **cor**, coronoid process; **corf**, coracoid foramen; **dpc**, deltopectoral crest; **ecte**, ectepicondylar tuber; **furc**, furcula; **glen**, glenoid; **h**, head; **mc**, medial condyle; **ole**, olecranon process; **pvp**, posteroventral process; **rad**, radius; **scap**, scapula; **scs**, scapula–coracoid suture; **st**, sternal plate; **str**, sternal ribs; **ul**, ulna.
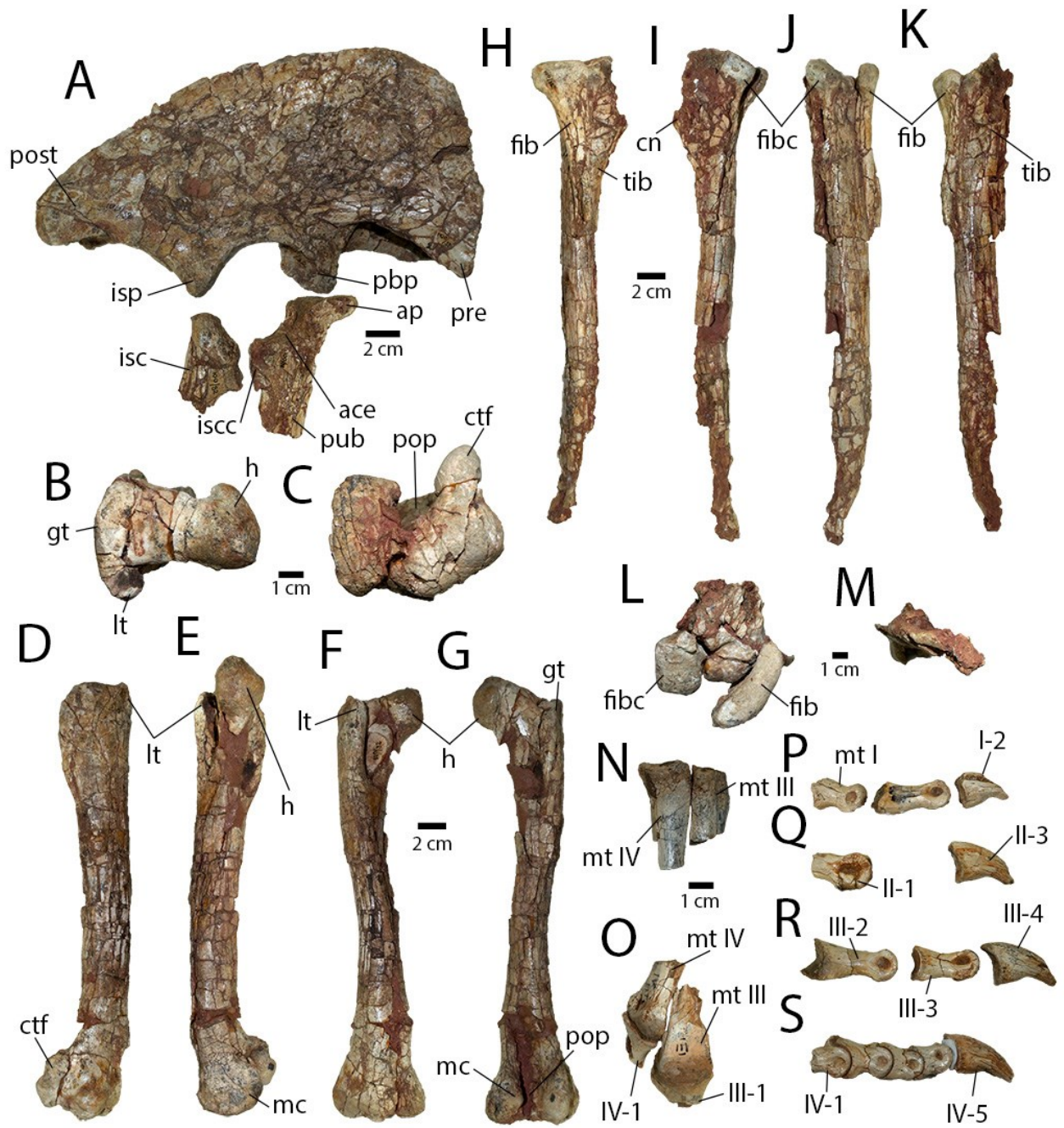
Fig. 4.23. Hindlimb elements of *Rinchenia mongoliensis*.

Pelvic elements of MPC-D 100/32-A in right lateral view (A). Right femur in proximal (B),

distal (C), lateral (D), medial (E), anterior (F), and posterior (G) views. Right tibia in lateral (H),

medial (I), posterior (K), anterior (K), proximal (L), and distal (M) views. Proximal ends of right

metatarsals III and IV in anterior (N) view. Distal ends of right metatarsals III and IV in anterior

(O) view. Lateral views of right pedal digits I (P), II (Q), III (R), and IV (S). **Abbreviations:**

ace, acetabulum; **ap,** anterior process; **cn**, cnemial crest; **ctf**, crista tibiofibularis; **fib**, fibula; **fibc**,

fibular condyle; **gt**, greater trochanter; **h**, head; **I-2**, pedal ungual I-2; **II-1**, pedal phalanx II-2; **II-**

3, pedal ungual II-3; **III-1**, pedal phalanx III-1; **III-2**, pedal phalanx III-2; **III-3**, pedal phalanx

III-3; **III-4**, pedal ungual III-4; **isc**, ischium; **iscc**, ischadic contact; **isp**, ischadic peduncle; **IV-1**,

pedal phalanx IV-1; **IV-5**, pedal ungual IV-5; **lt**, lesser trochanter; **mc**, medial condyle; **mt I**,

metatarsal I; **mt III**, metatarsal III; **mt IV**, metatarsal IV; **pbp**, pubic peduncle; **pop**, popliteal

fossa; **post**, postacetabular blade; **pre**, preacetabular blade; **pub**, pubis.
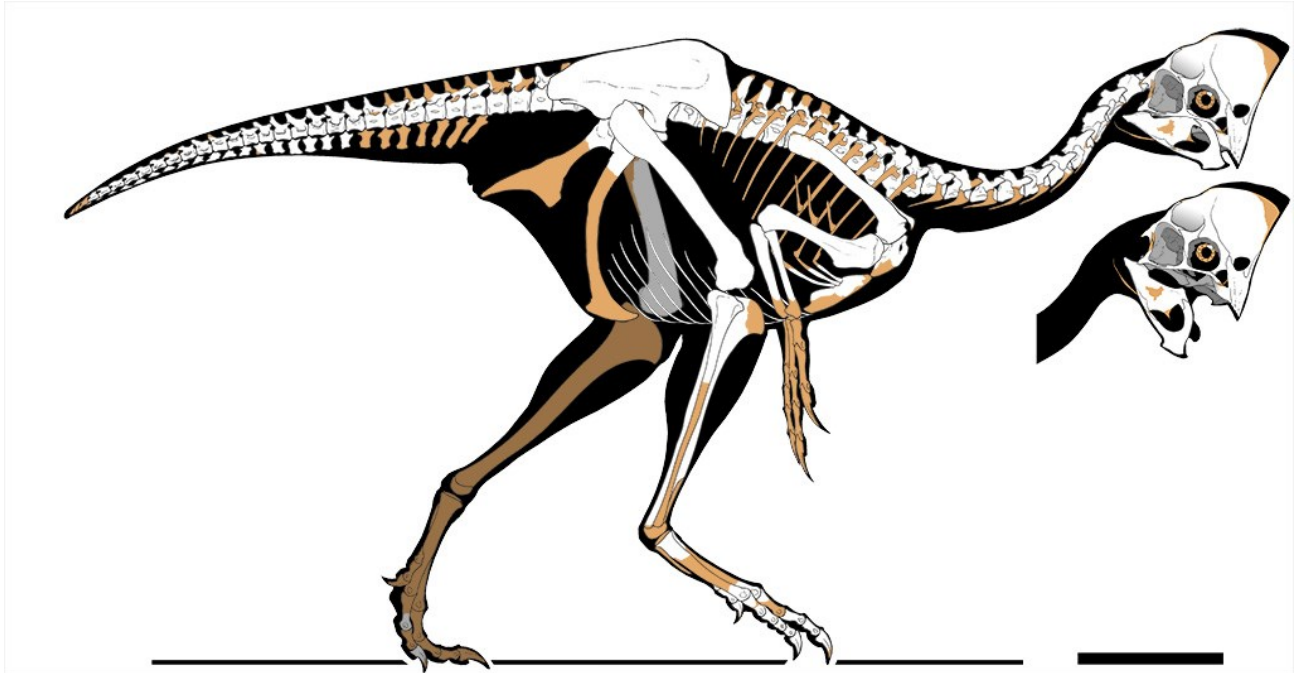
Fig. 4.24. Skeletal reconstruction of *Rinchenia mongoliensis*.

Skeletal reconstruction based on MPC-D 100/32-A. Known elements are white, missing regions

are shaded orange. Original artwork by Marco Auditore, used with permission.
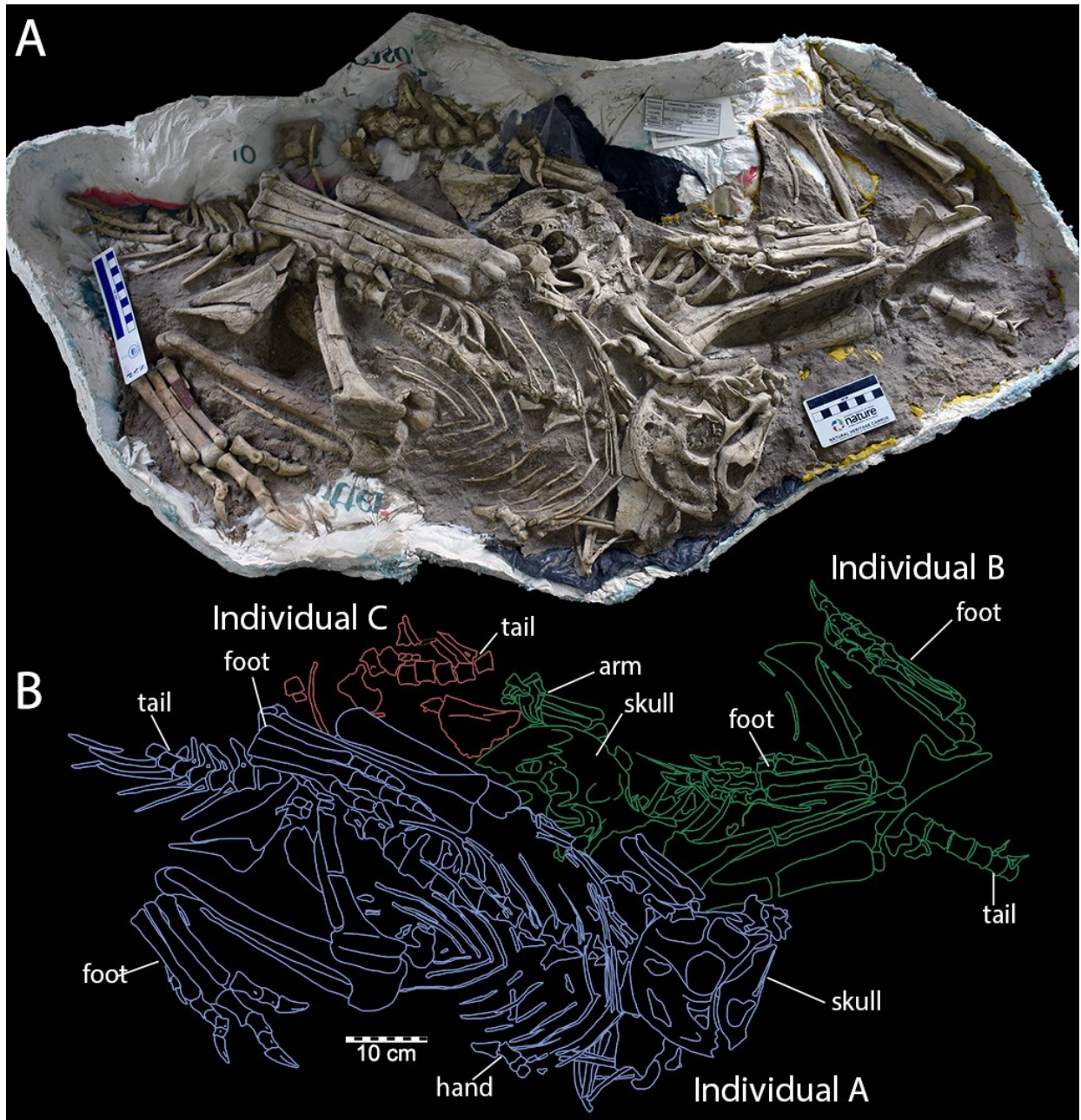
Fig. 4.25. Poached block of the Guriliin Tsav oviraptorid.

Photograph (A) and line drawing (B) of MPC-D 102/110. Colors correspond to different

individuals: A (blue), B (green), and C (red). Scale bars are 10 cm (left) and 8 cm (right).
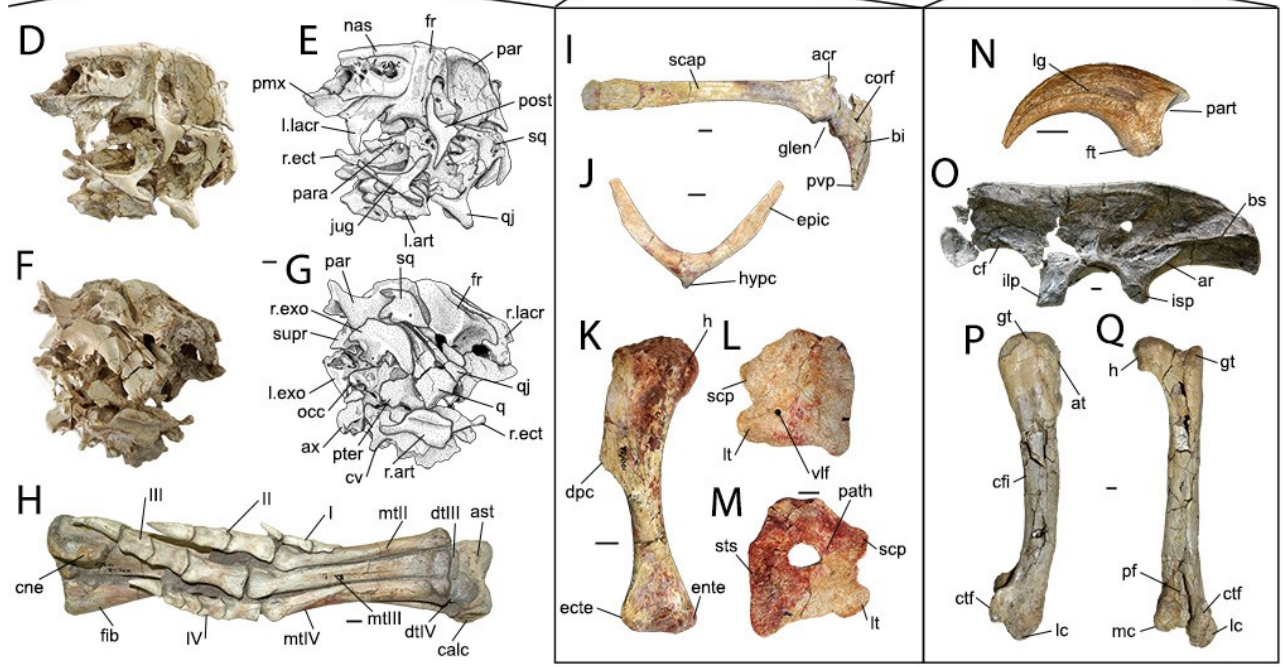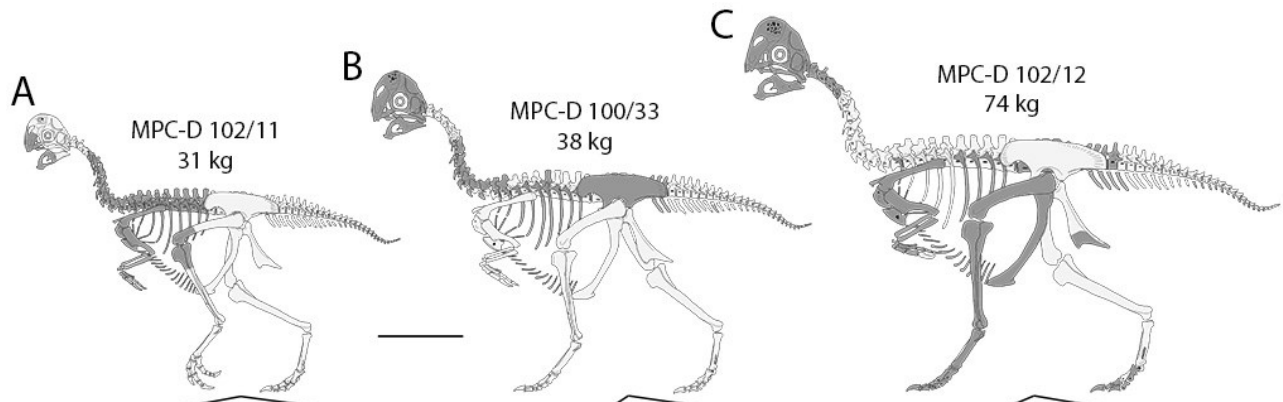
(Previous page)
Fig. 4.26. Other specimens of the Guriliin Tsav oviraptorid.

Reconstructions of MPC-D 102/11 (A), MPC-D 100/33 (B) and MPC-D 102/12 (C) showing scale skeletal representation (shaded elements are missing). Skull of MPC-D 102/11 in left lateral view (D) and illustration (E). Skull of MPC-D 102/11 in right ventrolateral view (F) and illustration (G). Tibiotarsus and foot of MPC-D 102/11 (H), showing exceptional preservation and articulation. Right scapulocoracoid of MPC-D 100/33 in right lateral view (I). Furcula of MPC-D 100/33 in anterior view (J). Right humerus of MPC-D 100/33 in anterior view (K). Right (L) and left (M) sternal plates of MPC-D 100/33 in anterior view. Left manual ungual I-2 of MPC-D 102/12 in lateral view (N). Right ilium of MPC-D 102/12 in medial view (O). Right femur of MPC-D 102/12 in lateral (P) and posterior (Q) views. Scale bars: A–C, 25 cm; D–Q, 1 cm. **Abbreviations: acr**, acromion process; **ar**, accessory ridge; **ast**, astragalus; **at**, anterior trochanter; **ax**, axis; **bi**, biceps tubercle; **bs**, brevis shelf; **calc**, calcaneum; **cf**, cuppedicus fossa; **cfi**, m. caudofemoralis insertion; **cne**, cnemial crest of tibia; **corf**, coracoid foramen; **ctf**, crista tibiofibularis; **cv**, cervical vertebra; **dpc**, deltopectoral crest; **dtIII**, distal tarsal III; **dtIV**, distal tarsal IV; **ecte**, ectepicondylar tuber; **epic**, epicleidium; **ente**, entepicondylar tuber; **fib**, fibula; **fr**, frontal; **ft**, flexor tubercle; **glen**, glenoid; **gt**, greater trochanter; **h**, head; **hypc**, hypocleidium; **I**, digit I; **II**, digit II; **III**, digit III; **IV**, digit IV; **ilp**, iliac peduncle; **isp**, ishiadic peduncle; **jug**, jugal; **l.art**, left articular; **l.exo**, left exoccipital; **l.lacr**, left lacrimal; **lc,** lateral condyle; **lg**, lateral groove; **lt**, lateral trabecula; **mc**, medial condyle; **mtII**, metatarsal II; **mtIII**, metatarsal III; **mtIV**, metatarsal IV; **nas**, nasal; **occ**, occipital condyle; **path**, pathology; **par**, parietal; **para**, parabasisphenoid; **part**, proximal articulation; **pf**, popliteal fossa; **pmx**, premaxilla; **post**, postorbital; **pter**, pterygoid; **pvp**, posteroventral process; **q**, quadrate; **qj**, quadratojugal; **r.art**, right articular; **r.ect**, right ectopterygoid; **r.exo**, right exoccipital; **r.lacr**, right lacrimal; **scap**,

scapula; **scp**, sternocoracoidal process; **sq**, squamosal; **supr**, supraoccipital; **sts**, sternal articulation surface; **vlf**, ventrolateral foramen.

B

C
nas fr
par
post
pmx
mx
dent
crtb
qj
q

D
rad
uln
slc

F
III-1
mc II
mc III
II-2
II-1
II-3
I-1
mc I
I-2

E
ulr
slc
radl
III-1
mc III

H
slc
int
ulr

J
epi
pl
cr

A

G
dist
prox

I
il
sac
dor
isc
pub
pbt

K
ns
spdf
tp
idpf

L
p1 p2
p3

M
ds sac cs
il
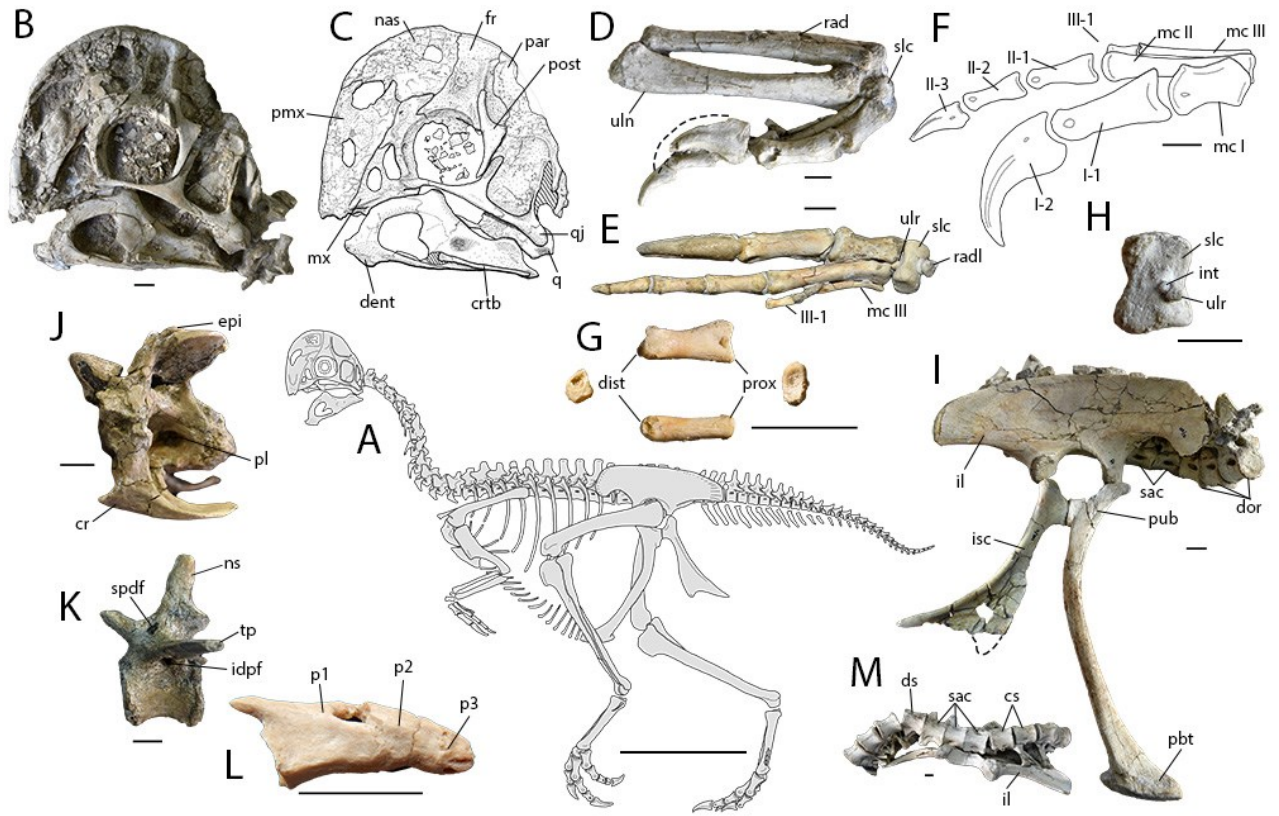
(Previous page)
Fig. 4.27. Overview of the anatomy of the Guriliin Tsav oviraptorid.

Composite reconstruction (A). Skull (MPC-D 102/110-a) in lateral view (B, C). Right antebrachium (MPC-D 102/110-a) in lateral view (D). Hand (MPC-D 102/110-a) in dorsal (E) and lateral (F, reconstructed) views. Manual phalanx III-1 (G) in lateral (top), distal (left), proximal (right) and dorsal (bottom) views, showing blunted, non-articular distal end. Carpals in distal view (H). Composite image of articulated pelvis and vertebrae (MPC-D 102/11) in lateral view (I; ischium is restored). Cervical vertebra (MPC-D 102/12) in lateral view (J). Caudal vertebra (MPC-D 102/12) in lateral view (K). Pygostyle (MPC-D 102/12) in lateral view (L). Sacral region (MPC-D 102/11) in ventral view (M), showing only three fused sacral vertebrae. Scale bars, A, 25 cm; B–M, 1 cm. **Abbreviations: cr**, cervical rib; **crtb**, ceratobranchial; **cs**, caudosacral vertebrae; **dent**, dentary; **dist**, distal end; **dor**, dorsal vertebrae; **ds**, dorsosacral; **epi**, epipophysis; **fr**, frontal; **I-1–2**, manual phalanges I-1–2; **II-1–3**, manual phalanges II-1–3; **III-1**, manual phalanx III-1; **idpf**, infradiapophyseal fossa; **int**, intermedium; **il**, ilium; **isc**, ischium; **mc I–III**, metacarpals I–III; **mx**, maxilla; **nas**, nasal; **ns**, neural spine; **p1–p3**, pygal vertebrae 1–3; **par**, parietal; **pbt**, pubic boot; **pl**, pleurocoel; **pmx**, premaxilla; **post**, postorbital; **prox**, proximal end; **pub**, pubis; **q**, quadrate; **qj**, quadratojugal; **rad**, radius; **sac**, sacral vertebrae; **slc**, semilunate carpal; **spdf**, supradiapophyseal fossa; **tp**, transverse process; **uln**, ulna; **ulr**, ulnare.
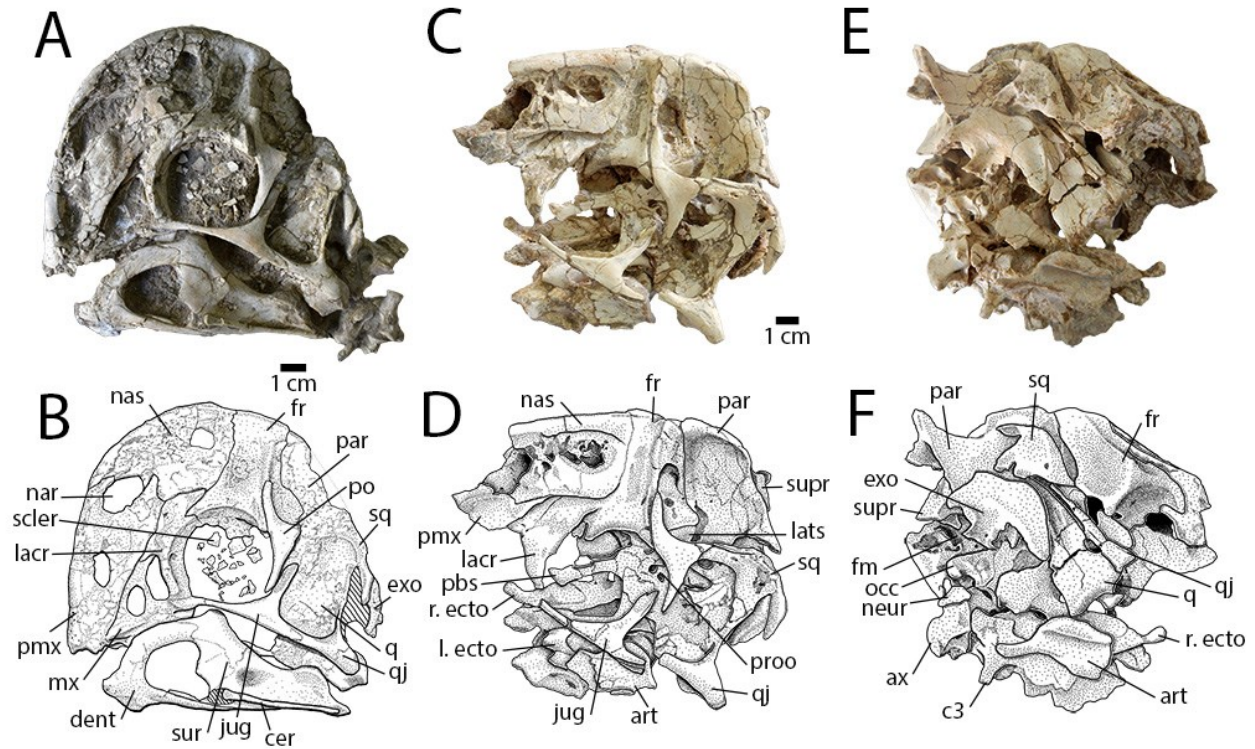
Fig. 4.28. Skulls of the Guriliin Tsav oviraptorid.

Photographs (A, C, E) and illustrations (B, D, F) of the skulls of MPC-D 102/110.a in left lateral view (A, B) and MPC-D 102/11 in left lateral (C, D) and right posterolateral (E, F) views.

Abbreviations: art, articular; **ax**, axis; **c3**, third cervical vertebra; **cer**, ceratobranchial; **dent**, dentary; **exo**, exoccipital; **fm**, foramen magnum; **fr**, frontal; **jug**, jugal; **l. ecto**, left ectopterygoid; **lacr**, lacrimal; **lats**, laterosphenoid; **mx**, maxilla; **nar**, naris; **nas**, nasal; **neur**, neuropophysis; **occ**, occipital condyle; **par**, parietal; **pbs**, parabasisphenoid; **pmx**, premaxilla; **po**, postorbital; **proo**, prootic; **q**, quadrate; **qj**, quadratojugal; **r. ecto**, right ectopterygoid; **scler**, sclerotic ossicles; **sq**, squamosal; **supr**, supraoccipital; **sur**, surangular.
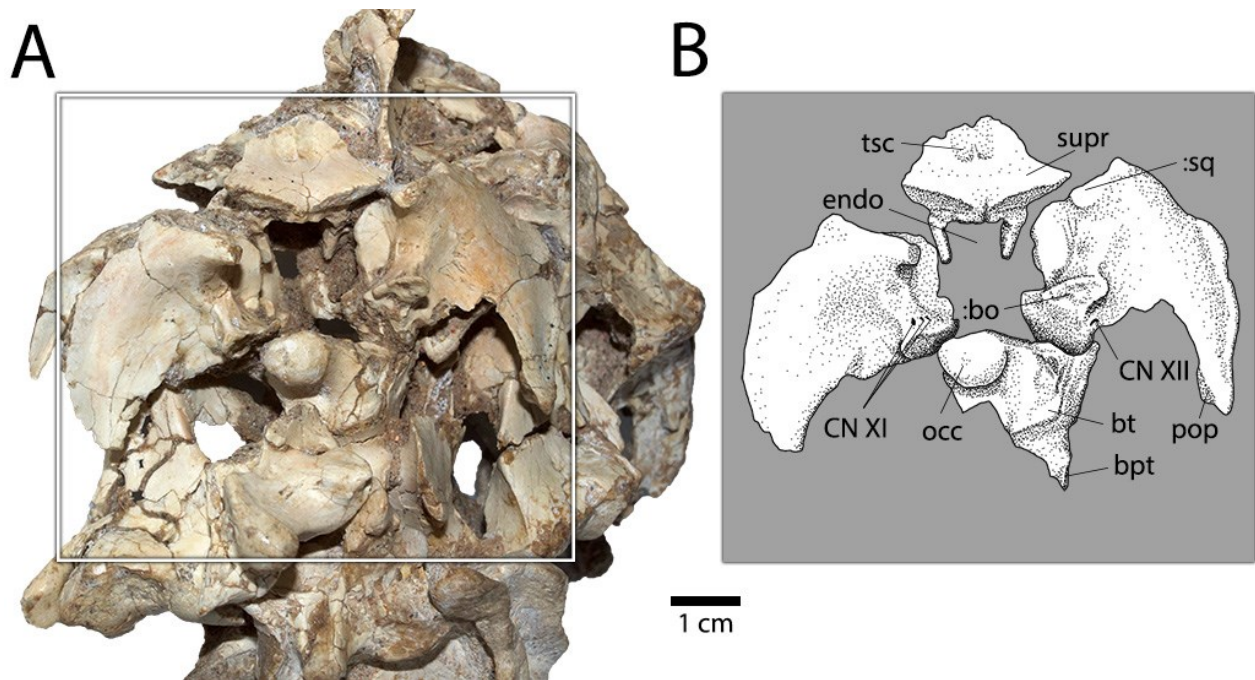
Fig. 4.29. Braincase of the Guriliin Tsav oviraptorid.

Photograph (A) and illustration (B) of the braincase of MPC-D 102/11 in posterior view. Box in (A) shows location of illustration B, only braincase elements are illustrated. **Abbreviations: :bo**, contact for basioccipital; **bpt**, basipterygoid process; **bt**, basal tuber; **CN XI**, foramen for cranial nerve XI; **CN XII**, foramen for cranial nerve XII; **endo**, endocranial cavity; **occ**, occipital condyle; **pop**, paroccipital process; **:sq**, contact for squamosal; **supr**, supraoccipital; **tsc**, insertion for *m. transversospinalis capitis*.
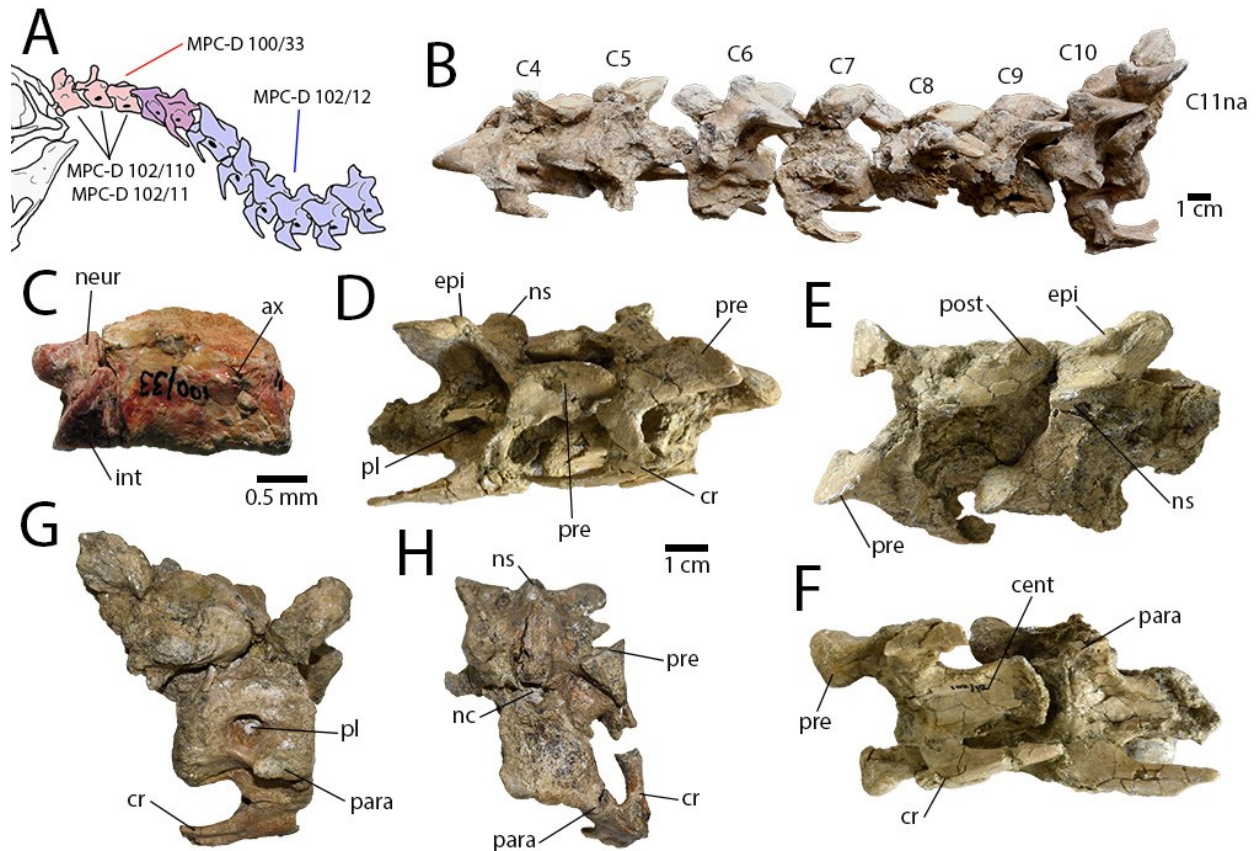
Fig. 4.30. Cervical vertebrae of the Guriliin Tsav oviraptorid.

Reconstruction (A) of cervical series showing which vertebrae are represented by which

specimens. Articulated series of middle to posterior cervical vertebrae of MPC-D 102/12 in left

lateral view (B). Atlas-axis of MPC-D 100/33 in left lateral view (C). Articulated anterior

cervical vertebrae of MPC-D 102/12 in right lateral (D), dorsal (E), and ventral (F) views.

Posterior cervical vertebra of MPC-D 102/12 in right lateral (G) and anterior (H) views.

Abbreviations: ax, axis; **C4–C10**, fourth to tenth cervical vertebrae; **C11na**, neural arch of

eleventh cervical vertebra; **cent**, centrum; **cr**, cervical rib; **epi**, epipophysis; **int**, atlas

intercentrum; **nc**, neural canal; **neur**, neuropophysis; **ns**, neural spine; **para**, parapophysis; **pl**,

pleurocoel; **post**, postzygapophysis; **pre** prezygapophysis.
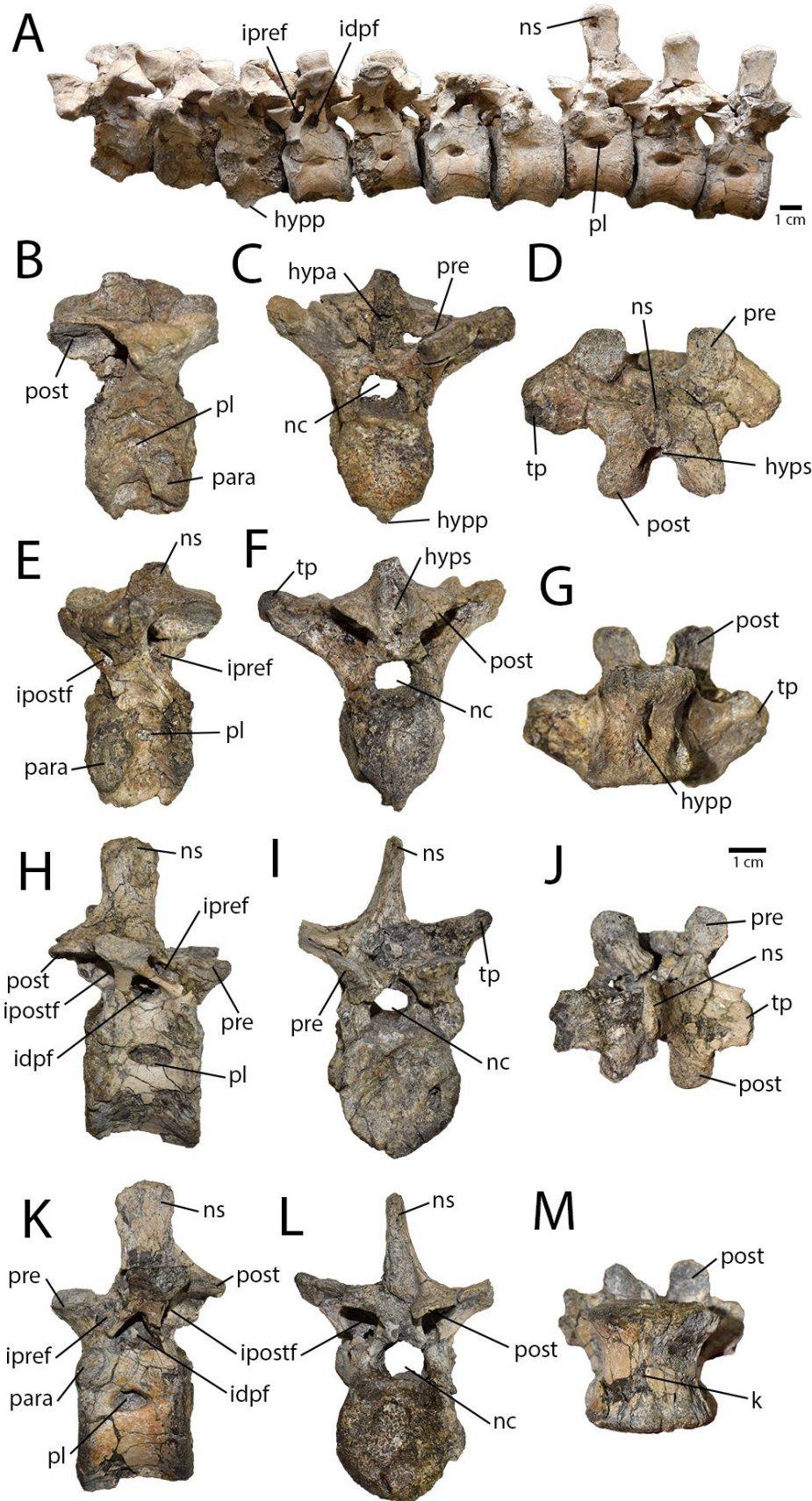
Fig. 4.31. Dorsal vertebrae of the Guriliin Tsav oviraptorid.

Dorsal vertebrae of MPC-D 102/12. Articulated dorsal series in left lateral view (A). Third cervicodorsal vertebra (B–G) in right lateral (B), anterior (C), dorsal (D), left lateral (E), posterior (F), and ventral (G) views. Posterior dorsal vertebra (H–M) in right lateral (H), anterior (I), dorsal (J), left lateral (K), posterior (L), and ventral (M) views. **Abbreviations: hypa**, hypantrum; **hypp**, hypapophysis; **hyps**, hyposphene; **idpf**, infradiapophyseal fossa; **ipref**, infraprezygapophyseal fossa; **ipostf**, infrapostzygapophyseal fossa; **k**, ventral keel; **nc**, neural canal; **ns**, neural spine; **para**, parapophysis; **pl**, pleurocoel; **post**, postzygapophysis; **pre**, prezygapophysis; **tp**, transverse process.
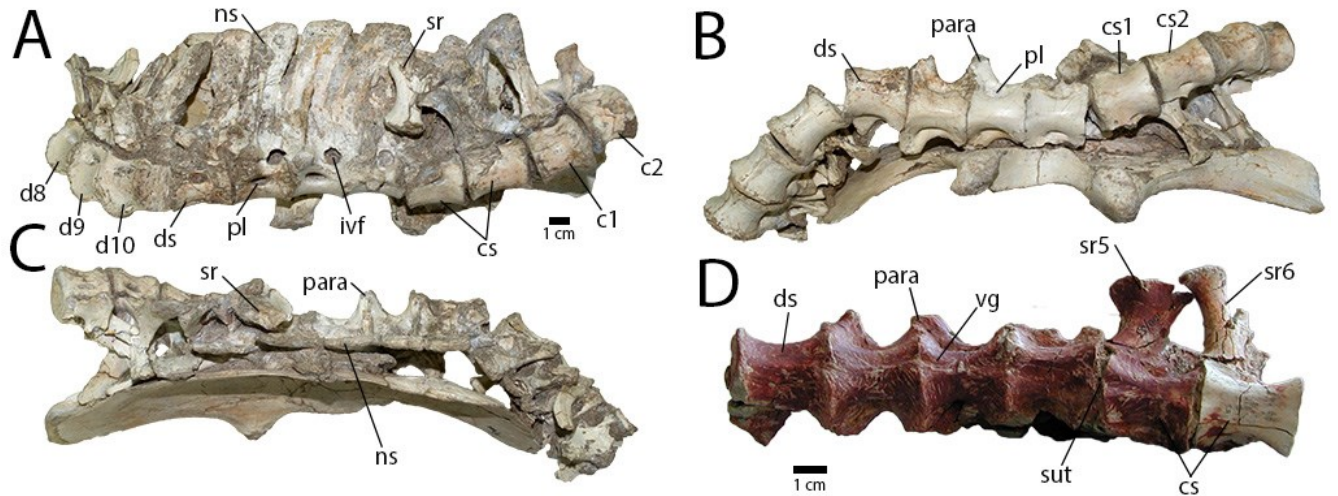
Fig. 4.32. Sacral vertebrae of the Guriliin Tsav oviraptorid.

Sacra of MPC-D 102/11 (A–C) and MPC-D 100/33 (D). Dorsal, sacral, and caudal vertebrae with associated right ilium of MPC-D 102/11 in left lateral (A), ventral (B) and dorsal (C) views. Sacrum of MPC-D 100/33 in ventral (D) view. **Abbreviations: c1–c2**, first and second caudal vertebrae; **cs**, caudosacral; **cs1–2**, first and second caudosacral vertebrae; **d8–d10**, eigth to tenth dorsal vertebrae; **ds**, dorsosacral; **ivf**, intervertebral fenestra; **ns**, neural spine; **para**, parapophysis; **pl**, pleurocoel; **sr**, sacral rib; **sr5–6**, fifth and sixth sacral ribs; **sut**, suture; **vg**, ventral groove.
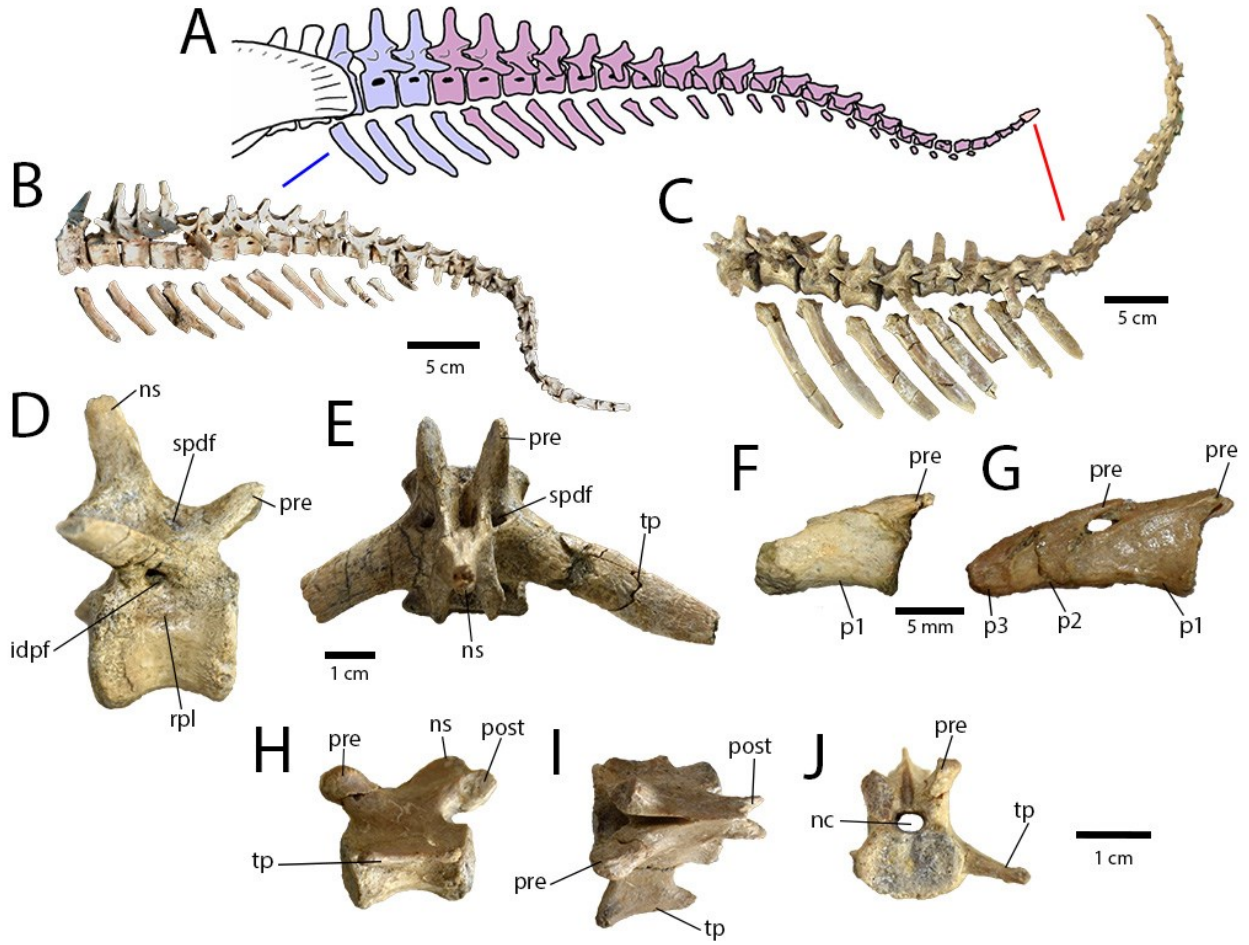
(Previous page)
Fig. 4.33. Caudal vertebrae of the Guriliin Tsav oviraptorid.

Reconstruction (A) of caudal series showing which vertebrae are represented by which specimens. Vertebrae shaded blue are preserved only in MPC-D 102/11 (B), whereas those shaded red (the pygal vertebrae) are preserved only in MPC-D 102/12 (C). Vertebrae shaded purple are represented by both specimens. Articulated caudal series of MPC-D 102/11 in left lateral view (B). Articulated caudal series of MPC-D 102/12 in right lateral view (C), mirrored to match the orientation of MPC-D 102/11. Proximal caudal vertebra of MPC-D 102/12 (D, E) in right lateral (D) and dorsal (E) views. Pygal vertebrae of MPC-D 102/11 (F) and MPC-D 102/12 (G), showing incorporation of additional vertebrae into the pygostyle. Distal caudal of MPC-D 102/12 (H–J) in left lateral (H), dorsal (I), and anterior (J) views. **Abbreviations: idpf**, infradiapophyseal fossa; **nc**, neural canal; **ns**, neural spine; **p1–p3**, first to third pygal vertebrae; **post**, postzygapophysis; **pre**, prezygapophysis; **rpl**, resorbed pleurocoel; **spdf**, supradiapophyseal fossa; **tp**, transverse process.
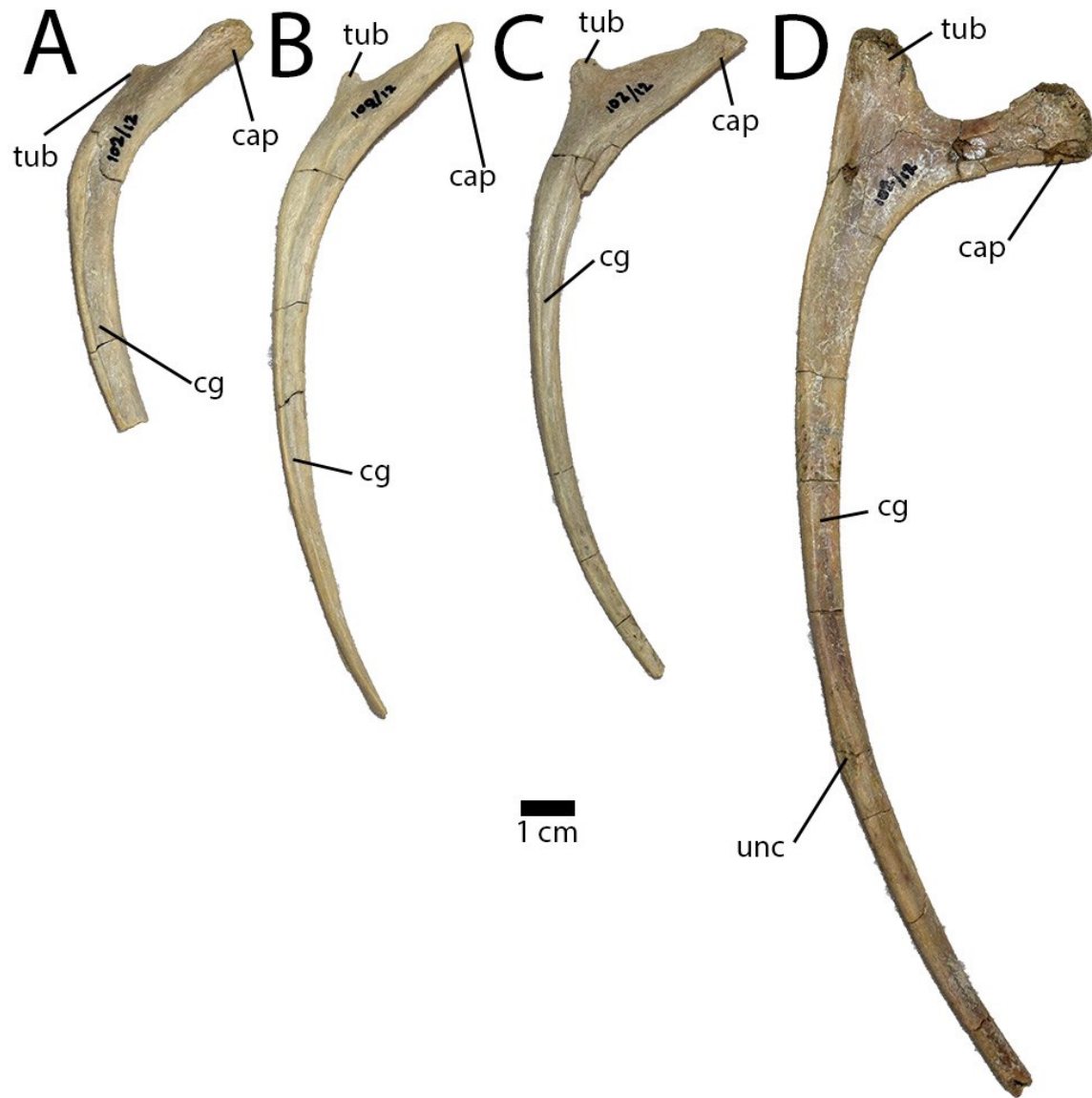
Fig. 4.34. Dorsal ribs of the Guriliin Tsav oviraptorid.

Right first dorsal rib (A), indeterminate anterior dorsal ribs (B, C), and middle dorsal rib (D) of MPC-D 102/12 in anterior view. **Abbreviations: cap**, capitulum; **cg**, costal groove; **tub**, tuberculum; **unc**, attachment for uncinate process.
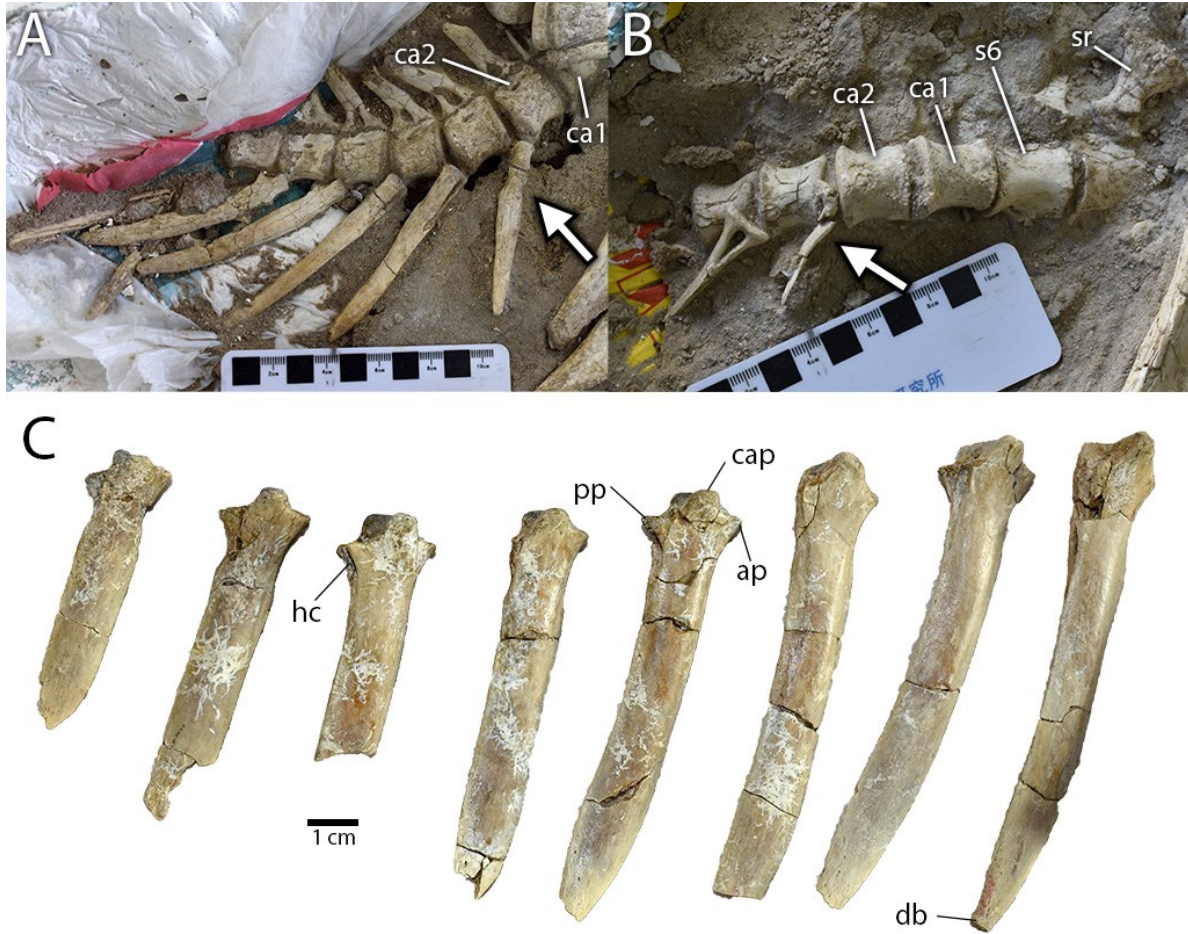
Fig. 4.35. Chevrons of the Guriliin Tsav oviraptorid.

Anterior chevrons of MPC-D 102/110.a (A) and MPC-D 102/110.b (B), showing disparity between size of the first chevron (arrows). Mid-caudal chevrons of MPC-D 102/12 in right lateral view (C). **Abbreviations: ap**, anterior process; **ca1–ca2**, first and second caudal vertebrae; **cap**, caudal articulating process; **db**, distal bulb; **hc**, haemal canal; **pp**, posterior process; **s6**, sixth sacral vertebra; **sr**, sacral rib.
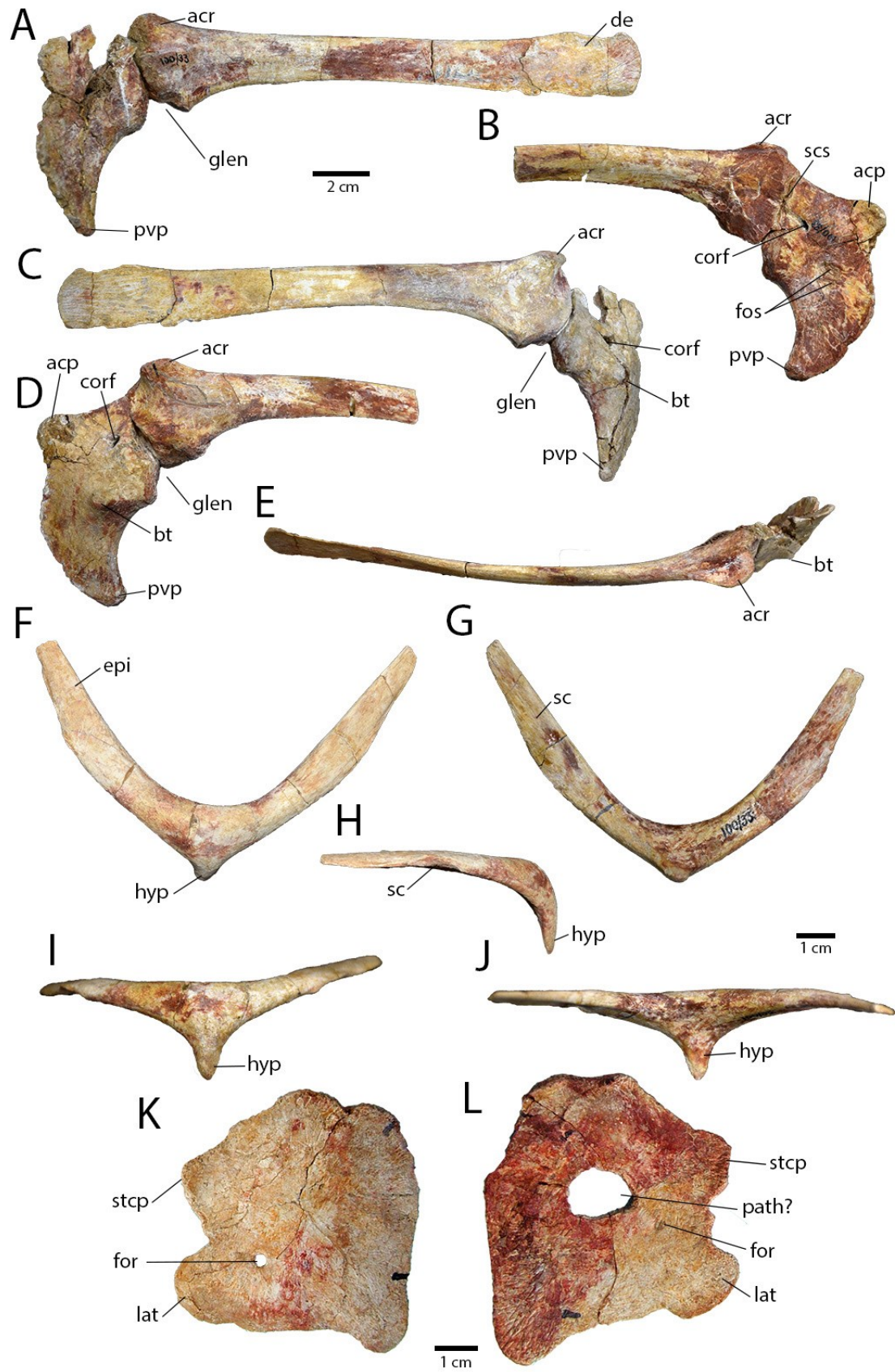
Fig. 4.36. Pectoral girdle of the Guriliin Tsav oviraptorid.

Pectoral girdle elements of MPC-D 100/33. Right scapulacoracoid in medial (A), lateral (C), and dorsal (E) views. Left scapulacoracoid in medial (B) and lateral (D) views. Furcula in anterior (F), posterior (G), right lateral (H), ventral (I) and dorsal (J) views. Right (K) and left (L) sternal plates in ventral view. **Abbreviations: acp**, acrocoracoid process; **acr**, acromion process; **bt**, biceps tubercle; **corf**, coracoid foramen; **de**, distal expansion; **epi**, epicleidal process; **for**, foramen; **fos**, fossa; **glen**, glenoid; **hyp**, hypocleidium; **lat**, lateral trabecula; **path?**, pathology?; **pvp**, posteroventral process; **sc**, scapular contact; **scs**, scapula–coracoid suture; **stcp**, sternocoracoidal process.
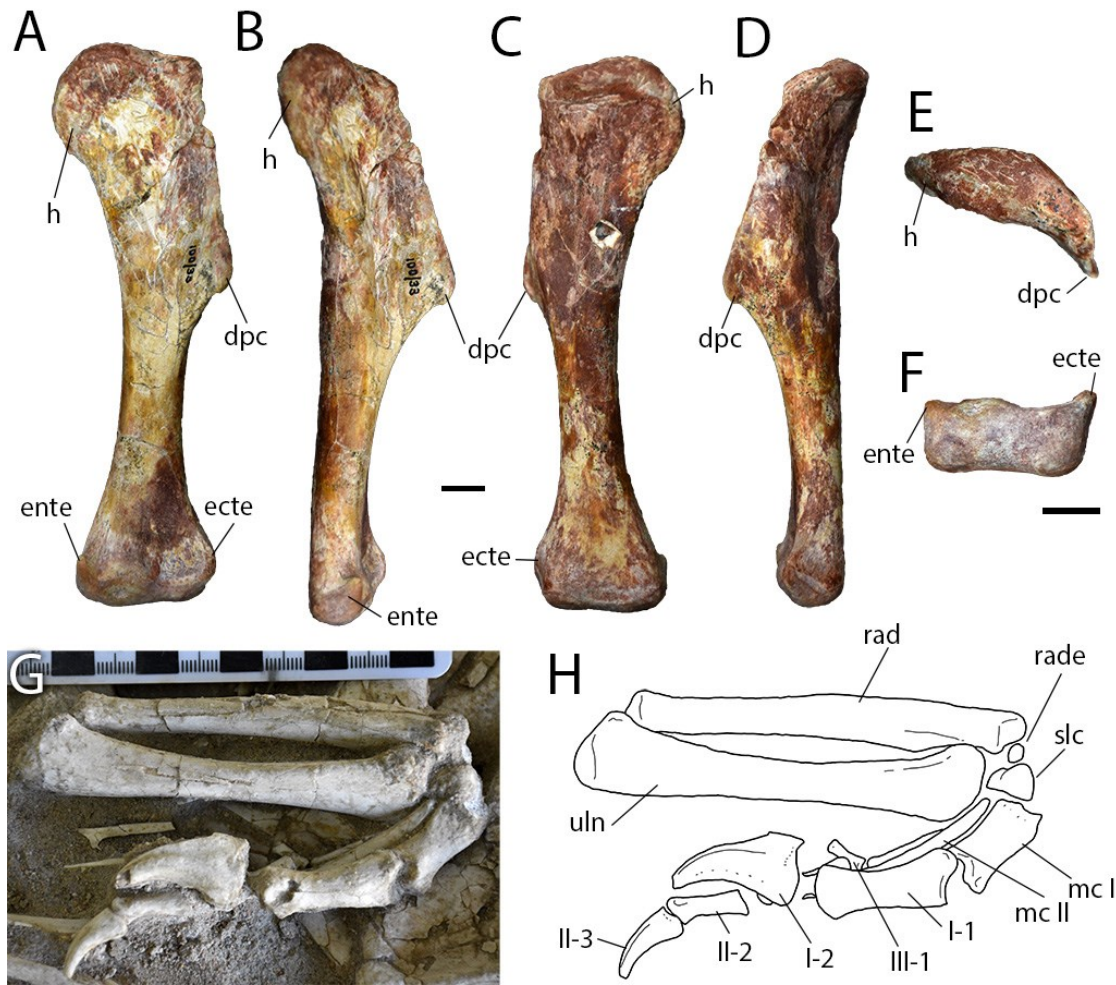
Fig. 4.37. Forelimb elements of the Guriliin Tsav oviraptorid.

Forelimb elements of MPC-D 100/33 (A–F) and MPC-D 102/110.a (G–H). Left humerus of MPC-D 100/33 in anterior (A), medial (B), posterior (C), lateral (D), proximal (E) and distal (F) views. Photograph (G) and illustration (H) of articulated antebrachium of MPC-D 102/110.a in ventral view. Scale bars in A–D and E–F are 1 cm. **Abbreviations: dpc**, deltopectoral crest; **ecte**, ectepicondylar tuber; **ente**, entepicondylar tuber; **h**, head; **I-1**, manual phalanx I-1; **I-2**, manual ungual I-2; **II-2**, manual phalanx II-2; **II-3**, manual ungual II-3; **III-1**, manual phalanx III-1; **mc I**, metacarpal I; **mc II**, metacarpal II; **rad**, radius; **rade**, radiale; **slc**, semilunate carpal; **uln**, ulna.
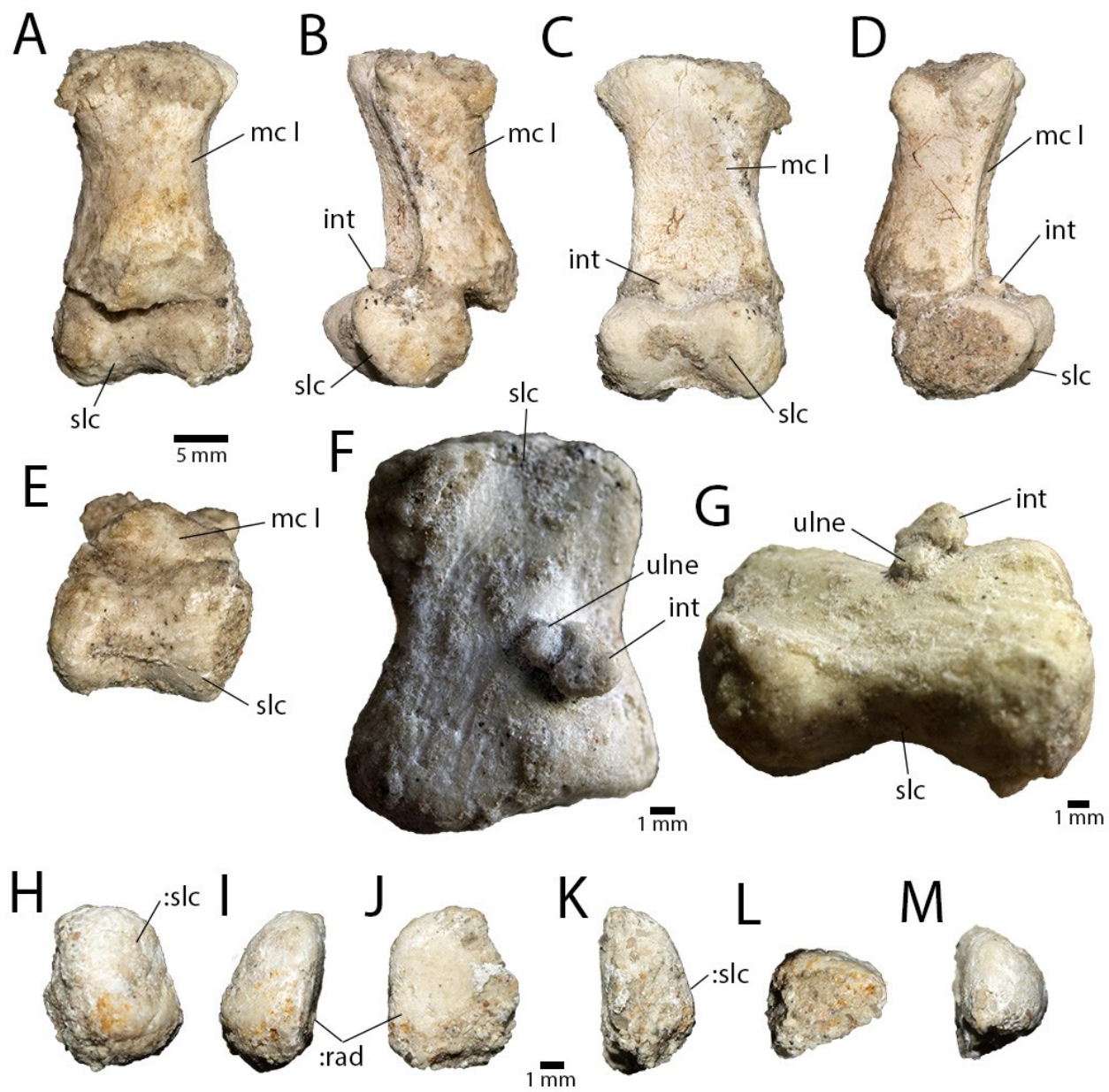
(Previous page)
Fig. 4.38. Carpals of the Guriliin Tsav oviraptorid.

Carpal elements of MPC-D 102/110.a. Left semilunate, intermedium, and ulnare carpals in

articulation with metacarpal I in medial (A), dorsal (B), lateral (C), ventral (D), and proximal (E)

views. Distal surface of semilunate carpal showing intermedium and ulnare in distal view (F) and

lateral (G) views. Right radiale of MPC-D 102/110.a in distal (H), medial (I), proximal (J),

lateral (K), ventral (L), and dorsal (M) views. **Abbreviations: int**, intermedium; **mc I**,

metacarpal I; **:rad**, contact for radius; **:slc**, contact for semilunate carpal; **slc**, semilunate carpal;

ulne, ulnare.

591

Fig. 4.39. Manus of the Guriliin Tsav oviraptorid.

Manual elements of the left hand of MPC-D 102/110.a. Digit I in lateral (A), dorsal (B), ventral (C), and medial (D) views. Metacarpal I in proximal (E) and distal (F) views. Digit II in lateral (G), dorsal (H), ventral (I) and medial (J) views. Metacarpal II in proximal (K) and distal (L) views. Digit III in medial (M) view. Phalanx III-1 in medial (N), lateral (O), ventral (P), dorsal (Q), proximal (R), and distal (S) views. Articulated left manus in dorsal (T) view.

Abbreviations: conc, concavity; **dc**, distal condyle; **dist**, distal end; **dp**, dorsal process; **ft**, flexor tubercle; **I-1–2,** phalanges of digit I; **II-1–3**, phalanges of digit II; **III-1**, phalanx III-1; **int**, intermedium; **ldc**, lateral distal condyle; **lp**, ligament pit; **mc I–III;** metacarpals I–III; **mdc**, medial distal condyle; **prox**, proximal end; **rade**, radiale; **slc**, semilunate carpal.
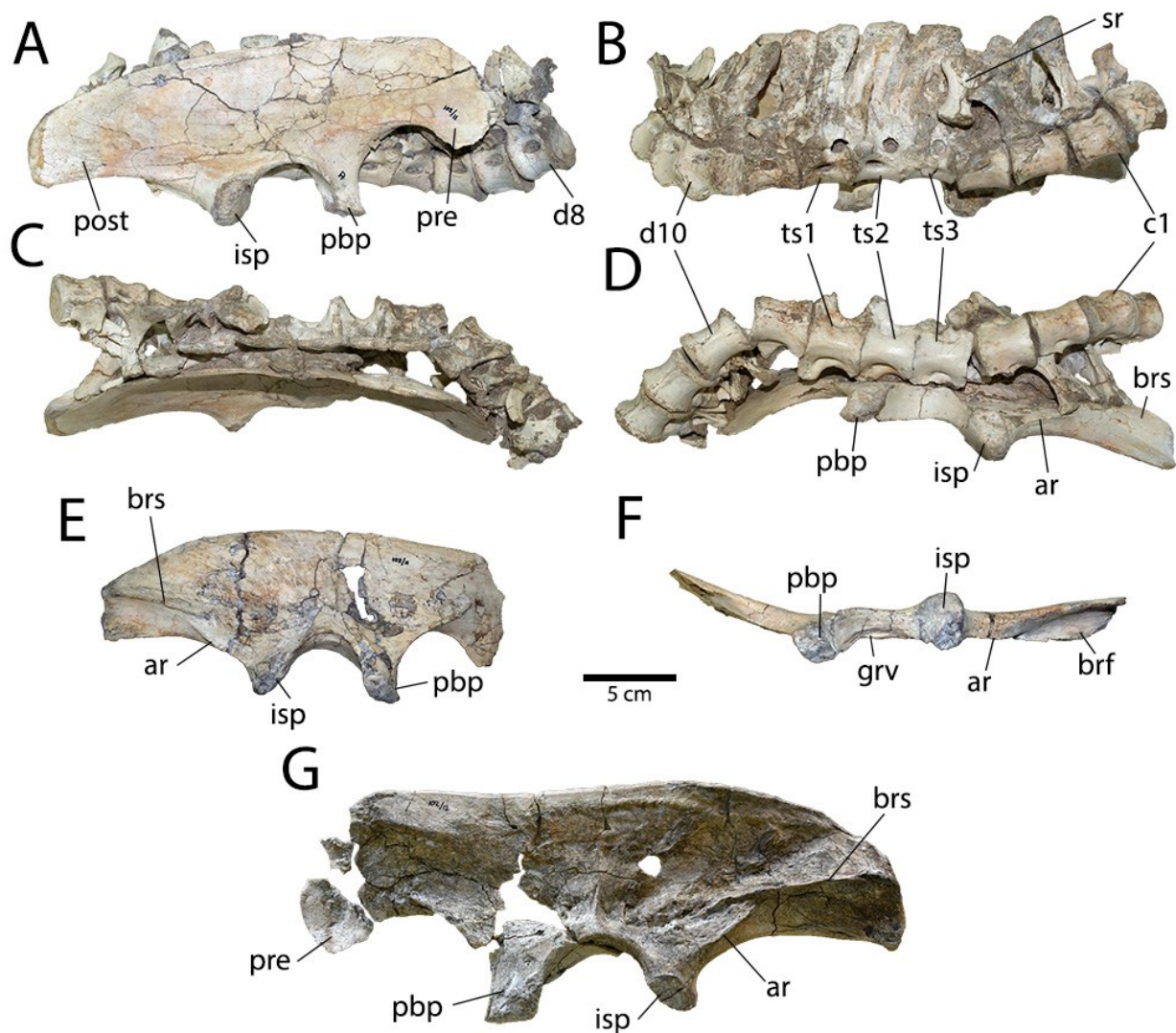
Fig. 4.40. Ilia of the Guriliin Tsav oviraptorid.

Ilia of MPC-D 102/11 (A–F) and MPC-D 102/12. Right ilium and associated vertebrae of MPC-D 102/11 in right lateral (A), medial (B), dorsal (C), and ventral (D) views. Left ilium of MPC-D 102/11 in medial (E) and ventral (F) views. Right ilium of MPC-D 102/12 in medial (G) view.

Abbreviations: ar, accessory ridge; **brf**, brevis fossa; **brs**, brevis shelf; **c1**, first caudal vertebra; **d8, d10**, eighth and tenth dorsal vertebrae; **grv**, groove; **isp**, ischiadic peduncle; **pbp**, pubic peduncle; **post**, postacetabular blade; **pre**, preacetabular blade; **sr**, sacral rib; **ts1–3**, first to third primordial sacral vertebrae.
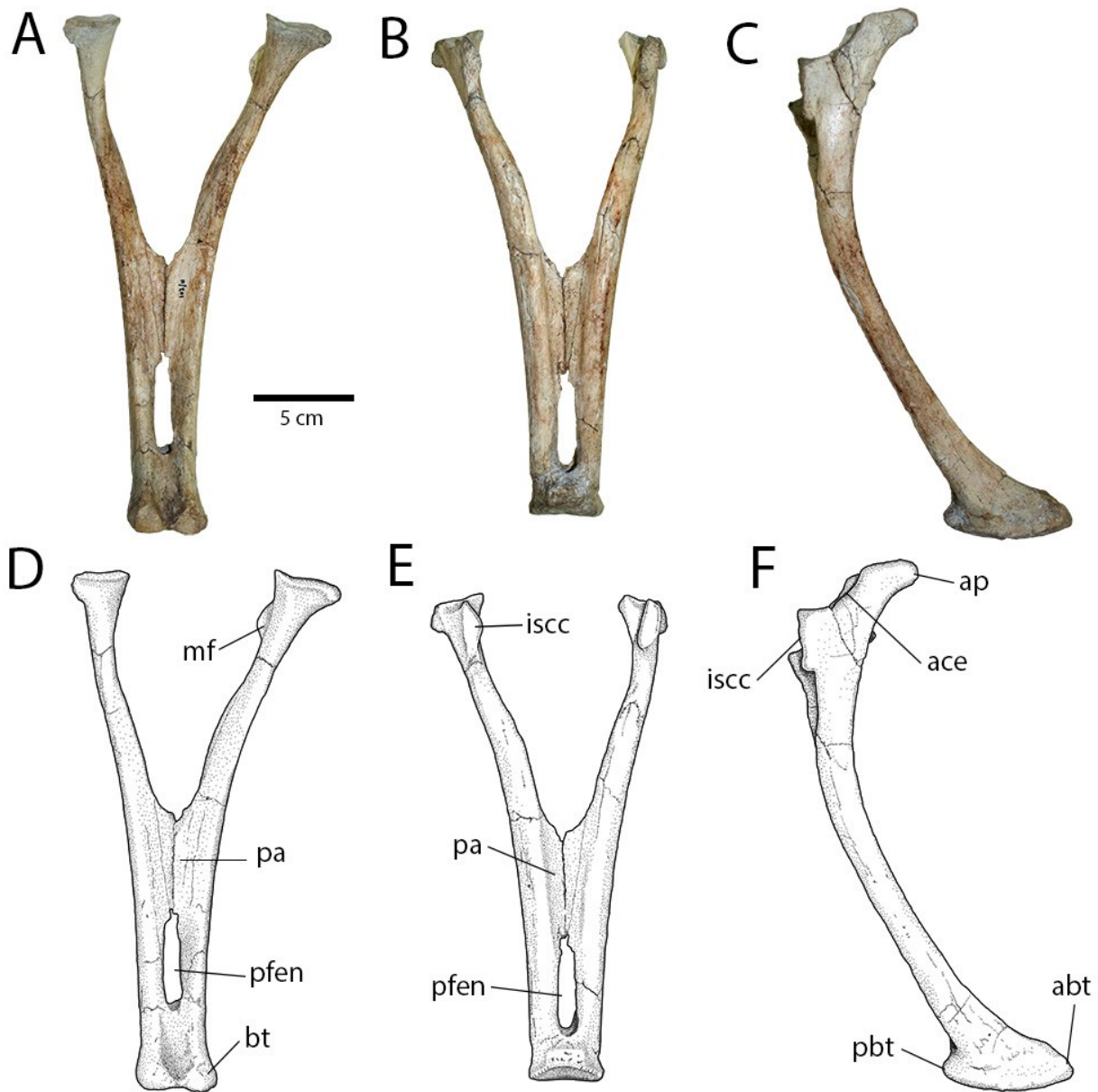
Fig. 4.41. Pubes of the Guriliin Tsav oviraptorid.

Photographs (A–C) and illustrations (D–F) of articulated pubes of MPC-D 102/11 in anterior (A, D), posterior (B, E), and right lateral (C, F) views. **Abbreviatons: abt**, anterior portion of pubic boot; **ace**, acetabulum; **ap**, anterior process; **bt**, pubic boot; **iscc**, ischiadic contact; **mf**, medial fossa; **pa**, pubic apron; **pbt**, posterior portion of pubic boot; **pfen**, pubic fenestra.

594
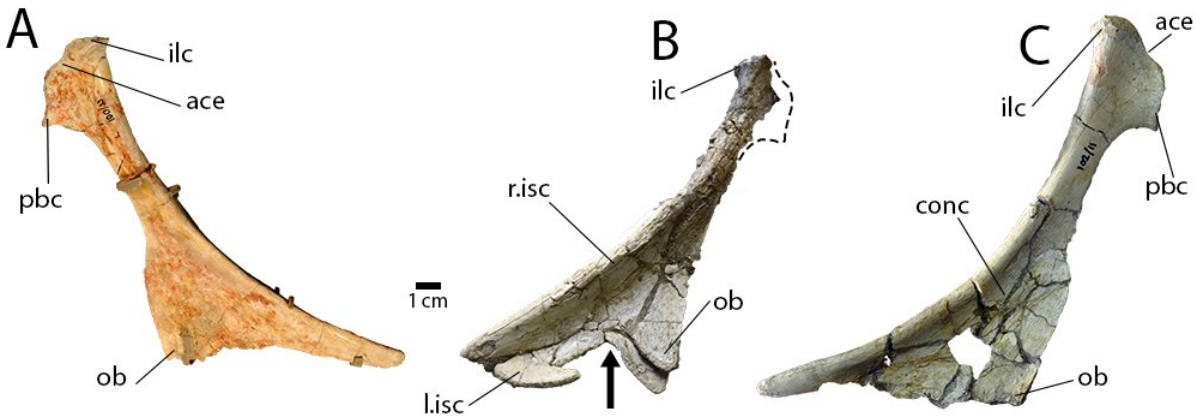
Fig. 4.42. Ischia of the Guriliin Tsav oviraptorid.

Ischia of MPC-D 100/33 (A), MPC-D 102/110.b (B), and MPC-D 102/11 (C). Left ischium of MPC-D 100/33 in lateral (A) view. Articulated ischia of MPC-D 102/110.b in right lateral view (B). Composite image of right ischium of MPC-D 102/11 in lateral view (C). **Abbreviations: ace**, acetabulum; **conc**, concavity; **ilc**, iliac contact; **l.isc**, left ischium; **ob**, obturator process; **pbc**, pubic contact; **r.isc**, right ischium.
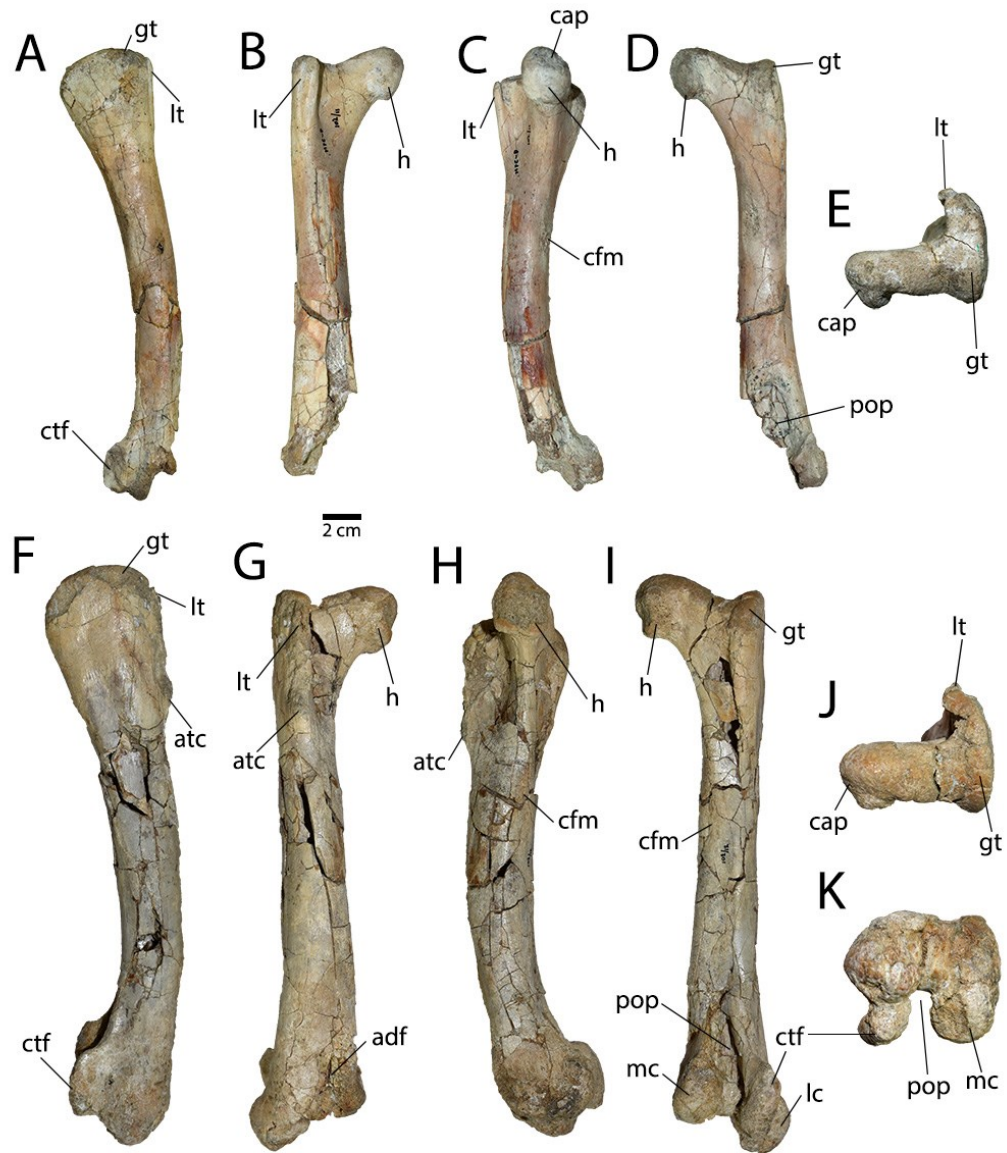
Fig. 4.43. Femora of the Guriliin Tsav oviraptorid.

Right femora of MPC-D 102/11 (A–E) and MPC-D 102/12 (F–K) in lateral (A, F), anterior (B, G), medial (C, H), posterior (D, I), proximal (E, J), and distal (K) views. **Abbreviations: adf**, adductor fossa; **atc**, accessory trochanteric crest; **cap**, capitate ligament scar; **cfm**, insertion of *m. caudofemoralis*; **ctf**, crista tibiofibularis; **gt**, greater trochanter; **h**, head; **lc**, lateral condyle; **lt**, lesser trochanter; **mc**, medial condyle; **pop**, popliteal fossa.
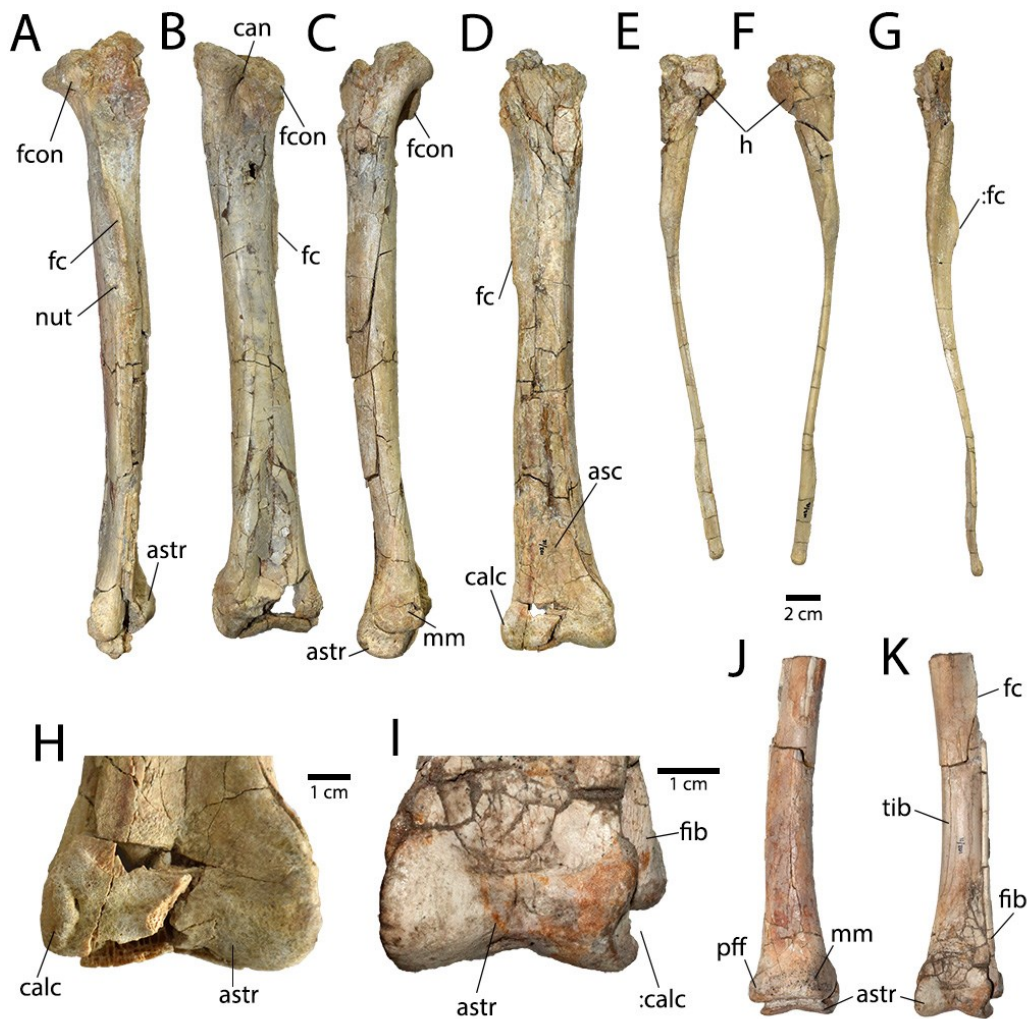
Fig. 4.44. Tibiotarsi of the Guriliin Tsav oviraptorid.

Tibiotarsus of MPC-D 102/12 in lateral (A), posterior (B), medial (C), and anterior (D) views.

Fibula of MPC-D 102/12 in posterior (E), anterior (F), and lateral (G) views. Detail (H, I) of

astragalocalcaneum of MPC-D 102/12 (H) and MPC-D 102/11 (I) in anterior view. Distal

tibiotarsus of MPC-D 102/11 in posterior (J) and anterior (K) views. **Abbreviations: astr**,

astragalus; **asc**, ascending process; **:calc**, contact for calcaneum; **calc**, calcaneum; **can**, canal

between fibular and femoral condyles; **fc**, fibular crest; :**fc**, contact for fibular crest; **fcon**, fibular

condyle; **h**, head; **mm**, medial malleolus; **nut**, nutrient foramen; **pff**, postfibular flange.

597
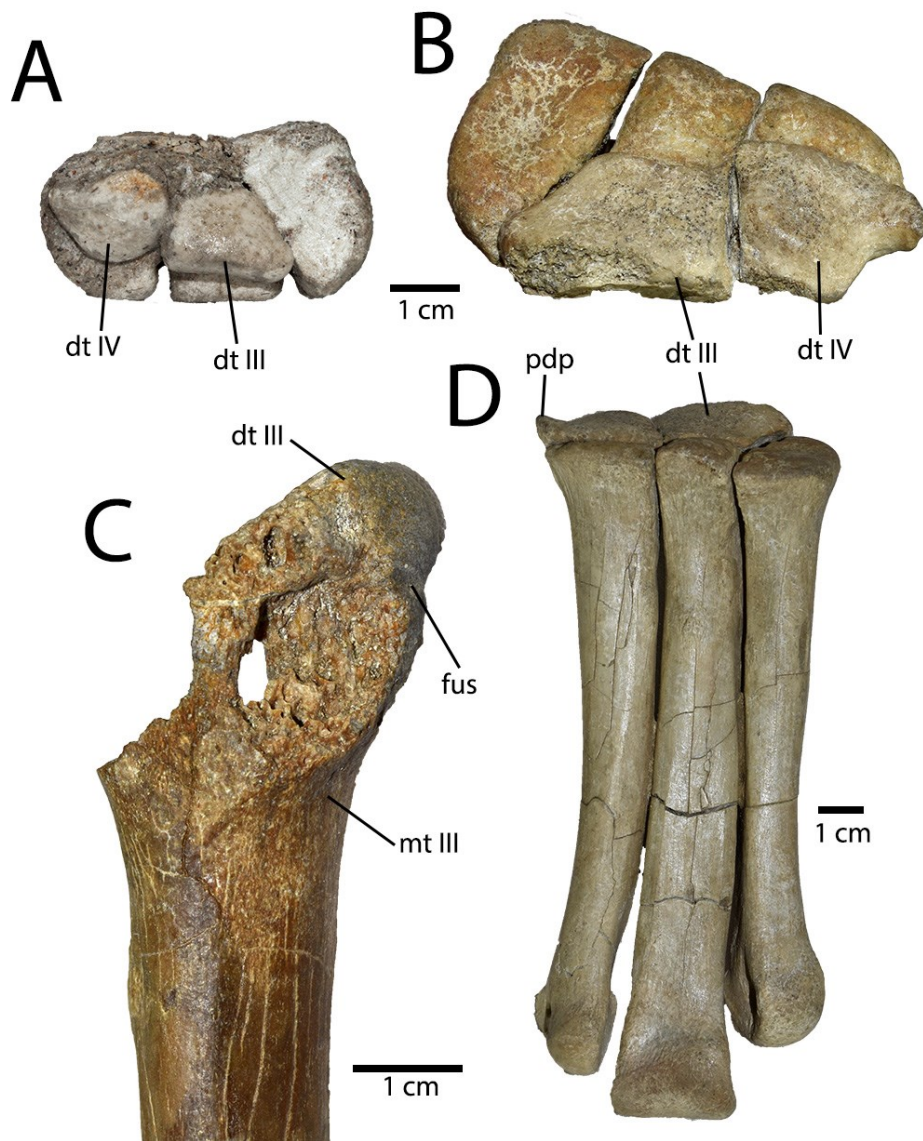
Fig. 4.45. Distal tarsals of the Guriliin Tsav oviraptorid.

Proximal tarsometatarsus of MPC-D 102/11 (A) and MPC-D 102/12 (B) in proximal view,

showing distal tarsals. Metatarsal III and partially fused distal tarsal III of MPC-D 102/12 in

posterolateral view (C). Tarsometatarsus of MPC-D 102/12 in anterior view (D), showing

proximodorsal process of distal tarsal IV. **Abbreviations: dt III**, distal tarsal III; **dt IV**, distal

tarsal IV; **fus**, fusion; **mt III**, metatarsal III; **pdp**, proximodorsal process.
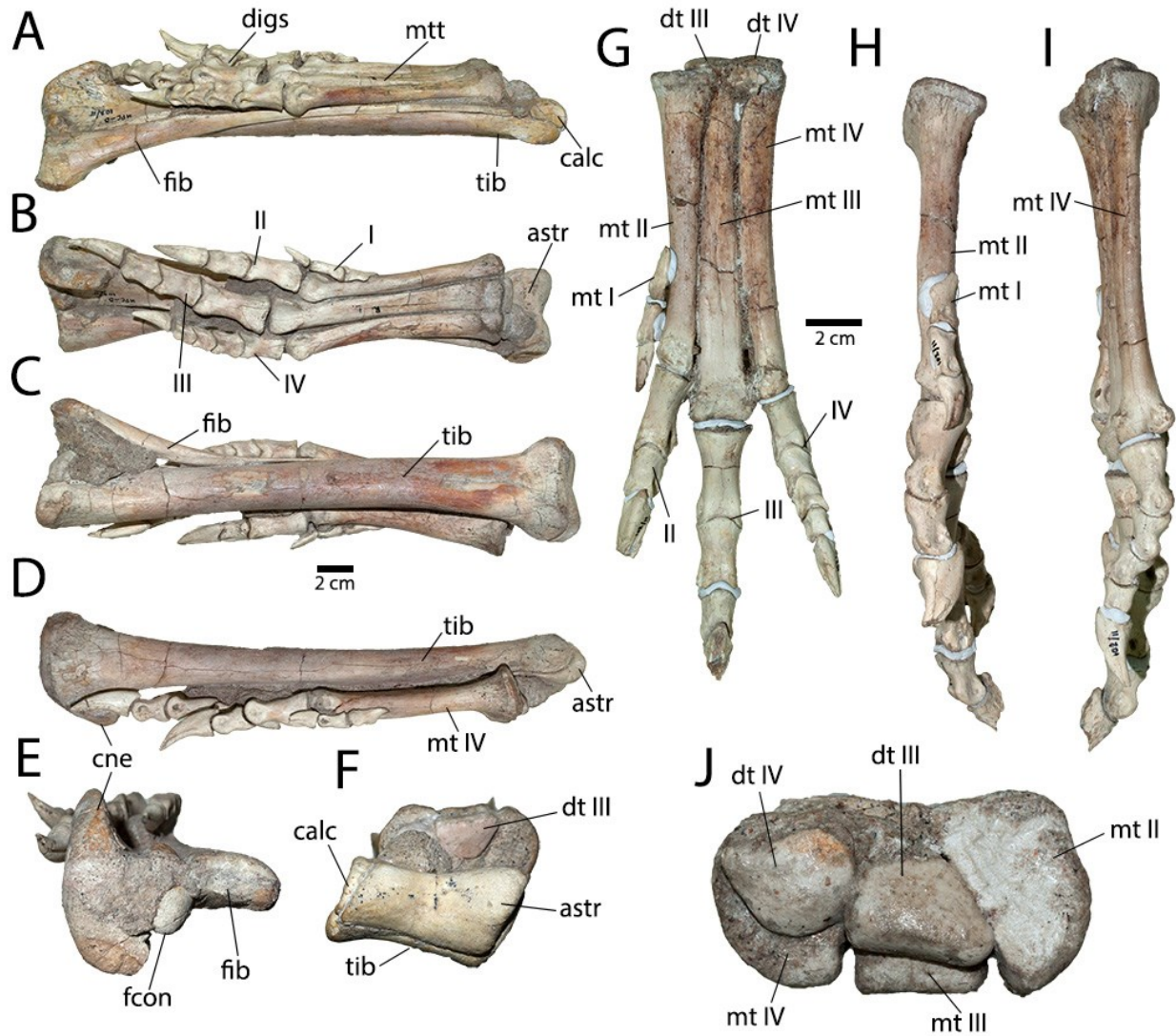
Fig. 4.46. Pes of the Guriliin Tsav oviraptorid.

Right foot with articulated tibiotarsus (A–F) and left foot (G–J) of MPC-D 102/11 in lateral (A, I), ventral (B), dorsal (C, G), medial (D, H), distal (E) and proximal (F, J) views. Tibiotarsus in images (E, F) is oriented opposite the foot: proximal view in (E), distal view in (F).

Abbreviations: astr, astragalus; **calc**, calcaneum; **cne**, cnemial crest; **digs**, digits; **dt III**, distal tarsal III; **dt IV**, distal tarsal IV; **fcon**, fibular condyle; **fib**, fibula; **I–IV**, pedal digits I–IV; **mt I–IV**, metatarsals I–IV; **tib**, tibia.
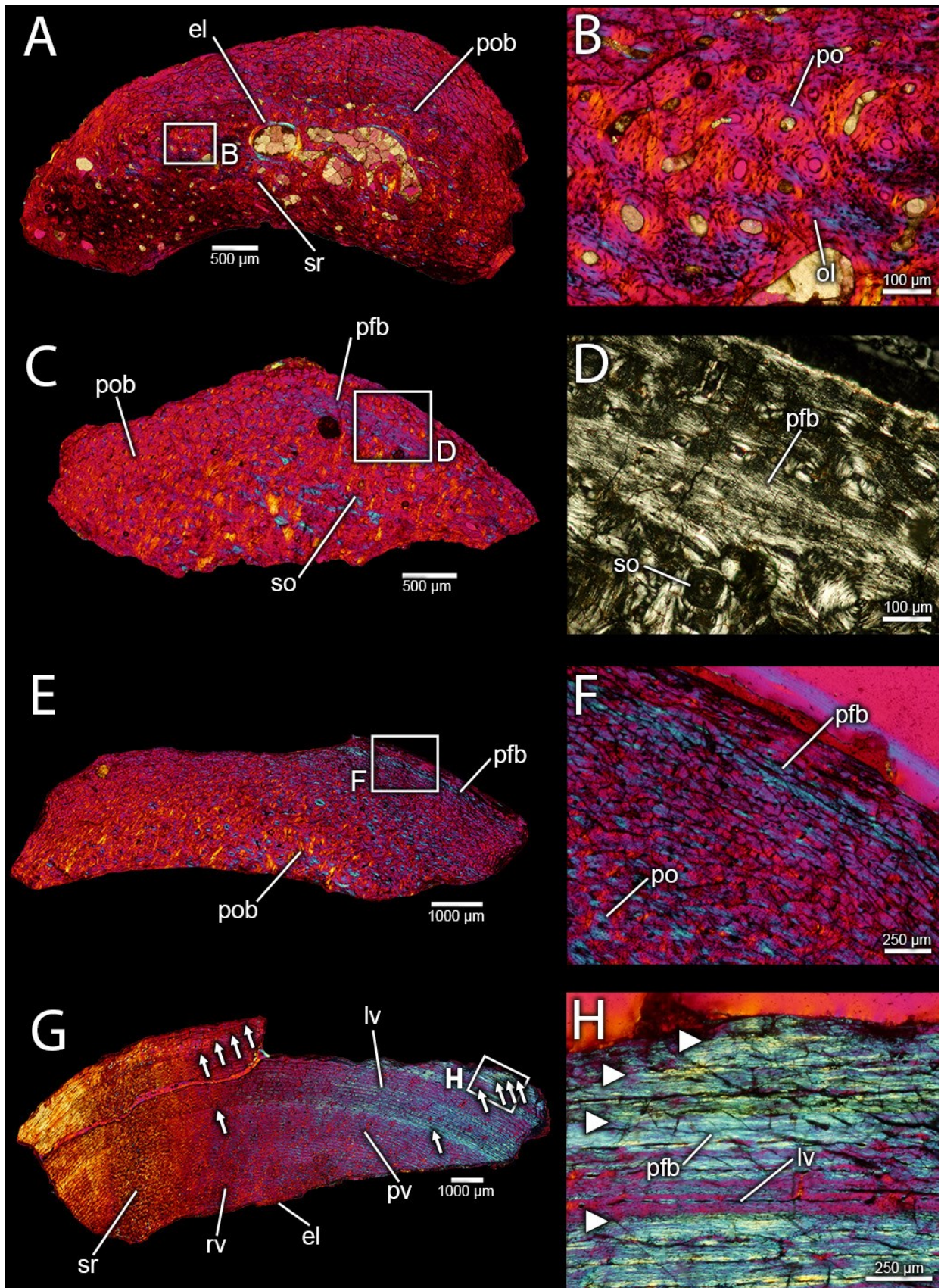
(Previous page)
Fig. 4.47. Osteohistology of the Guriliin Tsav oviraptorid.

Photographs under λ-filtered cross-polarized light (A–C, E–H) and unfiltered polarized light (D) of MPC-D 102/110a (A, B), MPC-D 102/110b (C, D), MPC-D 102/11 (E, F) and MPC-D 102/12 (G, H). Fibula of MPC-D 102/110a (A, B), showing lack of growth marks despite moderate secondary remodeling. Fibula of MPC-D 102/110b (B, C), showing zone of parallel-fibered bone possibly corresponding to the first growth mark. Femur of MPC-D 102/11 (E, F), showing lack of secondary remodeling and zone of parallel-fibered bone. Femur of MPC-D 102/12 (G, H), showing lines of arrested growth (arrows) preceded by zones of parallel-fibered bone, and development of an external fundamental system at the periosteal surface of the bone (H), indicating advanced age. Scale bars as indicated. **Abbreviations: el**, endosteal lamellae; **lv**, laminar vasculature; **ol**, osteocyte lacuna; **pfb**, parallel-fibered bone; **po**, primary osteon; **pob**, primary osteonal bone; **pv**, plexiform vasculature; **rv**, reticular vasculature; **so**, secondary osteon; **sr**, secondary remodeling.

Fig. 4.48. Life reconstruction of the Guriliin Tsav oviraptorid.

Artistic reconstruction of the Guriliin Tsav oviraptorids preserved in MPC-D 102/110, speculating upon the gregarious behaviours just prior to death and burial. Original artwork by Michael Skrepnick, used with permission.
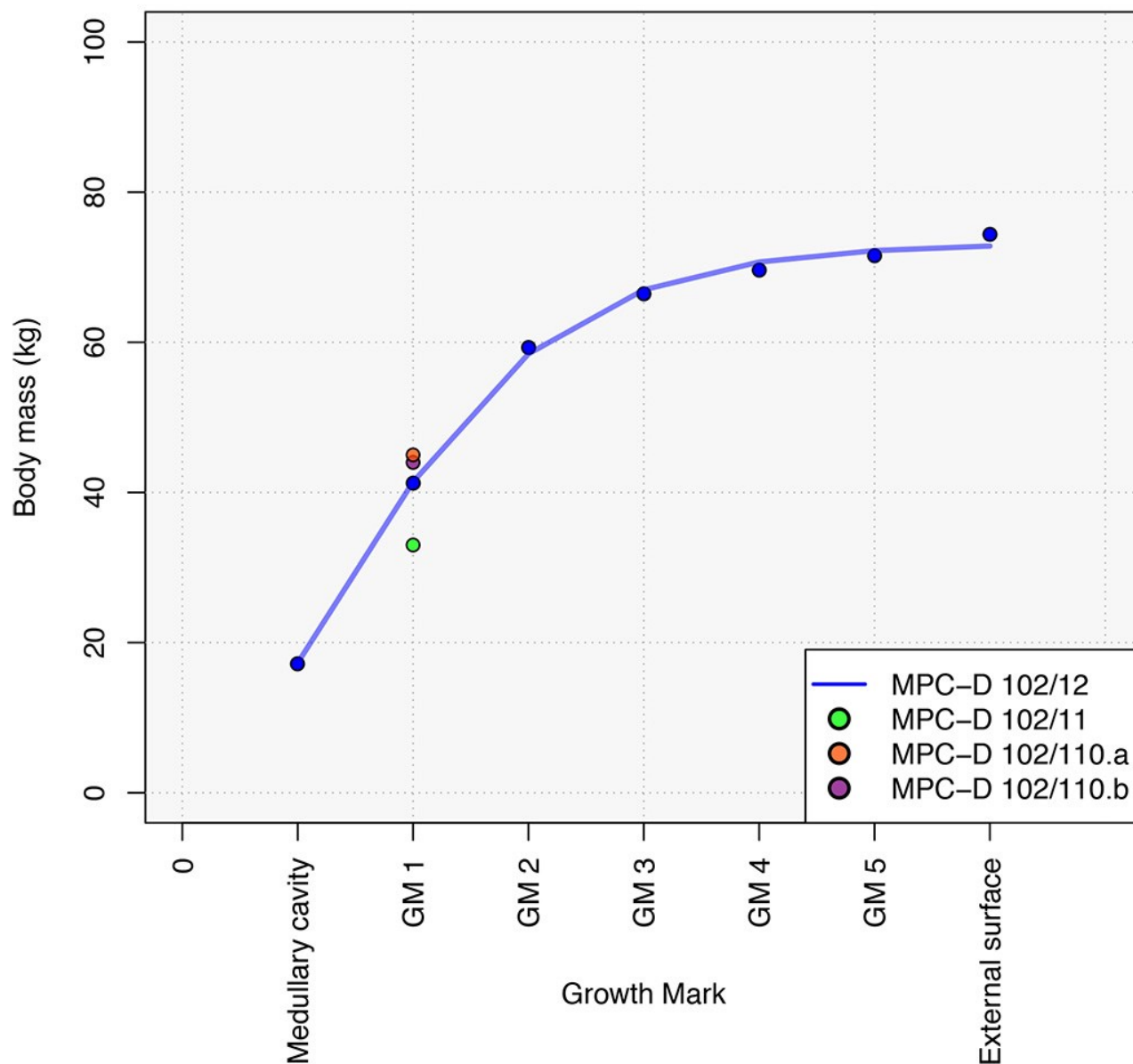
Fig. 4.49. Growth curve of the Guriliin Tsav oviraptorid.

Gompertz growth curve of growth mark against estimated body mass using the method of

Campione et al. (2014) for MPC-D 102/12. Other specimens are plotted on the chart using their

estimated body mass and age estimation from osteohistology.

Table 4.1. Taxonomic referral of oviraptorid specimens described in Chapter 4.

Taxon	Specimen	Material	Reference
Conchoraptor gracilis	MPC-D 100/20 (holotype)	Skull and partial mandible	Barsbold (1986)
	MPC-D NatGeo.2018.036	Block of >9 articulated skeletons	This study
	MPC-D 102/03	Articulated skeleton and tail of second individual	This study
Gen. et. sp. nov.	MPC-D 100/79-D	Skull, mandible, atlas-axis	This study
Heyuannia yanshini	MPC-D 100/30 (holotype)	Partial skeleton	Funston et al. (2018)
	MPC-D 100/31	Partial skeleton	Funston et al. (2018)
	MPC-D 100/32	Partial skeleton	Funston et al. (2018)
Rinchenia mongoliensis	MPC-D 100/32-A	Nearly complete skeleton	Funston et al. (2018)
Gen. et. sp. nov.: "Guriliin Tsav oviraptorid"	MPC-D 102/110	Block of three articulated skeletons	This study
	MPC-D 102/11	Partial articulated skeleton, possibly from same assemblage as MPC-D 102/110	This study
	MPC-D 102/12	Partial postcranial skeleton	This study
	MPC-D 100/33	Partial postcranial skeleton	This study

CHAPTER 5 – GREGARIOUS BEHAVIOUR, ECOLOGY, AND EVOLUTION

5.1 INTRODUCTION

Gregarious Behaviour:

Gregarious behaviour has been recorded in numerous theropod families (Maxwell and Ostrom, 1995; Kobayashi and Lü, 2003a; Kirkland et al., 2005a; Varricchio et al., 2008b; Eberth and Currie, 2010), but there remains much uncertainty about its prevalence within these families and the nature of the behaviours themselves (Roach and Brinkman, 2007). In oviraptorosaurs, the only published report of gregarious behaviour is the description of a bonebed of avimimids from the Nemegt Formation of Mongolia (Funston et al., 2016; Figs 5.1, 5.2). However, numerous unpublished oviraptorosaur assemblages are known, including additional avimimid bonebeds (Ryan et al., 2001a; Fig. 5.3) and associations of complete, articulated oviraptorid skeletons (Funston et al., 2017).

The avimimid bonebeds provide a wealth of information on the gregarious behaviour of avimimids and other oviraptorosaurs. The bonebeds are composed predominantly of disarticulated material (Fig. 5.4), especially hindlimbs, indicating that they were reworked after the initial mass death event. Regardless, the large number of individuals—as many as 18— provides a snapshot of the population dynamics of gregarious behaviour in these animals.

No definitive assemblage of multiple caenagnathid individuals is yet known, but there are several associations which may nonetheless provide some evidence of gregariousness. Most notable is the recovery of three partial associated skeletons of *Elmisaurus rarus* Osmólska 1981 (MPC-D 102/6, MPC-D 102/7, and MPC-D 102/9) from the Nemegt Formation in a small area in the North Sayr at Nemegt. The most distant of these specimens are separated by only 50 m,

and although no detailed stratigraphic information was collected, they appear to have been roughly at the same horizon. A second possible association was found at Bugiin Tsav. Approximately 20 m south of the type quarry of *Nomingia gobiensis* Barsbold et al. 2000b, fragments of a second partial caenagnathid skeleton were found as surface float. Unfortunately the horizon producing the elements could not be verified, but the majority of other fossils at the locality were produced by a layer continuous with the type quarry. The identity of this specimen is ambiguous (see Chapter 3: Section 3.3.6), but there are no features in which it differs from *Nomingia gobiensis* and it likely represents the same taxon. In any case, these two possible occurrences provide little certainty about the presence of gregarious behaviour in caenagnathids, and little information on the nature of those associations.

Numerous oviraptorid assemblages are now known, but none have been formally described or taphonomically studied. The most famous association is the articulated skeletons of *Khaan mckennai* Clark et al. 2001 affectionately nicknamed 'Sid and Nancy' or 'Romeo and Juliet' (Clark et al., 2001; Balanoff and Norell, 2012). However, the taphonomy of these specimens has not been described and they provide little information besides evidence of association prior to death. Several new assemblages (Fig. 5.5), in contrast, provide considerable data on the prevalence of gregarious behaviour and the interactions that these individuals engaged in. One of these, an uncatalogued block at the Central Museum of Mongolian Dinosaurs (a cast is catalogued as UALVP 54983; Fig. 5.5C), comprises five articulated juvenile skeletons of a new oviraptorid in death poses. Three other assemblages (MPC-D 102/3, MPC-D 102/110, and MPC-D NatGeo.2018.036; Fig. 5.5A, B, D) contain skeletons in life positions, although in each case some disarticulation has occurred. These assemblages provide information on the pre-

mortem behaviours these groups engaged in, as well as broader information on the prevalence of gregarious behaviour within Oviraptorosauria.

Ecology:

Oviraptorosaur ecology has been previously speculated upon, but few of these speculations have ever been rigorously tested. Previous analyses have focused mostly on the diet and environmental preferences of oviraptorosaurs. In his description of *Oviraptor philoceratops* Osborn 1924, Osborn (1924) speculated that the type specimen was preserved while pilfering a nest, but with the caveat that this "may entirely mislead us as to its feeding habits and belie its character" (Osborn, 1924, pg. 10). Recent analyses have suggested that Osborn's caveat was appropriate, and that the animal was more likely protecting its nest (Norell et al., 1995; Dong and Currie, 1996; Fanti et al., 2012). This has been supported by dietary studies, which suggest oviraptorosaurs were more likely herbivores or omnivores (Smith, 1992; Zanno and Makovicky, 2011; Funston and Currie, 2014). Regardless, the unusual palatal and mandibular structure of oviraptorosaurs would likely have enabled them to eat eggs as well (Currie et al., 1993).

The apparent environmental division between caenagnathids and oviraptorids has frequently been noted (Currie et al., 1993; Longrich et al., 2010, 2013; Tsuihiji et al., 2016), with oviraptorids showing a preference for xeric environments and caenagnathids more mesic environments. However, oviraptorids were still present in the mesic deposits of the Nemegt Formation, so the degree to which these families segregated is unclear.

The analyses presented here attempt to determine the ecological roles of oviraptorosaurs with more certainty, using the Baruungoyot and Nemegt Formations in the Nemegt Basin of Mongolia as a case study. The Baruungoyot and Nemegt Formations are home to a remarkable diversity of theropod dinosaurs, especially oviraptorosaurs. To date, seven oviraptorosaur genera

have been named from the Baruungoyot or Nemegt Formations (Fig. 5.11) and at least one new

genus from Guriliin Tsav has yet to be named (see Chapter 4: section 4.3.6). This abundant fossil

record offers ecological clues to the lifestyles of oviraptorosaurs. The Nemegt Formation in the

western Gobi desert is unique in that it is home to three groups of oviraptorosaurs—avimimids,

caenagnathids, and oviraptorids—and is the only place where the latter two families coexist.

Their distribution in the Baruungoyot and Nemegt Formations is therefore crucial for

understanding their behaviour and ecology.

The collection of Global Positioning System (GPS) data of sites in the Nemegt Basin

over the course of two decades has revealed the distribution of dinosaur skeletons (Fig. 5.12).

Combined with information from the literature, this allows nearly 500 dinosaur skeletons to be

incorporated into a community data set spanning the Nemegt interval (see Supplementary Tables

1–2 in Funston et al. (2018b)). Oviraptorosaur diversity and distribution can thus be compared to

the overall patterns of community composition in the Nemegt Formation. Here, I test whether

oviraptorosaur subfamilies overlapped in distribution, and whether their distributions show

environmental biases.

Evolution:

The evolution of oviraptorosaurs has never been systematically studied. Maryanska et al.

(2002) conducted the first rigorous phylogenetic analysis of oviraptorosaurs, but with the aim of

establishing their relationships to other maniraptorans. Incorporating some of these characters,

Osmólska et al. (2004) refined the analysis to examine the interrelationships of oviraptorosaurs,

and this data matrix is still built upon today. Both Maryanska et al. (2002) and Osmólska et al.

(2004) recovered the main clades of oviraptorosaurs recognized today: caenagnathids and

oviraptorids within Caenagnathoidea, and a series of stem oviraptorosaurs including avimimids and caudipterids. However, the relationships of those subgroups, particularly caenagnathids, remain volatile and poorly resolved. Some analyses (Senter, 2007; Zanno and Makovicky, 2011) differ drastically from the analysis of Osmólska et al. (2004) in terms of ingroup relationships of oviraptorosaurs. However, most of these studies are concerned with the wider relationships of coelurosaurs, maniraptorans, or paravians, and therefore character sampling does not encompass all of the variation in oviraptorosaurs. Numerous studies introducing new oviraptorosaur taxa have built upon the character matrix of Osmólska et al. (2004), with notable improvements made by Lamanna et al. (2014), Funston and Currie (2016), Lü et al. (2016), and Lü et al. (2017).

Despite the number of cladistic analyses of oviraptorosaurs, they have not been used for any subsequent analyses of character evolution, body mass evolution, or paleobiogeography. Lü et al. (2016) qualitatively assessed some trends in paleobiogeography based on the phylogenetic positions of oviraptorids from Ganzhou. However, this focused solely on a limited subset of oviraptorids and did not use any statistical techniques to support their assertions. Similarly, Funston et al. (2018a) spoke of paleobiogeography more widely in oviraptorosaurs, but did not support these claims quantitatively. Similarly, Yu et al. (2018) made some general comments on body size variation in oviraptorosaurs, but their analysis included few representatives of each oviraptorosaur clade and used a less accurate body mass estimation method. A major limitation of that study was the inability to examine body mass trends within the groups examined, and instead the authors focused on differences between oviraptorosaur families.

The analyses presented here aim to rectify some of these issues. In particular, increased taxonomic clarity of caenagnathid specimens (see Chapter 3) allows for more extensive character sampling of these taxa, and a better-resolved Caenagnathidae. Additionally, the inclusion of new

oviraptorid taxa and updates to their character scorings improves resolution in that part of the tree. For the first time, this well-resolved phylogeny is used for downstream analyses including the patterns of body size change, the evolutionary pattern of digit reduction in oviraptorids, and statistically-tested paleobiogeographical insights.

5.2 METHODS

5.2.1 Gregarious Behaviour

Collection—The Nemegt *Avimimus* Kurzanov 1981 bonebed was excavated systematically and mapped (Fig. 5.4) using a 1 m^2 grid system. Once mapped, specimens were collected and given coordinate numbers referring to their location within the map grid. Plan view, bi-directional orientations (azimuthal trends) of elements were obtained from the map using ImageJ 1.48v. These data were then plotted on a rose diagram divided into 45-degree quadrants (Fig. 5.4). Rao's Spacing and Raleigh Z tests from the R software package *circular* were used to assess whether the *in situ* assemblage exhibited statistically significant preferred orientations. Specimens were mechanically prepared at the MPC by "Dinosaurs of the Gobi" participants, using a combination of manual and air-pressured tools and a variety of consolidants (Butvar, cyanoacrylate).

The Iren Dabasu avimimid bonebed was sampled by surface collection of material from spoil piles left by the Sino-Soviet expedition (Fig. 5.3). Because no fresh excavation of the bonebed layer was conducted, the arrangement of bones could not be established and the site was not mapped.

Legally collected oviraptorid assemblages were excavated using standard palaeontological techniques. In the case of MPC-D 102/03, this did not include mapping the

specimen, as it was collected in a single block. Instead, this specimen was mapped after preparation (see Chapter 4: Section 4.3.1). For MPC-D NatGeo.2018.036, a sketch of the positions of the skeletons was made during collection, but time constraints precluded detailed mapping using a grid. Aerial images were taken during the excavation using a DJI Mavic Air and a photogrammetric model of the assemblage was produced using Agisoft Photoscan. Two other oviraptorid assemblages, MPC-D 102/110 and an uncatalogued block at the Central Museum of Mongolian Dinosaurs, were confiscated from poachers and no collection data exists. A cast of the uncatalogued block from the Central Museum of Mongolian Dinosaurs (UALVP 54983) was acquired through Gaston Design Inc., and was used to verify information derived from photographs of the specimen on exhibit.

Taphonomic analysis—Taphonomic bone-modification data (Eberth et al., 2007) were assessed through simple visual inspection of prepared elements for all assemblages. Skeletal representation was calculated for avimimids, but the articulated nature of the oviraptorid specimens did not necessitate these analyses. The adult skeletons of avimimids are characterized by the fusion of many bones into compound elements, reducing the number of discrete skeletal elements through ontogeny. As such, the mixture of fused and unfused compound elements in each bonebed makes it difficult to accurately assess skeletal element representation. Skeletal representation was therefore calculated separately for both a completely fused skeleton and a skeleton with no fused elements (Fig. 5.6). This provides minimum and maximum boundaries, although the true pattern is likely towards the maximum boundary, because in each assemblage, compound elements were more commonly fused than unfused. Minimum number of individuals (MNI) was estimated using the maximum number of unique elements. For the Nemegt bonebed, this was tibiae, whereas for the Iren Dabasu bonebed this was metatarsals. For the Nemegt

bonebed, combining this MNI estimate (n=13) with length estimates of tibia through regression analysis gave a better estimate of the number of tibiae of significantly different lengths (n=18).

Measurement—Calipers were used to measure small and medium size elements (< 150 mm in maximum dimension) to an accuracy of 0.5 mm. For large elements measuring more than 150 mm in maximum dimension, a fabric measuring tape was employed. For MNI information at the Nemegt bonebed, complete tibiae were measured and ratios of anteroposterior proximal width, transverse distal width, and transverse shaft diameter were correlated with tibia length. Regression analysis therefore allowed the lengths of partial tibiae to be estimated from other available measurements. None of the length estimates from opposite sides were close in value, so it is unlikely that two tibiae from which lengths were estimated belonged to the same individual.

5.2.2 Ecology

Data collection—Map data for plotting geographic distribution in the Nemegt Basin (see Supplementary File 1 of Funston et al. (2018b)) was gathered over the course of decades by P. Currie on expeditions organized by Nomadic Expeditions, the Korean-Mongolian International Dinosaur Project, and the MPC. Latitude, longitude, and altitude measurements were taken using a handheld Garmin Global Positioning System (GPS) unit for each site, to an accuracy of ± 5 m. Each site corresponds to a skeleton, which varies in completeness from partial to complete, and is at least associated, although the majority are articulated. A total of 358 sites were included in the map, each of which was identifiable at least to the superfamily level, and most to the species level. Two assemblage datasets were created with each locality as a separate sample: species occurrences and superfamily occurrences (see Supplementary Tables 1–2 in Funston et al. 2018b). Assemblage composition data was generated from the Google Earth map (Fig. 5.12) as

well as from reports in the published literature that were not included in the map (Kielan-Jaworowska, 1968, 1969, 1971, 1972, 1974, 1975, 1977, 1979, 1981, 1984; Ishii et al., 2000, 2004; Weishampel et al., 2008; Tsubamoto, 2010; Arbour et al., 2014; Currie, 2016; Tsuihiji et al., 2016) The sample was thereby improved from 364 identifiable occurrences (Currie, 2016) to 472 (species-level) or 476 (superfamily-level) occurrences. Although the duration of deposition at each locality is not known, each represents only a small portion of the ~350 m thick Baruungoyot-Nemegt interval. Furthermore, because the assemblages are time-averaged, the sample at each locality is probably reflective of broad-scale community structure at that site (Kidwell and Flessa, 1995; Kidwell, 2001). Locality assemblages are therefore regarded here as communities. Sites where multiple individuals of a single taxon occur, like the 'Dragon's Tomb' of *Saurolophus angustirostris* Rozhdestvensky 1952 (Bell et al., 2018) and the *Avimimus* bonebed (Funston et al., 2016), are taphonomic exceptions and, because they are not time-averaged, were counted as single occurrences. Counts were generated for 11 localities: Altan Uul II, Altan Uul III, Altan Uul IV, Bambuu Khudag, Bugiin Tsav, Guriliin Tsav, Hermiin Tsav, Khulsan, Nemegt, Tsagaan Khushuu, and Ulaan Khushuu.

 Taphonomic considerations—Taphonomic biases were not accounted for in the raw counts of the data, to maximize available data. It is likely that taphonomic processes influenced the relative proportions of taxa preserved between each formation, and that these influences differed between the Baruungoyot and Nemegt Formations, but it is unlikely that there was significant variation within each formation. There is, however, some evidence that taphonomic size-bias does not strongly influence the faunal composition of each formation. For example, although certain Baruungoyot-dominated localities preferentially preserve small animals (e.g. Khulsan), the presence of large ankylosaurs, *Nemegtosaurus* Nowinski 1971, and *Tarbosaurus*

Maleev 1955 in the Baruungoyot Formation suggests that large animals were capable of being preserved. Similarly, although the fluvial Nemegt Formation likely had a taphonomic bias against small animals (Brown et al., 2013), *Avimimus* and other small animals are still frequently collected. Furthermore, because the data at each locality are derived from many sites, rather than a single horizon or microsite, they are time-averaged and comprise a wide range of taphonomic conditions. This reduces the effect of any single taphonomic signal on the data set. The interfingering nature and the presence of several taxa in both Formations (e.g. *Conchoraptor gracilis* Barsbold 1986, *Gallimimus bullatus* Osmólska et al. 1972*, Nemegtomaia barsboldi* Lü et al. (2004), *Saurolophus angustirostris*, *Tarchia gigantea* Maryanska 1977), suggests that these ecosystems coexisted laterally and shared aspects of their dinosaur communities. This is also supported by their sedimentological interpretation (Gradziński, 1970; Gradziński and Jerzykiewicz, 1974; Jerzykiewicz and Russell, 1991; Jerzykiewicz, 1998; Eberth, 2018) as a proximal meander belt of an alluvial system (Nemegt Formation) grading distally into ephemeral lakes and aeolian sediments (Baruungoyot Formation). It is therefore reasonable to consider the Formations together as a single system. In the future, it may be possible to use other sources of information (e.g. eggs, footprints, or microsites) to correct taphonomic modification of community proportions.

Statistical methods—Sampling efficiency was tested through rarefaction curves using the rarecurve command (step = 1) in the *vegan* v2.4-5 package (Oksanen et al., 2017) of R statistical program. Data were rarified at both the species and superfamily level. Community structure was visualized in relative abundance plots using stacked-area percentage graphs using the stackpoly command of the *plotrix* v3.6-6 package (Lemon, 2006) of R. Family associations were visualized using non-metric multidimensional scaling (NMDS) on a matrix of Bray-Curtis

distances. Species that co-occur frequently plot more closely to each other on the resulting graph. Permutation tests were performed to test for uniformity in the occurrence of taxa among Nemegt-dominated localities. Taxa were considered uniformly distributed if their relative abundance remained constant between samples. To test for uniform superfamily composition in the samples, a hypothetical uniform distribution of taxa was calculated by converting all community abundance data into proportions and then calculating the average proportion of each taxon across samples. The similarity between the observed distribution and the uniform distribution was calculated using Bray-Curtis dissimilarity (Bray and Curtis, 1957) using *vegan* in R (Oksanen et al., 2017). This measure is appropriate for this study because it considers both presence-absence and relative abundance of taxa in its calculation of dissimilarity. This dissimilarity was then compared with the Bray-Curtis dissimilarity between the uniform distribution and 100,000 randomly generated distributions to generate a realized p-value (p_R). For each taxon, in each sample of each randomly generated distribution, the minimum number of individuals was zero, and the maximum number was equal to the observed number of individuals of that taxon in the total sample. Only whole numbers were used. The realized p-value is therefore the proportion of random distributions that are more similar than the observed distribution to the hypothesized uniform distribution. A low p_R indicates that the relative abundance of a taxon remains relatively consistent between samples. Oviraptorosaurs were split at the family level for permutation tests. Permutation tests were not performed on the Baruungoyot Formation fauna because, with only two Baruungoyot-dominated localities, the sample size was not sufficient to determine if taxon distributions were uniform.

5.2.3 Evolution

Matrix construction—A morphological character matrix for maximum parsimony (Appendix 2) was compiled based on the previous analyses of Osmólska et al. (2004), Lamanna et al. (2014), Funston and Currie (2016) and Lü et al. (2017). The tree was modified from these previous analyses mostly by dropping or consolidating caenagnathid taxa. In particular, *"Macrophalangia canadensis"* Sternberg (1932) and *"Caenagnathus sternbergi"* Cracraft (1971) were subsumed into *Chirostenotes pergracilis* Gilmore 1924, which was updated based on the new specimens described in Chapter 3. Characters scored for "Alberta Dentary Morph 3" were added to *Leptorhynchos elegans* Parks (1933), and the former OTU was removed. *Ojoraptorsaurus boerei* Sullivan et al. 2011 was also removed because it could be coded for relatively few characters (approximately 1%). *Leptorhynchos gaddisi* Longrich et al. (2013) was removed because it is represented only by the mandible and is therefore provides little data. A new taxon, the Guriliin Tsav oviraptorid, was added to the matrix and could be coded for nearly all of the characters (97.5%). Two notable taxa were not included in the analysis: *Beibeilong* Pu et al. 2017 and *Gobiraptor* Lee et al. 2019. The latter taxon was not added because, based on material presented in Chapter 4, it is likely the junior synonym of *Conchoraptor gracilis*. Despite its inclusion in previous analyses (Pu et al., 2017), *Beibeilong sinensis* was not included here because of its early ontogenetic stage and because it could not be observed firsthand. Regardless, it typically is allied with *Gigantoraptor erlianensis* Xu et al. 2007 and its position has little effect on the evolutionary trends discussed here. Despite their early ontogenetic stages, *Banji long* Xu and Han 2010, *Microvenator celer* Ostrom 1970, and *Yulong mini* Lü et al. 2013 were included in the analysis. Juvenile OTUs are typically recovered more basal than they should be, but this can be corrected by not scoring ontogenetically variable characters for these OTUs (Currie et al. 2016). Although caenagnathid ontogeny is more poorly known, analyses of oviraptorid ontogeny

in Chapter 4 indicate that few—if any—characters in the matrix are ontogenetically variable. Accordingly, these juvenile OTUs are likely to provide at least some important information.

Several characters were dropped from previous analyses because they were uninformative, ontogenetically variable, or poorly constructed. Character 110 of Lü et al. (2017), regarding the state of cervical rib fusion, was dropped because it varies through ontogeny. Character 215 on the position of muscle scars on the dorsal vertebrae was removed because it provided little information and the positions can change throughout both ontogeny and the axial series. Most of the characters removed were those added by Funston and Currie (2016), because these were poorly constructed and overweighted the influence of the manual phalanges and metatarsus. These characters were initially introduced to provide more information on the relationships of caenagnathids, but improved sampling of the taxa based on the data in Chapter 3 accomplishes the same task more rigorously. In addition to removing characters, all of the characters were treated as unordered. Previous ordered characters applied only to a few taxa and so served to force relationships artificially.

Three outgroups were included in the anaylsis: *Herrerasaurus ischigualastensis* Reig 1963, *Velociraptor mongoliensis* Osborn 1924, and *Archaeopteryx lithographica* Meyer 1861. Besides being the taxa already used by the matrix of Osmólska et al. (2004), these outgroups are appropriate because they polarize primitive characters within both Saurischia and Coelurosauria. *Herrerasaurus* is typically recovered as a basal saurischian or theropod, and therefore provides information on the ancestral characters of all theropods. *Velociraptor* and *Archaeopteryx* were both included in the matrix of Maryanska et al. (2002) and Osmólska et al. (2004) to test whether oviraptorosaurs were more closely related to birds than other theropods. Nonetheless, they each provide an appropriate polarization for paravian characters.

The resulting matrix had 42 taxa and 246 characters, which were a mix of binary and multistate characters. All multistate characters were treated as unordered. The matrix has a relatively high proportion of missing data: 51.7% of the characters could not be coded. As expected, much of this poor data quality comes from the caenagnathid portion of the tree, where only about one-third of the characters could be coded (68.7% missing data). This likely accounts for their volatility in previous analyses, typically resulting in a 13-tomy of caenagnathids more derived than *Gigantoraptor erlianensis.* Regardless, this is still a drastic improvement over previous analyses—for example, the caenagnathid portion of the matrix of Lü et al. (2017) has 80.6% missing data. Oviraptorids, in contrast, could be coded for more than half of the characters (46.0% missing data) and have been relatively stable in most analyses. However, some analyses have differed in the membership of each subfamily, and therefore better resolution in the oviraptorid portion of the tree is still important.

Tree search—A parsimony-based heuristic tree-search was run in TNT v.1.1 using 10000 replications of Wagner trees followed by tree bisection-reconnection (TBR) branch swapping, holding up to 10 trees each replication. A final round of TBR branch swapping was used on the resulting trees to find additional most parsimonious trees. Bremer support values were calculated using the *Bremer.run* package included with TNT v1.1. The analysis produced 9 most parsimonious trees of 641 steps, with relatively strong Bremer support for the major clades of Oviraptorosauria. The strict consensus tree (CI: 0.41, RI: 0.63) has a polytomy at the base of Oviraptorosauria within Caudipteridae, and a second polytomy within Oviraptoridae between non-heyuannine oviraptorids. Otherwise, the phylogeny is completely resolved. The majority-rules consensus tree (CI: 0.43, RI: 0.66) is completely resolved and was therefore used for the subsequent analyses.

Statistical methods—The phylogeny was time-scaled using age ranges published from the literature. Although the ages of most taxa could be determined relatively precisely, the stratigraphic ranges of oviraptorids from Southern China are poorly constrained. In these cases, stratigraphic ranges were taken from published estimates of the ages of the formations where the specimens were found. Time-scaling was done using the *paleotree* v3.3.0 package in R statistical package. Branch lengths were calculated using the equal dating method of Brusatte et al. (2008).

Body mass evolution was analyzed from body mass estimates based on femoral circumference using the method of Campione et al. (2014). Where body mass could not be estimated for a taxon, it was calculated by scaling the body mass estimate of a closely related taxon based on linear measurements of overlapping material. For example, the femur of *Leptorhynchos elegans* is unknown, so its body mass was estimated by scaling the known body mass of *Elmisaurus rarus* Osmólska 1981 based on the length of the tibiae, which are known for both taxa. *Yulong mini* and *Banji long*, both represented only by juvenile specimens, were dropped from the analysis to avoid skewing the pattern of body masses in oviraptorids. *Microvenator celer* was retained, despite its likely juvenile status, because of its important phylogenetic position. Body masses were plotted as a phenogram of $\log_{10}$BM (kg) versus time from the root of Oviraptorosauria using the phenogram function of *phytools* v0.6-44 in R (Revell, 2012). Phenogram branches were coloured based on biogeographic distributions (Asian or North American) and family membership (e.g. avimimids, caenagnathids, oviraptorids), to qualitatively assess factors influencing body mass.

To trace the patterns of digit reduction and loss in oviraptorids, a proxy for digit size was developed. Measurements for 73 complete digits (digit I, n = 32; digit II, n = 29; digit III, n = 12) of 31 oviraptorid specimens (15 taxa) showed that straight-line length of the ungual was strongly

correlated to the pre-ungual length of that digit ($0.82<R^2>0.93$). Therefore, the ratio of two ungual lengths could be used to determine the relative proportions of two digits, even where those digits were not complete. Based on these correlations, the ratio of ungual III-4 to I-2 was used because it maximized the availability of data: 19 of 42 taxa (n = 27) have both ungual I-2 and III-4, whereas only 9 of more than 100 measured oviraptorid specimens have complete first and third digits. The ratio of manual ungual III-4 to manual ungual I-2 was mapped as a quantitative character onto the phylogeny using Maximum Likelihood (via the *phytools* v0.6-44 package of R) to estimate ancestral states and missing tips. Warm colours indicate a low ratio of III-4:I-2 (i.e. smaller third digit), and cool colours represent a higher ratio of III-4:I-2 (i.e. larger third digit). A tree using Grafen branch lengths generated using the compute.brlen function of *phytools* v 0.6-44 was used in place of a time-calibrated tree, because phylogenetic distance between taxa is likely more informative for the pattern of morphological evolution than the stratigraphic distance. In addition to the ratio of ungual III-4 to I-2, the relative proportions of the digits for 14 oviraptorids with complete hands or scaled composites were plotted in a ternary plot. Digit length, including the ungual, was calculated from straight-line measurements of the long axes of each phalanx. The length of each digit was divided by the sum of the lengths of all digits and plotted as a percentage.

Paleobiogeography was examined by mapping the specimens using GPS coordinates and by creating discrete bins which were analyzed as a categorical character. To enhance relevance of these bins, they were chosen based on the biogeographic transition of interest in that part of the phylogeny. For example, to understand the dispersal of caenagnathids into North America, basal oviraptorosaurs and caenagnathids were coded as either "Asian" (purple) or "North American" (orange), without subdividing either of those regions. Because all oviraptorids are

found in Asia, two subdivisions were created: Southern China (blue) and Western Gobi (green). The history of oviraptorosaur biogeography was stochastically simulated based on the tip data for 1000 replicates using the make.simmap function of *phytools* v0.6-44, using a continuous-time reversible Markov model with equal rates of transformation. This allowed for estimation of ancestral biogeographic states and the posterior probability of each state at each node. In the future, it may be possible to increase the precision of the Markov model by scaling transformation rates based on biogeographic information, but this was not feasible for the present study. Biogeographic data was integrated with the digit reduction data by plotting biogeographic ancestral state likelihoods onto the nodes of a tree where digit reduction was mapped as a continuous character.

The evolution of gregarious behaviour was estimated using two methods, both of which suffer from a lack of definitive data. This issue stems from detecting absences of gregarious behaviour in the fossil record: at what sample size can we be confident in the absence of a conditionally-preserved trait? Although a threshold could be estimated by rarefaction of data where the trait is preserved or by creating a confidence index based on sample size and average skeletal completeness, these methods fail to adequately control for taphonomy, ontogenetic changes in behaviour, and other factors affecting the preservation of groups of individuals. In any case, these methods are beyond the current study. Instead, only two instances of the absence of gregarious behaviour were coded: *Herrerasaurus ischigualastensis* and *Velociraptor mongoliensis*. These were coded in this way because they serve as the outgroups to Oviraptorosauria and it is unlikely that gregarious behaviour in oviraptorosaurs was inherited from their coelurosaurian ancestor. Taxa for which gregarious assemblages are known were coded as present, and all other taxa were coded as ambiguous. Two analyses were run on two

trees each. The first analysis treated gregarious behaviour as a continuous character and estimated its ancestral states within Oviraptorosauria using maximum likelihood and estimating the states in missing tips. This was done for a time-calibrated tree and a tree scaled to Grafen branch lengths using the contMap command of *phytools* v0.6-44. The second analysis treated gregarious behaviour as a discrete character and estimated its posterior probability at each node by stochastically simulating its history over 1000 generations in a Markov model with equal rates of transformation. As in the first analysis, this was conducted for both a time-calibrated and a Grafen scaled tree.

<p align="center">5.3 RESULTS</p>

5.3.1 Gregarious Behaviour

Avimimid Bonebeds

Geological and Sedimentological Context:

 Nemegt Bonebed—The Nemegt *Avimimus* bonebed occurs in the lower portion of the alluvial Nemegt Formation, at the Nemegt locality within the Nemegt Basin (Gradzinski, 1970; Eberth et al., 2009; Fig. 5.1). Here, Upper Cretaceous strata of the Nemegt Formation interfinger with and overlie the Baruungoyot Formation (Eberth et al., 2009). In general the Nemegt Formation is characterized by abundant deposits of ephemerally active meandering channels, splays and sheetfloods, and ponds and wetlands (Gradzinski, 1970; Eberth et al., 2009). The Nemegt Formation has yielded few bonebed deposits; the only two recorded instances include an assemblage of *Saurolophus* (Ryan et al., 2011) and this *Avimimus* bonebed. The precise age of

the Nemegt Formation is difficult to determine because of the discontinuity of beds and exposures, absence of microfossil biostratigraphy, and lack of datable volcanics (Eberth et al., 2009). Nonetheless, based on the better-documented late Campanian to early Maastrichtian age of the underlying Djadokhta Formation (Tsogtbaatar et al., 2014) and the presence of Maastrichtian dinosaurs such as *Saurolophus* in the Nemegt Formation, an early Maastrichtian age for the Nemegt Formation is currently accepted.

The exposed Nemegt Formation around the bonebed is only 35 m thick due to truncation by a regionally-expressed Quaternary unconformity. The *Avimimus* bonebed occurs 10.5 m above an interfingered Nemegt-Baruungoyot contact and is associated with the lower portions of sigmoidal and offlapping inclined beds of silty, pebbly, fine- to medium-grained sandstone (Eberth et al., 2009; Fig. 5.2). Two types of matrix surround the bonebed. The base of the bonebed is a fine-grained sandstone, which is overlain by a coarse-grained sandstone with some clay rip-up clasts. Inclined beds are typically less than 5 cm thick, exhibit a total vertical relief of 40 cm, and dip toward the south and southwest, suggesting that they are offlapping deposits of a migrating point bar in a meandering river channel (Gradzinski, 1970; Eberth et al., 2009). Large-scale trough cross beds drape the toes of the point bar and immediately overlie the bonebed. Paleocurrent data collected from them indicate that flow at the base of the point-bar was toward the west-southwest, ranging from 240–280°. Bones are preserved in both matrix types, and some bones span the contact between the layers. This suggests that the beds were deposited in a single coarsening-upwards event, probably tied to the migration of the point bar. The presence of localized mudstone pebbles and *Avimimus* remains at the base of the beds, as well as non-predictable grain size changes between beds, poorly organized mixtures of trough and ripple cross-strata within beds, soft-sediment deformation structures, and localized millimeter-thick

clay drapes all suggest highly variable conditions through time at the bonebed site. These conditions include erosive hydraulic flow, standing water, subaerial exposure, and trampling by dinosaurs. Accordingly, at times this channel-hosted site may also have acted as a waterhole, attracting vertebrates in search of food and/or water.

Iren Dabasu Bonebed—The general age of the Iren Dabasu Formation is widely accepted as Late Cretaceous, but its precise age is debated. Granger and Berkey (1922) indicated a Cretaceous age, but did not speculate further. Morris (1936) hypothesized that the beds were Campanian, but others since have suggested an older age on the basis of a relatively primitive dinosaur fauna (Weishampel and Horner, 1986; Smith and Galton, 1990). Currie and Eberth (1993) reevaluated the biostratigraphy and sedimentology of the Iren Dabasu Formation and drew similarities with the Bayn Shiree Formation exposed at Bayshin Tsav. They concluded that these sediments were probably early Senonian (=Cenomanian–Santonian), but that several unusual members of the fauna (avimimids and troodontids) may point to a Campanian age. Van Itterbeeck et al. (2005) described microfossil data supporting a Campanian–Maastrichtian age for the formation and suggested it might correlate to the Nemegt Formation further west. Averianov and Sues (2012) used vertebrate biostratigraphy and found evidence for a Santonian age, arguing that the microfossil similarity of the Nemegt and Iren Dabasu Formations was the result of similarity in environment rather than age. Most recently, Bonnetti et al. (2014) used palynostratigraphy to support the assertion of Van Itterbeeck et al. (2005) that the Iren Dabasu (= Erlian) Formation is late Campanian–Maastrichtian.

Regardless of the equivocal age of the Iren Dabasu Formation, its paleoenvironment is well established. The sedimentology indicates a terrestrial fluvial system with braided channels in a semi-arid climate (Currie and Eberth, 1993). Preservation of egg nests, caliche and paleosols

indicates periodic subaerial exposure, and the presence of plesiosaurs and hybodont sharks indicates a river system with a marine connection. Because material was collected from spoil piles and no fresh excavation of the bonebed layer was conducted, the sedimentology of the bonebed deposit could not be assessed.

Assemblages:

  Nemegt Bonebed—The Nemegt Bonebed assemblage is dominated by *Avimimus*, which comprises 204 (91.8%) of the 222 accessioned specimens. The other 19 accessioned specimens include indeterminate dinosaur elements (6), an oviraptorid dorsal centrum, embryonic hadrosaur bones, a bird tarsometatarsus, a lizard vertebra, mammalian limb bones, eggshell, gastropod and bivalve casts, and wood. The relative abundance and dominance of *Avimimus* in the bonebed is underestimated because, in some cases, multiple elements are preserved in articulation or as fused single functional elements that were accessioned together. The non-poached, newly excavated part of the bonebed was collected exhaustively, so it is unlikely that there was a collection bias towards *Avimimus* at the expense of other taxa. *Avimimus* material collected includes a variety of cranial elements, vertebrae, forelimb material, some parts of the pelvis, and many hindlimb elements (see Chapter 2: section 2.3.2). Ontogenetic stage of elements from the bonebed was assessed using size and fusion of the elements. Although these qualities are not strictly tied to developmental age, similar criteria have been used previously to assess relative age in other assemblages where histological sections were unavailable (Ryan et al., 2001b; Currie and Azuma, 2006a). Adults were identified by fusion of the tibiotarsus or tarsometatarsus. The lengths of fused tibiatarsi (n=17) from the bonebed vary by less than 10% (246 mm – 280

mm), suggesting that adults were either all of a similar ontogenetic stage, or that growth was determinate in adult individuals. All tibiotarsi longer than 246 mm (n=17) are fused, and none shorter than 246 mm are fused, indicating that fusion of the tibiotarsus is strongly tied to body size. Non-adult individuals were identified by lack of hindlimb fusion. Most of these individuals, however, are similar in size to the largest fused individuals (tibiae >80% of 280 mm). Histological analysis of material from the Iren Dabasu Bonebed (see Chapter 2: Section 2.3.4) suggests that these individuals may still be young in age, even if they are approaching adult body size. Of the 33 tibiae recovered from the bonebed, only one tibia (MPC-D 102/38), an estimated 202 mm in length, fell below the 80% cutoff of the length of the largest tibia (280 mm), and can be considered a juvenile individual. The state of fusion for this individual cannot be assessed, because the distal end is missing. This suggests that the individuals in the bonebed are likely from the same cohort, rather than a representative sample of a population. Evidence from other bonebeds suggests that non-avian theropod dinosaurs had a tendency to form juvenile-dominated herds (Kobayashi and Lü, 2003a; Currie and Azuma, 2006a; Varricchio et al., 2008b; Erickson et al., 2010b). Adult-dominated bonebeds of non-theropod taxa also typically contain a small percentage of juvenile animals (Ryan et al., 2001b, 2011). The presence in the assemblage of small elements from *Avimimus*, such as phalanges, and small material from other taxa, including embryonic hadrosaur bones, a lizard vertebra, and mammal limb bones, suggests that the dearth of small *Avimimus* is real, rather than the result of winnowing. The Nemegt Bonebed is therefore unusual in its apparent near absence of juvenile individuals.

The minimum number of individuals (MNI) represented by the assemblage was estimated using tibiae. The distal ends of 13 right tibiae are present and indicate that at least this many individuals contributed to the assemblage. However, combining the measurements of these 13

specimens with data from left tibiae shows that there are at least 18 tibiae of different sizes in the assemblage. Thus, an MNI of 18 appears to be the best estimate for the number of individuals that contributed to the assemblage, which represents the largest monodominant assemblage of maniraptorans yet reported.

Iren Dabasu Bonebed—An exact calculation of monodominance at the Iren Dabasu Bonebed is not possible because the assemblage is not completely represented in the sample examined. Regardless, avimimids formed a high percentage of the assemblage, because other taxa (dromaeosaurs, ornithopods) are only represented by one or two specimens. Like the Nemegt Bonebed, the avimimid component of the Iren Dabasu Bonebed is dominated by fused compound elements, including tibiotarsi and tarsometatarsi. However, there is some variation in fusion: one tibiotarsus is only fused distally, and an isolated metatarsal IV was not yet fused proximally to metatarsal II. The Iren Dabasu and Nemegt Bonebeds therefore likely represent assemblages similar in age composition, although future systematic excavation of the Iren Dabasu Bonebed is necessary to confirm this suspicion. MNI was assessed using a mixture of unique elements and discrete size classes. Based on metatarsals, at least six individuals are represented by overlapping material or non-overlapping material of significantly different size.

Taphonomy:

Nemegt Bonebed—Given an MNI of 18 based on prepared material, overall skeletal element representation of *Avimimus* is low in the Nemegt bonebed (~5-6%, Fig. 5.6). Skeletal representation data was updated using the material accessioned in the 2016 catalogue, but MNI could not be updated without preparation of that material. Hindlimb elements are strongly overrepresented (~36-108%) in the assemblage compared to all other elements (Fig. 5.6).

Recovery of more than 100% representation of tarsometatarsi when assuming fusion of the compound bones (108%) suggests that an MNI of 18 is low. However, expected tarsometatarsi are only 36% represented when it is assumed that they were unfused, and so it is possible that this overrepresentation can be accounted for by variation in the degree of fusion between individuals. Long bones excavated from the quarry (Fig. 5.4) show a significantly preferred NE-SW orientation (Rao t=201, p<0.001; Raleigh Z: t=0.7211, p<0.001), subparallel to sedimentological indications of a SW-oriented paleochannel. All *Avimimus* bones recovered from the site share the same bone modification signature, lacking signs of prolonged subaerial exposure; insect feeding traces such as boring; tooth marks; or weathering. Small fragments of hadrosaur bones in the bonebed are typically abraded, weathered, and powdery, suggesting they have been subject to different taphonomic conditions. Most of the bones were preserved horizontally, but in the coarse-grained sandstone layer several elements (ilium, humerus, phalanges) were vertical or inclined, suggesting that they were moved from resting position and buried quickly. Few of the unfused elements are preserved in articulation, with the notable exceptions of two nearly articulated premaxillae (see Chapter 2: section 2.3.2) and eight distal caudal vertebrae found articulated. Most of the associated material comes from compound or fused elements, but the presence of some associated material (ilium and unfused sacral ribs) indicates that the bones were not transported far. The bones have been hydraulically sorted, so that small elements are rare—but still present—and there is a bias towards the preservation of thick-walled elements like femora and tibiae. Despite this, the bones show little to no abrasion, and delicate elements like cranial material and fibulae are unbroken, which suggests that hydraulic flows that sorted or reoriented elements were not intense or prolonged. Most of the broken bones from the assemblage were surface collected, suggesting that they were damaged by

the poachers. Only two theropod teeth (cf. *Velociraptor*) were recovered from the site, suggesting that scavenging, if present at all, was limited. It is unlikely for a number of reasons that the sediments surrounding the bonebed represent the first burial of the material. First, such an assemblage would be dominated by articulated or associated material, rather than isolated bones. Second, the matrix is representative of normal deposition in a channel, rather than a catastrophic flood capable of killing multiple *Avimimus*. The pristine condition of the bones suggests they were originally buried rapidly, which protected them from subaerial weathering, trampling and scavenging, but allowed most of the soft tissues to decompose over the course of months to years. The bonebed was then uncovered by a medium- to high-energy flow, represented by the two sandstones, which disarticulated most of the material and transported it a short distance. The second flow event had enough energy to reorient most of the long bones to a N-NE to S-SW orientation (Fig. 5.4), but was not powerful enough to remove large elements. Numerous examples of similar multistage depositional events in monodominant assemblages are known from North America (Britt et al., 2009; Eberth and Currie, 2010; Evans et al., 2015)

The predominance of thick-walled, hydrodynamically dense elements (Fig. 5.6) and the taphonomic signatures of the bones, combined with sedimentological and paleocurrent data, suggest that this assemblage represents a secondary deposit of previously buried skeletal material. The original death assemblage was probably formed by a catastrophic mass death event and the remains were then accumulated in the paleochannel during a second depositional event. The cause of the mass death cannot be determined with certainty, although the assemblage is somewhat similar to the ornithischian bonebeds from the Late Cretaceous of the Western Interior of North America. These include well-studied bonebeds such as the *Centrosaurus* Lambe 1904 bonebeds of Dinosaur Provincial Park (Ryan et al., 2001b) and the *Pachyrhinosaurus* Sternberg

1950 bonebeds of the Wapiti Formation (Fanti et al., 2015). These assemblages consist primarily of single species, although there are often isolated elements from other taxa. Larger individuals dominate, and assemblages are preserved as disarticulated, hydraulically sorted elements in channel lag deposits. These bonebeds are thought to result from the catastrophic deaths of many individuals in groups or herds, drowned during flooding events (Ryan et al., 2001b; Eberth, 2015; Fanti et al., 2015). The high proportion of distal hindlimb elements is unusual, especially considering that other dense elements, like sacra and the fused pelvic elements (Kurzanov, 1983), are underrepresented (Fig. 5.6). This may point to a miring event as the cause of the mass death. Unfortunately, any sedimentological indications of miring have been erased by the second flow event, and therefore the cause of death is ambiguous.

Iren Dabasu Bonebed— Skeletal representation at the Iren Dabasu bonebed is similar to the Nemegt Bonebed (4-5%; Fig. 5.6), but the elements themselves are less complete. As in the Nemegt Bonebed, thick-walled hindlimb elements are overrepresented, but so are vertebrae, which is not the case at the Nemegt Bonebed. It is likely that this is indicative of less reworking of the original material, and skeletal representation is lower by virtue of the methods of collection. The lack of *in situ* material from the site precludes detailed taphonomic analysis, but some information on the taphonomy can be gleaned from the bones themselves. The pristine surface condition of most material (see Chapter 2: section 2.3.3), especially considering that it had been exhumed for 30 years prior to collection, suggests that the bonebed material was buried relatively rapidly (Behrensmeyer, 1978). Regardless, many of the bones are broken and proximal and distal ends are more common than the intervening shafts. However, this is probably the result of secondary exposure and rough excavation via bulldozer, rather than pre-depositional breakage. The disarticulation of the bones, except for fused compound elements (tibiotarsi,

tarsometatarsi), indicates that they were exposed long enough for the flesh to decay.

Representation of a variety of elements from the entire skeleton (Fig. 5.6) argues against

hydraulic concentration of dissociated material and suggests that the individuals perished

together in a mass mortality (Rogers et al., 2014). Accordingly, the bonebed assemblage supports

previous suggestions of gregarious behaviour in avimimids (Funston et al., 2016). However,

some material from the bonebed pertains to other taxa, including a dromaeosaur and an

indeterminate ornithischian, and it is therefore possible that the assemblage was reworked after

initial deposition.

Oviraptorid Assemblages

Geological context:

Geological contexts are only known with certainty for two of the oviraptorid assemblages

described here. Both are from the Nemegt Basin, and both comprise specimens referable to

Conchoraptor gracilis (see Chapter 4: Section 4.3.1). However, some lines of evidence point to

the other assemblages being from the same region. Geochemical analysis of trace elements

preserved in the bones of MPC-D 102/110 indicates with 88% certainty that it is from the

Nemegt Formation (Fanti et al., 2018b), rather than the Baruungoyot or Djadokhta Formations,

which are the only other formations known to produce oviraptorids in Mongolia. The

sedimentology of the remaining matrix and the preservation of the bones themselves are

consistent with this interpretation. The Nemegt Formation is characterized by grey-brown

sandstones which starkly contrast with the bright red, oxidized sediments of the Baruungoyot and

Djadokhta Formations. The bones show no sign of taphonomic weathering (Fig. 5.7), whereas in

the Baruungoyot and Djadokhta Formations, bone is generally weathered and bored by dermestid beetles. Furthermore, bones that have been subaerially exposed after fossilization in MPC-D 102/110 (e.g. the left foot of individual 'A') have weathered to a pink-brown colour common in the Nemegt Formation, whereas fossils from the Baruungoyot and Djadokhta Formations typically remain bright white after exposure (G.F.F. pers. obs.). The provenance of the CMMD block (Fig. 5.8) is more difficult to establish because geochemical analysis is not available. In general, the sediments and bones more closely resemble Nemegt-style deposition than Baruungoyot or Djadokhta Formation deposits, especially in terms of matrix colour and bone surface modification. However, there are some peculiarities that may indicate it is from an as-yet-unknown locality. For example, the matrix is finer than typical in the Nemegt Formation and has a distinct green hue that is unlike any of the known oviraptorid-producing formations in Mongolia. Similarly, the bones vary in colour from white to distinctly pink to black, which contrasts with the more typical white or slightly pink-beige of the Nemegt and Baruungoyot Formations. In these aspects, the bones somewhat resemble those preserved in the Bayn Shiree Formation exposed at Shine Us Khudag in the Eastern Gobi Desert (Fig. 5.9). The Bayn Shiree Formation is inferred to be an earlier portion of the Late Cretaceous (Cenomanian–Santonian) than the Baruungoyot or Nemegt Formations (Campanian–Maastrichtian), and has not yet produced any certain oviraptorid material. Geochemical analysis or the recovery of similar oviraptorid material from the Bayn Shiree Formation would strengthen this claim.

With regards to the specimens of certain provenance, MPC-D 102/03 was collected from the Baruungoyot Formation exposed at Hermiin Tsav, whereas MPC-D NatGeo.2018.036 was collected from the Nemegt Formation in Guriliin Tsav. Recent work on stratigraphy and sedimentology suggest that parts of the Baruungoyot and Nemegt Formations overlap

temporally, and may represent a single ecosystem with different subenvironments and patterns of sedimentation through time (Eberth et al., 2009; Fanti et al., 2012, 2018a; Eberth, 2018). These Formations outcrop extensively in the Nemegt Basin, but most prominently at Altan Uul, Bugiin Tsav, Hermiin Tsav, and Nemegt. Correlation of the strata (Eberth, 2018) suggests that these localities form a transect of the Baruungoyot and Nemegt Formations, decreasing in age from Hermiin Tsav through Nemegt and Altan Uul, to the youngest deposits at Bugiin Tsav. Previous work on stratigraphy (Gradzinski, 1970; Gradziński et al., 1977) allows other localities from the Nemegt Basin to be incorporated into this stratigraphic sequence, and places Guriliin Tsav near the top of the section. MPC-D NatGeo.2018.036 was found in a fine-grained siltstone that was laterally continuous with two cross-bedded, concreted coarse sandstones. Accordingly, it likely represents a lower-energy interfluve deposit, which may have been critical for the preservation of individuals in life positions with minimal disarticulation (Fig. 5.10).

Assemblages:

Two individuals are preserved in MPC-D 102/3 (see Chapter 4: section 4.3.1). The more complete individual is represented by nearly the whole skeleton, missing only the tip of the snout and the middle to distal portions of the tail. The second individual is represented by a portion of the tail that overlaps with the first individual and is lying nearly perpendicular to the more complete skeleton. The ontogenetic stages of the individuals are difficult to establish without histological analysis, but the more complete individual has fused neurocentral sutures in the caudal and dorsal vertebrae, which are likely to have fused throughout ontogeny. It is the largest individual of *Conchoraptor gracilis* yet collected, with a femoral length (240 mm) and humeral length (125 mm) exceeding all other known specimens. It is likely, therefore, that this individual

can be considered an adult, although this is tentative. The tail of the second individual is comparable in size to that of the first individual, although its position within the caudal series is uncertain and this could be due to differences in which vertebrae are represented.

Two large blocks and several smaller jackets were collected from MPC-D NatGeo.2018.036 (Fig. 5.10), all but one of which still await preparation. Accordingly, the number of individuals contained within the blocks is not known with certainty, but at least eight skulls were uncovered during excavation, leading to an MNI of 8 individuals. However, based on the orientations of the skeletons, it is more likely that as many as 13 or 14 individuals are represented in the assemblage (Fig. 5.10F). Of these, nine will likely be represented by a significant portion of an articulated skeleton. The ages of the individuals cannot be determined without histological analysis, but it is clear that there is variation in the sizes of the animals represented. The smallest ilium completely exposed during excavation was approximately 70% of the length of the largest, although the ontogenetic stages of these individuals could not be established in the field. Caudal vertebrae associated with one individual approximately 80% the size of the largest individual had unfused neurocentral sutures, likely indicating an immature ontogenetic stage. More detailed analysis of the ages of the individuals in the assemblage will necessitate preparation of the blocks.

UALVP 54983 (=CMMD Block; Fig. 5.8) preserves at least four individuals based on skulls, but the positions of the skeletons suggest there were more likely six individuals. The skeletons are similar in size, ranging in femoral length from approximately 210 mm to 230 mm. Where they can be observed, neurocentral sutures of each individual are open (Fig. 5.8C), suggesting an early ontogenetic stage. This is supported by open sutures between the sacral vertebrae, which typically close relatively early in ontogeny in theropods.

Three individuals are preserved in MPC-D 102/110, but two of these are more complete than the third (Fig. 5.7A). A second specimen, MPC-D 102/11, was confiscated at the same time, is of the same taxon, and is preserved in the same style and posture (Fig. 5.7E). Associated with it are the quadrate, quadratojugal, and postorbital of a second individual. It is likely that these specimens were collected from the same quarry as MPC-D 102/110, but were separated for logistical reasons during excavation. Accordingly, they are interpreted here as members of the same assemblage, which brings the total to at least four individuals based on ilia. Osteohistological samples show that each of these individuals was young and growing rapidly (see Chapter 4: section 4.3.6). A growth mark consisting of an annulus of parallel-fibered bone were recovered towards the outer cortices of MPC-D 102/110.b and MPC-D 102/11, suggesting that these individuals were just over one year old. This is attested to by minimal sacral fusion in both individuals—only three of six vertebrae were fused—and lack of braincase fusion in MPC-D 102/11. This individual also retains a cleft between the anterior ends of the parietals and posterior ends of the nasals, as well as separated frontals that are not yet sutured together (see Chapter 4: section 4.3.6). These elements are typically fused even early in ontogeny (Lü et al., 2013), supporting the young age estimation based on osteohistology.

Taphonomy:

Each of the oviraptorid assemblages comprises nearly completely articulated skeletons, but some minor disarticulation has nonetheless occurred. Although the appendages and pelvis of MPC-D 102/03 are in life positions, they have settled somewhat and become disarticulated by dorsoventral crushing. This is especially evident in the pelvis, where the ilia and ischia have come to lay flat, rather than retaining their upright positions. The vertebral column is similarly

disarticulated and the dorsal vertebrae and ribs have fallen from their natural positions to lie along the ventral side of the body. Regardless, the feet and hands are naturally articulated and the limbs have apparently not changed position. This is evident in the forearm remaining oriented vertically in the sediment, and the left toes preserved grasping the substrate. The surfaces of the bones are pristine and do not show any evidence of scavenging nor insect boring. Similarly, they are not communited, which suggests that they were not subject to weathering. Together, the articulation of the specimen and the pristine conditions of the bones suggest that the skeleton was buried before the body could decompose. The disarticulation of the dorsal vertebrae can be explained by deflation of the thoracic cavity during decomposition after burial. The posture of the skeleton, with its legs crouched underneath the body and the belly against the ground suggest that it was not transported and may have been killed by the same event that buried it.

Additional preparation is necessary to establish the taphonomy of MPC-D NatGeo.2018.036 with more certainty, but some observations could be made in the field. Most of the bones were tightly articulated, although some elements on the southeastern side of the block (top right in Fig. 5.10A) had become disarticulated. This is likely the result of hydraulic action after the bodies had come to rest, as the sediments adjacent to this region are cross-bedded and concreted, suggesting a higher flow regime. Towards the northwestern side of the block, the skeletons are oriented belly-down with the limbs crouched underneath the bodies (Fig. 5.10D). In the center of the block, some individuals appear to be in death pose, although it is possible that these elements were incorrectly associated because no skeleton was completely exposed and the bonebed is dense (Fig. 5.10E). At least one individual appears to be curled up, with its head tucked towards the stomach in a pose resembling the fetal position (Fig. 510F, top left). Even in the naturally articulated skeletons, some local disarticulation has occurred. For example, one

exposed manus has had some separation of the phalanges from the metacarpals (Fig. 5.10C) and the right quadratojugal of a skull (Fig. 5.10B) was preserved under the left side of the braincase (see Chapter 4: section 4.3.1). The bones show no evidence of modification, and the bone surfaces are excellently preserved with no weathering or cracking. As is the case in MPC-D 102/03, these lines of evidence suggest that the skeletons were buried rapidly after death, possible in the same event. This would account for the preservation of some individuals in life postures. However, the skeletons were subject to some degree of hydraulic reworking, which was apparently more pronounced on the southeastern portion of the assemblage than the northwestern side.

The taphonomy of MPC-D 102/110 is remarkably similar to the northwestern portion of MPC NatGeo.2018.036. The orientation of the jacket can be established by the direction that preparation was undertaken, and early photographs show that the ventral sides of the skeletons remained buried in matrix. This indicates that this side was down in the field, and the specimen must have been detected by exposure of the dorsal sides of the skeletons. In this light, the skeletons are preserved with the legs crouched underneath the bodies and are, for the most part, tightly articulated, although some local disarticulation has occurred. The skeletons have slumped slightly so that the feet are not directly underneath the pelvis, but this likely occurred after burial as the skeletons decomposed. The surface conditions of the bone is virtually identical to MPC-D NatGeo.2018.036, with excellent preservation of the surface and no evidence of scavenging or weathering. Hydraulic action was apparently minimal, based on the preservation of delicate, easily transported elements like sclerotic plates. Accordingly, the specimen must have been buried quickly after death or by the same event.

The taphonomy of UALVP 54983 is difficult to assess with certainty because the specimen could not be examined in detail. Furthermore, little matrix is preserved with the specimen and no sedimentary structures can be observed in the matrix that is exposed. Regardless, some insights can be made. Most of the skeletons are naturally articulated, but rather than being preserved in life postures, they are all in death pose. Some local disarticulated has occurred, likely where unfused elements separated during decomposition. Unlike the other assemblages, there is considerably more evidence of compression in this specimen, and two of the skulls have been transversely crushed onto a single plane. Regardless, the hindlimb elements are uncrushed, so it is unclear how the crushing occurred. The skeletons appear to have a general trend in their orientation, parallel to the long axis of the block, but verifying this would require more detailed examination. In any case, the reorientation of the skeletons must have occurred before they decomposed, because the bones within the skeletons show no preferred orientations. In many areas the skeletons overlap, which is likely an indication of transport after death. The bone surface appears to lack signs of weathering and scavenging, but could not be observed in detail. Based on the available evidence, it is likely that these skeletons were killed in a mass death event and buried soon after in a hydraulic flow which had enough force to reorient the skeletons, but not enough to disarticulate the relatively fresh carcasses.

5.3.2 Ecology

Sampling efficiency—Rarefaction curves for species-level data (Fig. 5.13A) generally perform poorly, with three exceptions. Bugiin Tsav, Nemegt, and Hermiin Tsav are past the inflection points of their respective curves, but they are still slightly undersampled. The majority of the localities are low on their curves and therefore poorly sampled at the species level. Altan

Uul II is intermediately positioned, near the inflection point of its curve. Superfamily-level data (Fig. 5.13B) performed better because of lower richness. The results were similar to species-level data, except each site was further along its curve. Altan Uul II, which was at the inflection point using species-level data, was recovered closer to the asymptote using superfamily-level data. The results suggest that Bugiin Tsav, Hermiin Tsav, Nemegt, and possibly Altan Uul II, are well-sampled enough that species-level data are representative of their communities, but that other localities are not well-sampled enough. Most of the sites are well-sampled at the superfamily-level.

Community structure—Oviraptorosaurs comprise 12% of the entire Nemegt Basin sample, but their proportion of each community varies (Fig. 5.14). In the Baruungoyot Formation, they form on average 22.6% (n = 24 skeletons) of the community, but in Nemegt Formation, they contribute only 9.1% (n = 35 skeletons) of the fauna. *Tarbosaurus bataar* is by far the most abundant dinosaur from the Nemegt Basin (n = 127 skeletons; 27% of total sample), followed by *Gallimimus bullatus* (n = 96 skeletons; 20% of total sample) and *Saurolophus angustirostris* (n = 57 skeletons; 12% of total sample). Relative abundance plots (Fig. 5.14) reflect this dominance: these three taxa constitute on average 71% of the fauna at each site. The Nemegt Formation sites do not vary much in their overall composition, except for the proportion of rare taxa like alvarezsaurs and *Deinocheirus mirificus* Osmólska and Roniewicz 1970. In the Baruungoyot Formation, oviraptorids (n = 24 skeletons) form 21.2% of the fauna, whereas avimimids and caenagnathids are absent. Oviraptorids (n = 15 skeletons) contribute 4.0% of Nemegt Formation communities, whereas avimimids (n = 9 skeletons) and caenagnathids (n = 12 skeletons) are less common (2.4% and 3.0%, respectively). NMDS (Fig. 5.15) shows a clear division between the Nemegt Formation fauna and the Baruungoyot Formation fauna. The

Nemegt Formation fauna is characterized by tyrannosaurs, sauropods, and hadrosaurs, alongside therizinosaurs and ornithomimosaurs. The Baruungoyot Formation, on the other hand, has a higher proportion of ceratopsians, alvarezsaurs, and pachycephalosaurs, although these taxa do not co-occur frequently. Ankylosaurs, dromaeosaurs and oviraptorosaurs are intermediate, plotting close to each other but between the other groups. This suggests that they are more widely distributed between formations than the other taxa.

   Taxon distribution—Permutation tests on superfamily level data in the Nemegt Formation showed that hadrosaurs, sauropods, ornithomimosaurs, and tyrannosauroids (p_R = 0.007, 0.002, < 0.001, < 0.001, respectively) had a uniform distributions across Nemegt-dominated sites. Other superfamilies in the Nemegt Formation did not have uniform distributions but this may be due to small sample sizes, as these taxa reoccur in well-sampled sites. Oviraptorids had a uniform distribution, but avimimids and caenagnathids did not, which may be reflective of their smaller sample sizes. At well-sampled sites, avimimids and caenagnathids are consistently recovered, which suggests their absence at other sites is the product of poor sampling and their small numbers within the communities.

5.3.3 Evolution

Phylogeny:

   The cladistic analysis produced 9 most parsimonious trees of 641 steps. The strict consensus tree has polytomies near the base of Oviraptorosauria and within oviraptorids, but is otherwise well resolved (Fig. 5.16). The majority-rules tree is completely dichotomous (Fig. 5.16), and this exact topology is also recovered among the most parsimonious trees. Although the majority rules tree does not inherently add or resolve information to the analysis, most

downstream analyses require fully dichotomous trees. I have chosen to use the topology in the majority rules tree for these subsequent analyses, rather than randomly resolving dichotomies, because this topology is among the most parsimonious trees. In other words, it is a well-supported choice for a preferred topology.

Incisivosaurus gauthieri Xu et al. 2002 is recovered as the most primitive oviraptorosaur, followed by a paraphyletic Caudipteridae where *Similicaudipteryx yixianensis* He et al. 2008 is an outgroup to the sister taxa *Caudipteryx zoui* Qiang et al. 1998 and *Caudipteryx dongi* Zhou and Wang 2000 (Fig. 5.17). These species of *Caudipteryx* are sisters to a well-supported (decay index 2) group of *Avimimus* and Caenagnathoidea, referred to here as Edentoraptora based on the ubiquitous absence of teeth in these animals. The species of *Avimimus* are recovered as sister taxa to each other and together are sister to Caenagnathoidea. Caenagnathoidea is well-supported (decay index 3; Fig. 5.16) is divided at its base into Caengnathidae and Oviraptoridae.

The most primitive caenagnathid is *Microvenator celer*, followed by *Gigantoraptor erlianensis*, which is sister to the so-called 'derived caenagnathids'. These taxa are characterized by relatively small size and complexly textured occlusal surfaces of the fused dentaries. This group is relatively well-supported (decay index 2), and therefore referred to here as Caenagnathinae for clarity. The most primitive caengnathines are the sister taxa *Hagryphus giganteus* Zanno and Sampson 2005 and *Chirostenotes pergracilis* Gilmore 1924. The recovery of the latter taxon as sister to *Hagryphus giganteus* is based on manual characters, and their basal position is novel, but not unusual considering the unusual morphology of the pelvis of *Chirostenotes pergracilis* compared to more derived caenagnathids like *Anzu wyliei* Lamanna et al. 2014, *Caenagnathus collinsi* Sternberg 1940, *Leptorhynchos elegans*, and *Nomingia gobiensis* Barsbold et al. 2000b. The latter taxon, *Nomingia gobiensis*, is recovered between *Hagryphus*

giganteus + *Chirostenotes pergracilis* and a clade of the other caenagnathines, rather than as the sister to *Elmisaurus rarus*, which provides some support for its taxonomic distinction. *Nomingia gobiensis* has typically been recovered as an oviraptorid on the basis of the rounded preacetabular blade and the astragalus reaching the lateral margin of the tarsus. However, the discovery of these features in other caenagnathids draws it to the caenagnathid portion of the tree, which is more appropriate based on qualitative assessment of its morphology. *Elmisaurus rarus* and *Leptorhynchos elegans* are recovered as sister taxa, which is unsurprising considering the distinctiveness of their fused metatarsi. Their position within Caenagnathinae obviates the need for the name 'Elmisaurinae', although if future representatives of this lineage are discovered, Elmisaurini may be appropriate. *Apatoraptor pennatus* Funston and Currie 2016 is the sister taxon to a dichotomous pair of sister taxa, *Caenagnathasia martinsoni* Currie et al. 1993 and *Epichirostenotes curriei* Sullivan et al. 2011, as well as *Anzu wyliei* and *Caenagnathus collinsi*. The sister relationship of *Caenagnathasia martinsoni* and *Epichirostenotes curriei* is somewhat surprising, considering the disparate ages and body sizes of these taxa. However, there is some likelihood that the material referred to *Caenagnathasia martinsoni* by Sues and Averianov (2015) makes it a chimaera, because it combines a suite of relatively primitive oviraptorosaur postcranial features with derived features of the mandible. Furthermore, a specimen of *Caenagnathasia martinsoni* that bore teeth was allegedly collected (J. Stiegler pers. comm.), but was lost in transit. If this is true, it provides strong evidence that *Caenagnathasia* is not an edentoraptoran, but rather a late-surviving early oviraptorosaur that converged on the complex dentaries of caenagnathids. There is some support for this in the differing arrangement of the occlusal structures of *Caenagnathasia martinsoni* from other caenagnathines, the large

anterior occlusal groove, and the lack of lateral occlusal ridges. The union of *Anzu wyliei* and *Caenagnathus collinsi* is unsurprising based on their mandibles.

Oviraptoridae consists of *Nankangia jiangxiensis* Lü et al. 2013, *Oviraptor philoceratops* Osborn 1924, and *Yulong mini* as successive outgroups to two subfamilies of oviraptorids. The basal position of *Yulong mini* is likely the result of its early ontogenetic stage. The oviraptorid subfamilies appear to be divided based on the morphology of the manus (Fig. 5.16). One of the two groups is comprised of forms with elongate manus with digits roughly equal in robustness and an elongate third digit. Based on the exclusion of *Oviraptor philoceratops* from this group, it is inappropriate to refer to this family as 'Oviraptorinae', as in previous studies. Instead, it is hereby designated Citipatinae because *Citipati* Clark et al. 2001 is the oldest valid genus named in the family (Norell et al. 2001). Although *Rinchenia* Barsbold 1997 was coined earlier (Barsbold 1997), this genus was not properly diagnosed until its type species was synonymized with *"Oviraptor" mongoliensis* in 2004 (Osmólska et al. 2004). The most primitive citipatine is *Wulatelong gobiensis* Xu et al. 2013, and this is followed by a sister clade of *Rinchenia mongoliensis* and *Tongtianlong limosus* Lü et al. 2016. *Ganzhousaurus nankangensis* Wang et al. 2013 is the sister to a group of *Citipati osmolskae* and the Dzamyn Khondt oviraptorid as sister taxa and *Corythoraptor jacobsi* Lü et al. 2017 and *Huanansaurus ganzhouensis* Lü et al. 2015 as sister taxa. Notably, Citipatinae includes nearly all of the oviraptorids from Southern China. The other group of oviraptorids has been previously referred to as 'Ingeniinae', but because '*Ingenia*' is preoccupied, this subfamily name is inappropriate. *'Ingenia' yanshini* Barsbold (1981) was previously incorporated into *Heyuannia* as *Heyuannia yanshini*, and so this genus now lends its name to the subfamily: Heyuanninae. *Shixxingia oblita* Lü and Zhang 2005 is recovered as the most basal heyuannine, but this taxon is poorly known and it is volatile in the

phylogeny. *Khaan mckennai*, *Conchoraptor gracilis*, and *Machairasaurus leptonychus* Longrich et al. 2010 are successive outgroups to the remaining heyuannines, which form two sister clades of three taxa each. *Nemegtomaia barsboldi* Lü et al. (2004) is sister to the two species of *Heyuannia* on one side, and *Banji long* is sister to a clade of *Jiangxisaurus ganzhouensis* Wei et al. 2013 and the Guriliin Tsav oviraptorid on the other side.

Biogeography:

Based on the new phylogeny, the biogeography of oviraptorosaurs is fairly well constrained (Figs. 5.18, 5.19). Oviraptorosauria originated in Asia, and a major range expansion event to North America occurred in the Aptian at the base of Caenagnathidae (Fig. 5.19), but Caenagnathoidea likely had an Asian origin, rather than North American. Each caenagnathid clade has strong support for a North American origin (Fig. 5.19), indicating that Asian caenagnathids were migrants from North America, rather than dispersal back and forth between these regions. As expected, oviraptorids almost certainly originated in Asia, and more specifically, Southern China. One of the major differences in the results of this phylogeny from other recent phylogenies is that many of the Southern Chinese oviraptorids are grouped together within Citipatinae. This is reflected by the biogeography, which shows that many of these forms originated in Southern China and then some dispersed north to the Western Gobi (e.g. *Oviraptor philoceratops*, *Rinchenia mongoliensis*, *Citipati osmolskae*). A major range expansion event occurred in the Cenomanian from Southern China to the Western Gobi (Fig. 5.19), and this led to the radiation of Heyuanninae in the Western Gobi. This route was apparently only a minor barrier, because several taxa, both citipatines and heyuannines, crossed it in each direction throughout the Campanian and Maastrichtian. However, it appears that each of these regions

produced their own adaptive radiations of morphologically diverse oviraptorids, which nonetheless could inhabit both ecosystems successfully. The Late Cretaceous paleogeography of China is poorly studied, but those studies suggest that Southern China consisted of a series of marshes and lakes within intermontane basins with a relatively arid climate (Pei-ji, 1987). Accordingly, range expansion between Southern China and the Western Gobi may have been accomplished by successive small dispersals from basin to basin.

Body mass evolution:

Oviraptorosaurs comprised a wide range of body sizes (Fig. 5.20), nearly three orders of magnitude considering *Caenagnathasia martinsoni* (5 kg) and *Gigantoraptor erlianensis* (~2100 kg), if specimens of the former are mature. Early oviraptorosaurs were relatively small animals, approximately 10–20 kg, and these body sizes were inherited by avimimids. Caenagnathids and oviraptorids both increased body sizes, not only at their bases, but also throughout their evolution (Fig. 5.20). However, they appear to have done so independently of each other, rather than the common ancestor of Caenagnathoidea increasing in body mass. Further support for this claim would require the discovery of additional stem edentoraptorans. Caenagnathids encompassed the widest ranges of body size, represented by the miniscule *Caenagnathasia martinsoni* and the gigantic *Gigantoraptor erlianensis*. There appears to have been an initial increase in body mass at the base of Caenagnathinae, and a second upward divergence of body masses later in more derived caenagnathines including *Anzu wyliei, Caenagnathus collinsi*, and *Epichirostenotes curriei* (Fig. 5.20). In the Late Cretaceous of the Dinosaur Park Formation, caenagnathids varied in body size by an order of magnitude: *Leptorhynchos elegans* at ~22 kg and *Caenagnathus*

collinsi at ~275 kg. *Chirostenotes pergracilis* is intermediate (66 kg) between these forms, which may have had a role in niche partitioning.

Oviraptorids also experienced a body mass increase at their base, but a smaller one than caenagnathids. They increased slightly in body mass throughout their history, and the slope of this increase is relatively constant (Fig. 5.20). Late in their evolutionary history they were represented by a fairly narrow range of body masses, less than half an order of magnitude. The body masses of oviraptorids broadly overlapped with those of most caenagnathids, but were distinct from avimimids.

Digit reduction:

In general, the proportions of manual digits I and III varied little throughout Oviraptorosauria (Fig. 5.21C). In most oviraptorosaurs the ungual of digit III ranged between 75% and 100% of the length of manual ungual I-2, and the preceding digits can be expected to have followed the same pattern. A notable exception, however, occurred at the base of Heyuanninae, and more derived heyuannines had progressively shorter third digits compared to the first digit (Fig. 5.21A–C). This trend could be explained by either or both an increase in the size of digit I, or a decrease in the size of the lateral digits. However, considerable evidence suggests that manual disparity was caused solely by reduction of the lateral digits. Although digit I was apparently large in the Guriliin Tsav oviraptorid, *Conchoraptor gracilis*, *Nemegtomaia*, and other heyuannines, the ratios of manual ungual I-2 to the humerus and the forearm are consistent with those of other oviraptorids. One exception is *Heyuannia yanshini*, which had a slightly larger ungual I-2 compared to the rest of the arm, but this increase is not enough to account for the disparity in its digits. Instead, it appears as though digits II and especially III

were reduced in heyuannines, culminating in the loss of the third digit in the Guriliin Tsav oviraptorid. This is accompanied by a reduction in the transverse widths of metacarpal II and III, which suggests that these digits became less functional, rather than becoming more gracile to serve a particular function.

Gregarious behaviour:

The inability to confidently score absence of gregarious behaviour in oviraptorosaurs means that the trends recovered here are subject to considerable error and bias, and should be taken cautiously. Regardless, some general statements can be made about its prevalence in Oviraptorosauria. When treated as a continuous character, analyses on both trees recover gregarious behaviour as likely more widespread than currently recognized (Fig. 5.22), especially within oviraptorids. Significant differences exist between estimations based on Grafen distance and branch lengths scaled to time. Whereas the analysis based on Grafen distance recovers all heyuannines as likely to have been gregarious (Fig. 5.22B), the time-calibrated analysis suggests that it arose independently in each taxon where it is found (Fig. 5.22A). Similarly, the Grafen tree analysis suggests that citipatines and basal oviraptorids were more likely to have been gregarious than caenagnathids, whereas the time-calibrated analyses recovers both of these groups as equally likely to have been gregarious. The Grafen tree finds an increase in the likelihood of gregarious behaviour at the base of Edentoraptora, whereas in the time-calibrated tree this increase occurs at the base of Oviraptorosauria.

The overall patterns are similar when gregarious behaviour is considered as a discrete character (Fig. 5.22). In general, gregarious behaviour is estimated as more widespread than found, especially in oviraptorids. However, the differences between the trees are opposite: the

time-calibrated tree finds a high likelihood of gregarious behaviour in all oviraptorids and caenagnathids, which contrasts with the independent origins suggested by the continuous-character analysis. Furthermore, this tree finds a significant increase in the likelihood of gregarious behaviour at Edentoraptora, but even basal oviraptorosaurs are found to have been gregarious in more than 75% of the replicates. In contrast, the Grafen-scaled analysis finds high rates of gregariousness in heyuannines, but only 75% of the replicates show citipatines as gregarious, whereas this is nearly 90% in the time-calibrated tree (Fig. 5.22A). In the Grafen analysis, Edentoraptora has approximately 75% likelihood of gregariousness, but caenagnathids have a significantly lower likelihood (~60%), which contrasts with the discrete time-calibrated analysis and the continuous Grafen analysis.

5.4 DISCUSSION

5.4.1 Gregarious Behaviour

Avimimid bonebeds—The composition of the avimimid bonebeds and the high number of individuals have implications for the behaviour of *Avimimus*. The death assemblages strongly suggest that *Avimimus* engaged in gregarious behaviour, although the particular nature of that behaviour is not clear. The morphology of the mandible (see Chapter 2) in *Avimimus* is similar to oviraptorids and caenagnathids, which were probably herbivorous (Smith, 1992; Funston and Currie, 2014), so it is unlikely that the bonebed is evidence of pack hunting or a scavenging-driven assemblage. The presence of more than two adults in each assemblage suggests that the bonebeds do not represent isolated family groups. Other assemblages of multiple omnivorous or herbivorous theropods have been discovered, most notably therizinosaurs (Kirkland et al.,

2005b) and ornithomimids (Kobayashi and Lü, 2003b). Kirkland et al. (2005b) studied a paucispecific bonebed of *Falcarius* Kirkland et al. 2005, with more than 300 individuals and a range of developmental stages (Zanno and Erickson, 2006). The abundance of material (>2000 specimens) (Zanno and Erickson, 2006), and the 99% dominance of *Falcarius* at the site (Kirkland et al., 2005b) strongly suggest that the site is the result of a catastrophic mass death. The presence of multiple developmental stages indicates that the *Falcarius* assemblage reflects typical population structure, which suggests that it may represent a non-transient herd.

While the Nemegt Bonebed appears superficially to have a bias in the developmental stages represented, histological analysis of the material at the Iren Dabasu Bonebed brings that conclusion into question. In particular, the onset of tibiotarsal fusion in IVPP V16320, despite histological immaturity, suggests that fusion of compound bones in avimimids begins early in ontogeny, possibly within the first year of life, while the animals were still juvenile. Therefore, the absence of fusion in specimens at the Nemegt bonebed probably indicates that they are young juveniles, rather than subadults. This would resolve the unusual dearth of juvenile individuals in that bonebed and would suggest that a foraging assemblage is a more likely explanation for the assemblage than age-segregated lekking behaviour as suggested by Funston et al. (2016). Determining whether individuals with fused compound bones are juveniles or adults would require case-by-base histological assessment. Furthermore, it is possible that the onset of fusion was ontogenetically variable in avimimids and verification of ontogenetic stage in the *Avimimus nemegtensis* bonebed individuals will require future histological analysis of those specimens.

Regardless, the Iren Dabasu bonebed assemblage indicates that at least some avimimids grouped in mixed-age flocks, which is unusual in theropods (Varricchio et al., 2008a; Funston et al., 2016). Typically, non-avian theropod groups were formed exclusively of juveniles (Currie

and Azuma, 2006b; Varricchio et al., 2008a), although some bonebeds have more even representation of the population (Kirkland et al., 2005a; Erickson et al., 2010a). It is possible that mixed-age flocks were more common in avimimids because stunted growth restricted adults to a body size easily achievable by young juveniles. This possibility is supported by the similarity in size of IVPP V16320 and IVPP V16337, despite the young age of the former. Along these lines, the proximity in size of juveniles and adults probably reduced ontogenetic niche shift in avimimids. Evidence from other oviraptorosaurs suggests that avimimids were predominantly herbivorous (Smith, 1992; Zanno and Makovicky, 2011; Funston and Currie, 2014; Funston et al., 2018a) and it is likely that foraging patterns differed little between juveniles and adults. Ontogenetic niche shift was likely responsible to some degree for age-segregation in theropod groups and its absence may have facilitated mixed-age foraging behaviour in avimimids. The anti-predator effectiveness of flocking and communal roosting (Beauchamp, 1999) is documented especially well in birds (Bertram, 1980; Sullivan, 1984; Cresswell, 1994) and mammals (Hunter and Skinner, 1998; Childress and Lung, 2003; Cameron and Du Toit, 2005), among other animals. Multiple studies show that vigilance (Beauchamp, 2015) is reduced in larger groups, increasing foraging efficiency (Roberts, 1996; Brown, 1999). Kobayashi and Lu (2003b) described an assemblage of at least 14 articulated *Sinornithomimus* Kobayashi and Lü 2003 from China, with a high proportion of juveniles (Varricchio et al., 2008b), which they suggested is the result of a predator avoidance strategy. However, in the absence of a larger sample size and evidence of the cause of the mass death event, the specific behaviour that the *Avimimus* death assemblage represents cannot be assessed.

Oviraptorid assemblages—The oviraptorid assemblages are dominated by juveniles, which is similar to the previously recognized phenomenon of juvenile gregariousness in

theropods (Kobayashi and Lü, 2003b; Currie and Azuma, 2006b; Varricchio et al., 2008a). In most cases the individuals preserved appear to be relatively similar in size and ontogenetic stage, although there is some variation in size in MPC-D NatGeo.2018.036. In all cases the skeletons are articulated, and in all but the CMMD block some individuals in the assemblage are in life posture. This indicates minimal transport and therefore strongly supports the interpretation of gregariousness in these individuals. Where specimens are preserved in life postures, some conclusions can be made about the behaviours these animals were engaged in before death. The positions of the legs crouched underneath the body and the arms tucked towards the torso suggest in MPC-D 102/03 and MPC-D 102/110 that these individuals were resting together when they were killed and buried. The same is likely true for MPC-D NatGeo.2018.036, but confirmation will require complete preparation of the specimens. The taphonomy of MPC-D 102/03 is typical for specimens recovered from the aeolian portions of the Baruungoyot Formation, and probably indicates that this individual was killed by burial. The case of the burial cannot be established without more detailed analysis of the quarry, but it was apparently not violent based on the undisturbed position of the more complete skeleton.

The similarity between the taphonomy of MPC-D NatGeo.2018.036 and MPC-D 102/110 strongly supports the conclusion that the latter specimen is from the Nemegt Formation. However, the taphonomy of MPC-D 102/110 and MPC-D NatGeo.2018.036 raise more questions than answers. Like MPC-D 102/03, the individuals were probably resting together when they were killed and buried by some event, but their sedimentology indicates they were buried in fluvial depositional environments. This raises the perplexing issue of how specimens can be buried in life positions in fluvial environments, where sediment is transported by water. The gradient of articulation in MPC-D NatGeo.2018.036 may hold some clues. The variability in

articulation suggests that the skeletons were killed in an event prior to final burial, which allowed for some disarticulation of material that was either more decomposed or subject to higher flow rates. In this scenario, the group may have been killed by some event which buried and protected the skeletons as they decomposed, resulting in some local disarticulation. They were then uncovered by a second flow event which disarticulated some of the skeletons more extensively and resulted in the final burial of the material. How the skeletons remained unmodified in between these events is unclear, because typically exposed skeletons would be scavenged or bored by insects, but previously buried skeletons would have a mix of sediment from the first and second burials. The causes of death can only be speculated upon, but some information can be gleaned from the positions of the skeletons. Like in MPC-D 102/03, the crouched resting postures of the individuals in MPC-D 102/110 and MPC-D NatGeo.2018.036 indicates that the cause of death was non-violent. It is likely that these individuals were killed by exposure or some other environmental phenomenon, as otherwise they would likely have been making attempts to escape (Fastovsky et al., 2011; Hone et al., 2014). The first burial of the specimens likely followed their death or incapacitation, but was soon enough afterwards that scavenging was not possible. Recent evidence from stable isotopes suggests that the Nemegt Basin may have been subject to periodic monsoons (Owocki et al., 2019), and it is possible that these conditions were responsible for the deaths of the animals in these assemblages.

These specimens allow the nature of oviraptorid assemblages to be speculated upon. The assemblages represent three separate taxa, although all appear to be from the subfamily Heyuanninae (see Section 5.3.2). However, future phylogenetic analysis of the CMMD oviraptorid is necessary to verify this conclusion. Regardless, this suggests that gregariousness was relatively common, at least among heyuannines and possibly more broadly in oviraptorids

(see section 5.3). Although most of the assemblages are formed exclusively of juvenile individuals, the more complete individual in MPC-D 102/03 was probably an adult. This suggests that gregariousness was common among juveniles, but may have persisted throughout ontogeny into adulthood. Whether adults grouped together with juveniles or only with adults is unclear, but the absence of any adults in any of the juvenile assemblages suggests that most oviraptorid groups were age-segregated. Three of the assemblages preserve individuals that were apparently resting together, which provides evidence for communal roosting in oviraptorids. However, it must be noted that individuals succumbing to exposure would probably have adopted similar postures prior to their deaths. The close proximity of the skeletons to each other suggests that, at least in the case of MPC-D 102/110 and MPC-D NatGeo.2018.036, these individuals were huddled together, which may have conferred thermoregulatory benefits.

5.4.2 Ecology

Oviraptorosaur distribution—Although oviraptorids are present in both the Baruungoyot and Nemegt Formations, avimimids and caenagnathids have only been recovered from the Nemegt Formation. The absence of avimimids from the Baruungoyot Formation may be taphonomic, because they are smaller and have more delicate skeletons than oviraptorids. Caenagnathids, however, are, in most respects, taphonomically equivalent to oviraptorids, so it is unlikely that their absence in the Baruungoyot Formation is the result of differences in taphonomy. Instead, this supports previous suggestions (Currie et al., 1993; Tsuihiji et al., 2016) that caenagnathids preferred mesic environments, and may indicate that avimimids and caenagnathids overlapped in habitat, alongside oviraptorids.

The abundance of oviraptorids in the Baruungoyot Formation supports previous hypotheses of their preference for that environment (Longrich et al., 2010; Tsuihiji et al., 2016), but their presence in the Nemegt Formation suggests that they were not strictly limited to xeric environments. Indeed, they are both abundant and diverse in the mesic Nemegt Formation, but only Guriliin Tsav and Altan Uul II have produced more than one species of oviraptorid. This suggests that, at species level, oviraptorids were not uniformly distributed, either as a result of spatial or temporal separation. It is possible that this reflects spatial resource partitioning (Lyson and Longrich, 2011), or that there was rapid species turnover (Mallon et al., 2012) resulting in a succession of different species throughout the Nemegt Basin section. However, the latter seems unlikely because *Conchoraptor gracilis* is widely distributed, occurring at the bottom of the section (Hermiin Tsav and Khulsan), the middle (Altan Uul II), and at the top of the sequence (Guriliin Tsav), which suggests that species turnover rates were not high for all species. Both of these options suggest that oviraptorid species did not need to partition niches because they did not overlap in time and space. These explanations assume that the recovered distribution of oviraptorid species reflects the true pattern, but rarefaction curves (Fig. 5.13) suggest that nearly all the localities are undersampled at the species-level. It is possible, therefore, that these species co-occurred, in which case they must have partitioned resources through other means, if at all. In any case, oviraptorids were clearly diverse in the Nemegt Formation as well as the Baruungoyot Formation.

Oviraptorosaur co-occurrence—Permutation tests indicate that, as a family, oviraptorids occur in uniform proportions among samples in the Nemegt Formation. Caenagnathids and avimimids did not show the same uniformity among localities but still co-occurred with oviraptorids in well-sampled sites. This suggests that the co-occurrence of these

three families was a stable ecological arrangement, and that the perceived absence of avimimids and caenagnathids may be an artifact of sample size, given their low abundance when recovered. Numerous differences in mandibular and postcranial anatomy distinguish the functional morphology of oviraptorids and caenagnathids (Funston et al. 2016a). The sharp upturned beaks, long grasping fingers, and elongate arctometatarsalian hindlimbs of caenagnathids suggest that they were capable predators as part of an omnivorous diet (Funston et al., 2014). Oviraptorids, on the other hand, lack ornamented dentaries for enhanced shearing, had tall bony cheeks that decreased gape, and tended to reduce the hands and hindlimbs. Instead, they were possibly more strictly herbivorous than caenagnathids (Smith, 1992). It is therefore easy to conclude that caenagnathids and oviraptorids coexisted through dietary niche partitioning, as they are adapted for different diets. The coexistence of these two groups with avimimids, however, is more difficult to explain. Avimimids combine the cursorial postcranial adaptations of caenagnathids with a mandibular apparatus more similar to an oviraptorid. Their diet was probably more similar to oviraptorids, as their dentaries are neither highly ornamented nor strongly upturned. They may have avoided niche overlap with oviraptorids by virtue of their smaller body sizes. The elongate arctometatarsalian hindlimbs of avimimids may have evolved for predator avoidance instead of prey capture, which may also explain their gregariousness (Funston et al. 2016b).

Explaining the high species diversity of oviraptorids in the Nemegt is problematic. It is possible that resources in the Nemegt Basin were sufficient to sustain multiple species of oviraptorids. However, no other dinosaur superfamily was as diverse, and oviraptorids, despite their diversity, were small parts of Nemegt communities whose species apparently did not extensively overlap. It is possible that this simply reflects sampling intensity, but it is unusual nonetheless. Their uniform distribution through time at the family level suggests that their

ecological role in the overall community remained constant, but they either experienced high species turnover, were spatially separated, or partitioned resources in some other way. No option is conclusive given the available evidence.

Oviraptorosaur ecological roles—Oviraptorosaurs comprise a small portion of the Nemegt Formation fauna, typically forming less than 10% of the community. Although their anatomy is consistent with egg-eating and other modes of durophagy (Barsbold 1986; Currie et al. 1993), most analyses have recovered oviraptorosaurs as primarily herbivorous (Smith, 1992; Zanno and Makovicky, 2011). As herbivores, oviraptorids would have competed with ankylosaurs, hadrosaurs, ornithomimosaurs, and sauropods for food. Based on oral anatomy, it is reasonable to conclude that each of these superfamilies were adapted for different sources of vegetation. Oviraptorid jaws were specialized for a strong, nipping bite (Barsbold, 1986), which was emphasized by the shortening of the rostrum and associated muscular lever arms. This morphology is reminiscent of modern psittaciform birds (Sereno et al. 2010; Carril et al. 2015), which are specialized for a frugivorous diet that incorporates hard nuts and seeds. This function seems well suited to the anatomy of oviraptorids, as the maxillovomeral process and the robust palatal bones would have provided a reinforced surface for durophagy. Indeed, by the Late Cretaceous, angiosperms and their associated fruit were relatively widespread in Laurasia. This type of specialized diet may explain why oviraptorids were persistent but minor members of the communities. The consistent proportion of oviraptorids in Nemegt assemblages and their consistent morphology suggest that, despite changing species representation, oviraptorids occupied a stable niche in the Nemegt Formation. Accordingly, it seems likely that the fluvial systems of the Nemegt Formation acted as an 'oasis' that attracted oviraptorids.

Caenagnathids were likely more omnivorous than oviraptorids (Funston et al., 2014, 2016a), and are even less common than oviraptorids in the Nemegt Formation (2.7% of fauna). This suggests that they played a minor role in the Nemegt ecosystems. Their species composition is more ambiguous than that of oviraptorids, because they are known from more fragmentary material. It is possible that they are represented by as many as three species if *Elmisaurus rarus*, *Nomingia gobiensis*, and the dentaries from Bugiin Tsav (Tsuihiji et al. 2016) are all separate taxa, but this seems unlikely (see Chapter 3: section 3.4.1). The observed distribution of caenagnathids in the Nemegt Formation appears to be the result of sample size and rarity, as they are consistently recovered at well-sampled sites. They have not yet been recovered from the Baruungoyot Formation despite large sample sizes, which suggests a preference for the mesic environments represented by Nemegt.

Avimimids, as small animals, were likely more common than recovered, because of their small body size and delicate skeleton. This is supported by the *Avimimus* bonebed (Funston et al., 2016b), where exceptional taphonomic circumstances preserved a large assemblage of at least 18 individuals. Such 'flocks' of *Avimimus nemegtensis* Funston et al. 2018 may have been common in the Nemegt Basin. The oral anatomy of *Avimimus nemegtensis* is not well known, but the dentary and premaxilla are similar to those of oviraptorids and they may have had similar diets. Avimimids would have been highly cursorial, as evinced by their elongate hindlimbs, the reacquisition of a fourth-trochanter of the femur, and their arctometatarsalian pes.

5.4.3 Evolution

Biogeography:

Cretaceous communication between North America and Asia is well established (Russell, 1993; Cifelli et al., 1997; Farke et al., 2014), but oviraptorosaur biogeography has traditionally been difficult to explain because of poor phylogenetic resolution. Based on previous work and the analysis here, it is nearly certain that oviraptorosaurs had an Asian origin (Ji et al., 1998; Xu et al., 2002; Fig. 5.19). Some caenagnathoids dispersed to North America by the Albian (Makovicky and Sues, 1998) and radiated into the caenagnathids. Although a possible record of avimimids from North America has been reported (Ryan and Russell, 2001), reexamination of the material indicates it is not avimimid (GFF, PJC pers. obs., 2016). Avimimids are therefore best regarded as a uniquely Asian offshoot of the oviraptorosaur lineage, as recovered here. The increased resolution in the phylogeny of caenagnathids provides more clarity on their biogeography. Caenagnathidae has a high likelihood of a North American origin (Fig. 5.19), and Caenagnathinae even more so. Indeed, the recent description of macroelongatoolithid eggs from North America supports the origin of gigantic caenagnathids there (Simon et al., 2019), providing even stronger support for a North American origin of Caenagnathidae as a whole. The recovery of every caenagnathid clade as North American in origin suggests one way movement of caenagnathids from North America to Asia, rather than successive distributions back and forth. As recovered here, there was an early dispersal to Asia at some point between the Cenomanian and Santonian, which accounted for the presence of *Gigantoraptor erlianensis* and *Caenagnathasia martinsoni* in Asia. A second, later dispersal occurred either in the Maastrichtian or prior, indicated by *Elmisaurus rarus* and *Nomingia gobiensis*. Meanwhile, oviraptorids originated in Southern China and radiated into the Citipatinae (Fig. 5.19). Range expansion into the Western Gobi led to the radiation of Heyuanninae, and these regions maintained open connection resulting in exchange of taxa. Despite this connection, movement

between these regions must have been rare enough that each developed their own unique diversification of oviraptorids.

Range expansion, therefore, was clearly an important factor in the evolution and diversification of oviraptorosaurs. Two dispersals into new regions account for two of the major radiations of oviraptorosaurs: the caenagnathids in North America and the heyuannines in the Western Gobi. These range expansions led to the major anatomical divergences of Caenagnathoidea, specifically the mandibular adaptations of caenagnathids and the specialization of the manus in heyuannines, which may be adaptations for these new environments. Although previous analyses have suggested that oviraptorids were restricted to Asia (Fig. 5.18) because of their preference for xeric habitats, the results presented here show that oviraptorosaurs only experienced a single dispersal to North America, in the 'middle' Cretaceous during the height of the Cretaceous Terrestrial Revolution. It is possible that the rise of angiosperms created new niches in North America that were filled by basal caenagnathoids that dispersed from Asia and radiated into the caenagnathids. The basal caenagnathoids that remained in Asia diversified into oviraptorids, became specialized for new niches opened by the Cretaceous Terrestrial Revolution in Asia. However, the morphological disparity between caenagnathids and oviraptorids suggests that oviraptorosaur niches in Asia and North America were significantly different. It is likely, therefore, that after their initial range expansion and diversification, North American oviraptorosaur-suited niches were saturated by caenagnathids and movement of oviraptorids was not possible. The reverse was apparently not true, however: North American taxa successfully moved into Asia and Asian taxa frequently migrated between separate regions. Accordingly, Asian ecosystems were likely undersaturated, which allowed for free movement to new regions

and facilitated the exceptional diversity of oviraptorosaurs at both the family level and within these families in Asia.

Body mass evolution:

In general, oviraptorosaurs followed Cope's Rule of size increase throughout their evolutionary history. Notably, they also appear to have expanded their available size niches, and the range of body sizes increases throughout phylogeny (Fig. 5.20). This is particularly evident in Caenagnathidae, which comprises miniaturized forms (*Caenagnathasia martinsoni*) and gigantic forms (*Gigantoraptor erlianensis*) relative to their ancestral body mass. This contrasts with many other dinosaur groups, like tyrannosaurs and ornithomimids, which follow Cope's Rule but generally reduce the breadth of body mass range, becoming only larger. Instead, oviraptorosaurs show similar trends to dromaeosaurs, which also increase in body size throughout the evolutionary history (Turner et al., 2007), but retain small-bodied forms. However, dromaeosaur body size increase is restricted to smaller, disparate clades and dromaeosaurs never attain the large sizes of oviraptorosaurs.

The body mass evolution of oviraptorosaurs appears to be linked to biogeography (Fig. 5.23). Whereas Asian taxa show a generalized increase in body mass through time, this rate is relatively constant, and the range of body masses is fairly restricted. In contrast, caenagnathids experienced a considerable expansion of the range of body masses just after their dispersal to North America (Fig. 5.23). This is especially pronounced in *Gigantoraptor erlianensis* and *Caenagnathasia martinsoni*, which both likely had North American origins and migrated back to Asia. This is also reflected more subtly—but perhaps more importantly—in the larger body mass increase at the base of Caenagnathinae relative to Oviraptoridae. This suggests that early

caenagnathids were able to occupy larger body mass niches than oviraptorids, from which they expanded both upwards and downwards in body mass. It is likely that this is attributable to successful invasion of new niches after distribution to North America, as described previously. Accordingly, North America may have provided new ecosystems which allowed caenagnathids to experiment successful with body mass change, whereas taxa in Asia were restricted to certain body mass niches.

Digit Reduction:

The adaptive benefit of digit reduction in heyuannines is unclear. The pattern of reduction of the lateral digits is opposite their order of development, which is similar to digit loss in other vertebrates (Sanz-Ezquerro and Tickle, 2003; Shapiro et al. 2003; Kavanagh et al. 2013; Saxena et al. 2017; Towers, 2018). The presence of a single phalanx in the third digit of the Guriliin Tsav oviraptorid suggests that digit loss in this taxon was achieved by apoptosis after condensation of the digit, rather than changes in gene signaling (Cooper et al. 2014). It is unlikely that the highly reduced third digit in the Guriliin Tsav oviraptorid was adapted for a particular function, and it may be a byproduct of general reduction of the forelimb in heyuannines compared to citipatines and caenagnathids. Whereas most caenagnathoids showed an increase in humerus length (60–70% of femur length) relative to caudipterids (~45–50%), heyuannines reversed this trend (~50–60%). Heyuannines also changed the proportions of their forelimbs, decreasing the average length of the antebrachium (~75–85% of humerus length) and manus (~35–50%) to the humerus relative to citipatines (~100% and ~50%, respectively). However, citipatines may have increased the length of their antebrachium, because both caudipterids and caenagnathids had antebrachia about the same lengths as heyuannines. In any

case, it is likely that digit reduction accompanied generalized forelimb reduction, but the cause of this is unknown.

Interesting patterns emerge when digit reduction is compared to other aspects of oviraptorosaur evolution (Fig. 5.24). Reduction of the lateral digits appears to be strongly correlated to both biogeography and the evolution of gregarious behaviour, although the latter trend is poorly constrained (see subsequent discussion). In terms of biogeography, the onset of digit reduction begins at the estimated dispersal of heyuannines from Southern China into the Western Gobi (Fig. 5.24A). With the exception of *Citipati osmolskae* and the Zamyn Khondt oviraptorid, all clades with a reconstructed origin in the Western Gobi desert have reduced lateral digits, even if they redispersed to Southern China. The cause of this strong correlation is unclear with the available data, but its restriction to a single region suggests it that digit reduction was an adaptation for some aspect of the paleoenvironment of the Western Gobi. Indeed, *Citipati osmolskae* and the Zamyn Khondt oviraptorid have slightly reduced third digits compared to Southern Chinese citipatiines (Fig. 5.21). Regardless, dispersal of these specialized taxa back to Southern China indicates that this adaptation was beneficial in other ecosystems as well.

Heyuannines are also distinguished by an increased likelihood of gregarious behaviour (Fig. 5.24B). All gregarious assemblages of oviraptorids known to date are of heyuannines (see section 5.1), despite excellent preservation of many citipatines in similar environments (e.g. *Khaan mckennai* and *Citipati osmolskae*; *Heyuannia huangi* and other Guangdong oviraptorids). Whether the reduced forelimb and digits played some role in gregarious behaviour is unclear, but it is possible that they were both adaptations for the ecosystem in which heyuannines lived. This is supported by the appearance of these features in tandem with the dispersal to the Western Gobi (Fig. 5.24A). Paleoenvironmental reconstructions indicate that the Western Gobi was an arid

desert with sporadic lakes and possibly seasonal bursts of productivity (Gradziński and

Jerzykiewicz, 1974; Jerzykiewicz, 1998; Eberth, 2018). Gregarious foraging behaviour can

evolve in response to patchy resource distributions (Ward and Zahavi, 1973; Alexander, 1974;

Richner and Heeb, 1996). Similarly, reduction of the manus can occur as an adaptation for

scratch-digging (Senter, 2005), which may have facilitated foraging on roots and tubers during

periods of low productivity. This is tentatively supported by the retention of strong musculature

of the forelimb in heyuannines, despite reduction in its length, and the increased robustness of

the first manual digit and its ungual. Additional lines of support could come from better

qualification of resource distribution in the Late Cretaceous environments of the Western Gobi

and biomechanical analysis of the manus of heyuannines.

5.5 CONCLUSIONS

Three major aspects of the biology of oviraptorosaurs are examined. New records of gregarious behaviour provide more information on the prevalence of flocking behaviour in oviraptorosaur families, and the population structure of these groups. A second avimimid bonebed shows that at least some oviraptorosaurs gathered in mixed-age flocks. However, age segregation is evident in four oviraptorid bonebeds. These oviraptorid bonebeds show that these animals were resting together before they perished, suggesting they may have roosted communally. These assemblages support the hypotheses that gregarious behaviour was relatively widespread in Oviraptorosauria. Community ecology analyses of the Nemegt Basin show that oviraptorosaurs were a small but stable component of the fauna and thus may have been ecological specialists. Little overlap between oviraptorid species may be evidence of niche partitioning, but could also be the result of poor sampling. Non-uniform distributions of oviraptorosaur families, however, suggest that avimimids and caenagnathids were restricted to the mesic environments of the Nemegt Formation, whereas oviraptorids were also successful in the xeric Baruungoyot Formation. A new phylogeny of Oviraptorosauria has unprecedented resolution, allowing for characterization of biogeography, body mass evolution, digit reduction, and gregarious behaviour. Range expansion played a major role in the evolution of oviraptorosaurs, and dispersals to North America and the Western Gobi drove trends in body mass evolution and digit reduction, respectively. Digit reduction was gradual, rather than punctuated, and is correlated with gregarious behaviour, but more data is needed to establish the nature of this relationship. Concurrent onset of digit reduction and range expansion to the Western Gobi Desert may indicate an environmental pressure for digit reduction.

5.6 LITERATURE CITED

Alexander, R. D. 1974. The evolution of social behavior. Annual Review of Ecology and
Systematics 5:325–383.

Arbour, V. M., P. J. Currie, and D. Badamgarav. 2014. The ankylosaurid dinosaurs of the Upper
Cretaceous Baruungoyot and Nemegt formations of Mongolia: Ankylosaurids from
Mongolia. Zoological Journal of the Linnean Society 172:631–652.

Averianov, A. O., and H.-D. Sues. 2012. Correlation of Late Cretaceous continental vertebrate
assemblages in Middle and Central Asia. Journal of Stratigraphy 36:462–485.

Balanoff, A. M., and M. A. Norell. 2012. Osteology of *Khaan mckennai* (Oviraptorosauria:
Theropoda). Bulletin of the American Museum of Natural History 372:1–77.

Beauchamp, G. 1999. The evolution of communal roosting in birds: Origins and secondary
losses. Behavioral Ecology 10:675–687.

Beauchamp, G. 2015. Animal Vigilance: Monitoring Predators and Competitors. Academic
Press, London, pp.

Behrensmeyer, A. K. 1978. Taphonomic and ecologic information from bone weathering.
Paleobiology 4:150–162.

Bell, P. R., D. C. Evans, D. A. Eberth, F. Fanti, Kh. Tsogtbaatar, and M. J. Ryan. 2018.
Sedimentological and taphonomic observations on the "Dragon's Tomb" Saurolophus
(Hadrosauridae) bonebed, Nemegt Formation (Upper Cretaceous), Mongolia.
Palaeogeography, Palaeoclimatology, Palaeoecology 494:75–90.

Bertram, B. C. R. 1980. Vigilance and Group size in Ostriches. Animal Behaviour 28:278–286.

Bonnetti, C., F. Malartre, V. Huault, M. Cuney, S. Bourlange, X. Liu, and Y. Peng. 2014. Sedimentology, stratigraphy and palynological occurrences of the late Cretaceous Erlian Formation, Erlian Basin, Inner Mongolia, People's Republic of China. Cretaceous Research 48:177–192.

Bray, J. R., and J. T. Curtis. 1957. An ordination of upland forest communities of southern Wisconsin. Ecological Monographs 27:325–349.

Britt, B. B., D. a. Eberth, R. D. Scheetz, B. W. Greenhalgh, and K. L. Stadtman. 2009. Taphonomy of debris-flow hosted dinosaur bonebeds at Dalton Wells, Utah (Lower Cretaceous, Cedar Mountain Formation, USA). Palaeogeography, Palaeoclimatology, Palaeoecology 280:1–22.

Brown, C. M., D. C. Evans, N. E. Campione, L. J. O'Brien, and D. A. Eberth. 2013. Evidence for taphonomic size bias in the Dinosaur Park Formation (Campanian, Alberta), a model Mesozoic terrestrial alluvial-paralic system. Palaeogeography, Palaeoclimatology, Palaeoecology 372:108–122.

Brown, J. S. 1999. Vigilance, patch use and habitat selection: Foraging under predation risk. Evolutionary Ecology Research 1:49–71.

Brusatte, S. L., M. J. Benton, M. Ruta, and G. T. Lloyd. 2008. Superiority, competition, and opportunism in the evolutionary radiation of dinosaurs. Science 321:1485–1488.

Cameron, E. Z., and J. T. Du Toit. 2005. Social influences on vigilance behaviour in giraffes, Giraffa camelopardalis. Animal Behaviour 69:1337–1344.

Carril, J., F. J. Degrange, and C. P. Tambussi. 2015. Jaw myology and bite force of the monk parakeet (Aves, Psittaciformes). Journal of Anatomy 227:34–44.

Childress, M. J., and M. A. Lung. 2003. Predation risk, gender and the group size effect: does elk

    vigilance depend upon the behaviour of conspecifics? Animal Behaviour 66:389–398.

Clark, J. M., M. A. Norell, and R. Barsbold. 2001. Two new oviraptorids (Theropoda:

    Oviraptorosauria), Upper Cretaceous Djadokhta Formation, Ukhaa Tolgod, Mongolia.

    Journal of Vertebrate Paleontology 21:209–213.

Cooper, K. L., K. E. Sears, A. Uygur, J. Maier, K.-S. Baczkowski, M. Brosnahan, D. Antczak, J.

    A. Skidmore, and C. J. Tabin. 2014. Patterning and post-patterning modes of

    evolutionary digit loss in mammals. Nature 511:41–45.

Cresswell, W. 1994. Flocking is an effective anti-predation strategy in redshanks, Tringa totanus.

    Animal Behaviour 47:433–442.

Currie, P. J. 2016. Dinosaur of the Gobi: Following in the footsteps of the Polish-Mongolian

    Expeditions. Paleontologica Polonica 67:83–100.

Currie, P. J., and D. A. Eberth. 1993. Palaeontology, sedimentology and palaeoecology of the

    Iren Dabasu Formation (Upper Cretaceous), Inner Mongolia, People's Republic of China.

    Cretaceous Research 14:127–144.

Currie, P. J., and Y. Azuma. 2006a. New speciments, including a growth series, of Fukuiraptor

    (Dinosauria, Theropoda) from the Lower Cretaceous Kitadani Quarry of Japan. Journal

    of Paleontological Society of Korea 22:173–193.

Currie, P. J., and Y. Azuma. 2006b. New specimens, including a growth series, of *Fukuiraptor*

    (Dinosauria, Theropoda) from the Lower Cretaceous Kitadani Quarry of Japan. Journal

    of the Paleontological Society of Korea 22:173–193.

Currie, P. J., S. J. Godfrey, and L. Nessov. 1993. New caenagnathid (Dinosauria: Theropoda) specimens from the Upper Cretaceous of North America and Asia. Canadian Journal of Earth Sciences 30:2255–2272.

Dong, Z.-M., and P. J. Currie. 1996. On the discovery of an oviraptorid skeleton on a nest of eggs at Bayan Mandahu, Inner Mongolia, People's Republic of China. Canadian Journal of Earth Sciences 33:631–636.

Eberth, D. A. 2015. Origins of dinosaur bonebeds in the Cretaceous of Alberta, Canada. Canadian Journal of Earth Sciences 52:655–681.

Eberth, D. A. 2018. Stratigraphy and paleoenvironmental evolution of the dinosaur-rich Baruungoyot-Nemegt succession (Upper Cretaceous), Nemegt Basin, southern Mongolia. Palaeogeography, Palaeoclimatology, Palaeoecology 494:29–50.

Eberth, D. a., and P. J. Currie. 2010. Stratigraphy, sedimentology, and taphonomy of the Albertosaurus bonebed (upper Horseshoe Canyon Formation; Maastrichtian), southern Alberta, CanadaThis article is one of a series of papers published in this Special Issue on the theme Albertosaurus . Canadian Journal of Earth Sciences 47:1119–1143.

Eberth, D. A., M. Shannon, and B. G. Noland. 2007. A bonebeds database: classification, biases, and patterns of occurrence; pp. 102–220 in R. R. Rogers, D. A. Eberth, and A. R. Fiorillo (eds.), Bonebeds: genesis, analysis, and paleobiological significance. University of Chicago Press.

Eberth, D. A., D. Badamgarav, and P. J. Currie. 2009. The Baruungoyot-Nemegt Transition (Upper Cretaceous) at the Nemegt Type Area, Nemegt Basin, South Central Mongolia. Journal of the Paleontological Society of Korea 25:1–15.

Erickson, G. M., P. J. Currie, B. D. Inouye, and A. A. Winn. 2010a. A revised life table and
survivorship curve for *Albertosaurus sarcophagus* based on the Dry Island mass death
assemblage. Canadian Journal of Earth Sciences 47:1269–1275.

Erickson, G. M., P. J. Currie, B. D. Inouye, A. A. Winn, P. J. Currie, and E. B. Koppelhus.
2010b. A revised life table and survivorship curve for Albertosaurus sarcophagus based
on the Dry Island mass death assemblage. Canadian Journal of Earth Sciences 47:1269–
1275.

Evans, D. C., D. A. Eberth, and M. J. Ryan. 2015. Hadrosaurid (Edmontosaurus) bonebeds from
the Horseshoe Canyon Formation (Horsethief Member) at Drumheller, Alberta, Canada:
geology, preliminary taphonomy, and significance. Canadian Journal of Earth Sciences
52:642–654.

Fanti, F., P. J. Currie, and D. Badamgarav. 2012. New Specimens of *Nemegtomaia* from the
Baruungoyot and Nemegt Formations (Late Cretaceous) of Mongolia. PLoS ONE
7:e31330.

Fanti, F., P. J. Currie, and M. E. Burns. 2015. Taphonomy, age, and paleoecological implication
of a new Pachyrhinosaurus (Dinosauria: Ceratopsidae) bonebed from the Upper
Cretaceous (Campanian) Wapiti Formation of Alberta, Canada. Canadian Journal of
Earth Sciences 52:1–36.

Fanti, F., L. Cantelli, and L. Angelicola. 2018a. High-resolution maps of Khulsan and Nemegt
localities (Nemegt Basin, southern Mongolia): Stratigraphic implications.
Palaeogeography, Palaeoclimatology, Palaeoecology 494:14–28.

Fanti, F., P. R. Bell, M. Tighe, L. A. Milan, and E. Dinelli. 2018b. Geochemical fingerprinting as a tool for repatriating poached dinosaur fossils in Mongolia: A case study for the Nemegt Locality, Gobi Desert. Palaeogeography, Palaeoclimatology, Palaeoecology 494:51–64.

Fastovsky, D. E., D. B. Weishampel, M. Watabe, R. Barsbold, Kh. Tsogtbaatar, and P. Narmandakh. 2011. A nest of *Protoceratops andrewsi* (Dinosauria, Ornithischia). Journal of Paleontology 85:1035–1041.

Funston, G. F., and P. J. Currie. 2014. A previously undescribed caenagnathid mandible from the late Campanian of Alberta, and insights into the diet of *Chirostenotes pergracilis* (Dinosauria: Oviraptorosauria). Canadian Journal of Earth Sciences 51:156–165.

Funston, G. F., and P. J. Currie. 2016. A new caenagnathid (Dinosauria: Oviraptorosauria) from the Horseshoe Canyon Formation of Alberta, Canada, and a reevaluation of the relationships of Caenagnathidae. Journal of Vertebrate Paleontology 36:e1160910.

Funston, G. F., P. J. Currie, and C. Tsogtbaatar. 2017. A new oviraptorid (Dinosauria: Theropoda) provides a rare glimpse into social behaviour in dinosaurs. Journal of Vertebrate Paleontology Programs and Abstracts 2017:116.

Funston, G. F., S. E. Mendonca, P. J. Currie, and R. Barsbold. 2018a. Oviraptorosaur anatomy, diversity and ecology in the Nemegt Basin. Palaeogeography, Palaeoclimatology, Palaeoecology.

Funston, G. F., S. E. Mendonca, P. J. Currie, and R. Barsbold. 2018b. A dinosaur community composition dataset for the Late Cretaceous Nemegt Basin of Mongolia. Data in Brief 16:660–666.

Funston, G. F., P. J. Currie, D. A. Eberth, M. J. Ryan, T. Chinzorig, D. Badamgarav, and N. R. Longrich. 2016. The first oviraptorosaur (Dinosauria: Theropoda) bonebed: evidence of gregarious behaviour in a maniraptoran theropod. Scientific Reports 6:35782.

Gradzinski, R. 1970. Sedimentation of dinosaur-bearing upper cretaceous deposits of the Nemegt basin , gobi desert. Palaeontologia Polonica 21:147–229.

Gradziński, R. 1970. Sedimentation of dinosaur-bearing Upper Cretaceous deposits of the Nemegt basin, Gobi Desert. Palaeontologia Polonica 21:147–229.

Gradziński, R., and T. Jerzykiewicz. 1974. Sedimentation of the Barun Goyot Formation. Palaeontologica Polonica 30:111–146.

Gradziński, R., Z. Kielan-Jaworowska, and T. Maryańska. 1977. Upper Cretaceous Djadokhta, Barun Goyot and Nemegt formations of Mongolia, including remarks on previous subdivisions. Acta Geologica Polonica 27:281–318.

Granger, W., and C. P. Berkey. 1922. Discovery of Cretaceous and older Tertiary strata in Mongolia. American Museum Novitates 42:1–7.

Hone, D. W. E., A. A. Farke, M. Watabe, S. Shigeru, and K. Tsogtbaatar. 2014. A New Mass Mortality of Juvenile Protoceratops and Size-Segregated Aggregation Behaviour in Juvenile Non-Avian Dinosaurs. PLoS ONE 9:e113306.

Hunter, and Skinner. 1998. Vigilance Behaviour in African Ungulates: The Role of Predation Pressure. Behaviour 135:195–211.

Jerzykiewicz, T. 1998. Okavango Oasis, Kalahari Desert: A contemporary analogue for the Late Cretaceous vertebrate habitat of the Gobi Basin, Mongolia. Geoscience Canada 25:15–26.

Jerzykiewicz, T., and D. A. Russell. 1991. Late Mesozoic stratigraphy and vertebrates of the
    Gobi Basin. Cretaceous Research 12:345–377.

Kavanagh, K. D., O. Shoval, B. B. Winslow, U. Alon, B. P. Leary, A. Kan, and C. J. Tabin.
    2013. Developmental bias in the evolution of phalanges. Proceedings of the National
    Academy of Sciences 110:18190–18195.

Kidwell, S. M. 2001. Preservation of species abundance in marine death assemblages. Science
    294:1091–1094.

Kidwell, S. M., and K. W. Flessa. 1995. The quality of the fossil record: populations, species,
    and communities. Annual Review of Ecology and Systematics 26:269–299.

Kirkland, J. I., L. E. Zanno, S. D. Sampson, J. M. Clark, and D. D. DeBlieux. 2005a. A primitive
    therizinosauroid dinosaur from the Early Cretaceous of Utah. Nature 435:85–87.

Kirkland, J. I., L. E. Zanno, S. D. Sampson, J. M. Clark, and D. D. DeBlieux. 2005b. A primitive
    therizinosauroid dinosaur from the Early Cretaceous of Utah. Nature 435:84–87.

Kobayashi, Y., and J.-C. Lü. 2003a. A new ornithomimid dinosaur with gregarious habits from
    the Late Cretaceous of China. Acta Palaeontologica Polonica 48:235–259.

Kobayashi, Y., and J.-C. Lü. 2003b. A new ornithomimid dinosaur with gregarious habits from
    the Late Cretaceous of China. Acta Palaeontologica Polonica 48:235–259.

Kurzanov, S. M. 1983. New Data on the Pelvic Structure of Avimimus. Paleontological Journal
    4:115–116.

Lamanna, M. C., H.-D. Sues, E. R. Schachner, and T. R. Lyson. 2014. A New Large-Bodied
    Oviraptorosaurian Theropod Dinosaur from the Latest Cretaceous of Western North
    America. PLoS ONE 9:e92022.

Lemon, J. 2006. Plotrix: a package in the red light district of R. R-News 6:8–12.

Longrich, N. R., P. J. Currie, and D. Zhi-Ming. 2010. A new oviraptorid (Dinosauria:

    Theropoda) from the Upper Cretaceous of Bayan Mandahu, Inner Mongolia.

    Palaeontology 53:945–960.

Longrich, N. R., K. Barnes, S. Clark, and L. Millar. 2013. Caenagnathidae from the Upper

    Campanian Aguja Formation of West Texas, and a Revision of the Caenagnathinae.

    Bulletin of the Peabody Museum of Natural History 54:23–49.

Lü, J., R. Chen, S. L. Brusatte, Y. Zhu, and C. Shen. 2016. A Late Cretaceous diversification of

    Asian oviraptorid dinosaurs: evidence from a new species preserved in an unusual

    posture. Scientific Reports 6:35780.

Lü, J., P. J. Currie, L. Xu, X. Zhang, H. Pu, and S. Jia. 2013. Chicken-sized oviraptorid dinosaurs

    from central China and their ontogenetic implications. Naturwissenschaften 100:165–

    175.

Lü, J., G. Li, M. Kundrát, Y.-N. Lee, Z. Sun, Y. Kobayashi, C. Shen, F. Teng, and H. Liu. 2017.

    High diversity of the Ganzhou Oviraptorid Fauna increased by a new "cassowary-like"

    crested species. Scientific Reports 7.

Makovicky, P. J., and H.-D. Sues. 1998. Anatomy and phylogenetic relationships of the theropod

    dinosaur *Microvenator celer* from the Lower Cretaceous of Montana. American Museum

    Novitates 3240:1–27.

Maxwell, W. D., and J. H. Ostrom. 1995. Taphonomy and paleobiological implications of

    Tenontosaurus-Deinonychus associations. Journal of Vertebrate Paleontology 15:707–

    712.

Morris, F. K. 1936. Central Asia in Cretaceous time. Bulletin of the Geological Society of

    America 47:1477–1534.

Norell, M. A., J. M. Clark, L. M. Chiappe, and D. Dashzeveg. 1995. A nesting dinosaur. Nature 378:774–776.

Oksanen, J., G. Blanchet, M. Friendly, R. Kindt, P. Legendre, D. McGlinn, P. R. Minchin, R. B. O'Hara, G. L. Simpson, P. Solymos, M. H. H. Stevens, E. Szoecs, and H. Wagner. 2017. Vegan: Community Ecology Package. pp.

Osborn, H. F. 1924. Three new theropoda, *Protoceratops* zone, central Mongolia. American Museum Novitates 144:1–12.

Osmólska, H., P. J. Currie, and R. Barsbold. 2004. Oviraptorosauria; pp. 165–183 in D. B. Weishampel, P. Dodson, and H. Osmólska (eds.), The Dinosauria, 2nd ed. University of California Press, Berkeley, California.

Owocki, K., B. Kremer, M. Cotte, and H. Bocherens. 2019. Diet preferences and climate inferred from oxygen and carbon isotopes of tooth enamel of Tarbosaurus bataar (Nemegt Formation, Upper Cretaceous, Mongolia). Palaeogeography, Palaeoclimatology, Palaeoecology 109190.

Pei-ji, C. 1987. Cretaceous paleogeography in China. Palaeogeography, Palaeoclimatology, Palaeoecology 59:49–56.

Pu, H., D. K. Zelenitsky, J. Lü, P. J. Currie, K. Carpenter, L. Xu, E. B. Koppelhus, S. Jia, L. Xiao, H. Chuang, T. Li, M. Kundrát, and C. Shen. 2017. Perinate and eggs of a giant caenagnathid dinosaur from the Late Cretaceous of central China. Nature Communications 8:14952.

Revell, L. J. 2012. phytools: an R package for phylogenetic comparative biology (and other things): phytools: R package. Methods in Ecology and Evolution 3:217–223.

Richner, H., and P. Heeb. 1996. Communal life: honest signaling and the recruitment center hypothesis. Behavioral Ecology 7:115–119.

Roach, B. T., and D. L. Brinkman. 2007. A Reevaluation of Cooperative Pack Hunting and Gregariousness in *Deinonychus antirrhopus* and Other Nonavian Theropod Dinosaurs. Bulletin of the Peabody Museum of Natural History 48:103–138.

Roberts, G. 1996. Why individual vigilance declines as group size increases. Animal Behaviour 51:1077–1086.

Ryan, M. J., P. J. Currie, and A. P. Russell. 2001a. New material of *Avimimus portentosus* from the Iren Dabasu Formation (Upper Cretaceous) of the Erenhot region of Inner Mongolia. Journal of Vertebrate Paleontology 21:95A.

Ryan, M. J., A. P. Russell, D. a. Eberth, and P. J. Currie. 2001b. The Taphonomy of a Centrosaurus (Ornithischia: Certopsidae) Bone Bed from the Dinosaur Park Formation (Upper Campanian), Alberta, Canada, with Comments on Cranial Ontogeny. Palaios 16:482–506.

Ryan, M. J., D. C. Evans, P. R. Bell, K. Tsogtbaatar, and D. Badamgarav. 2011. Taphonomy of the "Dragon's Tomb" Saurolophus (Dinosauria: Hadrosauridae) Bonebed, Nemegt Formation (Late Cretaceous), Mongolia. Journal of Vertebrate Paleontology 31:183A.

Sanz-Ezquerro, J. J., and C. Tickle. 2003. Fgf Signaling Controls the Number of Phalanges and Tip Formation in Developing Digits. Current Biology 13:1830–1836.

Saxena, A., M. Towers, and K. L. Cooper. 2017. The origins, scaling and loss of tetrapod digits. Philosophical Transactions of the Royal Society B: Biological Sciences 372:20150482.

Senter, P. 2005. Function in the stunted forelimbs of *Mononykus olecranus* (Theropoda), a dinosaurian anteater. Paleobiology 31:373–381.

Senter, P. 2007. A new look at the phylogeny of coelurosauria (Dlnosauria: Theropoda). Journal
of Systematic Palaeontology 5:429–463.

Shapiro, M. D., J. Hanken, and N. Rosenthal. 2003. Developmental basis of evolutionary digit
loss in the Australian lizard *Hemiergis*. Journal of Experimental Zoology 297B:48–56.

Simon, D. J., D. J. Varricchio, X. Jin, and S. F. Robison. 2019. Microstructural overlap of
Macroelongatoolithus eggs from Asia and North America expands the occurrence of
colossal oviraptorosaurs. Journal of Vertebrate Paleontology e1553046.

Smith, D. 1992. The type specimen of *Oviraptor philoceratops*, a theropod dinosaur from the
Upper Cretaceous of Mongolia. Neues Jahrbuch Fur Geologie Und Palaontologie
Abhandlungen 186:365–388.

Smith, D., and P. M. Galton. 1990. Osteology of *Archaeornithomimus asiaticus*. Journal of
Vertebrate Paleontology 10:255–265.

Sues, H.-D., and A. Averianov. 2015. New material of *Caenagnathasia martinsoni* (Dinosauria:
Theropoda: Oviraptorosauria) from the Bissekty Formation (Upper Cretaceous:
Turonian) of Uzbekistan. Cretaceous Research 54:50–59.

Sullivan, K. a. 1984. The advantages of social foraging in downy woodpeckers. Animal
Behaviour 32:16–22.

Towers, M. 2018. Evolution of antero-posterior patterning of the limb: Insights from the chick.
Genesis 56:e23047.

Tsogtbaatar, K., D. B. Weishampel, D. C. Evans, and M. Watabe. 2014. A new hadrosauroid
(Plesiohadros djadokhtaensis) from the Late Cretaceous Djadokhtan fauna of southern
Mongolia; pp. 108–135 in D. A. Eberth and D. C. Evans (eds.), Hadrosaurs: Proceedings
of the International Hadrosaur Symposium. Indiana University Press.

Tsuihiji, T., M. Watabe, K. Tsogtbaatar, and R. Barsbold. 2016. Dentaries of a caenagnathid (Dinosauria: Theropoda) from the Nemegt Formation of the Gobi Desert in Mongolia. Cretaceous Research 63:148–153.

Turner, A. H., D. Pol, J. A. Clarke, G. M. Erickson, and M. A. Norell. 2007. A Basal Dromaeosaurid and Size Evolution Preceding Avian Flight. Science 317:1378–1381.

Van Itterbeeck, J., D. J. Horne, P. Bultynck, and N. Vandenberghe. 2005. Stratigraphy and palaeoenvironment of the dinosaur-bearing Upper Cretaceous Iren Dabasu Formation, Inner Mongolia, People's Republic of China. Cretaceous Research 26:699–725.

Varricchio, D. J., P. C. Sereno, Z. Xijin, T. Lin, J. A. Wilson, and G. H. Lyon. 2008a. Mud-Trapped Herd Captures Evidence of Distinctive Dinosaur Sociality. Acta Palaeontologica Polonica 53:567–578.

Varricchio, D. J., P. C. Sereno, Z. Xijin, T. Lin, J. A. Wilson, H. Lyon, D. J. Varricchio, P. C. Sereno, Z. Xijin, T. A. N. Lin, J. A. Wilson, and G. H. Lyon. 2008b. Mud−trapped herd captures evidence of distinctive dinosaur sociality. Acta Palaeontologica Polonica 53:567–578.

Ward, P., and A. Zahavi. 1973. The importance of certain assemblages of birds as "information-centres" for food-finding. Ibis 115:517–534.

Weishampel, D. B., and J. R. Horner. 1986. The Hadrosaurid dinosaurs from the Iren Dabasu Fauna (People's Republic of China, Late Cretaceous. Journal of Vertebrate Paleontology 6:38–45.

Weishampel, D. B., D. E. Fastovsky, M. Watabe, D. Varricchio, F. Jackson, K. Tsogtbaatar, and R. Barsbold. 2008. New oviraptorid embryos from Bugin-Tsav, Nemegt Formation

(Upper Cretaceous), Mongolia, with insights into their habitat and growth. Journal of Vertebrate Paleontology 28:1110–1119.

Yu, Y., K. Wang, S. Chen, C. Sullivan, S. Wang, P. Wang, and X. Xu. 2018. A new caenagnathid dinosaur from the Upper Cretaceous Wangshi Group of Shandong, China, with comments on size variation among oviraptorosaurs. Scientific Reports 8.

Zanno, L. E., and G. M. Erickson. 2006. Ontogeny and Life History of Falcarius utahensis, a primitive therizinosauroid from the Early Cretaceous of Utah. Journal of Vertebrate Paleontology 26:143A.

Zanno, L. E., and P. J. Makovicky. 2011. Herbivorous ecomorphology and specialization patterns in theropod dinosaur evolution. Proceedings of the National Academy of Sciences 108:232–237.

1968. Results of the Polish-Mongolian Palaeontological Expeditions Part I. Palaeontologica Polonica 19.

1969. Results of the Polish-Mongolian Palaeontological Expeditions Part II. Palaeontologica Polonica 21.

1971. Results of the Polish-Mongolian Palaeontological Expeditions Part III. Palaeontologica Polonica 25.

1972. Results of the Polish-Mongolian Palaeontological Expeditions Part IV. Palaeontologica Polonica 27.

1974. Results of the Polish-Mongolian Palaeontological Expeditions Part V. Palaeontologica Polonica 30.

1975. Results of the Polish-Mongolian Palaeontological Expeditions Part VI. Palaeontologica Polonica 33.

1977. Results of the Polish-Mongolian Palaeontological Expeditions Part VII. Palaeontologica Polonica 37.

1979. Results of the Polish-Mongolian Palaeontological Expeditions Part VIII. Palaeontologica Polonica 38.

1981. Results of the Polish-Mongolian Palaeontological Expeditions Part IX. Palaeontologica Polonica 42.

1984. Results of the Polish-Mongolian Palaeontological Expeditions Part X. Palaeontologica Polonica 46.

2010. Hayashibara Museum of Natural Sciences Research Bulletin Vol. 3 (T. Tsubamoto (ed.)). Hayashibara Museum of Natural Sciences, Okayama, Japan, pp.

2014. Bonebeds: Genesis, Analysis, and Paleobiological Significance (R. R. Rogers, D. A. Eberth, and A. R. Fiorillo (eds.)). University of Chicago Press, Chicago, pp.

2000. Hayashibara Museum of Natural Sciences Research Bulletin Vol. 1 (K. Ishii, M. Watabe, S. Suzuki, S. Ishigaki, R. Barsbold, and K. Tsogtbaatar (eds.)). Hayashibara Museum of Natural Sciences, Okayama, Japan, pp.

2004. Hayashibara Museum of Natural Sciences Research Bulletin Vol. 2 (K. Ishii, M. Watabe, S. Suzuki, S. Ishigaki, R. Barsbold, and K. Tsogtbaatar (eds.)). Hayashibara Museum of Natural Sciences, Okayama, Japan, pp.

5.6 FIGURES
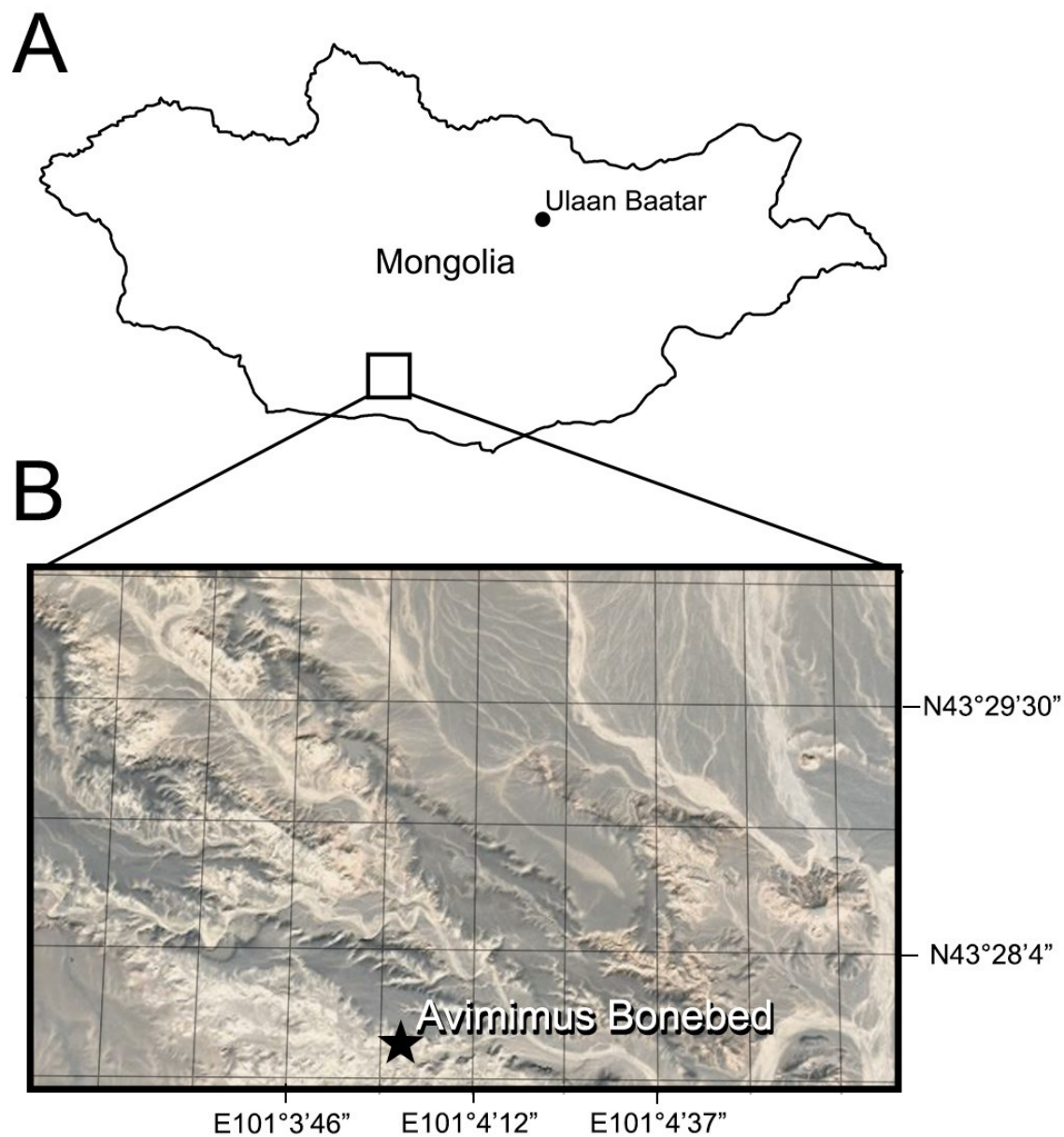
Fig. 5.1. Location of the Nemegt *Avimimus* bonebed.

Locality of *Avimimus* bonebed. Map (A) of Mongolia traced in Photoshop CS6

(www.adobe.com/photoshop), indicating the region of the Nemegt Locality (B). Detail (B) of the

Nemegt locality, indicating location of *Avimimus* bonebed (pointer). Map data in (A) and

satellite imagery in (B) from Google Maps (Map data: © Google), used under fair use terms.

681

Fig. 5.2. The Nemegt *Avimimus* bonebed.

Image of field locality of *Avimimus* bonebed, showing regional sedimentological structures. Note

people bottom right for scale.
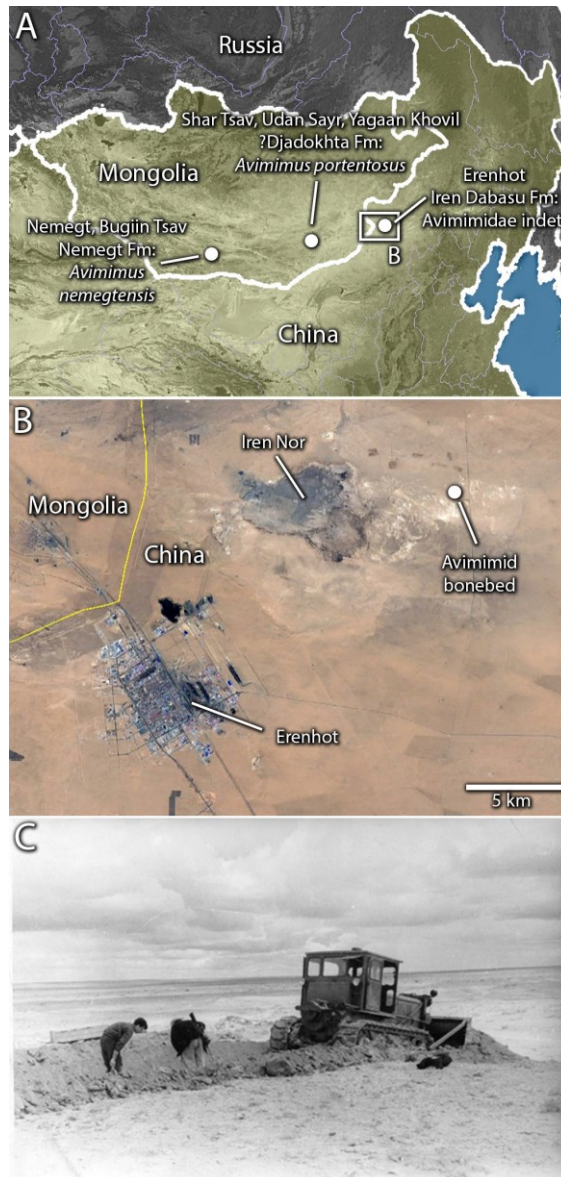
Fig. 5.3. Location of the Iren Dabasu avimimid bonebed.

Geographical setting of the Iren Dabasu avimimid bonebed. Map of Eastern Asia (A) showing

localities where avimimids have been found in China and Mongolia (highlighted; inset shows

location of image B). Satellite image (B) of Erenhot Region, showing Iren Nor and the location

of the Iren Babasu avimimid bonebed. Photograph (C) of Sino-Soviet expedition excavating the

site with a bulldozer in 1959.
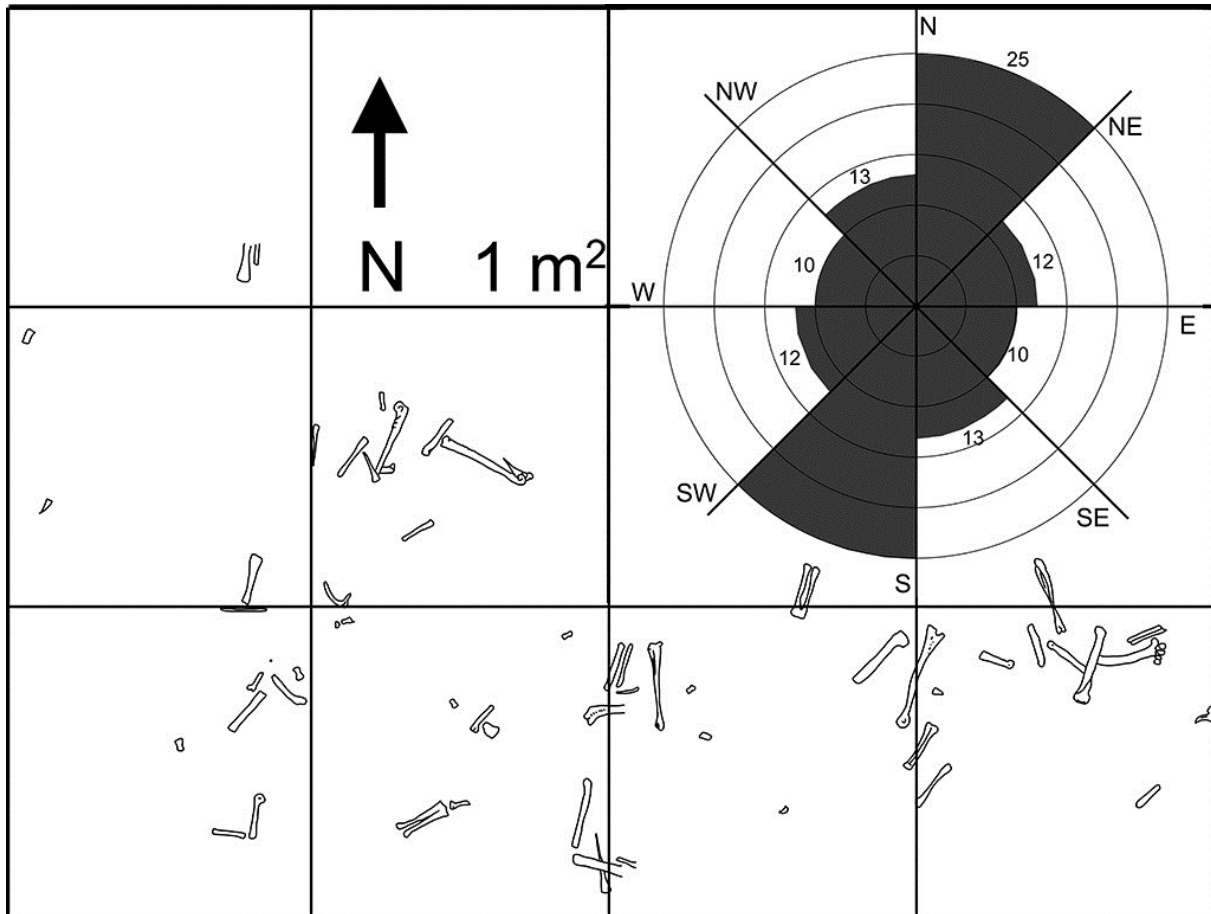
Fig. 5.4. Quarry map of Nemegt *Avimimus* bonebed.

Map of *Avimimus* bonebed, showing orientation and position of hindlimb bones *in situ*. Each square represents 1 m². Arrow indicates North. Mirrored rose diagram indicates orientations of *in situ* long bones in *Avimimus* bonebed. Shaded areas represent the number of bones within each range of orientations (n=60). Orientation measured from long axis of bones.
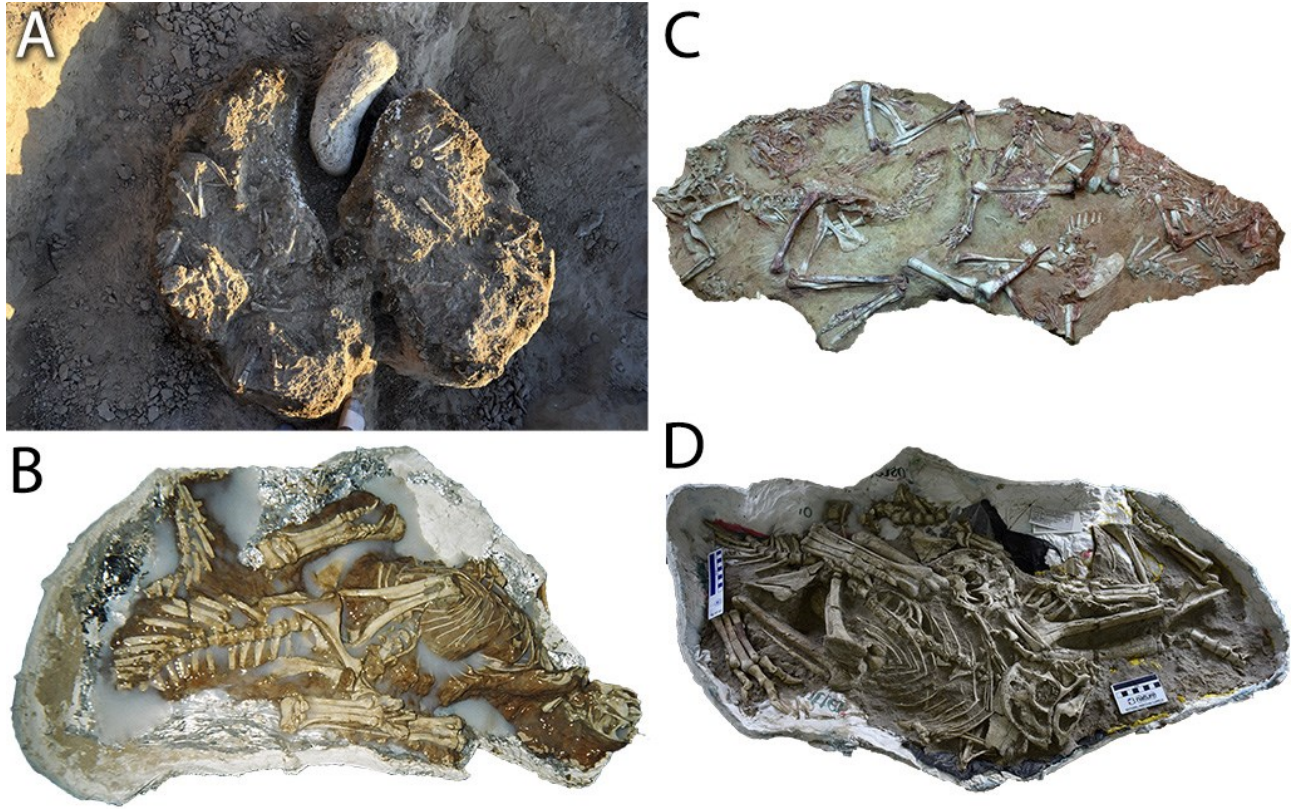
Fig. 5.5. Assemblages of gregarious oviraptorids.

Field photograph (A) of MPC-D NatGeo.2018.036 during excavation, showing numerous exposed bones of *Conchoraptor gracilis*. Photograph (B) of MPC-D 102/03 in ventral view during moulding, showing complete individual and partial tail of a second *Conchoraptor gracilis*. Uncatalogued block (C) on display at the Central Museum of Mongolian Dinosaurs in Ulaanbaatar, of at least five individuals of a new species of oviraptorid. MPC-D 102/110 (D) in ventral view, showing parts of three individuals of a new species of oviraptorid.
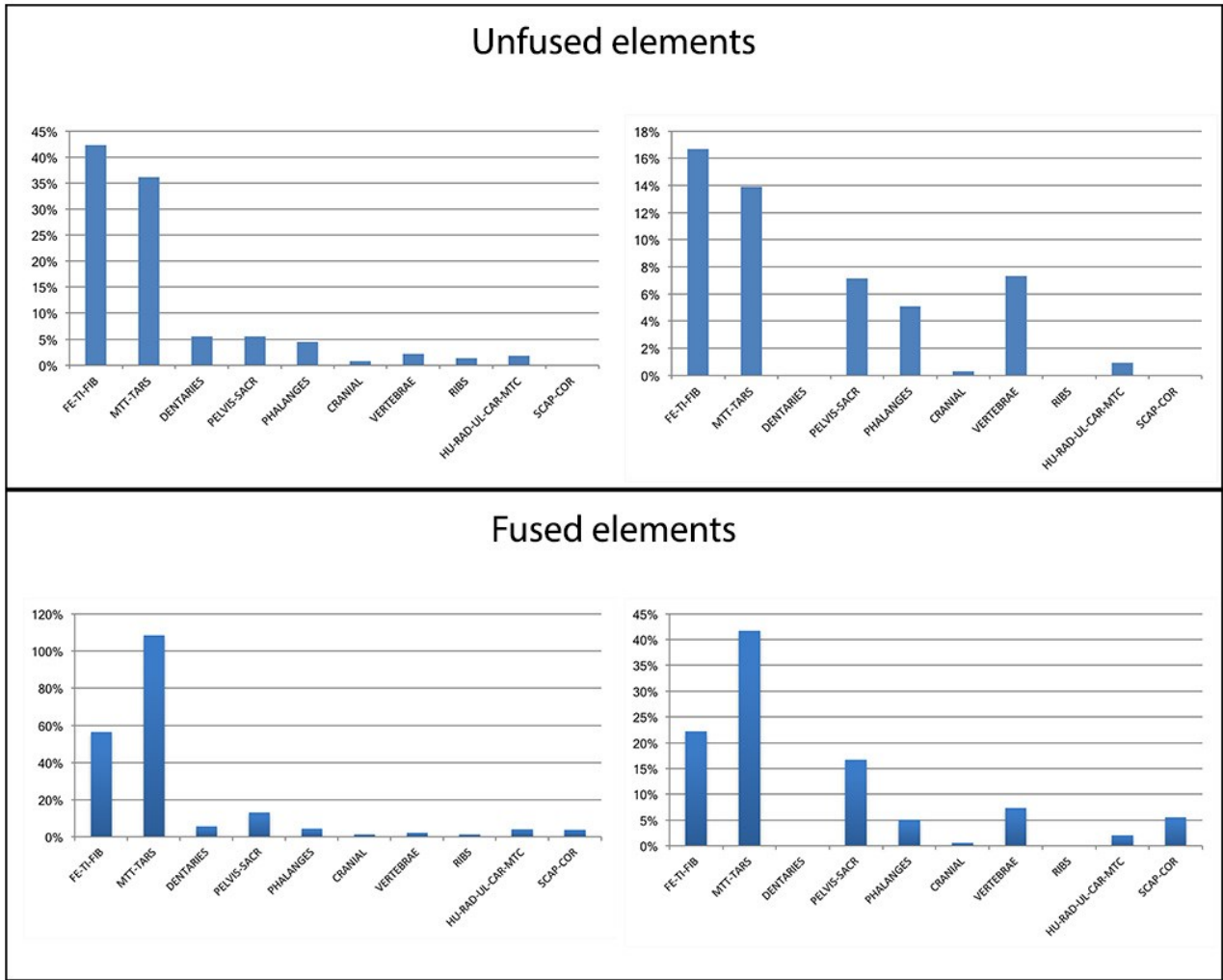
Fig. 5.6. Skeletal representation of avimimid bonebeds.

Skeletal representation at the Nemegt *Avimimus* bonebed (left) and the Iren Dabasu avimimid

bonebed (right), calculated assuming compound elements are unfused (top) and fused (bottom).
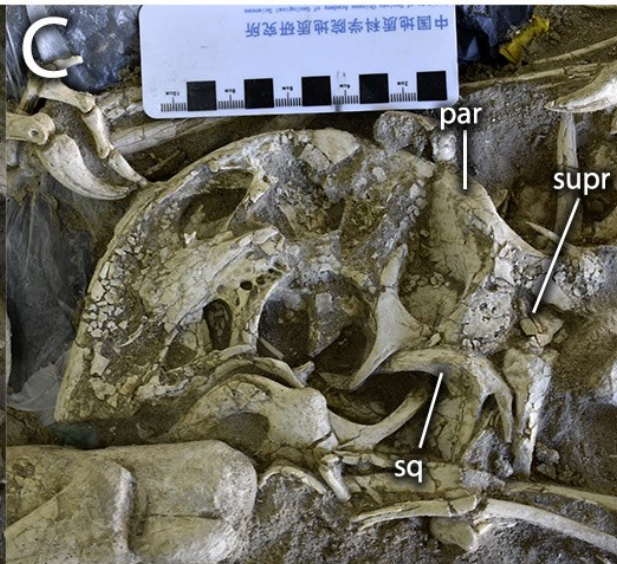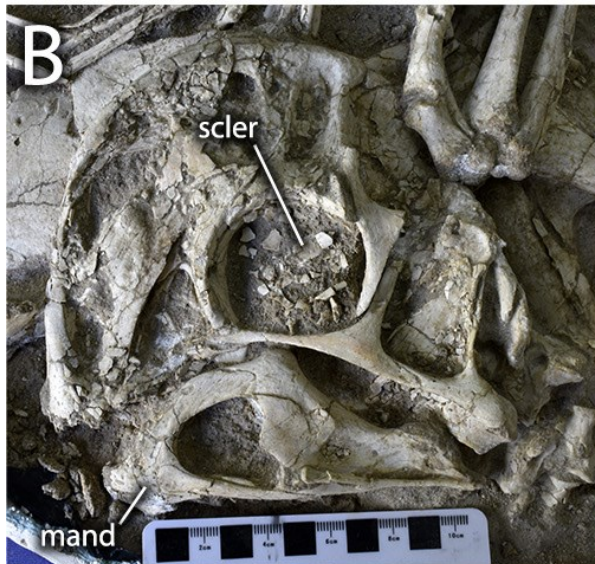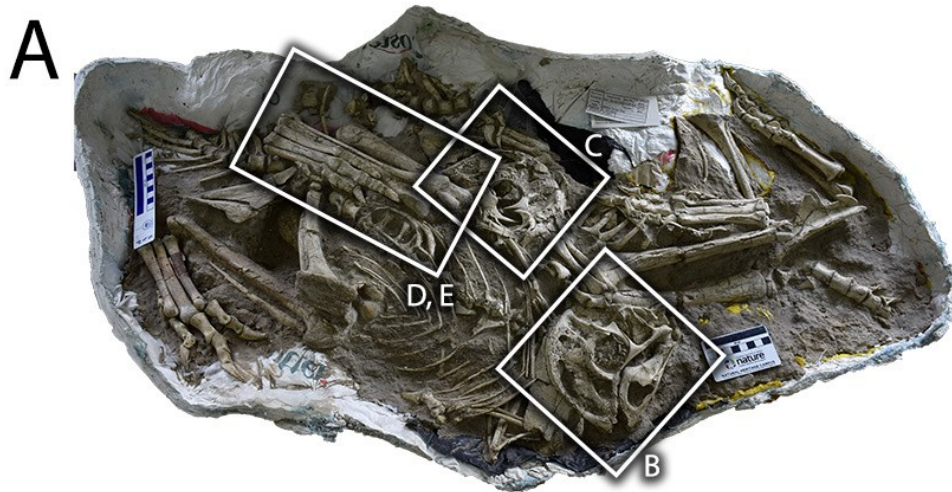
(Previous page)
Fig. 5.7. Details of MPC-D 102/110.

Photograph (A) of MPC-D 102/110, an assemblage of three partial skeletons, showing the arrangement of the skeletons and the locations of close-up images. Skulls (B, C) of MPC-D 102/110 in left lateral view, showing excellent preservation, including sclerotic plates, and local disarticulation of some elements (e.g. the braincase in C). Right leg (D) of MPC-D 102/110.a in right lateral view (ventral is up), showing excellent articulation and crouched posture. Comparison (E) of articulated tibia and pes of MPC-D 102/11 (left) and MPC-D 102/110.a (right), showing identical taphonomy, posture, and anatomy, suggesting that the specimens are from the same quarry. **Abbreviations: fem**, femur; **mand**, mandible; **par**, parietal; **pes**, foot; **scler**, sclerotic plates; **sq**, squamosal; **supr**, supraoccipital; **tib**, tibia.
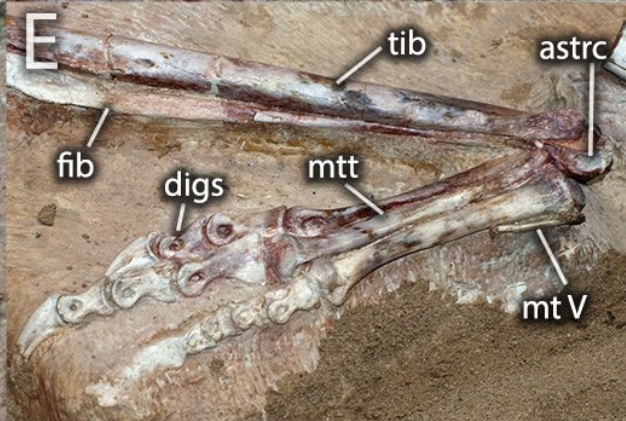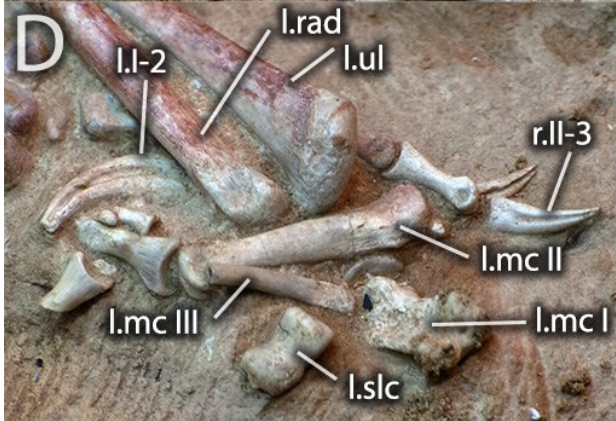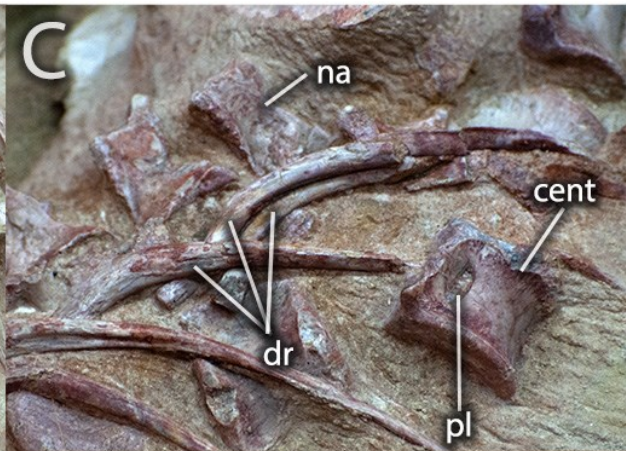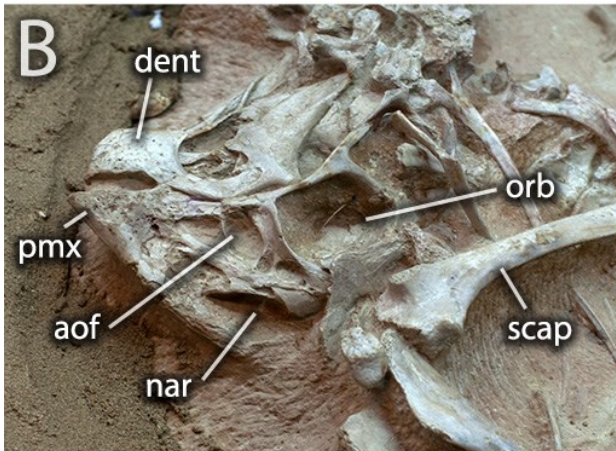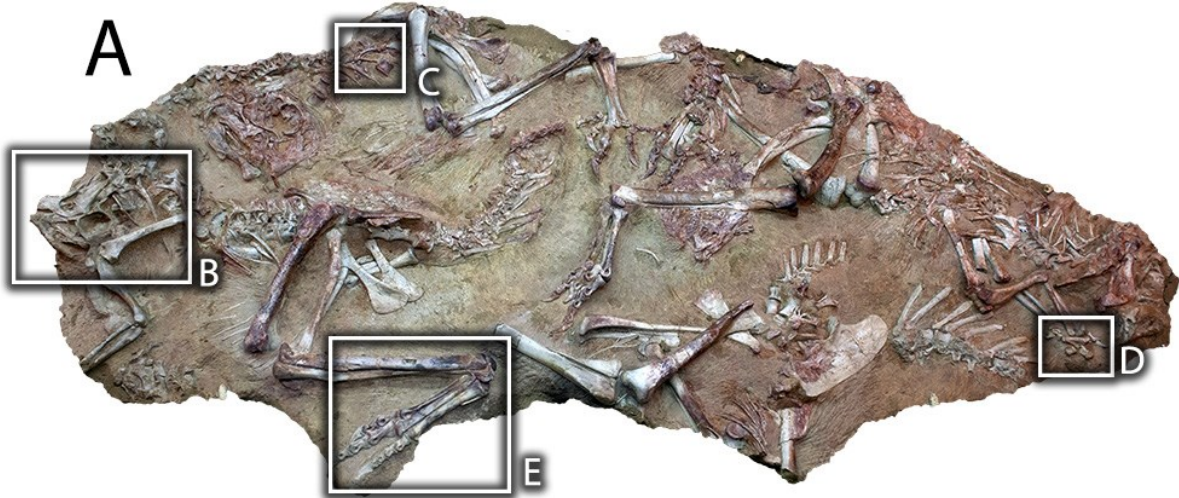
(Previous page)
Fig. 5.8. Details of the CMMD oviraptorid block.

Photograph (A) of the CMMD oviraptorid block, showing positions of skeletons and locations of close-up images. Photograph (B) of skull of most complete individual in right lateral view (ventral is up), showing excellent preservation and articulation. Photograph (C) of dorsal vertebrae and ribs, showing lack of neurocentral suture fusion and local disarticulation. Photograph (D) of left and right manus, showing disparity between unguals I-2 and II-3 typical of heyuannine oviraptorids, excellent preservation quality, and local disarticulation. Photograph (E) of left hindlimb of most complete individual, showing articulation and excellent preservation quality. **Abbreviations: aof**, antorbital fenestra; **astrc**, astragalocalcaneum; **cent**, centrum; **dent**, dentary; **digs**, digits; **dr**, dorsal rib; **fib**, fibula; **l.I-2**, left ungual I-2; **l.mc I**, left metacarpal I; **l.mc II**, left metacarpal II; **l.mc III**, left metacarpal III; **l.rad**, left radius; **l.slc**, left semilunate carpal; **l.ul**, left ulna; **mtt**, metatarsus; **mt V**, metatarsal V; **na**, neural arch; **nar**, naris; **orb**, orbit; **pl**, pleurocoel; **pmx**, premaxilla; **r.II-3**, right ungual II-3; **scap**, scapula.

Fig. 5.9. Preservation style in the Baynshiree Formation.

Field photograph of oviraptorosaur pubes excavated from the Baynshiree Formation exposed at

Shine Us Khudag, showing bone colouration and sediment similar to the CMMD oviraptorid

block. Note rock hammer for scale.
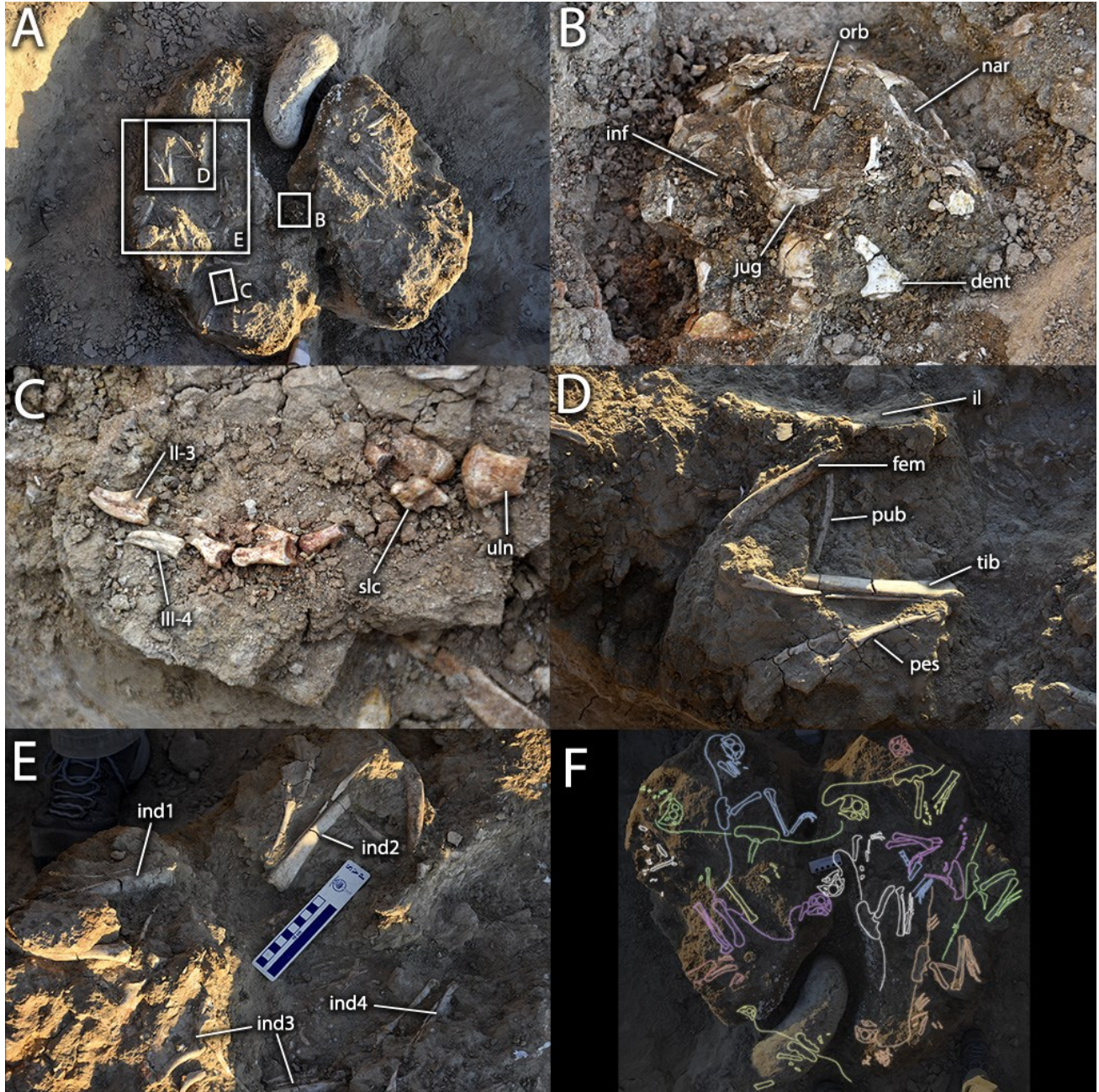
(Previous page)
Fig. 5.10. Details of MPC-D NatGeo.2018.036.

Field photographs (A–E) of MPC-D NatGeo.2018.036, and interpretive illustration of the positions of the skeletons (F). Overview (A), showing the three main blocks before removal of the jackets and locations of close-up photos. Skull (B) of MPC-D NatGeo.2018.036a in right lateral view before excavation. Left manus (C) of indeterminate individual showing local disarticulation and reduced lateral digits indicative of *Conchoraptor gracilis*. Left hindlimb (D) of indeterminate individual showing articulation and position of the hindlimb crouched underneath the body. Photograph (E) of northeastern portion of the block, showing densely packed individuals with hindlimbs articulated in a crouched position. Illustration (F) showing possible arrangements of skeletons based on observations in the field. **Abbreviations: dent**, dentary; **fem**, femur; **II-3**, manual ungual II-3; **III-4**, manual ungual III-4; **il**, ilium; **ind1–4**, first to fourth individuals; **inf**, infratemporal fenestra; **jug**, jugal; **nar**, naris; **orb**, orbit; **pes**, foot; **pub**, pubis; **slc**, semilunate carpal; **tib**, tibia; **uln**, ulna.
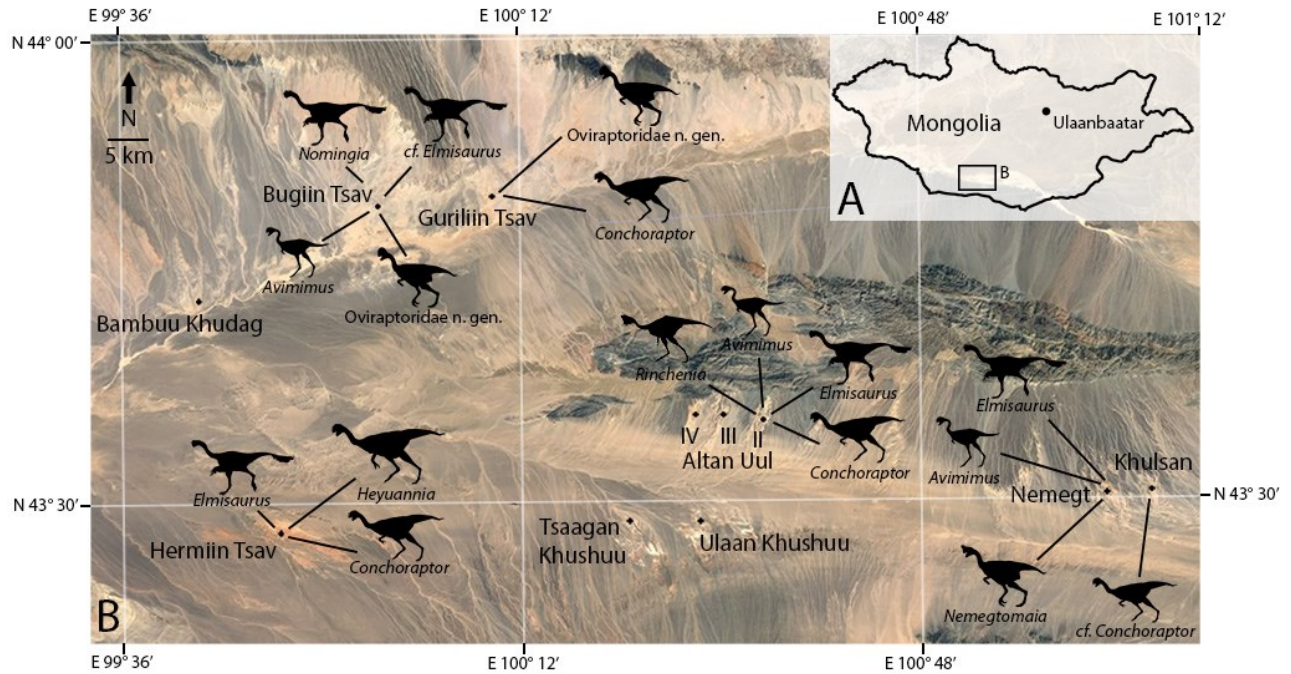
Fig. 5.11. Distribution of oviraptorosaurs in the Nemegt Basin.

Map of fossil localities and oviraptorosaur occurrences in the Nemegt Basin. Inset (A) shows location of Nemegt Basin within Mongolia. Satellite image from Google Earth, © Google, Landsat/Copernicus, used under fair use terms.
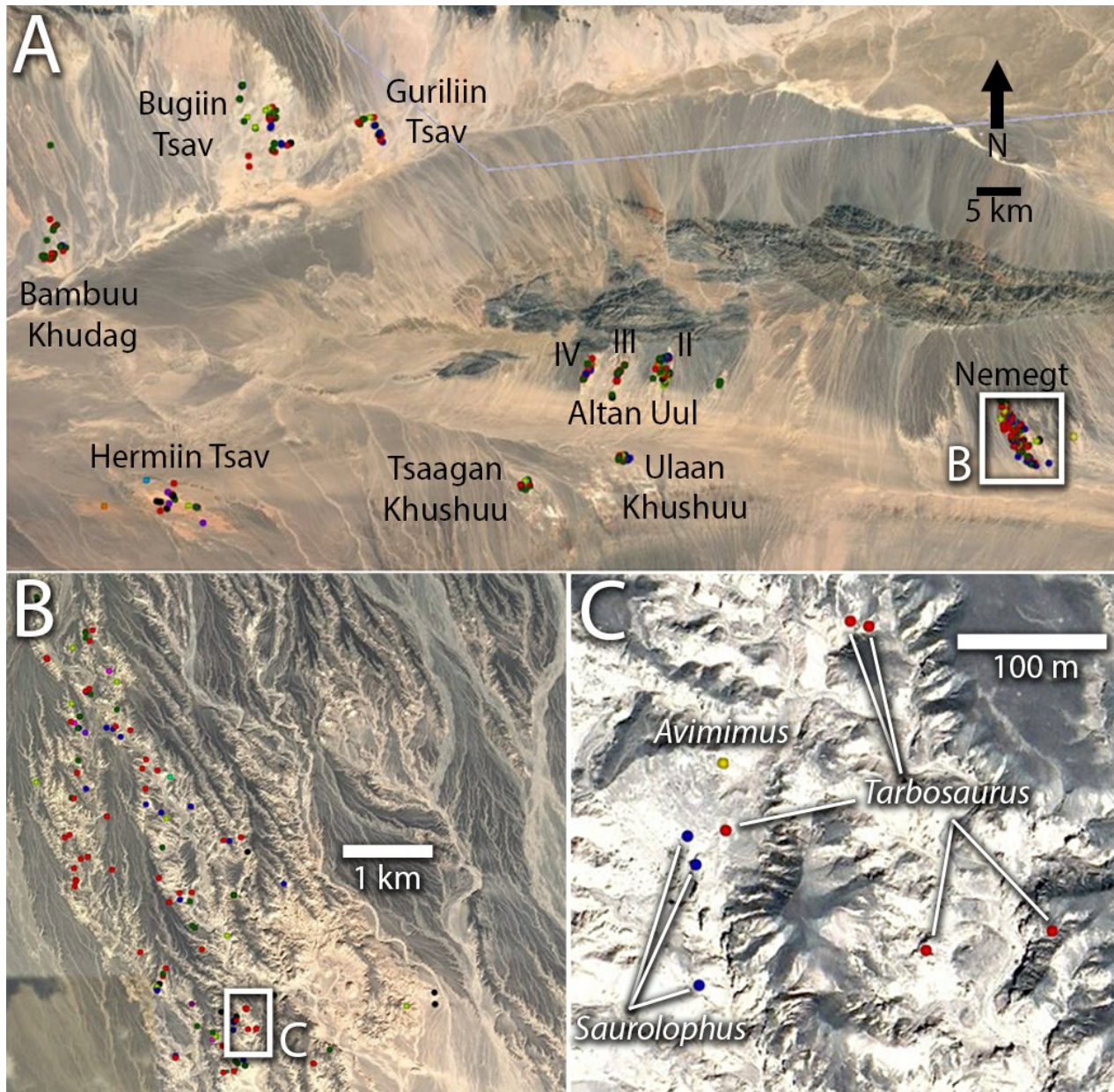
Fig. 5.12. Map data used for ecological analysis.

Example images from interactive map data. Overview (A) of Nemegt Basin, showing localities and clusters of GPS-acquired datapoints. Detail of Nemegt Locality (B), showing distribution of skeletons along sayrs. Close-up (C) of Central Sayr, showing fine-scale spatial resolution of data, and colour coding of different taxa. Scales as indicated. North is up in all images.
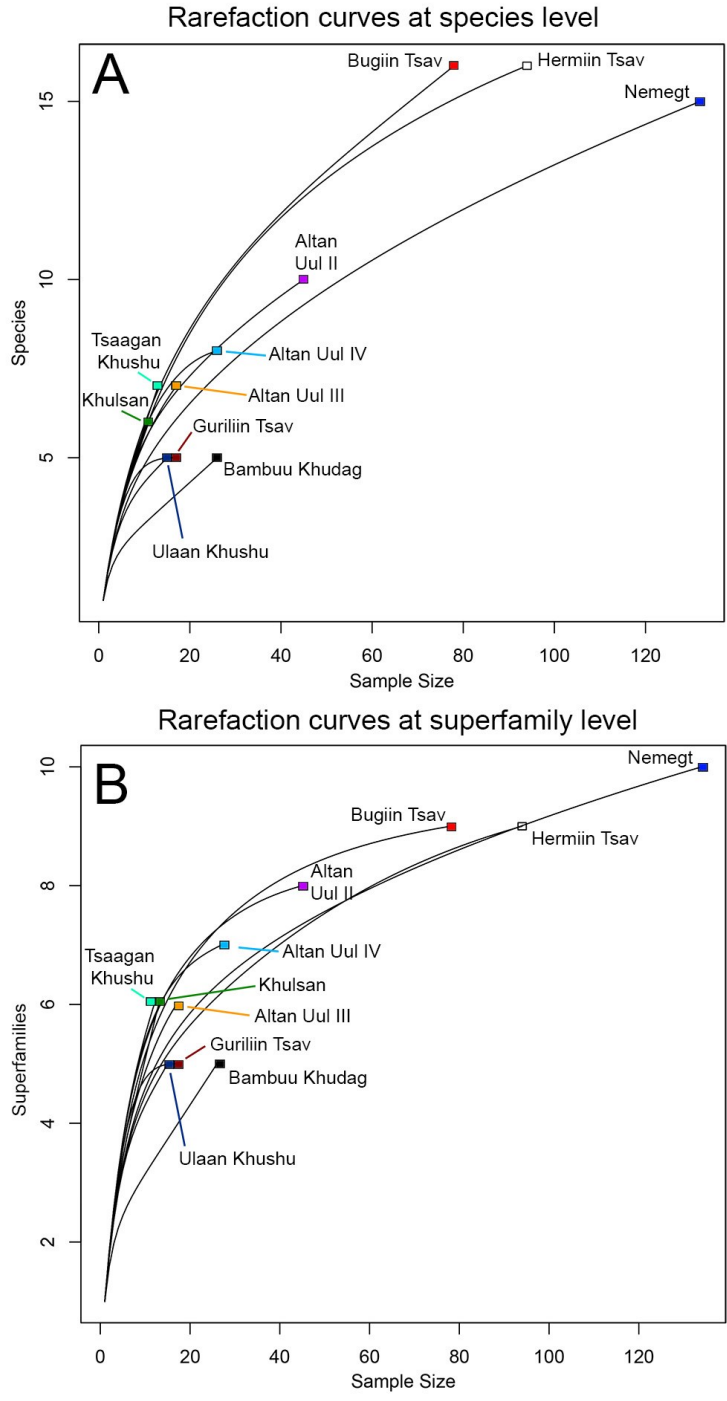
Fig. 5.13. Rarefaction curves of Nemegt Locality samples.

Rarefaction curves of Nemegt Basin sampling intensity at the superfamily level (A) and the

species level (B).
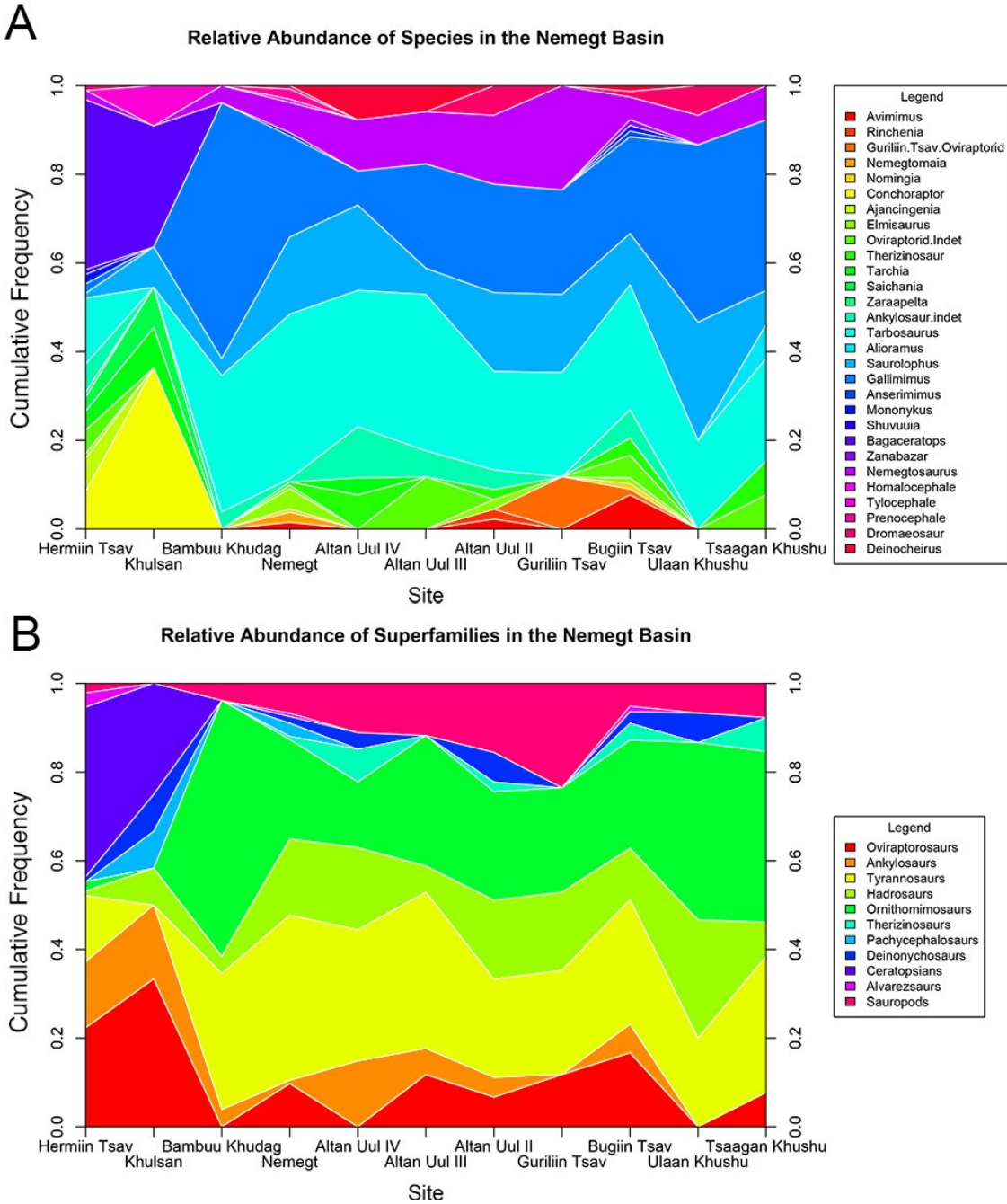
Fig. 5.14. Paleocommunity structure in the Nemegt Basin.

Relative abundance plots for species-level (A) and superfamily-level (B) data. Sites are arranged in approximate stratigraphic order.

NMDS Ordination of Nemegt Superfamilies
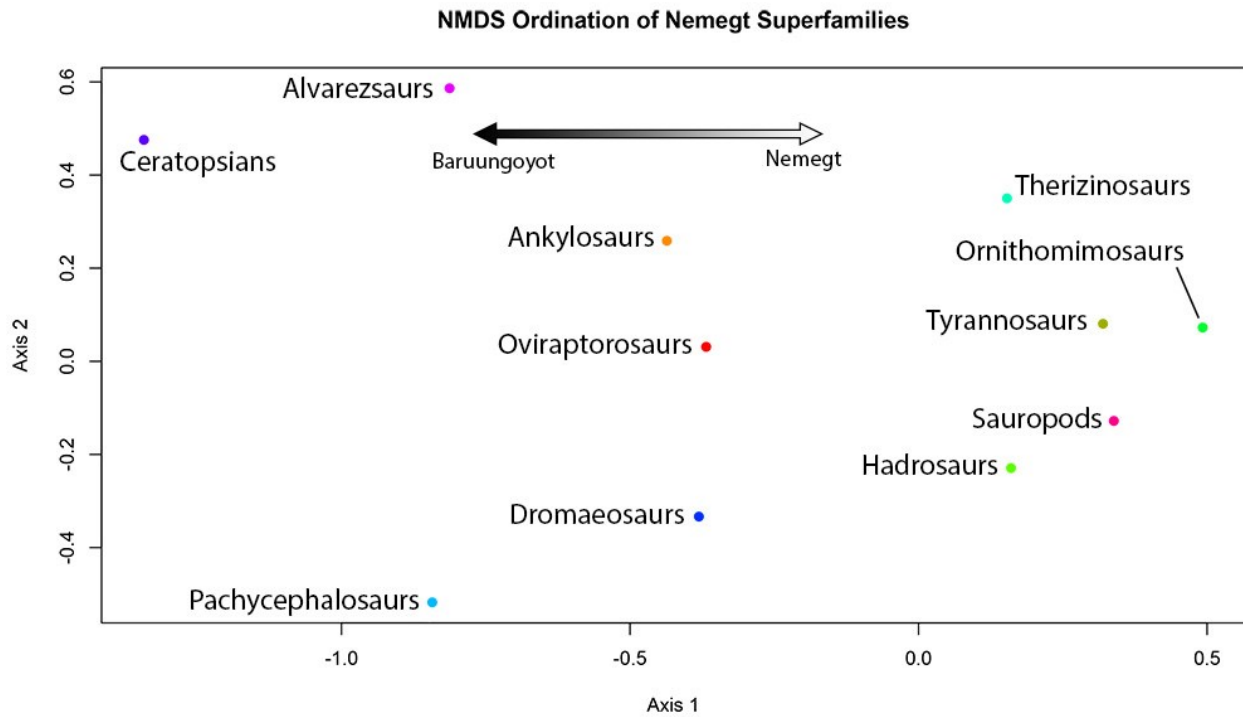
Fig. 5.15. Ordination of Nemegt Basin dinosaur superfamilies.

Non-metric multidimensional scaling of Nemegt dinosaur superfamilies, showing frequency of co-occurrence. Superfamilies that co-occur more often plot more closely together. Note division between Nemegt-typical superfamilies (e.g. Ornithomimosaurs, Tyrannosaurs) and Baruungoyot-typical superfamilies (e.g. Ceratopsians, Alvarezsaurs).
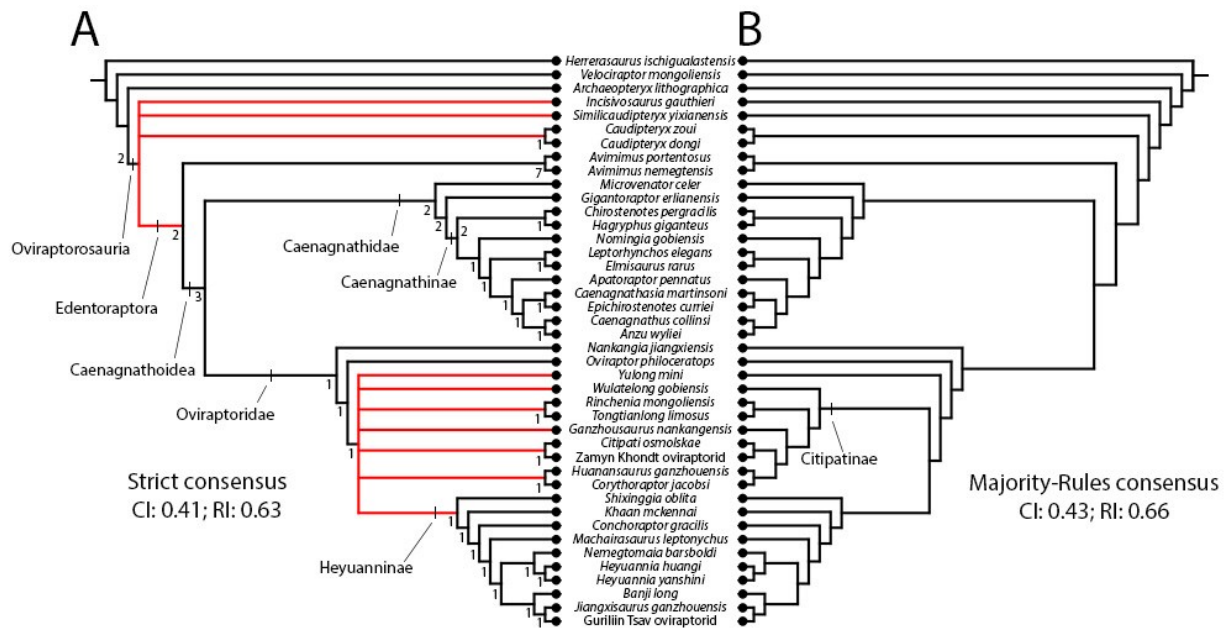
Fig. 5.16. Consensus trees of Oviraptorosauria.

Strict consensus (A) and majority-rules (B) consensus trees of Oviraptorosauria based on 9 most parsimonious trees of 641 steps generated by a matrix of 246 characters and 42 taxa. Polytomies in the strict consensus tree are in red, subclades used in the text are indicated.
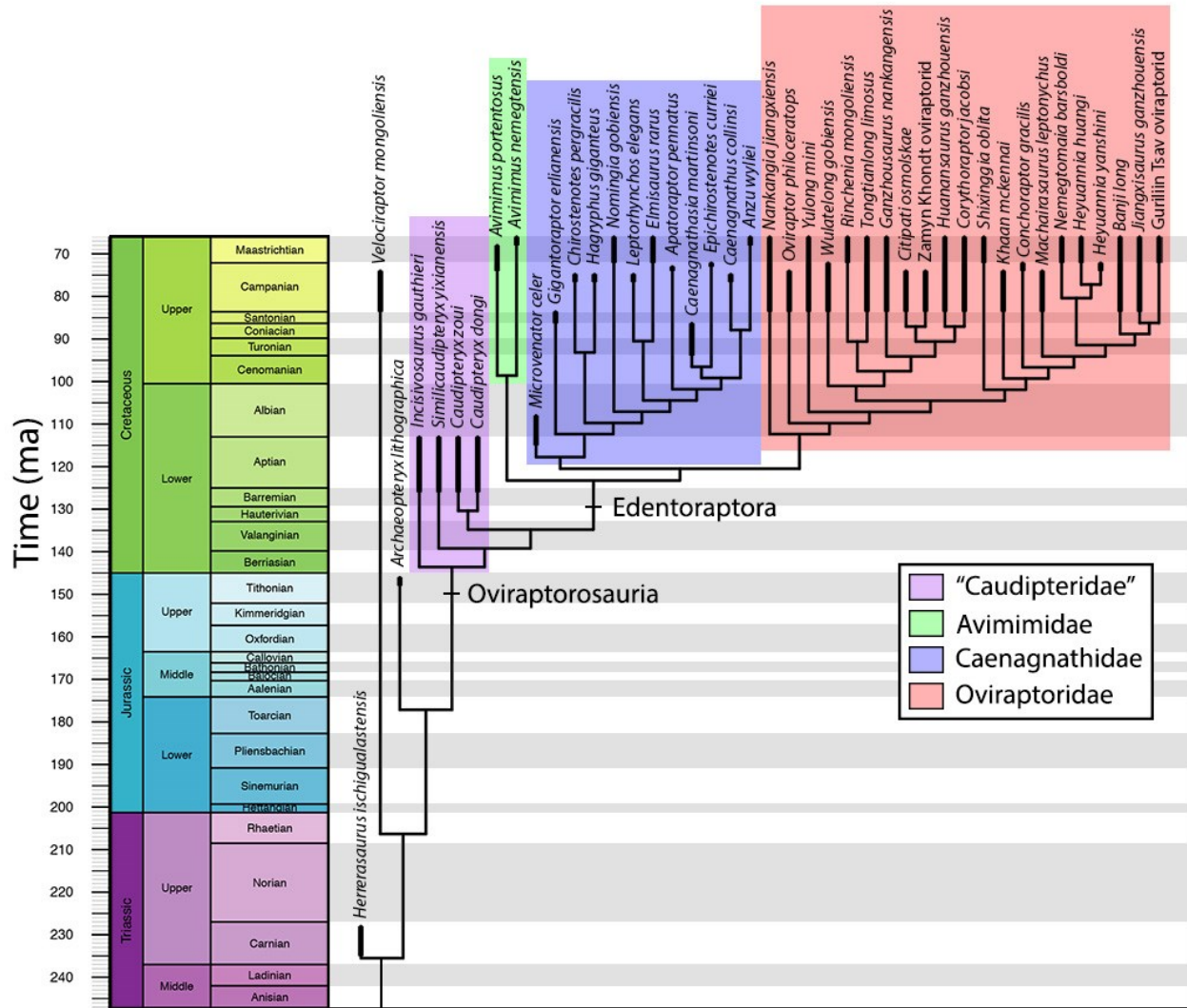
Fig. 5.17. Phylogeny of Oviraptorosauria.

Preferred topology based on majority-rules consensus tree of Oviraptorosauria, time-calibrated using the equal branch lengths method of Brusatte et al. (2008). Families of Oviraptorosauria indicated by coloured boxes.
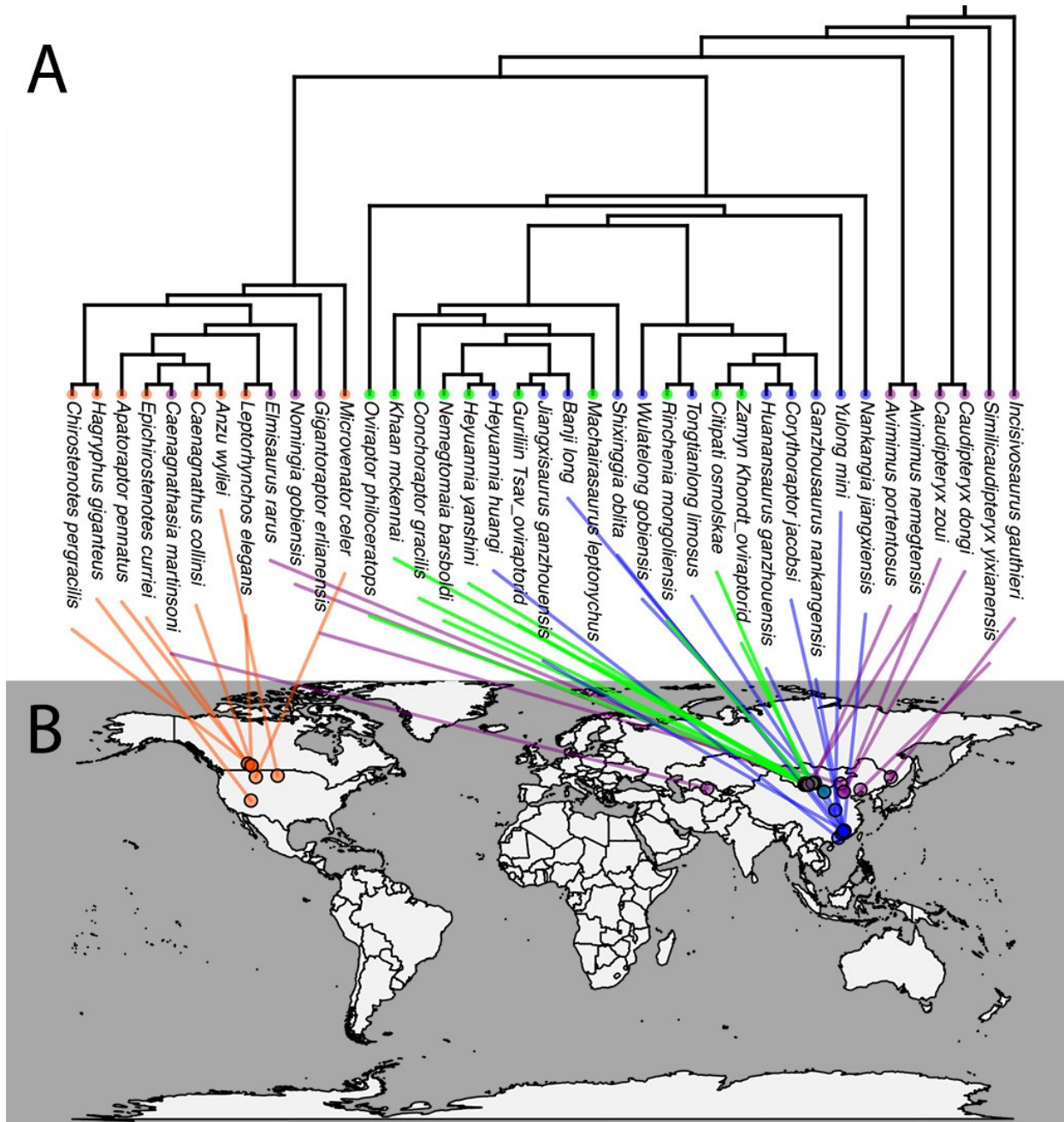
Fig. 5.18. Geographic distribution of Oviraptorosauria.

Preferred topology of Oviraptorosauria with provenance of each taxon indicated on a global map.
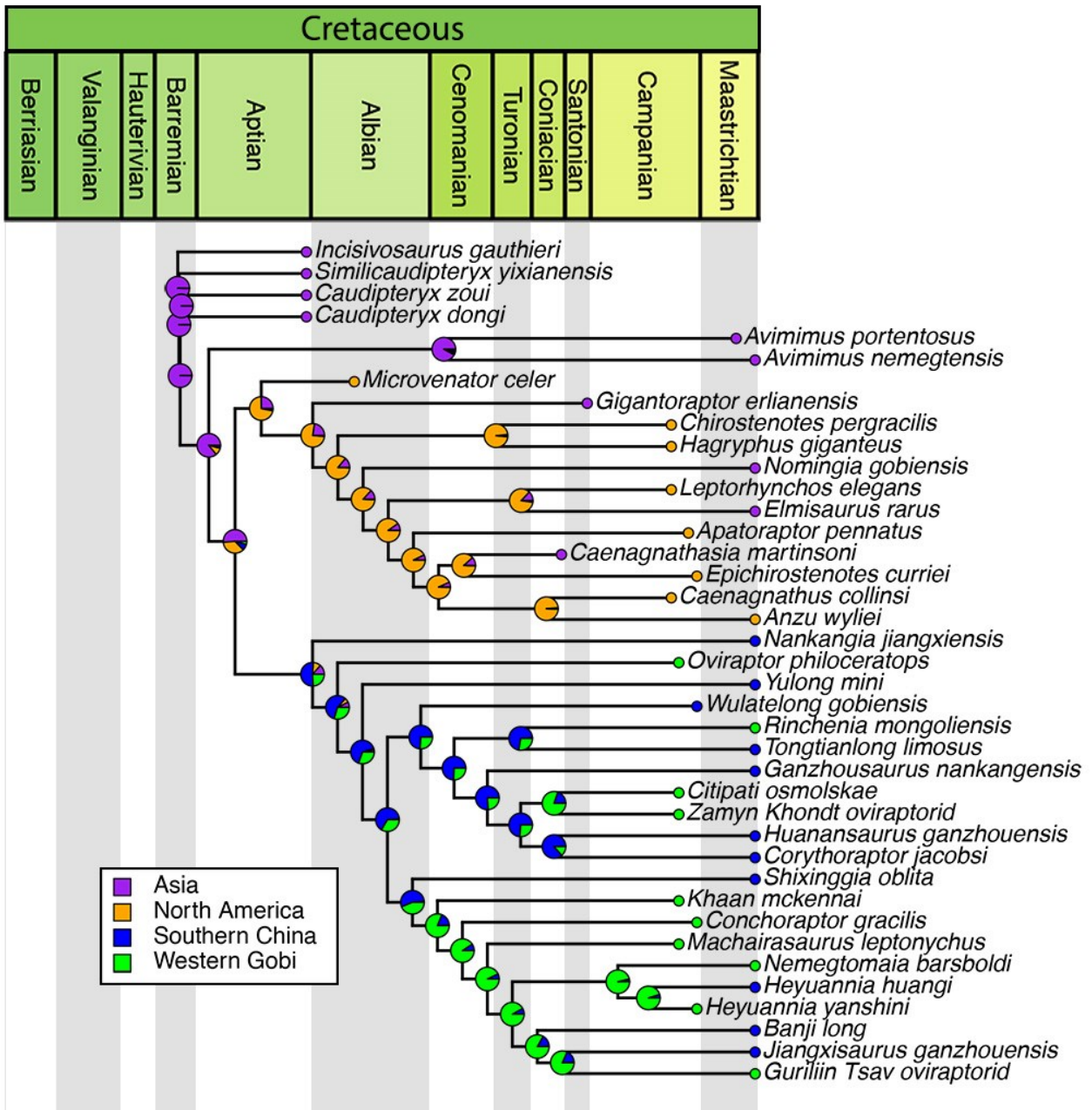
Fig. 5.19. Biogeography of Oviraptorosauria.

Estimation of ancestral biogeography of Oviraptorosauria based on stochastic character mapping of four discrete regions: Asia, North America, Southern China, and Western Gobi. Pie charts at nodes indicate proportion of ancestry estimations based on 1000 replicates of simulated character history using a Markov model.
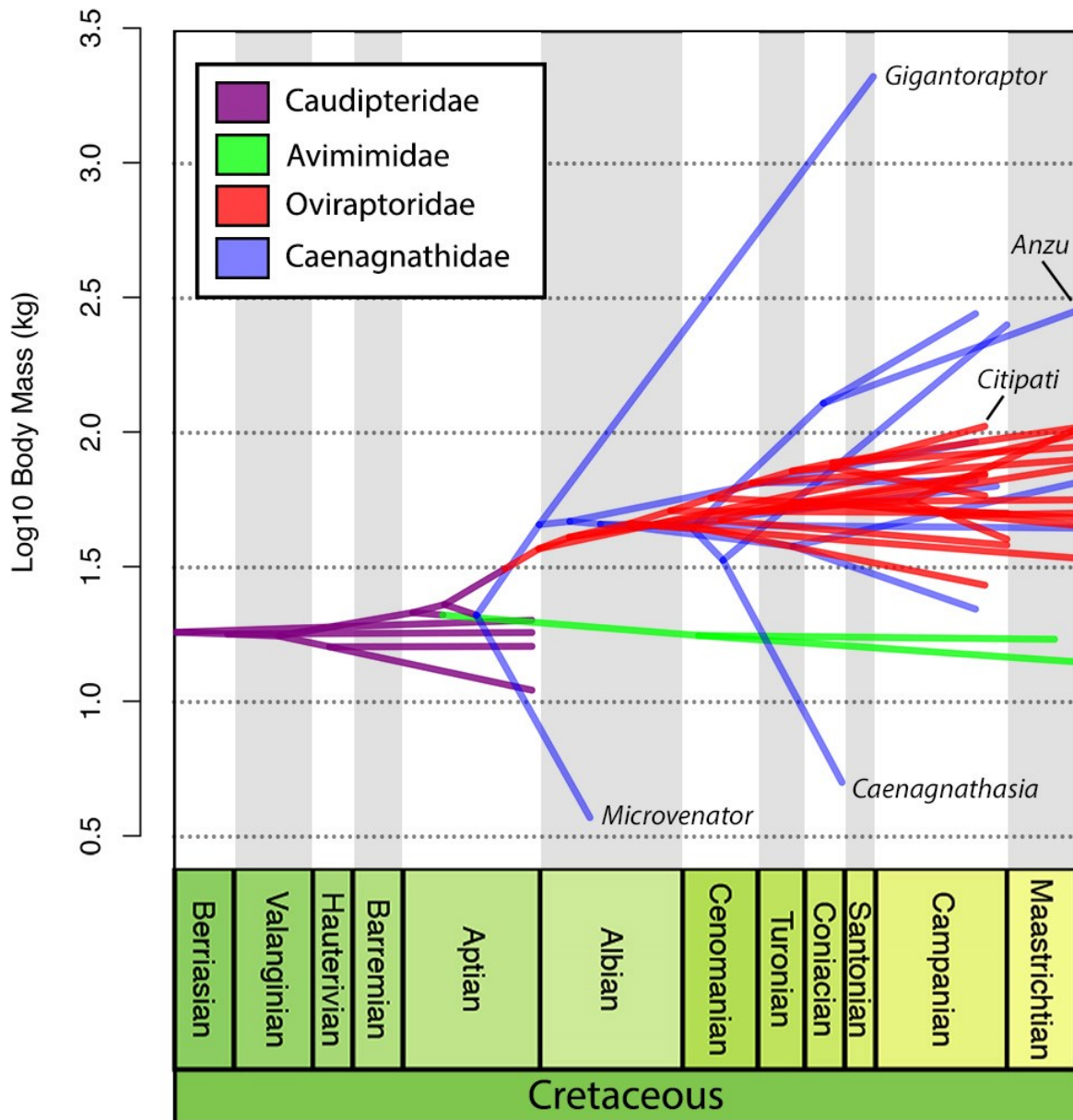
Fig. 5.20. Body mass evolution of Oviraptorosauria.

Phenogram of time-calibrated phylogeny plotted against log-transformed body mass (kg), with

families colour coded.
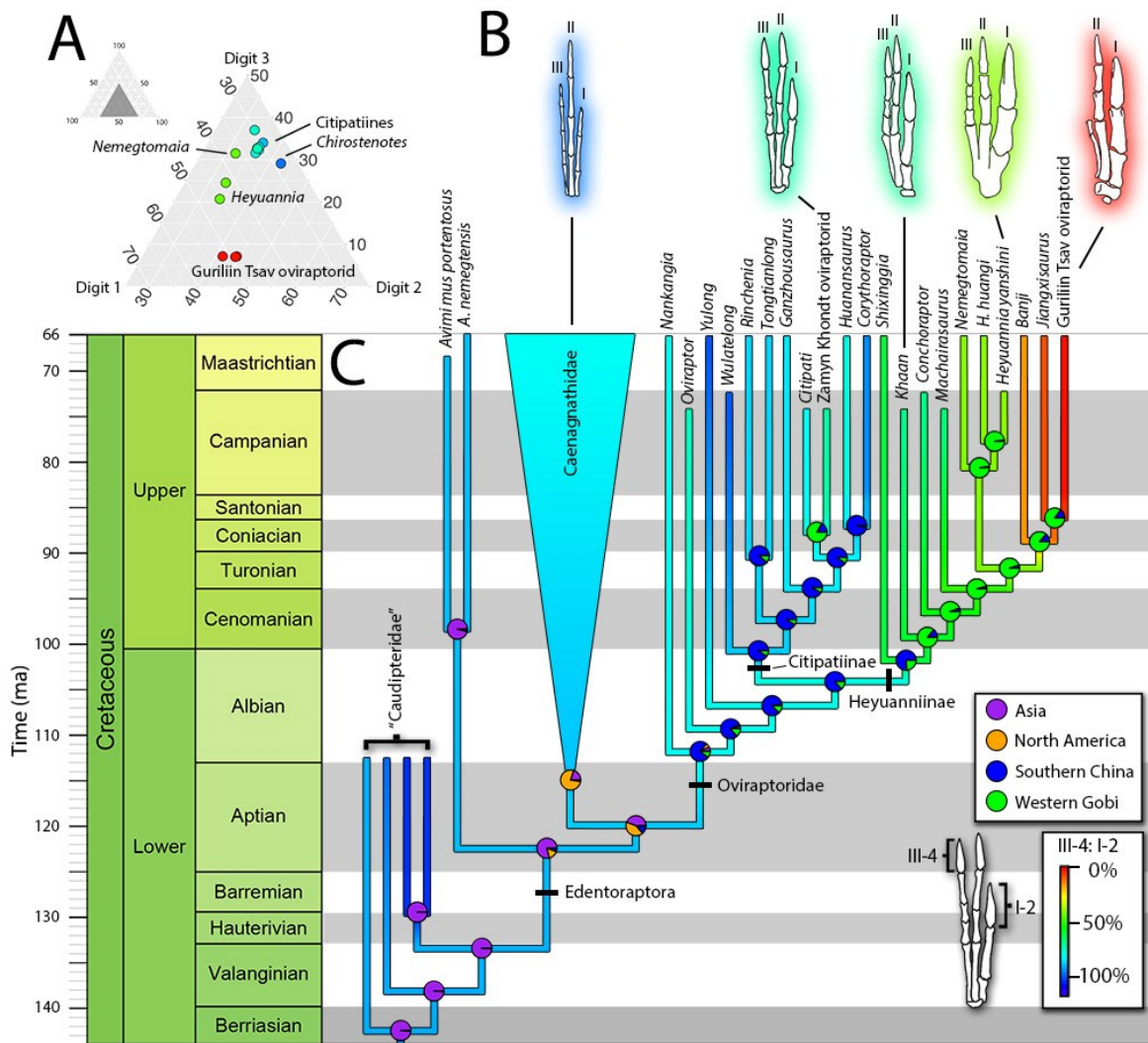
Fig. 5.21. Digit reduction in Oviraptorosauria.

Ternary plot (A) of manual digit proportions of selected oviraptorosauria. Illustrations (B) of general morphology of the manus of oviraptorosaurs, showing disparity between digits in Heyuanninae. Simplified phylogeny (C) of Oviraptorosauria with ratio of manual ungual III-4 to ungual I-2 mapped as a continuous character using Maximum Likelihood. Warm colours indicate lower ratios, indicative of lateral digit reduction. Pie charts at nodes indicate proportion of biogeographic ancestry estimations based on 1000 replicates of simulated character history using a Markov model.
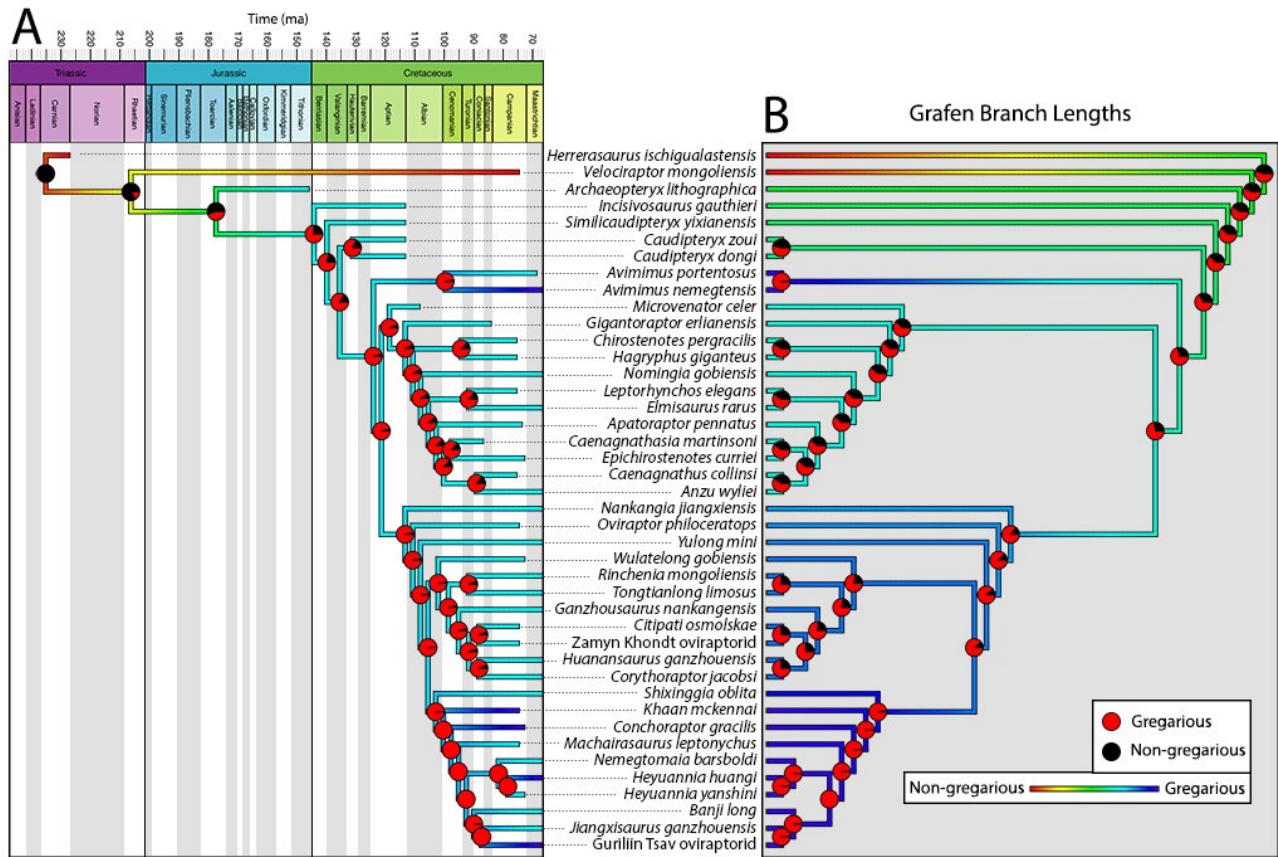
Fig. 5.22. Evolution of gregarious behaviour in Oviraptorosauria.

Ancestral state estimation of gregarious behaviour when treated as a continuous character (branch colour) and a discrete character (node labels), for trees calibrated to time (A) and branch length (B). Cooler colours indicate greater likelihood of gregarious behaviour estimated under Maximum Likelihood. Greater proportion of red in node labels indicates greater proportion of gregarious behaviour estimates based on 1000 replicates of simulated character history using a Markov model.
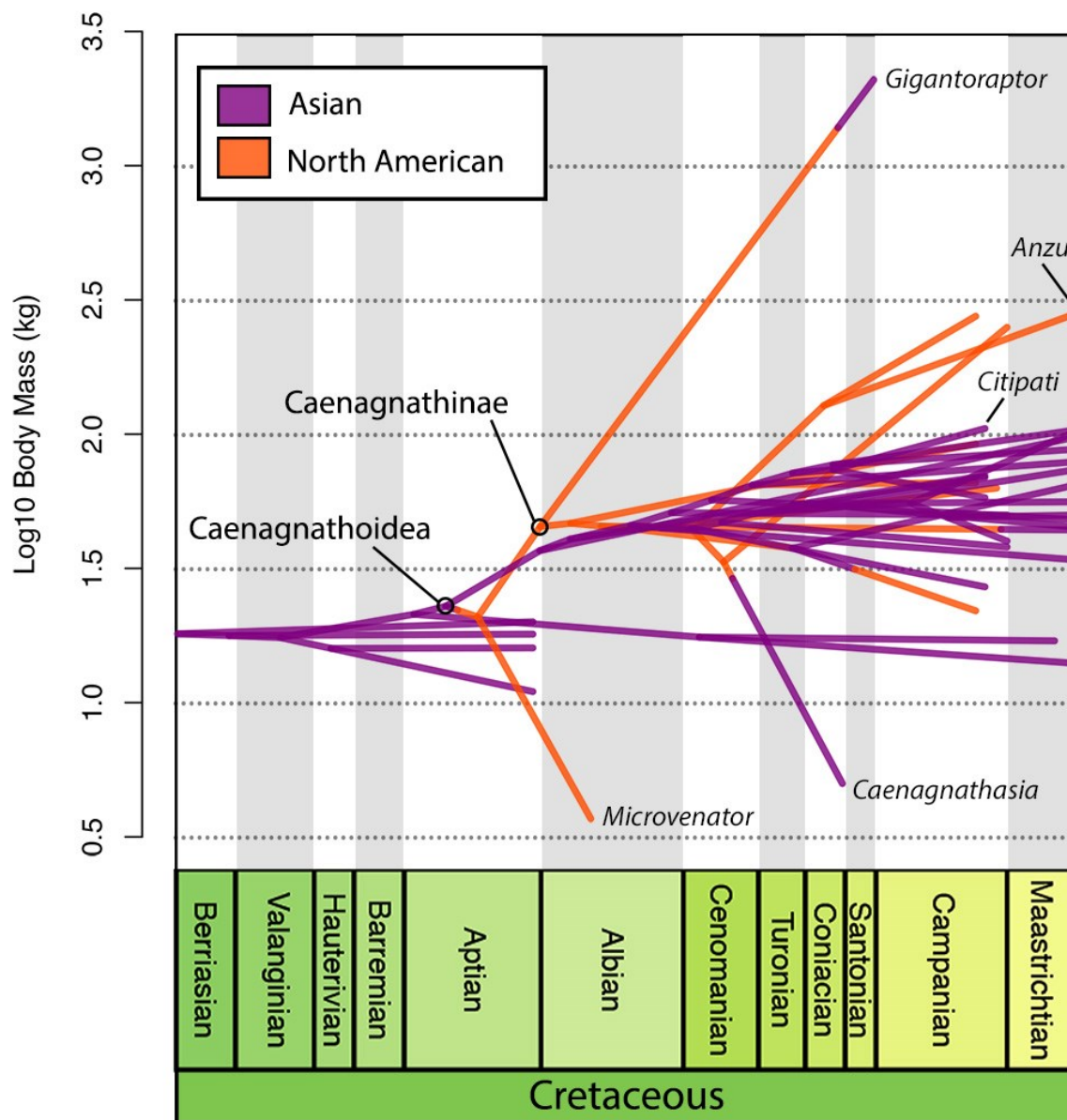
Fig. 5.23. Body mass and biogeography of Oviraptorosauria.

Phenogram of time-calibrated phylogeny plotted against log-transformed body mass (kg), with

biogeographic dispersal of caenagnathids to North America (orange) from Asia (purple) mapped

onto the tree.
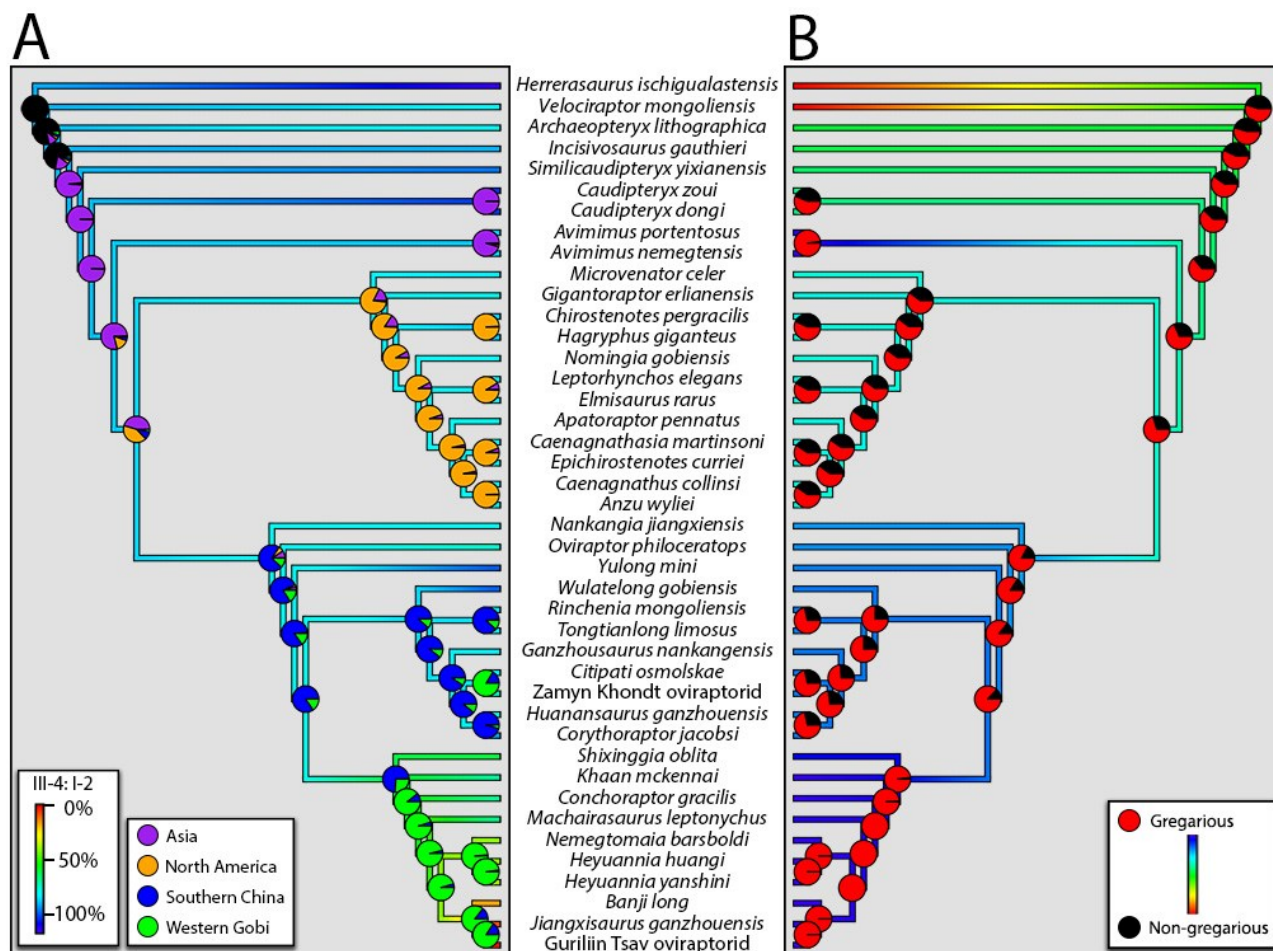
Fig. 5.24. Digit reduction and gregariousness in Oviraptorosauria.

Branch-length scaled phylogenies with the ratio of manual ungual III-4 to ungual I-2 (A) and

likelihood of gregarious behaviour (B) estimated under Maximum Likelihood mapped onto the

trees as continuous characters. Warm colours indicate shorter digits in (A) and cool colours

indicate greater likelihood of gregarious behaviour in (B). Node labels show ancestral estimates

of biogeography (A) and gregarious behaviour (B) based on 1000 replicates of simulated

character history using a Markov model.

CHAPTER 6 – CONCLUSIONS

The information presented here augments our knowledge of oviraptorosaur anatomy, and provides a foundation upon which future synthetic work can build. I have performed some of the first steps towards those analyses here, and I make preliminary comments on the diversity, growth, behaviour, ecology, and evolution of Oviraptorosauria.

I have described new avimimid specimens (Chapter 2) that include relatively complete skeletons and elements of the cranium, which fill in some of the gaps in our picture of these unusual animals. Material collected from a monodominant bonebed in Mongolia pertain to a new species, *Avimimus nemegtensis* Funston et al. 2018, distinguished from *Avimimus portentosus* Kurzanov 1981 by the cranium and pelvis. These results refute the hypothesis that all avimimid specimens are referable to the same taxon, and call into question biostratigraphic analyses relying on this tenet. A second bonebed in China consists of less complete material, and osteohistological analysis shows that both juveniles and adults flocked together. The osteohistological analyses show that fusion of the tibiotarsus—and presumably other bones of the skeleton—preceded skeletal maturity and is therefore an unreliable indicator of adulthood. These findings are major advances in the study of avimimids, which have always been enigmatic. Furthermore, they provide direction for future work, showing that the diversity, growth, and behaviour of avimimids are more complex than previously recognized.

I describe dozens of new caenagnathid specimens (Chapter 3), which provide more information about these poorly-known creatures. A partial caenagnathid skeleton from the Dinosaur Park Formation is a keystone to untangling the complex taxonomy of North American caenagnathids. The specimen unites a mandible with postcranial material, which allows for confident referral of isolated specimens to *Chirostenotes pergracilis* Gilmore 1924. Furthermore,

by exclusion from this *Chirostenotes pergracilis*, I refer new material to either *Caenagnathus collinsi* Sternerg 1940 and *Leptorhynchos elegans* Parks (1933) based on body size. These referrals are supported by osteohistological analysis, which reveals mature individuals at three separate body sizes, achieved by variation in growth rate rather than growth period. This supports hypotheses that three taxa can be delineated in the Dinosaur Park Formation and elucidates which specimens are referable to which taxa. I name a new genus of small caenagnathid—*Apatoraptor pennatus* Funston and Currie 2016—based on material from the Horseshoe Canyon Formation, and I describe more material of *Elmisaurus rarus* Osmólska 1981 from Mongolia. A suite of specimens from indeterminate taxa are intriguing nonetheless, and hint at an exciting future in the study of caenagnathids. Osteohistology of the mandibles of caenagnathids shows that they are useful for skeletochronology but that previously suggested external estimators of maturity are inappropriate. In light of this, I discuss some new variations that may potentially reflect maturity and I refute the hypothesis that caenagnathids exhibited ontogenetic edentulism. Osteohistology shows that caenagnathids grew much like other theropods and reached sexual maturity by 4–6 years of age.

I also describe the historic types of several Mongolian oviraptorids (Chapter 4), taking into account new information on the anatomy of oviraptorosaurs. I describe two important new specimens of *Conchoraptor gracilis* Barsbold 1986, revealing the cranium and postcranium in more detail. A mandible preserved with one of these specimens shows the same bizarre morphology ascribed to the new taxon *Gobiraptor minutus* Lee et al. 2019, and shows that it is a junior synonym of *Conchoraptor gracilis*. An unusual skull from Zamyn Khondt expands the diversity and functional morphology of oviraptorids in being adapted for a strong, crushing bite. I describe the osteology of *Rinchenia mongoliensis* Barsbold 1997 in detail for the first time,

unveiling a suite of unusual characters. I also discuss a spectacular block of poached oviraptorid skeletons that represents a new taxon, which is also known from less complete specimens from the Nemegt Formation exposed at Bugiin Tsav and Guriliin Tsav. Together, they comprise almost every bone from the skeleton, providing an unparalleled glimpse of oviraptorid anatomy. Unusually, the cranial crest is domed and incorporates the nasals, frontals, and parietals. Even more bizarre, the manus has only two functional digits, of which the first is nearly double the size of the second. The historic and new specimens strongly support conclusions of high species richness in Mongolian oviraptorids, and show variation that cannot be explained by ontogeny or allometry. Growth series of the Guriliin Tsav oviraptorid, alongside the new specimens of *Conchoraptor gracilis*, elucidate the changes in the skeleton throughout ontogeny, both in the cranium and postcranium. Specifically, these specimens show that cranial crests are positively allometric, but are present early in ontogeny, and their absence in embryonic oviraptorids is useful for taxonomy. Oviraptorids were similar to caenagnathids in terms of growth style and longevity.

The new assemblages of avimimids and oviraptorids provide information on their gregarious behaviour (Chapter 5), specifically the prevalence of flocking throughout their ontogeny and their phylogeny. Whereas avimimids formed mixed-age flocks, oviraptorids probably engaged in age-segregation, but both juveniles and adults apparently formed their own groups. Curiously, all evidence of gregarious behaviour in oviraptorids comes from Heyuanninae, but it is likely it was more widespread than currently recognized. Using the abundance of oviraptorids and other dinosaurs in the Nemegt Basin of western Mongolia, I perform an analysis of community ecology (Chapter 5), and show that oviraptorosaur families were adapted for different environments. Despite their diversity, oviraptorids in the Nemegt

Basin may not have needed to partition niches, as shown by the distribution of *Conchoraptor gracilis*.

Building on the information provided by the new specimens, I comprehensively revise the phylogeny of Oviraptorosauria (Chapter 5), resulting in unprecedented clarity in their relationships. This new framework allows me to characterize the biogeography, body size, digit reduction, and gregarious behaviour of oviraptorosaurs throughout their evolution for the first time. Range expansion played a major role in their diversification and evolution. Migration into North America led to the radiation of caenagnathids, and allowed for a drastic increase in the breadth of body sizes. In contrast, dispersal between basins in Southern China and the Western Gobi led to the divergence of heyuannines and citipatines, probably as a result of environmental differences. In the Western Gobi, heyuannines diversified and gradually reduced the lateral digits of the manus, culminating in the two functional fingers of the Guriliin Tsav oviraptorid. Digit reduction and gregarious behaviour are both strongly linked to biogeography, which suggests that they may have been adaptations for the harsh environments of the Western Gobi Desert in the Late Cretaceous of Mongolia.

The thesis therefore provides a significant contribution to our understanding of oviraptorosaurs, especially their taxonomy (Table 6.1), anatomy, growth, and their evolution. Nonetheless, numerous challenges remain, particularly regarding the taxonomy of caenagnathids, the behaviour of oviraptorids, and the evolution of growth styles throughout the group. Each of these issues is a promising candidate for successful research, and—if the recent explosion of oviraptorosaur diversity is any indication—numerous other avenues will continue to open for exploration.

Table 6.1 Current state of taxonomy of oviraptorosaur taxa examined.

Clade	Family	Genus	Species	Authority	Holotype	Referred specimens	Skeletal representation
Edentoraptora			nemegtensis	Funston et al. 2018	MPC-D 102/81	MPC-D 102/15–100	Partial skull and postcrania
						TMP 1985.043.0070,	Mandible foot pelvis
						TMP 1990.056.0006, TMP 1992.036.1237, TMP 1993.036.0181, TMP 2001.012.0012, TMP 2002.012.0103, UALVP 59400	
						TMP 1979.014.0001, TMP 1982.019.0222, TMP 1986.036.0323, TMP 1993.036.0197, TMP 1993.036.0198, TMP 1993.036.475, TMP 1993.036.0631, TMP 1993.075.0049, TMP 2009.003.0029, UALVP 55727, UALVP 56638, UALVP 59791	caudal vertebra, manual unguals, ilium, pubis, femur, astragalocalcaneum, metatarsals
						MPC-D 102/006–008	Frontal, vertebrae, pubis, ischium, femur, tibia, ilium, tibia, sacral vertebra,
						TMP 1979.008.0622, TMP 1981.023.0034–5 + 39, TMP 1982.016.0006, TMP 1984.163.0036, TMP 1986.036.0186, TMP 1988.036.0104, TMP 1992.036.0674, TMP 1992.040.0044, TMP 1993.036.0630, TMP 1994.012.0880, TMP 1996.012.0141, TMP 2005.049.0190, UALVP 55585, UALVP 55639, UALVP 59606	
		Nomingia	*gobiensis*	Barsbold et al. 2000	MPC-D 100/119	None	Partial postcranial skeleton
		Apatoraptor	*pennatus*	Funston and Currie 2016	TMP 1993.051.0001	None	Mandible and partial articulated postcranial skeleton
		Heyuannia				NatGeo.2018.0036, MPC-D 102/03	articulated postcranial skeleton
		Unnamed	Dzamyn Khondt	In preparation	MPC-D 100/79-D	None	Skull
		Unnamed	Gurilin Tsav	In preparation	MPC-D 102/110	MPC-D 102/11, MPC-D 102/12, MPC-D 100/32	Complete skeleton

LITERATURE CITED

Alexander, R. D. 1974. The evolution of social behavior. Annual Review of Ecology and Systematics 5:325–383.

Arbour, V. M., P. J. Currie, and D. Badamgarav. 2014. The ankylosaurid dinosaurs of the Upper Cretaceous Baruungoyot and Nemegt formations of Mongolia: Ankylosaurids from Mongolia. Zoological Journal of the Linnean Society 172:631–652.

Averianov, A. O., and H.-D. Sues. 2012. Correlation of Late Cretaceous continental vertebrate assemblages in Middle and Central Asia. Journal of Stratigraphy 36:462–485.

Bailleul, A. M., J. B. Scannella, J. R. Horner, and D. C. Evans. 2016a. Fusion patterns in the skulls of modern archosaurs reveal that sutures are ambiguous maturity indicators for the Dinosauria. PloS One 11:e0147687.

Bailleul, A. M., C. Nyssen-Behets, B. Lengelé, B. K. Hall, and J. R. Horner. 2016b. Chondroid bone in dinosaur embryos and nestlings (Ornithischia: Hadrosauridae): Insights into the growth of the skull and the evolution of skeletal tissues. Comptes Rendus Palevol 15:49–64.

Balanoff, A. M., and M. A. Norell. 2012. Osteology of *Khaan mckennai* (Oviraptorosauria: Theropoda). Bulletin of the American Museum of Natural History 372:1–77.

Balanoff, A. M., G. S. Bever, and M. A. Norell. 2014. Reconsidering the Avian Nature of the Oviraptorosaur Brain (Dinosauria: Theropoda). PLoS ONE 9:e113559.

Balanoff, A. M., G. S. Bever, T. B. Rowe, and M. A. Norell. 2013. Evolutionary origins of the avian brain. Nature 501:93–96.

Balanoff, A. M., M. A. Norell, A. V. C. Hogan, and G. S. Bever. 2018. The Endocranial Cavity
of Oviraptorosaur Dinosaurs and the Increasingly Complex, Deep History of the Avian
Brain. Brain, Behavior and Evolution 91:125–135.

Balanoff, A. M., X. Xu, Y. Kobayashi, Y. Matsufune, and M. A. Norell. 2009. Cranial Osteology
of the Theropod Dinosaur *Incisivosaurus gauthieri* (Theropoda: Oviraptorosauria).
American Museum Novitates 3651:1–35.

Barrett, P. M. 2005. The diet of ostrich dinosaurs (Theropoda: Ornithomimosauria).
Palaeontology 48:347–358.

Barsbold, R. 1976a. A new Late Cretaceous Family of Small Theropods (Oviraptoridae n. fam.)
in Mongolia. Doklady Akademii Nauk SSSR 226:685–688.

Barsbold, R. 1976b. On the evolution and systematics of the late Mesozoic carnivorous dinosaurs
[in Russian]. Paleontologiâ i biostratigrafiâ Mongolii. Trudy, Sovmestnaâ
Sovetsko−Mongol'skaâ paleontologičeskaâ èkspediciâ 3:68–75.

Barsbold, R. 1977. Kineticism and peculiarities in the maxillary structure of oviraptorids
(Theropoda, Saurischia). Transactions of the Joint Soviet Mongolian Paleontological
Expedition 4:37–47.

Barsbold, R. 1981. Toothless Dinosaurs of Mongolia. Transactions of the Joint Soviet Mongolian
Paleontological Expedition 15:28–39.

Barsbold, R. 1983. Carnivorous dinosaurs from the Cretaceous of Mongolia. Transactions of the
Joint Soviet Mongolian Paleontological Expedition 19:5–117.

Barsbold, R. 1986. The predatory dinosaurs - Oviraptors; pp. 210–223 in Herpetologische
Untersuchungen in der Mongolischen Volksrepublik. Academia Nauk SSSR.

Barsbold, R. 1988. The bony crest and helmet on the skull of predatory dinosaurs—oviraptors. Transactions of the Joint Soviet Mongolian Paleontological Expedition 34:77–80.

Barsbold, R. 1997. Oviraptorosauria; pp. 505–508 in P. J. Currie and K. Padian (eds.), Encyclopedia of Dinosaurs. Academic Press, Oxford, UK.

Barsbold, R., H. Osmólska, M. Watabe, P. J. Currie, and K. Tsogtbaatar. 2000a. A new oviraptorosaur (Dinosauria, Theropoda) from Mongolia: the first dinosaur with a pygostyle. Acta Palaeontologica Polonica 45:97–106.

Barsbold, R., P. J. Currie, N. P. Myhrvold, H. Osmólska, K. Tsogtbaatar, and M. Watabe. 2000b. A pygostyle from a non-avian theropod. Nature 403:155–156.

Beauchamp, G. 1999. The evolution of communal roosting in birds: Origins and secondary losses. Behavioral Ecology 10:675–687.

Beauchamp, G. 2015. Animal Vigilance: Monitoring Predators and Competitors. Academic Press, London, pp.

Beecher, R. M. 1977. Function and fusion at the mandibular symphysis. American Journal of Physical Anthropology 47:325–335.

Behrensmeyer, A. K. 1978. Taphonomic and ecologic information from bone weathering. Paleobiology 4:150–162.

Bell, P. R., P. J. Currie, and D. A. Russell. 2015. Large caenagnathids (Dinosauria, Oviraptorosauria) from the uppermost Cretaceous of western Canada. Cretaceous Research 52:101–107.

Bell, P. R., D. C. Evans, D. A. Eberth, F. Fanti, Kh. Tsogtbaatar, and M. J. Ryan. 2018. Sedimentological and taphonomic observations on the "Dragon's Tomb" *Saurolophus*

(Hadrosauridae) bonebed, Nemegt Formation (Upper Cretaceous), Mongolia. Palaeogeography, Palaeoclimatology, Palaeoecology 494:75–90.

Benner, E., T. M. Cullen, and D. C. Evans. 2016. Morphological and histological analysis of a new large-bodied caenagnathid specimen (Theropoda: Oviraptorosauria) from the Hell Creek Formation (Montana). Vertebrate Anatomy Morphology Palaeontology CSVP 2016 Abstracts:9.

Bertram, B. C. R. 1980. Vigilance and Group size in Ostriches. Animal Behaviour 28:278–286.

Bonnetti, C., F. Malartre, V. Huault, M. Cuney, S. Bourlange, X. Liu, and Y. Peng. 2014. Sedimentology, stratigraphy and palynological occurrences of the Late Cretaceous Erlian Formation, Erlian Basin, Inner Mongolia, People's Republic of China. Cretaceous Research 48:177–192.

Botha-Brink, J., D. Codron, A. K. Huttenlocker, K. D. Angielczyk, and M. Ruta. 2016. Breeding Young as a Survival Strategy during Earth's Greatest Mass Extinction. Scientific Reports 6.

Bray, J. R., and J. T. Curtis. 1957. An ordination of upland forest communities of southern Wisconsin. Ecological Monographs 27:325–349.

Britt, B. B. 1993. Pneumatic postcranial bones in dinosaurs and other archosaurs. Ph.D. Dissertation, University of Calgary, Calgary, 393 pp.

Britt, B. B., D. a. Eberth, R. D. Scheetz, B. W. Greenhalgh, and K. L. Stadtman. 2009. Taphonomy of debris-flow hosted dinosaur bonebeds at Dalton Wells, Utah (Lower Cretaceous, Cedar Mountain Formation, USA). Palaeogeography, Palaeoclimatology, Palaeoecology 280:1–22.

Brochu, C. A. 1996. Closure of neurocentral sutures during crocodilian ontogeny: implications for maturity assessment in fossil archosaurs. Journal of Vertebrate Paleontology 16:49–62.

Brochu, C. A. 2003. Osteology of *Tyrannosaurus rex*: Insights from a nearly complete skeleton and high-resolution computed tomographic analysis of the skull. Journal of Vertebrate Paleontology 22:1–138.

Bromage, T. G., R. S. Lacruz, R. Hogg, H. M. Goldman, S. C. McFarlin, J. Warshaw, W. Dirks, A. Perez-Ochoa, I. Smolyar, D. H. Enlow, and A. Boyde. 2009. Lamellar Bone is an Incremental Tissue Reconciling Enamel Rhythms, Body Size, and Organismal Life History. Calcified Tissue International 84:388–404.

Brown, C. M., D. C. Evans, N. E. Campione, L. J. O'Brien, and D. A. Eberth. 2013. Evidence for taphonomic size bias in the Dinosaur Park Formation (Campanian, Alberta), a model Mesozoic terrestrial alluvial-paralic system. Palaeogeography, Palaeoclimatology, Palaeoecology 372:108–122.

Brown, J. S. 1999. Vigilance, patch use and habitat selection: Foraging under predation risk. Evolutionary Ecology Research 1:49–71.

Brusatte, S. L., M. J. Benton, M. Ruta, and G. T. Lloyd. 2008. Superiority, competition, and opportunism in the evolutionary radiation of dinosaurs. Science 321:1485–1488.

Cameron, E. Z., and J. T. Du Toit. 2005. Social influences on vigilance behaviour in giraffes, *Giraffa camelopardalis*. Animal Behaviour 69:1337–1344.

Campione, N. E., D. C. Evans, C. M. Brown, and M. T. Carrano. 2014. Body mass estimation in non-avian bipeds using a theoretical conversion to quadruped stylopodial proportions. Methods in Ecology and Evolution 5:913–923.

Castanet, J., S. Croci, F. Aujard, M. Perret, J. Cubo, and E. de Margerie. 2004. Lines of arrested growth in bone and age estimation in a small primate: *Microcebus murinus*. Journal of Zoology 263:31–39.

Chatterjee, S. 1991. Cranial anatomy and relationships of a new Triassic bird from Texas. Philosophical Transactions of the Royal Society of London. Series B: Biological Sciences 332:277–346.

Chiappe, L. M., J. Shu'An, J. Qiang, and M. A. Norell. 1999. Anatomy and Systematics of the Confuciusornithidae (Theropoda: Aves) from the Late Mesozoic of Northeastern China. Bulletin of the American Museum of Natural History 242:1–89.

Childress, M. J., and M. A. Lung. 2003. Predation risk, gender and the group size effect: does elk vigilance depend upon the behaviour of conspecifics? Animal Behaviour 66:389–398.

Clark, J. M., M. Norell, and L. M. Chiappe. 1999. An oviraptorid skeleton from the late Cretaceous of Ukhaa Tolgod, Mongolia, preserved in an avianlike brooding position over an oviraptorid nest. American Museum Novitates 3265:1–36.

Clark, J. M., M. A. Norell, and R. Barsbold. 2001. Two new oviraptorids (Theropoda: Oviraptorosauria), Upper Cretaceous Djadokhta Formation, Ukhaa Tolgod, Mongolia. Journal of Vertebrate Paleontology 21:209–213.

Clark, J. M., M. A. Norell, and T. Rowe. 2002. Cranial anatomy of *Citipati osmolskae* (Theropoda, Oviraptorosauria), and a reinterpretation of the holotype of *Oviraptor philoceratops*. American Museum Novitates 1–24.

Cresswell, W. 1994. Flocking is an effective anti-predation strategy in redshanks, *Tringa totanus*. Animal Behaviour 47:433–442.

Cullen, T. M., D. C. Evans, M. J. Ryan, P. J. Currie, and Y. Kobayashi. 2014. Osteohistological variation in growth marks and osteocyte lacunar density in a theropod dinosaur (Coelurosauria: Ornithomimidae). BMC Evolutionary Biology 14:231.

Currie, P., G. Funston, and H. Osmolska. 2016a. New specimens of the crested theropod dinosaur *Elmisaurus rarus* from Mongolia. Acta Palaeontologica Polonica 61:143–157.

Currie, P. J., R. B. Holmes, M. J. Ryan, and C. Coy. 2016b. A juvenile chasmosaurine ceratopsid (Dinosauria, Ornithischia) from the Dinosaur Park Formation, Alberta, Canada. Journal of Vertebrate Paleontology 36:e1048348

Currie, P. J. 1987. Bird-like characteristics of the jaws and teeth of troodontid theropods (Dinosauria, Saurischia). Journal of Vertebrate Paleontology 7:72–81.

Currie, P. J. 1989. The first records of *Elmisaurus* (Saurischia, Theropoda) from North America. Canadian Journal of Earth Sciences 26:1319–1324.

Currie, P. J. 1992. Saurischian dinosaurs of the Late Cretaceous of Asia and North America; pp. in Aspects of Nonmarine Cretaceous Geology: International Symposium on Nonmarine Cretaceous Correlations. China Ocean Press, Beijing.

Currie, P. J. 1995. New information on the anatomy and relationships of *Dromaeosaurus albertensis* (Dinosauria: Theropoda). Journal of Vertebrate Paleontology 15:576–591.

Currie, P. J. 2003. Allometric growth in tyrannosaurids (Dinosauria: Theropoda) from the Upper Cretaceous of North America and Asia. Canadian Journal of Earth Sciences 40:651–665.

Currie, P. J. 2016. Dinosaur of the Gobi: Following in the footsteps of the Polish-Mongolian Expeditions. Paleontologica Polonica 67:83–100.

Currie, P. J., and D. A. Russell. 1988. Osteology and relationships of *Chirostenotes pergracilis* (Saurischia, Theropoda) from the Judith River (Oldman) Formation of Alberta, Canada. Canadian Journal of Earth Sciences 25:972–986.

Currie, P. J., and D. A. Eberth. 1993. Palaeontology, sedimentology and palaeoecology of the Iren Dabasu Formation (Upper Cretaceous), Inner Mongolia, People's Republic of China. Cretaceous Research 14:127–144.

Currie, P. J., and J.-H. Peng. 1993. A juvenile specimen of *Saurornithoides mongoliensis* from the Upper Cretaceous of northern China. Canadian Journal of Earth Sciences 30:2224–2230.

Currie, P. J., and Y. Azuma. 2006. New specimens, including a growth series, of *Fukuiraptor* (Dinosauria, Theropoda) from the Lower Cretaceous Kitadani Quarry of Japan. Journal of the Paleontological Society of Korea 22:173–193.

Currie, P. J., S. J. Godfrey, and L. Nessov. 1993. New caenagnathid (Dinosauria: Theropoda) specimens from the Upper Cretaceous of North America and Asia. Canadian Journal of Earth Sciences 30:2255–2272.

Currie, P. J., N. R. Longrich, M. J. Ryan, D. A. Eberth, and D. Badamgarav. 2008. A bonebed of *Avimimus* sp. (Dinosauria: Theropoda) from the Late Cretaceous Nemegt Formation, Gobi Desert: insights into social behaviour and development in a maniraptoran theropod. Journal of Vertebrate Paleontology 28:67A.

Dong, Z.-M., and P. J. Currie. 1996. On the discovery of an oviraptorid skeleton on a nest of eggs at Bayan Mandahu, Inner Mongolia, People's Republic of China. Canadian Journal of Earth Sciences 33:631–636.

Easter, J. 2013. A new name for the oviraptorid dinosaur *"Ingenia yanshini"* (Barsbold, 1981; preoccupied by Gerlach, 1957). Zootaxa 3737:184–190.

Eberth, D. A. 1990. Stratigraphy and sedimentology of vertebrate microfossil sites in the uppermost Judith River Formation (Campanian), Dinosaur Provincial Park, Alberta, Canada. Palaeogeography, Palaeoclimatology, Palaeoecology 78:1–36.

Eberth, D. A. 2015. Origins of dinosaur bonebeds in the Cretaceous of Alberta, Canada. Canadian Journal of Earth Sciences 52:655–681.

Eberth, D. A. 2018. Stratigraphy and paleoenvironmental evolution of the dinosaur-rich Baruungoyot-Nemegt succession (Upper Cretaceous), Nemegt Basin, southern Mongolia. Palaeogeography, Palaeoclimatology, Palaeoecology 494:29–50.

Eberth, D. a., and P. J. Currie. 2010. Stratigraphy, sedimentology, and taphonomy of the *Albertosaurus* bonebed (upper Horseshoe Canyon Formation; Maastrichtian), southern Alberta, Canada. Canadian Journal of Earth Sciences 47:1119–1143.

Eberth, D. A., and D. R. Braman. 2012. A revised stratigraphy and depositional history for the Horseshoe Canyon Formation (Upper Cretaceous), southern Alberta plains. Canadian Journal of Earth Sciences 49:1053–1086.

Eberth, D. A., M. Shannon, and B. G. Noland. 2007. A bonebeds database: classification, biases, and patterns of occurrence; pp. 102–220 in R. R. Rogers, D. A. Eberth, and A. R. Fiorillo (eds.), Bonebeds: genesis, analysis, and paleobiological significance. University of Chicago Press.

Eberth, D. A., D. Badamgarav, and P. J. Currie. 2009. The Baruungoyot-Nemegt Transition (Upper Cretaceous) at the Nemegt Type Area, Nemegt Basin, South Central Mongolia. Journal of the Paleontological Society of Korea 25:1–15.

Edington, G. H., and A. E. Miller. 1942. XII.—The Avian Ulna: Its Quill - Knobs. Proceedings of the Royal Society of Edinburgh. Section B. Biology 61:138–148.

Enlow, D. H. 1962. A Study of the Post-Natal Growth and Remodeling of Bone. American Journal of Anatomy 110:79–101.

Erickson, G. 2000. Growth curve of *Psittacosaurus mongoliensis* Osborn (Ceratopsia: Psittacosauridae) inferred from long bone histology. Zoological Journal of the Linnean Society 130:551–566.

Erickson, G. M., P. J. Currie, B. D. Inouye, and A. A. Winn. 2010. A revised life table and survivorship curve for *Albertosaurus sarcophagus* based on the Dry Island mass death assemblage. Canadian Journal of Earth Sciences 47:1269–1275.

Erickson, G. M., K. Curry Rogers, D. J. Varricchio, M. A. Norell, and X. Xu. 2007. Growth patterns in brooding dinosaurs reveals the timing of sexual maturity in non-avian dinosaurs and genesis of the avian condition. Biology Letters 3:558–561.

Evans, D. C., D. A. Eberth, and M. J. Ryan. 2015. Hadrosaurid (*Edmontosaurus*) bonebeds from the Horseshoe Canyon Formation (Horsethief Member) at Drumheller, Alberta, Canada: geology, preliminary taphonomy, and significance. Canadian Journal of Earth Sciences 52:642–654.

Fanti, F., P. J. Currie, and D. Badamgarav. 2012. New Specimens of *Nemegtomaia* from the Baruungoyot and Nemegt Formations (Late Cretaceous) of Mongolia. PLoS ONE 7:e31330.

Fanti, F., P. J. Currie, and M. E. Burns. 2015. Taphonomy, age, and paleoecological implication of a new *Pachyrhinosaurus* (Dinosauria: Ceratopsidae) bonebed from the Upper

Cretaceous (Campanian) Wapiti Formation of Alberta, Canada. Canadian Journal of Earth Sciences 52:1–36.

Fanti, F., L. Cantelli, and L. Angelicola. 2018a. High-resolution maps of Khulsan and Nemegt localities (Nemegt Basin, southern Mongolia): Stratigraphic implications. Palaeogeography, Palaeoclimatology, Palaeoecology 494:14–28.

Fanti, F., P. R. Bell, M. Tighe, L. A. Milan, and E. Dinelli. 2018b. Geochemical fingerprinting as a tool for repatriating poached dinosaur fossils in Mongolia: A case study for the Nemegt Locality, Gobi Desert. Palaeogeography, Palaeoclimatology, Palaeoecology 494:51–64.

Fastovsky, D. E., D. B. Weishampel, M. Watabe, R. Barsbold, Kh. Tsogtbaatar, and P. Narmandakh. 2011. A nest of *Protoceratops andrewsi* (Dinosauria, Ornithischia). Journal of Paleontology 85:1035–1041.

Funston, G. F., and P. J. Currie. 2014. A previously undescribed caenagnathid mandible from the late Campanian of Alberta, and insights into the diet of *Chirostenotes pergracilis* (Dinosauria: Oviraptorosauria). Canadian Journal of Earth Sciences 51:156–165.

Funston, G. F., and P. J. Currie. 2016. A new caenagnathid (Dinosauria: Oviraptorosauria) from the Horseshoe Canyon Formation of Alberta, Canada, and a reevaluation of the relationships of Caenagnathidae. Journal of Vertebrate Paleontology 36:e1160910.

Funston, G. F., and P. J. Currie. 2018. A small caenagnathid tibia from the Horseshoe Canyon Formation (Maastrichtian): Implications for growth and lifestyle in oviraptorosaurs. Cretaceous Research 92:220–230.

Funston, G. F., P. J. Currie, and M. Burns. 2016a. New elmisaurine specimens from North America and their relationship to the Mongolian *Elmisaurus rarus*. Acta Palaeontologica Polonica 61:159–173.

Funston, G. F., P. J. Currie, and C. Tsogtbaatar. 2017. A new oviraptorid (Dinosauria: Theropoda) provides a rare glimpse into social behaviour in dinosaurs. Journal of Vertebrate Paleontology Programs and Abstracts 2017:116.

Funston, G. F., W. S. Persons, G. J. Bradley, and P. J. Currie. 2015. New material of the large-bodied caenagnathid *Caenagnathus collinsi* from the Dinosaur Park Formation of Alberta, Canada. Cretaceous Research 54:179–187.

Funston, G. F., S. E. Mendonca, P. J. Currie, and R. Barsbold. 2018a. Oviraptorosaur anatomy, diversity and ecology in the Nemegt Basin. Palaeogeography, Palaeoclimatology, Palaeoecology.

Funston, G. F., S. E. Mendonca, P. J. Currie, and R. Barsbold. 2018b. A dinosaur community composition dataset for the Late Cretaceous Nemegt Basin of Mongolia. Data in Brief 16:660–666.

Funston, G. F., R. D. Wilkinson, D. J. Simon, A. R. H. LeBlanc, M. Wosik, and P. J. Currie. In Press. Histology of caenagnathid (Theropoda, Oviraptorosauria) dentaries and implications for development, ontogenetic edentulism, and taxonomy. The Anatomical Record.

Funston, G. F., P. J. Currie, D. A. Eberth, M. J. Ryan, T. Chinzorig, D. Badamgarav, and N. R. Longrich. 2016b. The first oviraptorosaur (Dinosauria: Theropoda) bonebed: evidence of gregarious behaviour in a maniraptoran theropod. Scientific Reports 6:35782.

Genbrugge, A., D. Adriaens, B. De Kegel, L. Brabant, L. Van Hoorebeke, J. Podos, J. Dirckx, P. Aerts, and A. Herrel. 2012. Structural tissue organization in the beak of Java and Darwin's finches. Journal of Anatomy 221:383–393.

Gilmore, C. W. 1924. A new coelurid dinosaur from the Belly River Cretaceous of Alberta. Canada Geological Survey Bulletin 38:1–12.

Gradziński, R. 1970. Sedimentation of dinosaur-bearing Upper Cretaceous deposits of the Nemegt basin, Gobi Desert. Palaeontologia Polonica 21:147–229.

Gradziński, R., and T. Jerzykiewicz. 1974. Sedimentation of the Barun Goyot Formation. Palaeontologica Polonica 30:111–146.

Gradziński, R., Z. Kielan-Jaworowska, and T. Maryańska. 1977. Upper Cretaceous Djadokhta, Barun Goyot and Nemegt formations of Mongolia, including remarks on previous subdivisions. Acta Geologica Polonica 27:281–318.

Granger, W., and C. P. Berkey. 1922. Discovery of Cretaceous and older Tertiary strata in Mongolia. American Museum Novitates 42:1–7.

He, T., X.-L. Wang, and Z.-H. Zhou. 2008. A new genus and species of caudipterid dinosaur from the Lower Cretaceous Jiufotang Formation of Western Liaoning, China. Vertebrata PalAsiatica 46:178–189.

Hedrick, B. P., C. Gao, A. R. Tumarkin-Deratzian, C. Shen, J. L. Holloway, F. Zhang, K. D. Hankenson, S. Liu, J. Anné, and P. Dodson. 2016. An Injured *Psittacosaurus* (Dinosauria: Ceratopsia) From the Yixian Formation (Liaoning, China): Implications for *Psittacosaurus* Biology: Psittacosaurus Fibular Fracture. The Anatomical Record 299:897–906.

Hone, D. W. E., A. A. Farke, M. Watabe, S. Shigeru, and K. Tsogtbaatar. 2014. A New Mass Mortality of Juvenile *Protoceratops* and Size-Segregated Aggregation Behaviour in Juvenile Non-Avian Dinosaurs. PLoS ONE 9:e113306.

Horner, J. R., A. De Ricqlès, and K. Padian. 2000. Long bone histology of the hadrosaurid dinosaur *Maiasaura peeblesorum* : growth dynamics and physiology based on an ontogenetic series of skeletal elements. Journal of Vertebrate Paleontology 20:115–129.

Horner, J. R., H. N. Woodward, and A. M. Bailleul. 2016. Mineralized tissues in dinosaurs interpreted as having formed through metaplasia: A preliminary evaluation. Comptes Rendus Palevol 15:176–196.

Hou, L., Z. Zhonghe, L. D. Martin, and A. Feduccia. 1995. A beaked bird from the Jurassic of China. Nature 377:616–618.

Hunter, and Skinner. 1998. Vigilance Behaviour in African Ungulates: The Role of Predation Pressure. Behaviour 135:195–211.

Hutchinson, J. 2001. The evolution of pelvic osteology and soft tissues on the line to extant birds (Neornithes). Zoological Journal of the Linnean Society 131:123–168.

Ingolfsson, A. 1970. The moult of remiges and retrices in Great Black-backed Gulls *Larus marinus* and Glaucous Gulls *L. hyperboreus* in Iceland. Ibis 112:83–92.

Jerzykiewicz, T. 1998. Okavango Oasis, Kalahari Desert: A contemporary analogue for the Late Cretaceous vertebrate habitat of the Gobi Basin, Mongolia. Geoscience Canada 25:15–26.

Jerzykiewicz, T., and D. A. Russell. 1991. Late Mesozoic stratigraphy and vertebrates of the Gobi Basin. Cretaceous Research 12:345–377.

Jollie, M. T. 1957. The head skeleton of the chicken and remarks on the anatomy of this region in other birds. Journal of Morphology 100:389–436.

Kidwell, S. M. 2001. Preservation of species abundance in marine death assemblages. Science 294:1091–1094.

Kidwell, S. M., and K. W. Flessa. 1995. The quality of the fossil record: populations, species, and communities. Annual Review of Ecology and Systematics 26:269–299.

Kirkland, J. I., and D. G. Wolfe. 2001. First definitive therizinosaurid (Dinosauria; Theropoda) from North America. Journal of Vertebrate Paleontology 21:410–414.

Kirkland, J. I., L. E. Zanno, S. D. Sampson, J. M. Clark, and D. D. DeBlieux. 2005. A primitive therizinosauroid dinosaur from the Early Cretaceous of Utah. Nature 435:85–87.

Kobayashi, Y., and J.-C. Lü. 2003. A new ornithomimid dinosaur with gregarious habits from the Late Cretaceous of China. Acta Palaeontologica Polonica 48:235–259.

Kobayashi, Y., and R. Barsbold. 2005. Reexamination of a primitive ornithomimosaur, *Garudimimus brevipes* Barsbold, 1981 (Dinosauria: Theropoda), from the Late Cretaceous of Mongolia. Canadian Journal of Earth Sciences 42:1501–1521.

Köhler, M., N. Marín-Moratalla, X. Jordana, and R. Aanes. 2012. Seasonal bone growth and physiology in endotherms shed light on dinosaur physiology. Nature 487:358–361.

Kundrát, M. 2007. Avian-like attributes of a virtual brain model of the oviraptorid theropod *Conchoraptor gracilis*. Naturwissenschaften 94:499–504.

Kundrát, M., and J. Janáček. 2007. Cranial pneumatization and auditory perceptions of the oviraptorid dinosaur *Conchoraptor gracilis* (Theropoda, Maniraptora) from the Late Cretaceous of Mongolia. Naturwissenschaften 94:769–778.

Kurzanov, S. M. 1981a. An unusual theropod from the Upper Cretaceous of Mongolia. Transactions of the Joint Soviet Mongolian Paleontological Expedition 15:39–49.

Kurzanov, S. M. 1981b. An unusual theropod from the Upper Cretaceous of Mongolia. Joint Soviet Mongolian Paleontological Expedition 15:39–49.

Kurzanov, S. M. 1982. Structural characteristics of the forelimbs of *Avimimus*. Paleontological Journal 3:108–112 [In Russian].

Kurzanov, S. M. 1983a. New Data on the Pelvic Structure of Avimimus. Paleontological Journal 4:115–116 [In Russian].

Kurzanov, S. M. 1983b. New data on the pelvic structure of *Avimimus*. Paleontological Journal 4:115–116 [In Russian].

Kurzanov, S. M. 1985. The skull structure of the dinosaur *Avimimus*. Paleontological Journal 4:81–89 [In Russian].

Kurzanov, S. M. 1987. Avimimidae and the problem of the origin of birds. Transactions of the Joint Soviet Mongolian Paleontological Expedition 31:1–92.

Lamanna, M. C., H.-D. Sues, E. R. Schachner, and T. R. Lyson. 2014. A New Large-Bodied Oviraptorosaurian Theropod Dinosaur from the Latest Cretaceous of Western North America. PLoS ONE 9:e92022.

LeBlanc, A. R. H., D. O. Lamoureux, and M. W. Caldwell. 2017a. Mosasaurs and snakes have a periodontal ligament: timing and extent of calcification, not tissue complexity, determines tooth attachment mode in reptiles. Journal of Anatomy 231:869–885.

LeBlanc, A. R. H., K. S. Brink, T. M. Cullen, and R. R. Reisz. 2017b. Evolutionary implications of tooth attachment versus tooth implantation: A case study using dinosaur, crocodilian, and mammal teeth. Journal of Vertebrate Paleontology 37:e1354006.

Lee, A. H., and S. Werning. 2008. Sexual maturity in growing dinosaurs does not fit reptilian growth models. Proceedings of the National Academy of Sciences 105:582–587.

Lee, S., Y.-N. Lee, A. Chinsamy, J. Lü, R. Barsbold, and K. Tsogtbaatar. 2019. A new baby

    oviraptorid dinosaur (Dinosauria: Theropoda) from the Upper Cretaceous Nemegt

    Formation of Mongolia. PLOS ONE 14:e0210867.

Lemon, J. 2006. Plotrix: a package in the red light district of R. R-News 6:8–12.

Longrich, N. R., P. J. Currie, and D. Zhi-Ming. 2010. A new oviraptorid (Dinosauria:

    Theropoda) from the Upper Cretaceous of Bayan Mandahu, Inner Mongolia.

    Palaeontology 53:945–960.

Longrich, N. R., K. Barnes, S. Clark, and L. Millar. 2013. Caenagnathidae from the Upper

    Campanian Aguja Formation of West Texas, and a Revision of the Caenagnathinae.

    Bulletin of the Peabody Museum of Natural History 54:23–49.

Lü, J. 2003. A new oviraptorosaurid (Theropoda: Oviraptorosauria) from the Late Cretaceous of

    southern China. Journal of Vertebrate Paleontology 22:871–875.

Lü, J., Y. Tomida, Y. Azuma, Z.-M. Dong, and Y.-N. Lee. 2004. New oviraptorid dinosaur

    (Dinosauria: Oviraptorosauria) from the Nemegt Formation of Southwestern Mongolia.

    Bulletin of the National Science Museum of Tokyo Series C 30:95–130.

Lü, J., R. Chen, S. L. Brusatte, Y. Zhu, and C. Shen. 2016. A Late Cretaceous diversification of

    Asian oviraptorid dinosaurs: evidence from a new species preserved in an unusual

    posture. Scientific Reports 6:35780.

Lü, J., P. J. Currie, L. Xu, X. Zhang, H. Pu, and S. Jia. 2013. Chicken-sized oviraptorid dinosaurs

    from central China and their ontogenetic implications. Naturwissenschaften 100:165–

    175.

Lü, J., G. Li, M. Kundrát, Y.-N. Lee, Z. Sun, Y. Kobayashi, C. Shen, F. Teng, and H. Liu. 2017. High diversity of the Ganzhou Oviraptorid Fauna increased by a new "cassowary-like" crested species. Scientific Reports 7.

Ma, W., J. Wang, M. Pittman, Q. Tan, L. Tan, B. Guo, and X. Xu. 2017. Functional anatomy of a giant toothless mandible from a bird-like dinosaur: *Gigantoraptor* and the evolution of the oviraptorosaurian jaw. Scientific Reports 7.

Makovicky, P. J. 2008. Telling time from fossils: a phylogeny-based approach to chronological ordering of paleobiotas. Cladistics 24:350–371.

Makovicky, P. J., and H.-D. Sues. 1998. Anatomy and phylogenetic relationships of the theropod dinosaur *Microvenator celer* from the Lower Cretaceous of Montana. American Museum Novitates 3240:1–27.

Maryanska, T., and H. Osmólska. 1997. The quadrate of oviraptorid dinosaurs. Acta Palaeontologica Polonica 42:361–371.

Maryanska, T., H. Osmólska, and M. Wolsan. 2002. Avialan status for Oviraptorosauria. Acta Palaeontologica Polonica 47.

Maxwell, E. E. 2009. Comparative ossification and development of the skull in palaeognathous birds (Aves: Palaeognathae). Zoological Journal of the Linnean Society 156:184–200.

Maxwell, W. D., and J. H. Ostrom. 1995. Taphonomy and paleobiological implications of *Tenontosaurus-Deinonychus* associations. Journal of Vertebrate Paleontology 15:707–712.

Mina, M. 2001. Regulation of Mandibular Growth and Morphogenesis. Critical Reviews in Oral Biology & Medicine 12:276–300.

Morris, F. K. 1936. Central Asia in Cretaceous time. Bulletin of the Geological Society of America 47:1477–1534.

Norell, M. A., and P. J. Makovicky. 1997. Important features of the dromaeosaur skeleton: information from a new specimen. American Museum Novitates 3215:1–28.

Norell, M. A., and P. J. Makovicky. 1999. Important features of the dromaeosaurid skeleton II: Information from newly collected specimens of *Velociraptor mongoliensis*. American Museum Novitates 3282:1–45.

Norell, M. A., J. M. Clark, and L. M. Chiappe. 2001. An Embryonic Oviraptorid (Dinosauria: Theropoda) from the Upper Cretaceous of Mongolia. American Museum Novitates 3315:1–20.

Norell, M. A., J. M. Clark, L. M. Chiappe, and D. Dashzeveg. 1995. A nesting dinosaur. Nature 378:774–776.

Norell, M. A., A. M. Balanoff, D. E. Barta, and G. M. Erickson. 2018. A Second Specimen of *Citipati Osmolskae* Associated With a Nest of Eggs from Ukhaa Tolgod, Omnogov Aimag, Mongolia. American Museum Novitates 3899:1–44.

Norell, M. A., J. M. Clark, D. Demberelyin, B. Rhinchen, L. M. Chiappe, A. R. Davidson, M. C. McKenna, P. Altangerel, and M. J. Novacek. 1994. A Theropod Dinosaur Embryo and the Affnities of the Flaming Cliffs Dinosaur Eggs. Science, New Series 266:779–782.

Norman, D. B. 1990. Problematic Theropoda: "Coelurosaurs"; pp. 280–305 in D. B. Weishampel, P. Dodson, and H. Osmólska (eds.), The Dinosauria, 1st ed. University of California Press, Berkeley.

O'Connor, J., G. M. Erickson, M. Norell, A. M. Bailleul, H. Hu, and Z. Zhou. 2018. Medullary bone in an Early Cretaceous enantiornithine bird and discussion regarding its identification in fossils. Nature Communications 9.

O'Connor, P. M. 2006. Postcranial pneumaticity: An evaluation of soft-tissue influences on the postcranial skeleton and the reconstruction of pulmonary anatomy in archosaurs. Journal of Morphology 267:1199–1226.

Oksanen, J., G. Blanchet, M. Friendly, R. Kindt, P. Legendre, D. McGlinn, P. R. Minchin, R. B. O'Hara, G. L. Simpson, P. Solymos, M. H. H. Stevens, E. Szoecs, and H. Wagner. 2017. Vegan: Community Ecology Package. pp.

Ortega, F., F. Escaso, and J. L. Sanz. 2010. A bizarre, humped Carcharodontosauria (Theropoda) from the Lower Cretaceous of Spain. Nature 467:203–206.

Osborn, H. F. 1924. Three new theropoda, *Protoceratops* zone, central Mongolia. American Museum Novitates 144:1–12.

Osmólska, H. 1976. New light on the skull anatomy and systematic position of *Oviraptor*. Nature 262:683–684.

Osmólska, H. 1981. Coossified tarsometatarsi in theropod dinosaurs and their bearing on the problem of bird origins. Palaeontologia Polonica 42:79–95.

Osmólska, H. 1996. An unusual theropod dinosaur from the Late Cretaceous Nemegt Formation of Mongolia. Acta Palaeontologica Polonica 41:1–38.

Osmólska, H. 2004. Evidence on relation of brain to endocranial cavity in oviraptorid dinosaurs. Acta Palaeontologica Polonica 49.

Osmólska, H., P. J. Currie, and R. Barsbold. 2004. Oviraptorosauria; pp. 165–183 in D. B. Weishampel, P. Dodson, and H. Osmólska (eds.), The Dinosauria, 2nd ed. University of California Press, Berkeley, California.

Ostrom, J. H. 1969. Osteology of *Deinonychus Antirrhopus*, an Unusual Theropod from the Lower Cretaceous of Montana. Bulletin 30 of the Peabody Museum of Natural History, Yale University, New Haven, Connecticut, 172 pp.

Owocki, K., B. Kremer, M. Cotte, and H. Bocherens. 2019. Diet preferences and climate inferred from oxygen and carbon isotopes of tooth enamel of *Tarbosaurus bataar* (Nemegt Formation, Upper Cretaceous, Mongolia). Palaeogeography, Palaeoclimatology, Palaeoecology 109190.

Padian, K., and E.-T. Lamm. 2013. Bone Histology of Fossil Tetrapods: Advancing Methods, Analysis, and Interpretation. University of California Press, Berkeley, 285 pp.

Parks, W. A. 1933. New species of dinosaurs and turtles from the Upper Cretaceous Formations of Alberta. University of Toronto Studies Geological Series 34:1–24.

Patterson, C. 1982. Morphological Characters and Homology; pp. 21–74 in K. A. Joysey and A. E. Friday (eds.), Problems of Phylogenetic Reconstruction. vol. Systematics Association Special Volume No. 21. Academic Press, London and New York.

Pei-ji, C. 1987. Cretaceous paleogeography in China. Palaeogeography, Palaeoclimatology, Palaeoecology 59:49–56.

Pu, H., D. K. Zelenitsky, J. Lü, P. J. Currie, K. Carpenter, L. Xu, E. B. Koppelhus, S. Jia, L. Xiao, H. Chuang, T. Li, M. Kundrát, and C. Shen. 2017. Perinate and eggs of a giant caenagnathid dinosaur from the Late Cretaceous of central China. Nature Communications 8:14952.

Qiang, J., P. J. Currie, M. A. Norell, and J. Shu-An. 1998. Two feathered dinosaurs from
    northeastern China. Nature 393:753–761.

Revell, L. J. 2012. phytools: an R package for phylogenetic comparative biology (and other
    things): phytools: R package. Methods in Ecology and Evolution 3:217–223.

Richner, H., and P. Heeb. 1996. Communal life: honest signaling and the recruitment center
    hypothesis. Behavioral Ecology 7:115–119.

Roach, B. T., and D. L. Brinkman. 2007. A Reevaluation of Cooperative Pack Hunting and
    Gregariousness in *Deinonychus antirrhopus* and Other Nonavian Theropod Dinosaurs.
    Bulletin of the Peabody Museum of Natural History 48:103–138.

Roberts, G. 1996. Why individual vigilance declines as group size increases. Animal Behaviour
    51:1077–1086.

Romer, A. S. 1923. The ilium in dinosaurs and birds. Bulletin of the AMNH; v. 48, article 5. .

Ryan, M. J., P. J. Currie, and A. P. Russell. 2001a. New material of *Avimimus portentosus* from
    the Iren Dabasu Formation (Upper Cretaceous) of the Erenhot region of Inner Mongolia.
    Journal of Vertebrate Paleontology 21:95A.

Ryan, M. J., A. P. Russell, D. a. Eberth, and P. J. Currie. 2001b. The Taphonomy of a
    Centrosaurus (Ornithischia: Certopsidae) Bone Bed from the Dinosaur Park Formation
    (Upper Campanian), Alberta, Canada, with Comments on Cranial Ontogeny. Palaios
    16:482–506.

Ryan, M. J., D. C. Evans, P. R. Bell, K. Tsogtbaatar, and D. Badamgarav. 2011. Taphonomy of
    the "Dragon's Tomb" *Saurolophus* (Dinosauria: Hadrosauridae) Bonebed, Nemegt
    Formation (Late Cretaceous), Mongolia. Journal of Vertebrate Paleontology 31:183A.

Sato, T. 2005. A pair of shelled eggs inside a female dinosaur. Science 308: 375–375.

Scott, J. E., A. S. Hogue, and M. J. Ravosa. 2012. The adaptive significance of mandibular
symphyseal fusion in mammals: Diet and mandibular symphyseal fusion. Journal of
Evolutionary Biology 25:661–673.

Senter, P. 2005. Function in the stunted forelimbs of *Mononykus olecranus* (Theropoda), a
dinosaurian anteater. Paleobiology 31:373–381.

Senter, P. 2007. A new look at the phylogeny of coelurosauria (Dlnosauria: Theropoda). Journal
of Systematic Palaeontology 5:429–463.

Simon, D. J., D. J. Varricchio, X. Jin, and S. F. Robison. 2019. Microstructural overlap of
Macroelongatoolithus eggs from Asia and North America expands the occurrence of
colossal oviraptorosaurs. Journal of Vertebrate Paleontology e1553046.

Smith, D. 1992. The type specimen of *Oviraptor philoceratops*, a theropod dinosaur from the
Upper Cretaceous of Mongolia. Neues Jahrbuch Fur Geologie Und Palaontologie
Abhandlungen 186:365–388.

Smith, D., and P. M. Galton. 1990. Osteology of *Archaeornithomimus asiaticus*. Journal of
Vertebrate Paleontology 10:255–265.

Smith, K. K. 1988. Form and function of the tongue in agamid lizards with comments on its
phylogenetic significance. Journal of Morphology 196:157–171.

Snively, E., A. P. Russell, and G. L. Powell. 2004. Evolutionary morphology of the
coelurosaurian arctometatarsus: descriptive, morphometric and phylogenetic approaches.
Zoological Journal of the Linnean Society 142:525–553.

Solheim, R. 2011. Moult pattern of primaries and secondaries in Eagle Owls *Bubo bubo*. Ornis
Norvegica 34:1–9.

Solheim, R. 2012. Wing feather moult and age determination of Snowy Owls *Bubo scandiacus*. Ornis Norvegica 35:48–67.

Sternberg, C. M. 1932. Two new theropod dinosaurs from the Belly River Formation of Alberta. The Canadian Field-Naturalist 46:99–105.

Sternberg, C. M. 1934. Notes on certain recently described dinosaurs. The Canadian Field-Naturalist 48:7–8.

Sternberg, R. M. 1940. A toothless bird from the Cretaceous of Alberta. Journal of Paleontology 14:81–85.

Sues, H.-D. 1997. On *Chirostenotes*, a Late Cretaceous oviraptorosaur (Dinosauria: Theropoda) from western North America. Journal of Vertebrate Paleontology 17:698–716.

Sues, H.-D., and A. Averianov. 2015. New material of *Caenagnathasia martinsoni* (Dinosauria: Theropoda: Oviraptorosauria) from the Bissekty Formation (Upper Cretaceous: Turonian) of Uzbekistan. Cretaceous Research 54:50–59.

Sullivan, K. a. 1984. The advantages of social foraging in downy woodpeckers. Animal Behaviour 32:16–22.

Sullivan, R. M., S. E. Jasinski, and M. P. A. Van Tomme. 2011. A new caenagnathid *Ojoraptorsaurus boerei*, n. gen., n. sp (Dinosauria, Oviraptorosauria), from the Upper Ojo Alamo Formation (Naashoibito Member), San Juan Basin, New Mexico. New Mexico Museum of Natural History and Science Bulletin 53:418–428.

Tanaka, K., D. K. Zelenitsky, and F. Therrien. 2015. Eggshell Porosity Provides Insight on Evolution of Nesting in Dinosaurs. PLOS ONE 10:e0142829.

Tanaka, K., D. K. Zelenitsky, J. Lü, C. L. DeBuhr, L. Yi, S. Jia, F. Ding, M. Xia, D. Liu, C. Shen, and R. Chen. 2018. Incubation behaviours of oviraptorosaur dinosaurs in relation to body size. Biology Letters 14:20180135.

Ten Cate, A. R. 1998. Oral Histology: Development, Structure, and Function, 5th ed. University of Michigan, Ann Arbor, pp.

Thulborn, R. A. 1984. The avian relationships of *Archaeopteryx*, and the origin of birds. Zoological Journal of the Linnean Society 82:119–158.

Tsogtbaatar, K., D. B. Weishampel, D. C. Evans, and M. Watabe. 2014. A new hadrosauroid (*Plesiohadros djadokhtaensis*) from the Late Cretaceous Djadokhtan fauna of southern Mongolia; pp. 108–135 in D. A. Eberth and D. C. Evans (eds.), Hadrosaurs: Proceedings of the International Hadrosaur Symposium. Indiana University Press.

Tsuihiji, T., M. Watabe, R. Barsbold, and K. Tsogtbaatar. 2015. A gigantic caenagnathid oviraptorosaurian (Dinosauria: Theropoda) from the Upper Cretaceous of the Gobi Desert, Mongolia. Cretaceous Research 56:60–65.

Tsuihiji, T., M. Watabe, K. Tsogtbaatar, and R. Barsbold. 2016. Dentaries of a caenagnathid (Dinosauria: Theropoda) from the Nemegt Formation of the Gobi Desert in Mongolia. Cretaceous Research 63:148–153.

Tsuihiji, T., L. M. Witmer, M. Watabe, R. Barsbold, K. Tsogtbaatar, S. Suzuki, and P. Khatanbaatar. 2017. New information on the cranial morphology of *Avimimus* (Theropoda: Oviraptorosauria). Journal of Vertebrate Paleontology e1347177.

Tumarkin-Deratzian, A. R. 2009. Evaluation of Long Bone Surface Textures as Ontogenetic Indicators in Centrosaurine Ceratopsids. The Anatomical Record: Advances in Integrative Anatomy and Evolutionary Biology 292:1485–1500.

Turner, A. H., P. J. Makovicky, and M. A. Norell. 2007a. Feather Quill Knobs in the Dinosaur *Velociraptor*. Science 317:1721–1721.

Turner, A. H., P. J. Makovicky, and M. A. Norell. 2012. A Review of Dromaeosaurid Systematics and Paravian Phylogeny. Bulletin of the American Museum of Natural History 371:1–206.

Turner, A. H., D. Pol, J. A. Clarke, G. M. Erickson, and M. A. Norell. 2007b. A Basal Dromaeosaurid and Size Evolution Preceding Avian Flight. Science 317:1378–1381.

Urano, Y., K. Tanoue, R. Matsumoto, S. Kawabe, T. Ohashi, and S. Fujiwara. 2018. How does the curvature of the upper beak bone reflect the overlying rhinotheca morphology? Journal of Morphology 279:636–647.

Van Hemert, C., C. M. Handel, J. E. Blake, R. M. Swor, and T. M. O'Hara. 2012. Microanatomy of passerine hard-cornified tissues: Beak and claw structure of the black-capped chickadee (*Poecile atricapillus*). Journal of Morphology 273:226–240.

Van Itterbeeck, J., D. J. Horne, P. Bultynck, and N. Vandenberghe. 2005. Stratigraphy and palaeoenvironment of the dinosaur-bearing Upper Cretaceous Iren Dabasu Formation, Inner Mongolia, People's Republic of China. Cretaceous Research 26:699–725.

Varricchio, D. J., P. C. Sereno, Z. Xijin, T. Lin, J. A. Wilson, and G. H. Lyon. 2008a. Mud-Trapped Herd Captures Evidence of Distinctive Dinosaur Sociality. Acta Palaeontologica Polonica 53:567–578.

Varricchio, D. J., P. C. Sereno, Z. Xijin, T. Lin, J. A. Wilson, H. Lyon, D. J. Varricchio, P. C. Sereno, Z. Xijin, T. A. N. Lin, J. A. Wilson, and G. H. Lyon. 2008b. Mud−trapped herd captures evidence of distinctive dinosaur sociality. Acta Palaeontologica Polonica 53:567–578.

Vickers-Rich, P., L. M. Chiappe, and S. M. Kurzanov. 2002. The enigmatic birdlike dinosaur

Avimimus portentosus, comments and a pictorial atlas; pp. 65–86 in L. M. Chiappe and L.

M. Witmer (eds.), Mesozoic Birds, Above the Heads of Dinosaurs. University of

California Press, Berkeley, California.

Wang, S., Q. Zhang, and R. Yang. 2018. Reevaluation of the Dentary Structures of Caenagnathid

Oviraptorosaurs (Dinosauria, Theropoda). Scientific Reports 8.

Wang, S., S. Zhang, C. Sullivan, and X. Xu. 2016. Elongatoolithid eggs containing oviraptorid

(Theropoda, Oviraptorosauria) embryos from the Upper Cretaceous of Southern China.

BMC Evolutionary Biology 16.

Wang, S., J. Stiegler, P. Wu, C.-M. Chuong, D. Hu, A. Balanoff, Y. Zhou, and X. Xu. 2017.

Heterochronic truncation of odontogenesis in theropod dinosaurs provides insight into the

macroevolution of avian beaks. Proceedings of the National Academy of Sciences

201708023.

Wang, X., A. J. McGowan, and G. J. Dyke. 2011. Avian Wing Proportions and Flight Styles:

First Step towards Predicting the Flight Modes of Mesozoic Birds. PLoS ONE 6:e28672.

Ward, P., and A. Zahavi. 1973. The importance of certain assemblages of birds as "information-

centres" for food-finding. Ibis 115:517–534.

Watabe, M., S. Suzuki, and K. Tsogtbaatar. 2006. Geological and geographical distribution of

bird-like theropod, *Avimimus* in Mongolia. Journal of Vertebrate Paleontology 26:136–

137A.

Watabe, M., K. Tsogtbaatar, S. Suzuki, and M. Saneyoshi. 2010a. Geology of dinosaur-fossil-

bearing localities (Jurassic and Cretaceous: Mesozoic) in the Gobi Desert: Results of the

HMNS-MPC Joint Paleontological Expedition. Hayashibara Museum of Natural Sciences Research Bulletin 3.

Watabe, M., D. B. Weishampel, R. Barsbold, K. Tsogtbaatar, and S. Suzuki. 2000. New nearly complete skeleton of the bird-like theropod, *Avimimus*, from the Upper Cretaceous of the Gobi Desert, Mongolia. Journal of Vertebrate Paleontology 20:77A.

Watabe, M., S. Suzuki, K. Tsogtbaatar, T. Tsubamoto, and M. Saneyoshi. 2010b. Report of the HMNS-MPC Joint Paleontological Expedition in 2006. Hayashibara Museum of Natural Sciences Research Bulletin 3:11–18.

Weishampel, D. B., and J. R. Horner. 1986. The Hadrosaurid dinosaurs from the Iren Dabasu Fauna (People's Republic of China, Late Cretaceous. Journal of Vertebrate Paleontology 6:38–45.

Weishampel, D. B., D. E. Fastovsky, M. Watabe, D. Varricchio, F. Jackson, K. Tsogtbaatar, and R. Barsbold. 2008. New oviraptorid embryos from Bugin-Tsav, Nemegt Formation (Upper Cretaceous), Mongolia, with insights into their habitat and growth. Journal of Vertebrate Paleontology 28:1110–1119.

Wiemann, J., T.-R. Yang, and M. A. Norell. 2018. Dinosaur egg colour had a single evolutionary origin. Nature 563:555–558.

Woodward, H. N. 2019. Maiasaura (Dinosauria: Hadrosauridae) Tibia Osteohistology Reveals Non-annual Cortical Vascular Rings in Young of the Year. Frontiers in Earth Science 7.

Woodward, H. N., J. R. Horner, and J. O. Farlow. 2011a. Osteohistological Evidence for Determinate Growth in the American Alligator. Journal of Herpetology 45:339–342.

Woodward, H. N., J. R. Horner, and J. O. Farlow. 2014. Quantification of intraskeletal histovariability in *Alligator mississippiensis* and implications for vertebrate osteohistology. PeerJ 2:e422.

Woodward, H. N., T. H. Rich, A. Chinsamy, and P. Vickers-Rich. 2011b. Growth dynamics of Australia's polar dinosaurs. PLoS One 6:e23339.

Woodward, H. N., E. A. Freedman Fowler, J. O. Farlow, and J. R. Horner. 2015. *Maiasaura*, a model organism for extinct vertebrate population biology: a large sample statistical assessment of growth dynamics and survivorship. Paleobiology 41:503–527.

Xu, X., X. Zheng, and H. You. 2010. Exceptional dinosaur fossils show ontogenetic development of early feathers. Nature 464:1338–1341.

Xu, X., Y.-N. Cheng, X.-L. Wang, and C.-H. Chang. 2002. An unusual oviraptorosaurian dinosaur from China. Nature 419:291–293.

Xu, X., Q. Tan, J. Wang, X. Zhao, and L. Tan. 2007. A gigantic bird-like dinosaur from the Late Cretaceous of China. Nature.

Yao, X., X.-L. Wang, C. Sullivan, S. Wang, T. Stidham, and X. Xu. 2015. *Caenagnathasia* sp. (Theropoda: Oviraptorosauria) from the Iren Dabasu Formation (Upper Cretaceous: Campanian) of Erenhot, Nei Mongol, China. Vertebrata PalAsiatica 53:291–298.

Yu, Y., K. Wang, S. Chen, C. Sullivan, S. Wang, P. Wang, and X. Xu. 2018. A new caenagnathid dinosaur from the Upper Cretaceous Wangshi Group of Shandong, China, with comments on size variation among oviraptorosaurs. Scientific Reports 8.

Zanno, L. E. 2006. The pectoral girdle and forelimb of the primitive therizinosauroid *Falcarius Utahensis* (Theropoda, Maniraptora): analyzing evolutionary trends within Therizinosauroidea. Journal of Vertebrate Paleontology 26:636–650.

Zanno, L. E., and S. D. Sampson. 2005. A new oviraptorosaur (Theropoda, Maniraptora) from the Late Cretaceous (Campanian) of Utah. Journal of Vertebrate Paleontology 25:897–904.

Zanno, L. E., and G. M. Erickson. 2006. Ontogeny and Life History of Falcarius utahensis, a primitive therizinosauroid from the Early Cretaceous of Utah. Journal of Vertebrate Paleontology 26:143A.

Zanno, L. E., and P. J. Makovicky. 2011. Herbivorous ecomorphology and specialization patterns in theropod dinosaur evolution. Proceedings of the National Academy of Sciences 108:232–237.

Zelenitsky, D. K., F. Therrien, G. M. Erickson, C. L. DeBuhr, Y. Kobayashi, D. A. Eberth, and F. Hadfield. 2012. Feathered Non-Avian Dinosaurs from North America Provide Insight into Wing Origins. Science 338:510–514.

Zhou, Z.-H., X.-L. Wang, F. Zhang, and X. Xu. 2000. Important features of *Caudipteryx* - evidence from two nearly complete new specimens. Vertebrata PalAsiatica 10:241–254.

1968. Results of the Polish-Mongolian Palaeontological Expeditions Part I. Palaeontologica Polonica 19.

1969. Results of the Polish-Mongolian Palaeontological Expeditions Part II. Palaeontologica Polonica 21.

1971. Results of the Polish-Mongolian Palaeontological Expeditions Part III. Palaeontologica Polonica 25.

1972. Results of the Polish-Mongolian Palaeontological Expeditions Part IV. Palaeontologica Polonica 27.

1974. Results of the Polish-Mongolian Palaeontological Expeditions Part V. Palaeontologica Polonica 30.

1975. Results of the Polish-Mongolian Palaeontological Expeditions Part VI. Palaeontologica Polonica 33.

1977. Results of the Polish-Mongolian Palaeontological Expeditions Part VII. Palaeontologica Polonica 37.

1979. Results of the Polish-Mongolian Palaeontological Expeditions Part VIII. Palaeontologica Polonica 38.

1981. Results of the Polish-Mongolian Palaeontological Expeditions Part IX. Palaeontologica Polonica 42.

1984. Results of the Polish-Mongolian Palaeontological Expeditions Part X. Palaeontologica Polonica 46.

2010. Hayashibara Museum of Natural Sciences Research Bulletin Vol. 3 (T. Tsubamoto (ed.)). Hayashibara Museum of Natural Sciences, Okayama, Japan, pp.

2014. Bonebeds: Genesis, Analysis, and Paleobiological Significance (R. R. Rogers, D. A. Eberth, and A. R. Fiorillo (eds.)). University of Chicago Press, Chicago, pp.

2000. Hayashibara Museum of Natural Sciences Research Bulletin Vol. 1 (K. Ishii, M. Watabe, S. Suzuki, S. Ishigaki, R. Barsbold, and K. Tsogtbaatar (eds.)). Hayashibara Museum of Natural Sciences, Okayama, Japan, pp.

2004. Hayashibara Museum of Natural Sciences Research Bulletin Vol. 2 (K. Ishii, M. Watabe, S. Suzuki, S. Ishigaki, R. Barsbold, and K. Tsogtbaatar (eds.)). Hayashibara Museum of Natural Sciences, Okayama, Japan, pp.

APPENDICES

Appendix 1: Selected measurements of oviraptorosaurian theropods.

[see supplementary electronic files].

Appendix 2: Characters and character matrix used for phylogenetic analysis

1. Ratio of the preorbital skull length to the basal skull length
        0 0.6 or more
        1 less than 0.6

2. Pneumatized crest-like prominence on the skull roof
        0 absent
        1 present

3. Ratio of the width (across premaxilla-maxilla suture) of the snout to its length
        0 less than 0.3
        1 0.3-0.4
        2 more than 0.4

4. Ratio of the length of the tomial margin of the premaxilla to the premaxilla height (ventral to the external naris)
        0 1.0-1.4
        1 more than 1.7
        2 0.7 or less

5. Inclination of the anteroventral margin of the premaxilla relative to the horizontally positioned ventral margin of the jugal
        0 vertical
        1 posterodorsal
        2 anterodorsal

6. Ventral projection of the premaxilla below the ventral margin of the maxilla
        0 absent
        1 present

7. Ventral projection of the premaxilla below ventral margin of maxilla
        0 small
        1 significant

8. Share of the premaxilla (ventral) in the basal skull length
        0 0.10 or less
        1 0.12 or more

9. Pneumatization of the premaxilla
        0 absent

1 present

10. Ratio of the length of the maxilla (in lateral view) to the basal skull length
      0 0.4-0.7
      1 less than 0.4

11. Subantorbital portion of the maxilla
      0 not inset medially
      1 inset medially

12. Palatal shelf of the maxilla with two longitudinal ridges and a tooth-like ventral process
      0 absent
      1 present

13. Ventral margins of maxilla and jugal
      0 margins form a straight line
      1 the ventral margin of the maxilla slopes anteroventrally, its longitudinal axis at an angle of ca. 120??? to the longitudinal axis of the jugal

14. Rim around antorbital fossa
      0 well pronounced
      1 poorly delimited

15. Antorbital fossa
      0 bordered anteriorly by the maxilla
      1 bordered anteriorly by the premaxilla

16. Accessory maxillary fenestrae
      0 absent
      1 at least one accessory fenestra present

17. Nasal along midline
      0 longer than frontal
      1 shorter than or as long as the frontal

18. Nasals
      0 separate
      1 fused

19. Subnarial process of the nasal
      0 long
      1 short

20. Shape of the narial opening
      0 longitudinally oval
      1 teardrop-shaped, slightly longer than wide

2 much longer than wide

21. Nasal recesses
    0 absent
    1 present

22. External naris position relative to the antorbital fossa
    0 naris and fossa widely separated
    1 posterior margin of the naris reaching the fossa
    2 overlapping anterodorsally most of the fossa

23. Ventral margin of the external naris
    0 at the level of the maxilla
    1 dorsal to the maxilla

24. Prefrontal
    0 present
    1 absent or fused with the lacrimal

25. Lacrimal shaft
    0 not projecting outward beyond the orbital plane and lateral surface of the snout
    1 the middle part of the shaft projecting laterally to form a flattened transverse bar in front of the eye

26. Lacrimal recesses
    0 absent
    1 present

27. Ratio of the length of the orbit to the length of the antorbital fossa
    0 0.7-0.9
    1 1.2 or more

28. Ratio of the length of the parietal to the length of the frontal
    0 0.6 or less
    1 1.0 or more

29. Pneumatization of the skull roof bones
    0 absent
    1 present

30. Sagittal crest along the interparietal contact
    0 absent
    1 present

31. Supratemporal fossa
    0 invading the frontal

1 not invading the frontal

32. Infratemporal fenestra
0 dorsoventrally elongate, narrow anteroposteriorly
1 subquadrate, its anteroposterior length comparable to the orbital length

33. Pneumatization of the squamosal
0 absent
1 present

34. Cotyle-like incision on the ventrolateral margin of the squamosal (for reception of the dorsal end of the ascending process of the quadratojugal)
0 absent
1 present

35. Ventral ramus of the jugal
0 deep dorsoventrally and flattened lateromedially
1 shallow dorsoventrally or rod-shaped

36. Jugal process of the postorbital
0 not extending ventrally below two-thirds of the orbit height
1 long, extending ventrally close to the base of the postorbital process of the jugal

37. Postorbital process of the jugal
0 posterodorsally inclined
1 perpendicular to the ventral ramus of the jugal

38. Postorbital process of the jugal
0 present
1 absent

39. Jugal-postorbital contact
0 present
1 absent

40. Quadratojugal process of the jugal in lateral view
0 forked
1 not forked
2 fused with the quadratojugal

41. Quadratojugal-squamosal contact
0 absent
1 present

42. Ascending (squamosal) process of the quadratojugal
0 bordering ca. the ventral half, or less, of the infratemporal fenestra

1 bordering the ventral two-thirds or more of the infratemporal fenestra

43. Ascending (squamosal) process of the quadratojugal
        0 present
        1 absent

44. Angle between the ascending and jugal processes of the quadratojugal
        0 ca. 90???
        1 less than 90???

45. Quadrate process of the quadratojugal
        0 well developed, extending posteriorly or posteroventrally beyond the posterior margin
of the ascending process
        1 not extending beyond the posterior margin of the ascending process

46. Dorsal part of the quadrate
        0 erect
        1 bent backward

47. Otic process of the quadrate
        0 articulating only with the squamosal
        1 articulating with the squamosal and the lateral wall of the braincase

48. Pneumatization of the quadrate
        0 absent
        1 present

49. Lateral accessory process on the distal end of the quadrate for articulation with the
quadratojugal
        0 absent
        1 present

50. Lateral cotyle for the quadratojugal on the quadrate
        0 absent
        1 present

51. Mandibular condyles of quadrate
        0 posterior to the occipital condyle
        1 in the same vertical plane as the occipital condyle
        2 anterior to the occipital condyle

52. Nuchal transverse crest
        0 pronounced
        1 not pronounced

53. Occiput position in relation to the ventral margin of the jugal-quadratojugal bar

0 about perpendicular
1 inclined anterodorsally

54. Paroccipital process
0 directed laterally
1 directed ventrally

55. Foramen magnum
0 smaller than or equal in size to the occipital condyle
1 larger than the occipital condyle

56. Basal tubera
0 modestly pronounced
1 well developed, widely separated

57. Pneumatization of the basisphenoid
0 weak or absent
1 extensive

58. Basipterygoid processes
0 well developed
1 strongly reduced

59. Basipterygoid processes
0 present
1 absent

60. Parasphenoid rostrum
0 horizontal or anterodorsally directed
1 sloping anteroventrally

61. Depression in the periotic region
0 absent
1 present

62. Pneumatization of the periotic region
0 absent or weak
1 extensive

63. Quadrate ramus of the pterygoid
0 distant from the braincase wall
1 overlapping the braincase

64. Pterygoid basal process for contact with the basisphenoid
0 absent
1 present

65. Ectopterygoid position
      0 lateral to the pterygoid
      1 anterior to the pterygoid

66. Ectopterygoid contacts with the maxilla and lacrimal
      0 absent
      1 present

67. Ectopterygoid
      0 short anteroposteriorly with a hook-like jugal process
      1 elongate, shaped like a Viking ship, without a hook-like process

68. Massive pterygoid-ectopterygoid longitudinal bar
      0 absent
      1 present

69. Palate extending below the cheek margin
      0 absent
      1 present

70. Palatine
      0 tetraradiate or trapezoidal
      1 triradiate, without a jugal process
      2 developed in horizontal, longitudinal, and transverse planes perpendicular to each other

71. Pterygoid wing of the palatine
      0 dorsal to the pterygoid
      1 ventral to the pterygoid

72. Maxillary process of the palatine
      0 shorter than the vomeral process
      1 longer than the vomeral process

73. Vomer
      0 distant from the parasphenoid rostrum
      1 approaching or in contact with the parasphenoid rostrum

74. Suborbital (ectopterygoid-palatine) fenestra
      0 well developed
      1 closed or reduced

75. Jaw joint
      0 distant from the midline of the skull
      1 close to the skull midline

76. Movable intramandibular joint
  0 present
  1 suppressed

77. Mandibular symphysis
  0 loose
  1 tightly sutured
  2 fused

78. Extended symphyseal shelf at the mandibular symphysis
  0 absent
  1 present

79. Downturned symphyseal portion of the dentary
  0 absent
  1 present

80. U-shaped mandibular symphysis
  0 absent
  1 present

81. Ratio of the length of the retroarticular process to the total mandibular length
  0 less than 0.05 or the process absent
  1 ca. 0.10

82. Dentary
  0 elongate
  1 proportionally short and deep, with maximum depth of dentary between 25% and 50% of dentary length (with length measured from the tip of the jaw to the end of the posterodorsal process)
  2 extremely short and deep, with maximum depth 50% or more of dentary length

83. Ratio of the height of the external mandibular fenestra to the length of the fenestra
  0 0.2-0.5
  1 0.7-1.0

84. External mandibular fenestra
  0 present
  1 absent

85. Ratio of the length of the external mandibular fenestra to total mandibular length
  0 0.15-0.20
  1 not more than 0.10 or fenestra absent
  2 0.25 or more

86. Process of the surangular dividing the external mandibular fenestra

0 absent
1 short and broad
2 elongate and spike-like

87. Co-ossification of the articular with the surangular
0 absent
1 present

88. Mandibular rami in dorsal view
0 straight
1 laterally bowed at midlength

89. Anterodorsal margin of dentary in lateral view
0 straight
1 concave
2 broadly concave

90. Posterior margin of the dentary
0 incised, producing two posterior processes
1 oblique

91. Posterodorsal process of the dentary long and shallow
0 present
1 absent

92. Posteroventral process of the dentary shallow and long, extending posteriorly at least to the posterior border of the external mandibular fenestra
0 absent
1 present

93. Coronoid process
0 posteriorly positioned and vertically projected
1 anteriorly positioned, near the midpoint of the jaw, with a medially hooked apex

94. Surangular foramen
0 present
1 absent

95. Mandibular articular facet for the quadrate
0 comprising the surangular and the articular
1 formed exclusively of the articular

96. Mandibular articular facet for the quadrate
0 with one or two cotyles
1 convex in lateral view, transversely wide

97. Position of the quadrate articular surface relative to the level of the adjoining dorsal margin of the mandibular ramus
    0 ventral
    1 moderately elevated, quadrate articulation grades smoothly into remainder of mandible
    2 highly elevated, anterior and posterior margins of quadrate articulation at nearly right angles to remainder of mandible

98. Anterior part of the prearticular
    0 deep, approaching the dorsal margin of the mandible
    1 shallow, strap-like, not approaching the dorsal mandibular margin

99. Splenial
    0 subtriangular, approaching the dorsal mandibular margin
    1 strap-like, shallow, not approaching the margin

100. Mandibular adductor fossa
    0 anteriorly delimited, occupying the posterior part of the mandible
    1 large, anteriorly and dorsally extended, not delimited anteriorly

101. Coronoid bone
    0 well developed
    1 strongly reduced

102. Coronoid bone
    0 present
    1 absent

103. Premaxillary teeth
    0 present
    1 absent

104. Maxillary tooth row
    0 extends at least to the level of the preorbital bar
    1 does not reach the level of the preorbital bar
    2 maxillary teeth absent

105. Dentary teeth
    0 present
    1 absent from tip of jaw but present posteriorly
    2 absent

106. Number of cervicals (excluding cervicodorsal)
    0 not more than 10
    1 more than 10

107. Anterior articular facets of the centra in the anterior postaxial cervicals

0 not inclined or only slightly inclined

1 strongly inclined posteroventrally, almost continuous with the ventral surfaces of the centra

108. Centra of the anterior cervicals

0 not extending posteriorly beyond their respective neural arches

1 extending posteriorly beyond their respective neural arches

109. Epipophyses on the postaxial cervicals

0 in the form of a low crest or rugosity

1 prong-shaped

110. Shafts of cervical ribs

0 longer than their respective centra

1 not longer than their respective centra

111. Lateral pneumatic fossae ("pleurocoels") on the dorsal centra

0 absent

1 present

112. Ossified uncinate processes on the dorsal ribs

0 absent

1 present

113. Number of vertebrae included in the synsacrum in adults

0 not more than 5

1 6

2 7-8

114. Sacral spines in adults

0 unfused

1 fused

115. Lateral pneumatic fossae on the sacral centra

0 absent

1 present

116. Transition point on the caudals

0 absent

1 present

117. Number of caudals with transverse processes

0 15 or more

1 fewer than 15

118. Lateral pneumatic fossae on the caudal centra

0 absent
1 present at least in the anterior part of the tail

119. Neural spines confined to
    0 at least 23 anterior caudals
    1 at most 16 anterior caudals

120. Number of caudals
    0 more than 35
    1 30 or fewer

121. Posterior caudal prezygapophyses
    0 overlapping less than half of the centrum of the preceding vertebra
    1 overlapping at least half of the centrum of the preceding vertebra

122. Hypapophyses in the cervicodorsal vertebral region
    0 absent
    1 small
    2 prominent

123. Posterior hemal arches
    0 deeper than long
    1 longer than deep

124. Ratio of the length of the scapula to the length of the humerus
    0 0.8-1.1
    1 1.2 or more
    2 0.7 or less

125. Acromion
    0 projecting dorsally
    1 projecting anteriorly
    2 everted laterally

126. Posteroventral process of the coracoid
    0 absent or short, not extending beyond the glenoid diameter
    1 long, posteroventrally extending beyond the glenoid

127. Orientation of the glenoid on the pectoral girdle
    0 posteroventral
    1 lateral

128. Deltopectoral crest
    0 low, its width equal to, or smaller than, the shaft diameter
    1 expanded, wider than the shaft diameter

129. Extent of the deltopectoral crest (measured from the humeral head to the apex)
    0 about the proximal third of the humerus length or less
    1 ca. 40%-50% of the humerus length

130. Shaft of the ulna
    0 straight
    1 bowed, convex posteriorly

131. Ratio of the length of the radius to the length of the humerus
    0 0.80 or less
    1 0.85 or more

132. Combined length of manual phalanges III-1 and III-2
    0 greater than the length of phalanx III-3
    1 less than or equal to the length of phalanx III-3

133. Ratio of the length of metacarpal I to the length of metacarpal II
    0 0.5 or more
    1 less than 0.5

134. Proximal margin of metacarpal I in dorsal view
    0 straight, horizontal
    1 angled due to a medial extent of carpal trochlea

135. Metacarpal II relative to metacarpal III
    0 shorter
    1 longer
    2 subequal

136. Ratio of the length of metacarpal II to the length of the humerus
    0 0.4 or less
    1 more than 0.4

137. Ratio of the length of the manus to the length of the humerus plus the radius
    0 0.50-0.65
    1 more than 0.65
    2 less than 0.50

138. Ratio of the length of the manus to the length of the femur
    0 0.3-0.6
    1 more than 0.7

139. Ratio of the length of the humerus to the length of the femur
    0 0.50-0.69
    1 0.70 or more

140. Dorsal margins of opposite iliac blades
    0 well separated from each other
    1 close to or contacting each other along their medial sections

141. Dorsal margin of the ilium along the central portion of the blade
    0 straight
    1 arched

142. Preacetabular process of the ilium relative to the postacetabular process (lengths measured from the center of the acetabulum)
    0 shorter or equal
    1 longer

143. Preacetabular process
    0 not expanded or weakly expanded ventrally below the level of the dorsal acetabular margin
    1 expanded ventrally well below the level of the dorsal acetabular margin

144. Morphology of the ventral margin of the preacetabular process
    0 cuppedicus fossa absent, margin transversely narrow
    1 cuppedicus fossa or a wide shelf present
    2 margin flat, wide at least close to the pubic peduncle

145. Anteroventral extension of the preacetabular process
    0 absent
    1 present

146. Anteroventral extension of the preacetabular process
    0 with rounded tip
    1 hook-like

147. Posterior end of the postacetabular process
    0 truncated or broadly rounded
    1 narrowed or acuminate

148. Anteroposterior length of the pubic peduncle
    0 about the same as that of the ischial peduncle
    1 distinctly greater than that of the ischial peduncle

149. Dorsoventral extension of the pubic peduncle
    0 level with the ischial peduncle
    1 deeper than the ischial peduncle

150. Ratio of the length of the ilium to the length of the femur
    0 0.50-0.79
    1 0.80 or more

151. Pelvis
    0 propubic
    1 mesopubic
    2 opisthopubic

152. Pubic shaft
    0 straight
    1 concave anteriorly

153. Pubic foot
    0 anterior and posterior processes about equally long
    1 anterior process absent or shorter than the posterior process
    2 anterior process longer than the posterior process

154. Posterior margin of the ischial shaft
    0 straight or almost straight
    1 distinctly concave

155. Greater trochanter of the femur
    0 weakly separated, or not separated, from the femoral head
    1 distinctly separated from the femoral head

156. Anterior and greater trochanters
    0 separated
    1 contacting

157. Dorsal extremity of the anterior trochanter
    0 well below the greater trochanter
    1 about level with the greater trochanter

158. Fourth trochanter
    0 well developed
    1 weakly developed or absent

159. Adductor fossa and the associated anteromedial crest on the distal femur
    0 weak or absent
    1 well developed

160. Distal projection of the fibular condyle of the femur beyond the tibial condyle
    0 absent
    1 present

161. Ascending process of the astragalus
    0 as tall as wide across the base
    1 taller than wide

162. Distal tarsals
  0 not fused with the metatarsus
  1 fused with the metatarsus

163. Proximal coossification of metatarsals II-IV
  0 absent
  1 present

164. Arctometatarsus
  0 absent
  1 present, but only proximal-most extreme of metatarsal III obscured from anterior view in articulated metatarsus
  2 present, proximal ~half of metatarsal III obscured from anterior view in articulated metatarsus

165. Length of metatarsal I constituting
  0 more than 50% of metatarsal II length
  1 less than 50% of metatarsal II length
  2 metatarsal I absent

166. Ratio of the maximum length of the metatarsus to the length of the femur
  0 0.4-0.6
  1 ca. 0.3
  2 0.7-0.8

167. Crenulated tomial margin of the premaxilla
  0 absent
  1 present

168. Frontals
  0 flat or weakly arched, not strongly projecting above orbit in lateral view
  1 strongly arched, projecting well above orbit in lateral view to contribute to nasal-frontal crest

169. Exoccipital
  0 short, weakly projecting
  1 strongly projects ventrally beyond squamosal in lateral view, approaching ventral end of the quadrate

170. Dentary posterodorsal ramus
  0 straight or weakly curved
  1 strongly bowed dorsally

171. Prominent symphyseal process on posteroventral surface of dentary symphysis
  0 absent

1 present

172. Dentary anteroventral margin in lateral view
0 straight or weakly downturned
1 strongly downturned

173. Lateral surface of dentary
0 smooth
1 bearing a deep fossa, sometimes with associated pneumatopore

174. Angular
0 contributes extensively to the border of the external mandibular fenestra
1 largely excluded from the border of the external mandibular fenestra by the surangular

175. Surangular with an anteroposteriorly elongate flange on the ventral edge
0 absent
1 present

176. External mandibular fenestra
0 elongate
1 height subequal to length

177. Dentary contribution to external mandibular fenestra
0 no more than 50% length of dentary
1 exceeds 50% length of dentary

178. Metacarpal I expanded ventrally to cover ventral surface of metacarpal II
0 absent
1 present

179. Unguals of manual digits II and III
0 strongly curved
1 weakly curved

180. Manual phalanx I-1
0 slender
1 more robust than II-1
2 more than 200% diameter of II-1

181. Manual phalanx III-3
0 longer than phalanx III-2
1 does not exceed length of III-2

182. Manual phalanx II-2
0 longer than II-1
1 subequal to or slightly shorter than II-1

2 distinctly shorter than II-1

183. Manual digit II
    0 elongate, with combined lengths of manual phalanges II-1 and II-2 longer than metacarpal II
    1 combined lengths of manual phalanges II-1 and II-2 subequal to metacarpal II

184. Ischium strongly bent posteriorly at midshaft distal end forms an angle of at least 60
    0 with proximal end
    1 absent
    2 present

185. Metatarsus
    0 elongate
    1 short, length does not exceed 300% of proximal width

186. Ilium
    0 tall
    1 low and anteroposteriorly elongate, height less than 25% of length

187. Anterior blade of ilium shallower than posterior blade
    0 absent
    1 present

188. External naris
    0 placed anteriorly
    1 extends posteriorly, with posterior end lying above antorbital fenestra

189. Premaxillae, nasal processes anteroposteriorly expanded and mediolaterally compressed to form a bladelike internarial bar
    0 absent
    1 present

190. Dentary, anterodorsal tip of beak projects
    0 upwards
    1 anterodorsally, tip of beak projecting at an angle of 45??? or less relative to the ventral margin of the symphysis

191. Dentary symphysis with interior surface bearing vascular grooves and associated foramina
    0 absent
    1 present

192. Dentary symphysis bearing an hourglass-shaped ventral depression
    0 absent
    1 present

193. Meckelian groove terminates
        0 on the inside of the dentary
        1 on the ventral surface of the symphysis

194. Lingual triturating shelf of dentary
        0 absent
        1 present

195. Dentary, symphyseal ridges inside the tip of the beak
        0 absent
        1 present but weakly developed
        2 present and well developed

196. Dentary, lingual ridges inside the lateral occlusal surface of beak
        0 absent
        1 present

197. Posteroventral process of dentary
        0 straight
        1 bowed ventrally

198. Dentaries pneumatized
        0 absent
        1 present

199. Dentary
        0 participates in dorsal border of the external mandibular fenestra
        1 excluded from dorsal border of external mandibular fenestra by anterior extension of
the surangular

200. Dentary
        0 participates in ventral border of external mandibular fenestra
        1 excluded from ventral border of external mandibular fenestra by anterior extension of
the angular

201. Surangular and angular divided by posterior extension of the external mandibular fenestra
        0 absent
        1 present

202. Posterior end of the surangular
        0 deep
        1 shallow, subequal to or shallower than angular

203. Surangular
        0 deep anteriorly
        1 strap-like

204. Retroarticular process extends
    0 posteriorly
    1 posteroventrally
    2 posterolaterally

205. Metacarpal I
    0 proportionately broad
    1 long and slender, diameter 20% of length

206. Manual phalanx I-1
    0 longer than II-2
    1 subequal to II-2
    2 shorter than II-2

207. Ischiadic peduncle of pubis with prominent medial fossa
    0 absent
    1 present

208. Ischium, obturator process located
    0 distally
    1 at midshaft of ischium

209. Anterior margin of obturator process
    0 straight or convex
    1 distinctly concave

210. Accessory trochanter of femur
    0 weakly developed
    1 prominent, subrectangular flange or finger-like process

211. Metatarsal III
    0 with an ovoid or subtriangular cross section
    1 anteroposteriorly flattened, with a concave posterior surface

212. Paroccipital process
    0 elongate and slender, with dorsal and ventral edges nearly parallel
    1 short and deep with convex distal end

213. Mandibular articulation surface
    0 as long as ventral end of quadrate
    1 twice or more as long as quadrate surface, allowing anteroposterior movement of mandible

214. Sternum, distinct lateral xiphoid process posterior to costal margin
    0 absent

1 present

215. Anterior edge of sternum
      0 grooved for reception of coracoids
      1 without grooves

216. Deltopectoral crest
      0 large and distinct, proximal end of humerus quadrangular in anterior view
      1 less pronounced, forming an arc rather than being quadrangular

217. Ischium
      0 more than two-thirds of pubis length
      1 two-thirds or less of pubis length

218. Lateral ridge of femur
      0 absent or represented only by faint rugosity
      1 distinctly raised from shaft, mound-like

219. Surangular, distinct groove on dorsal surface
      0 present
      1 absent

220. Vomer, position
      0 level with other palatal elements
      1 ventral to other palatal elements

221. Calcaneum
      0 excludes astragalus from reaching lateral margin of tarsus
      1 small process of astragalus protrudes through a circular opening in edge of calcaneum
to reach lateral margin of tarsus

222. Depression on lateral surface of dentary immediately anterior to external mandibular
fenestra
      0 absent
      1 present

223. Groove on ventrolateral edge of angular to receive posteroventral branch of dentary
      0 absent
      1 present

224. Posteroventral branch of dentary twisted so that lateral surface of branch faces somewhat
ventrally
      0 absent
      1 present

225. Premaxilla, large, presumably pneumatic foramen at anteroventral corner of narial fossa

0 absent
1 present

226. Accessory opening at anterodorsal extreme of snout
0 absent
1 present

227. Development of symphyseal shelf of mandible
0 limited, anteroposterior length of mandibular symphysis (as measured on midline) less than 20% total anteroposterior length of mandible
1 intermediate, length of symphysis greater than 20% but less than 25% length of mandible
2 extensive, length of symphysis greater than 25% mandibular length

228. Prominent flange or shelf arising from lateral surface of dentary
0 absent
1 present

229. Base of retroarticular process
0 considerably wider mediolaterally than tall dorsoventrally
1 approximately as wide as tall
2 considerably taller than wide

230. Posterior-most caudal vertebrae fused, forming a pygostyle-like structure
0 absent
1 present

231. Humeral shaft
0 straight or nearly straight
1 strongly bowed laterally

232. Proximodorsal "lip" on manual unguals
0 weak (i.e., continuous or nearly continuous with remainder of dorsal surface of ungual) and/or absent
1 prominent ("set off" from remainder of dorsal surface by distinct change in slope immediately distal to "lip")

233. Pubic process of ischium, "hooked" anterodistal extension
0 absent
1 present

234. Posterodistal margin of obturator process
0 straight
1 distinctly concave, apex of obturator process angled distally

235. Proximolateral edge of metatarsal IV attenuated into pointed process

0 absent
1 present

236. Frontal anteriorly divided by slot for nasal and possibly lacrimal
    0 absent
    1 present

237. Infradiapophyseal infraprezygapophyseal and infrapostzygapophyseal fossae on cervical and dorsocervical vertebrae
    0 one or more absent
    1 all three present

238. Ratio of the length of the metatarsus to the length of the tibia
    0 <0.5
    1 >0.5

239. Tibia ratio of the transverse width of the distal condyles to the length
    0 0.20 or greater
    1 <0.20

240. Ratio of minimum transverse width to length of tarsometatarsus
    0 >0.20
    1 <0.20

241. Fusion of distal tarsals III and IV at maturity
    0 absent
    1 present

242. 'Hook-like' posterodorsal process of distal tarsal IV
    0 absent
    1 present

243. Posterior protuberance on proximal end of tarsometatarsus caused by coossification of distal tarsals III and IV, plus MT II, III and IV
    0 absent
    1 present

244. Anterior margin of metatarsal V in lateral view
    0 straight or slightly curved
    1 tightly curved

245. Concavity on posterior surface of tarsometatarsus in cross section
    0 absent or shallow
    1 prominent and deep

246. Transverse groove between flexor tubercle and proximal articular surface of manual ungual I-2

      0 absent
      1 present

Character Matrix:

Herrerasaurus_ischigualastensis
000100-
0000000000000000000000000000000000000000000000000000000000000000000000001
0000000000000000000000001?0000000000100?0000101??000100000000-
00001010000000000000100000?000?00001101101 00??000??00001 01??00??0000??00?1000?00
0000?00000?????000?00

Velociraptor_mongoliensis
000200-
00000010100101001010001000000000010000000001 00001000000000000000000000000000
000011000000000000100101011110110101 1111-
1101011120211000011011112020011100010010000000000?0000000111000?0000??00100001
00000000010011?000?000000000000000???000000

Archaeopteryx_lithographica
000?10-0000001011010011000100 01?1000-
1110??0?1??0020????000????0000001?1???1000010-10000011-01000000-
10100??001?00?1101100101110011111111111011010-
111020201?0100?1101200?0000?0?0?00000101000?0000??001?000000?0100100?111??00?00
000?0000?00????000000

Incisivosaurus_gauthieri
100210-
101000011?0111210011?01?00?00000?100010?0??200111?10?10?01??111?0101?2101110020
??00011??11?11100 11???00000
000100?????????00100000000000000?? ??? ?? 1?????? 00???01000??????? 0????? ???? 0

Caudipteryx_zoui
10?210-
?01??0?1110?0?21?01?10???011000011100100????????????????????0????????0??1111??2???00
01??????11??0220????010????0?1??11???1011?1010200?0012110110?021100???1000121??0?
??0??0?00?001000?000?00000000?01000?0010??0101????0?00000?0000000??????0000

Avimimus_portentosus
?0??????????0???????????????10110??1?-0021-
101??00?101111?10???????????????0?1??111???01?0???11000???-
11?2100010?110??0???2?12100111?1?????00000?1110?100201010011112221000 10000?0????
???00??00?00????0??0000??0??1011??11110????????0?0?00100?1111000?

Avimimus_nemegtensis
?0?2???01???????011202??????01?0???????2110011100?10111101011011??????????0?2101?1
?0????00????????????1?2?????0??????0???2??21000?????????00012111 00???2?10100111122
?1?00100??????????000100100000?00??????????101???1?1??????0??0?00???1?0?1111100?

Microvenator_celer
??1111?2?0???
12001????????????2???0?1?????????0????1?0011??1????0???1111?10?112?1011101????????0
101???0011?????00??0000000?0??????0?1??1?????1?0??11????00??00????1?1???????

Oviraptor_philoceratops
1????????????1?11?????21????????1??10000???0????????????????????????1????????1?12102
2??00011???1??1???22???0?1??????????????2???101101?212????????????????????????0?????0?
??001001000000??0??1??????????????0?????????0??11?0?0???0??00???0?????????0

Rinchenia_mongoliensis
11102??0111110111???1211111111?11110100111000111111?11111-
11?1111111121111111111112102?01100111111111-
1122111011?1010010102?22101000??????011011111101???111111?0????1101?001011????
????00111?????00000001????????110???1110?0?0?0??????????????0

Citipati_osmolskae
11202111111110110111121111111111111111001110111?1??11111??101111?1111121?111111
1112102201100111111111110122??????1????????????????0?101?1??????????????????????
0????11011001011?01010?0??11000000000000000100?????01100?01110?001000100?0?0????0
0?0?0

Zamyn_Khondt_oviraptorid
11202111111110111111121111111111111111001110111111111111111-
11111111111121111111111121022011001111111111-
1122111011?1010010102102101011011121010012101001112111111110001111101?001011?0
000010??110?0000000000?0100??00?1100??11???001?0??00??00?????????0

Khaan_mckennai
10201101?1111011?11212111111111?110000111000?111?111111???0??1?????1?????11111
1210210110011111111???1221110?1????00?0102??210??1101011210?0001100001?1211111?
11000111001100100100101011111110?000?001000001000000?011100?1?10101000?0000100?
???000000

Conchoraptor_gracilis
10101101111110111121211111111111000011100?1111111?1111-
11111111111211111111111?102?01100111111111-
1122111011?2010010101221011110011121010002100001112111111110001110 1?????????11
0???1??11??????????????0??????1?00?011?0?0000011?0??000???000000

Machairasaurus_leptonychus
??
?????????????????2??????????????????????0011??????????????????????????????????????
???111110????????????????00???????????????????????1?????????????0

Nemegtomaia_barsboldi

1110010111111011111112111111111?11000010101011?111111?1??11?1111111211111111
1112102?11100111111?11-
1122111011?201????????????????????10002???00?1????11????0????10111101011?12?11
??1111000000010000001000??0??1??1??11?1?1?0001?000??00????????0

Heyuannia_huangi
???????????????????????????????1???????????????????????????????????????1??21021
??1001????1??????21???1-
12????1?????221?11000001?20???01?10100111?1??????0???????1?1?1011112?2111?1??????
???0?00000100?0?0?011?00?1?11?0???0?00001?????000000

Heyuannia_yanshini
????????1??????????????11?????1?11000011 10?0111111???111???11?1?1??111?1???11111112
102?01100111111111-
1122?11011?2010010101022101100001100001001210000111211111111100011?011?10101111
21211111110000000000000100?0000?1100001?1??0???0?000010?0000000000

Gigantoraptor_erlianensis
??112111120020
11200111112?????1?2??????????0010?0??10?00000?11?1??1????????????1??1111111000?1??
?0001010000??????????0???0001001110100??0?????1?????110??112?10????????010?01

Caenagnathasia_martinsoni
???2101?1?????
120???????????????2?100?1???1???????????????????????????????????10?1???????????000
1???0????????????0111111?1????????????????????????0????????0?????????

Leptorhynchos_elegans
??12101?1?0??
11200???????1?????2?????????1?????????????????????0??1??011????????????111????00
01???????????000??0111121?111??????????1?????????1????10??????1??11111101?

Chirostenotes_pergracilis
??112101110020
11200111112111110122?1001??111001010?1??10????0????1??1111111101???1111111100111
???00010100?000102000??01111211111111112?1111?1????01?1111??101??1000?1110010111

Caenagnathus_collinsi
??112101110020
11200111111111-
1??2???????????1?????????????????????0?1110?10?10??1111111001????00010100?0?????
?00??1111121011111 11??1??1???????01?0010??201??1???????????0??0

Anzu_wyliei
?1??10-
1100?1100?????????????????0?0000???????1011??100?10??1??0?011?????112101110020112

001111111?1-
1122111011?1?100101020121000l0????1210??1111?010110211111111001??1?000010100000
??02000?011112111011111??1111111101101?00101021201ll00?1?1??1?010

Hagryphus_giganteus
???
???0010?????????????????????????????????????
???000010??????????????????2????????????????????????1?????????????1

Elmisaurus_rarus
???????????????????????????1?0???2101?1?0??
??200????????????2???????1?1??????2??2?1????001??????????????10??111????111?0?0?0
001????000010?0????0111121?1??????111??11?????0???1????10???10?111111111011

Nomingia_gobiensis
???
????????????????????0?1?1110010102l?????????????????111111001011001111l111?????????
????????????2?00????????????????????1111??????10??1????????1??00??1?1???????

Epichirostenotes_curriei
??????????01?010??????1???????????????????????????110?10?1??0?????????????????????
???????????????2??????1?111??1???2???????????????????????021???????????????0???
??????????2????????????????????111??0????1??????????????10??0?????????

Banji_long
11?010-
111???0111102121111111011??111001?????0??11?1111?????????1111121?0111??11?21021??
000110??1?11??122?1???1111100
1011??????????110??????0?00000???????????????00?0?000?0???????0??????????

Caudipteryx_dongi
???
???????????????????????01?0????????????0010?1?10200?011?11011000211?????100012????
????????00?001000????????????????01?10????0??1????????????000000???00000?

Ganzhousaurus_nankangensis
???11111?210?2
011001?????111????2???????????0???0???????????????????????????????????????0001????1?
001?11???????1???????000?1?10????????0??????????011???0????????????00000?

Jiangxisaurus_ganzhouensis
1??????????1?????????????11???????1?0001????????112?????1-
1?????1?01121??0111111210211100111111?????122??10?11??1??1?????221?1110?0120???
?0?????1??????????????????1??110010111?2?????????111??0?0100000100??????11?0?????0
011?00??00??????????????

Nankangia_jiangxiensis
???11101?2?0??
??000?????????????2?????1???1??1??0?0111001?????????011011011111211111111????????
1100??????????2?00??11?????0?0???1????111?????01???1010??00??0?10??0?0???????

Shixinggia_oblita
??
???????????????????????1?2?1??1???????????????????????110000-
000?????1????1???????????????????????01??
??????????????

Similicaudipteryx_yixianensis
??
??????????????????????011?0?1?0??1?2???????1???????0?001?111110?????????0??0?12??????
?????????????00???????????????????????0?????????????????10????00???000?0?

Wulatelong_gobiensis
11?02101?11?1?1???02121?111?1??1?1110001???00??11??????????????????1111??????????????
??101????1??11?????12??????1???100????2?????????1??????1100?1111111121???????000?1
1?????????0??????011????????????000????1????110?101????????????0??00????????0?

Yulong_mini
102110-
1110110110111121010111010?0100001110010?111110110???0???????0?????1111111210220
11001111111?1-
?122?100?1????001?10??2??0000101?11110?110?100??0??1?1?0??110001110?11001011?110
00?100110??????0?0000010???????1?????1110?01000??00???0???000?0?

Huanansaurus_ganzhouensis
1120211111111101101?11211111111111?110001110111?11100111?????1???11?11?????11111
11210220110011111?????122?11011????????????????001101?112????????????????????????
????11011000011?01000????1?1?0????0100000110?????01??0??1??011??101?01???00???????
00

Tongtianlong_limosus
10202111111111101?011212111111101111110001100001111?21110?????011?????1?????11110
11210210110011011??????122111001??01?01??0?02?1001?0???????01??????????1121??????1
000?111010001011??????11??111??????01000001???10?101010??1?100010001?0??00000??0?
?000

Corythoraptor_jacobsi
1121111111111001???21211111?1??01?11000??????????2?1??????????????????1?????11111?2
102???0001??????1???122111011?111??1???2?????001101?11100110111110111121111111?1
001111?1100101100101010001100000001000?0?00?1000????110??0110110??01010000?10
00000

Apatoraptor_pennatus
??0?1???12111110020
11100111111111-
1??21100111?????????2?1211001001120211???1110????????111101?????????00010100000?1
0??????01?11?111111111110???1??1101?01??011??101?01????1????????0

Guriliin_Tsav_oviraptorid
11?2111011111001010012111111110011000001110001110120011101011111111111???000121
11121022111100111111??1-
11221110111111001010201210100001120200100121000011121111101110010111101010101111
2-1111101100000000010000110001010010000010101000001000010010000000000